Dielectric resonators and filters for cellular base-stations

Vanessa Evelyne Guillemette Walker

Submitted in accordance with the requirements for the degree of Doctor of Philosophy.

The candidate confirms that the work submitted is her own and that appropriate credit has been given where reference has been made to the work of others.

The University of Leeds

Department of Electronic and Electrical Engineering

December 2003

Abstract

The investigation into three types of dielectric resonators for use in base-station filtering applications is presented.

The triple-mode cubic $TE_{01\delta}$ resonator is shown to have good performance for high Q applications. Its suitability for realising conventional narrowband selective bandpass filter responses is proved. The effect on the response of spurious inter-cavity couplings through irises is studied. The triple-mode cubic $TE_{01\delta}$ resonator is also used for the realisation of a novel type of filter, the even-odd hybrid mode reflection filter, which eliminates the need for cross-couplings for any symmetrical frequency response. The insensitivity of the new type of filter to most spurious couplings is shown in the case of a sixth degree elliptic filter. The drawbacks of this type of filter are also described.

The new dual-mode conductor-loaded dielectric resonator is presented. An exact model of the resonator is necessary for an accurate study of this resonator. The axial mode-matching technique is used. The relative numbers of modes to use in each section of the model for optimum convergence primarily depend on the mode type and the relative diameters of the dielectric cylinder and the metal disc. The convergence of the resonant frequencies is good. That of the quality factors is slower but still provide useful approximate results. These convergences are affected respectively by large electric and magnetic field amplitudes in singularity regions. The resonant frequency and Q_u of the fundamental mode are primarily dependent on the diameter and height of the dielectric cylinder respectively. The resonator geometry is optimised for Q_u and spurious separation at 900 MHz and trade-offs between the two criteria are quantified. The resonator is found to be particularly suited for medium Q applications, i.e. between 4000 and 7000.

The third resonator, the dielectric-loaded TE_{011} resonator, is shown to be well suited for applications around 2 GHz and requiring Q_u's of a few thousands. The

optimum cavity cross-section dimensions for maximum Q_u/volume are almost constant over a wide range of cavity diameters. The trade-off between Q_u and spurious separation is explained. Coupling bandwidth limitations in the case of off-line cavities are found to be solvable by using off-centred resonators. 80 MHz wide filters, optimised for ease of manufacturing, are built.

Contents

Acknowledgments

I would like to thank my supervisors, Prof. Ian Hunter and Dr. Vasil Postoyalko for their support and interest in this research project.

I am very grateful for the opportunity that was given to me by Filtronic Plc to carry out this work as well as for their sponsoring, and the use of their facilities.

Thank you to everybody in the Filtronic R&D lab, for their continuous encouragements, to Dr. David Iddles for his patient proof-reading of the section on ceramic materials and to Andy Panks and Ben Senior for their help with the text editing software. My parents should also be mentioned, for their discrete but ever so precious moral support.

Finally, I would like to thank Stewart, my husband, for all his help and moral support.

List of Figures

List of Tables

List of Principal Abbreviations

DR	Dielectric resonator
E mode	Electric dipole mode
EH	Hybrid mode in dielectric-loaded waveguide or dielectric resonator
FBAR filter	Thin-film bulk acoustic resonator filter
FD-TD	Finite-difference time-domain method
FEM	Finite element method
GFRP	Graphite fiber reinforced plastic
H mode	Magnetic dipole mode
HE	Hybrid mode in dielectric-loaded waveguide or dielectric resonator
LNA	Low noise amplifier
PA	Power amplifier
PEW	Perfect electric wall
PMW	Perfect magnetic wall
Q	Quality factor
RF	Radio frequency
Rx	Receive
SAW filter	Surface acoustic wave filter
TE	Transverse electric
TEM	Transverse electromagnetic
TM	Transverse magnetic
Tx	Transmit

List of Principal Symbols

Note: In the text of the thesis, some symbols will be followed by one or several subscripts, defining for example the region of the resonator or the mode to which the symbol applies. Most of these subscripts will be defined within the text itself.

B, B'	Susceptance value
c	Speed of light in vacuum
c	Half-length of cubic resonator
C	Capacitor value
C_{xypm}	Correlation between modes p and m of waveguides x and y respectively
d_1, d_2, d_3	Respectively diameter of metal disc, dielectric resonator and cavity for the dual-mode conductor loaded DR
b_1, b_2, b_3	Coordinates of interfaces in the TE_{011} mode dielectric loaded resonator mode-matching structure
D	Diameter of cylindrical dielectric resonator
$d\omega$	Angular bandwidth of filter
$\mathbf{E}$	Electric field
$\mathbf{E_t}$	Transverse part of the electric field
E_x	Electric field component in the x direction
$\hat{\mathbf{e}}$	Transverse part of the electric field
$\overline{\mathbf{e}}$	Transverse variations of the transverse part of the electric field
$\overline{e}_x$	Transverse variations of E_x
f	Frequency
f_0	Resonant frequency
F_r	Frequency ratio of closest spurious and mode of interest

G	Conductance value
G_c	$G_c = 0$ is the characteristic equation for hybrid modes in the dielectric loaded waveguide
g_i	Reactance of element i of low-pass prototype
h	Height of the TE_{011} mode dielectric loaded resonator
$\mathbf{H}$	Magnetic field
$\mathbf{H_t}$	Transverse part of the magnetic field
H_x	Magnetic field component in the x direction
$\hat{\mathbf{h}}$	Transverse part of the magnetic field
$\overline{\mathbf{h}}$	Transverse variations of the transverse part of the magnetic field
$\overline{h}_x$	Transverse variations of H_x
h_A	Height of dielectric resonator
h_B	Height of metal disc
h_C	Gap between metal disc and cavity top
$\mathrm{I_n}$	Modified Bessel function of order n
$J_{i-1,i}$	Admittance of inverter between nodes $i-1$ and i
$\mathrm{J_n}$	Bessel function of the first kind of order n
k	Wave number
$K_{i-1,i}, K'_{i-1,i}$	Admittance or impedance of inverter between nodes $i-1$ and i
$K(\omega^2)$	Expression defining the frequency response of the low-pass prototype
k_0	Wave number in free space
k_{yn}	Wave number of a mode in waveguide n in the y direction
$\mathrm{K_n}$	Modified Bessel function of order n
L	Inductor value
L_A	Insertion loss level
L_d	Dielectric resonator length
l_{pm}	z coordinate of interface between regions P and M
L_R	Return loss level
l_1, l_2, l_3	z coordinates of the regions in the three section mode-matching geometry
$\mathbf{M}$	Matrix defining the mode-matching system to solve
$\mathbf{M_c}$, $\mathbf{M'_c}$	Coupling matrix defining the even and odd mode network

N	Scaling factor for the nodal matrix of the network
Na, Nb, Nc	Number of modes used in regions A, B and C
P_c	Power dissipated in the conductive surfaces of the structure
P_{cs}	Power dissipated in the side of the conductive disc
P_d	Power dissipated in the dielectric regions of the structure
p_i	Intensity of oscillator i in ceramic material
P_{xp}	Inner-product of mode p in waveguide x
P_{xypm}	Cross-product of modes p and m in waveguide x and y
$Q_{x\ pm}$	Cross-product for power orthogonality of modes p and m in waveguide x
Q_c	Quality factor due to conductor losses
Q_d	Quality factor due to dielectric losses
Q_u	Unloaded Q factor
R	Resistor value
$\mathbf{R}_{i-1,i}$	Rotation matrix between $i-1^{\text{th}}$ and i^{th} rows and columns
r_1, r_2, r_3	Respectively radius of metal disc, dielectric resonator and cavity for the dual-mode conductor loaded DR
r_c	r_1/r_3
r_d	r_2/r_3
R_{lin}	Ratio of linear dimensions of waveguides A (or C) and B
R_s	Surface resistivity of a conductor
S	Interface surface area
S_c	Cross-section area of TE_{011} dielectric loaded cavity
S_f	Ratio of stopband to passband frequency
$\tan\delta$	Loss tangent of the ceramic material
TC_f	Temperature coefficient of resonant frequency of the material
T_e	Temperature coefficient of the relative permittivity of the material
$T_n(\omega)$	Chebyshev polynomial
V	Volume of cavity
V_d	Volume of dielectric resonator
W	Total stored energy of the structure
W_d	Cylindrical waveguide diameter
W_E	Electric energy

W_{Et}	Energy contained in $\mathbf{E_t}$
W_{Ez}	Energy contained in E_z
W_H	Magnetic energy
x_i^+, x_i^-	Forward and reverse coefficients of mode i in region x
X_n	Functions of Bessel functions defined in Appendices C and D X is for A, B, C, Q, P, W, X, S or Z
Y_n	Bessel function of the second kind of order n
$Y(p)$	Input admittance
Y_e, Y_o	Even and odd mode admittance of network
$Z(p)$	Input impedance
Z_e, Z_o	Even and odd mode impedance of network
α	$\omega_0/d\omega$
α_T	Linear thermal coefficient
γ	Propagation constant of a mode
Γ_e, Γ_o	Even and odd mode reflection coefficient of network
γ_i	Damping factor of oscillator i in ceramic material
δ	Skin depth of the conductor
δ	Amount of field variation between 0 and 1 radian in mode nomenclature
$\Delta f/f$	Normalised frequency variation
ε	Permittivity of the medium $\varepsilon = \varepsilon' - j\varepsilon''$
ε_0	Vacuum permittivity
$\varepsilon_{E(XY)}$	Electric field error between waveguides X and Y
$\varepsilon_{H(XY)}$	Magnetic field error between waveguides X and Y
ε_r	Relative permittivity of the medium
ε_∞	Permittivity of the ceramic material at optical frequencies
ζ	Wave number of a mode in the radial direction (ζ =jξ)
θ_i	Angle of rotation i
κ	Coefficient defining the proportion of TE and TM modes in hybrid mode
λ	Wavelength
λ_0	Wavelength in free space
μ_0	Vacuum permeability

ξ	Wave number of a mode in the radial direction
σ	Conductivity of the material
ϕ	Phase length
χ	Argument of J_n and J_n', eigenvalue of mode in cylindrical waveguide
ψ	Phase of transmitted signal
ω	Angular frequency
ω_0	Angular resonant frequency
ω_c	Cut-off angular frequency
ω_p	Passband angular frequency
ω_s	Stopband angular frequency
ω_{T_i}	Relaxation frequency of oscillator i in ceramic material

Chapter 1

Introduction

1.1 Applications for RF filtering in cellular base stations

RF filtering plays an important part in cellular base station systems. It is employed at different stages of the base station front end and often needs to meet very demanding specifications driven by the extremely rapid development of the mobile telecommunication market. Several examples of RF filtering in a base station are described below.

Example 1

A first example is the diplexer present in the front end of each sector of a base station as shown in Fig. 1.1. This diplexer provides the isolation between transmit and receive signals sharing the same antenna. The high power transmit signal, typically greater than 20 W, must be prevented from overloading the receiver. This requires the Rx filter to have high attenuation levels over the transmit frequency band. The

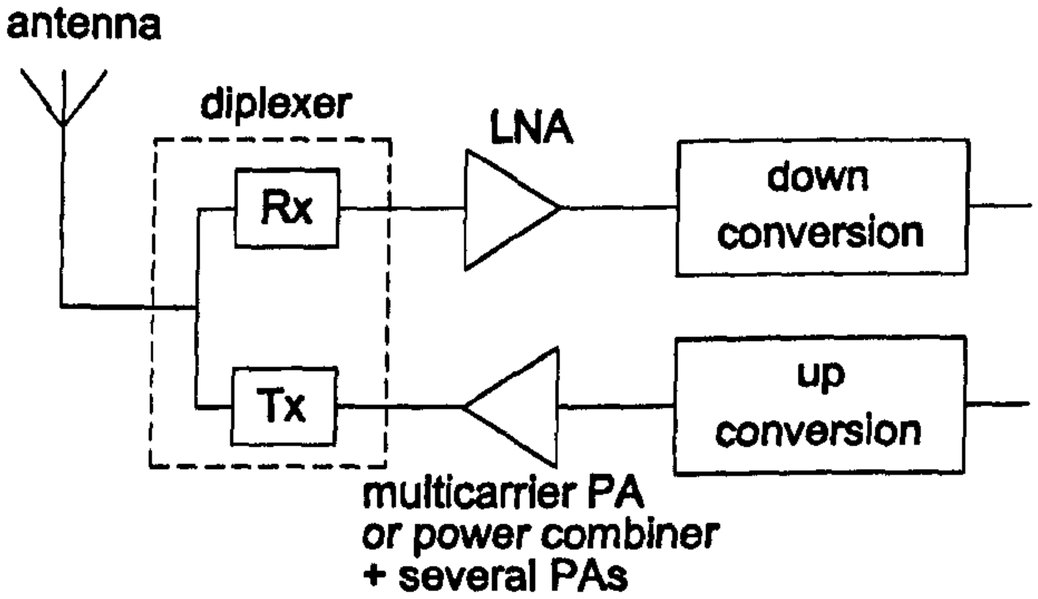

Figure 1.1: Block diagram of a base station front end

Tx filter also has stringent requirements on its stopband attenuation as it has to prevent out-of-band harmonics generated by the power amplifier being transmitted. In addition, it has to suppress the noise generated by the power amplifier in the receive band, which would otherwise affect the sensitivity of the receiver. The diplexer should also generate very low passive intermodulation [6], as intermodulation products of the signals in the transmit band could fall into the receive band and cause interference. Finally, both filters must have low insertion loss. Extra loss created by the filter in the transmit band would need to be compensated for by a bigger, more expensive power amplifier and decrease the efficiency of the base station. On the receive side, insertion loss decreases the sensitivity of the receiver. Typical insertion loss specifications differ, depending on the surface area covered by the base station. Although all base stations are required to be small to comply with planning restrictions, low power base stations covering small cells have extreme size limitations. Small cells are usually created in urban areas in order to increase the network's capacity and the base station will need to be easily deployed, for example, on the side of buildings. As a result, their insertion loss specification can be relaxed as the need for size reduction outweighs the need for efficiency and sensitivity. Table 1.1 and Fig. 1.2 show typical specifications and the spectral mask of the receive branch for a PCS front end diplexer.

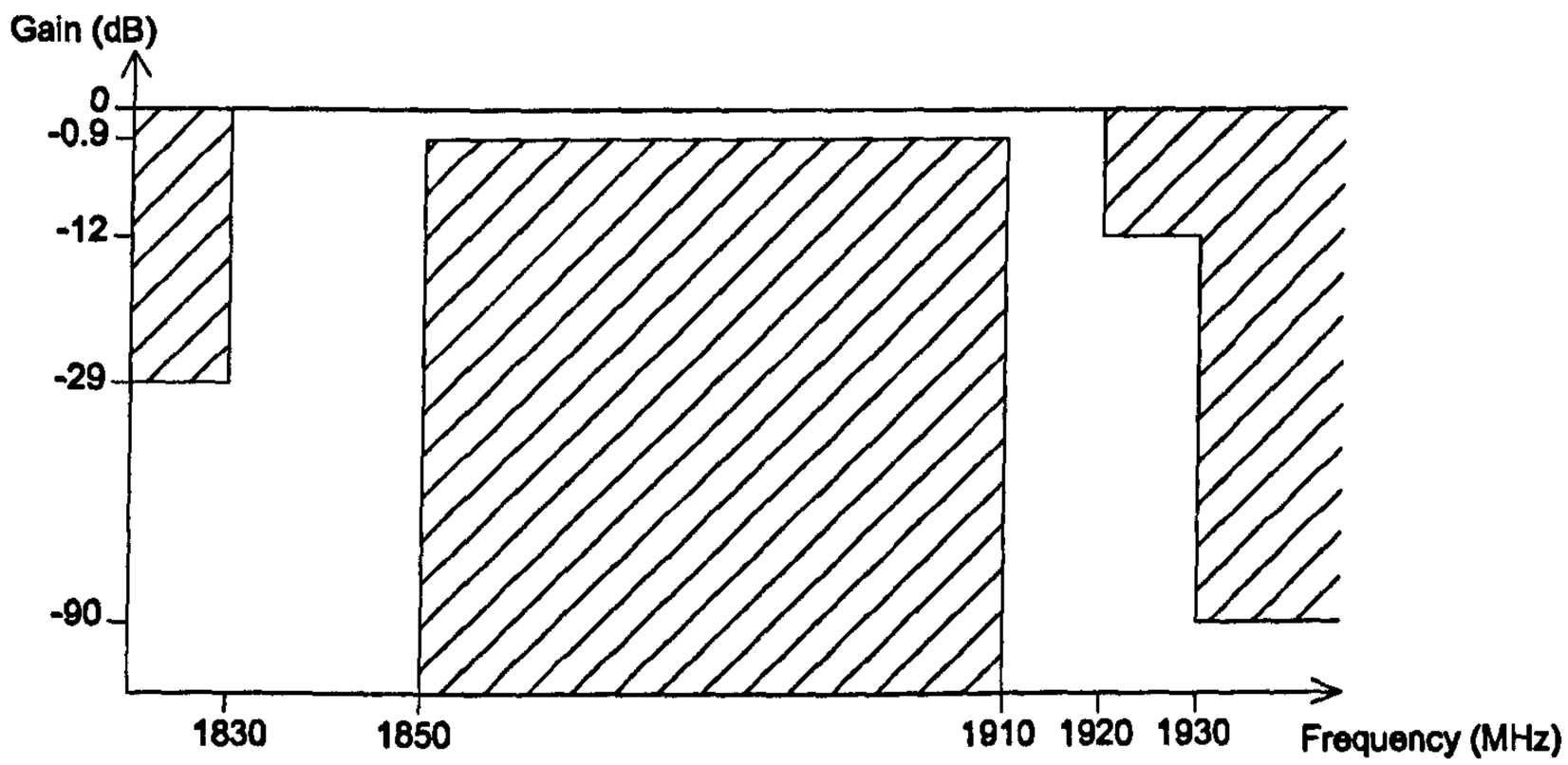

Figure 1.2: Spectral mask of receive branch of PCS diplexer

Table 1.1: *Typical specification for a PCS base-station diplexer*

	Receive (1850-1910 MHz)	Transmit (1930-1990 MHz)
Insertion loss (dB)	< 0.9	< 0.9 (1932-1988 MHz) < 1.0 (1930-1932 MHz) < 1.0 (1988-1990 MHz)
Insertion loss variation (dB)	< 0.4	< 0.3 (1932-1988 MHz) < 0.5 (1930-1932 MHz) < 0.5 (1988-1990 MHz)
Return loss (dB)	> 18	> 18
Rejection (dB)	−29 at 1830 MHz −12 at 1920 MHz −90 at 1930 MHz	−90 at 1910 MHz −16 at 1920 MHz −16 at 2000MHz
Group delay distortion (ns) in 5 MHz band	< 20	< 20
Intermodulation (dBm) (two +44.3 dBm tones in Tx)	−97	−36
Peak power handling (dBm)	+25	+63

Example 2

If a base station's range is limited by its receive power, the receive signal might have to be amplified close to the antenna at the top of the mast. This stops its signal to noise ratio from being degraded by the loss of the cable which runs down the mast, which is typically several decibels. Fig. 1.3 shows the block diagram of a tower top low noise amplifier. The Rx and Tx signals are split and recombined on each side of the amplifier by diplexers. The loss, rejection and intermodulation requirements of these diplexers are similar to those given in Table 1.1. The rejection specification should also be adequate to ensure that the amplifier is prevented from oscillating.

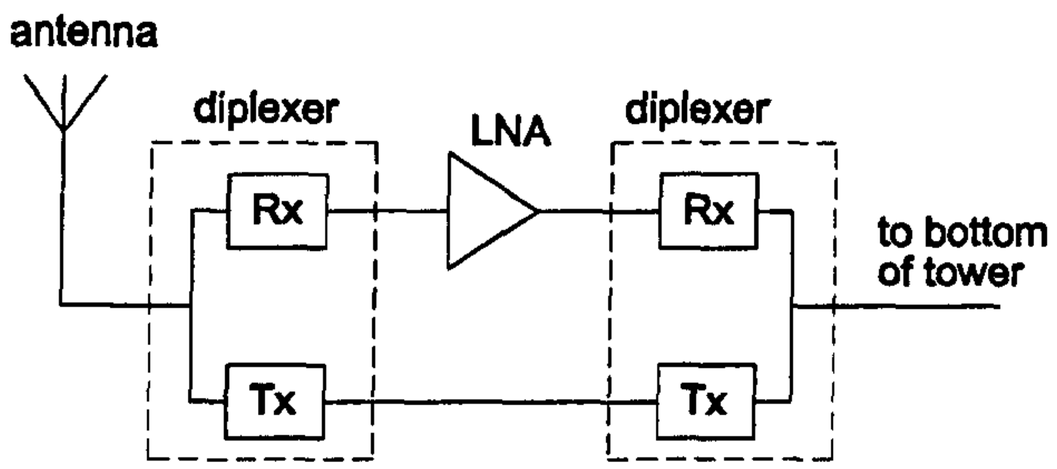

Figure 1.3: Block diagram of the tower top low noise amplifier

Example 3

RF filtering is also present in the feedforward amplifiers [7], which are used as multicarrier power amplifiers in base stations. The signals typically need amplifying by 50 dB while keeping the intermodulation levels 50 to 60 dB below the main signal average power. Feedforward amplifiers are also used for single carrier signals when the modulation used is not constant envelope, as for example with IS95 and WCDMA. The typical layout of a feedforward amplifier is shown in Fig. 1.4. Non linearities in the main amplifier generate distortion. This distortion is isolated from the main signal by adding a portion of the amplified signal out of phase with some of the undistorted input signal. The distortion is then amplified and re-injected out of phase into the output signal to leave only the wanted amplified signal. Delay filters are needed in each loop of the feedforward cancellation process to mimic the delays of the main and the error amplifiers. These delays, between 10 and 30 ns, are due to the physical length of the signal path and the narrowband matching circuits of the amplifiers. The main requirements for these filters are a flat amplitude and a

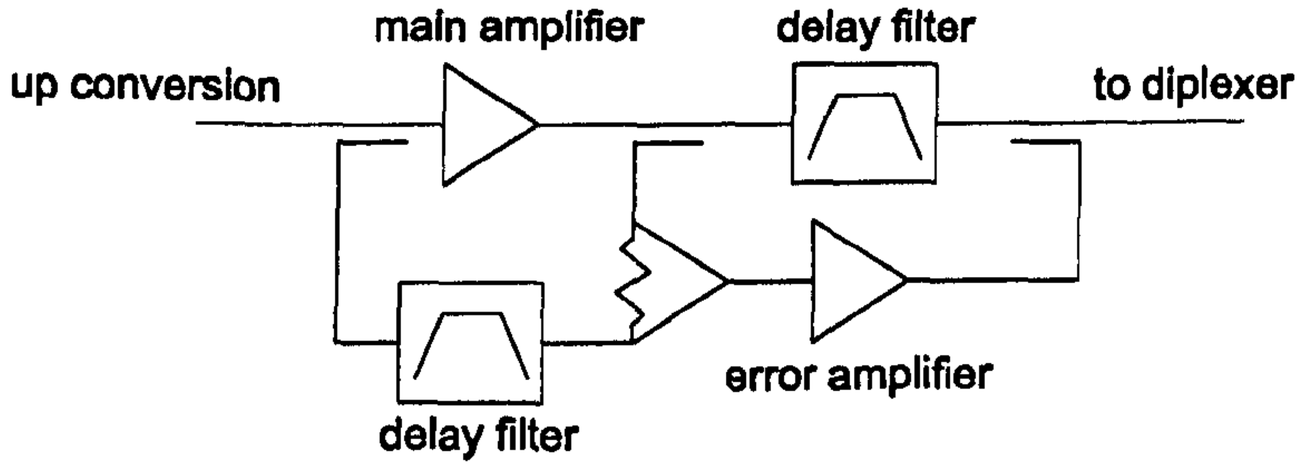

Figure 1.4: Block diagram of a feed forward amplifier

linear phase (i.e. flat group delay). Phase deviations of less than $\pm$ 1^o over the full system bandwidth (e.g. 60 MHz for PCS and UMTS systems) are usually needed. The insertion loss of the second loop filter, situated straight after the main amplifier is critical and is usually less than a few tenths of a dB.

Example 4

Multicarrier amplifiers such as feedforward amplifiers are not always able to meet the system specifications on distortion levels. As a result, power combiners, combining the outputs of single carrier power amplifiers are used, mainly for the GSM and PCN systems, where spurious levels of more than 70 dB below the main signal are required. Fig. 1.5 shows how several carriers are combined by means of narrowband filters centred on each carrier frequency. The manifold ensures that, at the common junction, all other branches present an open circuit to the signal coming from one of the power amplifiers. The filters need to be narrow band, each wide enough only for one carrier. They also must be low loss. Typical values are 1 dB insertion loss at the centre frequency for each carrier. However, these filters are usually realised using single resonators as each of them often has to be automatically tuned to the changing centre frequency of its input signal. These requirements are conflicting as will be discussed in the next section and very demanding in terms of resonator performance. Two section filters are sometimes used for manually tuned CDMA combiners, as the need to reconfigure the frequency plan of the network is not as great. Table 1.2 summarises the requirements for a GSM power combiner.

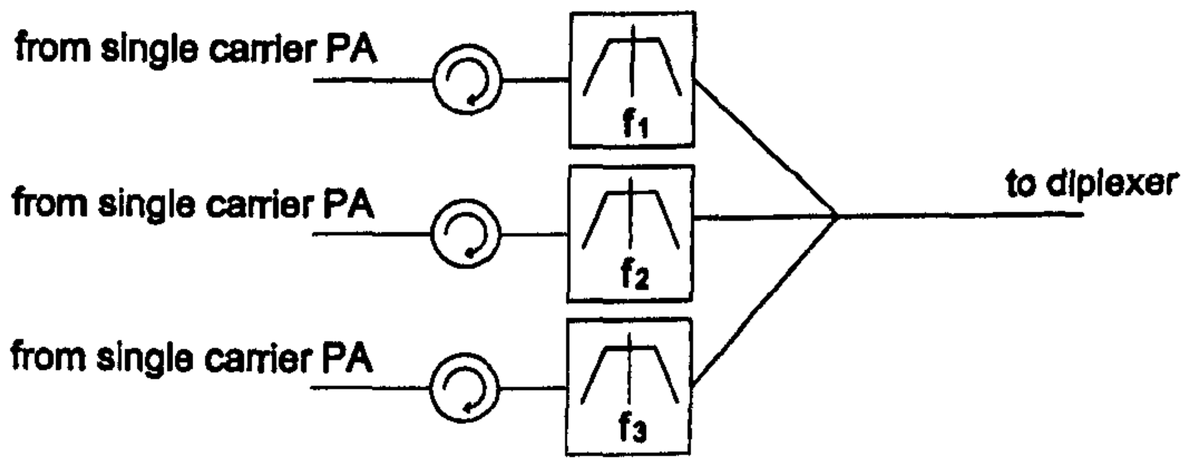

Figure 1.5: Block diagram of a power combiner

Table 1.2: *Specifications for a GSM power combiner filter*

Signal bandwidth	270 kHz
Carrier spacing	1 MHz
Insertion loss	1 dB
Rejection at +/− 1 MHz	7 dB

Example 5

A final application for filtering within the base station is best described by Fig. 1.6., representing the frequency allocations of two operators of the American AMPS system. It is possible that mobiles of operator A could be transmitting at maximum power while physically located close to a base station of operator B. This operator then needs to be able to get the signals from these mobiles attenuated before they reach its receiver as they could cause intermodulation products in its receive band. This is achieved by a very selective notch filter which rejects the 1.5 MHz of operator A inserted within its band. Table 1.3 summarises the specifications for the notch filter.

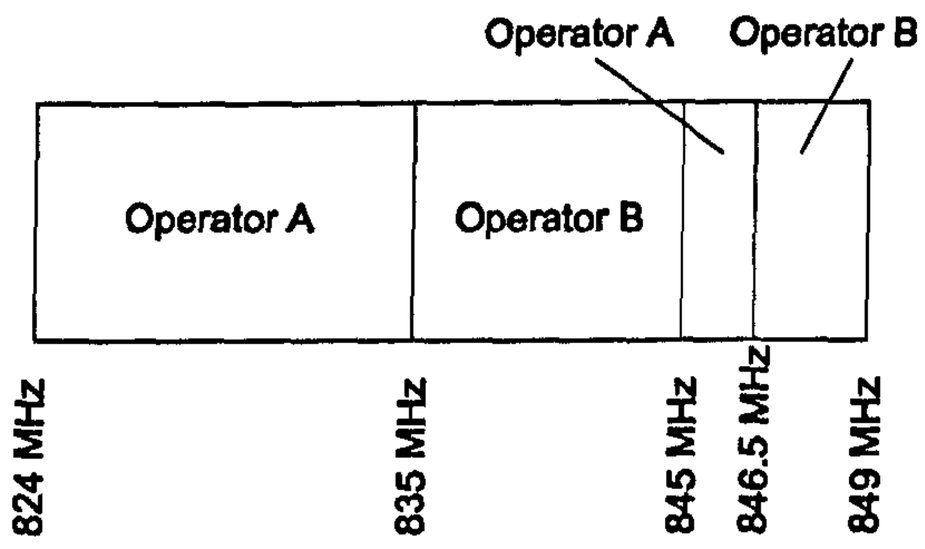

Figure 1.6: Frequency allocations for two operators in the AMPS band

1.2 Overview of filter design

The first step of filter design consists of synthesising a low-pass prototype network. This is a lumped or distributed reciprocal lossless and passive two-port network operating from a 1 Ω generator into a R Ω load as shown in Fig. 1.7.

Table 1.3: *Specifications for the operator B notch filter*

Frequency (MHz)	Insertion loss relative to passband (dB)
845	−1.5
845.2	−20.0
846.3	−20.0
846.5	−1.5

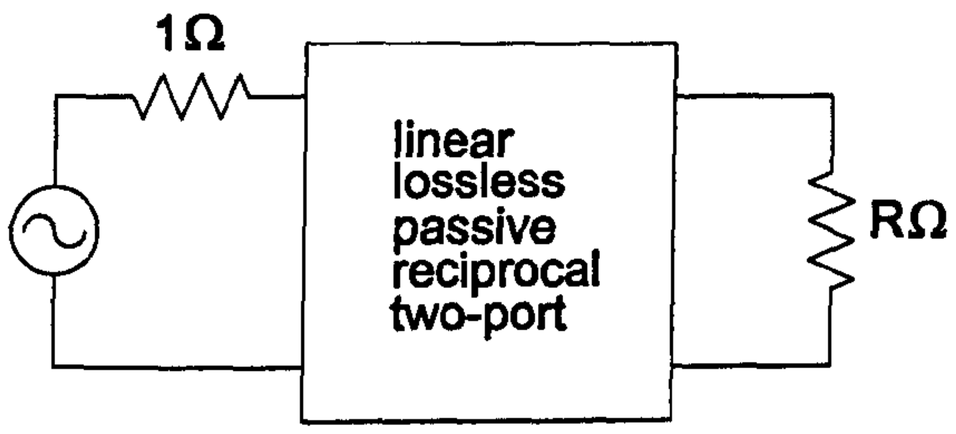

Figure 1.7: Low-pass prototype

Let us consider a network with a transmission coefficient $S_{12}(p)$, which is a bounded real function. If the network is passive and lossless, its reflection coefficient, $S_{11}(p)$, also a bounded real function, can be deduced from the unitary condition:

$$|S_{11}(j\omega)|^2 + |S_{12}(j\omega)|^2 = 1 \tag{1.1}$$

$Z(p)$, the input impedance of the network then follows from the bilinear transformation

$$Z(p) = \frac{1 \pm S_{11}(p)}{1 \mp S_{11}(p)} \tag{1.2}$$

and is a positive real function. As demonstrated by Darlington, this means that the two-port network considered here can be synthesised as a lossless passive reciprocal network terminated by a non-negative resistor [8]. The synthesis of a low-pass prototype thus follows from the definition of the bounded real $S_{12}(p)$.

The transmission characteristic of an ideal low-pass filter is shown in Fig. 1.8. The amplitude of the transmission coefficient is unity below the cut-off angular frequency ω_c and 0 above. However, the transmission coefficient of a lumped or distributed network is a finite rational function and cannot present any discontinuity at ω_c [9]. As a result, several low-lass prototypes have been created that approximate

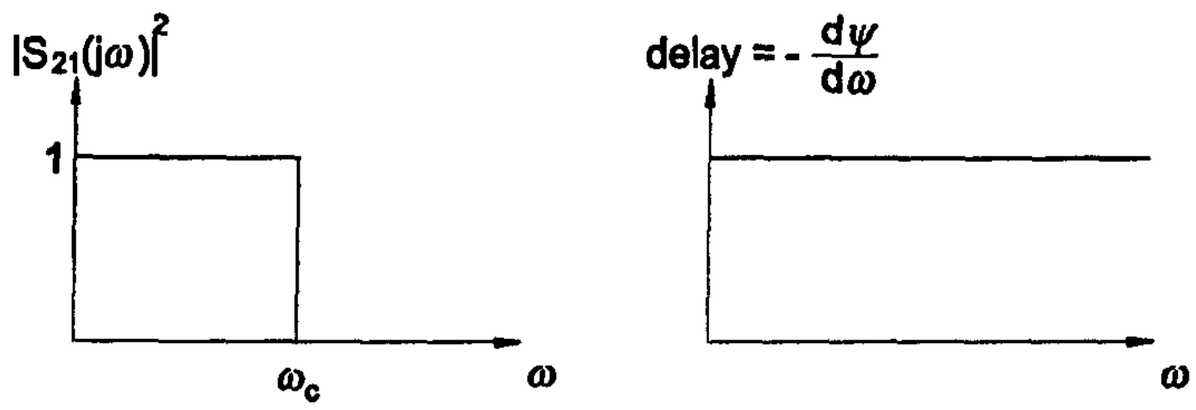

Figure 1.8: Ideal low-pass prototype response

the amplitude response of the ideal low-pass filter. Fig. 1.9 shows the typical template for the amplitude and the group delay of the low-pass prototype transmission coefficient.

It can be shown [5] that $|S_{12}(j\omega)|^2$ can be written as $1/(1+K(\omega^2))$ where $K(\omega^2) = h(\omega^2)/f(\omega^2)$. The zeros of $h(\omega^2)$ are then the attenuation zeros of the network whereas the zeros of $f(\omega^2)$ are its transmission zeros. A summary of the expressions for $K(\omega^2)$ of several prototypes are given in Table 1.4, as well as formulas for calculation of the minimum network degree to achieve a specified selectivity.

The maximally flat approximation is so called because its transmission characteristic is maximally flat at 0 and infinity. The expression for $|S_{12}(j\omega)|^2$ is obtained by equating its first $2n-1$ derivatives (for a n^{th} degree filter) to 0 at $\omega = 0$ and infinity. This implies that all the attenuation zeros of the filter are at $\omega = 0$ and all its transmission zeros are at infinity. This all-pole approximation is a very simple but also limited approximation of the ideal low-pass amplitude characteristic as its rolls-off very slowly. The filter selectivity can be improved by allowing $|S_{12}(j\omega)|^2$ to oscillate in the passband. It can be shown [4] that the greatest selectivity is given by an equiripple oscillation. Solving the differential equation setting n turning points to the minimum and maximum oscillation values in the passband gives the expression for the Chebyshev polynomial, $T_n(\omega)$. The equiripple or Chebyshev approximation thus has its attenuation zeros spread over the passband but all its transmission zeros are still at infinity. The inverse Chebyshev approximation does exactly the opposite. Its transmission zeros are distributed over the stopband. The expression for $|S_{12}(j\omega)|^2$ of the inverse Chebyshev is deduced from that of $|S_{11}(j\omega)|^2$ for the Chebyshev as the two are symmetrical around $\omega = 1$. Chebyshev and inverse

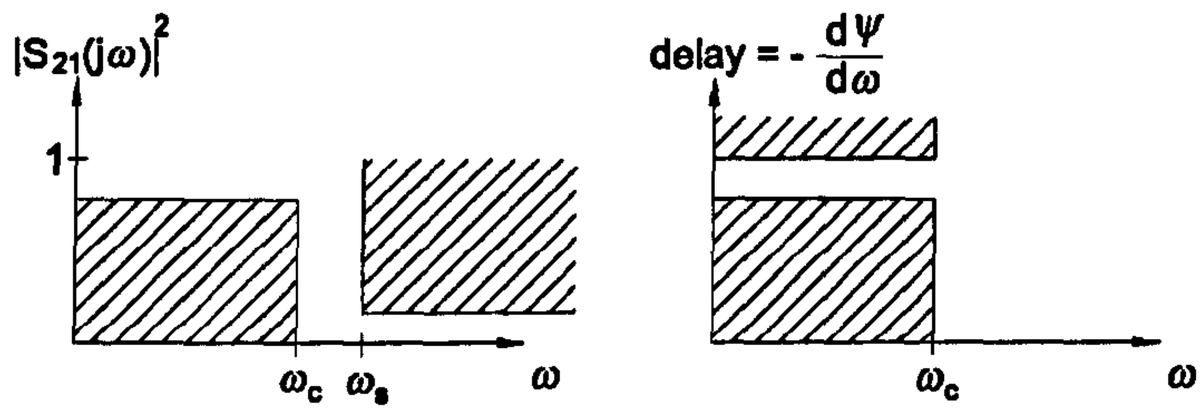

Figure 1.9: Low-pass prototype template

Table 1.4: *Expressions for $K(\omega^2)$ and formulas for degree calculation for common amplitude approximation low-pass prototypes, L_A minimum insertion loss at $\omega \geq \omega_s$, L_R minimum return loss at $\omega \leq \omega_p$, $S_f = \omega_s/\omega_p$ [4, 5]*

Prototype	$K(\omega^2)$	Minimum degree network $N \geq$
Maximally flat	$(\omega^2)^n$	$\frac{L_A+L_R}{20\log_{10}(S_f)}$
Chebyshev	$\varepsilon^2 T_n^2(\omega)$ $\varepsilon = (10^{L_R/10}-1)^{-1/2}$ $T_n(\omega) = \cos(n\cos{-1}(\omega))\ \ \omega \leq 1$ $T_n(\omega) = \cosh(n\cosh{-1}(\omega))\ \ \omega \geq 1$ $T_{n+1}(\omega) + T_{n-1}(\omega) = 2\omega T_n(\omega)$	$\frac{L_A+L_R+6}{20\log_{10}(S_f+(S_f^2-1)^{1/2})}$
Inverse Chebyshev	$\frac{1}{\varepsilon^2 T_n^2(1/\omega)}$ $\varepsilon = (10^{L_A/10}-1)^{-1/2}$ T_n as above	$\frac{L_A+L_R+6}{20\log_{10}(S_f+(S_f^2-1)^{1/2})}$
Elliptic	$F_n^2(\omega)$ $F_n(\omega) = \frac{(\omega^2-\omega_1{}^2)(\omega^2-\omega_2{}^2)\ldots}{(\omega^2-\omega_A^2)(\omega^2-\omega_B^2)\ldots}$ where $\omega_1, \omega_2\ldots, \omega_A, \omega_B\ldots$ are fixed by L_R and L_A	$\frac{K(m)}{K'(m)}\frac{L_A+L_R+12}{13.65}$ with $K(m)$ and $K'(m)$ in [4]
Generalised Chebyshev	$\varepsilon^2 T_n^2(\omega)$ $\varepsilon = (10^{L_R/10}-1)^{-1/2}$ $T_n(p) = \cos\sum_{r=1}^{n}\cos^{-1}(j\frac{1+pp_r}{p-p_r})$ p_r transmission zeros	Must be computed

Chebyshev approximations of the same degree have the same selectivity. A more selective response still is achieved by the elliptic approximation, where both passband and stopband are made equiripple. Here again, a differential equation gives the expression for $F_n(\omega)$, the ratio of polynomials which defines the transmission characteristic of the filter. As with the Chebyshev and inverse Chebyshev approximations, the frequencies of the turning points of $F_n(\omega)$ are fixed. However, it might be desirable to control the location of the attenuation poles of a filter. One reason is that the rejection specification of filters usually varies over the stopband. Diplexers in particular have very asymmetric attenuation specifications, with a lot more rejection required from each filter over the passband of the other filter. If it is the case, it is possible to meet the same rejection requirements with a smaller degree filter, by locating attenuation zeros in the frequency bands where the maximum rejection is needed, instead of achieving the maximum required rejection over the whole stopband. An arbitrary number of transmission zeros can be added to the Chebyshev response at chosen finite frequencies by modifying the Chebyshev polynomial $T_n(\omega)$ so that it still oscillates over the passband but also tends to infinity at the transmission zeros frequencies. The filter is then called a generalised Chebyshev filter. As well as real frequency axis poles, imaginary and complex poles can be added, for example for group delay equalization.

To prevent phase distortion of the signal, the group delay of the network needs to be constant, as represented in the ideal lowpass filter response in Fig. 1.8. Linear phase approximations [9] such as the maximally flat or the equidistant linear phase prototypes are optimised for group delay flatness. The former has maximally flat group delay at $\omega = 0$. Its transmission coefficient is derived by truncating the function $S_{12}(p) = K/(\cosh(Ap) + \sinh(Ap))$, which has constant group delay A at all frequencies, but is not realisable because its polynomial form would be of infinite degree. The latter gives a response much flatter than the maximally flat response. Its expression for $|S_{12}(j\omega)|^2$ is obtained by equating the phase of the degree n filter network to a linear function of ω at n equidistant points starting from the origin $\omega = 0$. Both previous approximations achieve some degree of phase linearisation, but at the expense of amplitude selectivity. Similarly, a selective filter network will exhibit sharp group delay variations, especially close to its bandedges. When both selectivity and phase linearity are important criteria, combined amplitude and

phase approximations can be used [9]. One option is to cascade an allpass network with the initial network. The amplitude response stays unchanged and the allpass network is defined so that the overall network has the required phase linearity. However, this approach is not very efficient as the number of constraints applied to the phase by the allpass network is small when compared with its degree. The opposite approach, where the phase response of the initial network is retained and the amplitude response improved, is also possible. However, it leads to bandwidths of flat amplitude always significantly smaller than the bandwidths of linear phase. The best option is to realise a simultaneous approximation of amplitude and phase, with a maximum number of constraints shared between both of them.

All the approximations previously described lead to a bounded real $S_{12}(p)$ from which the positive real function $Z(p)$ is deduced and the filter network synthesised. To synthesise $Z(p)$ as a lossless two port network terminated in a non-negative resistance, one can always successfully use cascade synthesis [8]. It can be shown that the zeros of transmission of the network are the zeros of the even part of $Z(p)$ and the poles common to $Z(p)$ and $Z(-p)$. The latter correspond to transmission zeros on the real frequency axis and can be extracted under the Foster form. For the remaining zeros, subnetworks can be successively extracted for each set of zeros, in any order. The networks that are extracted are Brune sections, C sections and D sections for imaginary axis (real frequency axis), real axis and complex transmission zeros, respectively [8].

More particularly, all-pole networks, i.e. networks with all transmission zeros at infinity, can be synthesised as ladder networks. This is the case of maximally flat and Chebyshev amplitude approximations as well as maximally flat and equidistant linear phase approximations. Fig. 1.10(a) and Fig. 1.10(b) show a typical low-pass ladder filter network and how it can be transformed into a network consisting only of capacitors (or inductors) by introducing impedance inverters.

The synthesis of generalised Chebyshev prototypes, which includes the elliptic prototype as a special case, can take different forms depending on the symmetry or asymmetry of the transmission zeros [4, 10]. In a general manner, the network can be presented in a cross-coupled form, shown in Fig. 1.11, where only one kind of element, L or C, is needed.

Once the low-pass prototype network has been synthesised, several transforma-

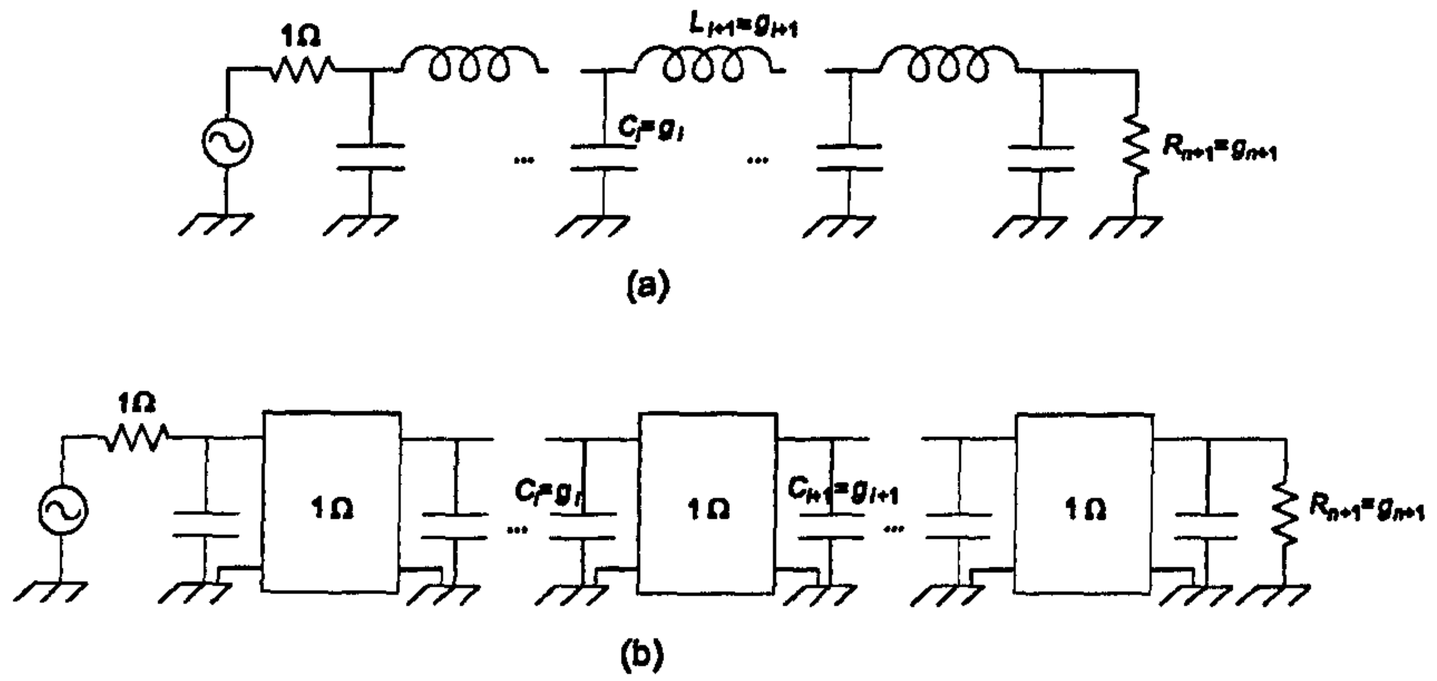

Figure 1.10: Ladder and equivalent inverter coupled low pass prototype networks

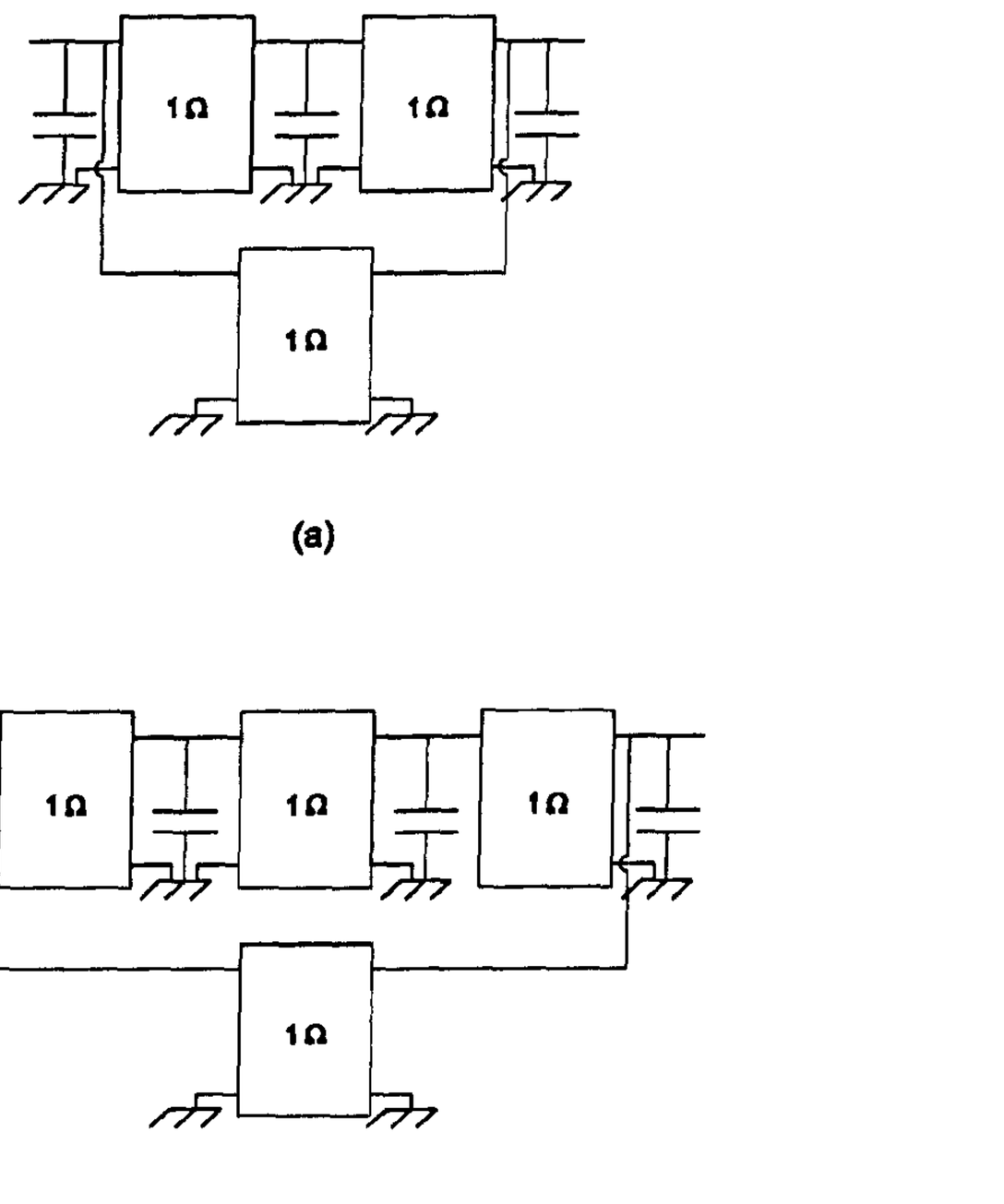

Figure 1.11: Asymmetrically and symmetrically located transmission zeros low-pass prototypes

tions are applied to customise it to the exact filter specifications. The prototype, which was designed in a 1 Ω system, can be transformed into another impedance system Z_0, usually 50 Ω, by multiplying all impedances and dividing all admittances by Z_0. Frequency transformations can be used to turn the low-pass prototypes into high-pass, band-pass or band-stop filters. For a low-pass to band-pass transformation, for example, the transformation is $\omega \rightarrow \alpha(\omega/\omega_o - \omega_o/\omega)$ where $\alpha = \omega_o/d\omega$, with ω_o the centre frequency and $d\omega$ the bandwidth of the filter. Inductors and capacitors are transformed into series and shunt resonant circuits respectively. Fig. 1.12 shows the result of the bandpass transformation on the inverter coupled filter of Fig. 1.10(b). Fig. 1.12 also includes the effect of the dissipation loss of the resonators. This dissipation is expressed in terms of the quality factor (Q) of the resonator, which is defined as

$$Q = \omega \frac{\text{total energy stored}}{\text{average power loss}} \tag{1.3}$$

Series resistances and shunt conductances of value $R = \omega L/Q$ and $G = \omega C/Q$ are added to series and shunt resonators respectively. Fig. 1.13 illustrates the effect of a finite resonator Q on the insertion loss of the filter. It can be seen that the loss increases rapidly at the vicinity of the bandedges, which corresponds with the regions where the signal experiences the most time delay. If all the resonators have same Q, the loss at centre frequency is given by the formula [11]

$$\text{Insertion Loss} = 4.343 \frac{\alpha}{Q} \sum_{i=1}^{n} g_i \tag{1.4}$$

where g_i is the i^{th} reactance element of the low-pass prototype. This shows that the insertion loss of a filter is inversely proportional to its bandwidth and to the Q of its resonators. It is also increasing with the filter degree. As a result, the Q needed

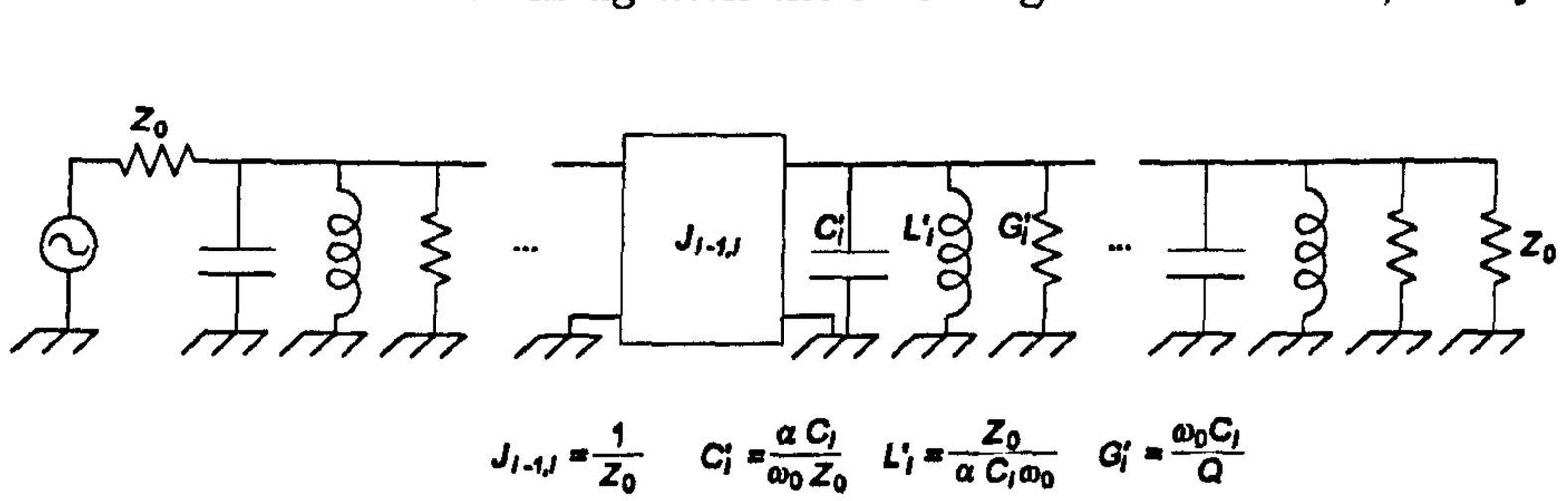

Figure 1.12: Finite Q bandpass filter prototype

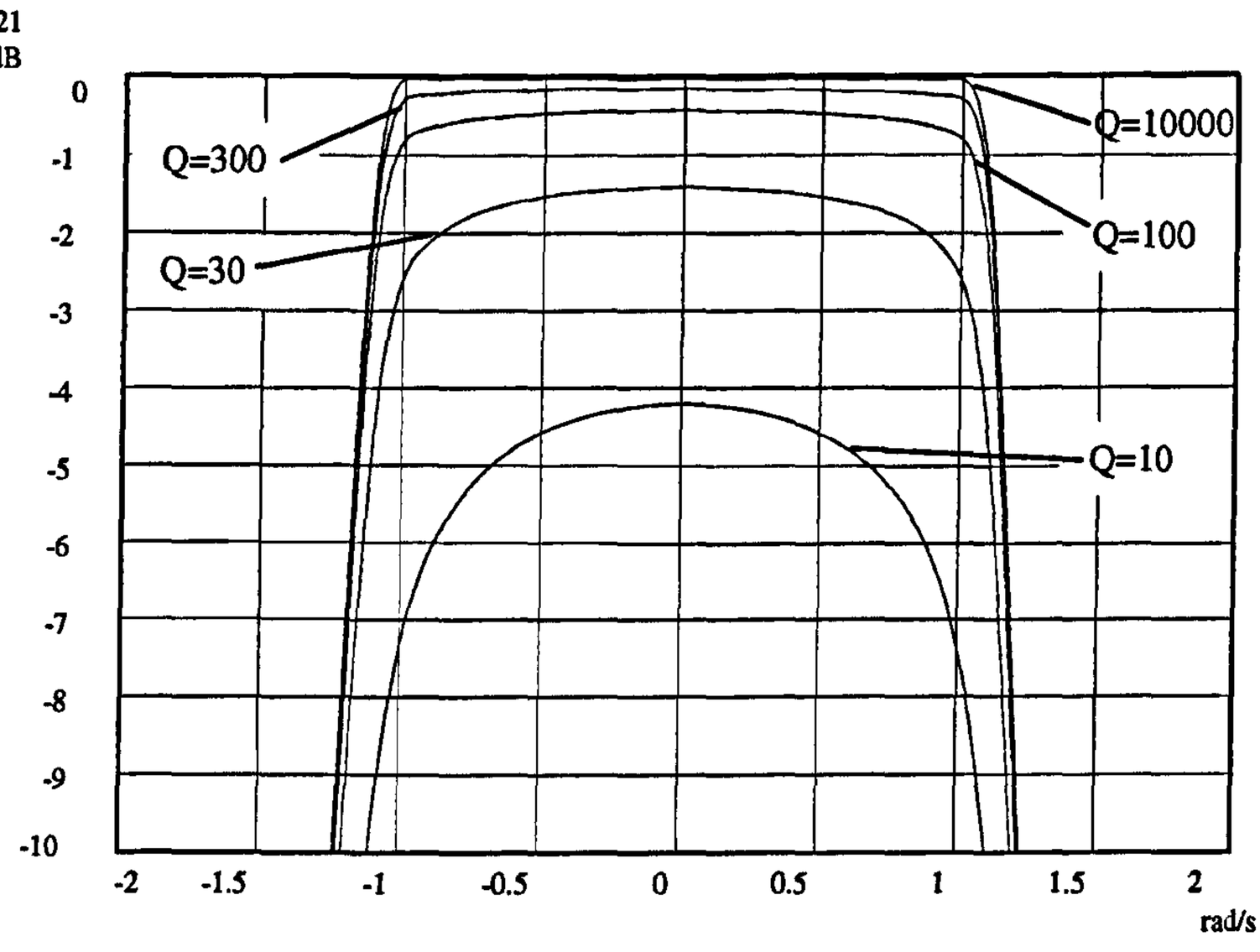

Figure 1.13: Effect of the finite Q of the resonators on the insertion loss of a filter

by the resonators will depend on the individual specifications of each application. For microwave resonators, this quality factor, as defined by Eq. 1.3, is called the unloaded quality factor, or Q_u. Referring back to the applications described in Section 1.1, diplexer filters for the PCS system will require Q_u's between 3,000 and 6,000, mainly depending on the insertion loss specification. The delay filters in feedforward amplifiers also have requirements on absolute delay and phase linearity of the transmitted signal. The former is related to Q_u and insertion loss by the formula [12]:

$$\text{Group Delay (s)} = \frac{Q_u \text{ Insertion Loss (dB)}}{27.3\ f\ \text{(Hz)}} \tag{1.5}$$

To get linear phase over a wide enough bandwidth, the filter usually need to be made significantly wider than the full system bandwidth. A typical Q_u value for a 10 ns UMTS delay filter with 0.15 dB insertion loss is 7,000. In the case of power combiners, combined low insertion loss (1 dB at centre frequency) and very narrow bandwidth (smaller than 1 MHz) require Q_u between 25,000 and 50,000. Finally, similar Q_u values will be needed in the case of the notch filter described in the previous section, as the passband loss and bandwidth specifications are equally

demanding.

Resonant circuits can also be represented by open and short circuited lengths of transmission lines. This representation allows the physical length of distributed network resonators, which can be of the same order of magnitude as the wavelength at high frequencies, to be taken into account. This is the representation originally used for the modelling of filters where the dominant mode of propagation is TEM or quasi-TEM, e.g. for combline or interdigital filters. In these cases, the filter model usually originates from the theory of coupled lines [13]. Even for non-TEM filters, e.g. DR filters, it is practical to simplify the filter model into the form shown in Fig. 1.14. This is because, in the case of microwave bandpass filters, the physical network consists of cavity resonators interacting together through coupling of their electromagnetic fields. The shunt stub-inverter bandpass prototype network is thus easy to identify with the physical realisation. It can be shown that the filters represented in Fig. 1.12 and Fig. 1.14 are equivalent around ω_o, the resonant frequency, for the elements values given in Fig. 1.14.

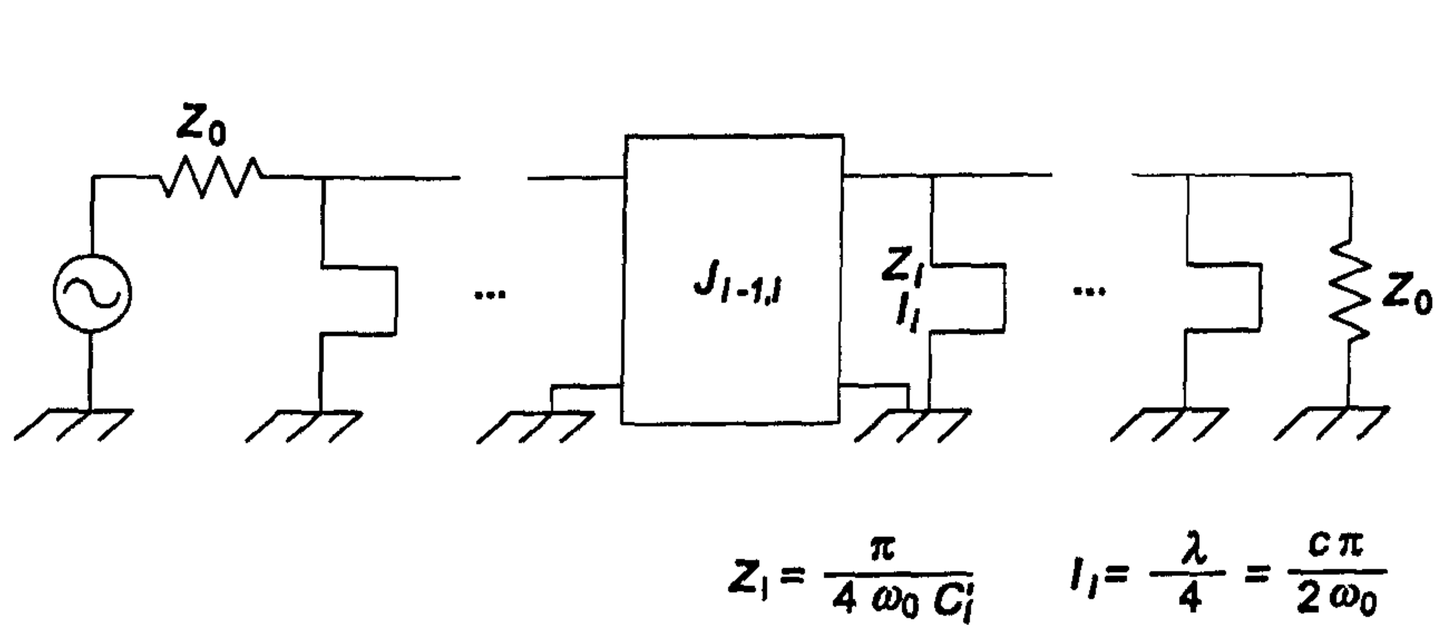

Figure 1.14: Shunt stub-inverter coupled bandpass equivalent circuit

Finally, if all the resonators of a filter are physically identical, it can be desirable to equate the impedance of all the resonators of the network to the same value. The impedance at any point of the network can be scaled by a factor N by multiplying corresponding row and column of the nodal admittance matrix by $1/\sqrt{N}$ [4]. Obviously, if the resonators are physically different, each point in the filter network can be scaled to a different impedance.

1.3 Properties of ceramic resonator materials

Early defense and satellite communications filtering applications first used a variety of different metal resonator structures, such as waveguide, combline and interdigital structures. But with the very demanding volume and weight restrictions these applications required, the miniaturisation offered by DR's was extremely interesting. As a result, ceramic materials were first introduced in the above filtering applications, and later spread to others such as the large mobile communications market. Ceramic resonator materials are non-metallic, inorganic compounds with high permittivity [14]. Such a material has the property of reducing the velocity and wavelength of electromagnetic waves by the square root of the permittivity. As a result, it allows significant size reductions of microwave resonators. The permittivity is a function of the molecular polarizability, which is due to displacements of particles when an electric field is applied to the crystal. At microwave frequencies, the polarization in low-loss ceramics is mainly due to the displacement of ions in the material [15]. The complex relative permittivity, also called complex dielectric constant, can be approximated for simple crystal structures by considering the ions as harmonic oscillators excited by the applied field. It is given by

$$\frac{\varepsilon(\omega)}{\varepsilon_0} = \varepsilon_\infty + \sum_i \frac{{\omega_{Ti}}^2 \; 4\pi p_i}{{\omega_{Ti}}^2 - \omega^2 - j\gamma_i\omega} \tag{1.6}$$

where ε_∞ is the permittivity of the material at optical frequency and p_i, γ_i and ω_{Ti} are the intensity, the damping factor and the relaxation frequency of the oscillator, respectively [16, 17]. The damping factors represent losses due to the ions' vibrations in the crystal. The relaxation frequencies, which are the resonant frequencies of the optical mode lattice vibrations, are very large compared to microwave frequencies. As a result, one can simplify the expressions for the real (ε') and imaginary (ε'') parts of the permittivity and write

$$\frac{\varepsilon'}{\varepsilon_0} = \varepsilon_r = \varepsilon_\infty + \sum_i 4\pi p_i \tag{1.7}$$

$$\tan\,\delta = \frac{\varepsilon''}{\varepsilon'} = \frac{\sum_i 4\pi p_i ({\gamma_i}/{{\omega_{Ti}}^2})\omega}{\varepsilon_\infty + \sum_i 4\pi p_i} \tag{1.8}$$

where $\tan\,\delta$ is the loss tangent of the material. Often, it is the quality factor, $Q = 1/\tan\,\delta$, which is used to characterise the material performance. At RF frequencies, the oscillator model predicts that the product of Q and frequency, $Q.f$,

is a constant [17, 18]. However, experimental data between 1 GHz and 10 GHz of commercially available ceramics generally show a significant increase with frequency.

The temperature coefficient of resonant frequency of the material (TC_f) is the parameter that prevented the widespread development of dielectric resonators until the 1970's. Before then, all known low loss ceramics had very poor temperature stability. TC_f is defined as $-(\frac{1}{2}T_\epsilon+\alpha_T)$ [19] where α_T is its linear thermal expansion coefficient and T_ϵ the temperature coefficient of the relative permittivity. For most microwave ceramic materials, α_T is approximately +10ppm/°C. Temperature stable dielectric resonators are then obtained by controlling T_ϵ. The latter is linked to small changes in the crystal structure, called tilt transitions, happening between major state changes. TC_f is usually controllable between +10ppm/°C and −10ppm/°C. All three parameters mentioned above (ε_r, Q and TC_f) require very good control of each step of the manufacturing process: purity and particle size of the raw materials, mixing, sintering, firing, cooling rates. Table 1.5 gives a list of the most common ceramic resonator materials.

Table 1.5: *Characteristics of the most commonly used ceramic materials*

Material	ε_r	$Q.f$ (GHz)	Reference
$MgTiO_3$ - $CaTiO_3$	21	55 000	[17]
$Ba(Mg, Ta)O_3$	24	300 000	[1]
$Ba(Sn, Mg, Ta)O_3$	25-24	200 000-240 000	[17, 20, 21]
$Ba(Zn, Ta)O_3$	30	168 000	[17]
$Ba(Zr, Zn, Ta)O_3$	30	100 000	[17]
$(Zr, Sn)TiO_4$	38	50 000-32 000	[17, 22, 23]
$Ba_2Ti_9O_{20}$	40	32 000	[17, 24]
$CaTiO_3 - NdAlO_3$(CTNA)	45	43 000	[25]
$ZrTiO_4 - ZnNb_2O_6$(ZTZN)	45	55 000	
$BaO - PbO - Nd_2O_3 - TiO_2$	90	5 000	[17]

1.4 Dielectric resonators and filters

1.4.1 Cylindrical dielectric rod waveguides and dielectric loaded waveguides

The understanding of the modes existing in these two waveguides is essential for the study of dielectric resonators. In both waveguides, the modes are only transverse electric (TE) or transverse magnetic (TM) modes in the absence of angular variation. Otherwise, they become hybrid modes, and have been noted HEM modes or also HE and EH modes. These notations are usually followed by two subscripts, giving for example HE_{nm}. n describes the number of angular variations. m is the number of the solution to the waveguide eigenvalue equation for a given n [19]. The distinction between HE and EH modes is made by evaluating the ratio of axial magnetic field to axial electric field [26, 27]. The HE and EH modes are associated with TE and TM modes of the homogeneous metallic waveguide respectively. For a given n, the successive solutions for m are in turn HE and EH modes [19]. If the electric and magnetic fields are interchanged, the HE and EH modes distributions are then similar to those of the TE and TM modes of the homogeneous waveguide surrounded by a perfect electric wall (PEW) [20]. Otherwise, they are similar to the field distributions of the TM and TE modes respectively in the case of the waveguide consisting of the rod surrounded by a perfect magnetic wall (PMW).

The variations of the fields inside the dielectric rod are expressed in terms of J_n and J'_n, the Bessel function of the first kind and its derivative. Outside the rod, the decay of the fields in the radial direction is ensured by using K_n and K'_n, modified Bessel function the second kind and its derivative. Each mode is defined by its eigenvalue, commonly the argument χ of J_n and J'_n. By opposition to homogeneous waveguides, these eigenvalues depend on the frequency and the radius of the waveguide. As a result, the variations of χ, or of the propagation constant of the mode, are usually plotted against the radius of the rod normalised with frequency [19].

For the fields of the mode to be decaying outside the dielectric, the arguments of K_n and K'_n have to be real. This condition defines the cutoff frequency of the mode, although not in the usual sense as the propagation constant of the waveguide never becomes real [26]. It also means that, for a given n, there are only a finite

number of solutions to the characteristic equation. HE_{11}, the dominant mode, has a zero cutoff frequency. However, the smaller the value of the normalised rod radius, the more the fields extend outside the rod. The mode is then loosely bound. As the normalised radius becomes infinitely small, all the propagating energy is outside the rod [26, 28].

All other modes do have a cutoff frequency, at which the ratio of transmitted power inside and outside the rod is finite. Plots of the phase coefficient variations show that cutoff happens for the same normalised radius for each pair of TE_{0m} and TM_{0m} modes as well as for each EH_{1m} and $HE_{1(m+1)}$ pair [20, 26].

As for the dielectric rod waveguide, the modes in the cylindrical dielectric loaded waveguide split between TE, TM and hybrid modes. Hybrid modes tending towards a TE mode as the waveguide becomes homogeneously filled are called HE modes. Those tending towards a TM mode are called EH modes. It has to be noted that for some normalised dimensions and permittivities of the inhomogeneous waveguide, the appearance of the modes can change. In particular, the HE_{11} mode can actually be a TM mode at cutoff [29]. The field patterns of the first modes have been published [30]. The expressions for the fields and the characteristic equations can be found in Appendix A. Plots of the phase coefficient variations are more complex than for the dielectric rod waveguide, due to the existence of backward waves and complex modes. The conditions for the existence of backward waves have been studied extensively [31, 29]. For a range of waveguide to rod ratios and for a given permittivity and normalised waveguide radius, the cutoff frequency of two hybrid modes can coincide. For these ratios, backward waves can then exist provided the permittivity of the rod is above a certain value. For the fundamental pair of hybrid modes, the range of ratios extends from 0 to 1. For higher order modes, the range narrows quickly. Backward waves have been associated with the existence of complex modes, so that a particular waveguide supporting backward waves in a given range of frequencies will also support complex modes of propagation across a certain frequency range. However, the converse is not true. The range of cavity to rod radius ratios over which complex modes exist totally overlaps that of the backward waves. The maximum ratio is the same in both cases, but the range for complex modes extends to smaller ratios [31].

1.4.2 First investigations into dielectric resonators

The concept of the dielectric resonator (DR) was first thought of by Richmyer in 1938, who illustrated his idea with the study of a dielectric sphere and a circular ring resonator [32]. The potential of DR's for microwave applications such as oscillators [19], slow wave structures [33] and bandpass and bandstop filters [34] became clear in the early 1960's. One of their attractions was their ease of integration in microstrip circuits [35]. During this period, the research effort concentrated in the modelling of the DR (usually of cylindrical shape as shown in Fig. 1.15) which resulted in the characterisation of the different modes of resonances and the drawing of the first mode charts. The modelling of DR's will be discussed in further details in the next section. Modes were split into H and E modes, depending on their field distribution. Notations differ, but modes with magnetic fields resembling magnetic dipoles (or multipoles) are commonly called H modes while those with electric fields resembling electric dipoles (or multipoles) are called E modes [34, 36, 37, 38]. Studies of the electrical and mechanical properties of the materials available at the time confirmed the possibility of resonators with Q_us higher than that of metal cavities at very low temperatures [34]. However, the limitations of the materials also became obvious, mainly due to their very high temperature dependence. Single crystal rutile TiO_2 and strontium titanate $SrTiO_3$, the two most commonly used crystals at the time, have TC_f of +450 ppm/°C and around +1 700 ppm/°C respectively. Nevertheless, the first high Q bandpass filters using rutile were designed in the late 1960's.

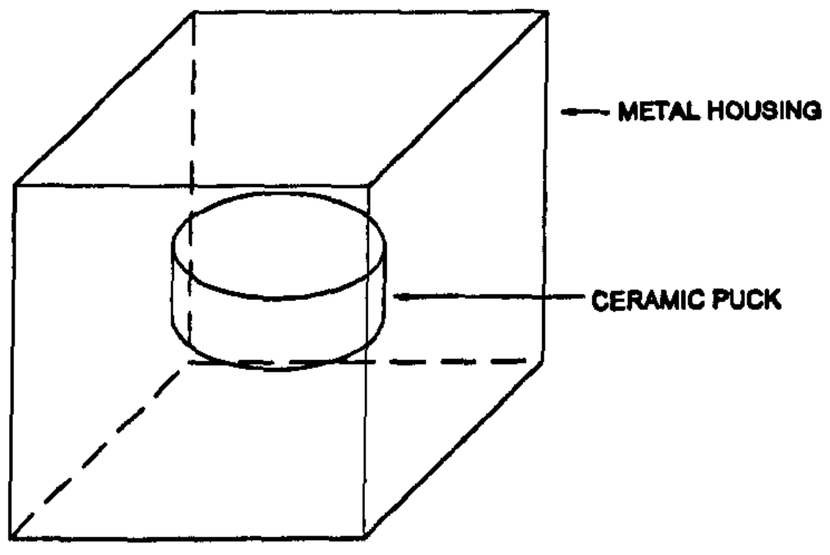

Figure 1.15: Cylindrical dielectric resonator

1.4.3 $TE_{01\delta}$ resonator filters

The first designs of bandpass DR filters used the $TE_{01\delta}$ mode, an H mode which is the fundamental mode of a cylindrical puck with length/diameter (L_d/D) ratio smaller than unity. The field distributions of the $TE_{01\delta}$ mode are shown in Fig. 1.16. DR's are traditionally located in a metallic enclosure to prevent any radiation. In the case of the $TE_{01\delta}$, the electromagnetic fields are very concentrated in the dielectric region. As a result, little current is induced in the cavity walls and Q_us close to the Q of the ceramic material are achievable in reasonable size cavities. A rule of thumb to preserve high Q_u is to keep the enclosure twice as large as the biggest dimension of the dielectric cylinder. The first design procedures for the design of DR bandpass filters were established by Cohn [39]. The resonators were placed axially or transversally in a metallic cavity below cutoff, as shown in Fig. 1.17(a). Magnetic wall and dipole moment models were used to get approximations of the resonant

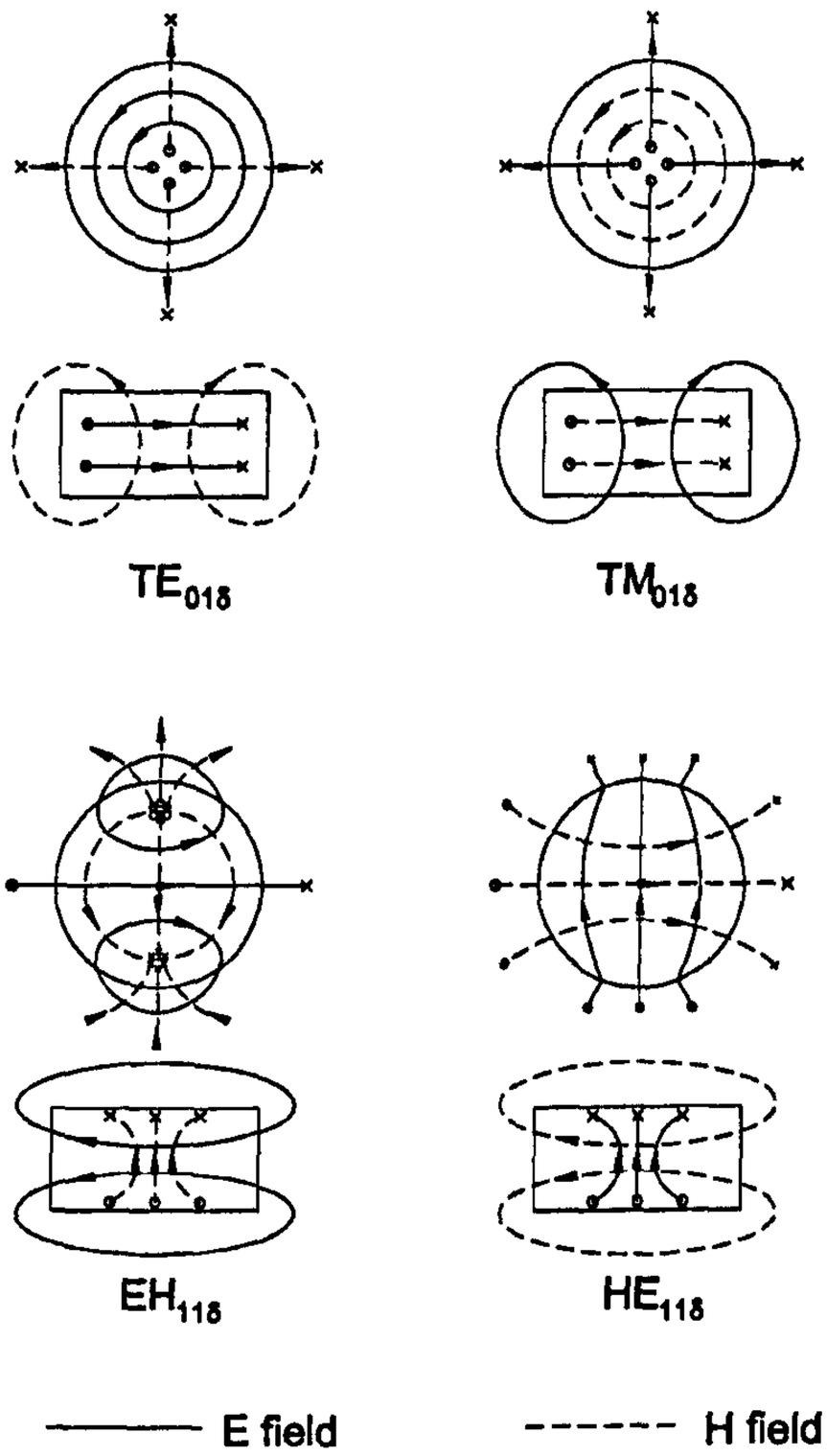

Figure 1.16: Mode patterns for lowest modes of suspended resonator [1]

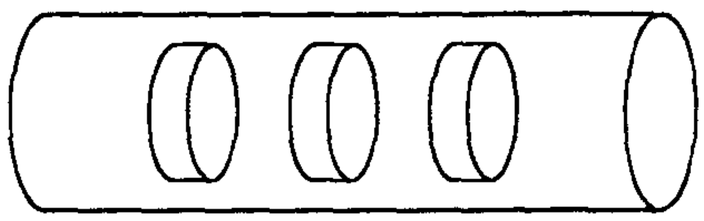

(a) Cutoff waveguide layout

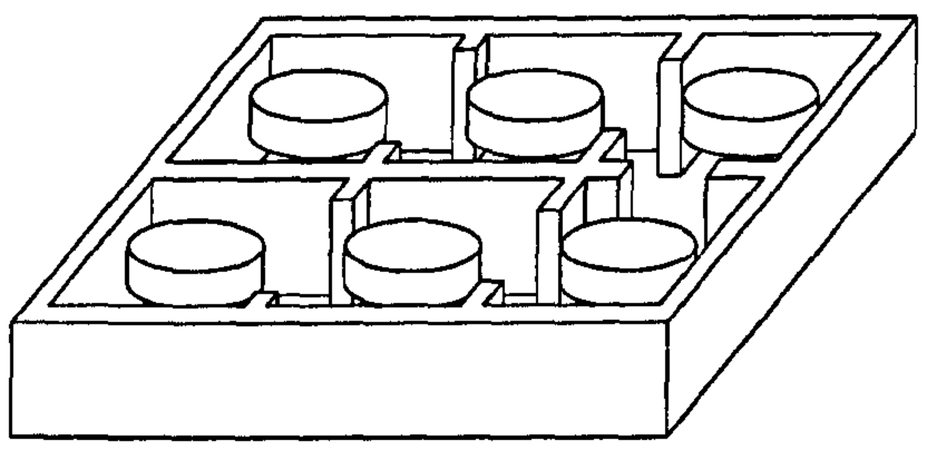

(b) Planar layout

Figure 1.17: Cutoff waveguide and planar filter layout

frequencies (see next section) and the couplings between consecutive resonators, respectively. Several $TE_{01\delta}$ filters were designed following the same method around the same time [40, 41].

Various methods such as the double resonator [42, 43] were developed to temperature compensate filters made with these early materials. But the development of DR filters only took off in the early 1970's when the first temperature stable ceramic materials were made available. Near perfect temperature stability of the DR was obtained by considering not only the variation of the ceramic material properties but also the temperature dependence of the enclosure dimensions and the resonator support permittivity and dimensions [44, 45]. Various modelling techniques were also used to optimise the resonator dimensions for Q_u and spurious performance [44]-[46]. A L_d/D of about 0.4-0.5 gave spurious to fundamental frequency ratios (F_r) of 1.3, with $HE_{11\delta}$ and $EH_{11\delta}$ as the first spurious modes [38]. Modifying the shape of the resonator into a ring improved F_r to 1.5 as the $HE_{11\delta}$ frequency increases dramat-

ically. The optimum inner diameter is then about 0.4 times the disc diameter and the first spurious is now the $TM_{01\delta}$ [38, 44, 20].

In the 1970's and 1980's, the bandpass $TE_{01\delta}$ filter configuration remained the same as the one described by Cohn with in-line resonators suspended in a circular or rectangular waveguide enclosure as shown in Fig. 1.17 [44, 47, 45]. Bandstop filters were also designed, by locating cavities loaded with DR's $3\lambda/4$ apart and coupling either to a propagating waveguide [48] or a microstrip line [24]. Today, $TE_{01\delta}$ filters are widely used for narrowband and low loss applications in mobile phone base-stations. Currently, Q_u values around 30,000 are achievable with ceramic material of permittivity 29 in 130 cm^3 at 2 GHz. With $\varepsilon_r = 44$, the Q_u/volume is a bit lower with a Q_u of 18,500 in 85 cm^3 [2]. However, the waveguide in-line configuration is not well suited for the wide-band, cross-coupled, high volume, low cost filter units that the cellular market requires. The layout generally adopted in this case is a planar layout, shown in Fig. 1.17(b). The magnetic fields of two adjacent resonators couple through irises, which are made narrow in order to limit the coupling of the $TM_{01\delta}$ mode. As well as being easier to manufacture, this layout provides the maximum flexibility for the realisation of single and multiple cross-couplings. The sign of the coupling can be changed for example by placing a metal resonator in the iris, resonating below the operating bandwidth of the filter.

1.4.4 $TM_{01\delta}$ resonator filters

From 1980, other modes were considered for the design of DR filters. The use of the $TM_{01\delta}$ mode was first proposed by Guillon et al. [49] as an alternative to the $TE_{01\delta}$ mode. $TM_{01\delta}$ resonators can have Q_u's even higher than $TE_{01\delta}$ resonators because of the smaller percentage of electric field concentrated in the ceramic in the case of the $TM_{01\delta}$ mode. This is of course most significant when the loss tangent of the ceramic material considered is relatively high. The field distributions of the $TM_{01\delta}$ mode, which is an E mode, are shown in Fig. 1.16. As for the first $TE_{01\delta}$ filters, the first $TM_{01\delta}$ filters consisted of resonators placed in-line in cutoff waveguides. Simple models were first applied to calculate resonant frequencies and couplings. The direct coupling between the fields of transversal adjacent resonators was considered in [50]. It was found to be mainly due to direct coupling between resonators [51] rather than through the evanescent fields of the cutoff waveguide, as considered [39]. In almost

all the rest of the literature, coaxially located resonators were considered.

The same extensive modelling that had been done for the $TE_{01\delta}$ resonator was applied to optimise the $TM_{01\delta}$ resonator for spurious performance, size and Q_u [52, 53, 54]. The spurious performance of the $TM_{01\delta}$ could in theory be quite restricted as this mode is not the fundamental for conventional disc L_d/D ratios. However, for most applications, the use of probe coupling on the end faces of the waveguide to realise the external Q of the filter prevents the excitation of any mode other than TM_0 modes [52, 53], which guarantees good stopband attenuation. To realise a filter with small dimensions, the dielectric cylinder diameter to waveguide diameter, D/W_d, should be fairly big (D/W_d around 0.7 for ε_r 30 [54]). The opposite is true to optimise the filter for high Q_u (D/W_d around 0.3 for ε_r 30). Filters with the $TM_{01\delta}$ mode as the fundamental mode were developed for cases where probe coupling was not possible, as for example, for high power applications [1]. This was realised by using very long and thin discs (or rods), nominally with L_d/D of 5. Spurious separations comparable to that of $TE_{01\delta}$ are then achievable, with F_r around 1.5, but are usually accompanied by a decrease of the Q_u. Finally, recently, the $TM_{01\delta}$ mode was considered for base station applications [54]. As well as higher Q_u, the $TM_{01\delta}$ also offers more coupling between adjacent resonators disposed in a planar filter layout (Fig. 1.17(b)) than $TE_{01\delta}$ resonators. Using vertical irises, the coupling is also much more tunable. The drawback of the $TM_{01\delta}$ filter over the $TE_{01\delta}$ filter is a significant increase of the filter dimensions.

1.4.5 Multimode resonator filters

Dual-mode DR filters can present the same very high Q_u as $TE_{01\delta}$ and $TM_{01\delta}$ DR filters and simultaneously offer significant volume reduction. They support modes which are degenerate due to the symmetry of the resonator geometry (e.g. the axial symmetry of a cylindrical puck). The use of multimode resonant cavities was first mentioned in the early 1950's [55] for metal air filled cavity filters. During the 1970's, satellite applications created a demand for filters with lightweight and small size as well as very high Q. A first volume reduction of about 50% over the conventional single-mode metal cavity filter was realised by using dual-mode TE_{011} metal cavity filters [56]. The next step, consisting of replacing the air cavities by DR loaded cavities, was proposed in 1980 by Guillon et al [57], but the first complete study of

dual-mode dielectric-loaded cavity filters was realised by Fiedziuszko in 1982 [58]. It used the $HE_{11\delta}$ mode, which is an H mode. Its field variations are shown in Fig. 1.16. In this thesis, the denominations of hybrid modes will follow the notation by Kobayashi [38, 46]. A mode is a HE mode, or EH mode, if its axial electric, or magnetic field, is dominant, respectively. When L_d/D is not much smaller than unity, the $HE_{11\delta}$ resonates closely above the $TE_{01\delta}$. In fact, the two modes would be degenerate in a 3D symmetrical resonator structure, as for example in a cube. The Q_u of the $HE_{11\delta}$ mode in a given cavity is thus similar to that of the $TE_{01\delta}$. As a result, volume reductions close to 50% compared with $TE_{01\delta}$ filters are achievable with the $HE_{11\delta}$. Another advantage of the dual-mode DR filters over metal filters is their excellent temperature stability, which is much better than that of Invar or graphite fiber reinforced plastic (GFRP) filters.

The physical realisation of the filter by Fiedziuszko uses the coaxial in-line configuration in cut-off waveguide of Fig. 1.17(a). The dual-mode aspect of the design followed from the work on air cavities [56]. Intra-cavity and inter-cavity couplings were obtained by 45° metal screws and cross shaped irises, respectively. A planar or "engine-block" type filter was also developed [59]. As for the $TE_{01\delta}$, this layout is easier to assemble and makes a better use of the space than the in-line cavities. Non-adjacent couplings are more difficult to realise, but can be obtained for example by a combined iris and probe coupling through the separating wall.

The optimal L_d/D for $HE_{11\delta}$ resonators was estimated to 0.5 by Fiedziuszko. The spurious performance of the resonator was then similar to that of TE_{111} metal cavities, provided the $TE_{01\delta}$ was not excited by the input and output coupling mechanisms. Optimisation of L_d/D for maximum F_r by mode-matching modelling [38] gives $L_d/D = 0.59$ and $F_r = 1.15$. The $TE_{01\delta}$ and $TM_{01\delta}$ modes are then at equal spacings below and above the $HE_{11\delta}$ resonant frequency, respectively.

The $EH_{11\delta}$ mode has also been used in the design of dual-mode DR filters [60, 61]. Its field patterns are shown in Fig. 1.16. For best F_r, L_d/D is chosen around 0.35. Once again F_r is about 1.15 and the $EH_{11\delta}$ mode is then sandwiched between the $TE_{01\delta}$ and the $HE_{11\delta}$ modes.

Dual-mode filter designs suffer from the fact that couplings of different magnitude might be needed through the same separating wall. In the canonical filter form, both inter-cavity couplings between any two given cavities need to have the same

magnitude, which allows the use of circular irises [62, 60]. As we move away from the input-output cavity, the coupling magnitude decreases, resulting in small irises with tight tolerances. These can be eliminated in the case of DR filters by using evanescent waveguide coupling [61, 63]. In other filter designs, such as longitudinal or canonical asymmetric designs, the problem due to the difference in magnitude between the couplings can be minimised by optimisation of the filter design [64].

Several triple-mode DR's use the fundamental mode of a resonator, made triply degenerate by using a geometry identical in the three dimensions. Triple-mode DR's achieve Q_u's similar to single-mode ones, for a given mode of resonance. They can use the suspended DR's, as for the dual-mode resonators listed above. For example, a triple-mode $TE_{01\delta}$ resonator consisting of interlocking discs has already been considered [65]. A new triple-mode $TE_{01\delta}$ resonator, consisting of a suspended cubic DR will be studied in detail in Chapter 2. Triple-mode resonators can also consist of a complete loading of the cavity with dielectric, creating a loaded waveguide cavity, as with a triple-mode cube resonator in [66].

In another type of multimode cavity, the resonator geometry is adjusted so that modes of different types resonate at the same frequency. They usually combine a dual-mode with a TM [67, 68, 69] or a TE [70] mode to create a triple-mode dielectric-loaded cavity. L_d/D can be chosen so that the resonant frequencies of the $EH_{11\delta}$ and the $TM_{01\delta}$ merge when they were the least sensitive to the distance between the resonator and the top and bottom walls of the cavity [68]. These two particular modes were also chosen because they had dissimilar field patterns at the junction between cavities, facilitating selective coupling through slots. In [70], the resonator took the form of a flat square plate, which lowers the resonant frequency of the $EH_{11\delta}$ mode enough to become degenerate with $TE_{01\delta}$ mode. Instead of using screws at 45°, intra-cavity couplings were realised by machining away part of the resonator itself. This method had already been used for dual-mode DR's [71]. Inter-cavity coupling used metallic loops instead of the conventional irises.

1.4.6 Improvement of spurious performance

One of the major drawbacks of DR's is their poor spurious performance when compared with metal filters. In the case of base station diplexers, clean stopbands are usually required up to 13 GHz. As a result, very selective clean-up filters are needed,

adding volume and insertion loss to the filter.

Improving the spurious separation of the DR by altering its shape only has a limited effect [72] and often adds complexity and cost to the manufacturing of the resonator. Another solution consists in eliminating some of the spurious resonant modes by forcing symmetry planes of the resonator into perfect electric (PEW) or magnetic walls (PMW). The latter are in theory realised by infinite discontinuities in the material permittivity. With the high permittivity materials available nowadays, an air-ceramic interface can provide a good approximation to the PMW. In [22], electric boundaries are used to reduce the $TE_{01\delta}$ resonator to one quarter of its original size. The two orthogonal metal walls also prevent the TM_{0nm} and the hybrid modes with odd numbers of angular variations to be supported by the structure. However, the ceramic material is then in direct contact with the conductive enclosure, which significantly decreases the Q_u of the resonator.

To improve the stopband of a DR filter, Snyder [73] proposed the use of resonant couplings. Each iris is tuned to be resonant at the centre frequency of the filter and provide an extra 6 dB/octave attenuation in the stopband. However, these resonant couplings are very sensitive. The input and output couplings can also be made resonant. For example, the DR can be coupled into by a $\lambda/4$ long metal post. This method has the advantage of short-circuiting the ports of the filter at twice the passband frequency, which provides very good rejection levels around the frequency of the second harmonic [47]. Alternatively, the input and output posts can replace the first and last resonators of the filter [74]. Mixing the type of resonators within the same filter improves the spurious response as higher modes can only propagate at common resonant frequencies. Posts, or coaxial resonators have very good spurious performance but also restricted Q_u. Other metal resonators such as the HE_{11} metal disc resonator can be used. This has a better Q_u than coaxial resonators but also a good spurious separation [75]. In [76], a HE_{11} metal disc filter was terminated by $HE_{11\delta}$ DR's. For very low loss applications, it is possible to mix different types of DR's. In [77], $HE_{11\delta}$ filters were terminated by $TE_{01\delta}$ resonators. The overall size of the filter was not increased significantly as the $TE_{01\delta}$ resonators have a smaller volume than $HE_{11\delta}$ resonators for a given frequency. Finally, a planar filter interleaving $TE_{01\delta}$ and $HE_{11\delta}$ resonators was presented in [78]. The $HE_{11\delta}$ cavities were made asymmetrical and only one of each of the dual-modes was used.

The filter dimensions were reduced over conventional filter dimensions because the distance between resonators required to realise the coupling between $TE_{01\delta}$ and $HE_{11\delta}$ resonators is small.

1.4.7 Conductor loading of dielectric resonators

All the suspended DR structures previously mentioned exhibit very high Q_u but are too big and bulky for most applications, especially in the cellular base station market. Solutions to realise physically smaller resonators, while retaining the maximum Q_u are then needed. Volume reduction can be obtained by introducing surfaces of contact between the ceramic and some conductive material. Each of the modes studied above can be loaded in different ways, which will make it optimum for different Q_u and volume ranges. Besides, for all structures where the ceramic is in direct contact with the housing, the power handling of the filter is greatly improved. The quarter-cut $TE_{01\delta}$ resonator mentioned before [22] offers a four fold volume reduction over the conventional $TE_{01\delta}$ version. Q_u's between 5,000 and 9,000 at 800 MHz are achievable. These values are representative of what is required for macrocell base station diplexers. Another alternative to load the $TE_{01\delta}$ mode was proposed in [79]. The periphery of the disc is metallised to create a dielectric slug. The spurious performance of the resonator is good as no current can flow on the flat faces of the slug. As a result, no modes other than the TE_{0nm} can be supported. Q_u's of 3,200 in 13.4 cm^3 at 2 GHz are reported and correspond to a Q_u/volume of 238 cm^{-3}. A potential application for this resonator would be microcell base station diplexers.

Contrarily to the $TE_{01\delta}$ mode, the $TM_{01\delta}$ mode is usually loaded on the flat walls of the cylindrical puck. One of the resulting resonator structures is the dielectric combline filter, where the inner conductor of a coaxial resonator has been replaced by ceramic. The dominant mode is the $TM_{01\delta}$, with improved spurious performance over the conventional suspended $TM_{01\delta}$ DR due to the combined effects of a large L_d/D, the metal contact on the base of the cylinder and the small capacitive gap at its top. An F_r of 1.6 is achievable and, because of the limited surface area in contact with the enclosure, high Q_u's are retained. A Q_u of 10,000 in 36 cm^3 (Q_u/volume = 280 cm^{-3}) at 1.87 GHz was reported [80], giving a 1.8:1 improvement over metal coaxial resonators.

If the metal enclosure is to make contact with both ends of the dielectric combline cylinder, the δ variation is prevented and the mode then becomes the TM_{010}. This resonator is actually very similar to the quarter-cut $TE_{01\delta}$ resonator [22] in terms of field distributions. The potential of this mode was first pointed out by Kobayashi et al. [81] in 1978. Varying the height of the resonator only has an effect on Q_u, not on the resonant frequency. This makes the TM_{010} very versatile as a wide range of Q_u's and volume reductions applicable to both micro and macrocell applications can be achieved. For example, at 880 MHz, Q_u's of 3,000 and 7,000 require 36 cm^3 and 108 cm^3 respectively. This corresponds to Q_u/volume ratios of 83 and 65 cm^{-3} respectively, compared with 55 and 26 cm^{-3} for metal coaxial cavities of same Q_u [23]. Comparably good performances are possible at 1800 MHz [82]. At the same time, F_r can be as high as 2 [81]. Numerous filter designs have been made, in most of which the cylinders were placed standing parallel to each other. However, the coupling between adjacent resonators can be decreased by introducing a certain angle between their axis. This can be used to reduce the filter dimensions or to create cross-couplings between non-adjacent resonators in cut-off waveguides [3, 83]. Further volume reduction can be obtained by intersecting the cylinders and making the mode doubly [84] or triply [85] degenerate. A 880 MHz dual version is reported to have a Q_u of 7,000 in 180 cm^3 (Q_u/volume = 77 cm^{-3}) but the best improvement happens for the triple-mode version with $Q_u = 8,500$ in 175 cm^3 (Q_u/volume = 145 cm^{-3}). The drawback of the triple-mode resonator is a fairly small F_r of 1.25 due to the presence of ceramic in all three directions.

The conductor loading of hybrid modes has also been studied. The resonant frequency of the $HE_{11\delta}$ mode decreases as the DR is lowered on the base of the cavity. If L_d/D is kept smaller than 1, the $HE_{11\delta}$ becomes the fundamental mode [86]. Further volume reduction and spurious separation is achieved by adding a metal disc on the top flat face of the DR. This resonator structure will be studied in detail in Chapter 3.

Another way to load a hybrid mode is to start from the metal disc dual-mode resonator [75]. As this resonator exhibits good spurious separation but relatively low Q_u, a compromise is reached by loading it with dielectric discs directly above and/or below it [87, 88]. Extremely good theoretical volume reductions are reported: Q_u of 7,730 in 46.9 cm^3 at 1.9 GHz, i.e. Q_u/volume = 329 cm^{-3}. F_r is quoted between

1.5 and 1.7.

Previously in this section, the TM_{010} resonator was mentioned as a good candidate for filter designs requiring Q_u's between 2,000 and 5,000. Below these values, the technology which has been the most often considered is the dielectric-loaded coaxial resonator. Its main current application is the handset duplexer, but its Q_u would also be high enough to meet the insertion loss duplexer requirements of the smallest cells (e.g. picocell) base stations. In the late 1970's and 1980's, Wakino et al. studied the dielectric loading of coaxial resonators at both 900 and 1800 MHz. They increased the frequency of the first re-resonance of an open-ended $\lambda/2$ resonator by filling the central region ($\lambda/4 \pm \Delta\lambda$) with a lower permittivity material than the rest of the resonator [89]. A Q_u above 1,800 in 7.7 cm^3 at 835 MHz was reported, which corresponds to a Q_u/volume of 233 cm^{-3}. $\lambda/4$ resonators followed [90], with similar Q_u in 57% of the volume. The frequency of the first spurious resonance was this time increased by reducing the impedance of the grounded end of the resonator [91]. Both types of resonators were placed in-line along their direction of propagation. The open ends of the resonators coupled capacitively through lengths of evanescent air waveguides. The short-circuit ends coupled inductively through apertures in their common ground plane. In the 1990's, the design of dielectric coaxial resonator filters switched to the conventional combline layout. Quarter wavelength long coupled lines in homogeneous media form an all-stop network. To solve this problem, the electric length of the resonators can be reduced by capacitive end loading [92]. The medium can also be made inhomogeneous by drilling out air regions between the resonators [93]. Other options are to manufacture the resonators separately and either leave an air gap between them [94] or block part of their interface with metallisation [95].

Miniaturisation techniques similar to metal combline resonators were used for the dielectric-loaded coaxial resonators, namely capacitive loading and impedance stepping. The latter can be obtained, as for the spurious optimisation, by changing the effective relative permittivity of the material along the resonator length [96]. The resulting resonators achieve Q_u's of the order of 800 in 2 cm^3 at 900 MHz (Q_u/volume = 400 cm^{-3}). Today, dielectric-loaded coaxial resonator filters have reached the size limit achievable with conventional dielectric materials, and a full AMPS duplexer with 2.2 dB insertion loss fits in 0.9 cm^3. Stripline versions of $\lambda/4$

resonator filters were also reported [97, 98]. They consist of several layers of ceramic on which the resonators and the coupling patterns are printed. Finally, both single and dual-mode helical ceramic resonators have been recently described as offering significant volume reduction over the ceramic coaxial resonators [99].

In spite of the great amount of research into dielectric-loaded coaxial resonators, these are now very seriously challenged over the handset duplexer market by alternative technologies such as surface acoustic wave (SAW) filters and thin-film bulk acoustic resonator (FBAR) filters. The former are very small but suffer from higher insertion loss than dielectric coaxial resonator filters at RF frequencies and low power handling [100]. Volume reductions of a factor 14 [101] compared with dielectric coaxial filters are possible. FBARs also have quality factors up to 1000 and power handling of a few Watts. Another advantage is that FBARS can be grown on silicon or gallium arsenide, which opens the possibility of the integration of the handset duplexer on chip and the development of the whole phone front end as a single module.

One other alternative to the dielectric coaxial resonator filter for the very low Q applications is the dielectric waveguide filter technology. It has been mainly considered for use at high frequencies (5 GHz - 10 GHz) where it gives better Q_u than dielectric coaxial resonators. Recently, however, dielectric waveguide filters at 1.35 GHz [102] and 2.5 GHz [103] have been presented. At the latter frequency, a resonator of Q_u 480 in 1 cm^3 was reported. As the height of the resonator has no influence on the resonant frequency, the filters can be made very low profile (between 1 and 5 mm), which facilitates their integration. Fully loaded versions of dielectric waveguide filters strongly resemble air-filled metal ones [104]. One difference is the possibility of realising inter-resonator couplings with an air or low permittivity waveguide section of same cross section as the resonators. These evanescent sections also have the effect of increasing the resonant frequency of the next higher modes up to twice the operating frequency [105]. Otherwise, inductive coupling can be obtained by separating resonators with sections of smaller widths. For capacitive couplings, one can remove the metallisation all around the waveguide cross sections over a certain length [17]. By alternating capacitive and inductive couplings, quarter wave resonator bandpass filters can be designed. In order to ease the manufacture of the filter, each resonator can be machined separately [106]. Metal patterns are

then printed on their end faces to control the inter-resonator coupling. The use of external elements such as chip capacitors connected to the resonators by microstrip lines to realise negative couplings was also reported [102].

The symmetry plane half way across the width of these dielectric waveguide resonators can be approximated to a large extent by an dielectric-air interface. As a result, cutting the resonators along this plane results in volume reductions of 50% with only a marginal increase of the resonant frequency. Two section dual-mode $\lambda/4$ filters were realised in this manner [107]. The open-end cut can be done along the whole length of the filter, which is then known as a dielectric E-plane waveguide filter. A detailed study of this type of filters is presented in [17] and developed in [103]. In these, an alternative realisation for inductive couplings consists of metal strips printed on the open-end to connect the top and the bottom of the waveguide.

1.4.8 High temperature superconducting resonators

In the resonator structures described above, more volume reduction means more loss due to current induced in the conductors. High temperature superconductivity (HTS) can drastically reduce these losses. As an example, the surface resistivity of $YBa_2Cu_3O_{7-x}$ (YBCO) is less than 0.4 mΩ at 77 K and 10 GHz compared with 15 mΩ for copper. The Q_u of the resonators is then mainly limited by the loss tangent of the ceramic materials. The dielectric loss that this loss tangent causes can in turn be minimised by choosing one of the ceramic materials which exhibit extremely high Q at low temperatures. For example, $Ba(MgTa)O_3$ has a Q higher than 140 000 at 77 K [46]. The drawbacks of HTS are mainly linked to the cryogenic unit necessary for cooling, which reduces the miniaturisation and adds reliability issues, and the nonlinearity of the HTS resonators which causes intermodulation problems [108].

HTS resonators have been considered for many types of DR's including the quarter and half cut $TE_{01\delta}$ resonators, the HE_{111} resonator and the TE_{011} post resonator filters [109]. In the latter case, a Q_u of 50,000 was expected at 77 K and 9 GHz with resonators of diameter just above 1 cm. The largest conductor loss occurs at the surfaces where the fields are of biggest magnitude, which is where the DR is in contact with the metal. Limiting the HTS metallisation to these surfaces by only depositing a thin film of superconducting material on the ceramic will then still eliminate most of the conductor loss. Dual-mode microstrip, stripline and suspended

substrate patch resonators were evaluated [110]. The suspended substrate resonator was singled out as its fields are less concentrated in the ceramic and the resonator more easy to tune. A 80 MHz wide filter with 0.05 dB insertion loss at 8.2 GHz was built. The same kind of structure, but with patches on both sides of the substrate was also studied [87]. Finally, HTS has also been applied to conventional suspended DR, mainly to high-power $TM_{01\delta}$ resonators [60]. The resonator dimensions were optimised for temperature stability. Variations of 1.7 ppm/K between 20 K and 300 K were achieved along with a Q_u of 150,000 at 12 GHz and 20 K.

1.5 Modelling of dielectric resonators and filters

1.5.1 Cavity models

With the exception of a few simple geometries such as the spherical resonator, the field equations of the vast majority of DR's cannot be solved analytically. Nowadays, various numerical methods to solve these equations exist that take advantage of the ever increasing capacity of modern computers. Previously, solutions were restricted to simpler approximation methods, which can still be used today as a starting point for a more rigorous analysis.

The first and most simple approximation consists in considering all dielectric to air interfaces as PMW's [34, 111]. Tangential magnetic and normal electric fields are forced to vanish at the interfaces. Resonant frequencies of E modes are approximated to within a few percent. However, the error for H modes, which include the $TE_{01\delta}$, can be as large as 20%. The accuracy of the model improves with the order of the mode.

Better results are obtained by using a second order approximation, first described by Okaya [34]. It is also referred to as the magnetic wall model, or the Cohn model, as it was used by Cohn [39] for one of the first $TE_{01\delta}$ filter designs. In the case of a cylindrical resonator, the air region around the periphery of the disc is replaced by a magnetic wall. But, by contrast with the first approximation model, the air regions on each side of the end faces are retained. The radial dependence of the fields in the dielectric region is fixed by the PMW condition. As the transverse fields need to be continuous over the two flat end interfaces, the same radial dependence is used in the air regions. Equating the transverse fields at the interfaces then leads

to a transcendental equation to solve for ω. In the longitudinal direction, the fields are propagating in the dielectric region and evanescent in the air regions. The longitudinal field variation within the dielectric is no longer an integer number of half wavelengths. In the case of the $TE_{01\delta}$, the variation is only a fraction of half a wavelength δ, where $\delta = L\gamma/\pi$ with γ the propagation constant in the dielectric region. The $TE_{01\delta}$ mode has been extensively studied by the Cohn model [112], with errors on the resonant frequency between 5 and 10%. The effect of the cavity ends can be partially simulated by making the air regions on each side of the resonator of finite length [113]. The Cohn model has also been used successfully in [58] to approximate the resonant frequency of the $HE_{11\delta}$ mode, with a similar accuracy. A dual of the Cohn model also exists for E modes and consists in considering the end faces of the resonator as PMW's and equating the fields over the periphery of the dielectric cylinder.

The accuracy of the Cohn model can be improved, sometimes down to 1%, by using the variational or the perturbation method. In both cases, some field is allowed to exist outside the PMW boundary, of surface S. In the variational method, the magnetic wall impedance is varied from infinity and the change in resonant frequency is obtained by applying the stationary condition on S [114]. In the perturbation method, it is deduced from the perturbation principle [115]. Even though, in the case of the $TE_{01\delta}$, the longitudinal magnetic field has to be forced to zero outside the boundary to prevent any discontinuity, this method gives very good results, especially for isolated resonators.

An extension of the Cohn model is the dielectric waveguide model. It is also called the Itoh and Rudokas model [116] although first described by Chow in 1966 [117]. It only differs from the Cohn model in that the dielectric waveguide section is replaced by a dielectric-loaded waveguide section, thus taking into account the air region surrounding the periphery of the resonator. However, the air regions on each side of the flat ends of the resonator are still considered to be of diameter D. As a result, the dielectric waveguide model works best for shielded resonators. For isolated resonators, the error on the resonant frequency of $TE_{01\delta}$ DR's can deteriorate from 1 to 7%.

Other techniques based on the previous models include the effective dielectric constant method [118]. In this method, the radial wave number of the dielectric

region is deduced from the characteristic equation for an infinite dielectric-loaded waveguide of equivalent relative permittivity. Another method [119] uses successive approximations of first order models, the Cohn model and the dielectric waveguide model. Effective dimensions for the resonator, calculated by alternative use of both first methods, give a lower bound for the resonant frequency when used in the first order approximation model. Then, the dielectric waveguide model is applied, using the actual resonator dimensions, to give a higher bound. The approximated resonant frequency is then taken as the average of both frequencies and is accurate to 1% for isolated resonators.

1.5.2 Rigorous numerical methods

Many numerical methods developed for the general study of RF structures have been applied to the analysis of dielectric resonators. All have in common an extremely good accuracy provided CPU time and large storage capacity are available. The field simulation packages used in several instances in this thesis are based on some of these methods. This is also the case of the programs written to study the resonators of Chapter 3 to 5. The most commonly used techniques will be briefly described here.

The problem to solve is an eigenvalue problem, set by the Helmholtz equations and the boundary conditions of the structure. One approach is to apply the moment method [120] directly to the eigenvalue equation. The eigenfunctions of the problem, i.e. the electric and magnetic vector fields, are expanded into a linear combination of basis functions. By taking the innerproducts of the equations with carefully chosen test functions, the equation is discretised into an infinite matrix eigenvalue equation, which only has solutions for the eigenvalues, i.e. the resonant frequencies, of the problem. Basis and test functions are commonly chosen to be the same. The method is then called Galerkin's method. Obvious functions for the study of DR cavities are the electric and magnetic vector fields of empty or dielectric post cavities. This is a somewhat crude use of the moment method, which generally exhibits fairly slow convergence rates. To improve the convergence, more adequate basis functions need to be used, which is challenging for complex structures. To overcome this problem, several methods limit the fields expansions over a number of smaller and simpler regions, as will be described next.

When the DR geometry is separable into a succession of homogeneous waveg-

uides, the transversal fields of each mode in each waveguide section can be chosen as the basis functions. The equations to solve then become the continuity equations of the transverse fields at each interface between waveguides. This is the fundamental idea of the mode-matching method [121]. This method is very well adapted to the case of shielded DR's of simple shapes and will be considered in more detail in the next section.

Other methods are more versatile and adapted to irregular geometries. One example is the finite element method (FEM), where the basis functions are defined as polynomials over small and simple shaped (often triangular or tetrahedrical) elements [122]. Field continuity is enforced by an adequate choice of polynomials. The Helmholtz equation can then once again be solved by a method similar to the moment method, the weighted-residual method [19]. Another formulation of the finite element method is based on the variational method. The basis functions are substituted into a stationary form of the problem and the Rayleigh-Ritz conditions are applied to lead to a set of equations equivalent to the one obtained by Galerkin-weighted residual method. In the following chapters, numerous simulations will be realised using two different FEM softwares: MicroWaveLab^{TM} and HFSS^{TM}, both from Ansoft.

A method related to the finite element method and sharing the same versatility is the finite difference method [49]. In this method, the derivative operators of the differential (Helmholtz) equation are discretised. The field is defined at discrete points on a rectangular grid and the equation is rewritten at each point as a linear function of the fields at neighboring points. The resulting matrix eigenvalue problem is then solved as in the previously described methods.

The unknowns in the Helmholtz equation (i.e. the resonant frequencies and the field expression) can be expanded in terms of ascending powers of $1/\sqrt{\epsilon_r}$. The Helmholtz equation is then split into a series of equations solved iteratively by the finite element method. Each iteration increases the accuracy of the results. This is known as the perturbational method and also as Van Bladel's method [19].

In a different approach, the DR problem can also be solved from one of two integral equation formulations. The first one, the volume integral method, requires knowledge of the Green's functions for the entire structure and, as a result, is easier to use in the case of open DR's. A variant of the volume integral method, the

spectral domain analysis method deals with both the determination of the Green's functions and the resolution of the equation in the spectral domain [122]. For complex structures, the second formulation, called the surface integral method, simplifies the Green's functions expressions by using the equivalence principle [19]. The material properties of partial regions of the structure are replaced by equivalent magnetic and electric surface currents on the boundaries of these regions. Imposing continuity of tangential fields on these boundaries then leads to a simplified integral equation which can be solved by method moment for the unknown currents.

Other numerical methods set out to solve the Maxwell's equations in the time domain. The transmission-line matrix method models the resonator structure by a transmission line network where the voltages and currents of three-dimensional cells represent the six field components at equidistant points of the structure [123]. The distance between cells induces a certain propagation time of the signal from one cell to the next. The network response to an impulse stimulus is computed over many time units (or iterations) as the signals are scattered between the cells. The response to any waveform is then available from the impulse response by convolving the two. The frequency response of the structure can then be deduced by Fourier transform. This method is very versatile and is said to require less CPU time than the finite element and the finite difference methods. With no matrix equations to solve, it avoids the problems of convergence and spurious responses.

Further CPU time savings can be made by using the finite-difference time-domain (or FD-TD) method [124]. Here, finite difference equations are used to relate the field components at interlaced points of the structure. Maxwell's equations are also discretised in time so that the steady state response of the structure to an adequately chosen excitation can be computed iteratively. The spectrum of this steady state solution is then extracted by a discrete Fourier transform.

1.5.3 Mode-matching method

The mode-matching technique has often been used to solve waveguide discontinuity problems for which the analytical methods such as the static [125], variational [125], residue calculus [126, 127] and Wiener-Hopf [126] methods were not adapted. The method was pioneered by Wexler [121] and Clarricoats et al. [128]. It has been used to study bifurcations [121], irises [129, 127, 130], steps in rectangular and cylindrical

waveguides [128, 131, 132], steps in dielectric-loaded circular waveguides [128, 133], coplanar waveguide discontinuities [134], finline discontinuities [135], microstrip discontinuites [136] and waveguide T junctions [137].

For this method [121, 128, 133, 138], the structure under study is divided in sections of waveguides, all directed along the same axis of propagation. In each waveguide, the fields are expanded as an infinite series of the fields of the waveguide modes. The transverse fields at both sides of each interface between sections are then equated. This results in $2n$ doubly infinite equations, with n the number of interfaces. Next, the fields variations across each interface section are eliminated by realising cross-products of the electric (magnetic) fields at the interface with the magnetic (electric) fields of one of the two waveguides. By choosing the appropriate fields, and because all modes within each waveguide are orthogonal, many products disappear and each equation results in a infinite set of equations retaining only one infinite summation. These equations can then be put in the form of a matrix equation. The unknowns of this equation are the coefficients of the modes in each waveguide section. The mode-matching technique relies on the fact that the higher modes of each waveguide, modes with high γ^2, have less and less effect on the behaviour of the structure as they get attenuated very fast after being generated at a discontinuity. This means that the matrix equation can be truncated and still be a meaningful representation of the structure [122, 128]. Provided the number of modes in each region is chosen carefully, the coefficients deduced from this truncated equation will converge towards the exact solution as the size of the matrix tends to infinity [127, 131]. The matrix equation then takes the form

$$[\mathbf{M}][\mathbf{A}] = [\mathbf{B}] \tag{1.9}$$

with $\mathbf{M}$ a square matrix. The column vector $\mathbf{A}$ composed of the mode coefficients is retrieved by Gaussian inversion.

The $\mathbf{S}$ matrix or the $\mathbf{T}$ matrix [139, 72, 53] of each waveguide interface can also be extracted. This is particularly interesting for more complex geometries since, as the number of interfaces is increased, so is the number of unknowns, which dramatically increases the computation time. Rather than directly cascade successive discontinuities, the characteristic matrix of each interface can be independently computed and later cascaded through waveguide sections. Structures such as dielectric-

loaded [140, 141], corrugated [141] and smooth-walled conical horns [140], DR TE mode filters [105] and E-plane filters [72] have been studied in this manner.

If boundary conditions are added at each extremity of the cascade of waveguides, the matrix equation becomes:

$$[\mathbf{M}][\mathbf{B}] = 0 \tag{1.10}$$

with $\mathbf{M}$ again a square matrix. Non-trivial solutions for the mode coefficients $\mathbf{B}$ in Eq. 1.10 only exist when the determinant of the matrix is zero. This will happen at the resonant frequencies of the now closed structure. A wide range of resonators were studied this way including combline [93, 142, 143], conductor-loaded [142, 75], dielectric combline [80], multilayered cylindrical [144] and suspended dielectric [145, 146, 147, 52, 38, 21, 148, 20, 86] resonators.

1.6 Scope of present work

The purpose of this work is to investigate new dielectric resonators and filters for use in cellular base-station applications. Three types of resonators will be studied, which are promising structures for different ranges of Q_u and thus adequate for different types of applications. The main aim of this work is to present data which gives a thorough understanding of the first resonant modes of the resonators, and allow the design of the optimum resonators for any given filter specification. The most critical parameters for the suitability of a resonator are its Q_u, Q_u/volume and spurious performance. Other filter design related criteria, such as the maximum coupling to adjacent resonators and the frequency tuning available, also need to be considered.

In the case of very high Q_u filter applications, the single-mode $TE_{01\delta}$ resonator filter technology has been extensively proven. Dual-mode $HE_{11\delta}$ and $EH_{11\delta}$ resonator filters are also becoming more common. With triple-mode resonators, the extra complexity added to the filter design means that only a few examples have been published. The majority of them combine a dual-mode and a single-mode [70, 69, 68], which means that different frequency tuning behaviours coexist within the same cavity. The only exception is the resonator made of three $TE_{01\delta}$ ring resonators [65], which has an unpractical shape. The first resonator which will be studied in the present work is the cubic triple-mode $TE_{01\delta}$ resonator. As for the previous resonator, its fundamental mode is a triply degenerate H mode. This should make it optimal

for applications requiring very high Q_u and large volume reduction. In Chapter 2, the performance of the cubic $TE_{01\delta}$ resonator will be examined and the performances of the two triple-mode $TE_{01\delta}$ resonators will be compared.

A complication of multi-mode resonator filters is the multiplicity of inter-cavity couplings which have to occur through the same physical wall. The second part of Chapter 2 will present the theory for the design of a novel type of filter, the even-odd mode hybrid reflection filter, which eliminates the need for any cross-coupling in the case of symmetrical filter responses. Advantage will be taken of the triple degeneracy of the cubic $TE_{01\delta}$ resonator to design a sixth degree elliptic bandstop filter for the receive notch application described in Section 1.1. The last part of Chapter 2 will be concerned with the use of triple-mode $TE_{01\delta}$ cubic resonators for the design of conventional bandpass transmission mode filters with the most general frequency response. The suitability of the resonator for small bandwidth (0.25% fractional bandwidth), selective filters will be assessed at 2 GHz.

For medium and low Q_u applications, the technology which is currently widely used is the combline resonator. Several dielectric resonator structures have been reported previously in this chapter, which present significant improvement over this technology. In the case of macrocell base-station filters, the Q_u's required are still sufficiently large for multimode resonators to offer attractive volume reductions in spite of their added aligning complexity. E modes are then the best option, combining good Q_u/volume with compactness. The second resonator studied in this work will be the dual-mode conductor-loaded DR. The aim of Chapters 3 and 4 is to study this new resonator at approximately 900 MHz, so that the variations of its electrical performance with respect to the various geometrical parameters of the structure can be understood and the geometry optimised.

In Chapter 3, approximate and mode-matching modelling of the dual-mode conductor-loaded resonator will be investigated. The accuracy of the modelling methods and the problem of the convergence of the mode-matching results will be discussed. The results of the resonator study will be presented in Chapter 4. They will include the optimisation of the geometry for best Q_u and best F_r.

The third resonator to be studied will be the TE_{011} dielectric-loaded waveguide resonator (TM_{010} in cylindrical coordinates). It will be investigated for the lower Q_u range of base station filter applications. For these applications in particular, the

accent is put on a small filter volume but also on ease of manufacture and low cost. The single-mode TE_{011} resonator, with very good spurious separation, then presents an advantage compared to the more compact but also more complex dual and triple-mode resonators such as the multimode TM_{010} resonators and the conductor-loaded dual-mode DR. The aim of Chapter 5 is to complement the data available in the litterature in the case of microcell base-station filters at 2 GHz. In particular, the influence of filter requirements such as bandwidth, spurious performance or the need for cross-couplings on the performance of the resonator will be considered. Other aspects of the filter design, such as frequency tuning and the resonator mounting, will also be studied to be best adapted to the manufacturing of a wide bandwidth, low-cost filter.

1.7 Original work

The original contributions of this work are listed below. Concerning the novel hybrid reflection mode filter, they are:

- The synthesis of the filter and the study of its limitations.
- In the case of a sixth degree filter, the study of the realisation of the two third degree networks with the presence of spurious cross-couplings.

Concerning the triple mode $TE_{01\delta}$ cubic resonator, they are:

- The evaluation of the performance of the resonator.
- The study of the suitability of the resonator for selective narrowband filters, including the optimisation of the tuning and coupling mechanisms, and more particularly the location of inter-cavity irises to limit the effects of spurious couplings on the response of transmission mode bandpass filters.

Concerning the dual-mode conductor loaded resonator, they are:

- The investigation of simple models and explanation of their limited accuracy.
- The evaluation of the axial mode-matching technique for resonant frequency and Q simulations. The study determines the number of modes to use in the geometry and evaluates the convergence and accuracy of the results.

- A thorough study of the variations of resonant frequencies and Q with all the geometry parameters, which sets key parameters for optimisation of the resonator at 900 MHz.

- A more systematic study of these variations resulting in optimum geometries for Q_u and spurious performance at 900 MHz.

- The evaluation of the performance of the resonator and comparison with existing geometries.

Concerning the dielectric-loaded waveguide resonator, they are:

- The first study of the feasibility of wide (80 MHz) bandpass cross-coupled filters at 2 GHz using this resonator. This considers:

  - The effect of offset cavities and dielectric slabs on the coupling bandwidth, studied by mode-matching.

  - The trade-off between coupling bandwidth and performance of the resonator itself (spurious separation and Q_u/volume).

Chapter 2

Triple-Mode $TE_{01\delta}$ Filters

2.1 Introduction

As explained in Chapter 1, some of the most demanding filtering applications in base station systems require very high Q_u resonators. This is usually to meet low insertion loss and small insertion loss variation requirements over their passband.

In a few cases, as for the receive notch filter mentioned in Section 1.1, the absolute level of insertion loss is not critical. Using the absorptive reflection mode filter synthesis technique [149], it is then possible to design a filter network which has the same passband insertion loss variation as a filter of infinite Q, but has some constant level of insertion loss. This absorptive filter consists of a cascade of resistors and coupled resonators of finite Q. If the tolerable insertion loss level is high enough, this finite Q will be significantly lower than the Q required from a conventional filter with the equivalent performance in terms of selectivity and passband insertion loss variation. However, in most cases, an extra constant level of insertion loss is not acceptable. The use of very high Q_u DR is then the only available option, and minimising the size of the resonators is desirable.

2.2 The triple-mode $TE_{01\delta}$ cubic resonator

The most intuitive way of realising a high Q_u triple-mode resonator is to intersect three $TE_{01\delta}$ ring resonators together [65]. The resulting resonator supports three degenerate modes of Q_u similar to that of the single-mode $TE_{01\delta}$ resonator in a volume less than 1.5 times that of the single-mode cavity. However, the spurious separation of the single-mode is not retained. F_r, the ratio of the first spurious frequency to the fundamental frequency, decreases from 1.5 to values close to 1.3 as

the two added rings are optimally located to bring one of the dual $HE_{21\delta}$ modes down in frequency. A second drawback of this resonator is its complicated shape, which, if realised by joining simpler separate parts together, tends to create significant variations between the resonant frequencies of the three modes. These are not acceptable as the resonator only has a very limited amount of frequency tuning. Indeed, single-mode $TE_{01\delta}$ resonators are conventionally tuned either by a dielectric plunger partly inserted in the resonator hole, or by a dielectric tuning disc brought at proximity of one of the flat faces of the resonator. Because of the presence of the two other rings, neither of these methods is possible.

Considering the previous points, it was felt that the triple-mode cubic resonator presented a better alternative. Flat square resonators have previously been used as single-mode resonators [41]. The fundamental mode of such resonators is a perturbation of the $TE_{01\delta}$ mode of the cylindrical resonator. Following the notation derived from the Cohn model field expressions in rectangular coordinates, this mode is the $TE_{11\delta}$ mode. However, to avoid confusion when referring to other resonator studies in the literature, especially when considering higher order modes, the cylindrical coordinates and the denomination $TE_{01\delta}$ will be used in the rest of this chapter.

The first resonant modes of the square resonator have been studied by FEM simulations. Plotting the resonant frequencies of the $TE_{01\delta}$ and the first spurious modes with respect to the resonator height, as in Fig. 2.1, shows how the fundamental triple-mode of the cubic resonator appears as the single $TE_{01\delta}$ and the dual $HE_{11\delta}$ modes become degenerate. Fig. 2.2 illustrates the spurious separation of the triple-mode $TE_{01\delta}$ cubic resonator as the ratio of the cavity length to the dielectric length, or dielectric filling ratio, is increased. The dielectric constant of the resonator is chosen to be 44. The optimum occurs for a 38% filling ratio after which the normalised resonant frequency of the triple $TM_{01\delta}$ mode decreases to eventually cross over the $TE_{01\delta}$ mode and become the fundamental resonant frequency. With a filling ratio of 38%, F_r is equal to 1.3, which is comparable with the spurious separation obtainable from the intersecting discs triple-mode resonator. Fig. 2.3 shows the cavity volume reduction and the decrease in Q_u at 2 GHz as the filling ratio is increased. The cavity is considered silver plated and the loss tangent of the ceramic material is estimated at 5.55×10^{-5}. A 38% filling ratio appears adequate for high Q applications as the Q_u is still 95% of that of the ceramic material. The

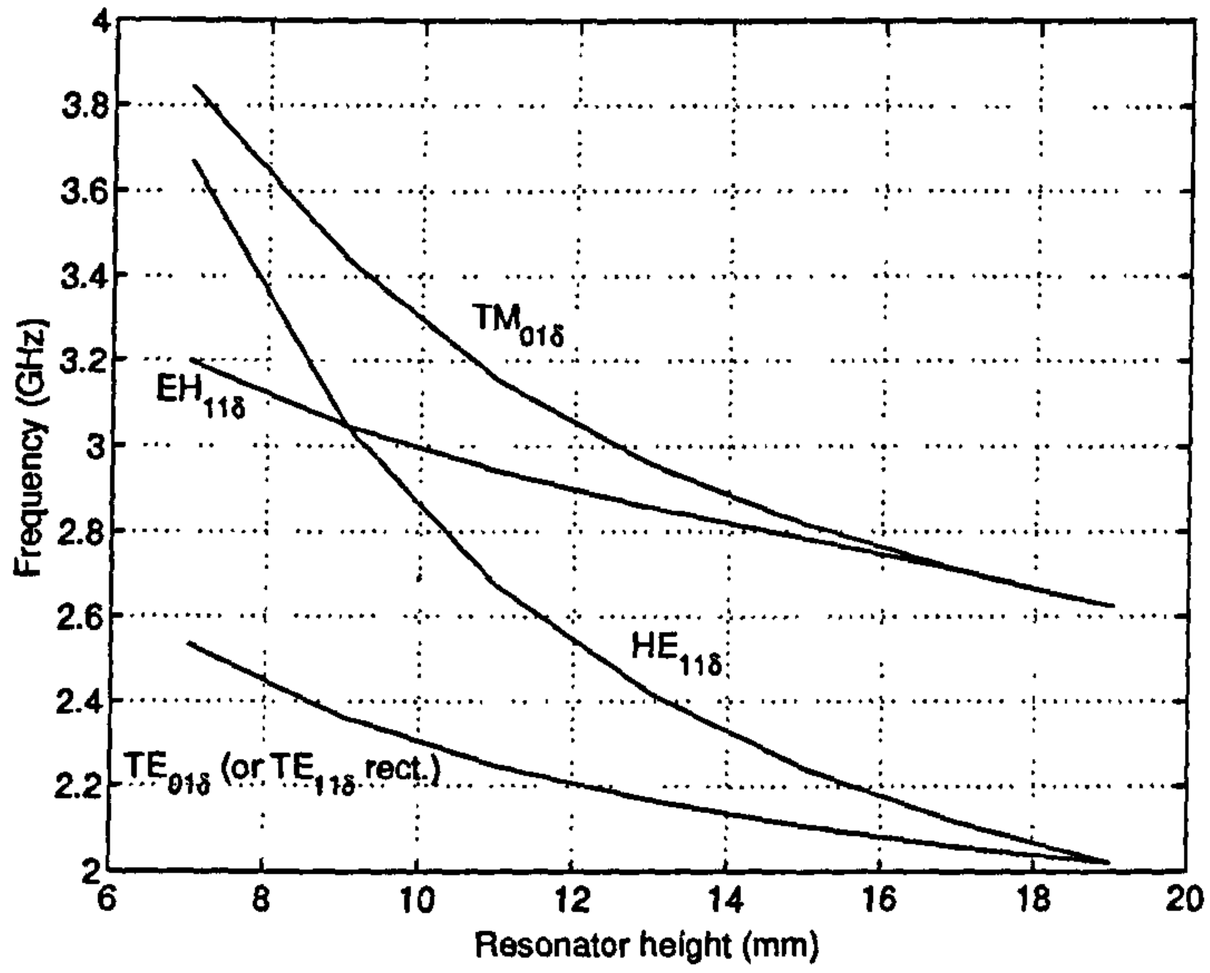

Figure 2.1: Frequency variation of the first resonant modes of a square resonator with resonator height. Cubic cavity of length 50 mm. Resonator of length 19 mm and dielectric constant 44.

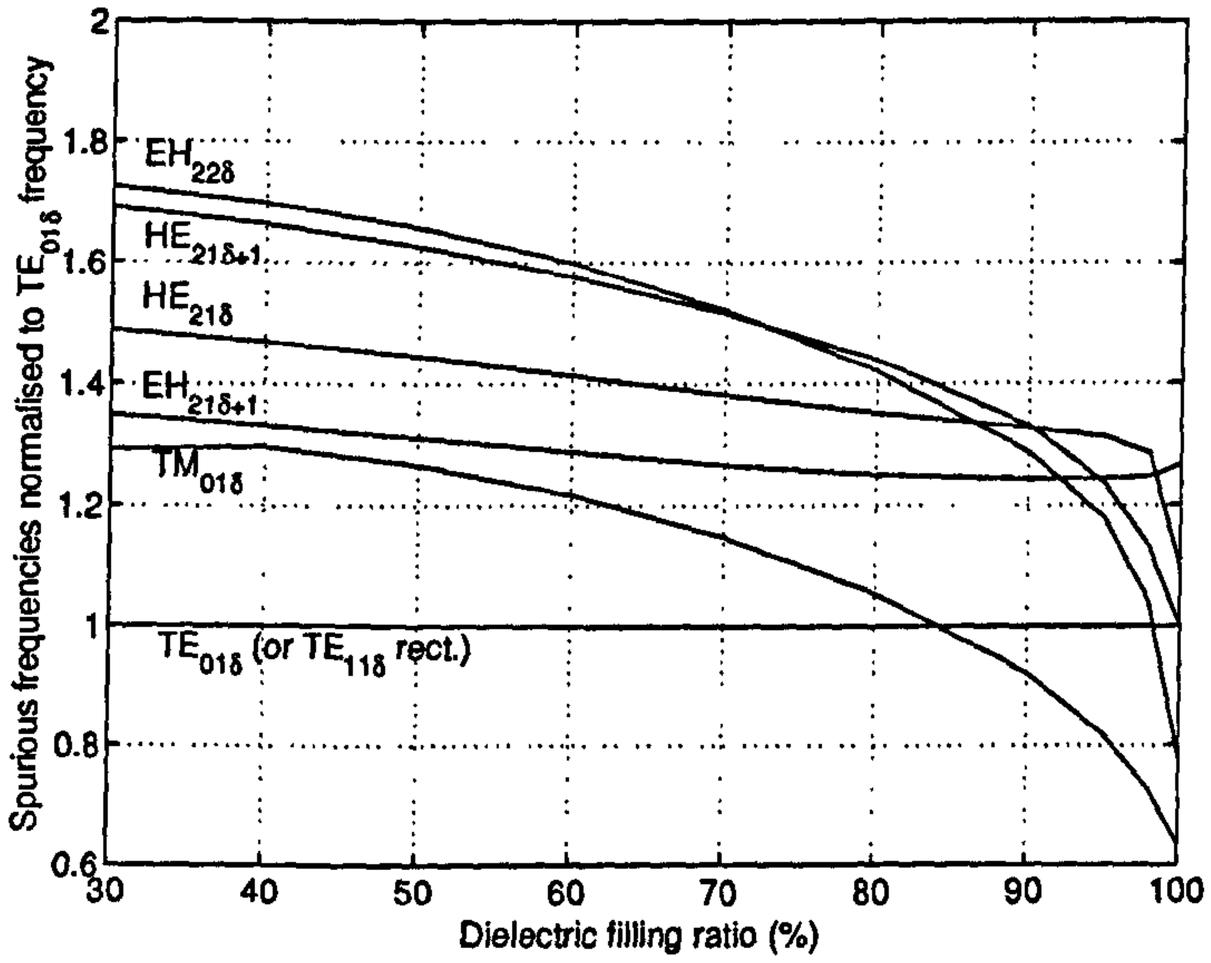

Figure 2.2: Variation of the first resonant frequencies of the cubic resonator normalised to the $TE_{01\delta}$ mode resonant frequency with the dielectric filling ratio. Resonator of dielectric constant 44.

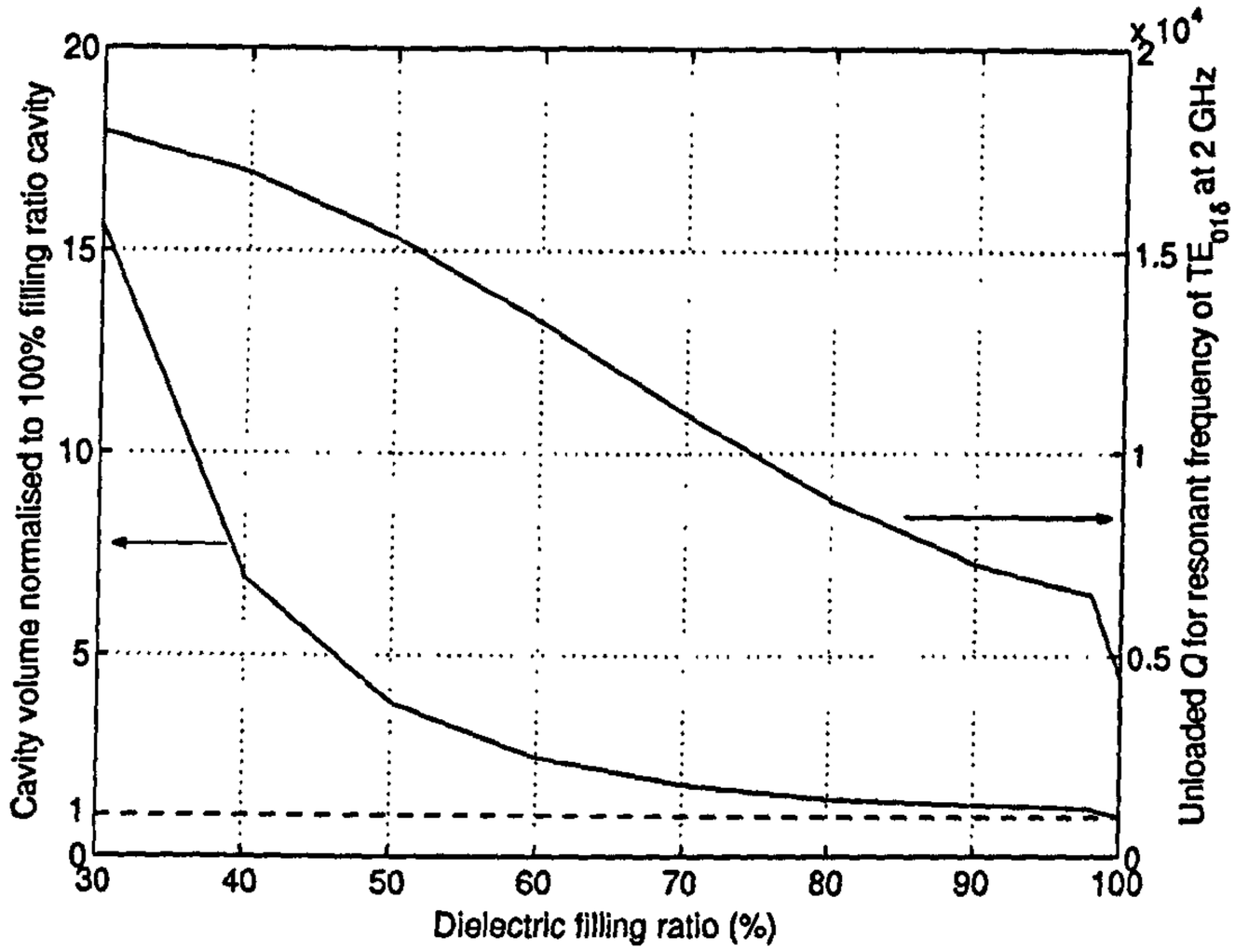

Figure 2.3: Variation with dielectric filling ratio of cavity volume and Q_u at 2 GHz for the $TE_{01\delta}$ mode cubic resonator. Resonator of dielectric constant 44 and loss tangent 5.55×10^{-5}. Silver plated cavity.

volume reduction compared to a single-mode $TE_{01\delta}$ resonator is then significant. A Q_u/volume of 217 cm^{-3} has been quoted [2] for a single-mode $TE_{01\delta}$ resonator with a Q_u of 18,500 at 2 GHz. FEM simulations give Q_u's/volume around 450 cm^{-3} for the triple-mode $TE_{01\delta}$ with similar Q_u, or a volume reduction of 50%.

Even more so than its single-mode counterpart, the triple-mode $TE_{01\delta}$ cubic resonator is best adapted for very high Q applications. Indeed, for high Q_u factors (i.e. large cavity dimensions), the triple-mode $TE_{01\delta}$ has the double advantage of good spurious performance and low dielectric filling ratio over the next modes of higher resonant frequencies, in particular the triple-mode $TM_{01\delta}$. For example, at 2 GHz and in a 63 mm cubic cavity, the ceramic material occupies 6.4% of the cavity volume in the case of the $TM_{01\delta}$, and 1.5% in the case of the $TE_{01\delta}$. For smaller Q_u values, these advantages disappear as the resonant frequencies and resonator dimensions for the two modes converge rapidly. While for a single-mode $TE_{01\delta}$, it is possible to keep good spurious separation down to Q_u values of 8,000 at 2 GHz, $TE_{01\delta}$ and $TM_{01\delta}$ modes are degenerate for a triple-mode DR of similar Q_u. Also, it is to be remembered that $TM_{01\delta}$ mode resonators usually have higher Q_u than $TE_{01\delta}$ mode resonators, particularly when the loss tangent of the dielectric material

used is not too low (as here with 5.55×10^{-5}) [52, 49, 54]. The difference is not too significant for large cavities (16% for 63 mm cavities at 2 GHz), but increases rapidly for smaller cavities (72% for 28 mm cavities at 2 GHz). It is then more interesting to use the $TM_{01\delta}$ mode for smaller Q applications (smaller than 10,000) and devise a resonator shape which gives good spurious performance. The combined dual-mode $TM_{01\delta}$ (or $EH_{11\delta}$), single-mode $TE_{01\delta}$ resonator [70] is a very good illustration of this.

The main field variations of the $TE_{01\delta}$ mode are plotted in Fig. 2.4 to 2.6. The axis origin and directions are shown in Fig. 2.7. The typical variations of the $TE_{01\delta}$ cylindrical resonator can be recognised. The maximum intensity of the electric field on the top and bottom faces of the resonator ($z = \pm c$ in Fig. 2.6) is 71% of that of the electric field on the same faces of a conventional single-mode $TE_{01\delta}$ resonator with $L_d/D = 0.4$. Significant frequency tuning should then still be achievable from a tuning element placed in proximity to one of the faces of the triple resonator.

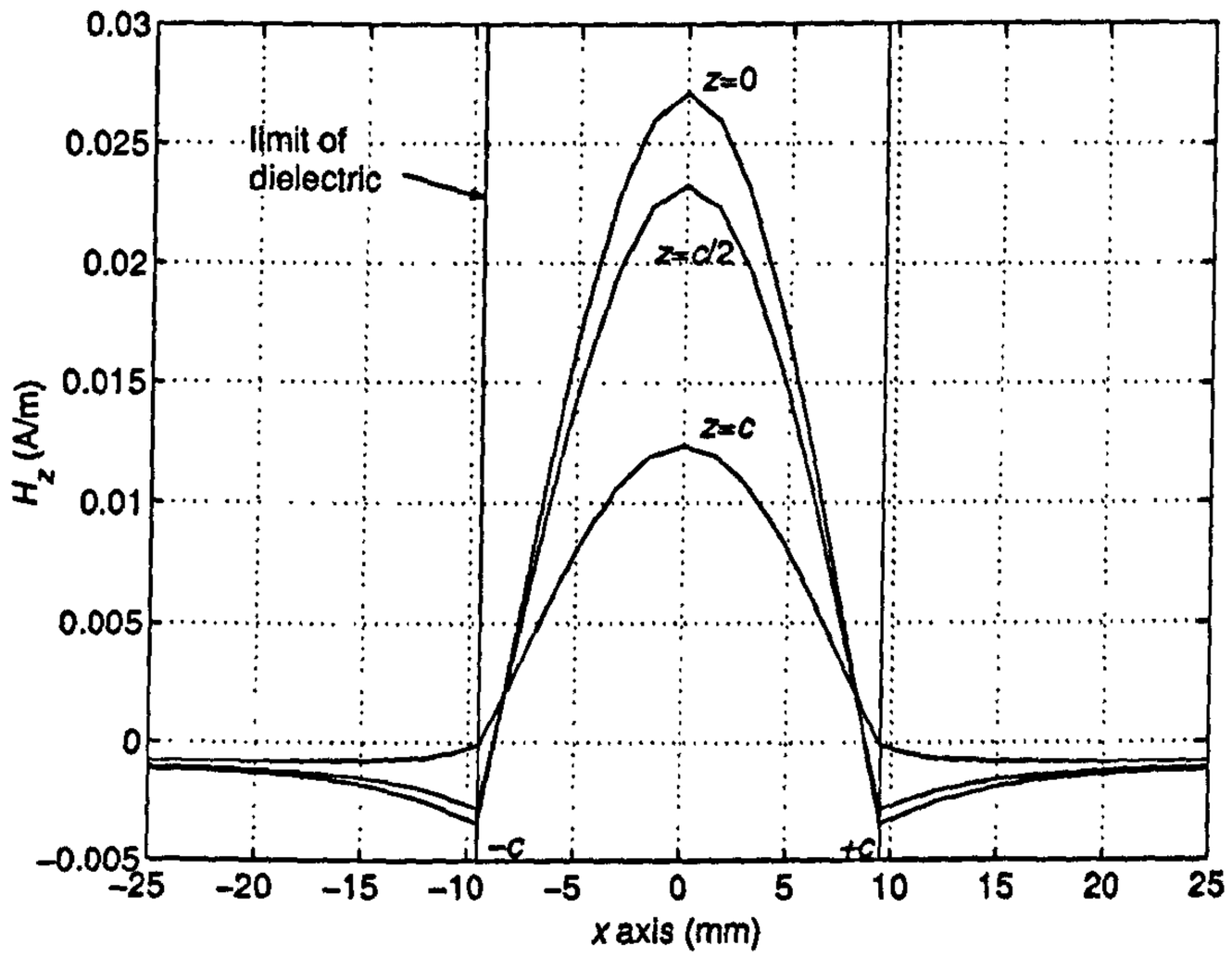

Figure 2.4: H_z field magnitude across the cubic resonator at $y = 0$

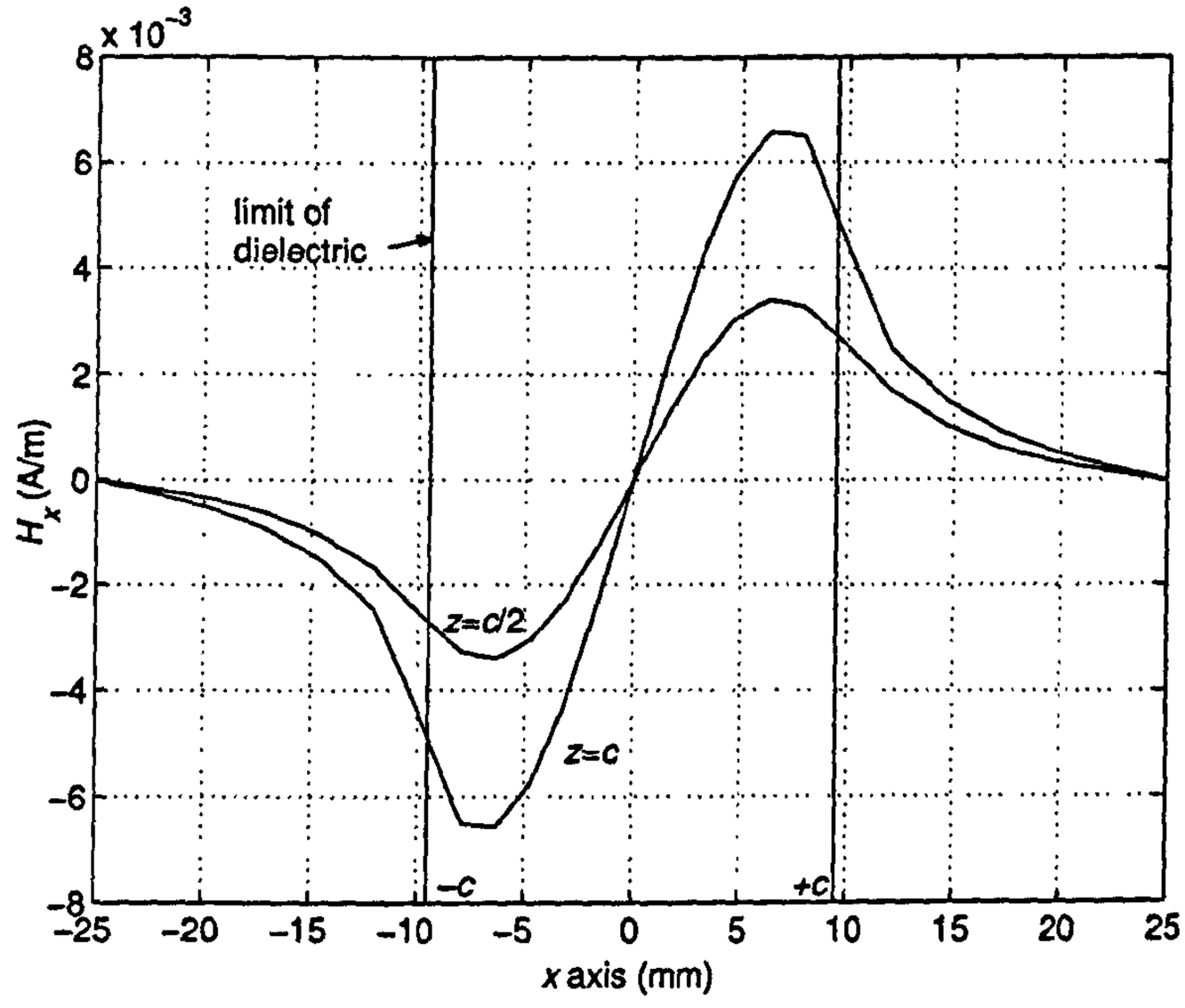

Figure 2.5: H_x field magnitude across the cubic resonator at $y = 0$

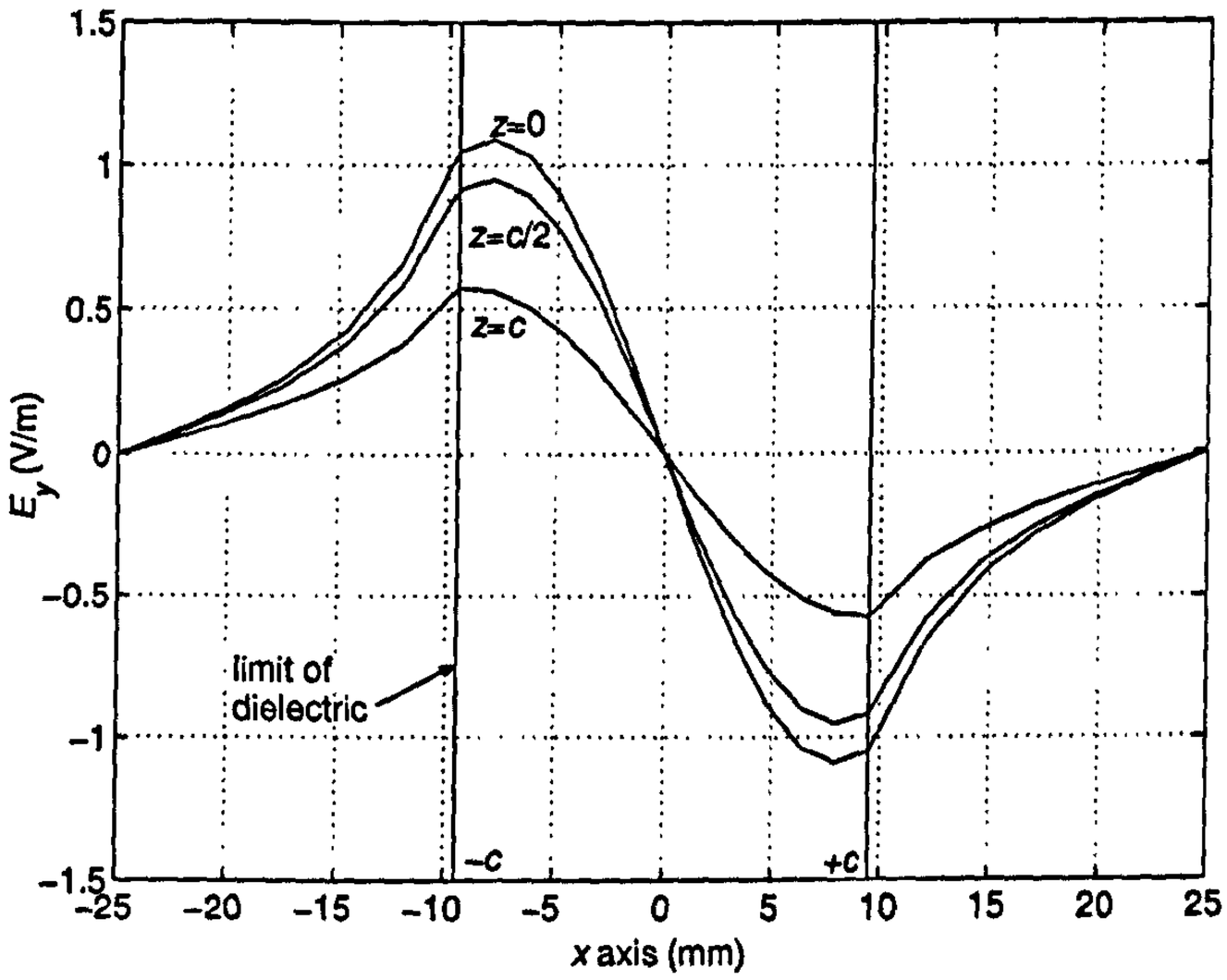

Figure 2.6: E_y field magnitude across the cubic resonator at $y = 0$

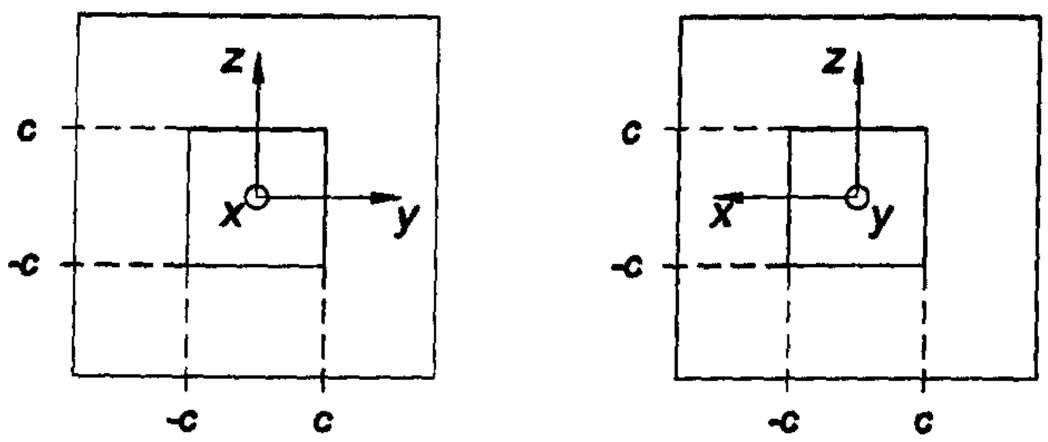

Figure 2.7: Definition of axis origin and orientations for plots of fields of the cubic resonator

2.3 Triple-mode even-odd mode $TE_{01\delta}$ hybrid reflection filters

2.3.1 Hybrid reflection filter theory

It is known that a bandstop filter response can be obtained by connecting a symmetrical bandpass filter across the outputs of a 90° hybrid, as in Fig. 2.8 [150]. The scattering parameters of the bandpass filter, $S_{11}^A(p)$ and $S_{12}^A(p)$, are related to its odd and even mode admittances, Y_o^A and Y_e^A by

$$S_{11}^A = \frac{1 - Y_e^A Y_o^A}{(1 + Y_e^A)(1 + Y_o^A)} \tag{2.1}$$

and

$$S_{12}^A = \frac{Y_e^A - Y_o^A}{(1 + Y_e^A)(1 + Y_o^A)} \tag{2.2}$$

As the network in Fig. 2.8 also has a line of symmetry, its scattering coefficients, $S_{11}^B(p)$ and $S_{12}^B(p)$, can be defined in a similar manner in terms of Y_o^B and Y_e^B.

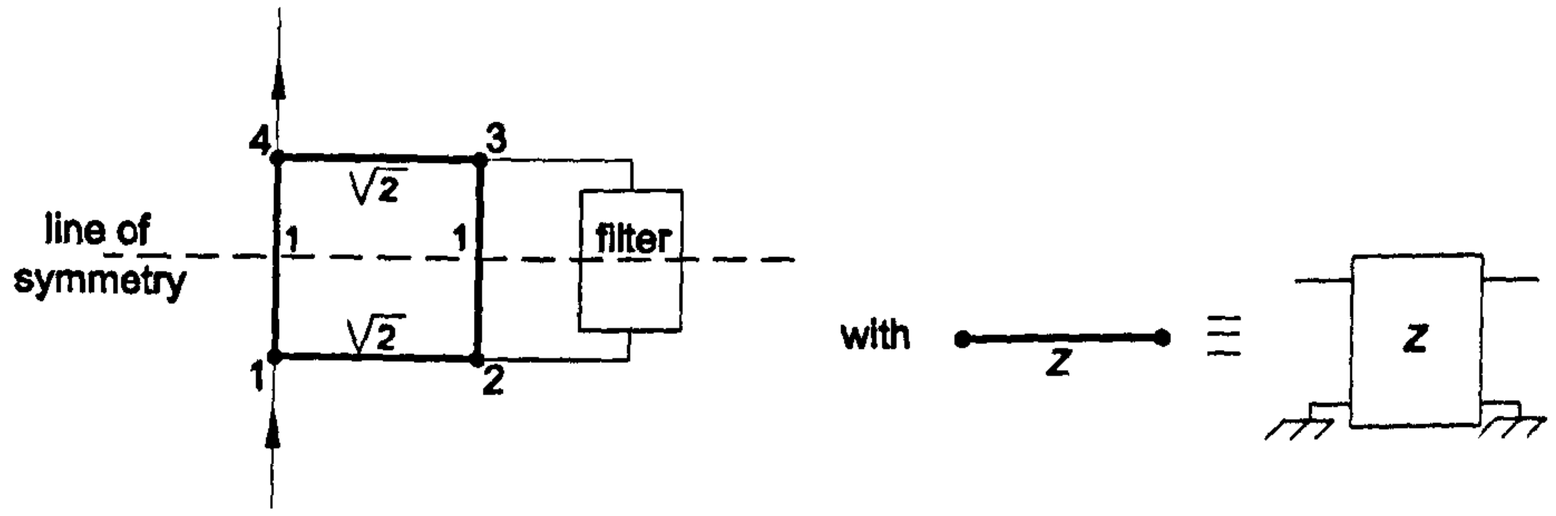

Figure 2.8: Reflection mode hybrid filter

Expressing Y_o^B and Y_e^B in terms of Y_o^A and Y_e^A and after manipulations, it is shown that

$$S_{11}^B = -jS_{12}^A \tag{2.3}$$

$$S_{12}^B = -jS_{11}^A \tag{2.4}$$

The scattering parameters are interchanged except for a constant phase shift of -90^o. With this method, bandstop filters can be realised without the need for $\lambda/4$ or $3\lambda/4$ lines between resonators.

Moreover, one can connect the odd and even mode networks of the bandpass filter, rather than the filter itself, across the outputs of the hybrid as shown in Fig. 2.9. To find the new expressions for $S_{11}^B(p)$ and $S_{12}^B(p)$, let us consider the scattering matrix of the hybrid:

$$\left[\mathbf{S}^{\mathbf{hybrid}}\right] = \frac{-1}{\sqrt{2}} \begin{bmatrix} 0 & j & 1 & 0 \\ j & 0 & 0 & 1 \\ 1 & 0 & 0 & j \\ 0 & 1 & j & 0 \end{bmatrix} \tag{2.5}$$

A signal incoming on port 1 of the hybrid will split equally between ports 2 and 3. The transmission coefficients are $-j/\sqrt{2}$ to port 2 and $-1/\sqrt{2}$ to port 3. The signals are then reflected by the even and odd mode networks of reflection coefficients Γ_e and Γ_o respectively. Each of these are in turn split between ports 1 and 4. The signal transmitted to port 4 is the transmission coefficient of the network S_{12}^B:

$$S_{12}^B = \frac{-1}{\sqrt{2}} \underbrace{\left(\frac{-j\Gamma_o}{\sqrt{2}}\right)}_{\text{from port 2}} + \frac{-j}{\sqrt{2}} \underbrace{\left(\frac{-\Gamma_e}{\sqrt{2}}\right)}_{\text{from port 3}} = \frac{j}{2}(\Gamma_o + \Gamma_e) \tag{2.6}$$

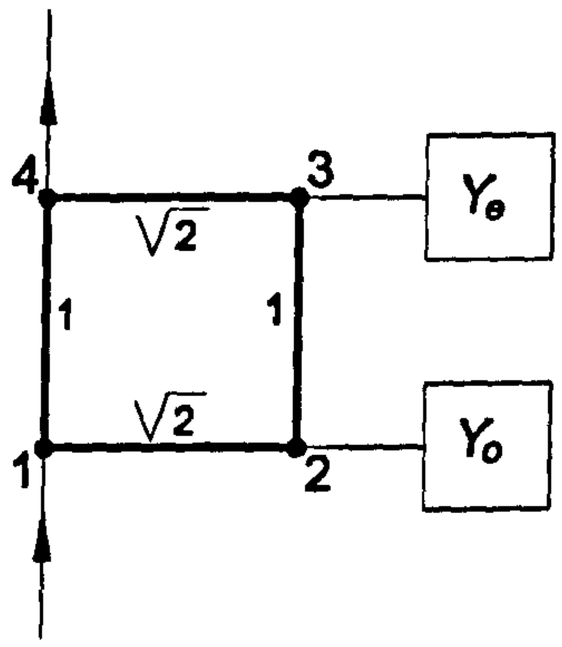

Figure 2.9: Odd and even mode alternative for the reflection mode hybrid filter

and the reflection coefficient S_{11}^B is:

$$S_{11}^B = \frac{-j}{\sqrt{2}} \underbrace{\left(\frac{-j\Gamma_o}{\sqrt{2}}\right)}_{\text{from port 2}} + \frac{-1}{\sqrt{2}} \underbrace{\left(\frac{-\Gamma_e}{\sqrt{2}}\right)}_{\text{from port 3}} = \frac{1}{2}(\Gamma_e - \Gamma_o) \tag{2.7}$$

As

$$\Gamma_e = \frac{Y_e^A - 1}{Y_e^A + 1} \tag{2.8}$$

and

$$\Gamma_o = \frac{Y_o^A - 1}{Y_o^A + 1} \tag{2.9}$$

it follows that

$$S_{12}^B = j\frac{-1 + Y_e^A Y_o^A}{(1 + Y_e^A)(1 + Y_o^A)} = -jS_{11}^A \tag{2.10}$$

$$S_{11}^B = j\frac{Y_e^A - Y_o^A}{(1 + Y_e^A)(1 + Y_o^A)} = S_{12}^A \tag{2.11}$$

So the basic behaviour of the network of Fig. 2.8 is retained, except for the phase shift of S_{11}^B.

If the odd and even networks are interchanged, the previous results still hold but S_{11}^B incurs a 180° phase shift. If a bandpass response is wanted from the network, an extra inverter can be added between the hybrid and either the even or the odd mode network. In the former case, the new network parameters are

$$S_{12}^B = -jS_{12}^A \tag{2.12}$$

$$S_{11}^B = S_{11}^A \tag{2.13}$$

In the latter case,

$$S_{12}^B = jS_{12}^A \tag{2.14}$$

$$S_{11}^B = -S_{11}^A \tag{2.15}$$

The even and odd mode admittances of the symmetrical filters considered here are reactance functions. They can be synthesised as ladder networks of the form shown in Fig. 2.10. Over a narrow bandwidth, which is usually the case for high Q_u resonator filters, the frequency invariant susceptances can be absorbed by the capacitors and inductors, effectively changing the resonant frequency and impedance of each resonator. With the exception of the first frequency invariant susceptance, these networks can thus be realised as a cascade of coupled resonators. In the case of a degree six filter, both the even and odd mode networks are readily realisable by the three resonators of a triple-mode DR cavity. This eliminates the need for couplings between cavities to realise symmetrical cross-coupled filters responses.

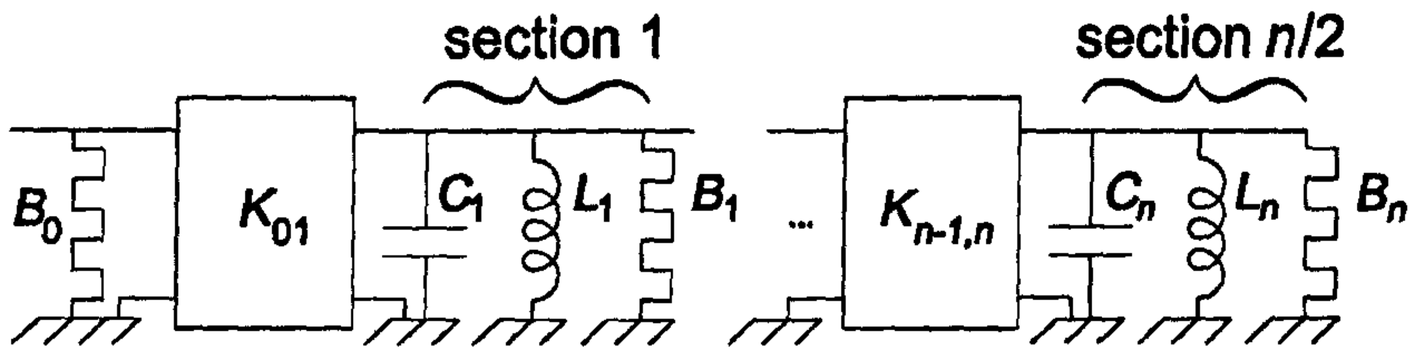

Figure 2.10: Odd and even mode network of symmetrical degree n bandpass filter

2.3.2 Design example: degree 6 elliptic bandstop filter

Network synthesis

The reflection mode filter method combined with the triple-mode $TE_{01\delta}$ cubic resonator technology is particularly interesting in the case of the receive bandstop filter presented in Section 1.1. The specifications for this filter are repeated in Table 2.1.

Table 2.1: *Specifications for receive notch filter*

Frequency (MHz)	Insertion loss relative to passband (dB)
845	−1.5
845.2	−20.0
846.3	−20.0
846.5	−1.5

They are met by an elliptic filter with the following characteristics:

- Degree : 6

- 3 dB bandwidth : 1.31 MHz

- Q factor : 30,000

- Stopband insertion loss ripple level : 22 dB

- Passband return loss ripple level : 22 dB

Because both ripple levels are equal, we have:

$$|S_{11}(j\omega)|^2 = |S_{12}(j/\omega)|^2 \tag{2.16}$$

The expression for the insertion loss is then

$$|S_{11}(j\omega)|^2 = \frac{F_n^2(\omega)}{1 + F_n^2(\omega)} \tag{2.17}$$

with

$$F_n = \frac{(\omega^2 - \omega_1^2)(\omega^2 - \omega_2^2)(\omega^2 - \omega_3^2)}{(1 - \omega^2\omega_1^2)(1 - \omega^2\omega_2^2)(1 - \omega^2\omega_3^2)} \tag{2.18}$$

The transmission zeros are located at ω_1, ω_2 and ω_3. The poles of $|S_{12}(j\omega)|^2$ are at $1/\omega_1$, $1/\omega_2$ and $1/\omega_3$. ω_1, ω_2 and ω_3 are the zeros of F_n and are calculated from the equations derived in [151, 9]. We obtain $\omega_1 = 0.9484$, $\omega_2 = 0.8155$ and $\omega_3 = 0.3649$. Retaining the left half-plane poles of $|S_{11}(j\omega)|^2$ as poles of $S_{11}(p)$ yields

$$S_{11}(p) = \frac{-0.9968p^6 - 1.6922p^4 - 0.8039p^2 - 0.0794}{p^6 + 1.9920p^5 + 3.734p^4 + 4.0252p^3 + 3.7347p^2 + 1.9920p + 1} \tag{2.19}$$

$$S_{12}(p) = \frac{0.0794p^6 + 0.8039p^4 + 1.6922p^2 + 0.9968}{p^6 + 1.9920p^5 + 3.734p^4 + 4.0252p^3 + 3.7347p^2 + 1.9920p + 1} \tag{2.20}$$

Y_o and Y_e follow from $S_{11}(p)$ and $S_{12}(p)$ since

$$Y_e(p) = \frac{1 - S_{11}(p) + S_{12}(p)}{1 + S_{11}(p) - S_{12}(p)} \tag{2.21}$$

and

$$Y_o(p) = \frac{1 - S_{11}(p) - S_{12}(p)}{1 + S_{11}(p) + S_{12}(p)} \tag{2.22}$$

The even and odd admittances of symmetrical cross-coupled ladder networks have to be complex conjugates. Considering Eq. 2.21, Eq. 2.22 and the fact that the numerator of $S_{12}(p)$ is an even polynomial, this is achieved by multiplying $S_{12}(p)$ by j. Then,

$$Y_e(p) = \frac{25.1499jp^3 - 15.6939p^2 + 29.2789jp - 18.4900}{p^3 + 25.7127jp^2 - 7.0843p + 17.0766j} \tag{2.23}$$

and

$$Y_o(p) = \frac{-25.1499jp^3 - 15.6939p^2 - 29.2789jp - 18.4900}{p^3 - 25.7127jp^2 - 7.0843p - 17.0766j} \tag{2.24}$$

Finally, continued fraction expansion of $Y_e(p)$ and $Y_o(p)$ yields the component values of the even and odd mode networks in Table 2.2. At a later stage of the network synthesis, the frequency invariant susceptances B_1 to B_3 will be absorbed in the resonators. However, B_0 cannot be associated with any resonator. Rather than realising it separately, for example by approximating it to a short or open-circuited stub at the filter frequency, it is more convenient to modify the first part of each network as shown in Fig. 2.11. The first susceptance B_0 and first admittance inverter

Table 2.2: *Element values for the even and odd mode networks. Network layout as in Fig. 2.10*

Element	Even mode network	Odd mode network
B_0 (Ω^{-1})	25.1499	−25.1499
K_{01} (Ω^{-1})	25.1193	25.1193
C_1 (F)	1	1
B_1 (Ω^{-1})	25.3839	−25.3839
K_{12} (Ω^{-1})	0.780961	0.780961
C_2 (F)	1	1
B_2 (Ω^{-1})	−0.561404	0.561404
K_{23} (Ω^{-1})	0.389350	0.389350
C_3 (F)	1	1
B_3 (Ω^{-1})	0.890178	−0.890178

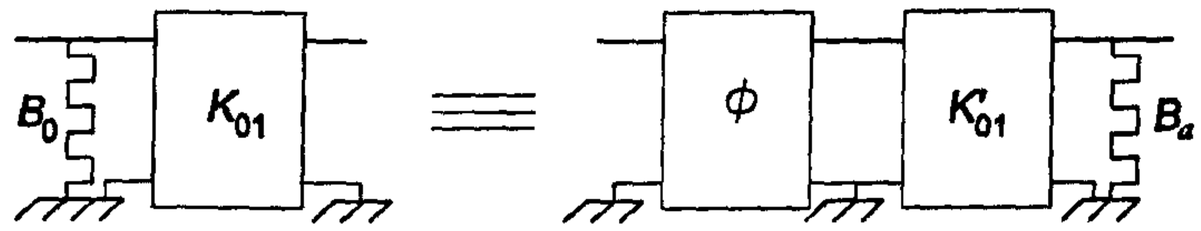

Figure 2.11: Substitution for the first two elements of the even and odd networks

K_{01} are substituted by a phase shifter of impedance 1 Ω followed by an inverter of admittance K'_{01} and a shunt frequency invariant susceptance B_a. The latter will be absorbed into the first resonator together with B_1. The transfer matrices of the original network is:

$$[\mathbf{T_1}] = \begin{bmatrix} 1 & 0 \\ jB_0 & 1 \end{bmatrix} \begin{bmatrix} 0 & j/K_{01} \\ jK_{01} & 0 \end{bmatrix} = \begin{bmatrix} 0 & j/K_{01} \\ jK_{01} & -B_0/K_{01} \end{bmatrix} \tag{2.25}$$

The transfer matrix of the substitute network is:

$$\begin{aligned} [\mathbf{T_2}] &= \begin{bmatrix} \cos\phi & j\sin\phi \\ j\sin\phi & \cos\phi \end{bmatrix} \begin{bmatrix} 0 & j/K'_{01} \\ jK'_{01} & 0 \end{bmatrix} \begin{bmatrix} 1 & 0 \\ jB_a & 1 \end{bmatrix} \\ &= \begin{bmatrix} -K'_{01}\sin\phi - B_a\frac{\cos\phi}{K'_{01}} & j\frac{\cos\phi}{K'_{01}} \\ jK'_{01}\cos\phi - jB_a\frac{\sin\phi}{K'_{01}} & -\frac{\sin\phi}{K'_{01}} \end{bmatrix} \end{aligned} \tag{2.26}$$

Equating the two gives the expressions for K'_{01}, B_a and ϕ:

$$K'_{01} = \frac{K_{01}}{\sqrt{1 + B_0^2}} \tag{2.27}$$

$$B_a = -\frac{K_{01}^2 B_0}{1 + B_0^2} \tag{2.28}$$

$$\phi = \sin^{-1}\left(\frac{K'_{01} B_0}{K_{01}}\right) \tag{2.29}$$

Table 2.3 shows the new element values for the networks of Table 2.2.

The lowpass networks are then customised as described in Section 1.2. The capacitors are transformed into bandpass LC resonators at 845.75 MHz, in which the frequency invariant susceptances are absorbed using the reactance slope parameter method [9]. The LC resonators are then converted into short circuited stub resonators, by equating the resonant frequency and the slope of the admittance of the two resonators at this frequency (see Section 1.2). Finally, both networks are normalised to 50 Ω. The final filter network and its frequency response are shown in Figs. 2.12 and 2.13. Here, the transformation from LC resonators to short circuited stubs is accurate because all the susceptances absorbed by the resonators were relatively small. As a result, none of the resonant frequencies was differing significantly from the centre frequency of the filter passband. Had the substitution of Fig. 2.11 not happened, B_0 would have not cancelled most of B_1. The susceptances associated with the first resonator of each subnetwork would have been very large, resulting in resonant frequencies of 862.6 MHz and 829.3 MHz. In this case, the transformation into stub resonators should have been executed differently, by equating the absolute value and the slope of the resonator reactances at the centre of the filter passband frequency.

Table 2.3: *Modified first element values for the even and odd mode networks. Network layout as in Fig. 2.10*

Element	Even mode network	Odd mode network
ϕ (°)	87.66	−87.66
K'_{01} (Ω^{-1})	0.997993	0.997993
B_a (Ω^{-1})	−25.0491	25.0491

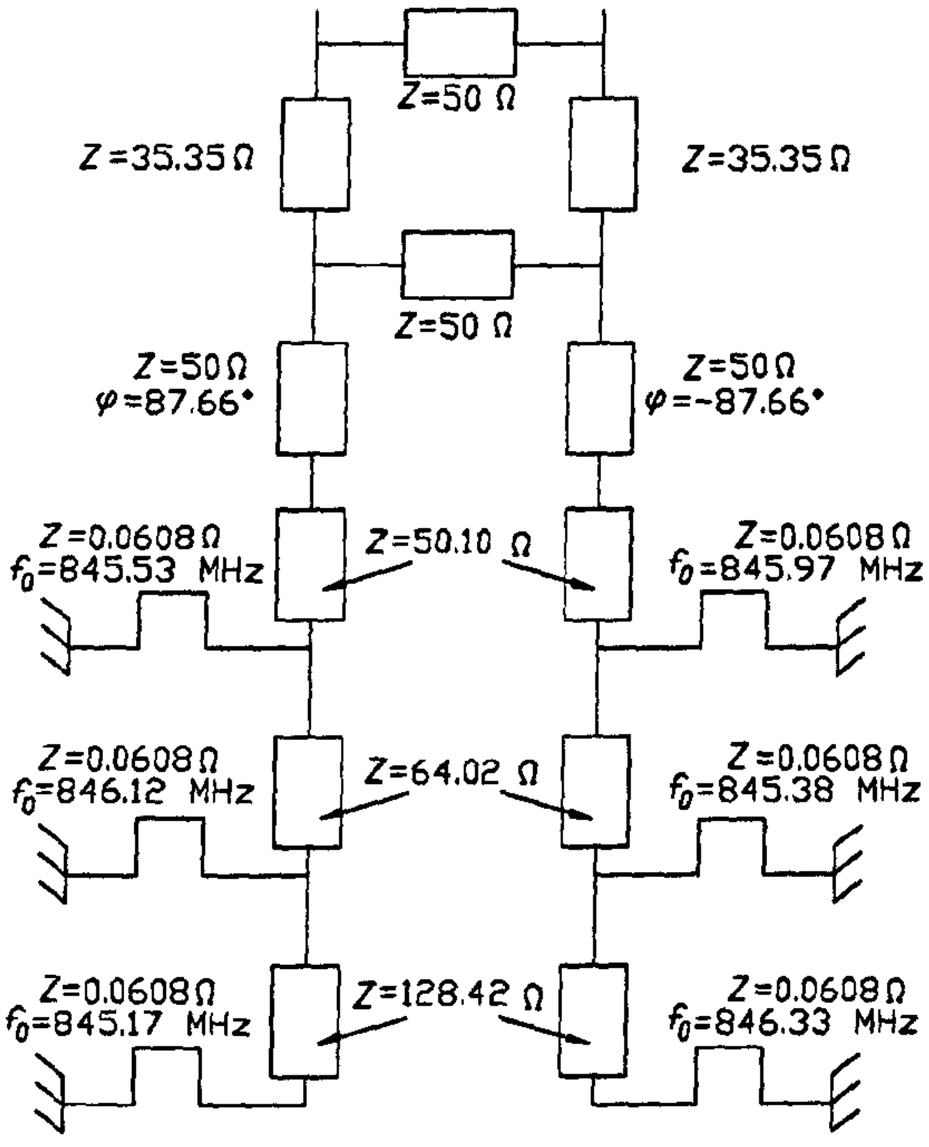

Figure 2.12: Final equivalent network for the degree 6 reflection mode hybrid elliptic filter

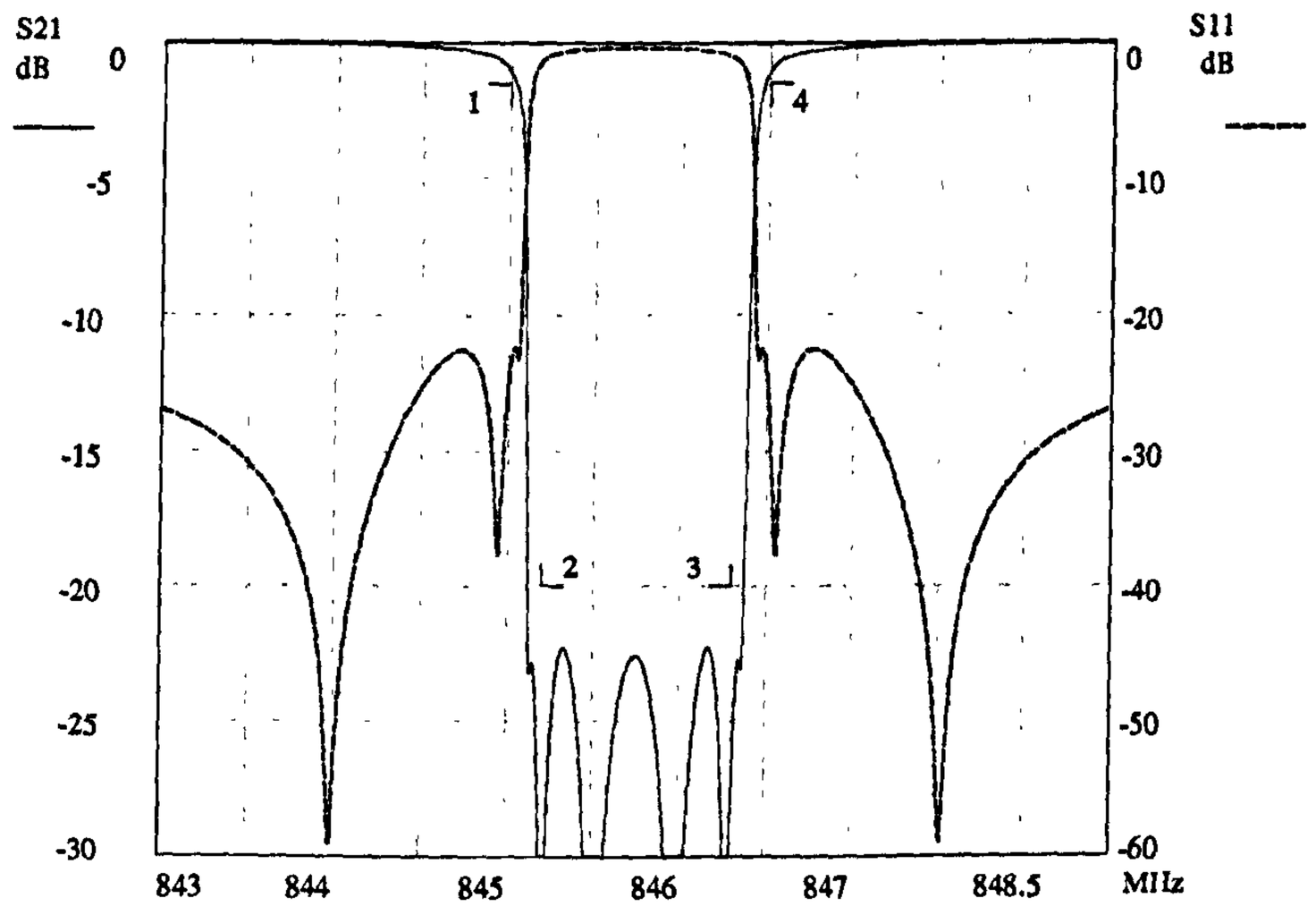

Figure 2.13: Simulated response of the degree 6 elliptic hybrid reflection mode cubic resonator filter

Cancellation of spurious couplings

An advantage of the hybrid even-odd mode layout is its immunity to unwanted couplings. These are very difficult to eliminate in conventional multimode cavity filters. They can be due to misalignment of the resonator and its support. Also, as the tuning elements and the coupling mechanisms are inserted in the cavity, some spurious couplings appear, although careful design usually keeps them at a limited level. In the case of a triple-mode resonator, a first spurious coupling can occur between modes 1 and 3. One could add an extra coupling tuning element in the cavity in order to cancel this coupling. However, this is unnecessary as the effect of this coupling can be counteracted by modifying the values of the existing couplings as follows.

The coupling matrices [152] of both the odd or even mode lowpass networks synthesised previously in this section have the following form:

$$[\mathbf{M_c}] = \begin{bmatrix} B_0 & K_{01} & 0 & 0 \\ K_{01} & B_1 & K_{12} & 0 \\ 0 & K_{12} & B_2 & K_{23} \\ 0 & 0 & K_{23} & B_3 \end{bmatrix} \tag{2.30}$$

Let us suppose that a spurious coupling between modes 1 and 3 of value K'_{13} exists when the network is effectively tuned. The other couplings can be modified accordingly to a new value B'_i or K'_{ij} by applying a rotation to the coupling matrix $[\mathbf{M_c}]$ [152]. In this case, a rotation of angle θ of its second row and column with respect to its third row and column is used. The coupling matrix $[\mathbf{M_c}]$ is post- and pre-multiplied by the rotation matrix $[\mathbf{R_{23}}]$ and its transpose $[\mathbf{R_{23}^T}]$ respectively to give the coupling matrix of the new network $[\mathbf{M'_c}]$.

$$[\mathbf{M'_c}] = [\mathbf{R_{23}^T}][\mathbf{M_c}][\mathbf{R_{23}}] \tag{2.31}$$

with

$$[\mathbf{M'_c}] = \begin{bmatrix} B'_0 & K'_{01} & 0 & 0 \\ K'_{01} & B'_1 & K'_{12} & K'_{13} \\ 0 & K'_{12} & B'_2 & K'_{23} \\ 0 & K'_{13} & K'_{23} & B'_3 \end{bmatrix} \tag{2.32}$$

and

$$[\mathbf{R_{23}}] = \begin{bmatrix} 1 & 0 & 0 & 0 \\ 0 & 1 & 0 & 0 \\ 0 & 0 & \cos(\theta) & \sin(\theta) \\ 0 & 0 & -\sin(\theta) & \cos(\theta) \end{bmatrix} \tag{2.33}$$

The expression for K'_{13} can be found after expanding the right hand side of Eq. 2.31:

$$K'_{13} = \sin(\theta)\ K_{12} \tag{2.34}$$

This yields the value for θ:

$$\theta = \sin^{-1}\left(\frac{K'_{13}}{K_{12}}\right) \tag{2.35}$$

Substituting for θ in Eq. 2.31, expressions for all B'_i and K'_{ij} are derived as a function of B_i, K_{ij} and K'_{13}. Solutions for θ only exists for values of $|K'_{13}|$ less than $|K_{12}|$. In practice, this does not represent a restriction as the spurious coupling should only be a fraction of an intentional coupling such as K_{12}.

Other spurious couplings in the triple-mode cavity can exist when the input coupling loop also couples into modes 2 and 3. In these cases, two successive rotations are necessary to recover the initial coupling matrix. For a coupling between input and mode 2, a rotation of angle θ_1 of row and column 2 with respect to row and column 3 is applied to $[\mathbf{M_c}]$ as before. It is then followed by a rotation of angle θ_2 of row and column 1 with respect to row and column 2:

$$[\mathbf{M'_c}] = [\mathbf{R_{12}^T}][\mathbf{R_{23}^T}][\mathbf{M_c}][\mathbf{R_{23}}][\mathbf{R_{12}}] \tag{2.36}$$

with

$$[\mathbf{M'_c}] = \begin{bmatrix} B'_0 & K'_{01} & K'_{02} & 0 \\ K'_{01} & B'_1 & K'_{12} & 0 \\ K'_{02} & K'_{12} & B'_2 & K'_{23} \\ 0 & 0 & K'_{23} & B'_3 \end{bmatrix} \tag{2.37}$$

Expanding the right hand side of Eq. 2.36 gives

$$K'_{02} = \sin(\theta_2)\ K_{01} \tag{2.38}$$

or

$$\theta_2 = \sin^{-1}\left(\frac{K'_{02}}{K_{01}}\right) \tag{2.39}$$

Also, because of the first rotation, the expression for K'_{13} has to be forced to zero, giving θ_1 as the solution of the Eq. 2.40, which can be solved numerically.

$$z^4 + \frac{2(\sin\theta_2(B_2 - B_3) + \cos\theta_2 K_{12})}{\sin\theta_2 K_{23}} z^3 - 6z^2 + \frac{2(\sin\theta_2(B_3 - B_2) + \cos\theta_2 K_{12})}{\sin\theta_2 K_{23}} z + 1 = 0 \tag{2.40}$$

with

$$z = \tan\frac{\theta_1}{2} \tag{2.41}$$

Values of K'_{02} that can be cancelled are restricted by Eq. 2.39, as $|K'_{02}|$ needs to be less than $|K_{01}|$. This would normally be the case and, as such, does not present a real limitation. It can also be shown that Eq. 2.40 does not present any further restriction as it always has a solution. Rearranging Eq. 2.40 yields:

$$\tan\theta_2 = \frac{\sin\theta_1 K_{12}}{0.5\sin 2\theta_1(B_2 - B_3) + \cos 2\theta_1 K_{23}} \tag{2.42}$$

As K'_{02} ranges from $-K_{01}$ to K_{01}, the left hand side of Eq. 2.42 ranges from $-\infty$ to $+\infty$. However, so does the right hand side as θ_1 is varied from $\frac{1}{2}\tan^{-1}\frac{2K_{23}}{B_3 - B_2}$ to $\frac{1}{2}\tan^{-1}\frac{2K_{23}}{B_3 - B_2} + \pi$, so that a solution can always be found.

Couplings from the input to mode 3 are dealt with by a rotation of angle θ_1 of row and column 2 with respect to row and column 3 followed by a rotation of angle θ_2 of row and column 1 with respect to row and column 3:

$$[\mathbf{M'_c}] = [\mathbf{R^T_{13}}][\mathbf{R^T_{23}}][\mathbf{M_c}][\mathbf{R_{23}}][\mathbf{R_{13}}] \tag{2.43}$$

with

$$[\mathbf{M'_c}] = \begin{bmatrix} B'_0 & K'_{01} & 0 & K'_{03} \\ K'_{01} & B'_1 & K'_{12} & 0 \\ 0 & K'_{12} & B'_2 & K'_{23} \\ K'_{03} & 0 & K'_{23} & B'_3 \end{bmatrix} \tag{2.44}$$

The same procedure as above gives

$$\theta_2 = \sin^{-1}\left(\frac{K'_{03}}{K_{01}}\right) \tag{2.45}$$

and

$$\cos\theta_2\sin\theta_2(B_3 - B_1) + (2(\cos\theta_2^2 - \sin\theta_2^2)K_{12} + 4\cos\theta_2\sin\theta_2 K_{23})z^3 - 2\cos\theta_2\sin\theta_2((B_1 + B_3) + 2B_2)z^2 + (2(\cos\theta_2^2 - \sin\theta_2^2)K_{12} - 4\cos\theta_2\sin\theta_2 K_{23})z + \cos\theta_2\sin\theta_2(B_3 - B_1) = 0 \tag{2.46}$$

with

$$z = \tan\frac{\theta_1}{2} \tag{2.47}$$

as the system of equations yielding θ_1 and θ_2. Similarly to the previous restrictions, $|K'_{03}|$ should be smaller than $|K_{01}|$. However, this time, Eq. 2.46 cannot always be solved for θ_1 real and imposes a further restriction on K'_{03}. For the filter example considered previously, $|K'_{03}|$ has to be inferior to 0.7554 Ω^{-1}, which represents about 3% of the intentional input coupling K_{01}.

This demonstrates that, in most cases and with a careful design, the exact filter response will be obtainable in spite of the existence of some spurious couplings.

Physical realisation

Two triple-mode cubic resonators were used to realise the odd and even mode networks. The resonators consist of 100 mm cubic cavities in the centre of which are located 46 mm cubes of ceramic with relative dielectric constant 44. The alumina supports, of large diameter, decrease the resonant frequencies of the three modes by the same amount (see Section 2.4.1). Each network is tuned separately by setting the reflected delay to have the right frequency response. The resonant frequency of each mode is tuned by conventional dielectric tuning discs perpendicular to the symmetry axis of the mode. However, these only provide a differential tuning. As a given mode is intentionally tuned down by the corresponding tuning disc, the resonant frequencies of two other modes decrease even more rapidly. With tuning discs of permittivity 44 and diameter 28 mm, 1.9 MHz of differential tuning is achieved. A more detailed study of the frequency tuning of the triple-mode resonator is presented in Section 2.4.1. As for single-mode $TE_{01\delta}$ filters, the different couplings are realised through the magnetic fields of the modes, as the electric fields are almost entirely concentrated in the dielectric. The input coupling into the first mode is realised by a grounded metal loop. The coupling between modes 1 and 2 and modes 2 and 3 are created by conductive loops, isolated on a plastic screw and located on the side opposite the third mode frequency tuning disc. The resonator layout is illustrated in Fig. 2.14. The modes are represented according to the notation in Fig. 2.15.

The hybrid is realised as coaxial air transmission lines with a ground plane spacing of 10 mm, contributing an extra 0.03 dB to the bandedge loss if silver plated. The photograph in Fig. 2.16 pictures the filter and hybrid assembly. An extra

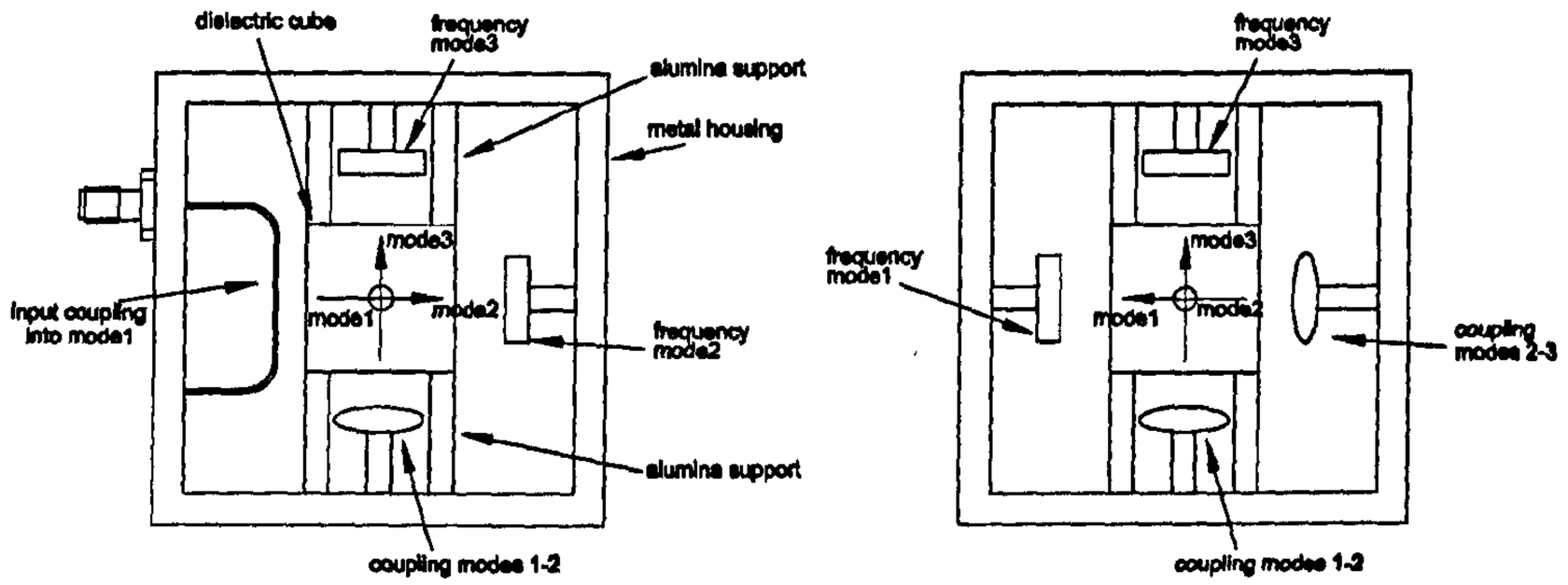

Figure 2.14: Triple-mode resonator layout for the even and odd networks

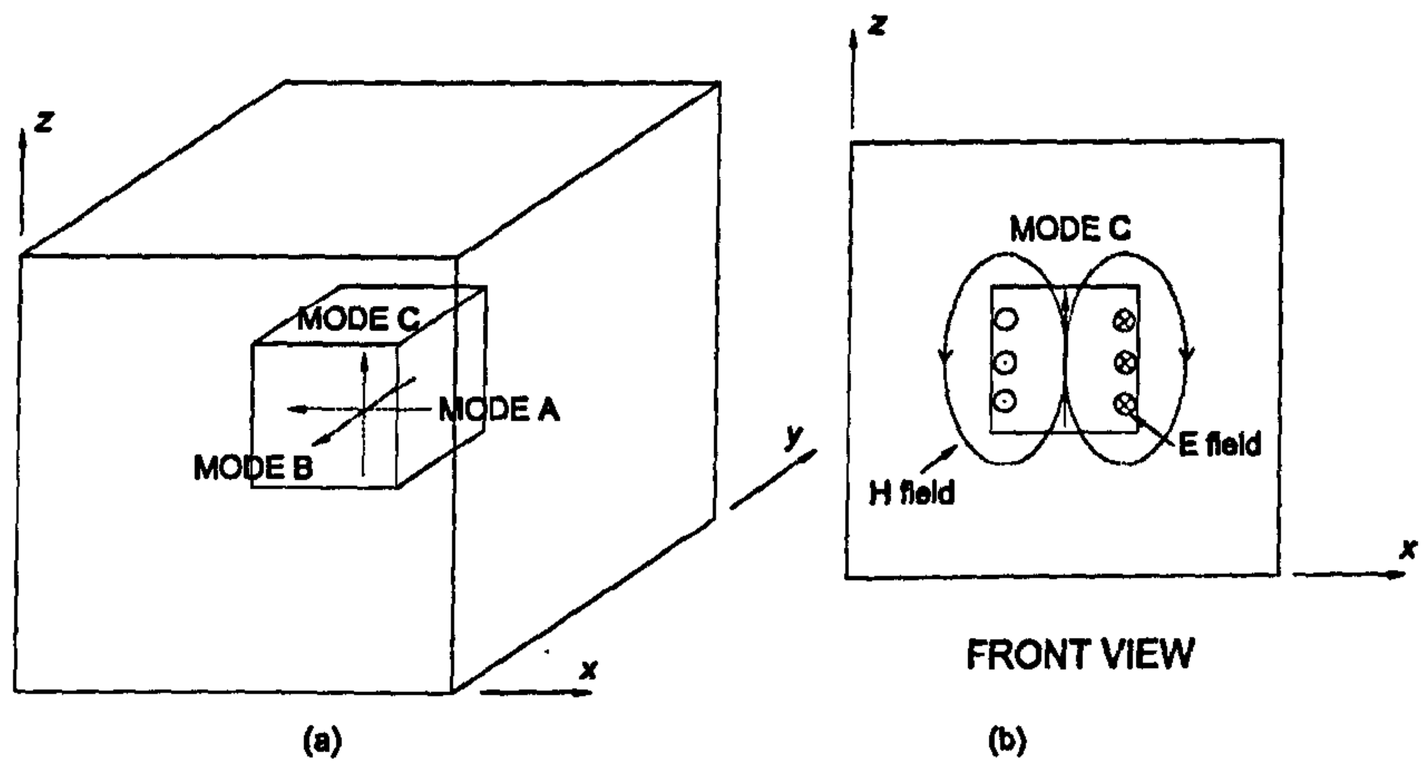

Figure 2.15: (a) Symbolic representation for the three modes of the cubic resonator. (b) Fields and representation for mode C.

length of line at the even mode output port of the hybrid provides the necessary $2 \times \phi = 2 \times 87.66^o = 175.32^o$ of phase shift. The measured difference in phase between the two outputs is 267.29^o instead of the theoretical $175.32^o + 90^o = 265.32^o$, corresponding to a 0.7% inaccuracy. Fig. 2.17 and Fig. 2.18 show the measured hybrid response at the even mode output port.

The filter response, shown in Fig. 2.19, has a centre frequency of 835 MHz. This lower frequency is due to the combined effect of the dielectric tuners and the alumina supports. It is also more lossy than the simulated response for a filter with unplated cavities and hybrid. After correction for the difference in stopband bandwidth, the extra loss is calculated to be 0.5 dB, which corresponds to an average Q_u of only 16,000. It is believed to be due mainly to contamination of the resonators. However,

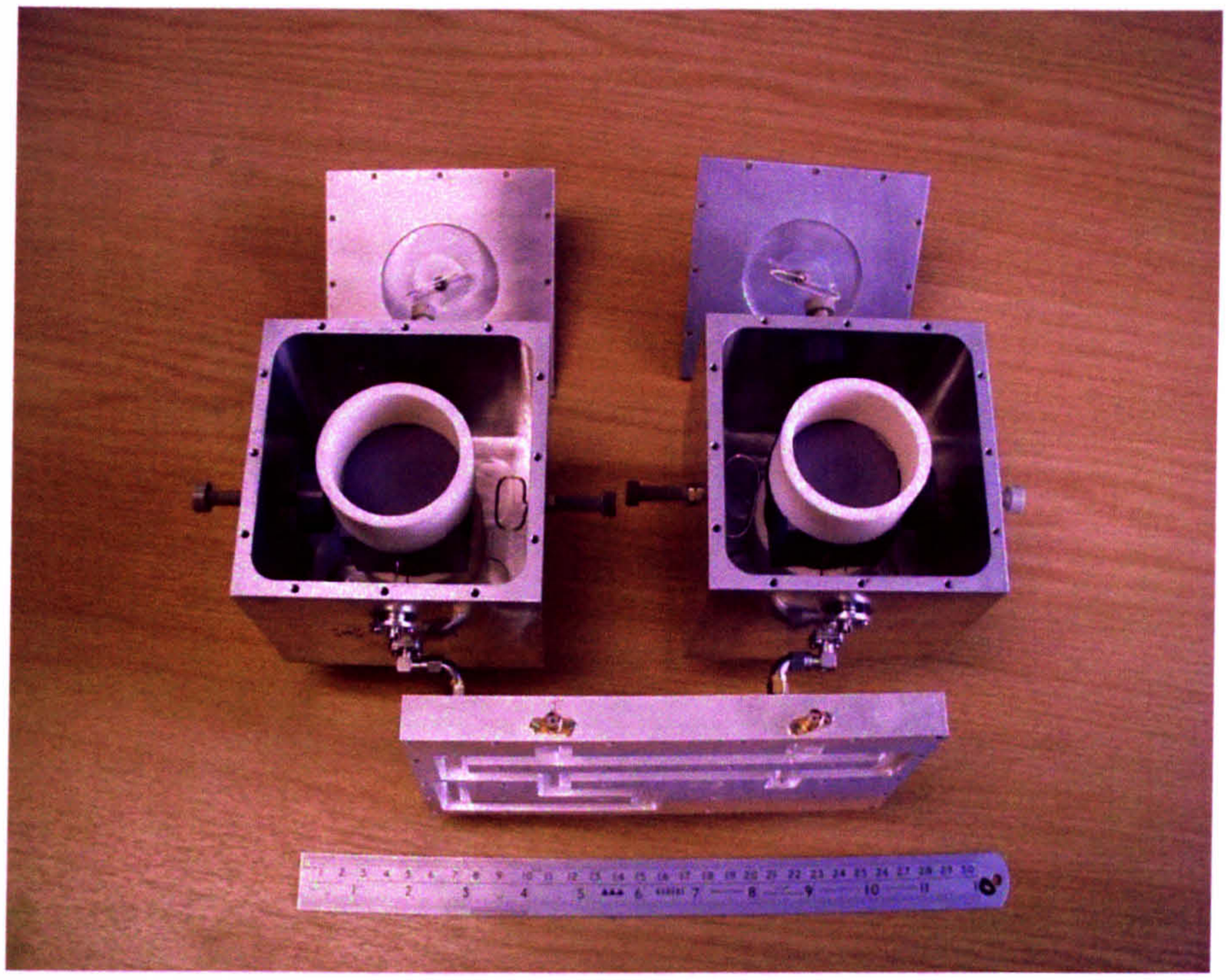

Figure 2.16: Filter and hybrid assembly

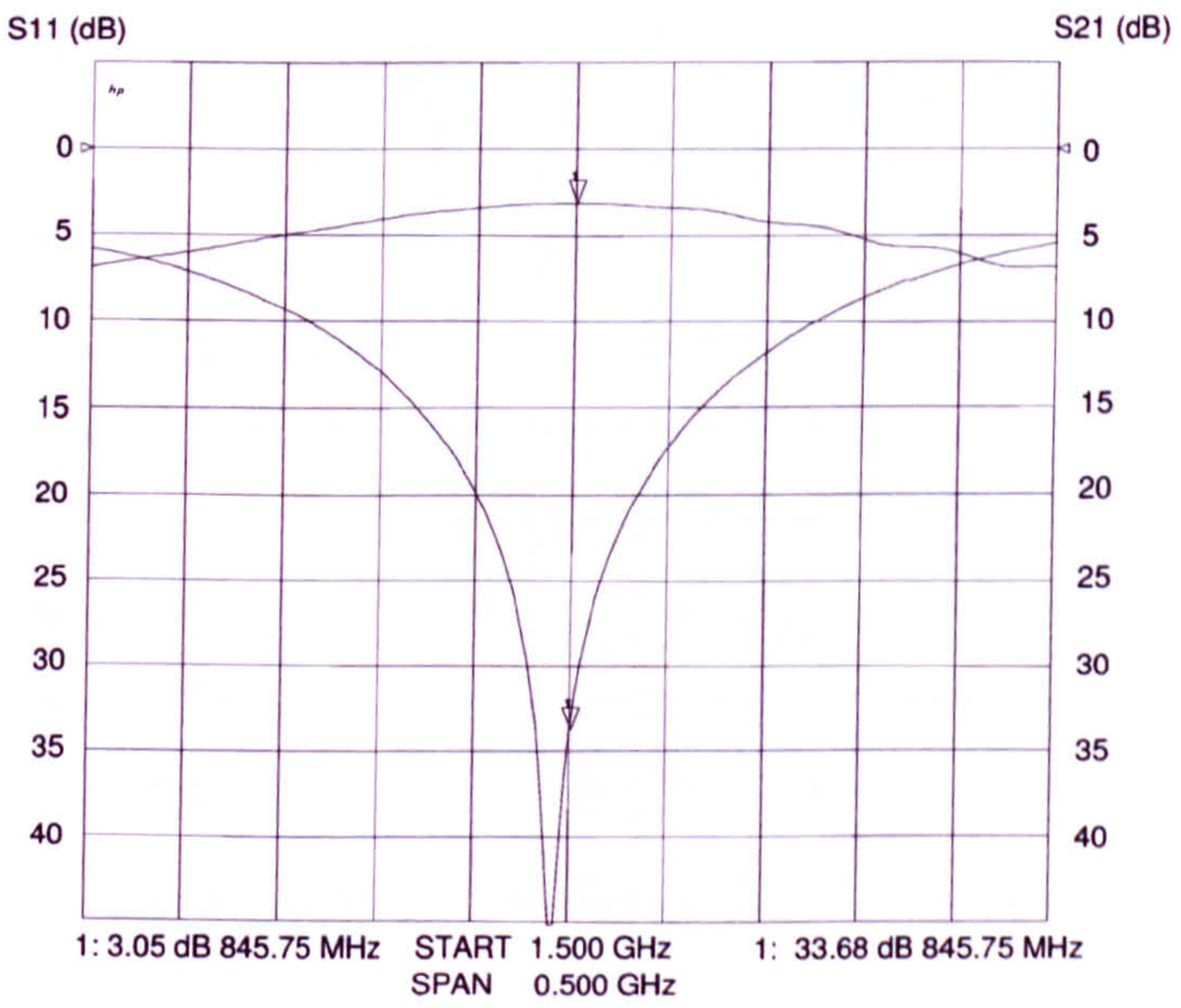

Figure 2.17: Hybrid response at the even mode output port. Input on port diagonally opposite. Magnitude.

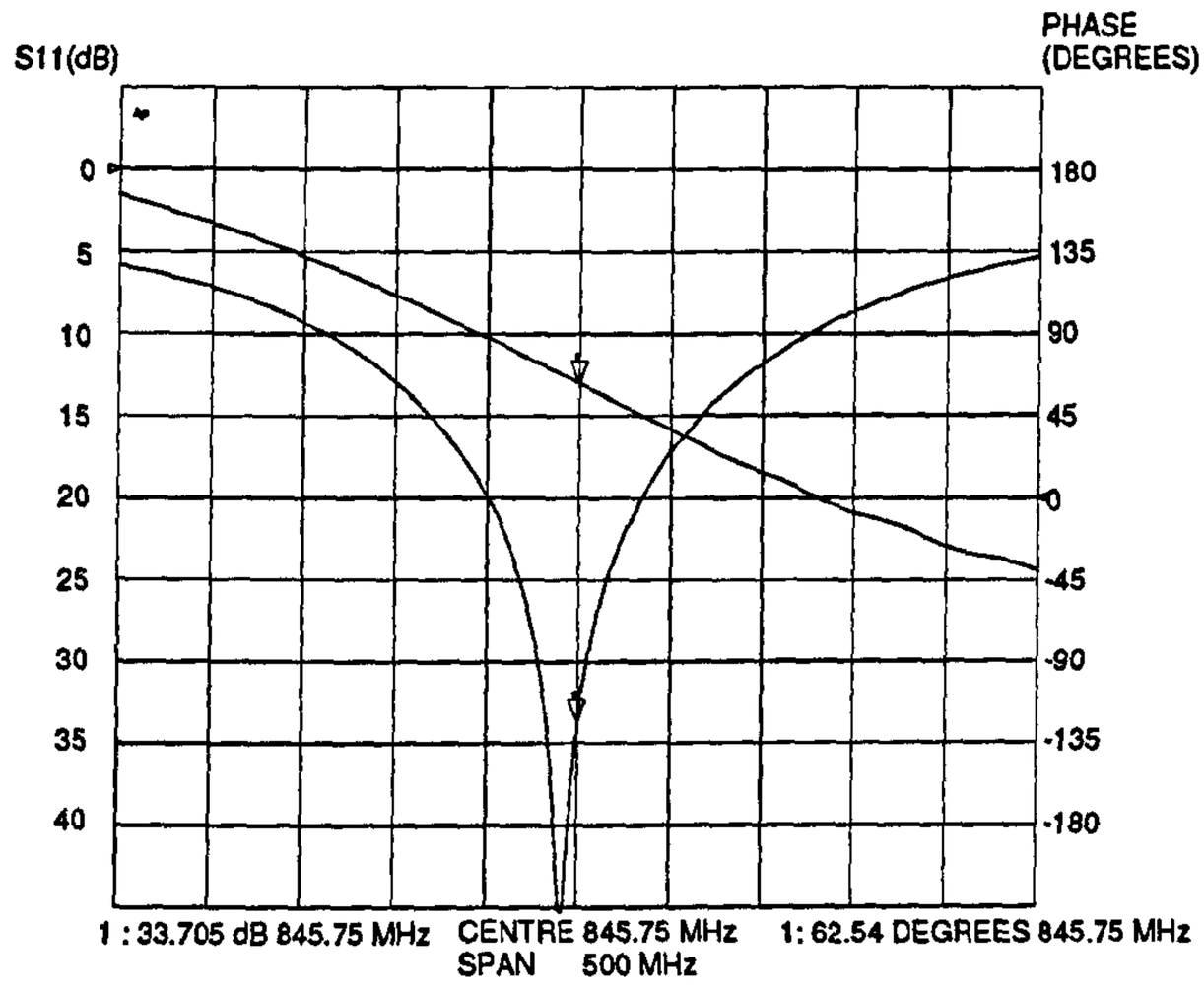

Figure 2.18: Hybrid response at the even mode output port. Input on port diagonally opposite. Phase.

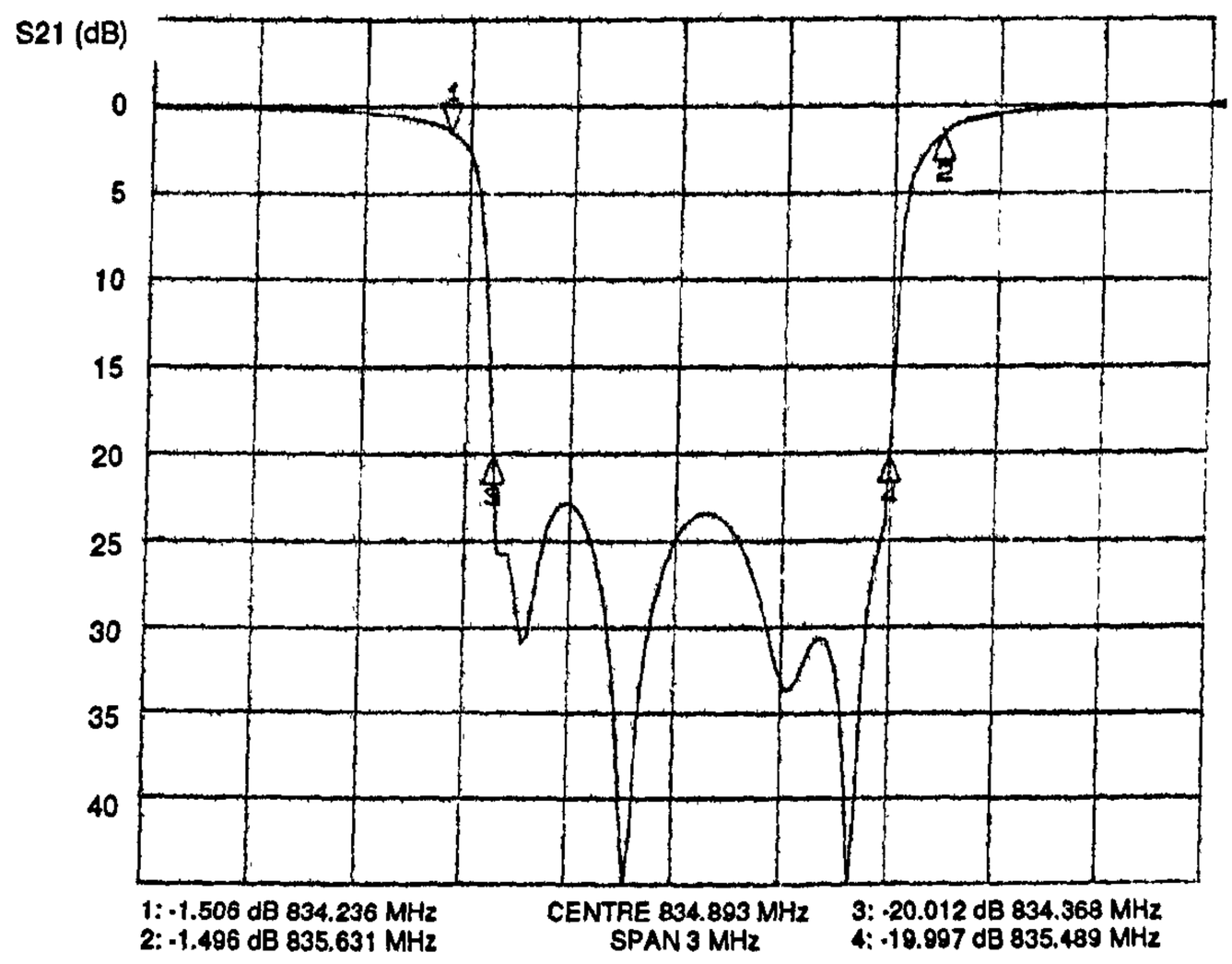

Figure 2.19: Measured transmission response of the degree 6 elliptic hybrid reflection mode cubic resonator notch filter. Both cavities and hybrid unplated.

the object of this section was primarily to demonstrate the principle of the even-odd mode reflection filter.

2.3.3 Limitations of the even-odd mode hybrid reflection filter

The simulated wideband filter response (Fig. 2.20) shows that, because of the finite bandwidth of the hybrid, the passbands of the bandstop filter are actually limited [150]. With a perfectly matched hybrid, reflection levels greater than 40 dB are possible only over a 5% bandwidth. This also means that, if the bandstop filter is converted back to a bandpass filter by means of an extra inverter, its rejection levels will suffer from the same limitations. Even within the bandwidth of the hybrid, manufacturing accuracy will limit the rejection levels of the bandstop (and the reflection levels of the bandpass) to 20 or 30 dB.

Another drawback of the even-odd mode reflection filter is the sensitivity of its response to the resonators resonant frequencies. Because the cross-couplings inverters are incorporated in the adjacent resonators, their values are modified as the

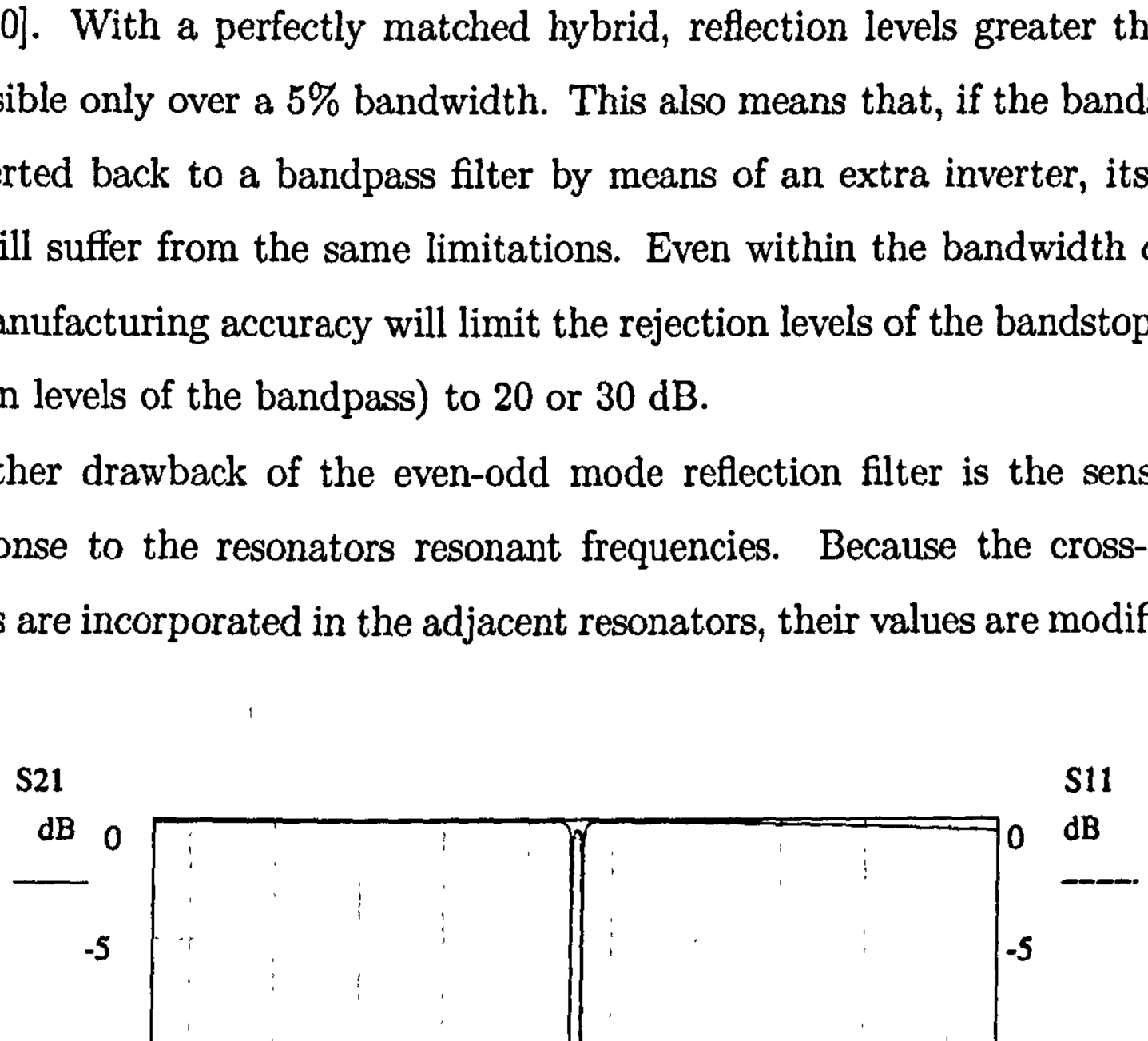

Figure 2.20: Simulated wideband frequency response of the degree 6 elliptic hybrid reflection mode cubic resonator filter

resonant frequencies of the latter are changed. Relative detuning of the resonators will happen when the filter is subject to a temperature change. In the case of the triple-mode cubic resonator, the thermal expansion of the geometry will not be symmetrical due to the presence of the alumina support in one direction only, which will potentially create further drift between the resonant frequencies. Fig. 2.21 illustrates the change of the response of the degree six elliptic filter when the first resonator is detuned by 10 ppm, or 85 kHz. The response is plotted for both a conventional cross-coupled filter and a even-odd mode reflection filter. For the latter, a model with LC resonators and input shunt reactances is used as a change of the first resonator characteristics would otherwise also induce changes to the input coupling and the input-output cross-coupling due to the substitution of Fig. 2.11. It can be seen that the locations of the transmission zeros are significantly changed for the even-odd mode reflection filter, thus making difficult the realisation of very selective and high rejection filter responses.

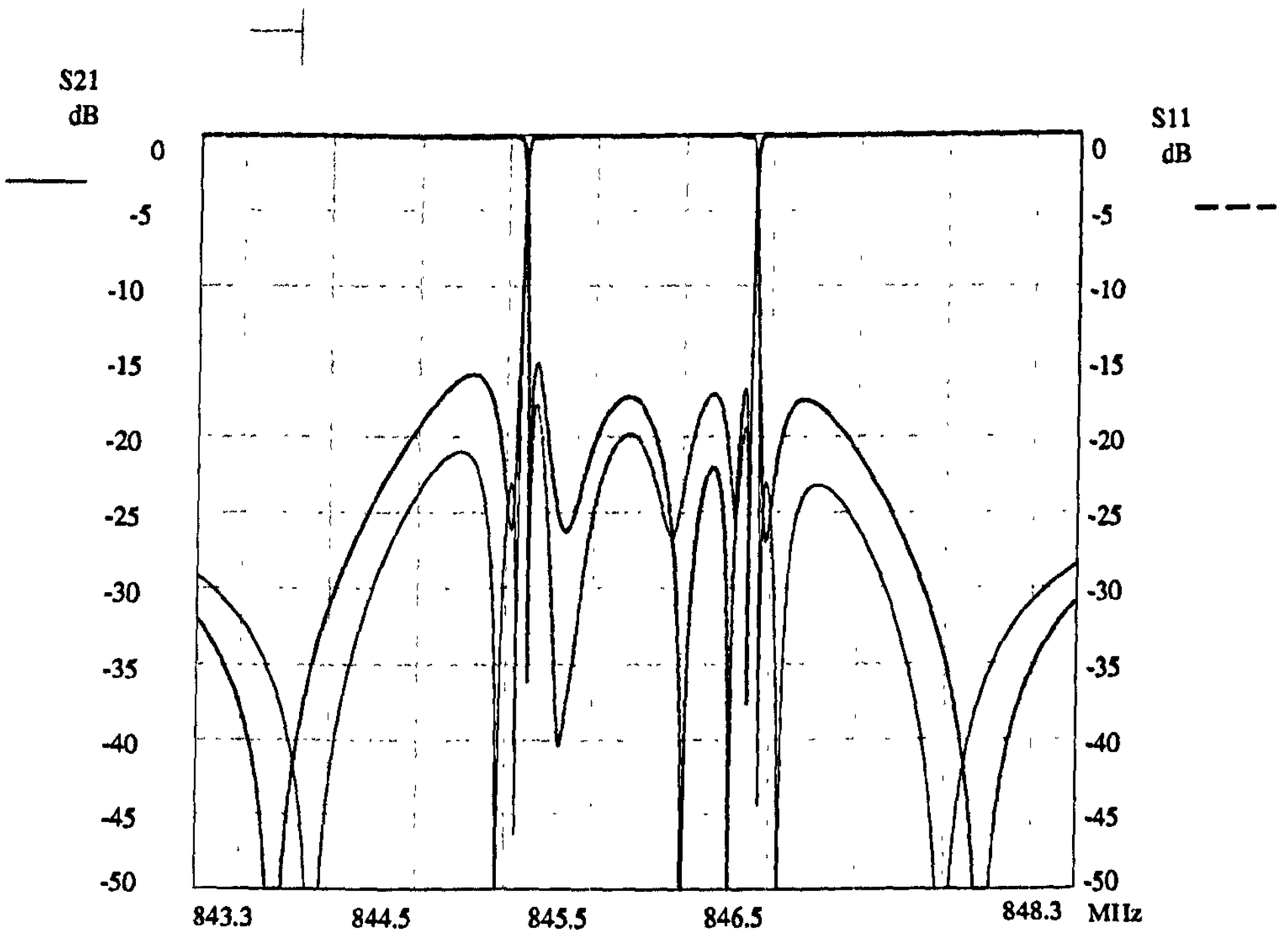

Figure 2.21: Simulated frequency response of conventional cross-coupled (in black) and even-odd mode reflection (in blue) bandpass filters with detuning of one input resonator by 0.01%. Model is with LC resonators and input shunt reactances instead of phase shifter of Fig. 2.11

Finally, the hybrid even-odd mode reflection filters are limited to symmetrical frequency responses.

2.4 Triple-mode $TE_{01\delta}$ transmission filters

With the hybrid reflection filters subject to the limitations explained above, it is necessary to investigate the filter design of conventional transmission triple-mode $TE_{01\delta}$ bandpass filters. The study is made at 2 GHz, with a dielectric filling ratio optimum for spurious separation. The resonator is a 19×19×19 mm cube of dielectric constant 44 ceramic. The cavity is 50×50×50 mm. A small alumina support of outside diameter 10 mm and wall thickness 1 mm is chosen to maximise the space available for tuning elements. Unfortunately, this also creates a difference in frequency of 2.6 MHz between the three modes. As a result, extra frequency tuning is required. A silver plated test cavity exhibited a triple-mode resonance with one mode at 2.0056 GHz and of Q_u 18,800, very close to the 18,910 simulated by FEM analysis. The two other modes were at 2.0030 GHz.

2.4.1 Frequency tuning

The need is for a frequency tuning mechanism which provides as much independent tuning as possible, without inducing much spurious coupling between the different modes. It is known that a dielectric tuning disc positioned as in Fig. 2.22 decreases the frequency of mode 2 as for the single-mode $TE_{01\delta}$. However, it also tunes significantly modes 1 and 3. From Fig. 2.6, it can be seen that the maximum electric

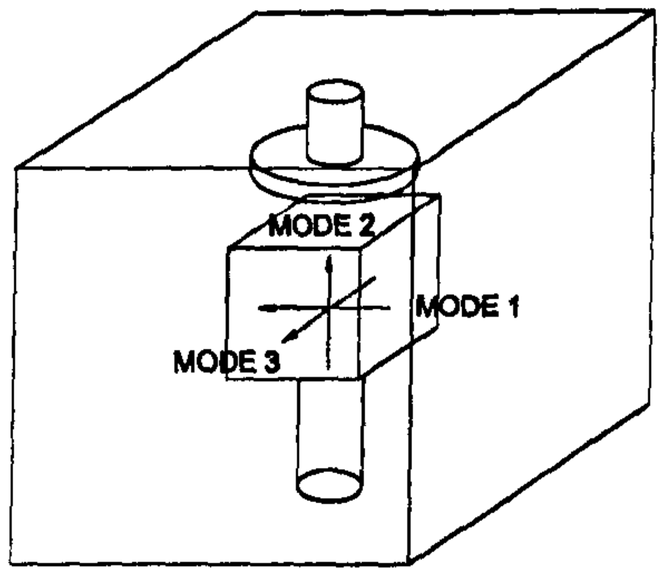

Figure 2.22: Frequency tuning of mode 2

fields of mode 2 at the top of the resonator ($z = c$) are around the edges of the cube. The fields of mode 1 and 3 on the same face can be deduced from the same figure by interchanging the x and z axis. They are strongest at the centre of the cube face. As a result, to tune mode 2 further than modes 1 and 3, tuning discs with large diameters will be needed. The top left graph of Fig. 2.23 shows the effect of a 25 mm diameter disc of dielectric constant 44. Mode 2 is tuned by the largest amount, and up to 12 MHz of differential tuning is achievable. Further differential tuning is expected to be achievable by using a doughnut-shaped disc, as the effect on mode 1 and 3 should be minimised. Unfortunately, large tuning discs will also generate large spurious coupling levels compared with the coupling bandwidths required for narrowband filters. For example, a FEM analysis shows that two tuning discs positioned 6.5 mm away from the cavity walls (each giving 11 MHz of differential tuning) create 2 MHz of coupling between the modes they predominantly tune. With smaller tuning discs, these couplings become negligeable and some differential tuning could still be possible, this time by predominantly tuning modes 1 and 3 rather than mode 2. However, in practice, the tuning of modes 1 and 3 only predominates when the tuning disc is less than 2 mm from the resonator. The effect of small discs is illustrated for diameters of 15 and 10 mm in Fig. 2.23.

This frequency behaviour with different tuning discs qualitatively explains the effect of different alumina support diameters. The smaller supports used in this section pulled the frequencies of mode 1 and 3 down relative to mode 2, similarly to a small tuning disc. In the previous section at 850 MHz, a larger diameter support had just as much effect on mode 2 as mode 1 and 3, behaving more like a large tuning disc.

Metal tuning discs were found to be the only alternative to dielectric ones. They were mounted on an insulating plastic screw so as not to perturb the $TM_{01\delta}$ modes. 13 MHz of independent tuning is achievable, creating a maximum of 0.6 MHz of spurious coupling, when simulated by FEM analysis with 17 mm diameter discs 8 mm away from the cavity walls. However, this is accompanied by a decrease of the Q_u of the tuned mode by 9%. The effect of a 17 mm metal tuning disc on the three resonant frequencies is shown in Fig. 2.23.

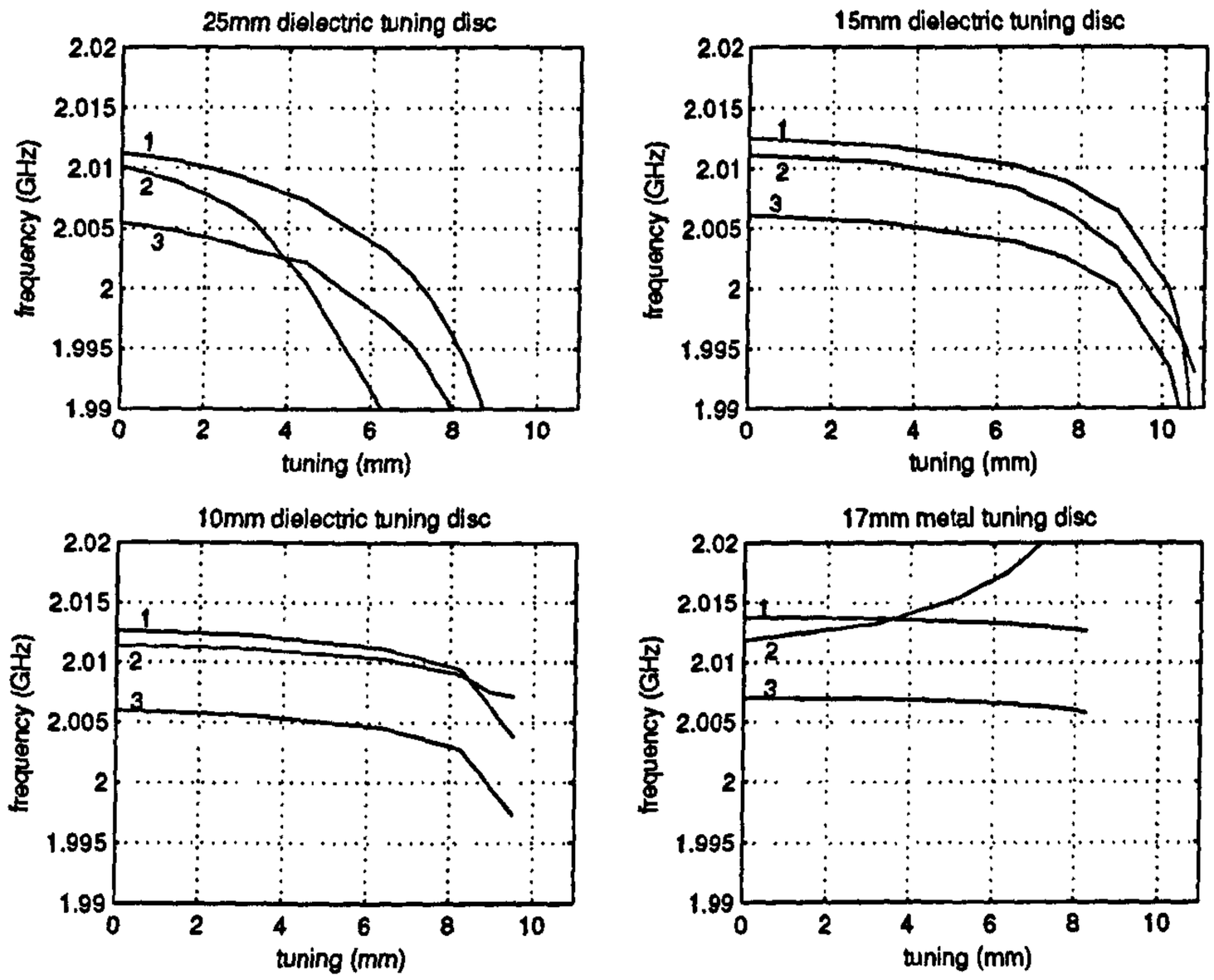

Figure 2.23: Variation of the resonant frequencies with displacement of tuning disc from cavity wall. Modes numbered as in Fig. 2.22. Dielectric cube: ε_r 44, length 19 mm. Cavity: length 50 mm. Dielectric tuning disc: ε_r 44. Total travel varies because of differing tuning element thickness and mounting.

2.4.2 Intra-cavity couplings

In the hybrid triple-mode filter of the previous section, the couplings between modes of the same cavity were realised by conducting loops located opposite the frequency tuning discs. This is not possible in the case of multi-cavity filters, where at least two walls of each cavity are required for external couplings. No other location is adequate for a metal or dielectric insert to create the values of coupling necessary for filters wider than a few megahertzs. As a result, most of the coupling needs to be created by discontinuities on the dielectric cube itself, such as chamfers, as shown in Fig. 2.24 [71]. The variation of the coupling with respect to the chamfer dimension, calculated by even-odd mode analysis with the FEM simulation software, is shown in Fig. 2.25.

Additional fine tuning up to 1 MHz is achieved by conductive loops positioned as in Fig. 2.24.a. Fig. 2.26 illustrates the magnetic coupling happening for different positions of the loop. The numerical values were obtained experimentally. These

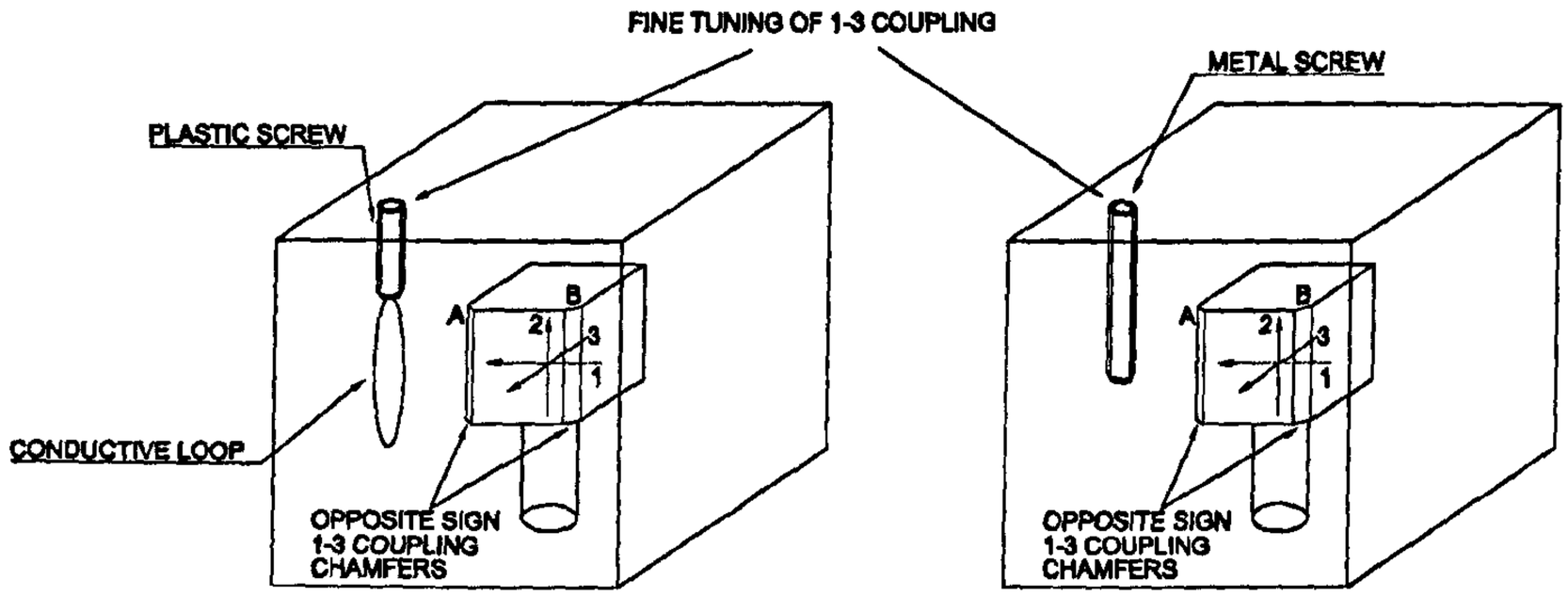

Figure 2.24: Intra-cavity coupling mechanism

coupling values are to be added to the coupling created by a chamfer situated next to the loop, as chamfer A of Fig. 2.24, or at 180° from it. They should be subtracted if the chamfer is situated as chamfer B. Overall, 1 MHz of tuning is available.

However, these conductive loops were found to be difficult to make in a repeatable manner and were replaced by 1/4" metal screws parallel to the chamfer as in Fig. 2.24.b. 1 MHz of tuning is also available. The screw in Fig. 2.24.b decreases the coupling created by the chamfer A and increases that of chamfer B. Tuning screws in similar positions can also be used without being associated to a chamfer to can-

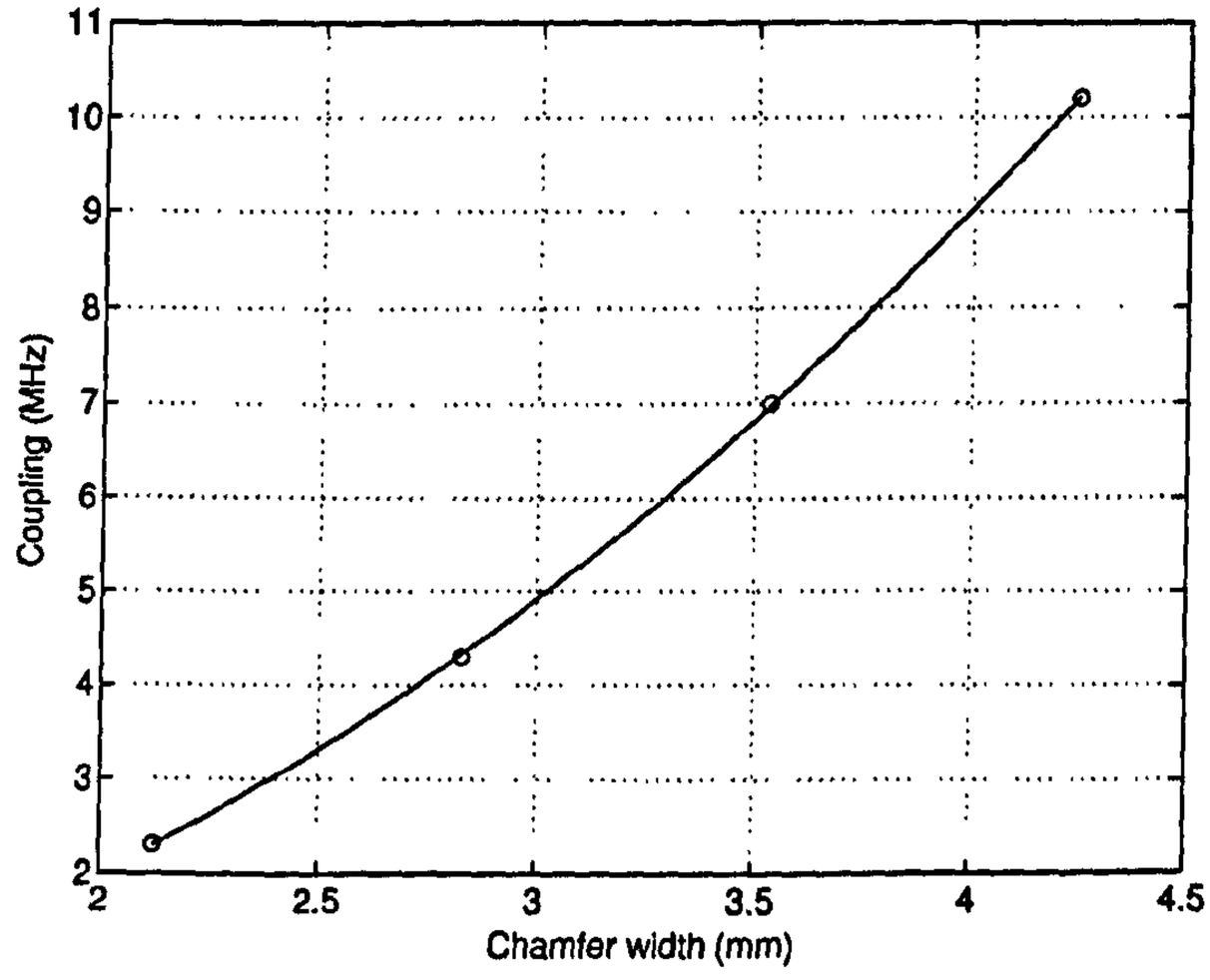

Figure 2.25: Coupling variation with chamfer size

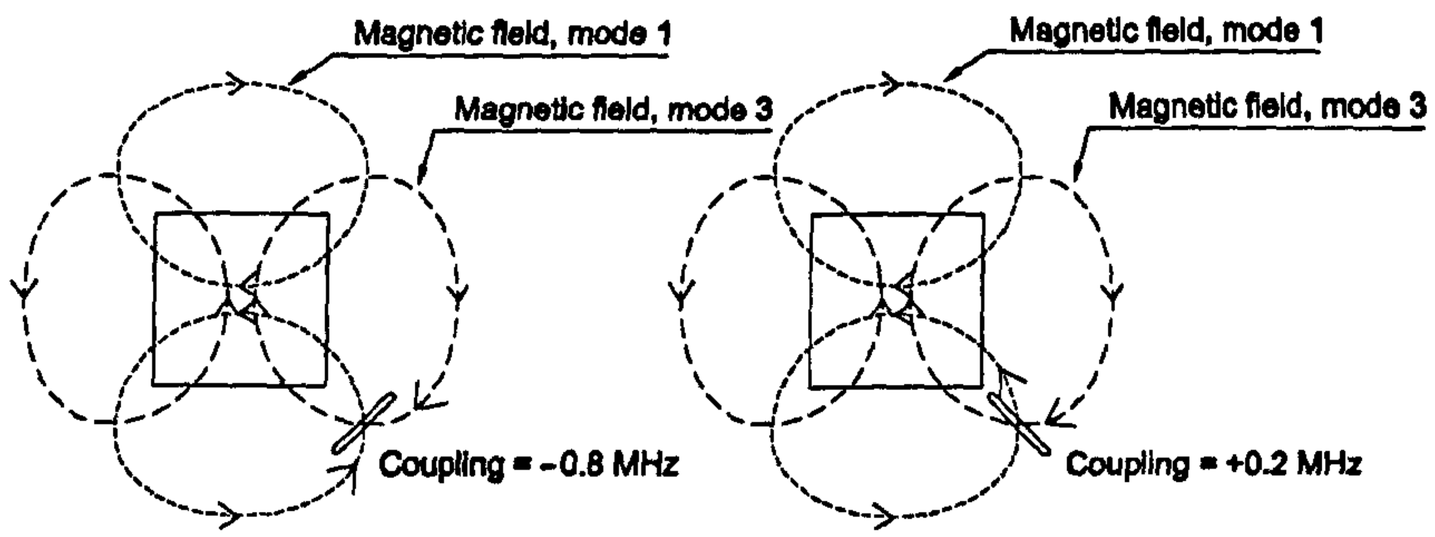

Figure 2.26: Coupling of magnetic fields through conductive loop

cel any spurious coupling which could exist between modes. For example, a tuning screw inserted in between two metal frequency tuning discs will tend to cancel the spurious coupling created by the discs themselves.

2.4.3 Inter-cavity couplings

Within each cavity, a cross-coupling of any sign between modes 1 and 3 is readily obtainable by machining chamfers along all three axis of the dielectric cube. This allows the realisation of some asymmetrical filter responses. Further cross-couplings require the existence of multiple inter-cavity couplings though the same cavity wall. Traditionally independent couplings through the same wall, both in air and DR multimode filters, are obtained by opening apertures that each predominantly couple one set of modes [68, 153]. The key point is then to identify the optimum location for these irises, by considering the distribution of the transversal fields of the three $TE_{01\delta}$ modes at the wall interface. The directions of the magnetic fields are illustrated in Fig. 2.27.

As a first step, the optimum iris location for the coupling of modes A in Fig. 2.27 is investigated in order to minimise the couplings of the two other set of modes. The first obvious choice for a coupling aperture is a long and narrow iris, parallel to the magnetic fields, and located at the centre of the wall. Such a iris is conventionally used in single-mode $TE_{01\delta}$ filters. However, it is difficult to machine. As a result, the coupling through a similar shaped iris, but running along one edge of the wall was considered. Such an iris is also easy to access and convenient to tune: a metal

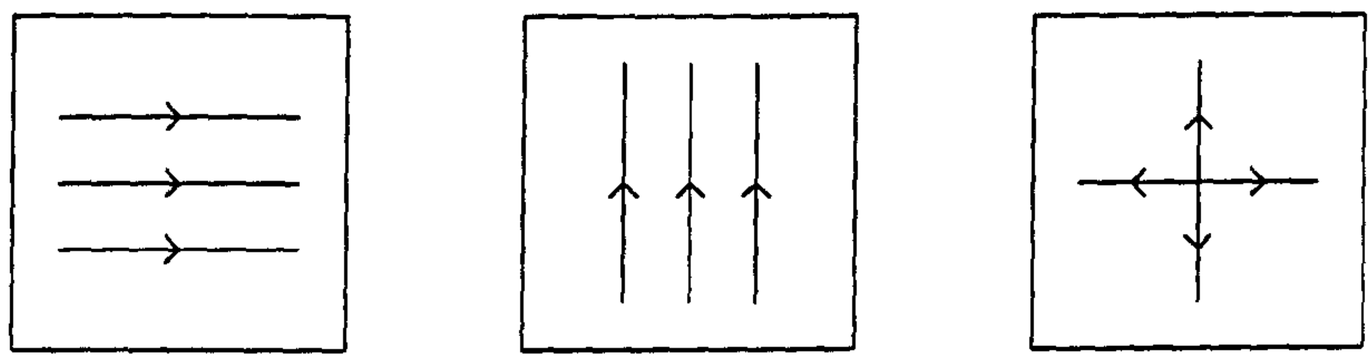

Figure 2.27: Directions of magnetic fields for the three modes at a cavity wall

screw inserted across it increases the iris coupling, thus limiting the necessary iris size and, as a result, the amount of spurious couplings. A FEM simulation predicts a coupling of 2.5 MHz through a 30 mm×10 mm iris in a 4 mm thick wall. The couplings for the two other set of modes are much weaker: 0.0 ±0.1 MHz for modes B and 0.1 ±0.1 MHz for modes C. Although these values are very small, they could still cause a significant change of the filter response, as they introduce cross-couplings between distant nodes of the network. To better evaluate the amount of spurious couplings, a filter was designed and built. The case of a degree 6, 5 MHz wide Chebyshev filter was considered. Its equivalent circuit, as well as the ones of all subsequent filters in this chapter, was derived by the Filtronic in-house filter design software using the same synthesis method as in Section 1.2. The "short-circuit stub resonator-inverter coupling" network model, recalled in Fig. 2.28 was chosen. The filter coupling bandwidths are listed in Table 2.4.

In the absence of cross-couplings, the signs of the main path couplings would not matter and the chamfers could be located in any of the appropriate positions described in Section 2.4.2. However, spurious couplings occur through the iris and have a sign that cannot be chosen. As a result, the signs of the main path couplings relative to those of the spurious cross-couplings will dictate the overall response of the filter. The couplings through the iris are inductive. The inverters representing them in the model then have a positive impedance, in order to create the same sign of phase shift as an inductor. As a result, an inductive coupling will also be called here a positive coupling. Let us represent such a positive coupling by drawing the fields of the two modes with opposite orientations on each side of the iris, as illustrated in Fig. 2.29.a [2]. Also, let us suppose that a coupling created by a chamfer is positive when the chamfer is located between the two heads of the mode symbolic arrows,

Table 2.4: *Chebyshev filter coupling bandwidths. Equiripple bandwidth:* 5 MHz, *return loss:* 25 dB.

Nodes	Coupling BW (MHz)
input-1	6.09
1-2	4.70
2-3	3.24
3-4	3.06
4-5	3.24
5-6	4.70
6-output	6.09

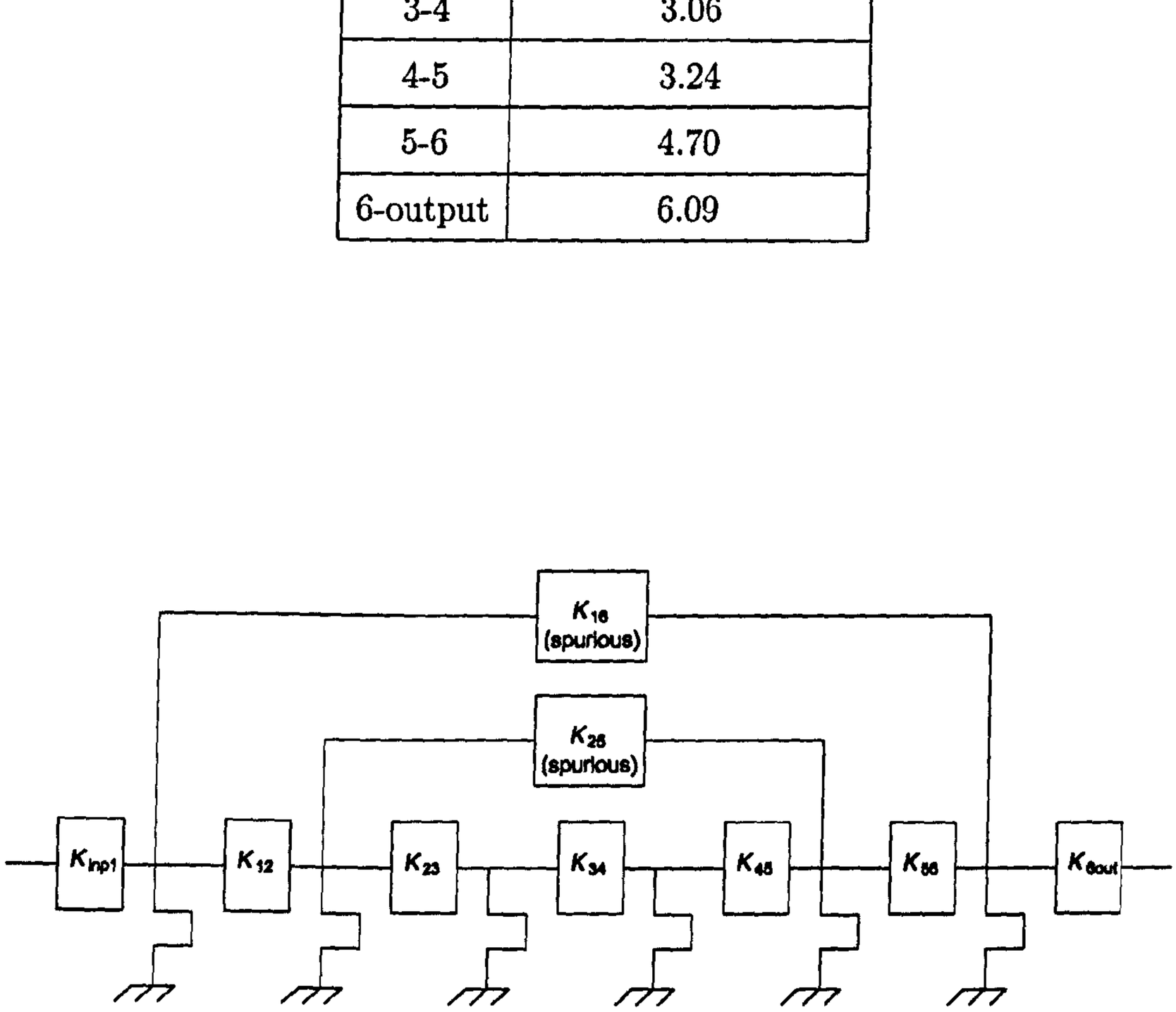

Figure 2.28: General filter equivalent circuit network

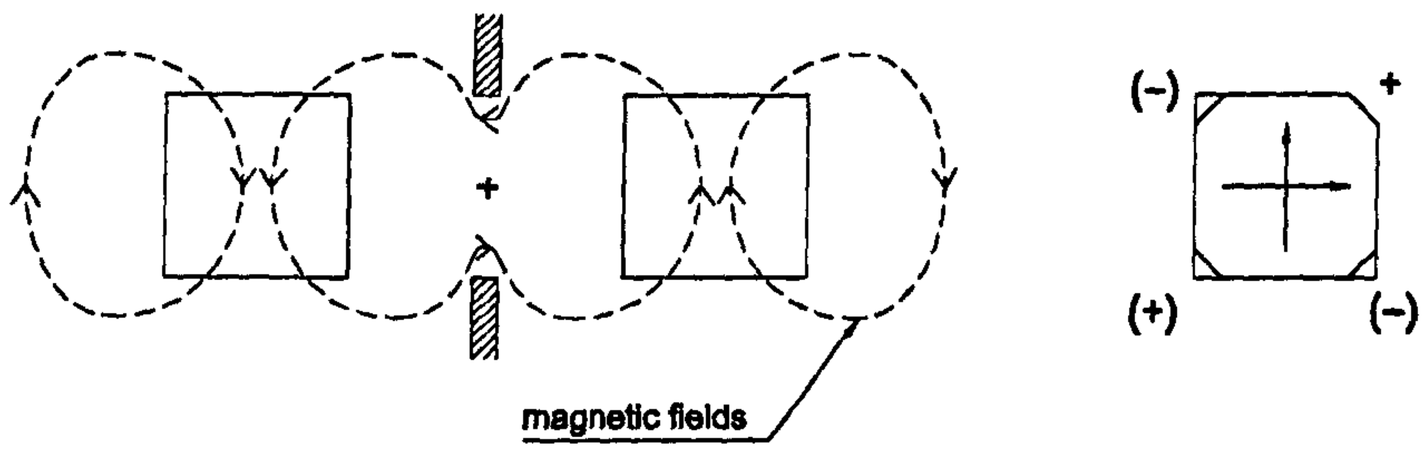

Figure 2.29: Sign conventions for iris couplings (a) and chamfer couplings (b). (a) is taken from [2].

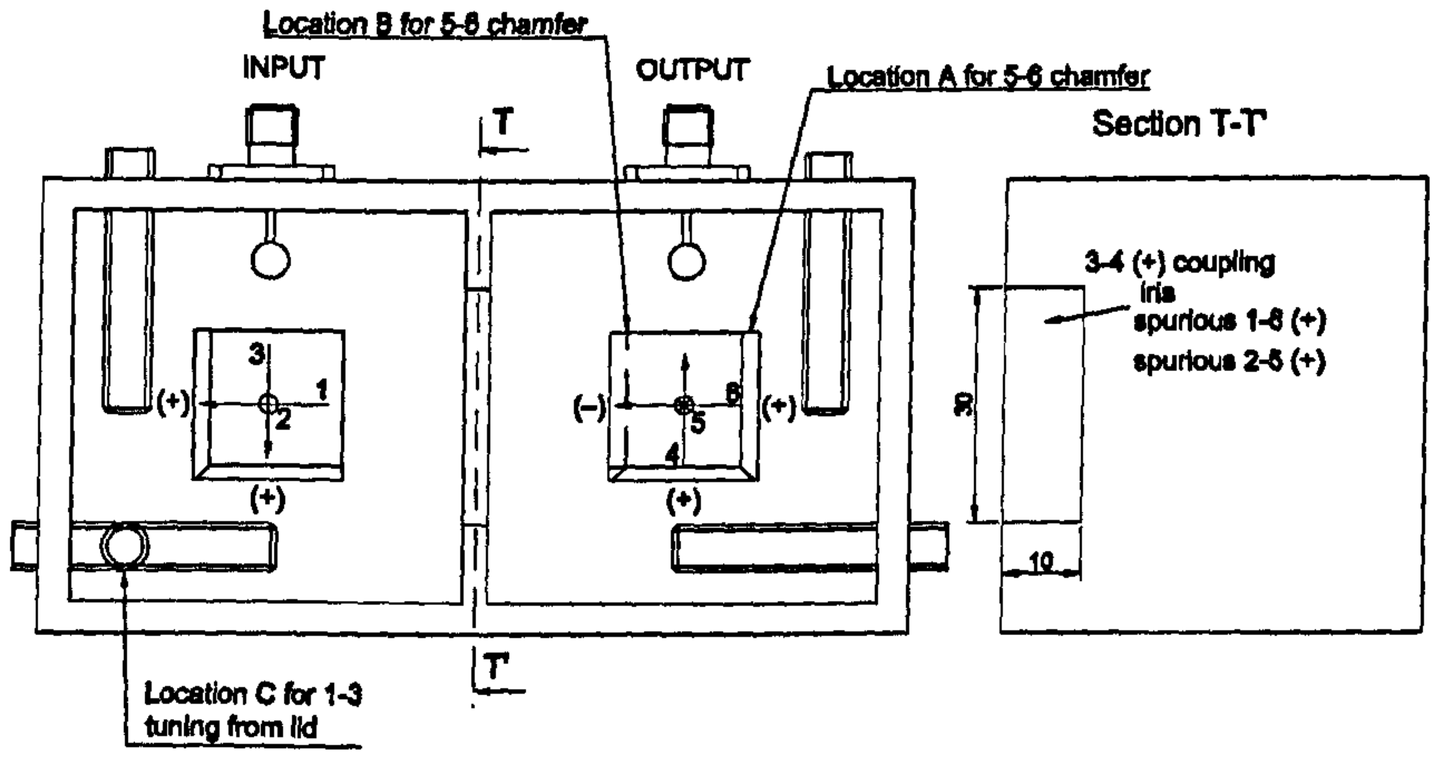

Figure 2.30: Layout of Chebyshev filter with top iris

as in Fig. 2.29.b, or at 180° from them. The relative sign of each coupling can then be deduced, by setting all chamfer couplings but one as positive and deducing the sign of the last coupling from the field orientations. The convention in Fig. 2.29.b is arbitrary. However, this is not restrictive at this stage as the filter studied here is symmetrical: any sign change (180° phase shift) occurring for a given chamfer in one cavity is reproduced symmetrically in the other cavity, and the overall response remains the same. For asymmetrical filters, the knowledge of the correct absolute sign would however be useful. It will be deduced later on in this section.

The filter was tuned for both signs of the 5-6 coupling. The filter layout is shown in Fig. 2.30. TEM transformers resonating above the passband couple into mode 1 and out of mode 6. Intra-cavity couplings are tuned by 1/4" metal tuning screws,

increasing the coupling already created by the chamfers. The filter responses are shown in Fig. 2.32 to 2.34. As expected, rotating the 5-6 coupling chamfer transforms the delay equalisation present in Fig. 2.32 into real frequency axis transmission zeros in Fig. 2.34. These are correctly predicted from the coupling signs in Fig. 2.30 deduced from Fig. 2.29. The plots also put in evidence the significant effect of the 1-6 coupling on the response. The latter can be deduced from the shoulder levels of Fig. 2.32 and 2.34.

The filter responses in both Fig. 2.32 and 2.34 exhibit some degree of asymmetry in their rejection levels below and above the passband. As with more conventional filters (combline, single-mode $TE_{01\delta}$), some asymmetry is expected due to the frequency dependence of the coupling mechanisms and the proximity of the closest spurious modes. Other contributions to the asymmetry come from spurious couplings between odd numbers of nodes in the filter network. The 1-3 and 4-6 couplings, mainly due to the presence of the frequency tuning elements and misalignement of the dielectric resonators, can be cancelled entirely by tuning screws inserted between the discs. Small amounts of input-2 and 5-output couplings also exist, but their effect on the response is much more limited. Finally, if the iris is offset relative to the symmetry lines of the field distributions at the wall interface, as it is the case for the top iris for example, couplings between different set of modes, e.g. 1-5 coupling, will also occur [154]. However, their effect is expected to be less significant than that of the inter-cavity and the 1-6 couplings. The modelling of the asymmetry is restricted to the use of impedance inverters which have impedances that vary linearly with frequency around the centre frequency of the filter. These provide a good model for the higher selectivity present at lower frequencies, which is believed to be mainly due to the frequency dependence of the coupling mechanisms and the proximity of spurious modes. The tuning elements only have a secondary effect. Indeed, the change of asymmetry of the response when changing the sign of the 5-6 coupling was only small, and could be explained by a spurious 4-6 coupling of +0.3 MHz, for example through the tuning discs. Also, both 1-3 and 4-6 couplings due to the tuning discs should, according to the models of Fig. 2.29, both be positive and increase the selectivity on the high side of the passband, which means that it is actually partly cancelling other more important effects. In any case, the way the asymmetry is modelled is not critical for the following evaluation of the spurious

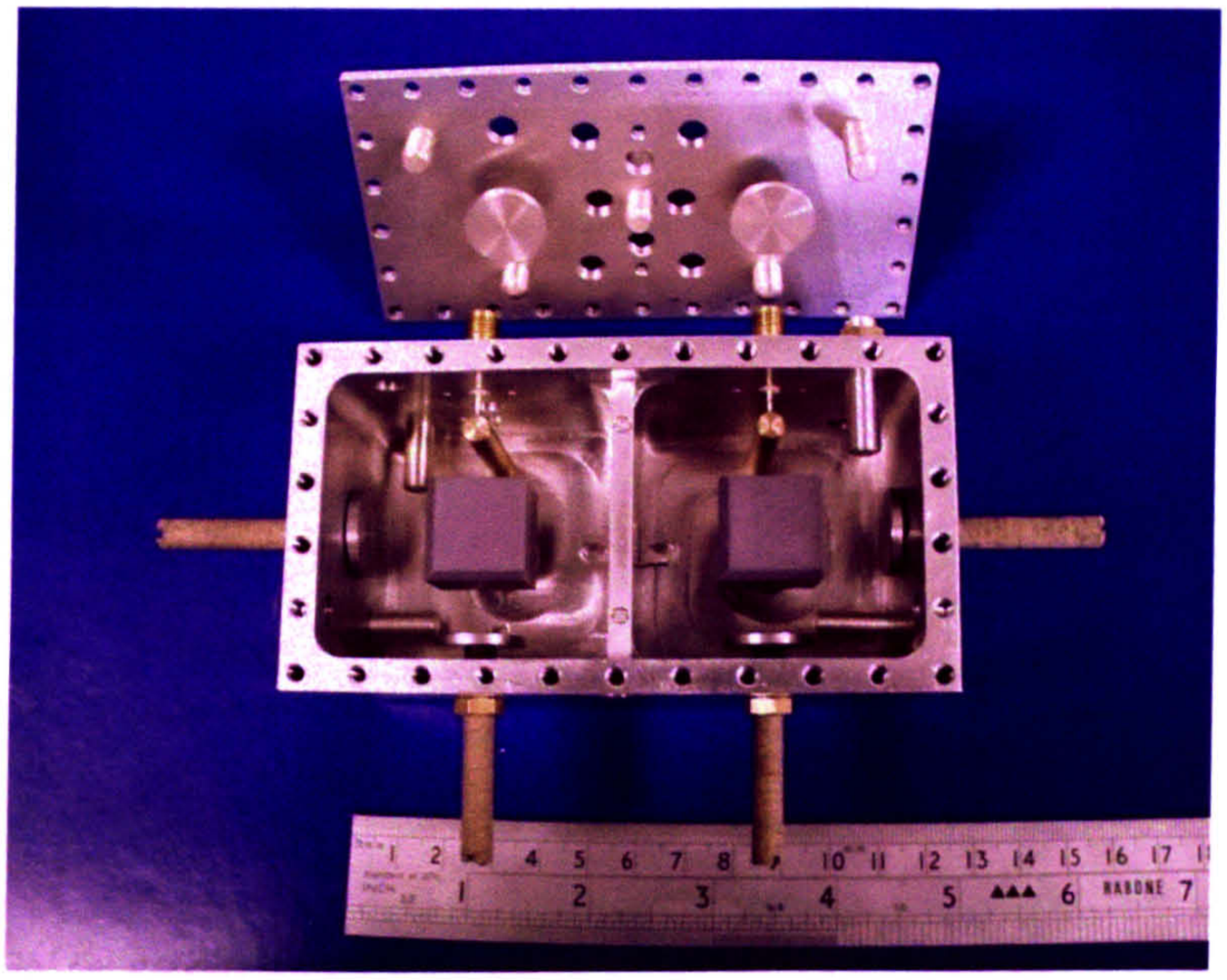

Figure 2.31: Picture of the Chebyshev filter with top iris. Central iris dimensions modified.

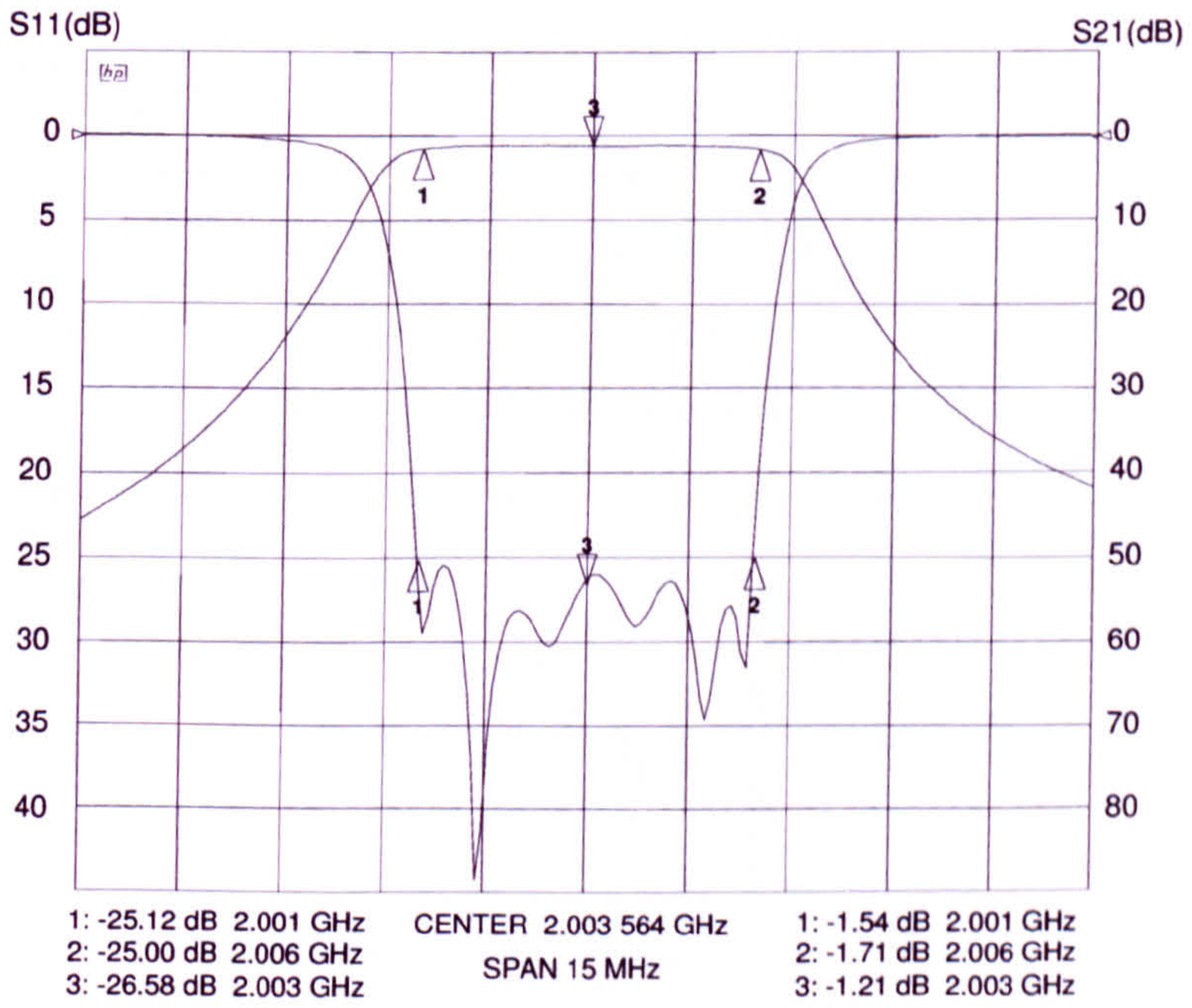

Figure 2.32: Measured narrowband frequency response of the Chebyshev filter with top iris and 5-6 chamfer in A

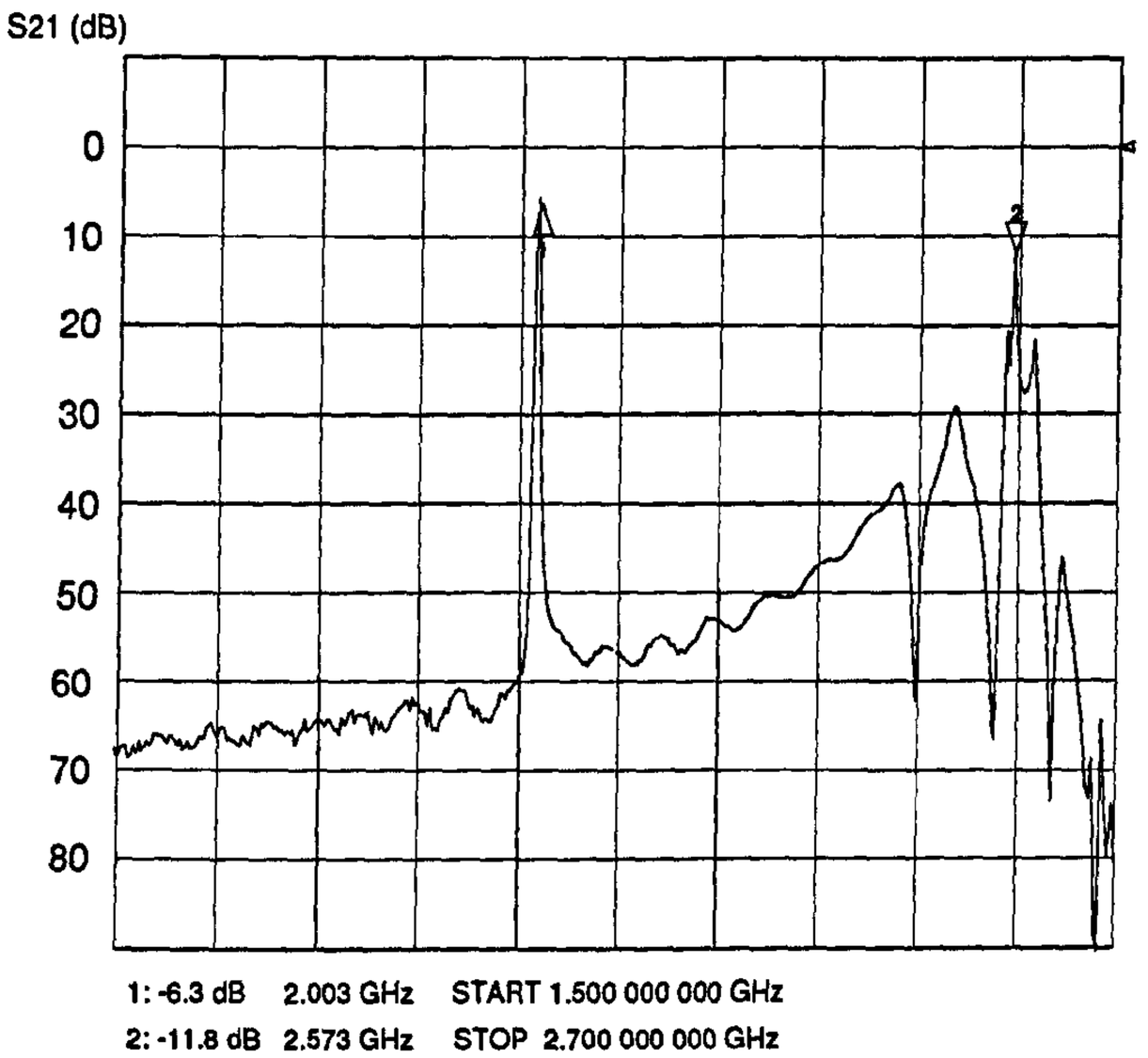

Figure 2.33: Measured wideband frequency response of the Chebyshev filter with top iris and 5-6 chamfer in A

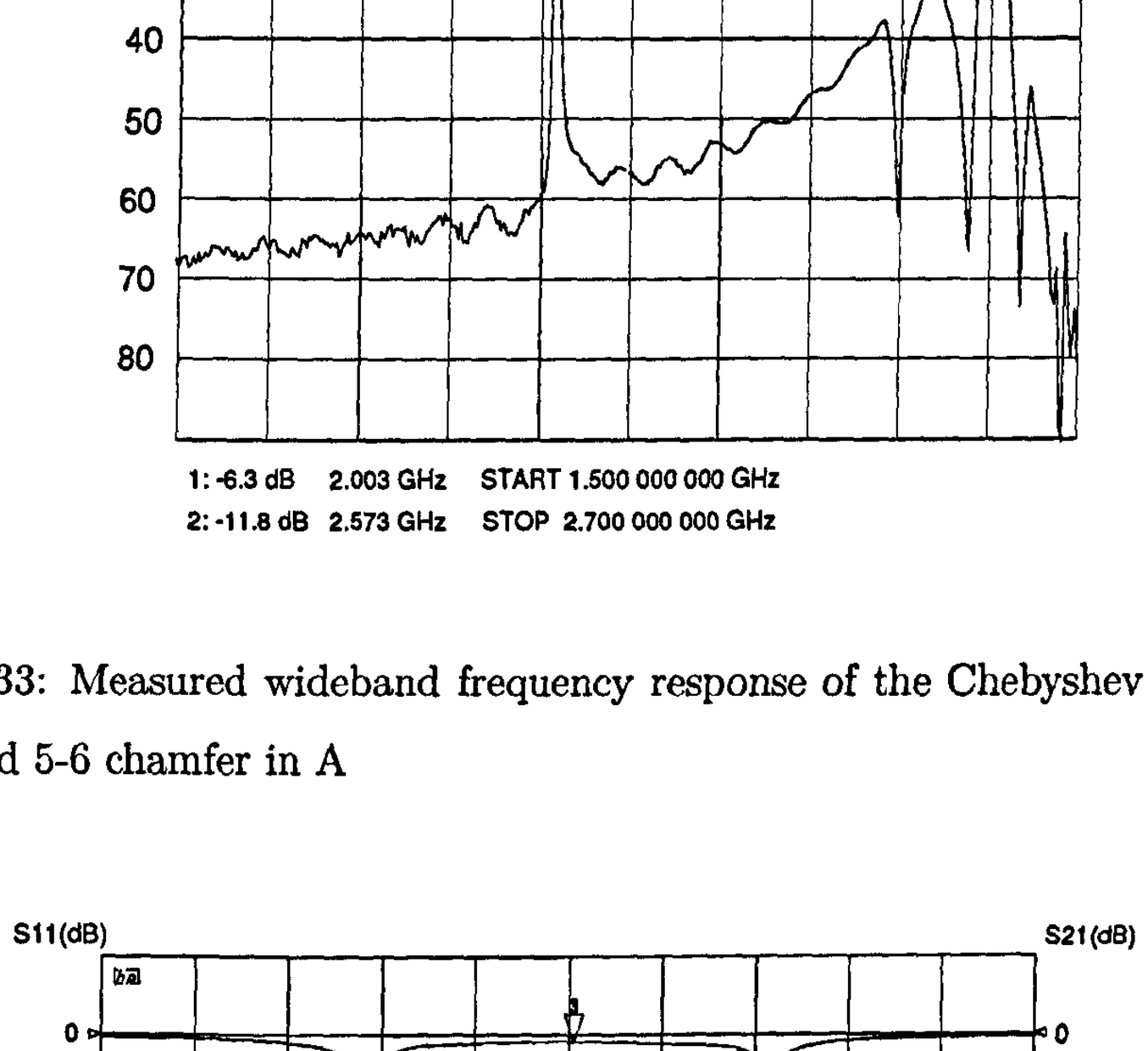

Figure 2.34: Measured narrowband frequency response of the Chebyshev filter with top iris and 5-6 chamfer in B

couplings occurring through the iris.

The fact that some 2-5 spurious coupling occurs through the iris only creates a small uncertainty on the estimation accuracy of the 1-6 coupling. The former was simulated to be between −0.1 MHz and +0.1 MHz by the FEM simulation, but in fact is restricted to positive values. Supposing 0 MHz of 2-5 spurious coupling, +0.105 MHz and +0.100 MHz of 1-6 coupling is estimated from Fig. 2.32 and 2.34 respectively. With 0.1 MHz of 2-5 coupling, these values change to +0.095 MHz and +0.113 MHz respectively. As the value for both spurious couplings should be the same in both experiments, and assuming a linear variation in the interval between the two measured cases, their values are deduced as +0.103 MHz for the 1-6 coupling and +0.022 MHz for the 2-5 coupling, or 3.36% and 0.72% of the main path coupling respectively. These values are slightly influenced by the positioning of the dielectric resonators. When accurate positioning is realised using a jig, the previous results are repeatable with less than 15% variation. Also, input-3 and 4-output spurious couplings might affect the measurements although their effect is equal to that of a 2-5 coupling with a sixth of the magnitude.

By inserting a metal tuning screw from the lid in C in Fig. 2.30, a negative 1-3 coupling should be created. That is because the tuning screw introduces a coupling of opposite sign to that of a chamfer in the same location. The measured response of the filter in Fig. 2.35 shows that the lower band edge of the filter becomes more selective. This is in agreement with the filter model. On the other hand, if all chamfers had created the opposite sign of coupling (negative for the same arrow orientations), then the 1-3 coupling would have been negative and the higher band edge should have become more selective. This demonstrates that the conventions used in Fig. 2.29 were correct.

To maximise the flexibility of the new triple-mode filter, the spurious couplings across both four and six nodes should not influence the response significantly. With the top iris in the previous layout, the 1-6 coupling is too large. To minimise its effect on the response, modes 1 and 6 would need to be interchanged with modes 2 and 5 respectively, which restricts the layout possibilities. On the other hand, the 1-6 coupling might be minimised by an iris in a different location. With this in mind, the central iris previously mentioned was again considered. The filter layout is shown in Fig. 2.36. The 3-4 coupling is this time decreased by inserting a 1/4" metal

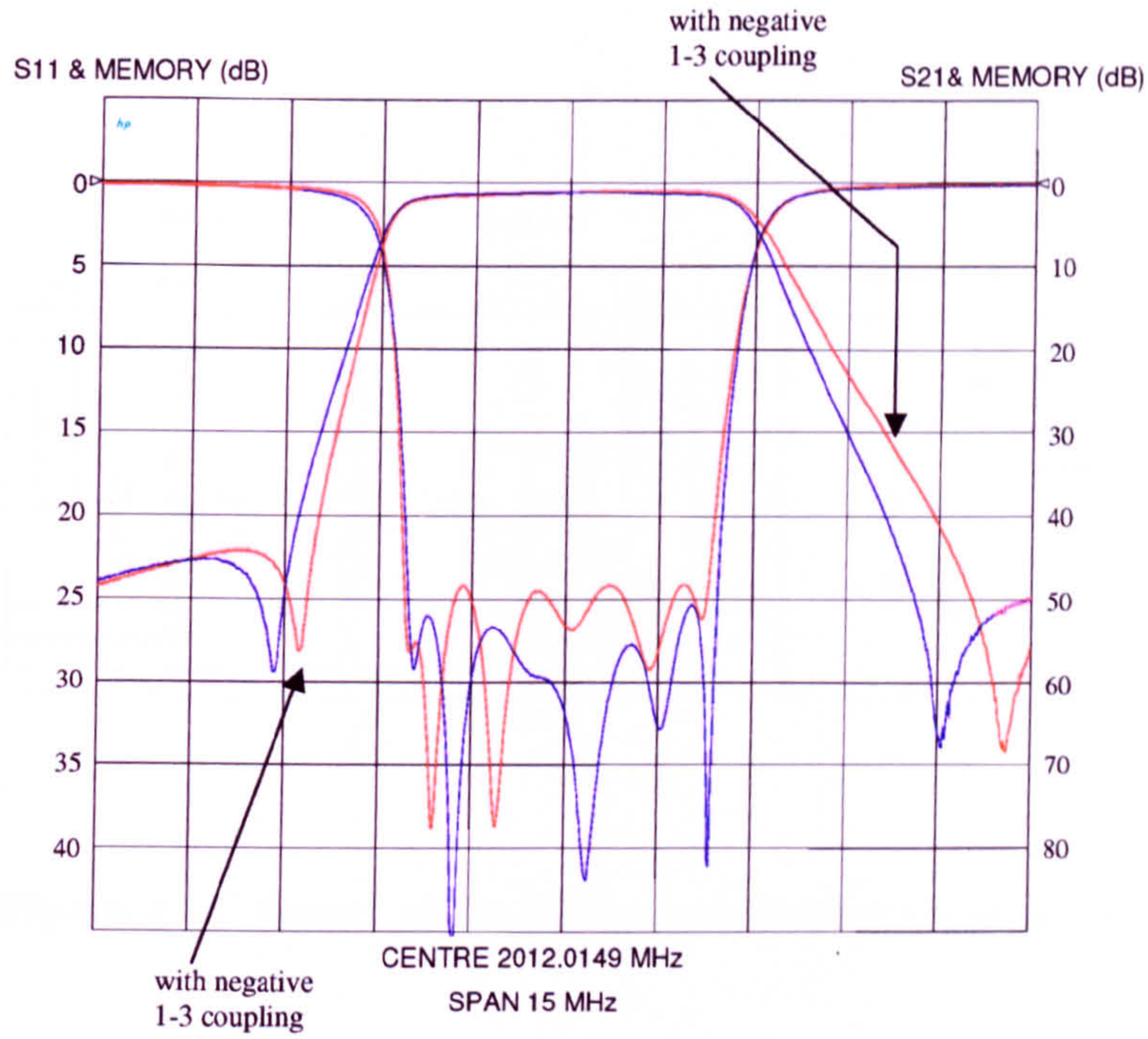

Figure 2.35: Measured response of filter with top iris, chamfer in B and tuning screw in C

tuning screw along its length. A FEM simulation predicted a coupling through a 30 mm×7 mm iris in a 4 mm thick wall of 3.1 MHz for modes A, 0.1 ±0.1 MHz for modes B and 0.2 ±0.1 MHz for modes C. A filter with a central aperture was built and its response is shown in Fig. 2.37. The deduced 1-6 coupling is between 0.16 MHz (or 5.2% of the main path coupling) and 0.193 MHz (or 6.3% of the main path coupling). This is considering a 2-5 spurious coupling between 0 and 0.2 MHz, as given by FEM simulation.

This result is worse than with the top iris. As previously, modes 2 and 5 might couple less than 1 and 6 through the central iris, as suggested by the FEM simulation. This was checked by retuning the filter after swapping modes 1 and 5 with modes 2 and 6 respectively, although, as already explained, this would restrict the possibilities of realisable filter layouts. The layout of the new filter is shown in Fig. 2.38 and its response in Fig. 2.39. The new 1-6 spurious coupling is estimated at 5.2% and 3.7% of the main coupling, considering 0.1 and 0.3 MHz of 2-5 coupling respectively. This is less than before the modes were swapped, although the shoulder levels are similar to those in Fig. 2.37. This is due to the fact that, in the latter case, the effects of

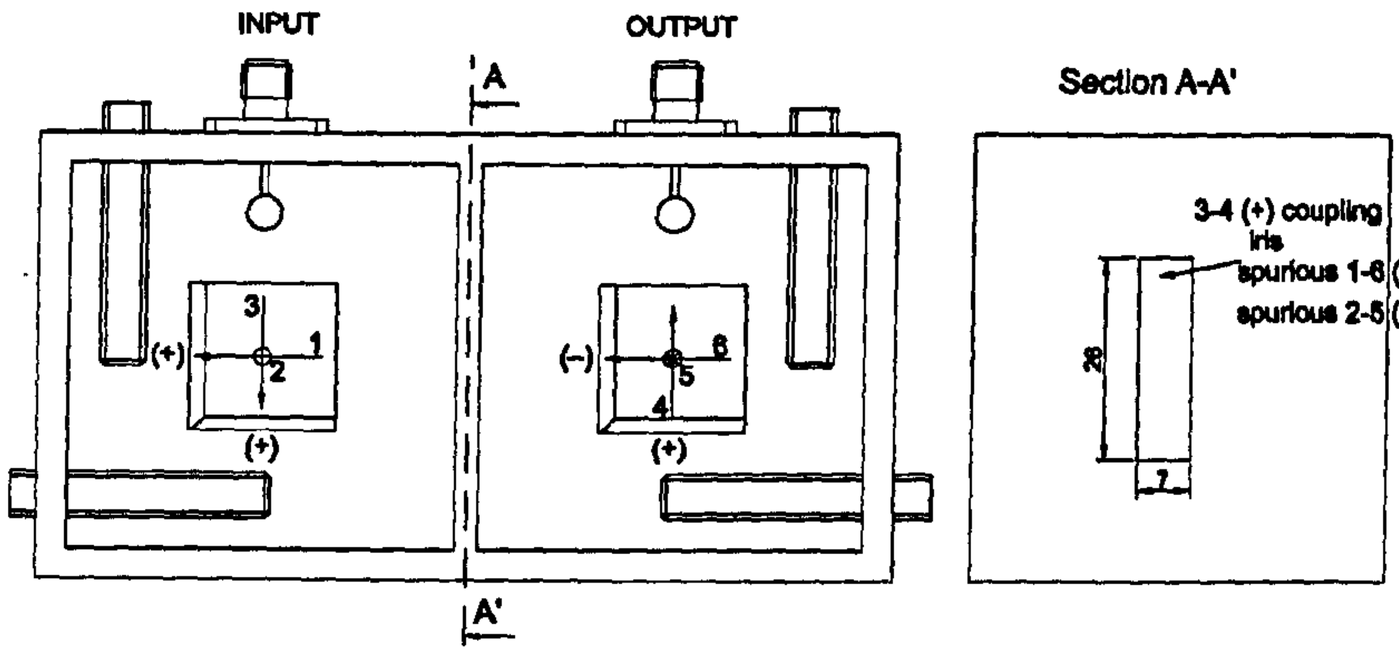

Figure 2.36: Layout of the Chebyshev filter with central iris

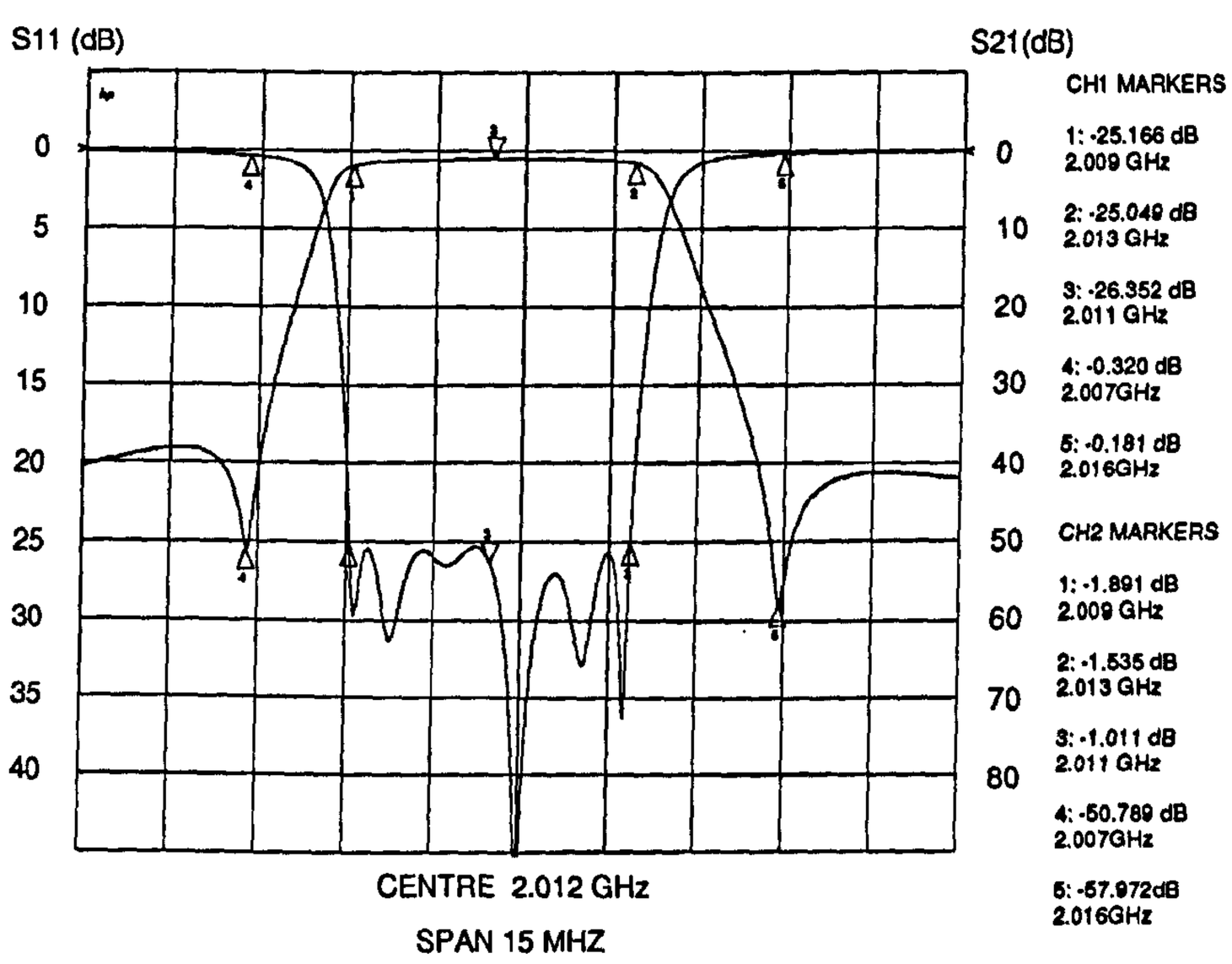

Figure 2.37: Measured frequency response of the Chebyshev filter with central iris

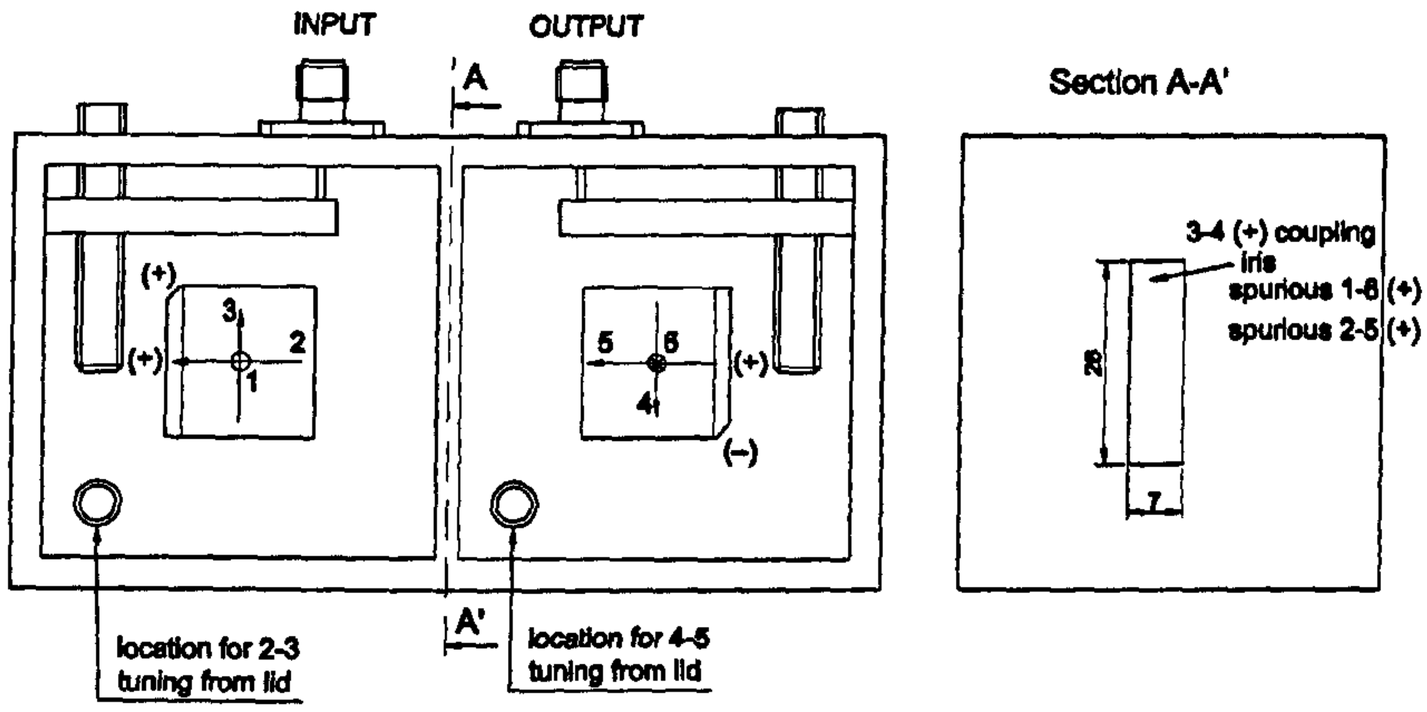

Figure 2.38: Layout of Chebyshev filter with central iris and modes swapped

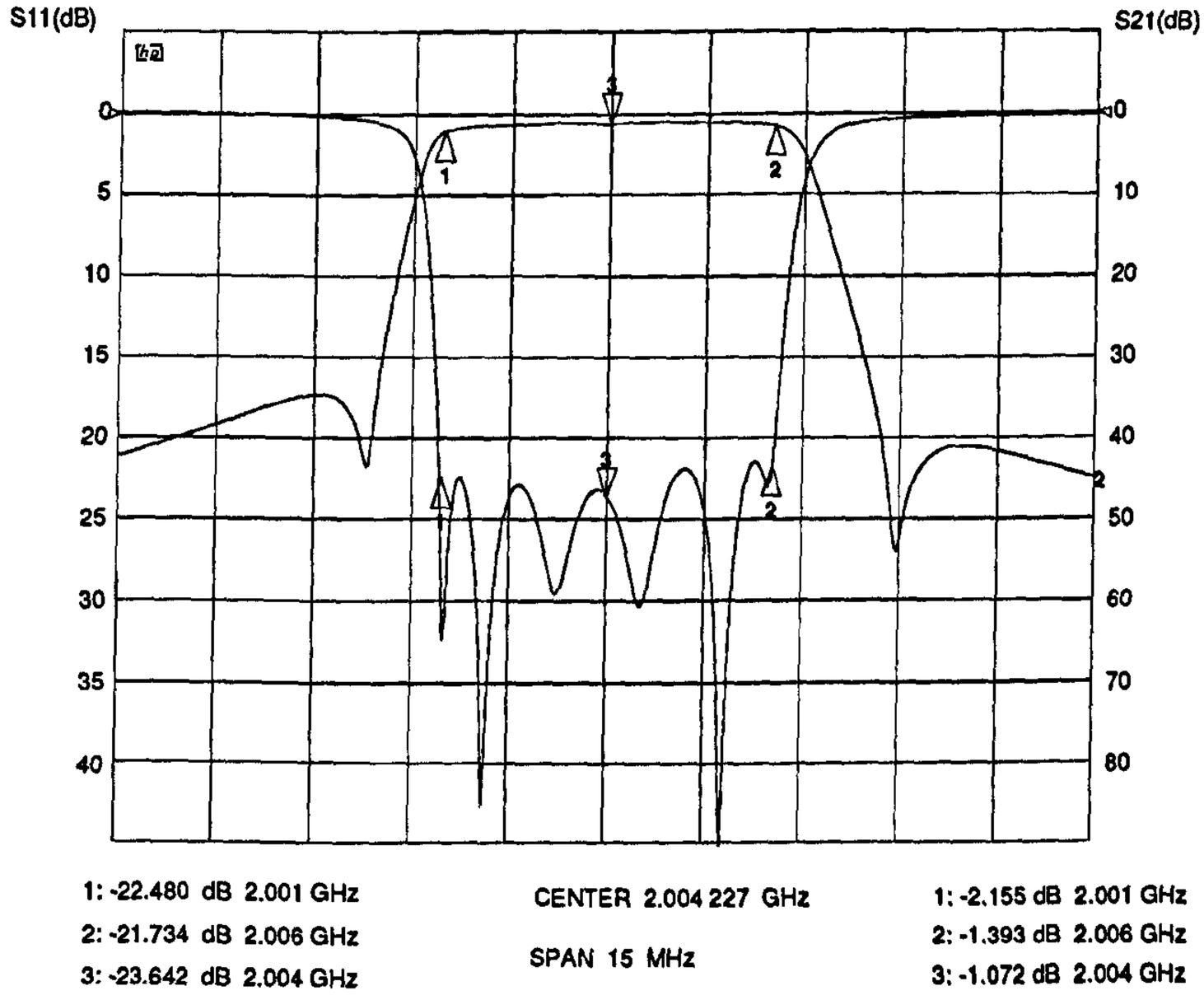

Figure 2.39: Measured frequency response of the Chebyshev filter with central iris and modes swapped

the two spurious couplings are adding up while they were previously cancelling. In any case, the 1-6 coupling level once again is worse than for the top iris.

It was felt that, in the general case, no iris will provide the amount needed for the main line coupling without introducing a significant amount of spurious cross-coupling. As a result, if this cross-coupling needs to be cancelled to achieve the desired frequency response, an additional coupling path has to be created.

For some filter networks, the 1-6 coupling, considered up to now as a spurious coupling, is actually needed. In this case, independent control of its level is necessary to easily tune the filter to the right response. Although the magnetic fields of the three modes are significantly different at the irises previously considered, very little independent tuning can be achieved. For example, the fields of modes A at the top iris of Fig. 2.30 are predominantly directed along the iris length where they have half a cosine variation. The fields of modes C are also significantly oriented along the iris length, although less so than modes A, but exhibit a full sine variation. As a result, a tuning screw across the centre of the iris should proportionally increase the coupling of modes A with respect to modes C, compared to tuning screws offset on each side of the centre. However, this effect is very limited, as the offset screws are not located in a null for the fields of modes 3 and 4 and still predominantly increase the 3-4 coupling. As an example, Fig. 2.40 shows the response of the filter in Fig. 2.30, first tuned with a tuning screw at the centre of the iris, as in Fig. 2.34, and secondly with tuning screws offset by 10 mm from each side of the centre. As expected, the second response shows an increase of the 1-6 coupling, even though this increase is estimated at only 10.6 %. As a result, a separate path is necessary to tune the spurious coupling. This will be discussed in the next section.

2.4.4 Cross-coupled filter with separate path to control the 1-6 coupling

In the general case, a fully cross-coupled filter response might be required. As a first step, a degree 6 filter with 2-5 iris cross-coupling is designed. The control of the 1-6 cross-coupling is then investigated.

Table 2.5 lists the coupling bandwidths for a 5 MHz wide, degree 6 filter with 30 dB rejection 1 MHz either side of the passband. The layout in Fig. 2.41 shows the

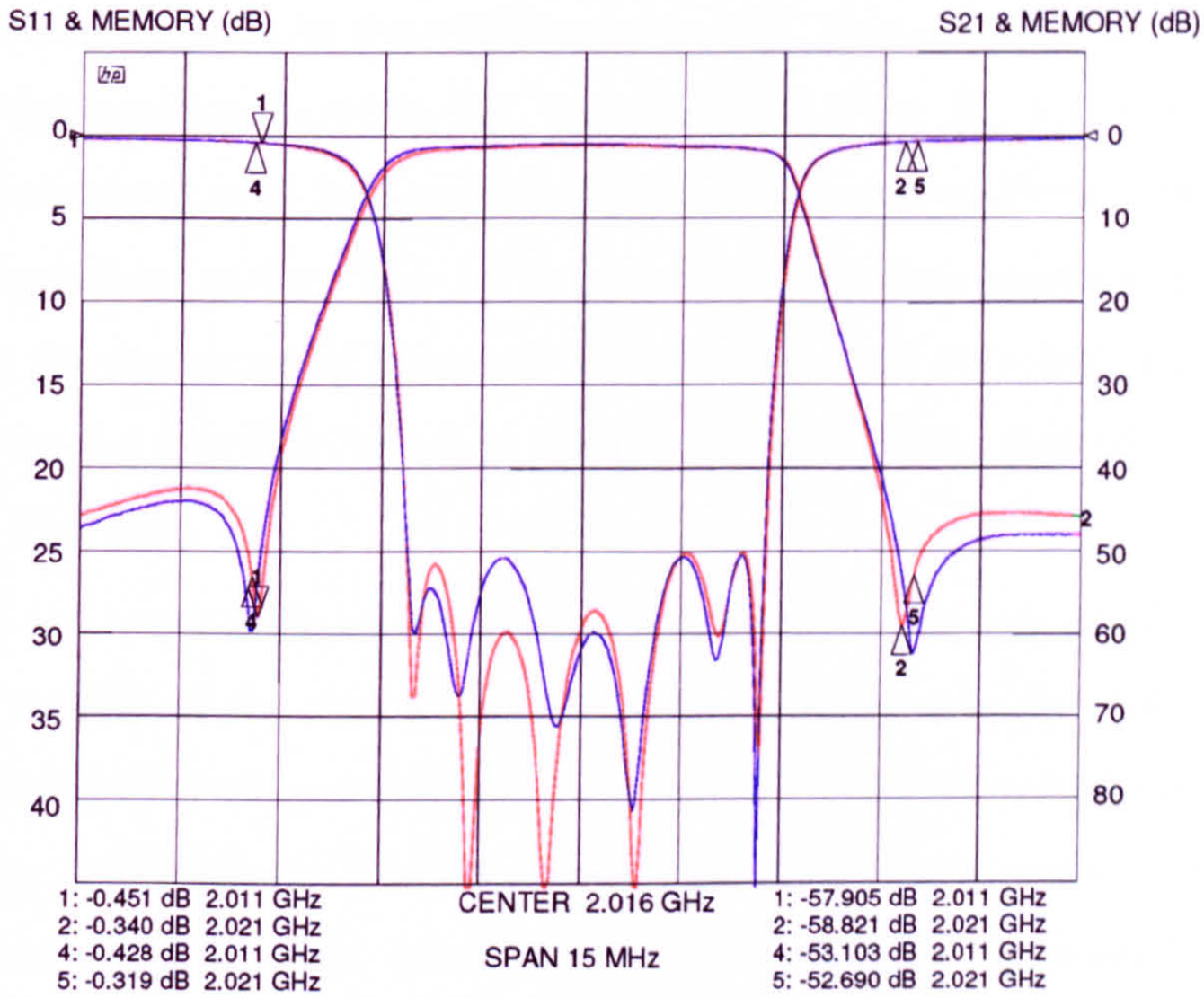

Figure 2.40: Measured frequency response of the Chebyshev filter with central tuning (in blue) and offset tuning (in red) of the top iris.

Table 2.5: *Cross-coupled filter coupling bandwidths. Equiripple bandwidth:* 5 MHz, *return loss:* 25 dB, 30 dB *shoulder level.*

Nodes	Coupling BW (MHz)	Nodes	Coupling BW (MHz)
input-1	6.03		
1-2	4.55		
2-3	2.95		
3-4	3.75	2-5	0.93
4-5	2.95		
5-6	4.55		
6-output	6.03		

locations of the chamfers so that both the wanted the 2-5 and spurious 1-6 couplings create transmission zeros on the real frequency axis. The measured narrowband and wideband responses are shown in Fig. 2.43 and 2.44. From Eq. 1.5, the overall Q of the filter is estimated at 15 700, equivalent to a reduction of 15.3% over the simulated Q_u of an aluminium cavity. The 1-6 spurious coupling now happens through both irises. From the experimental response, we deduce that the 1-6 coupling is 0.19 MHz, or 5.0% of the 3-4 coupling, which is slightly less than twice that of the single iris coupling of Fig. 2.31.

In order to cancel some of the existing 1-6 coupling, an iris would have to introduce a coupling of the opposite phase to the existing coupling, i.e. an electric coupling. However, electric coupling occurs through the field component normal to the iris plane, which modes 1 and 6 do not have [154]. As a result, in the general case, an extra coupling path, other than an iris, needs to be created. The configuration presented in Fig. 2.45 was used. To achieve selective coupling of modes 1 and 6, probes parallel to the electric field were inserted opposite the input and output transformers, and connected externally by means of a length of transmission line. The determination of the different circuit parameters in order to achieve the required change in 1-6 coupling level is described below.

The two capacitive probes are inserted and one is connected to a 50 Ω line. The measured reflected delay and phase shift at the end of the line are used to deduce the coupling, with an equivalent capacitance value C, and the phase shift ϕ_1 created by the probe. These values can then be used in the filter network model. As the

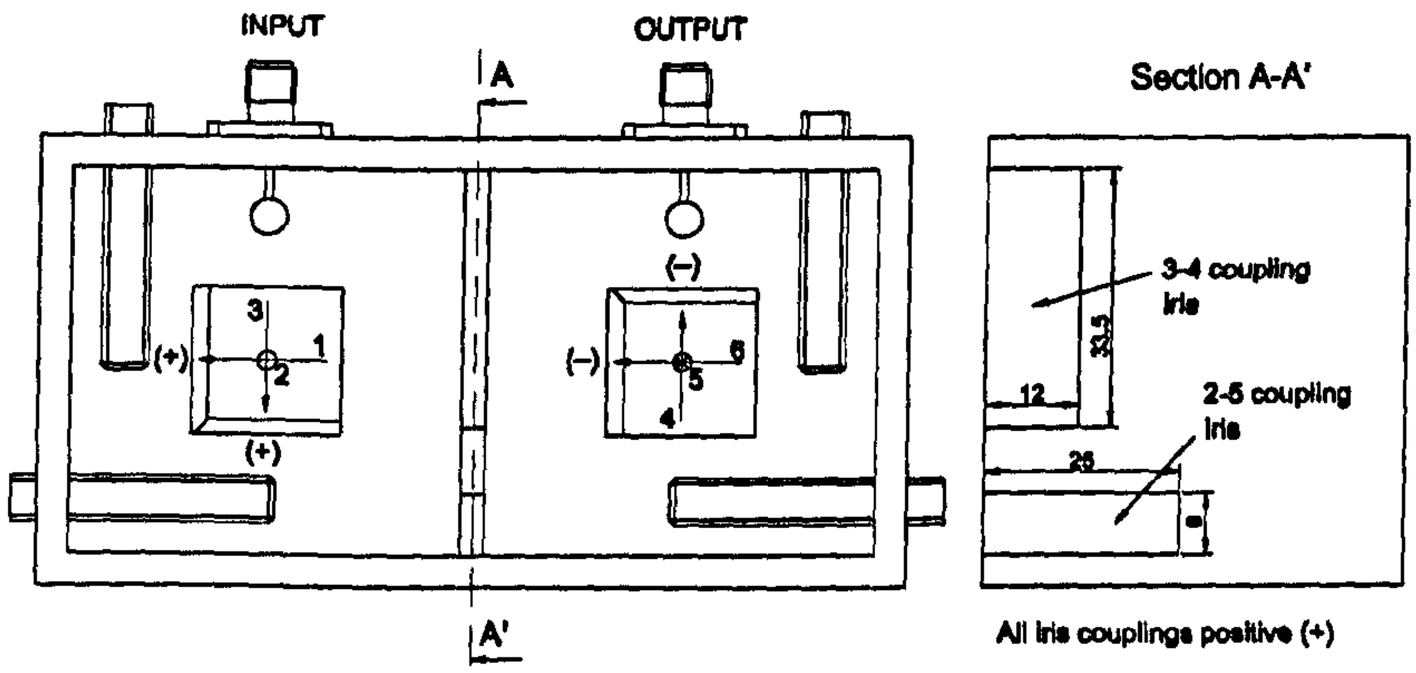

Figure 2.41: Layout of cross-coupled filter

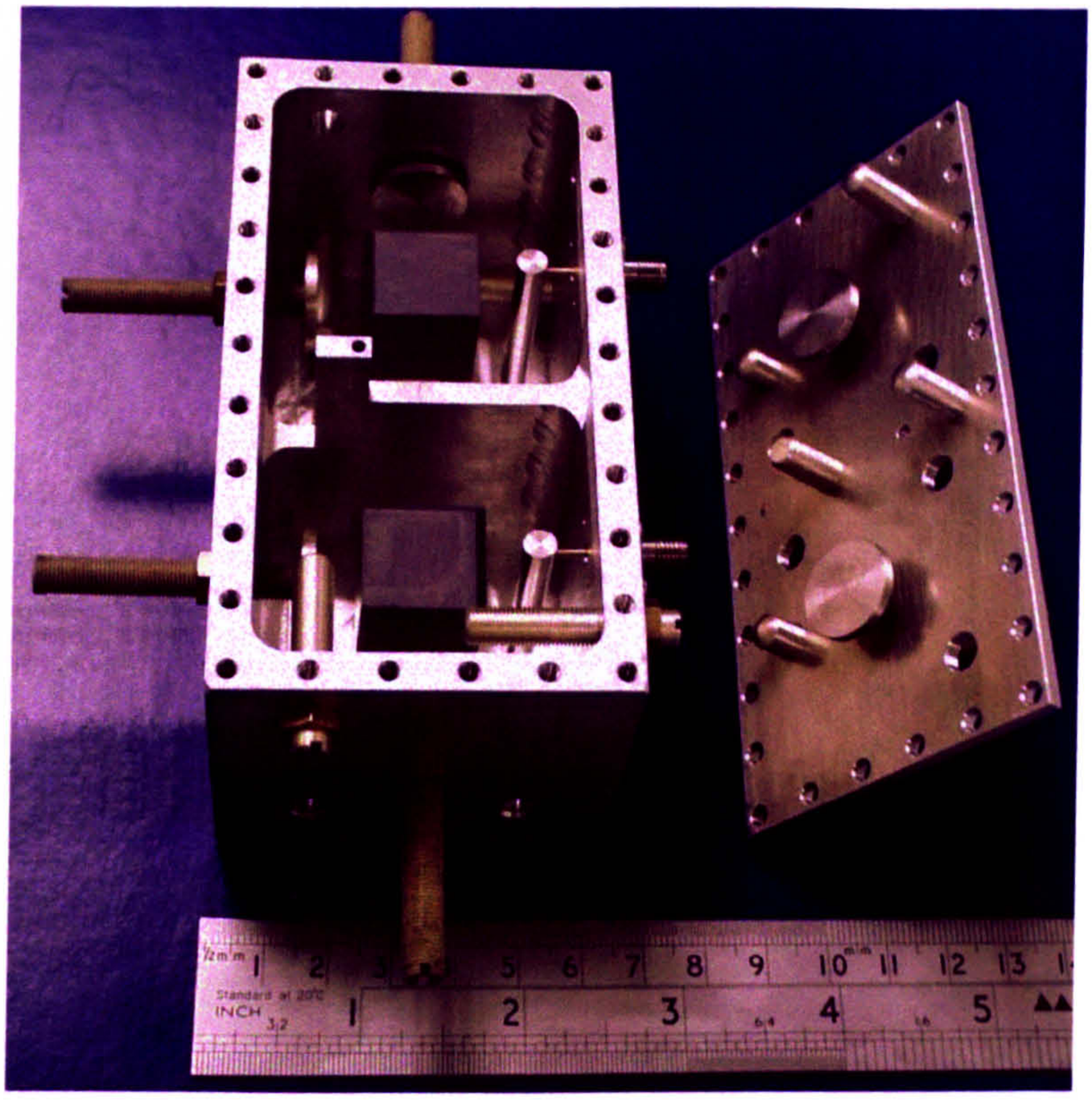

Figure 2.42: Picture of the cross-coupled filter

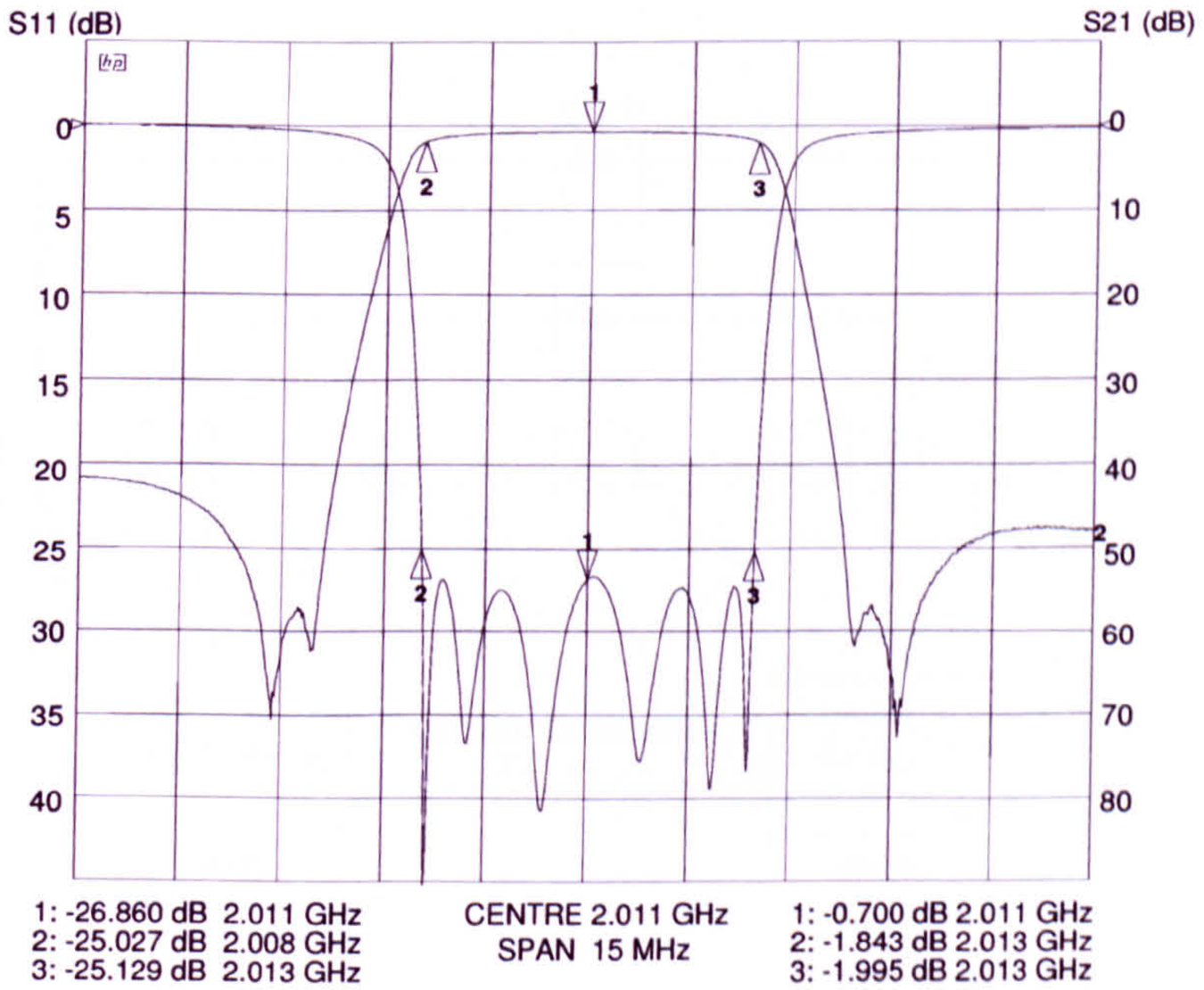

Figure 2.43: Measured narrowband frequency response of the cross-coupled filter

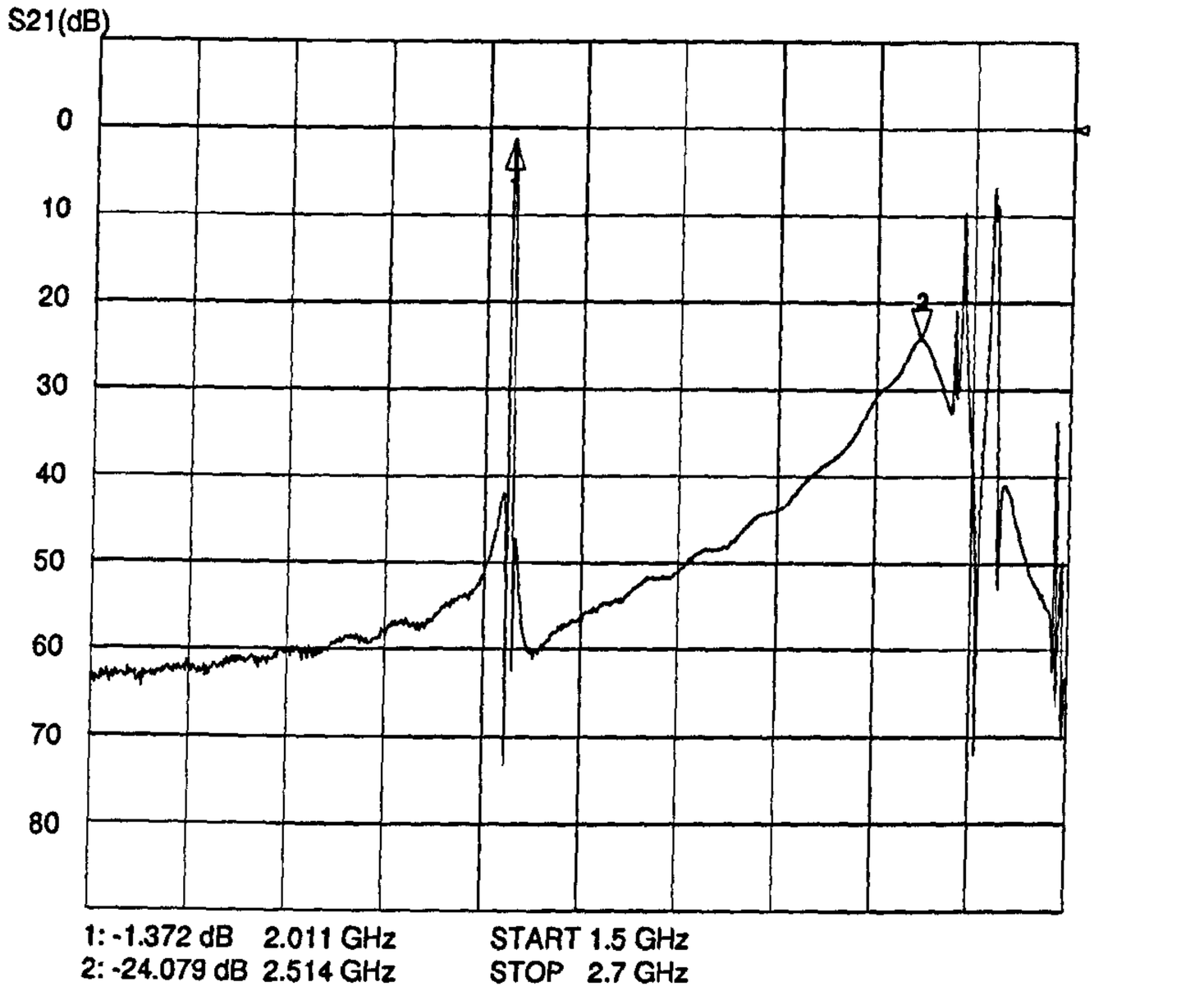

Figure 2.44: Wideband measured frequency response of the cross-coupled filter

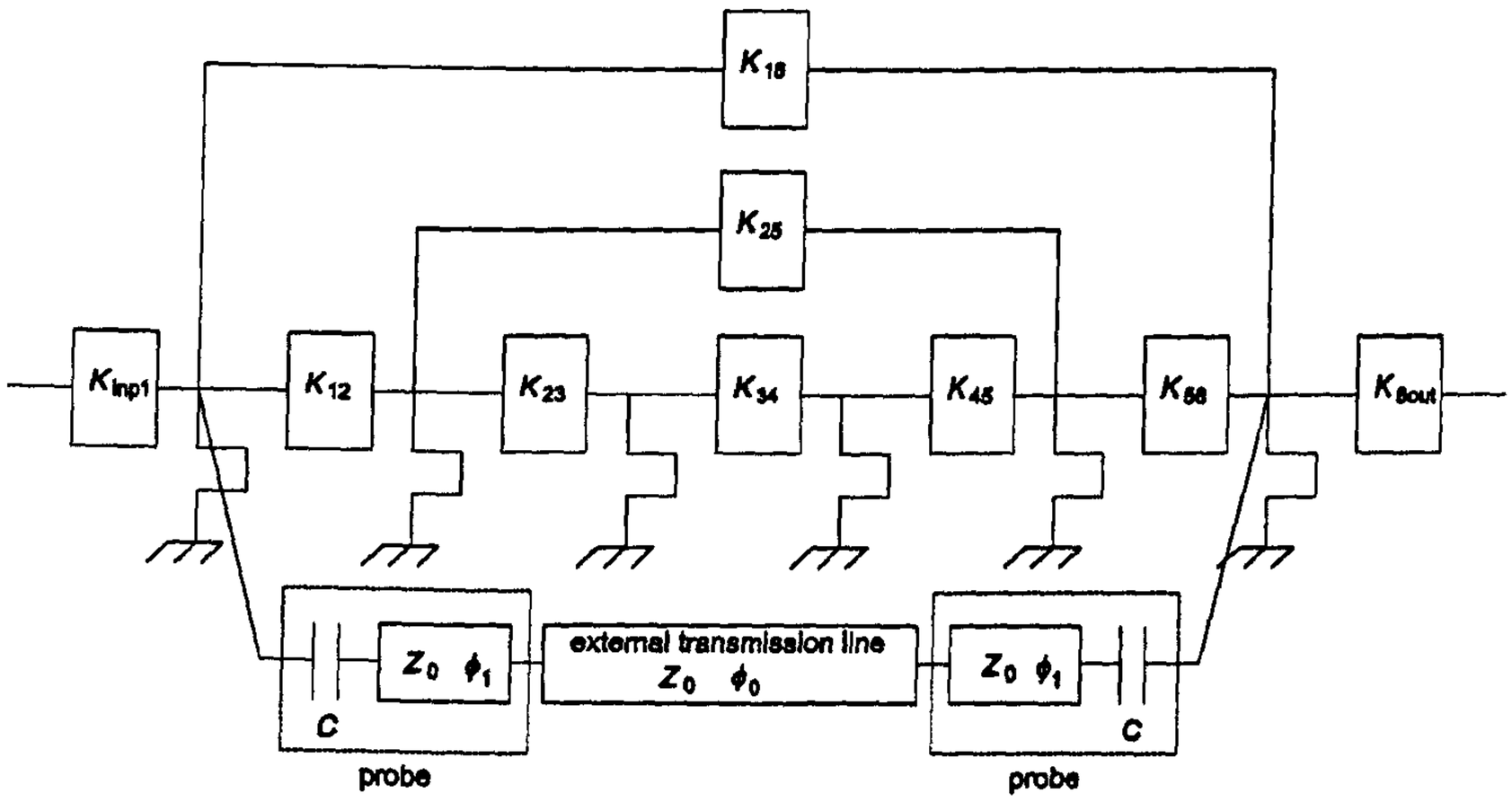

Figure 2.45: External 1-6 cross-coupling

capacitance is difficult to tune without physically changing the length of position of the probe, it was decided to keep a fixed capacitor value and study the possibility of creating the new coupling by adequately choosing the other circuit parameter values: impedance and length of the connecting line. These are linked to the desired inverter impedance K'_{16} by equating the transfer matrix of the latter with that of the network in Fig. 2.46.

$$\begin{bmatrix} 1 & 0 \\ jB & 1 \end{bmatrix} \begin{bmatrix} 1 & \frac{1}{jC\omega} \\ 0 & 1 \end{bmatrix} \begin{bmatrix} \cos\phi & jZ_0\sin\phi \\ \frac{j\sin\phi}{Z_0} & \cos\phi \end{bmatrix} \begin{bmatrix} 1 & \frac{1}{jC\omega} \\ 0 & 1 \end{bmatrix} \begin{bmatrix} 1 & 0 \\ jB & 1 \end{bmatrix} = \begin{bmatrix} 0 & jK \\ \frac{j}{K} & 0 \end{bmatrix} \tag{2.48}$$

This can be re-written as

$$\begin{bmatrix} 1 & \frac{1}{jC\omega} \\ 0 & 1 \end{bmatrix} \begin{bmatrix} \cos\phi & jZ_0\sin\phi \\ \frac{j\sin\phi}{Z_0} & \cos\phi \end{bmatrix} \begin{bmatrix} 1 & \frac{1}{jC\omega} \\ 0 & 1 \end{bmatrix} = \begin{bmatrix} 1 & 0 \\ -jB & 1 \end{bmatrix} \begin{bmatrix} 0 & jK \\ \frac{j}{K} & 0 \end{bmatrix} \begin{bmatrix} 1 & 0 \\ -jB & 1 \end{bmatrix} \tag{2.49}$$

which yields

$$\cos\phi + \frac{\sin\phi}{Z_0 C\omega} - KB = 0 \tag{2.50}$$

$$\frac{\sin\phi}{Z_0} - \frac{1}{K} + B^2K = 0 \tag{2.51}$$

and

$$K + \frac{2\cos\phi}{C\omega} + \frac{\sin\phi}{Z_0C^2\omega^2} - Z_0\sin\phi = 0 \tag{2.52}$$

Choosing a value for Z_0, Eq. 2.52 is solved numerically for ϕ. Not all values of Z_0 give a solution. ϕ_0 is then deduced from ϕ to give the length of external line. B is calculated from Eq. 2.51. Eq. 2.50 is automatically satisfied as the terms of the reciprocal network transfer matrices satisfy $AD - BC = 1$.

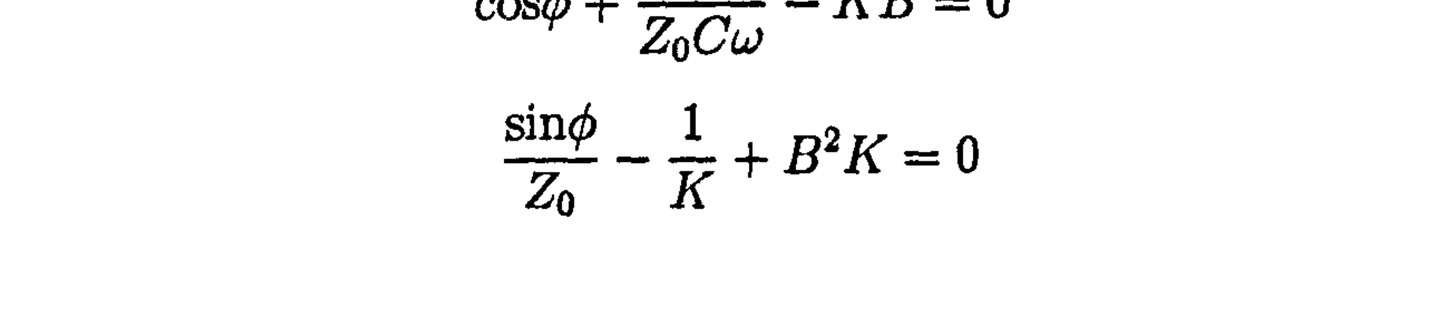

Figure 2.46: External cross-coupling equivalent network

As an example, the spurious 1-6 coupling is cancelled completely. The measured response of Fig. 2.43 is reproduced with an equivalent circuit model as in Fig. 2.28. The impedance of the stub resonators is set to 0.12 Ω. This is entirely arbitrary: if a different impedance is chosen, new values of C and ϕ_1 are extracted from the measured reflected signal and the external line length calculated from Eq. 2.51 and Eq. 2.52 remains the same. The inverter value to synthesise is $-K_{16} = -1811.6\ \Omega$. C is evaluated at 0.277 pF and ϕ_1 at 29°. A solution to Eq. 2.51 and Eq. 2.52 exists for $Z_0 = 46.8\ \Omega$. It is $B = -3.391\ m\Omega^{-1}$ and $\phi = 72°$ or 432°. Choosing the longer length, the external line then needs to be $\phi - 2\phi_1 = 374°$ in air or 97 mm of microstrip line on 30 thou Taclam. Fig. 2.47 shows the simulated response before and after cancelling. A resonance below passband is visible on the simulated wideband response in Fig. 2.48, which is due to the long electrical length of the external line. The filter hardware is shown in Fig. 2.49. The measured responses are shown in Fig. 2.50 and Fig. 2.51. This shows that this technique works as a method of cancelling the 1-6 coupling.

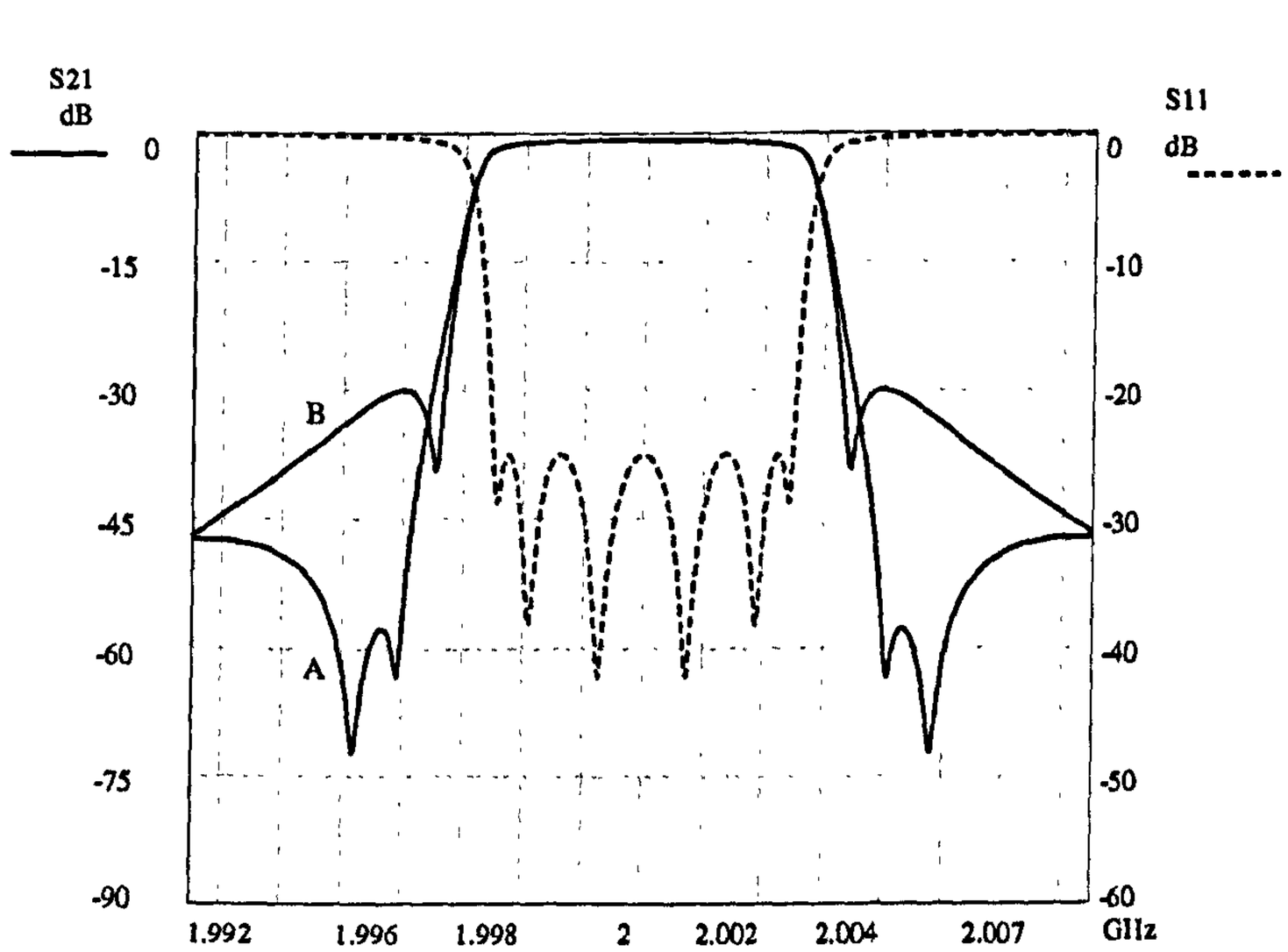

Figure 2.47: Simulated response of the cross-coupled filter before (A) and after (B) cancelling of the 1-6 coupling

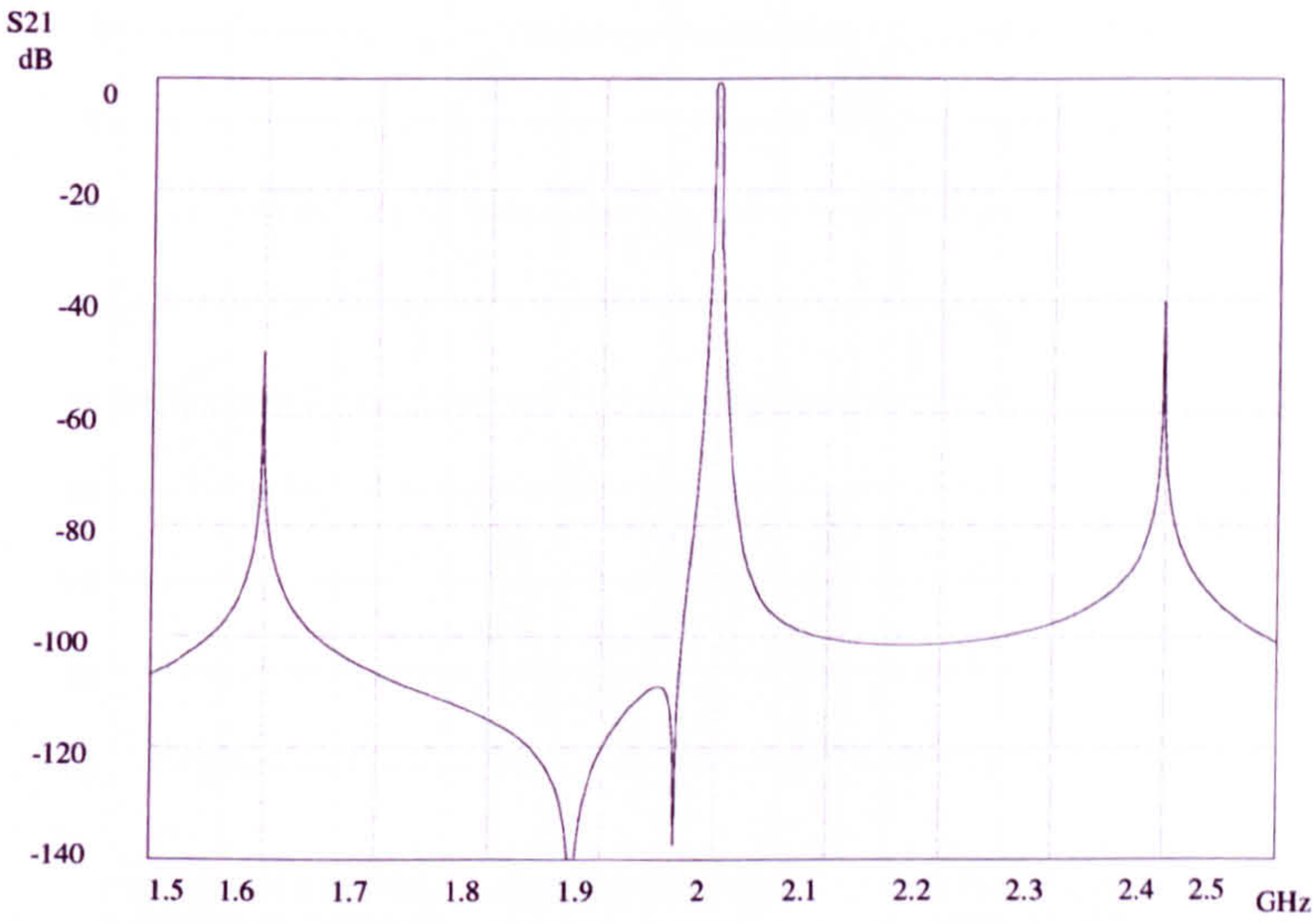

Figure 2.48: Simulated wideband response of the cross-coupled filter after cancelling of the 1-6 coupling

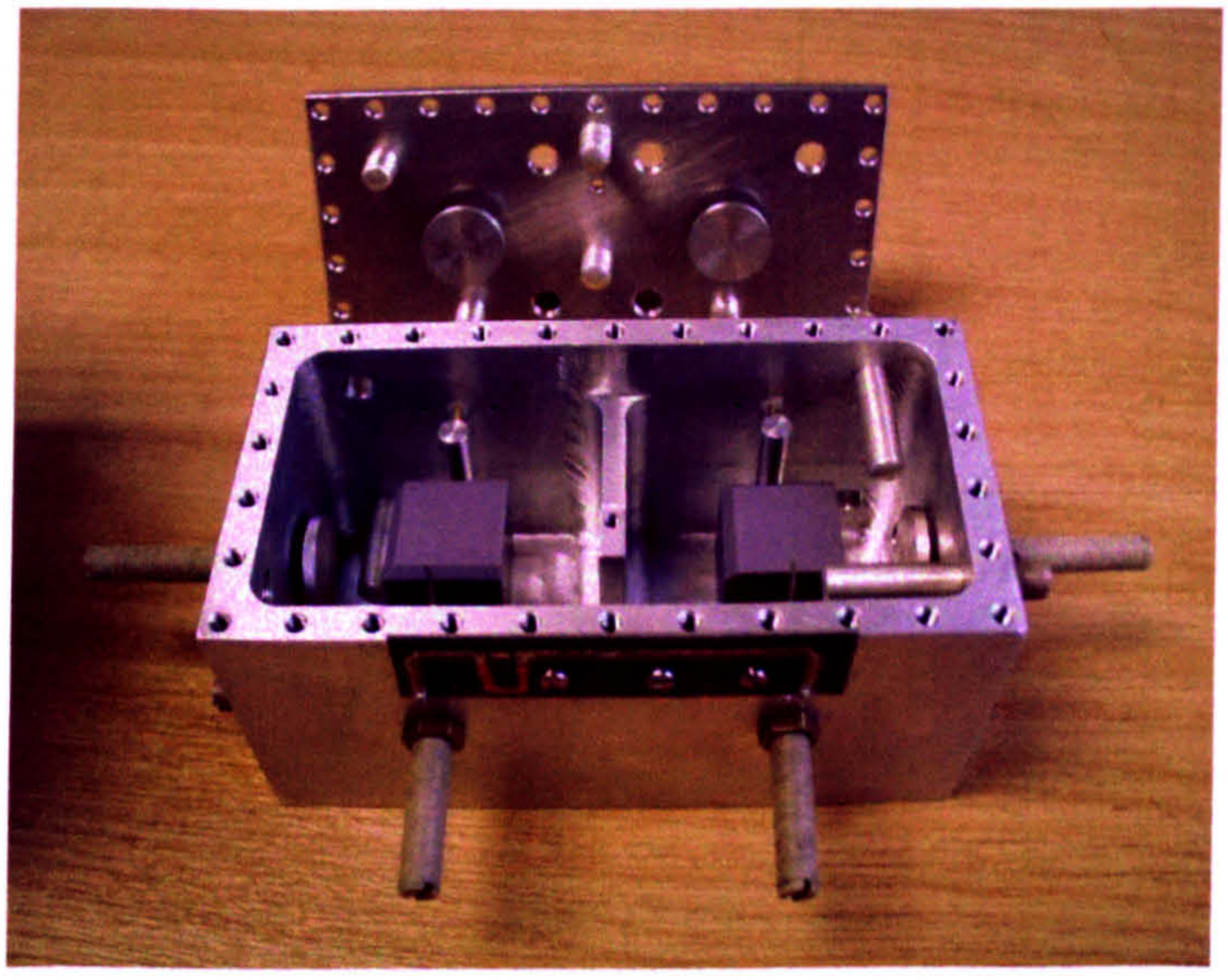

Figure 2.49: Picture of the cross-coupled filter with cancelling of the 1-6 coupling

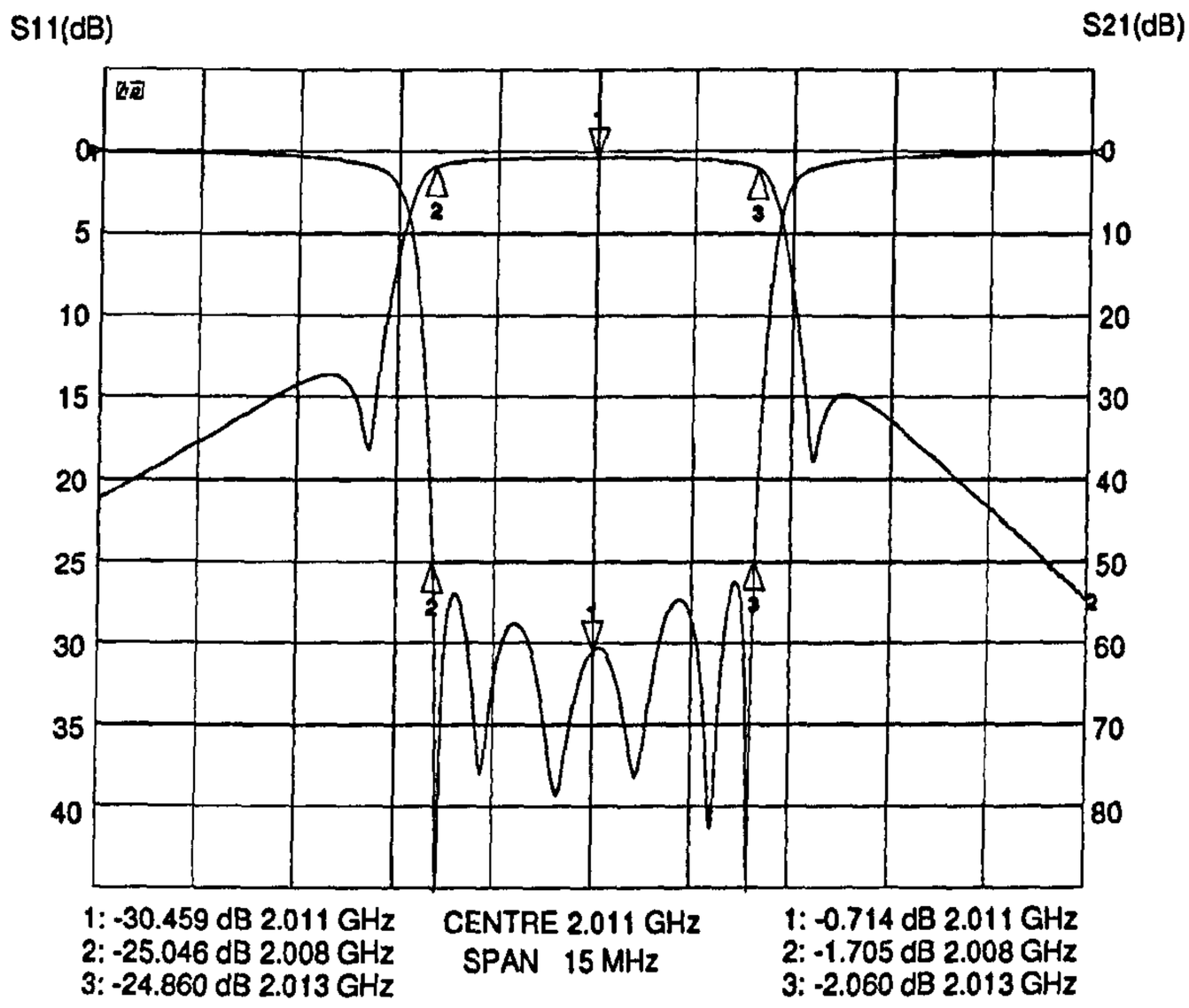

Figure 2.50: Measured response of the cross-coupled filter after cancelling of the 1-6 coupling

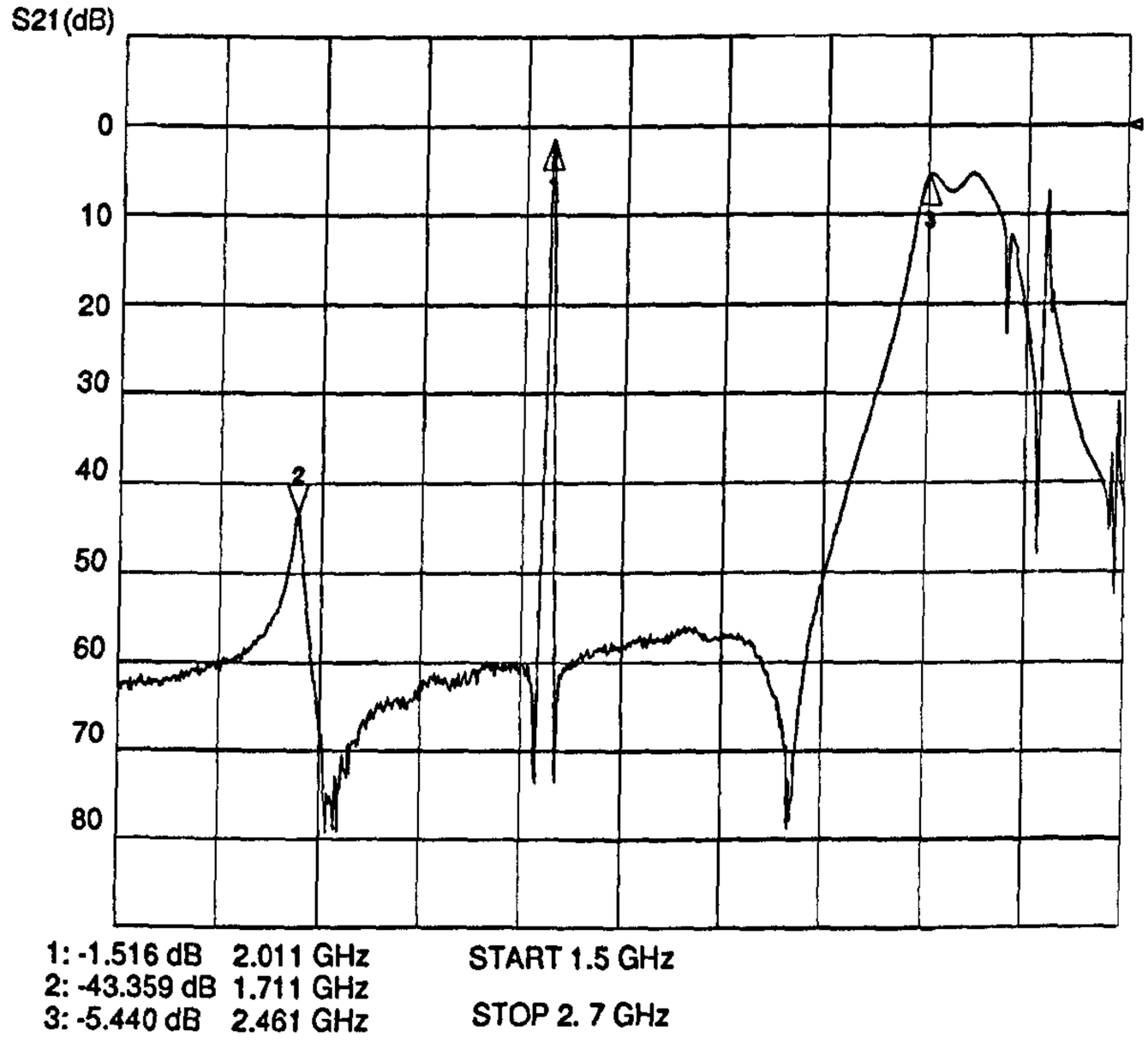

Figure 2.51: Measured wideband response of the cross-coupled filter after cancelling of the 1-6 coupling

2.5 Conclusion

In this chapter, the good performance of the new triple-mode $TE_{01\delta}$ was demonstrated. Its simple shape and small size while retaining a good spurious performance makes it an attractive alternative to the single-mode $TE_{01\delta}$. This resonator is best adapted for narrowband low loss applications, where high Q_u are needed and the coupling bandwidths required are limited. Reductions of 50% of the cavity volume over single-mode $TE_{01\delta}$ are achievable.

It was shown that conventional narrowband transmission filters can be designed and tuned, with only restricted and simple modifications to the basic cubic shape of the resonator. Different methods for frequency tuning and coupling of the modes were investigated. A wide range of filter responses is achievable through the choice of the coupling signs created by the chamfers and the realisation of inter-cavity cross-couplings. The sign of each coupling can be predicted. However, it was concluded that the realisation of three independent iris couplings between cavities was not possible, which somewhat restricts the ease of use of the new filters. A method for cancelling spurious couplings between modes in adjacent cavities was demonstrated. Q_u/volume improvements of 67% compared with single-mode $TE_{01\delta}$ filters were demonstrated from the passband insertion loss of the measured filters.

Also, the triple-mode $TE_{01\delta}$ cubic resonator was used to demonstrate a new type of filter: the reflection mode even-odd mode hybrid filter. Symmetrical cross-coupled filter responses can be realised in this manner with the double advantage of consisting only of two ladder networks (no physical cross-couplings required) and little sensitivity to most spurious couplings. However, drawbacks such as sensitivity to detuning with temperature and limited hybrid bandwidth restrict the use of this new filter realisation.

Chapter 3

Modelling of Dual-Mode Conductor-Loaded Dielectric Resonators

3.1 Introduction

In Section 2.2 of Chapter 2, it was shown that the $TM_{01\delta}$ modes become the fundamental modes of the suspended dielectric resonator as the dielectric filling ratio is increased. Being E modes, or electric dipole modes, their electric fields can terminate on two opposite conducting walls and their field distribution is little affected by the proximity of these walls to the ceramic. As the walls normal to the electric fields get closer to the ceramic, the amount of variation of the fields magnitude along the E field direction is decreased. When the metal is in contact with the ceramic, the resonator is in fact a dielectric-loaded waveguide resonator (TM_{010}) and the fields are uniform along one direction. This resonator will be studied extensively in Chapter 5.

Rather than terminating the fields on two opposite ends as for the TM_{010} mode, two degenerate E modes can be forced to be the two fundamental modes by lowering the dielectric resonator down to the bottom of the cavity. These two modes are, to start with, two of the three $TM_{01\delta}$ modes of the suspended DR. As the resonator is lowered, they decrease in frequency and cross over with the $TE_{01\delta}$ mode. When the resonator is in contact with the cavity, their electric field is terminated on the surface where the dielectric and metal contact. The two modes are then similar to half-cut $TE_{01\delta}$ resonators. As the contact between ceramic and the housing is only on one plane, the temperature behaviour of the resonator is easily controllable. However, a drawback of the resonator is its fairly poor spurious performance, with the $TE_{01\delta}$ mode resonant frequency around 1.3 times that of the fundamental mode.

To improve this, the frequency of the fundamental can be decreased by placing a conducting disc on the top of the resonator. Finite element field simulations have shown that this eliminates most of the field variations of both electric and magnetic fields along the axis normal to the disc and cavity base (as for the TM_{010} resonator). The $TE_{01\delta}$ mode resonant frequency increases, as the metallic boundary is created parallel to its electric field. The spurii of other E modes come down in frequency, as their electric fields can now, like that of the fundamental mode, terminate on the two parallel metallic planes. The new first spurii are the $EH_{11\delta+1}$ and the $TM_{01\delta}$ modes. Overall, however, Fr is improved.

3.2 Approximate models of the resonator

3.2.1 Description of the resonator structure

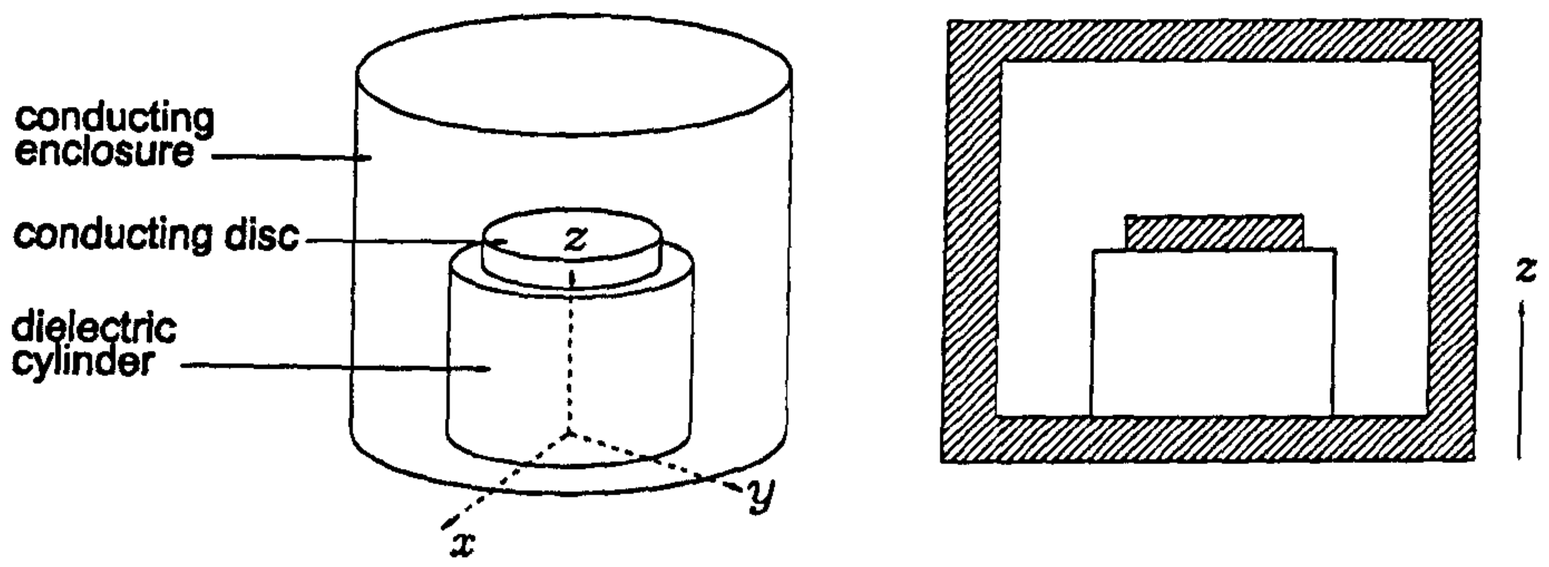

Figure 3.1: Dual-mode conductor-loaded dielectric resonator geometry

In order to simplify the calculations both in the following approximate studies and in the more detailed modelling of Section 3.3, the dielectric resonator, metal disc and cavity are considered to be of cylindrical shape and concentric. Fig. 3.1 shows such a resonator. However, resonators with the same basic structure but with different cross-sections, e.g. square, for the dielectric, disc or cavity in the $x-y$ plane would have very similar characteristics. This is provided the geometry has a rotational symmetry through 90° around the z axis.

The running time of exact models such as finite element analysis or mode-matching models can be very important. Approximate models that give a reasonable accuracy of the resonant frequencies of the first resonant modes are then valuable.

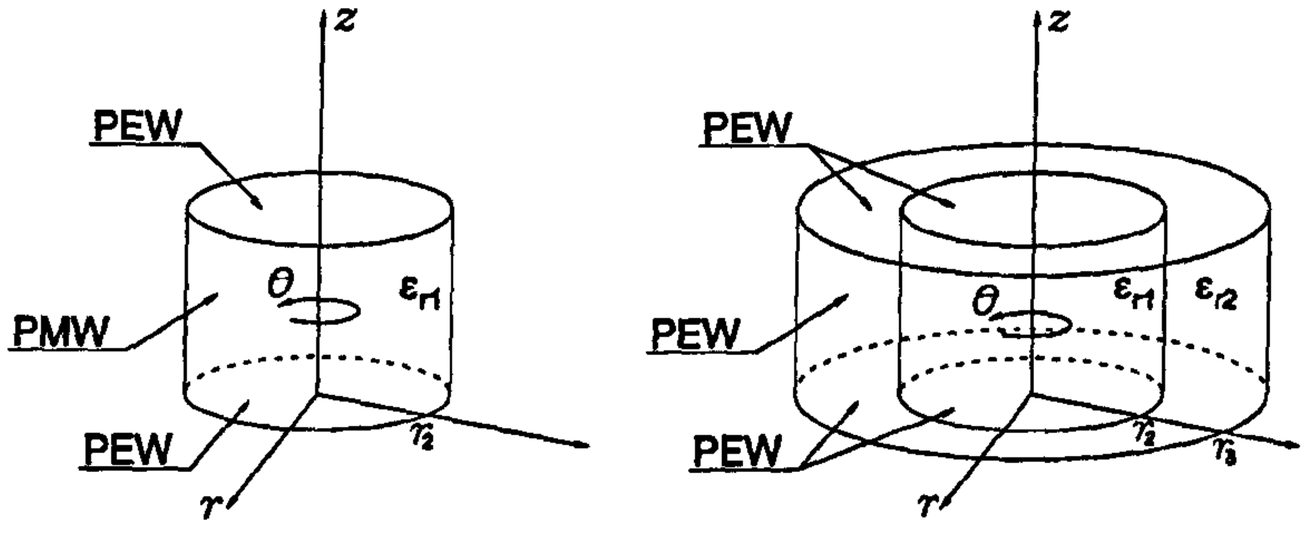

Figure 3.2: Approximation models of the dual-mode conductor-loaded dielectric resonator

The two simple models considered here are shown in Fig. 3.2. First, the basic cavity model, where only the dielectric region is retained, is considered. As mentioned in Section 1.5.1, this is a good first approximation as most of the fields of the modes are concentrated within this region. The top and bottom of the dielectric resonator are approximated to perfect electric conductors. Because of the large value of the ceramic permittivity, the periphery of the resonator is approximated to a perfect magnetic conductor. In the second model, the air region surrounding the dielectric is kept. The model then consists of a piece of dielectric-loaded waveguide terminated at both extremities by a perfect electric conductor. Of course, these models will be more accurate if the metal disc is relatively large with respect to the dielectric cylinder.

A resonator with the following dimensions is considered:

Cavity :	Diameter : 65 mm	Height : 40 mm	
Resonator :	Diameter : 38 mm	Height : 23 mm	ϵ_r : 44
Disc :	Diameter : 30 mm	Height : 3 mm	

In order to assess the accuracy of the models, the resonant frequencies of the first five resonant modes, obtained by finite element analysis with HFSS^{TM}, are listed in Table 3.1. Fig. 3.3 shows the field patterns of the modes.

Table 3.1: *Simulated resonant frequencies of the five first modes of the dual-mode conductor-loaded DR with $HFSS^{TM}$. 8705 nodes, 1810 elements (quarter of geometry only)*

Mode	$HE_{11\delta}$	$EH_{11\delta+1}$	$TM_{01\delta}$	$HE_{21\delta}$	$TE_{01\delta}$
Simulated f_0 (GHz)	0.9201	1.299	1.340	1.449	1.473

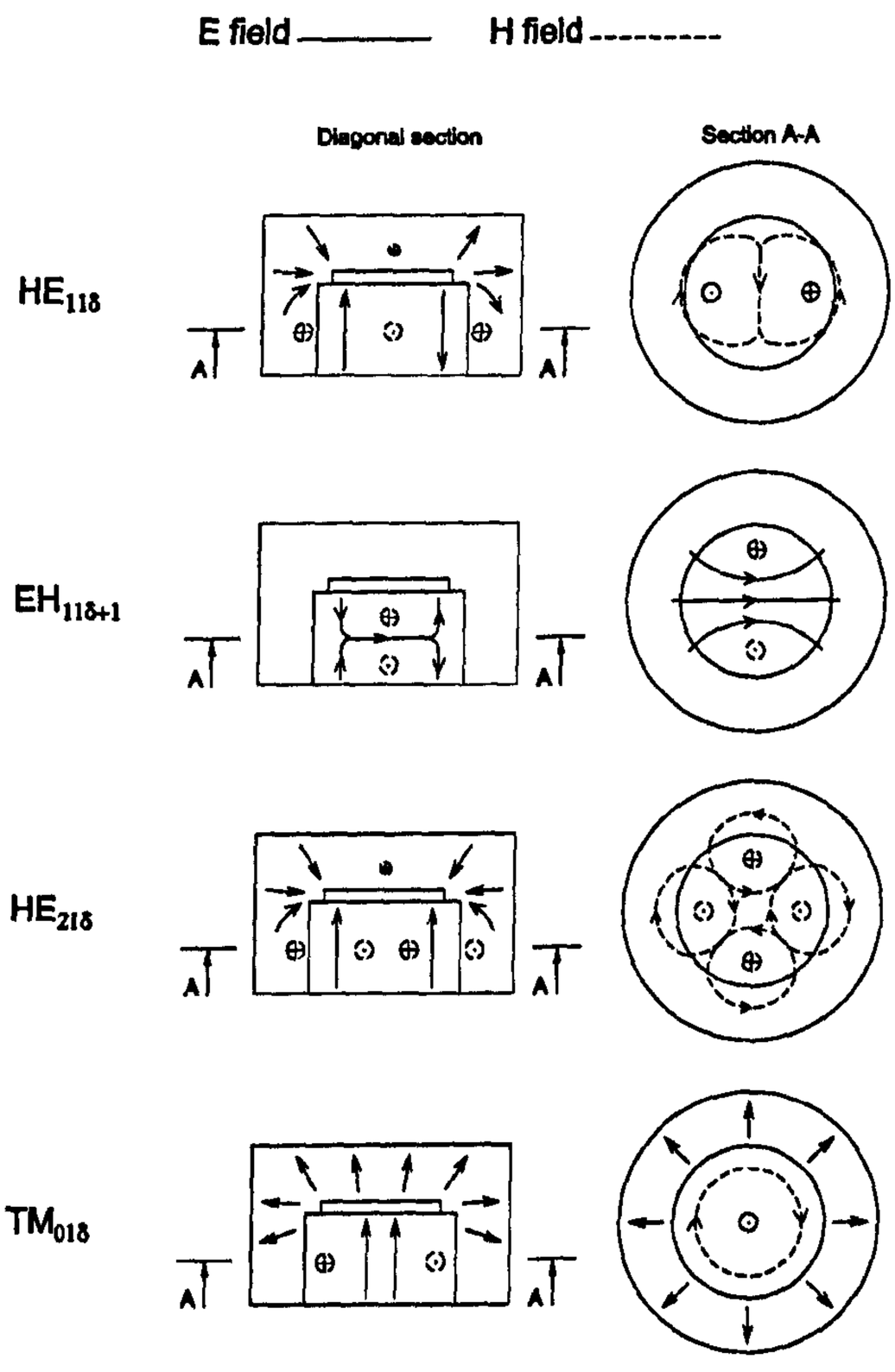

Figure 3.3: Field patterns of the first five resonant modes of the dual-mode conductor-loaded dielectric resonator

3.2.2 Hybrid modes

Cavity model

As the fields of the $HE_{11\delta}$ mode vary very little along the z axis, the corresponding mode in the cavity model is the TM_{110}. Let us consider a waveguide homogeneously filled with dielectric. The field expression of the TM_{11} in this waveguide can be deduced from the general expressions for homogeneous cylindrical waveguides listed in Section A.3. Ensuring a perfect magnetic wall at the periphery of the dielectric region $r = r_2$ yields:

$$H_\theta = \frac{k^2}{j\omega\mu_0\xi} J_1'(\xi r_2)\cos\theta = 0 \tag{3.1}$$

where J_n is the Bessel function of the first kind of order n and

$$\xi = \sqrt{k^2 + \gamma^2} \tag{3.2}$$

All the notations are introduced in Appendix A. ξr_2 is then root of $J_1'(x)$. The first root of $J_1'(x)$ is 1.8412. ξ is then deduced and the resonant frequency f_0 of the TM_{110} mode is found as the frequency which verifies:

$$\gamma = \sqrt{\xi^2 - k^2} = 0 \tag{3.3}$$

For the resonator diameter given above, $\xi = 96.9$ m^{-1} and $f_0 = 697.04$ MHz, which is 24.2% below the finite element field simulation result. This can be partially explained by the fact that some field variation along the z axis actually exist for the $HE_{11\delta}$ mode. However, the main reason for this discrepancy is thought to be the presence of the PMW which forces a null for H_θ and a maximum for E_z and H_r at the edge of the resonator. In the actual resonator, these points are located inside the dielectric region, which results in the fields being concentrated over a smaller region. It is especially critical in the case of E_z as the whole of the electric field is shifted towards the inside of the dielectric region.

In the case of the $EH_{11\delta+1}$ mode, Eq. 3.3 becomes

$$\gamma = \sqrt{\xi^2 - k^2} = \frac{j\pi}{h_A} \tag{3.4}$$

with h_A the height of the dielectric resonator. We find $f_0 = 1.2046$ GHz, which is 7.3% below the actual $EH_{11\delta+1}$ resonant frequency. Indeed, for this mode, a bigger part of the RF energy is situated at the centre of the puck, around the region of

radial electric field which is maximum at $r = 0$. As a result, the outward shift due to the PMW of the cavity model is less critical. This is not the case for the $HE_{21\delta}$ mode, which can then also be expected to be significantly underestimated by the cavity model. Referring to Section A.3, the PMW imposes the following condition to the magnetic field of the $HE_{21\delta}$ mode:

$$H_\theta = \frac{k^2}{j\omega\mu_0\xi} J_2'(\xi r_2)\cos 2\theta = 0 \tag{3.5}$$

or ξr_2 first root of $J_2'(x)$. From Eqs. 3.5 and 3.3, f_0 for the TM_{210} mode is estimated at 1.167 GHz, which corresponds to an underestimation of 20.2%.

Dielectric-loaded waveguide model

The field expressions and characteristic equation of a dielectric-loaded circular waveguide are given in Section A.1. They are listed for both a wave propagating and attenuating radially in the air region. In the first case, the wave number in the air region ξ_2 is real and the radial variations are described by J_n and Y_n, Bessel functions of the first and second kind. In the second case, ξ_2 is imaginary and is replaced by $\zeta_2 = j\xi_2 = j\sqrt{k_2^2 + \gamma^2}$ in modified field expressions using I_n and K_n, the modified Bessel functions [115, 30]. The resonant frequency is found by solving Eq. A.22 or Eq. A.31 with Eq. A.6 numerically. The value for γ is replaced by 0 for the $HE_{11\delta}$ and $HE_{21\delta}$ modes, and $\frac{\pi}{h_A}$ for the $EH_{11\delta+1}$ mode. As for the cavity model, the estimation of the $EH_{11\delta+1}$ mode is the most accurate, with an error of -0.7%. As before, the number of axial half sine variations is forced to 1 rather than $\delta+1$, which can explain that the resonant frequency is underestimated. On the other hand, the resonant frequencies of the $HE_{11\delta}$ and $HE_{21\delta}$ modes are overestimated by 12.6% and 3.1% respectively. In the case of the $EH_{11\delta+1}$ mode, the electric field terminating on the disc is forced to enter the dielectric region by crossing it radially. This is not the case for the two other hybrid modes. For these two modes, the electric fields are located at the fringe of the dielectric and terminated on the bottom of the cavity. As a result, part of the electric field can easily be shifted out of the dielectric region as the metal disc becomes larger than the dielectric resonator. The limiting case is that of the dielectric-loaded waveguide model. This explains why the resonant frequencies of the $HE_{11\delta}$ and $HE_{21\delta}$ modes were overestimated by the dielectric-loaded waveguide model. It is clear at this stage that the fields for these two modes are

very different from those of a classical waveguide mode, and that a more complex model will need to be build to predict their resonant frequencies and Q_u's with a good accuracy.

3.2.3 $TE_{01\delta}$ mode

Cavity model

This time H_z needs to be forced to 0 at $r = r_2$. Thus, from Eq. A.3,

$$H_z = \frac{\gamma}{j\omega\mu_0} J_0(\xi r_2) = 0 \tag{3.6}$$

or ξr_2 first root of $J_0(x)$. Using Eq. 3.4, the resonant frequency of the TE_{011} is estimated at 1.340 GHz, which is underestimated by 9.0%. As previously for the hybrid modes, the PMW is forcing a slower radial variation than in the actual resonator. In the latter, the axial magnetic field changes sign in the dielectric region rather than just vanishing at the resonator periphery, which explains the low calculated frequency.

Dielectric-loaded waveguide model

The fields of the $TE_{01\delta}$ mode are highly concentrated in the dielectric region. As a result, the metal disc will have a effect similar to a cavity lid sandwiching the dielectric material, particularly in the case of resonators with metal discs and dielectric resonators of comparable diameter. As a result, the dielectric-loaded waveguide model is expected to give an accurate approximation of the $TE_{01\delta}$ mode resonant frequency. The characteristic equations A.39 or A.43 are solved, substituting the wave numbers ξ for each region with Eq. A.6 and considering that $\gamma = \frac{\pi}{h_A}$. The result is 1.501 GHz, 1.9% above the frequency obtained by finite element field simulation.

3.2.4 $TM_{01\delta}$ mode

Cavity model

Similarly to the hybrid case, the PMW boundary condition at $r = r_2$ yields:

$$H_\theta = \frac{k^2}{j\omega\mu_0\xi} J_0'(\xi r_2) = 0 \tag{3.7}$$

or ξr_2 first root of J_0'. Considering the TM_{010} mode as the most adequate model for the $TM_{01\delta}$ mode, Eq. 3.3 has to be verified, which gives a resonant frequency of 1.452 GHz. The overestimation (8.3%) is explained by the fact that Eq. 3.7 forces some extra radial variation on the fields. For example, the axial electric field E_z of the actual resonator changes sign just before $r = r_2$, by opposition to $r = 0.63 \times r_2$ for the cavity model.

Dielectric-loaded waveguide model

This model is less accurate than the cavity model. Indeed, this second model does not allow any change of sign of E_z along the radial direction at all. The region of maximum fields is then extended towards the outside of the dielectric region and the resonant frequency is significantly underestimated. From Eqs. A.50, A.54 and A.6 and with $\gamma = 0$, the resonant frequency is estimated at 606 MHz, 54.8% below the actual resonant frequency. The change in sign of E_z in the actual resonator happens as the radial fields in the region outside the disc extend to the air region around the dielectric region. The electric field in this air region is then tilted vertically, but in the opposite direction to that of the E_z in the centre of the dielectric region, as seen in Fig. 3.3.

3.2.5 Conclusion on the models' accuracy

Even though the dielectric-loaded waveguide model does predict the resonant frequencies of the $TE_{01\delta}$, $EH_{11\delta+1}$ and $HE_{21\delta}$ modes within a few percent, both the fundamental frequency and the $TM_{01\delta}$ modes are badly estimated. For these, the use of an exact model, considering the whole of the geometry, is needed.

3.3 Mode-matching model of the resonator

In order to realise a systematic study of the resonator, it was decided to write a program based on the mode-matching technique. Such a program would allow the determination of the resonant frequencies, the Q_u's and the field distributions of resonator modes. This program will provide more detailed information than a commercially available software package. For example, the field magnitudes can be plotted individually for each waveguide mode, giving a better understanding of

their contribution to the overall resonant mode. The mode-matching technique was thought to be an efficient method for the study of the present resonator: it is a shielded resonator, for which the method is best adapted [19], as suggested by the numerous mode-matching studies of DR's already available. It is composed of a cascade of simple waveguides and its shape is unlikely to change drastically, and as such does not necessitate the use of the more versatile FEM [155].

3.3.1 Description of the modelled structure

The mode-matching technique has been extensively used for the past fifteen years to model cylindrical DR's. These studies are using either the radial technique [75, 38, 138, 156], where the waveguide sections consist of tubular parallel plate waveguides matched along the r direction, or the longitudinal mode-matching technique [52, 145, 146, 148, 138] where the matching is done along z. The former has in most cases the advantage of a shorter computing time, as no computation of Bessel functions are necessary for the calculation of the propagation constants of the waveguides normal modes [138]. However, it was also reported to offer slower convergence rates for modes having a large axial electric field (E_z) [38]. This is because this field component has a singularity near the edges of the dielectric resonator. It is then difficult to model with the waveguide modes in the tubular air region surrounding the dielectric, which have continuous variations in the z direction. It was suggested [19] that the axial technique would similarly have difficulties modelling modes with high radial electric fields. The mode that primarily needs to be matched here is the fundamental mode. Its first approximation is the TM_{110} mode, for which the electric fields are entirely longitudinal. In the general case, because of the proximity of the disc, many modes will contain high levels of E_z in the regions near the dielectric edge. However, as pictured in Fig. 3.3, the radial electric fields of these modes around the perimeter of the disc are also large, making it difficult to choose between the two methods.

Both methods divide the geometry into three waveguides. One future change to the geometry, which would improve the spurious ratio of the resonator, might be to change the solid resonator into a ring shape [157]. With the radial technique, this introduces a fourth waveguide region. With the axial technique, the number of regions is kept to three, but the resolution of the dielectric-loaded region characteris-

tic equation, in Appendix A, is made significantly more difficult. Another situation arises if the disc diameter is made larger than that of the dielectric resonator. In the case of the axial technique, the only changes necessary are the expression of a cross-coupling integral and a few of the Q_u analytical formulas. In the radial case however, the changes are more important as the metal then exists over two regions.

The axial technique was chosen and the resonator was split into three cylindrical waveguide sections as shown in Fig. 3.4. The structure can then be identified as a special case of the geometry studied in Section B.1.

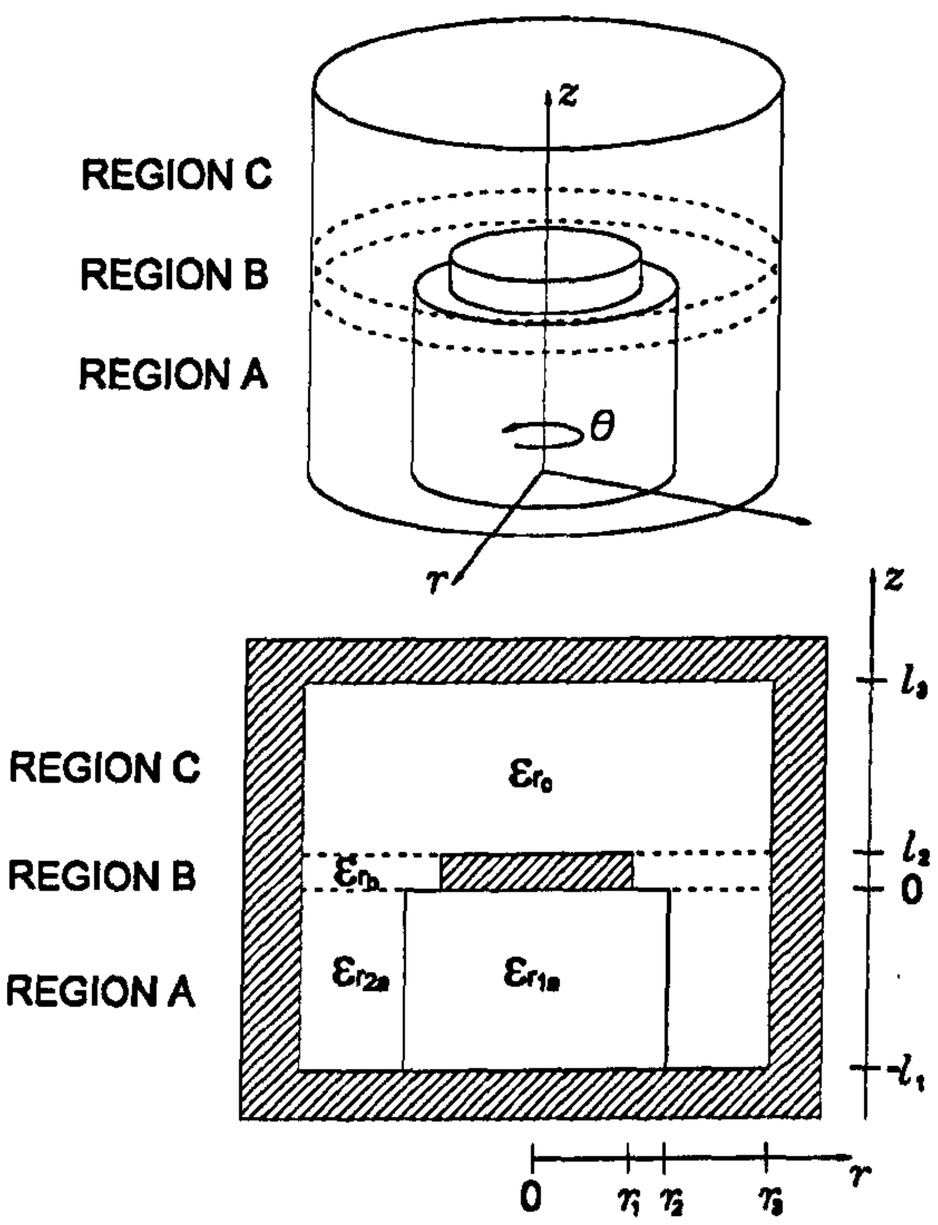

Figure 3.4: Subdivision of the resonator structure for mode-matching modelling

3.3.2 Computation of the waveguide modes propagation characteristics

All the mode characteristics (wave numbers ξ and propagation constants γ) follow from the resolutions of the characteristic equations detailed in Section A. The notations are essentially those introduced by [146], and used in their modelling work of cylindrical DR's.

Air waveguide (section C)

Such a circular waveguide supports TE and TM modes [158]. The resolution of their respective characteristic equations, A.75 and A.81, is an iterative process which could take a significant amount of CPU time, as it requires many evaluations of bessel functions. However, it only requires solving once for all frequencies and all waveguide dimensions. Noting $x = \xi r_3$, the equations

$$J'_n(x) = 0 \tag{3.8}$$

and

$$J_n(x) = 0 \tag{3.9}$$

with

$$J'_n(x) = \frac{n}{x} J_n(x) - J_{n+1}(x) \tag{3.10}$$

are solved with a simple routine using the Bessel evaluation functions of Matlab^{TM}. The characteristics of mode i in region C are then deduced from the i^{th} value of x, x_i, as:

$$\xi_i = \frac{x_i}{r_3} \tag{3.11}$$

$$\gamma_i = \sqrt{\xi_i^2 - k_c^2} \tag{3.12}$$

with k_c the vacuum wave number in region C. As the routine is not used repeatedly, it is kept as a simple and relatively slow routine, evaluating the value of the left-hand side of Eq. 3.8 or Eq. 3.9 at equidistant and increasing values of $x > 0$, and searching for a zero by the bisection method when two consecutive evaluations are of opposite signs. This is possible as both functions are continuous over the interval of interest.

Coaxial waveguide (section B)

A coaxial waveguide supports TE, TM and TEM modes [158]. A similar method to that used for the air circular waveguide is applied here for the study of the TE and TM modes. Noting $x = \xi r_3$ and $r_c = r_1/r_3$, their respective characteristic equations, Eqs. A.60 and A.66, simplify to

$$Y'_n(xr_c)J'_n(x) - J'_n(xr_c)Y'_n(x) = 0 \tag{3.13}$$

and

$$Y_n(xr_c)J_n(x) - J_n(xr_c)Y_n(x) = 0 \tag{3.14}$$

Note that Eq. 3.10 also holds for Y_n and Y_n'.

Here again, the values for x are independent of the frequency and the absolute values of the outer diameter r_3 and inner diameter $r_1 = r_3 r_c$ of the waveguide. They only depend on the inner to outer diameter ratio r_c. As a result, a new set of solutions for x will need to be extracted for every different value of r_c. This extraction presents no difficulty as the left-hand side of Eq. 3.13 and Eq. 3.14 are continuous for $x > 0$. Then,

$$\xi_i = \frac{x_i}{r_3} \tag{3.15}$$

$$\gamma_i = \sqrt{\xi_i^2 - k_b^2} \tag{3.16}$$

are deduced at any frequency and for any value of r_3.

The case of the TEM mode is trivial as it is fully defined by its characteristic equation, Eq. A.69:

$$\gamma = jk_b \tag{3.17}$$

Partially loaded dielectric waveguide (section A)

This waveguide supports hybrid modes (HE modes) except in the case of modes which are uniform along the θ direction, for which they split into two independent sets of TE and TM modes [159]. The characteristic equations for the HE, TE and TM modes are given in Eqs. A.22-A.31, A.39-A.43 and A.50-A.54 respectively. Let us call $G_c(\gamma^2)$ the left-hand side of these equations. The choice of γ^2 as the variable is arbitrary as all parameters of the mode (γ^2, ξ_1, and ξ_2 or ζ_2) are inter-related in a unique manner. In the literature, the variable ($\xi_1 r_2$) is more often used [160]. As ξ_1, and ξ_2 (or ζ_2), are related through

$$\xi_1^2 - \xi_2^2 = \xi_1^2 + \zeta_2^2 = \omega\mu_0\mu_r\varepsilon_0(\varepsilon_{r1} - \varepsilon_{r2}) \tag{3.18}$$

it is not possible to find the zeros of G_c as a function of any variable independently of the frequency, as was done for the two previous waveguides. As a result, $G_c(\gamma^2)$ will have to be scanned for its first zeros for each frequency of the study. Also, the extraction of the zeros is more difficult because $G_c(\gamma^2)$ has discontinuities, in the vicinity of which its gradient varies very rapidly. However, the relationships between the discontinuities and zeros of $G_c(\gamma^2)$ have been studied by Da Silva [160]. The study states that, in each interval between two consecutive discontinuities, $G_c(\gamma^2)$

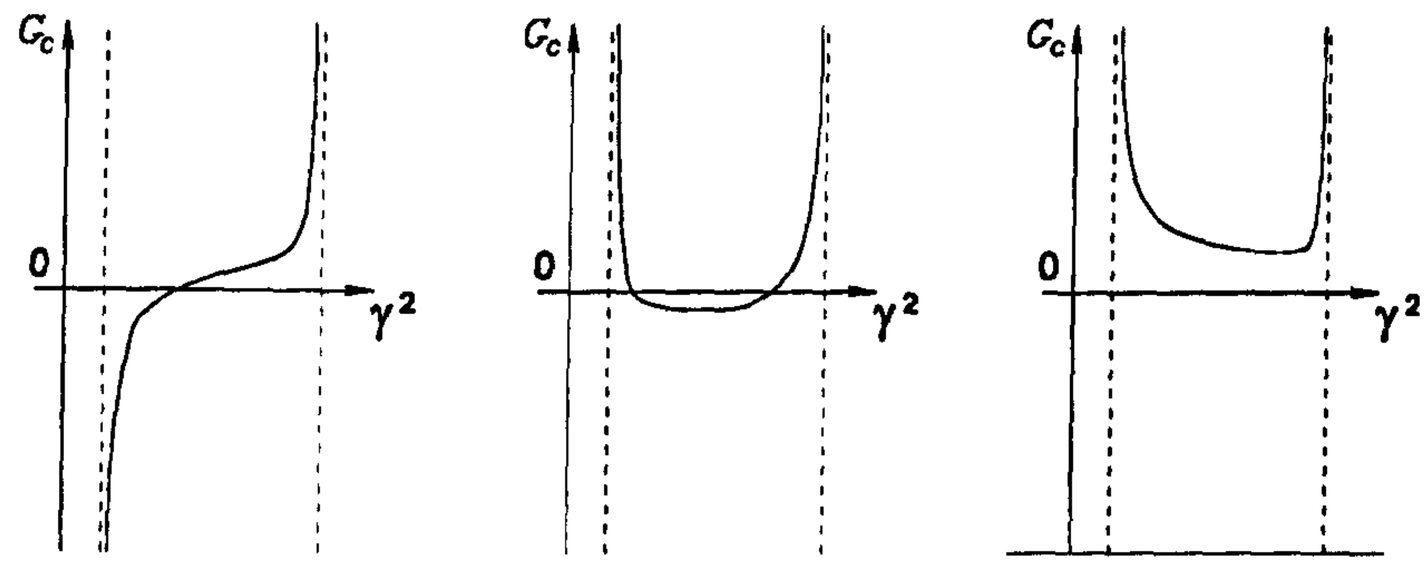

Figure 3.5: Possible variations of $G_c(\gamma^2)$ over each interval

has either one real, two real or two complex conjugate zeros. Fig. 3.5 shows the variations of $G_c(\gamma^2)$ in each case. As a result, the search for the zeros is greatly simplified. The first step consists of computing the discontinuities of $G_c(\gamma^2)$. For TM modes, they are $-k_2^2$, and the values of γ^2 verifying Eq. 3.9 with $x = \xi_1 r_2$ and Eq. 3.14 with $x = \xi_2 r_3$ and $r_d = r_2/r_3$. The latter two sets are available directly from the values of x previously computed for the two other waveguides. For the TE modes, they are $-k_2^2$, and the values of γ^2 verifying Eq. 3.9 with $x = \xi_1 r_2$ and the following equation with $x = \xi_2 r_3$ and $r_d = r_2/r_3$.

$$Y_n(xr_d)J_n'(x) - J_n(xr_d)Y_n'(x) = 0 \tag{3.19}$$

For the HE modes, all the previously listed zeros are combined.

The zeros of $G_c(\gamma^2)$ can then be computed on each interval. A real zero is extracted by the bisection method when the sign of $G_c(\gamma^2)$ is different at both limits of each interval. When the sign is the same, the minimum of $|G(\gamma^2)|$ is computed with the minimum finding routine of Matlab™. In the case of real zeros, the bisection method is applied twice to extract the two zeros. Because of the rapid variations of $G_c(\gamma^2)$, it was found to converge more reliably and sometimes faster than interpolation methods of higher degree, such as the secant method. For complex modes, γ^2 assumes complex values, which are extracted using Müller's method [138, 160]. It converges by successive parabolic interpolations of $G_c(\gamma^2)$ [161]. As γ is complex, so are ξ_1 and ξ_2, and the Bessel functions of the first and second kind are used to represent the variations of a localised propagating wave [115]. Müller's

method will converge on a value of γ^2, leading to two values of γ, $\gamma_1 = a + jb$ and $-\gamma_1 = -a - jb$. Two other values, $\gamma_2 = a - jb$ and $-\gamma_2 = -a + jb$ are also solutions of the characteristic equation, giving a total of four complex waves. The existence of complex modes in the circular dielectric-loaded waveguide was first demonstrated by Clarricoats et al. [31]. They have been reported in many other types of guiding structures with inhomogeneous dielectric filling, such as finlines [135, 139], shielded dielectric image guides [162] and microstrip lines [163]. General constraints for the existence of complex modes have been established, first by Chorney, and more recently in the case of reciprocal inhomogeneous isotropic waveguides in [159, 164, 165]. Their properties have been derived from these constraints, showing that a complex mode, of propagation constant $\gamma_1 = a + jb$, does not carry by itself any real nor reactive power. That is because its electric field does not couple to its magnetic field. However, it does couple to the magnetic field of the complex wave with $\gamma_2 = a - jb$. As a result, these two modes cannot exist independently and should always be considered together. A pair of complex modes (γ_1,γ_2) then carries only reactive power (as do evanescent waves) and represent an attenuated standing wave, localised near the point where it has been generated, e.g. at a discontinuity [166]. The vanishing of the real, or time-averaged, power has been explained by the fact that the power flowing in the dielectric and air regions are of equal magnitude but in opposite directions in the dielectric image guide [162] and the dielectric-loaded circular waveguide studied here [166].

In the case of the mode-matching technique, the necessity of considering the complex modes to obtain convergence has been shown [133, 167]. It is especially important to always consider the two modes of a pair together as, otherwise, the conservation of complex power across the discontinuity will not be ensured [135].

3.3.3 Self-coupling integrals

The expression for the self-coupling integrals is defined in Appendix B by Eq. B.19. In cylindrical coordinates, the integral for mode p in waveguide x becomes

$$P_{xp} = \int_S (\overline{e}_{r\,xp} \times \overline{h}_{\theta\,xp} - \overline{h}_{r\,xp} \times \overline{e}_{\theta\,xp}) r dr d\theta \tag{3.20}$$

with S the cross-section of the waveguide. As mentioned previously, the complex modes have to be considered simultaneously when power orthogonality are consid-

ered because, for them,

$$\int_S \bar{\mathbf{e}}_{\mathbf{xp}} \times \bar{\mathbf{h}}^*_{\mathbf{xp}} dS = 0 \qquad \int_S \bar{\mathbf{e}}_{\mathbf{xp}} \times \bar{\mathbf{h}}^*_{\mathbf{xm}} dS = Q_{x\,pm} \quad \textbf{if } p \neq m \tag{3.21}$$

However, the two complex modes are still orthogonal in the sense defined by Eq. B.19, i.e:

$$\int_S \bar{\mathbf{e}}_{\mathbf{xp}} \times \bar{\mathbf{h}}_{\mathbf{xp}} dS = P_{xp} \qquad \int_S \bar{\mathbf{e}}_{\mathbf{xp}} \times \bar{\mathbf{h}}_{\mathbf{xm}} dS = 0 \quad \textbf{if } p \neq m \tag{3.22}$$

and can be considered separately.

All self-coupling integrals can be evaluated analytically. In the case where ξ_2 is purely imaginary, the alternative field expressions using the modified Bessel functions would lead to slightly different expressions for the P_{xp} than the ones using the first and second kind functions. The two expressions are however equivalent. With the view to minimise the number of alternative expressions used in the mode-matching program, it was decided to keep the general expression using J_n and Y_n and a complex wave number ξ_2. Indeed, using different expressions at this stage would create different expressions for the cross-coupling products, but also for all further processing using the matrix elements (e.g.: Q_u calculations, plot of field distributions). The results of the coupling integrals are listed in Appendix C.

3.3.4 Cross-coupling integrals

Their expression in cylindrical coordinates, derived from Eq. B.20, is

$$P_{xypm} = \int_{S_x} (\bar{e}_{r\,xp} \times \bar{h}_{\theta\,ym} - \bar{h}_{r\,ym} \times \bar{e}_{\theta\,xp}) r dr d\theta dz \tag{3.23}$$

for modes p and m in waveguides x and y respectively, and with S_x as the cross-section of waveguide x. These can also be evaluated analytically and are listed in Appendix D.

The cross-coupling coefficient P_{xypm} is a measure of the correlation between modes p and m of waveguides x and y respectively. If the two modes are orthogonal (if they do not couple together), then $P_{xypm} = 0$. The modes in the three waveguides can be sorted into separate sets, in between which all $P_{xypm} = 0$ are null. As a result, the analysis can be realised independently for the separate sets of modes, each time leading to a separate set of resonances of the structure. This greatly reduces the size of the matrix $\mathbf{M}$ to solve in Eq. B.25. The orthogonality relations between the modes in adjacent waveguides are as follows:

- Modes with different numbers of variations n along the θ axis will not couple together.

- For $n = 0$, TE and TM modes are orthogonal.

- The TEM mode in the coaxial waveguide is orthogonal to TE modes in adjacent waveguides.

- For $n \neq 0$, only the TM modes in the coaxial waveguide and the TE modes in the air waveguide are orthogonal.

As a result, the analysis can be run separately for each value of n. For each n, all types of modes need to be considered simultaneously, except when $n = 0$, for which TE modes on one hand, and TM and TEM modes on the other, form two independent sets.

3.3.5 Convergence study of the $HE_{11\delta}$ mode

The resonator with dimensions listed in Section 3.2.1 was analysed. It was found that, as the number of modes was increased, very poor conditioning of the matrix could lead to inaccurate determinant calculations. This is due to the fact that high order hybrid modes in waveguide A can have very different field amplitudes due to large disparities of the κ variable (see Eq. A.21 in Appendix A). The conditioning of the matrix was then improved by normalising all modes by forcing:

$$P_{xp} = 1 \tag{3.24}$$

for any mode p in any waveguide x. As a result, the field coefficients of mode p in waveguide x need to be divided by $\sqrt{|P_{xp}|}$. Fig. 3.6 shows how the calculated resonant frequency of the $HE_{11\delta}$ mode varies as the matrix size is increased. The results are plotted for three different values for the ratios of number of modes between regions A and B (Na/Nb) and between regions C and B (Nc/Nb). It can be seen that the speed of the convergence is highly dependent on the mode ratios. A first criterion used to quantify the level of convergence is the rate of change of the resonant frequency $\Delta f/f_0$ each time the matrix size is increased [145, 146]. Another criterion, giving an absolute evaluation of the convergence consists in calculating the degree of matching of the transverse fields at each interface. This method is commonly used to

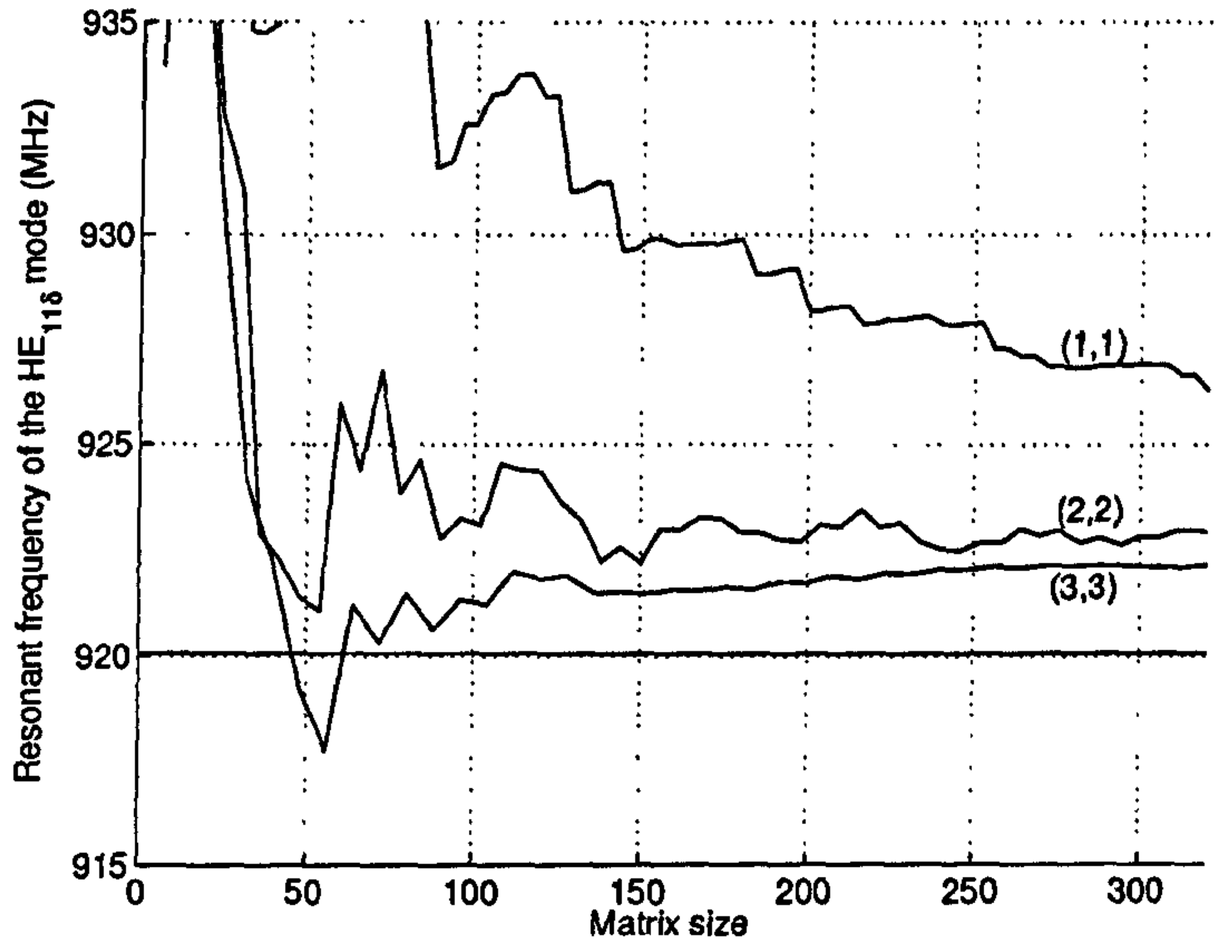

Figure 3.6: Resonant frequency variation with matrix size for the $HE_{11\delta}$ mode. Parameter:$(Na/Nb, Nc/Nb)$.

assess the accuracy of the modelling of waveguide discontinuities [168, 169, 170, 133]. Let us define

$$\varepsilon_{E(AB)} = \frac{\int_{S_B} |\mathbf{Et}_A - \mathbf{Et}_B|^2 \, dS}{\int_{S_B} |\mathbf{Et}_A|^2 \, dS} \qquad \varepsilon_{H(AB)} = \frac{\int_{S_B} |\mathbf{Ht}_A - \mathbf{Ht}_B|^2 \, dS}{\int_{S_B} |\mathbf{Ht}_A|^2 \, dS} \tag{3.25}$$

where S_B is the section of the waveguide B. $\mathbf{Et}_x$ and $\mathbf{Ht}_x$ are the transverse electric and magnetic fields of waveguide x at the dielectric to coaxial interface. Similarly, the field errors at the coaxial to empty interface are defined as

$$\varepsilon_{E(BC)} = \frac{\int_{S_B} |\mathbf{Et}_C - \mathbf{Et}_B|^2 \, dS}{\int_{S_B} |\mathbf{Et}_C|^2 \, dS} \qquad \varepsilon_{H(BC)} = \frac{\int_{S_B} |\mathbf{Ht}_C - \mathbf{Ht}_B|^2 \, dS}{\int_{S_B} |\mathbf{Ht}_C|^2 \, dS} \tag{3.26}$$

Fig. 3.7 and Fig. 3.8 show the variations of $\Delta f/f_0$ and the field errors for the $HE_{11\delta}$ mode. The values of $\Delta f/f_0$ are averaged over five samples as including different types of modes (e.g. TE, TM) at successive iterations result in a very variable $\Delta f/f_0$. The ratios giving best frequency convergence also show best matching of the electric fields at the dielectric to coaxial interface. The three other field errors all show similar level of convergence for the three mode ratios. However, only with the 3 to 1 ratio does $\varepsilon_{E(AB)}$ reach a similar level, i.e. inferior to 2% for when the matrix size exceeds 160. Figs. 3.9 to 3.11 are plots of the radial electric fields on each side of the dielectric to coaxial interface. E_θ behaves in a similar manner, showing an oscillation of always larger amplitude in the air region as the ratios of modes are

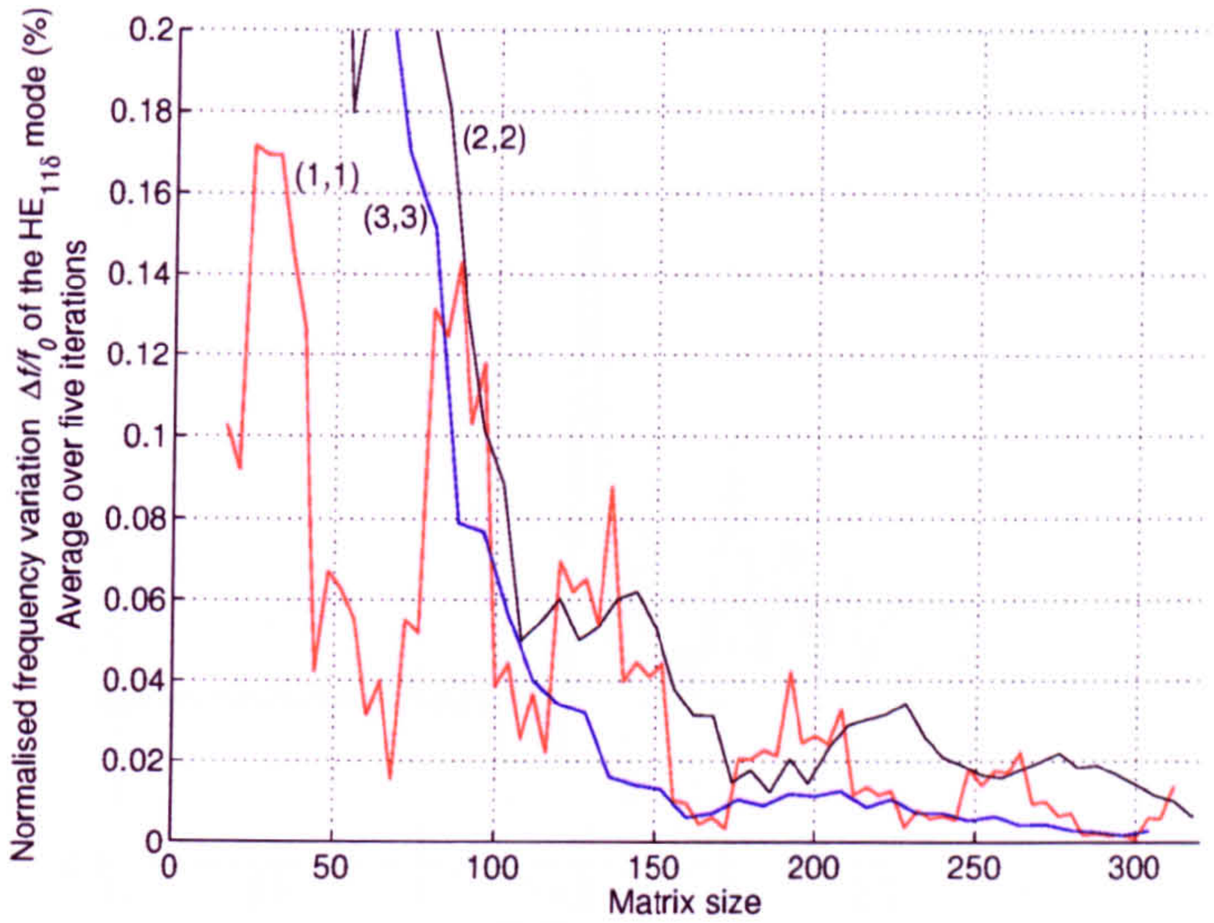

Figure 3.7: $\Delta f/f_0$ over last iteration ($Nb-1 \rightarrow Nb$) versus matrix size for the $HE_{11\delta}$ mode. Absolute value of $\Delta f/f_0$ is averaged over five samples (from $Nb-2$ to $Nb+2$). Parameter: $(Na/Nb,Nc/Nb)$.

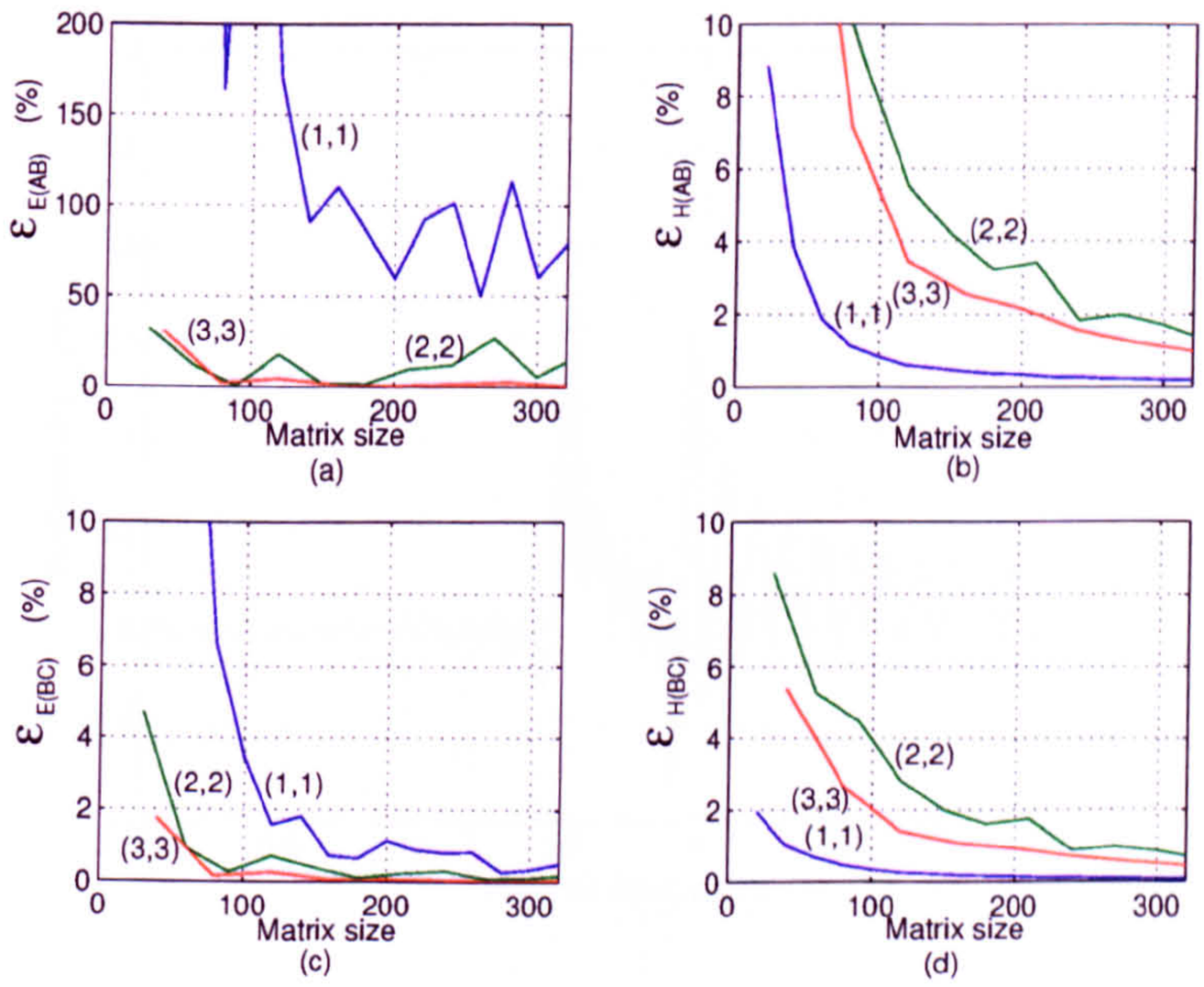

Figure 3.8: Field errors variations with matrix size for the $HE_{11\delta}$ mode. Parameter: $(Na/Nb,Nc/Nb)$.

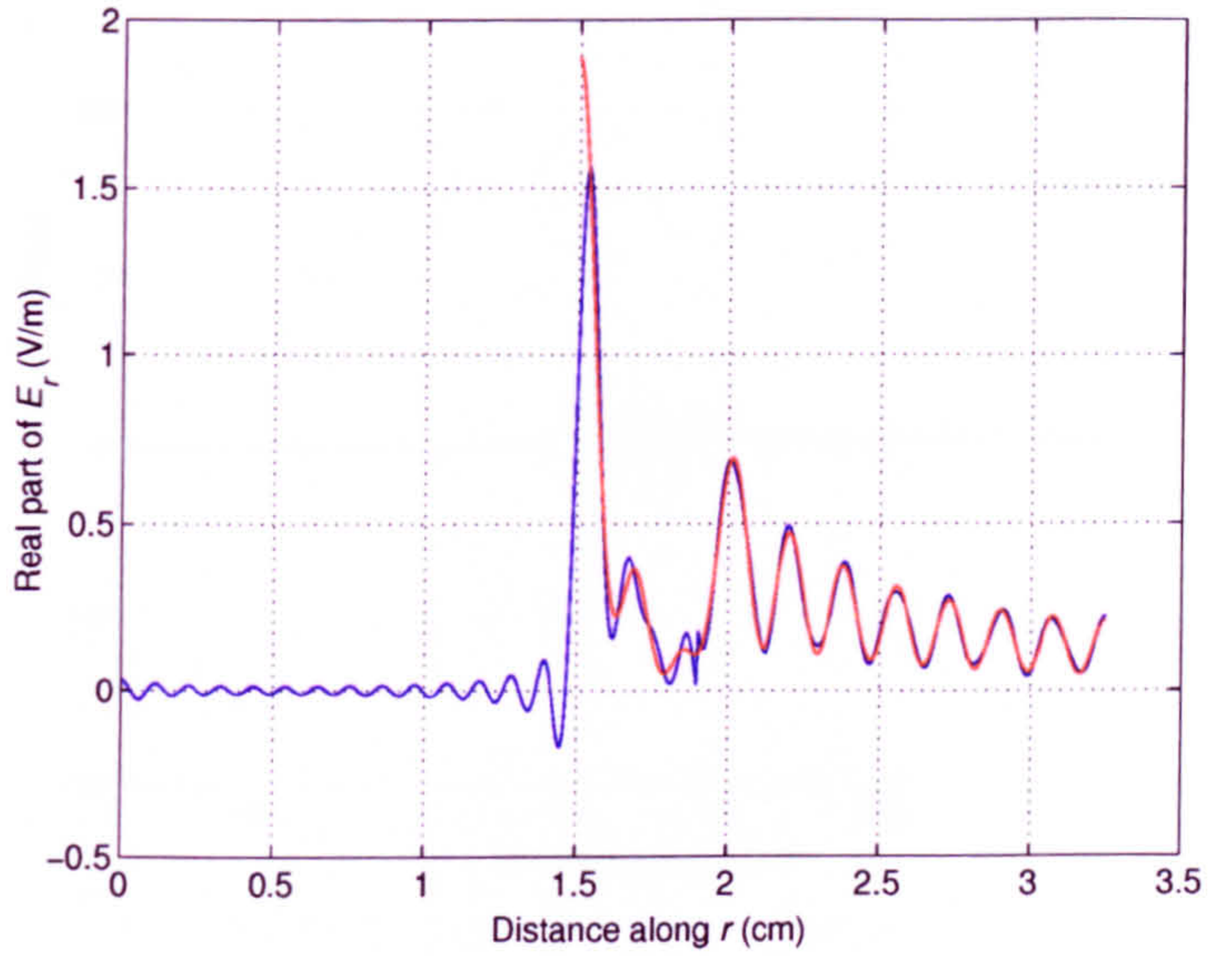

Figure 3.9: Real part of the radial electric field of the $HE_{11\delta}$ mode at the interface between regions A and B. $Na = 120$, $Nb = 40$, $Nc = 120$. $f = 922$ MHz. Region A in blue, region B in red.

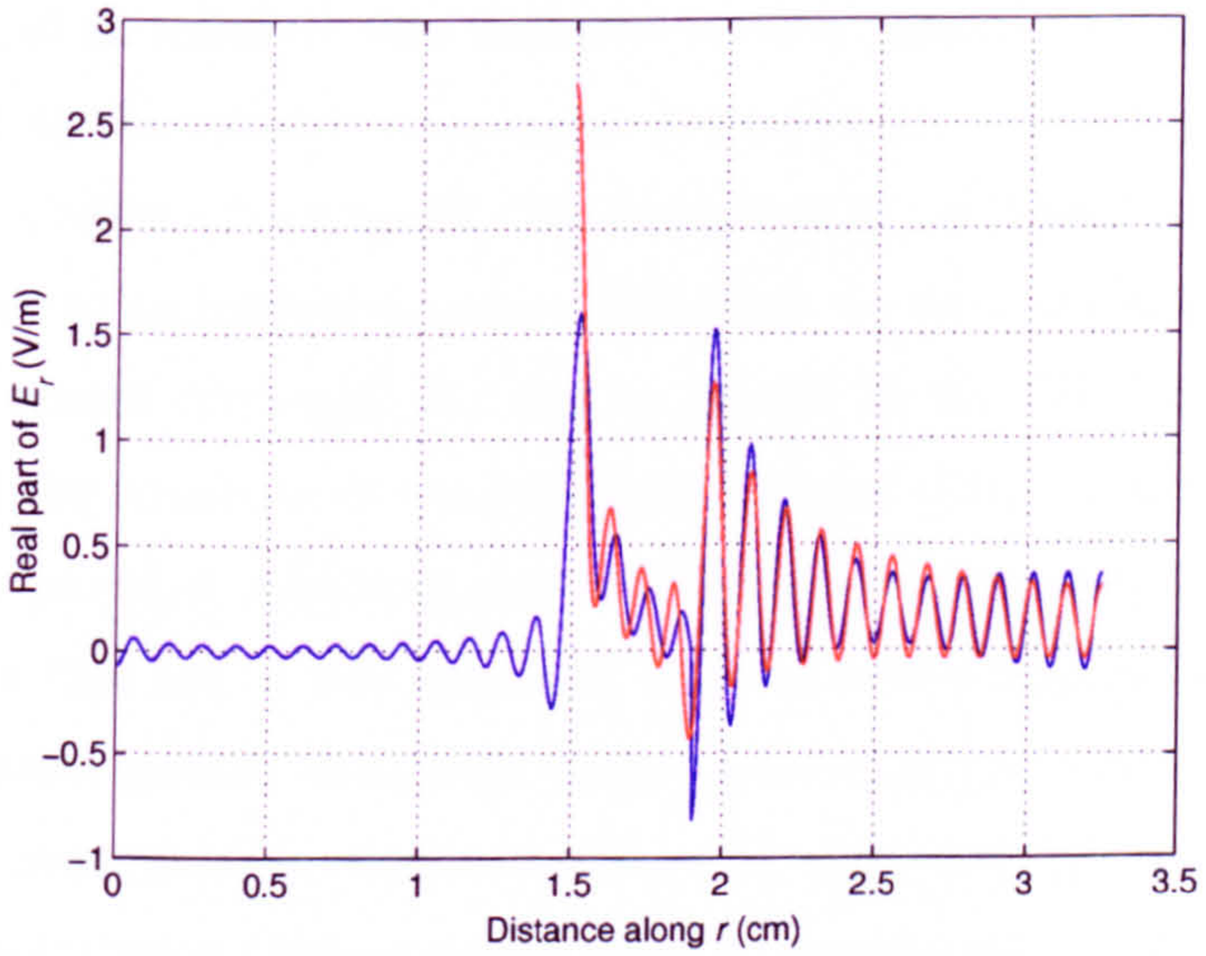

Figure 3.10: Real part of the radial electric field of the $HE_{11\delta}$ mode at the interface between regions A and B. $Na = 120$, $Nb = 60$, $Nc = 120$. $f = 922$ MHz. Region A in blue, region B in red.

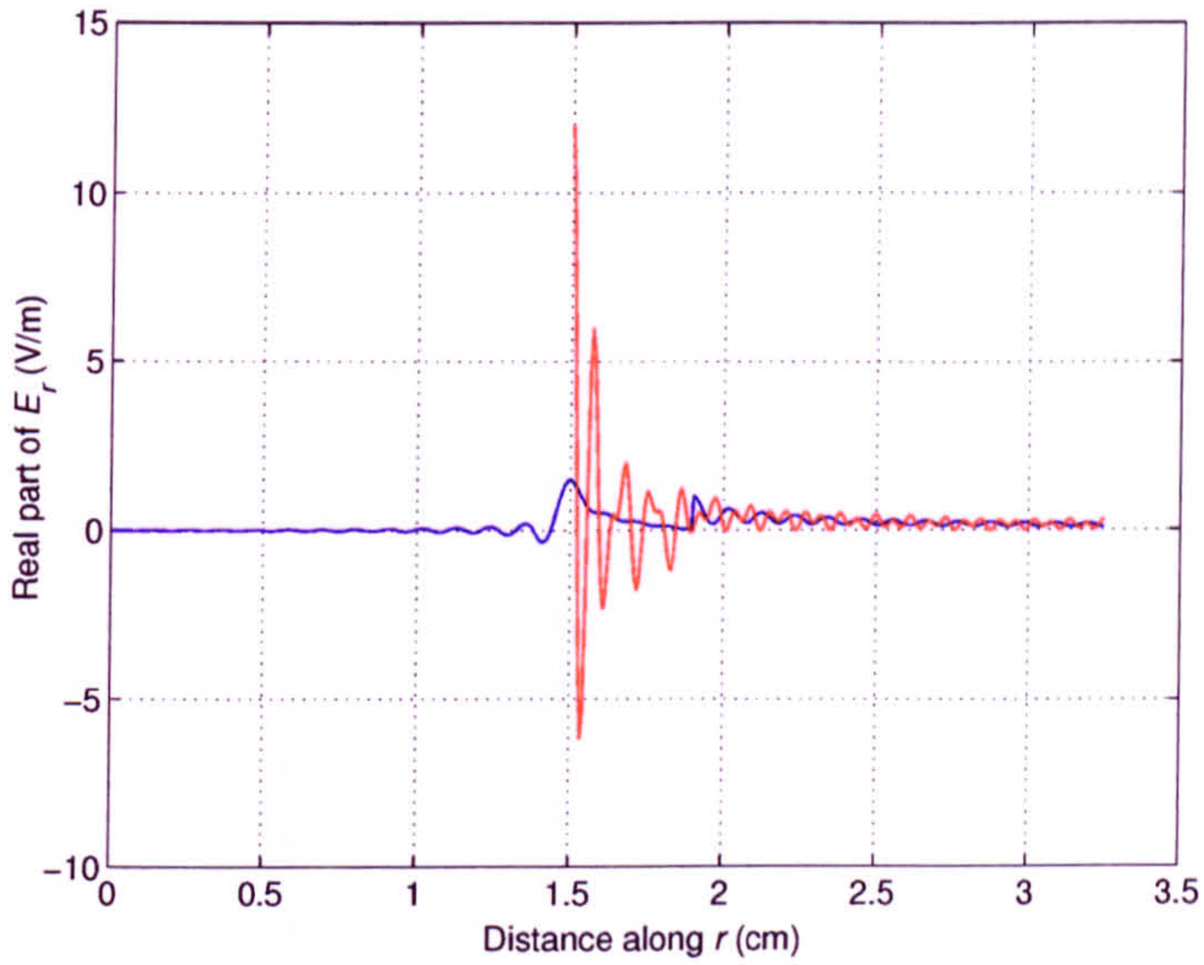

Figure 3.11: Real part of the radial electric field of the $HE_{11\delta}$ mode at the interface between regions A and B. $Na = 120$, $Nb = 120$, $Nc = 120$. $f = 922$ MHz. Region A in blue, region B in red.

decreased. The increasingly poor match of the fields as the relative number of modes in the region of smaller cross-section is increased was also observed in the case of the modelling of an infinitely thin inductive iris in a parallel plate waveguide [127]. It was linked to the relative convergence phenomenon, occurring in many cases during the resolution of waveguide discontinuities by mode-matching or moment method applied to an integral equation [127]-[131]. In these problems, the solution to which the system converged was seen to depend on the ratio of modes used in each region of the structure. It has been demonstrated [171] that this phenomenon will not occur provided the linear system to solve is well conditioned. In the case of an infinitely thin iris, it was suggested that the modes considered in the larger waveguides should include those with similar field variations to that of the modes in the smaller waveguide. In order to achieve this, the correlation between modes is studied. The correlation between modes p and m in waveguides x and y respectively is defined as

$$C_{xypm} = \frac{P_{xypm}}{\sqrt{P_{xp}}\sqrt{P_{ym}}} \tag{3.27}$$

Fig. 3.12 and Fig. 3.13 show the correlation plots of two modes of waveguide B with modes in waveguides C and A respectively. One of the two modes of waveguide B is

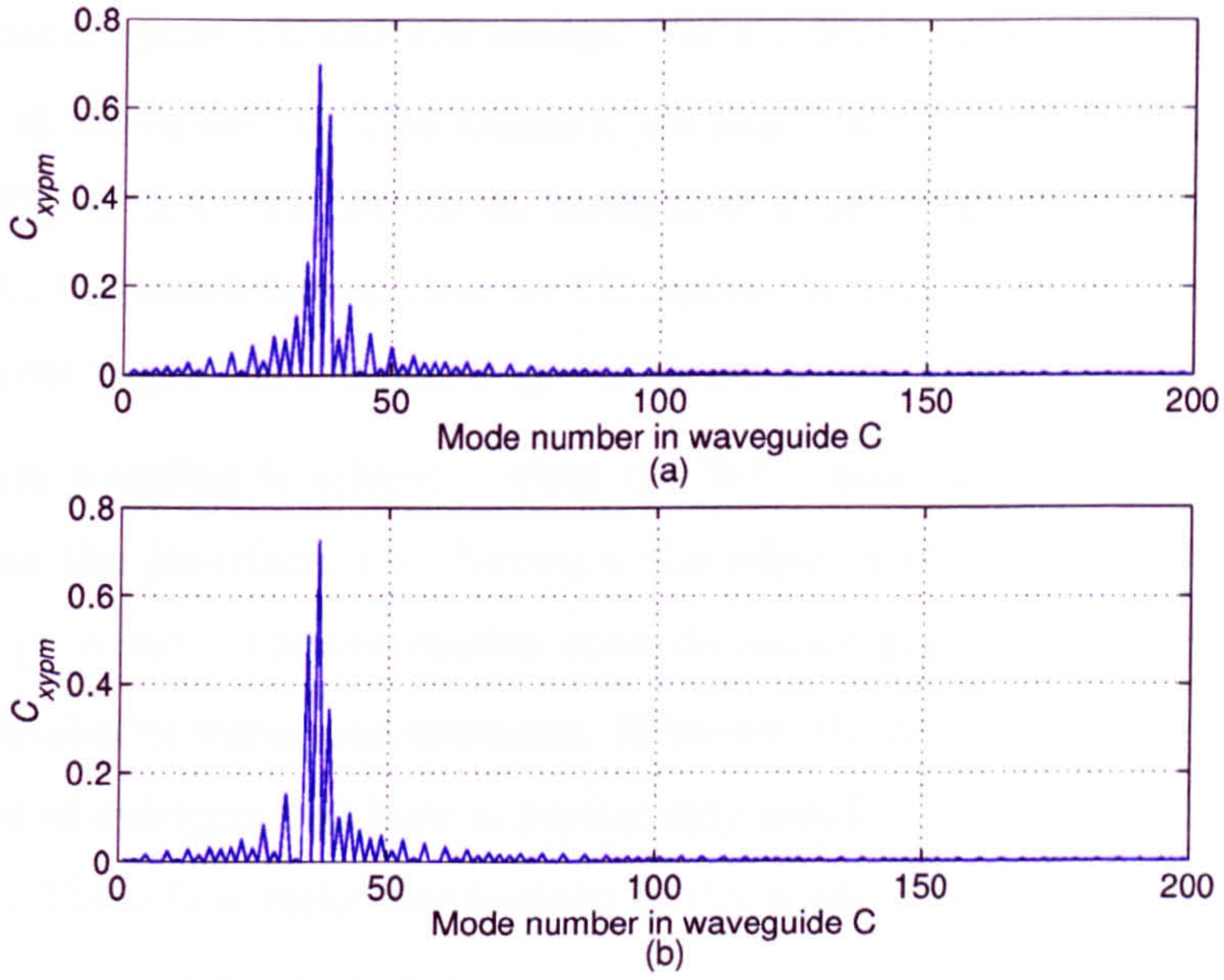

Figure 3.12: Correlation C_{xymp} of 20^{th} (a) and 21^{th} (b) modes of waveguide B with modes of waveguide C. $n = 1$, $f = 922$ MHz.

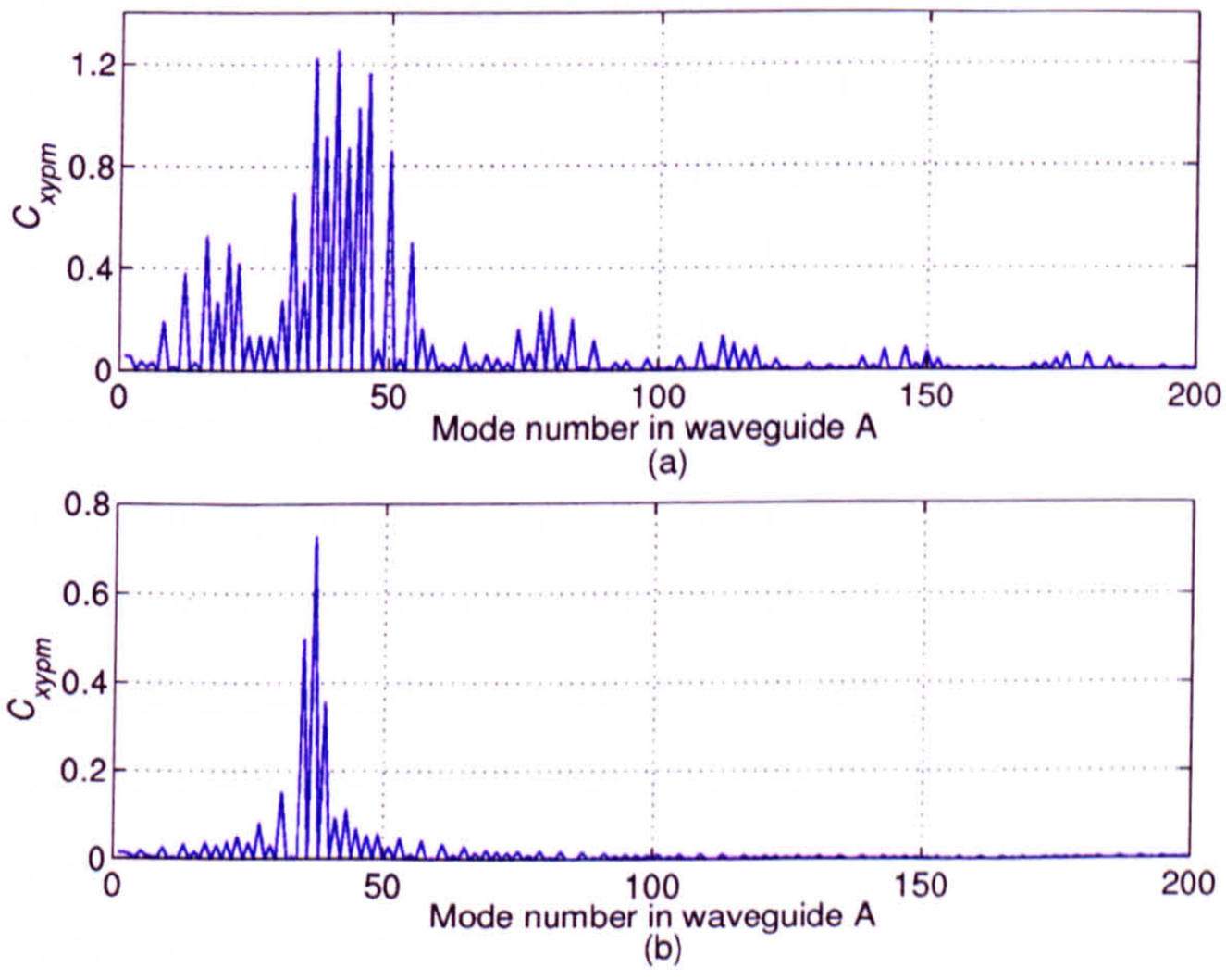

Figure 3.13: Correlation C_{xymp} of 20^{th} (a) and 21^{th} (b) modes of waveguide B with modes of waveguide A. $n = 1$, $f = 922$ MHz.

a TM mode (20^{th} mode) and the other is a TE mode (21^{st} mode). In waveguides B and C, modes are pure TE and TM modes. TM modes in waveguide B only couple to TM modes in waveguide C. This explains the fact that every second value of C_{xypm} is zero in Fig. 3.12.a. TE modes in waveguide B do couple to the TM modes in waveguide C, but much less so than to TE modes, because of the relative amplitude of the different fields. As a result, Fig. 3.12.b looks very similar to Fig. 3.12.a.

Maximum coupling is achieved when the fields have the same number of variations across the interface, i.e. between the edge of the disc ($r = r_2$) and the cavity wall ($r = r_3$). The correlation then decreases quickly as the difference between the number of variations increases. However, the decrease in not monotonous. Some modes of waveguide C have a particularly small correlation (e.g. mode 44 in Fig. 3.12.a). These fast variations happen as the fields of the modes on each side of the interface go in and out of phase.

Fig. 3.13 shows that a larger number of modes of waveguide A couples to a given TM mode than to a TE mode in waveguide B. Even though modes in waveguide A are hybrids, most of them have predominantly the characteristics of either TE (large values of κ in Appendix A) or TM modes (small values of κ). As a result, TE and TM modes in waveguide B will predominantly couple to the TE-like and TM-like modes respectively. Also, the field variations of the TE-like modes are very similar to those of the TE modes in waveguide C. As a result, Fig. 3.13.b and 3.12.b look very similar. By opposition, the variations of the TM-like modes can be very different to those of the corresponding modes in waveguide C. In the air region of waveguide A in particular, the amplitudes of E_r and H_θ can differ significantly between TM-like modes. The values of P_{ap} and P_{bapm} then vary greatly from mode to mode and result in the large spread of the C_{xypm} plot in Fig. 3.13.a.

At this stage, it is necessary to choose the minimum Na/Nb and Nc/Nb that will ensure good convergence of the results. Using more modes than necessary in waveguide A and C does not improve the accuracy of the frequency calculation. However, it does not degrade it either [130, 129]. The only drawback is the unnecessary size of the system to solve. One could choose the ratios so that all modes with a correlation above a certain percentage of the maximum correlation are included. Only the ratios for TM modes need to be calculated because they have a larger correlation spread with the modes in waveguide A.

In the case of the test cavity studied here ($r_1/r_3 = 0.4615$ and $r_2/r_3 = 0.5846$), the 10% and 20% correlations for the TM modes are achieved for $Na/Nb = 113/20 = 5.65$ and $Na/Nb = 55/20 = 2.75$ respectively. In the former case, ignoring mode 112 of waveguide A drops Na/Nb to $85/20 = 4.25$. For Nc/Nb, the ratios become $47/20 = 2.35$ and $43/20 = 2.15$ respectively. The variations of the resonant frequency of the $HE_{11\delta}$ mode with Nb is plotted for different ratios of Na/Nb and Nc/Nb in Figs. 3.14 and 3.15. For large values of Nb, choosing Na/Nb larger than 3 does not change the resulting frequency significantly. Even more clearly, increasing Nc/Nb above 2 does not bring any improvement. As a result, in the case of $Nb = 20$, the 20% criterion appears to be sufficient.

However, one needs to know how these ratios vary with other parameters such as frequency, the resonator dimensions, the number of angular variations n, and the number of modes Nb used in the resolution. Only minute changes in the correlation plots appeared when run at very different frequencies or for different values of $n > 0$. The study of the optimum Na/Nb and Nc/Nb depending on the radial dimensions of the resonator is more complex. Fig. 3.16 shows the variations of Na/Nb with the disc radius to cavity radius ratio r_1/r_3, in the case of a TE mode in waveguide B. Three of the curves correspond to different criteria: the first one plots the value of Na/Nb for which the maximum correlation happens. The second and third curves plot the minimal value of Na/Nb which needs to be used to ensure that all modes with a correlation above 20% and 10% of the maximum correlation respectively are included. These curves are independent of the dielectric cylinder to cavity radius ratio r_2/r_3, and are almost identical for Nc/Nb in both cases of a TE or a TM mode in waveguide B. All curves are closely approximated by the ratio of the linear dimensions of the two waveguides $R_{lin} = r_3/(r_3 - r_1)$. This ratio can be compared to the ratio of waveguide widths which was used to define the ratio of modes in [129] and [127]. In a general manner a Na/Nb of $R_{lin} \times 1.11$ and $R_{lin} \times 1.20$ will include all modes with more than 20% and 10% of the maximum correlation respectively. In the case of a TM mode in waveguide B, Na/Nb is similar to R_{lin} for the maximum correlation case only. The case of Na/Nb for 10% and 20% correlations are shown in Fig. 3.17. The R_{lin} variations are only followed for $r_1 > r_2$. Otherwise, Na/Nb needs to be increased up to 6 above the value of R_{lin} required for 10% correlation and 4 above that required for 20% correlation. The worst case always happens when

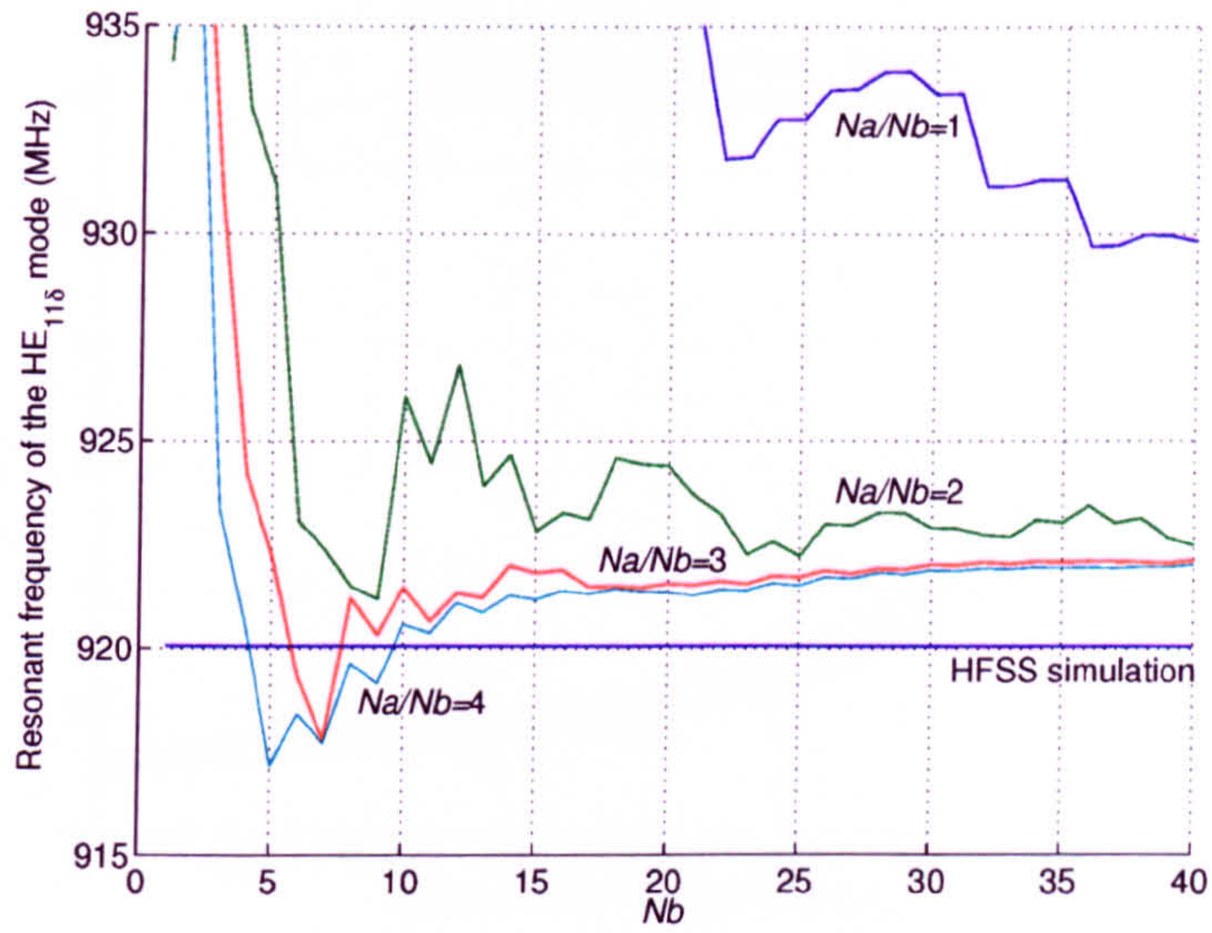

Figure 3.14: Resonant frequency variation with Nb for the $HE_{11\delta}$ mode for various Na/Nb. $Nc/Nb = 4$.

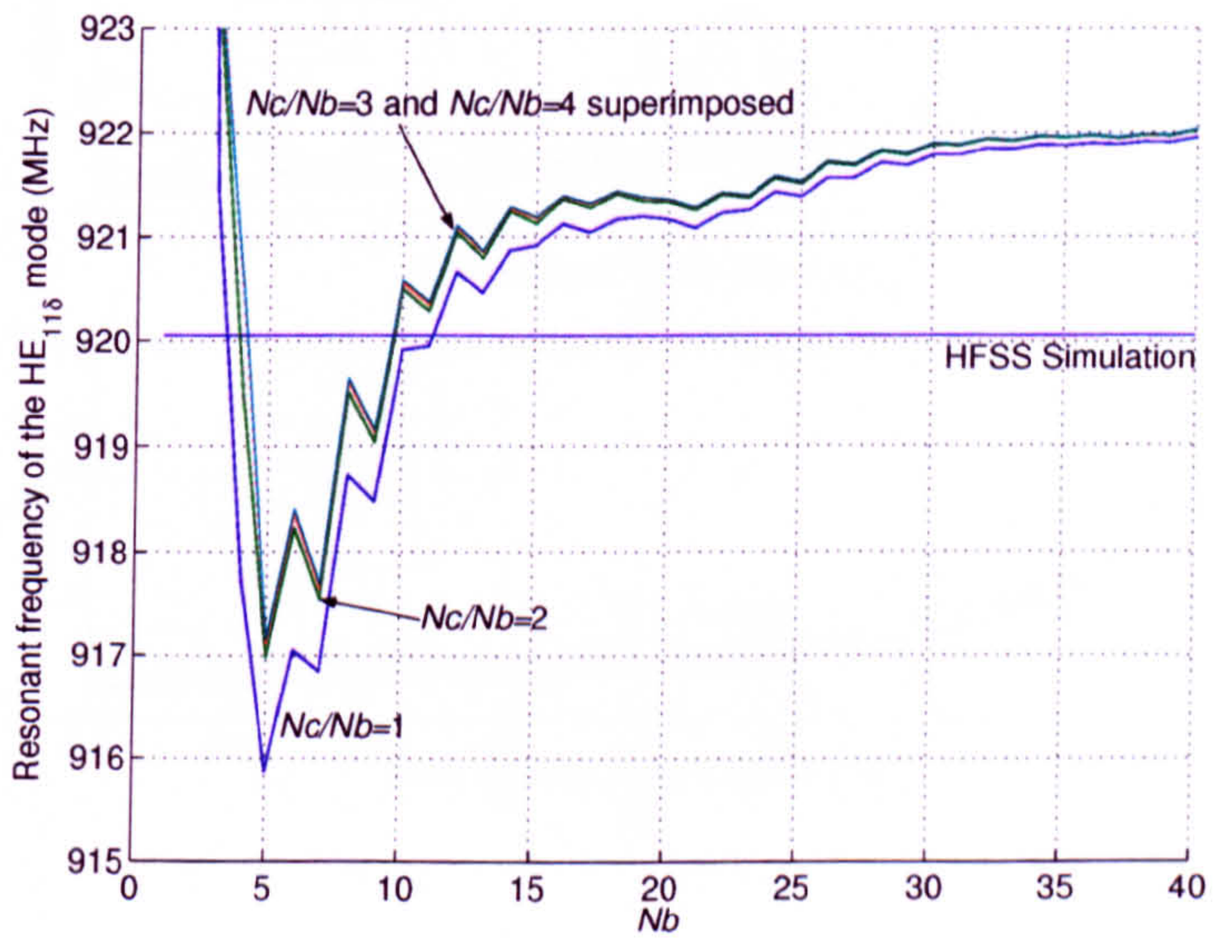

Figure 3.15: Resonant frequency variation with Nb for the $HE_{11\delta}$ mode for various Nc/Nb. $Na/Nb = 4$.

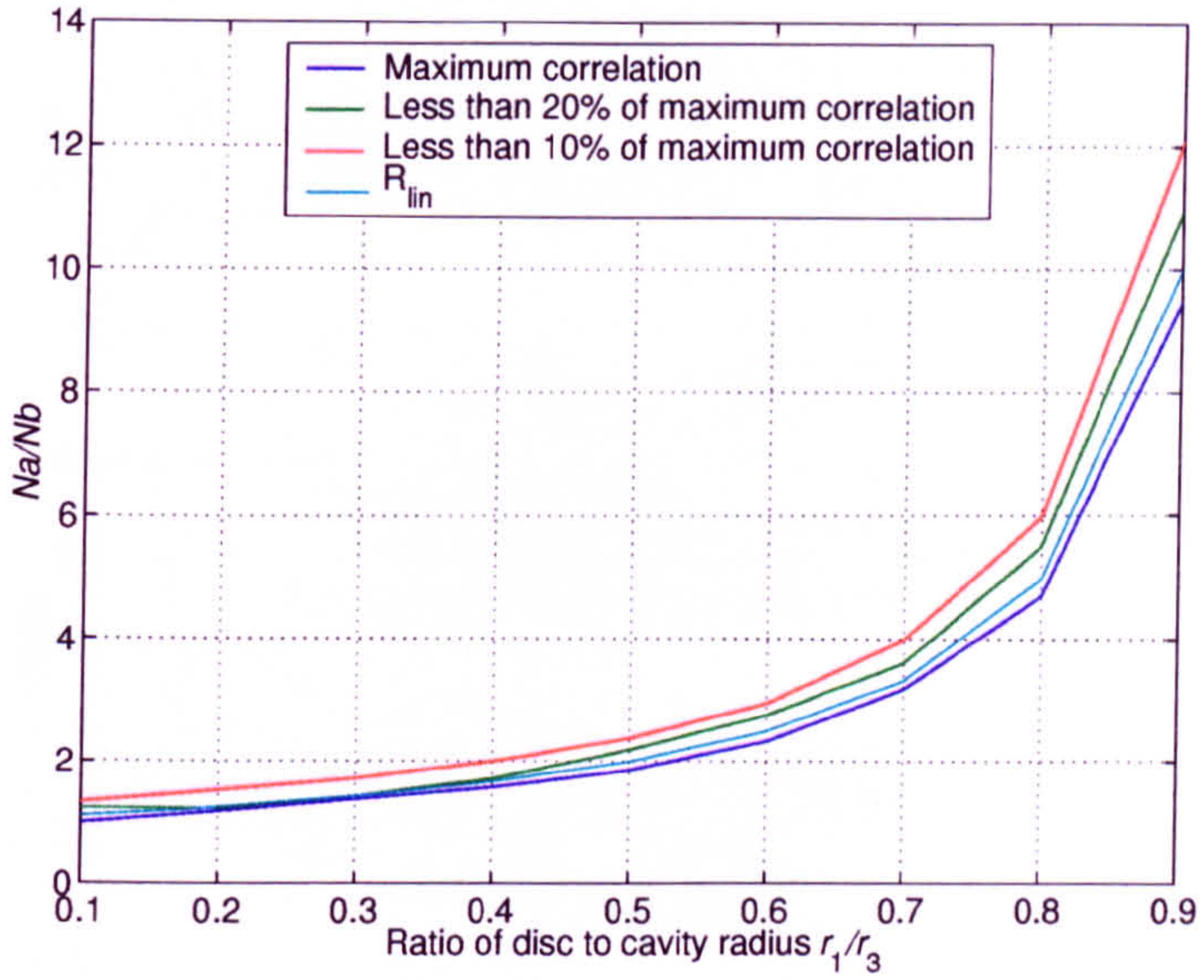

Figure 3.16: Na/Nb variation with disc to cavity radius ratio r_1/r_3 for different convergence criteria. Mode in waveguide B is a TE mode: $Nb = 21$. $f = 922$ MHz.

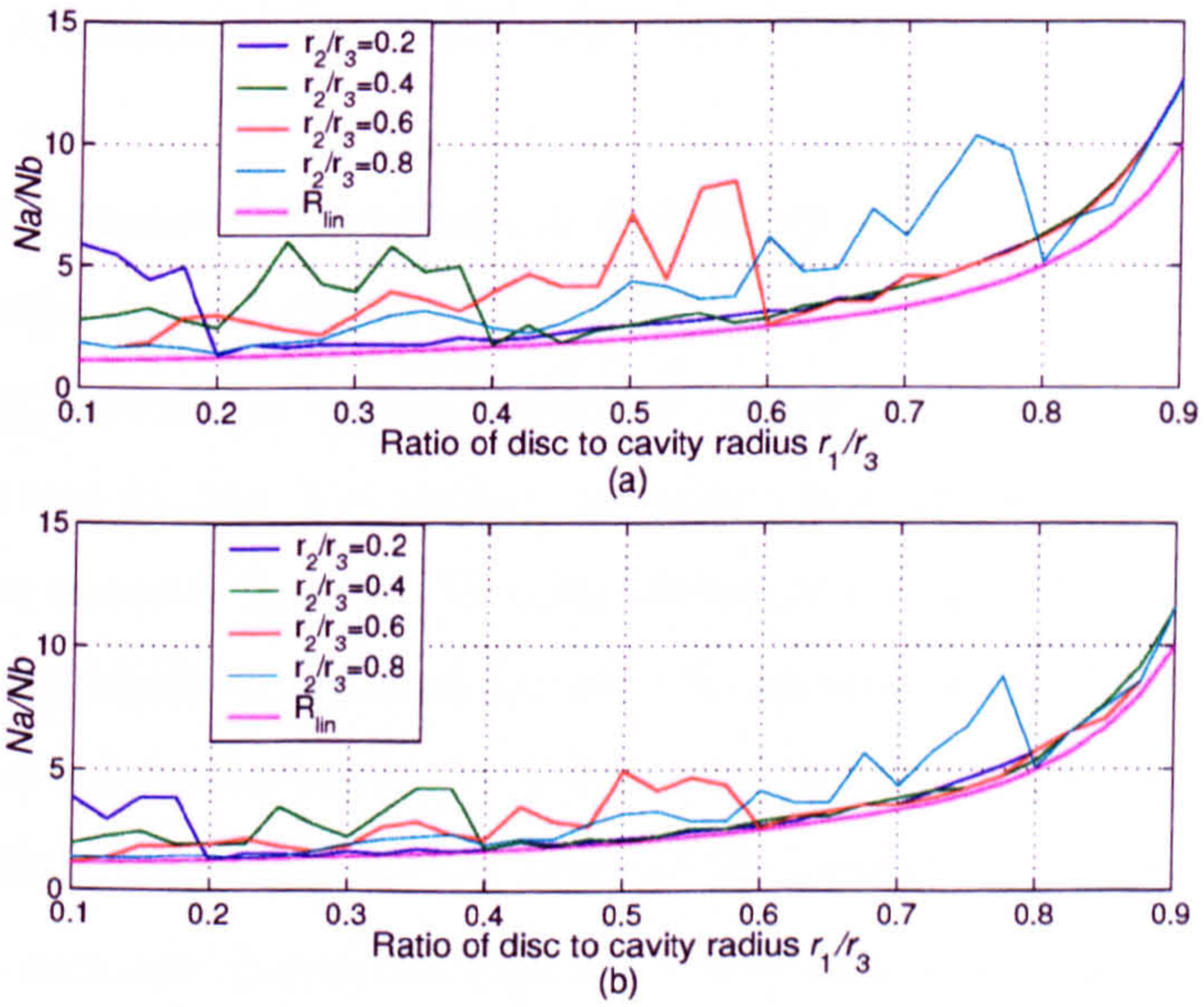

Figure 3.17: Na/Nb ratio variation with the disc to cavity radius ratio r_1/r_3 for different dielectric cylinder to cavity radius r_2/r_3 for hybrid modes and $n = 1$. Mode in waveguide B is a TM mode: $Nb = 20$. $f = 922$ MHz. (a) 10% correlation, (b) 20% correlation.

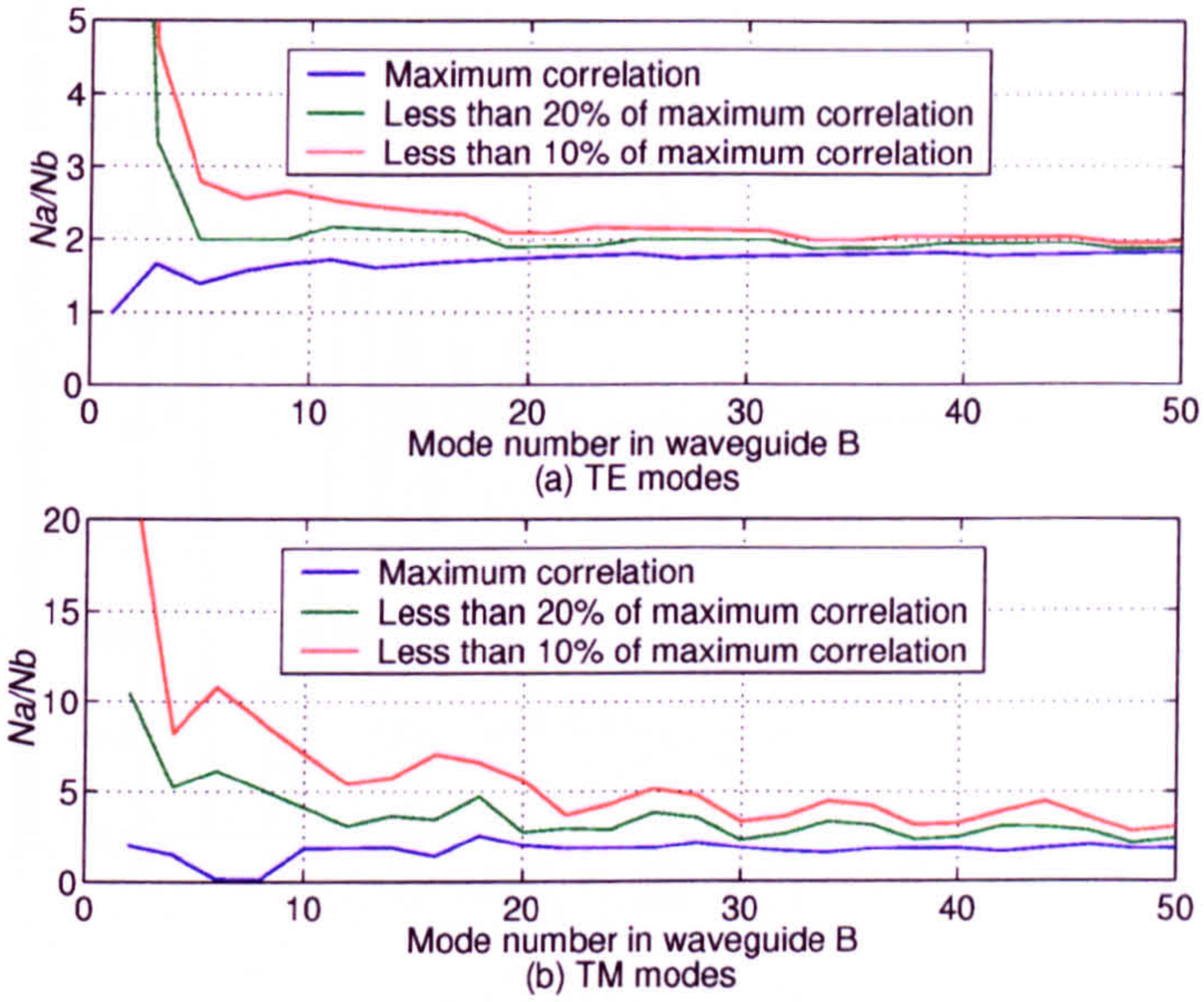

Figure 3.18: Na/Nb ratio variation with Nb for different convergence criteria. The TE modes (a) and TM modes (b) in waveguide B are considered separately.

the dielectric cylinder diameter is slightly larger than that of the metal disc, because several fields singularities then exist very close to each other, as explained later in this section.

Finally, an example of variations of Na/Nb with Nb is shown in Fig. 3.18 for the three criteria defined above. The variations for Nc/Nb are virtually identical to those of Fig. 3.18.a. As expected, Na/Nb converges faster for the TE modes in waveguide B than for the TM modes. In both cases, all curves seem to converge towards a ratio close to R_{lin}. As Nb is increased, the 10 and 20% curves are on the whole decreasing which means that the relative correlation spread is reduced. As a result, it will be safe to choose the Na/Nb and Nc/Nb ratios assuming the minimum value for Nb likely to be used and to increase Nb later if more accuracy is needed.

Once the ratios are chosen through the correlation plots, one has to decide on the minimum Nb to use, for example by using the $\Delta f/f_0$ and error plots for the chosen ratios. The latter approach necessitates more computing time. In the case of the $HE_{11\delta}$, let us consider $Na/Nb = 3$ and $Nc/Nb = 2$ (Fig. 3.19). For $Nb = 15$, $\Delta f/f_0$ is only marginally worse than for $Nb = 20$, with 0.022% instead of 0.011%. $\varepsilon_{E(AB)}$ increases from 3 to 5%. Results would be obtainable much more quickly with $Nb = 5$ and would still give a reasonable approximation of the resonant frequency

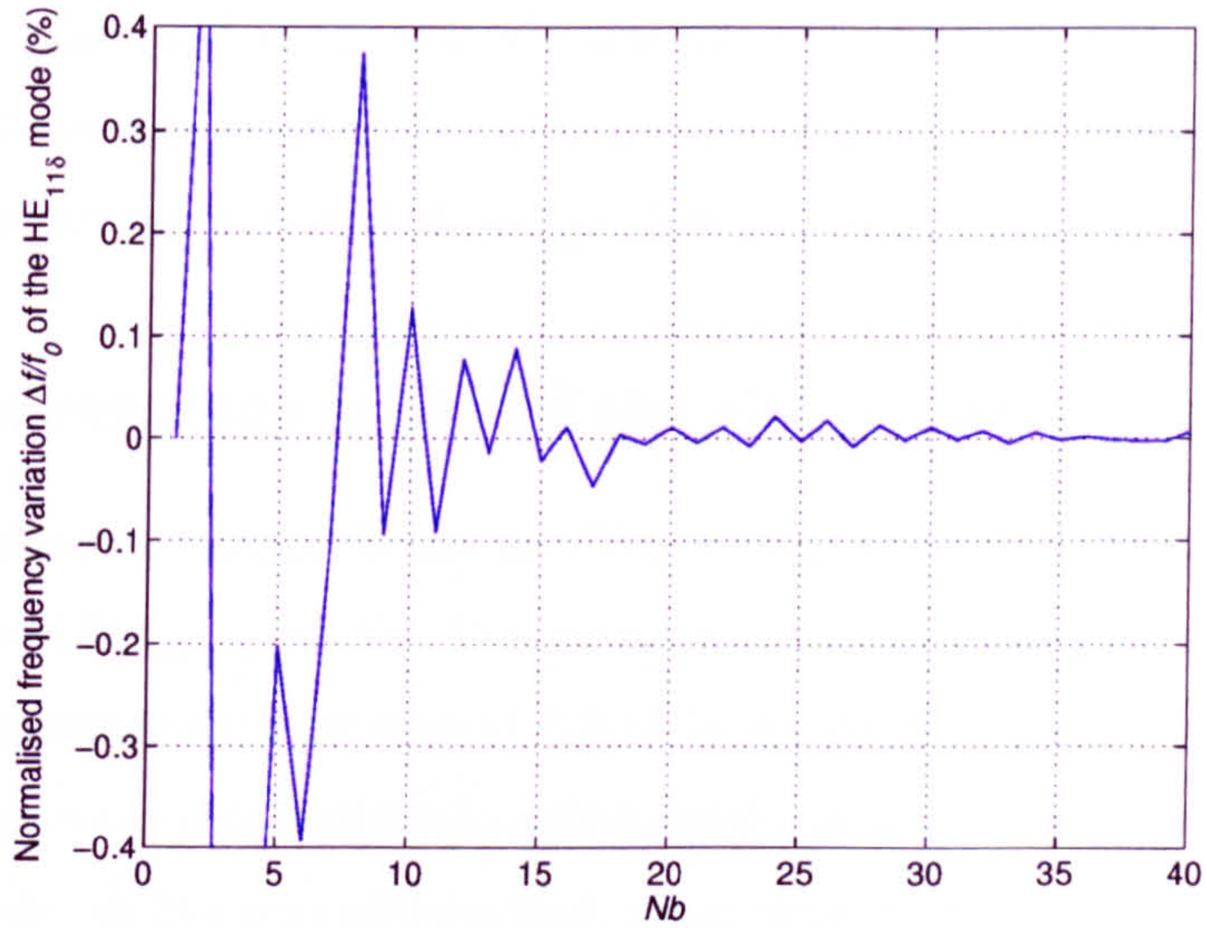

Figure 3.19: Change of resonant frequency over last iteration ($Nb-1 \rightarrow Nb$) versus Nb for the $HE_{11\delta}$ mode. $(Na/Nb,Nc/Nb) = (3,2)$.

($\Delta f/f_0 = 0.202\%$). However, the field distributions are still very approximate as $\varepsilon_{E(AB)}$ is larger than 30%.

Studying the variations of the fields at the interface, like those of E_r in Fig. 3.9 to 3.11, one can see the difficulties encountered when trying to create the fields of the $HE_{11\delta}$ mode from a superposition of waveguide modes. The field variations for 180, 60 and 120 modes in region A, B and C respectively is shown in Appendix E. First, E_r is singular at the approach of the edge of the metal disc ($r = 15$ mm). This is in agreement with the edge condition, which predicts that E_r and E_z should tend to infinity as r decreases and approaches r_1 at the $z = 0$ and $z = l_2$ planes [172]. The matching is all the more difficult for E_r as the metal disc forces its value to 0 for $r < r_1$. Also, a similar singularity exists for E_r and E_z at dielectric edge ($r = r_2$, $z = 0$) [173]. In [38], this was presented as the reason why the TM and EH modes of suspended DR's converge much more slowly by radial mode-matching than TE and HE modes. At $r = r_2$ too, the values for E_r must go through a large discontinuity as $E_r(r = r_2^+)/E_r(r = r_2^-) = 44/1$. Similarly, $E_z(z = 0^+)/E_z(z = 0^-) = 44/1$ for $r_1 < r < r_2$. The matching of E_z in Appendix E is in fact still very approximate in this region.

Unlike the electric field, H_r and H_z are only singular at the metallic edges [173]. As a result, their match is as good at $z = 0$ as at $z = l_2$. Finally, E_θ and H_θ remain

finite at both edges and are potentially less difficult to match [172, 173].

All this above agrees with the error plots of Fig. 3.8: the electric fields at the interface between region A and B are the slower to converge.

3.3.6 Convergence study of the $EH_{11\delta+1}$ and $HE_{21\delta}$ modes

All the difficulties mentioned in the previous section will also exist for the matching of the $HE_{21\delta}$ and $EH_{11\delta+1}$ modes. The correlation distributions look almost identical at higher frequencies such as around 1.3 GHz where the $EH_{11\delta+1}$ mode resonates. As a result, the same choice of mode ratios should be adequate. This is also true for the $HE_{21\delta}$ mode, as the correlations look again very similar for $f = 1.45$ GHz and $n = 2$. This can be verified in Figs. 3.20 to 3.23, which show the convergence of the $EH_{11\delta+1}$ and $HE_{21\delta}$ modes for different Na/Nb and Nc/Nb ratios. It can be seen in Fig. 3.24 that all modes converge at very similar speeds with Nb. The $HE_{11\delta}$ and $HE_{21\delta}$ modes especially are extremely similar, which could be expected as the only important difference in their field patterns is the number of angular variations. All the field singularities are however the same. The $EH_{11\delta+1}$ mode converges somewhat faster. This can be explained by the fact that there is a smaller proportion of E_r around the dielectric edge as shown in Fig. 3.25 (see also Section 4.3) as well as H_r along the top edge of the disc (see Figs. 3.37 and 3.40 in Section 3.3.9).

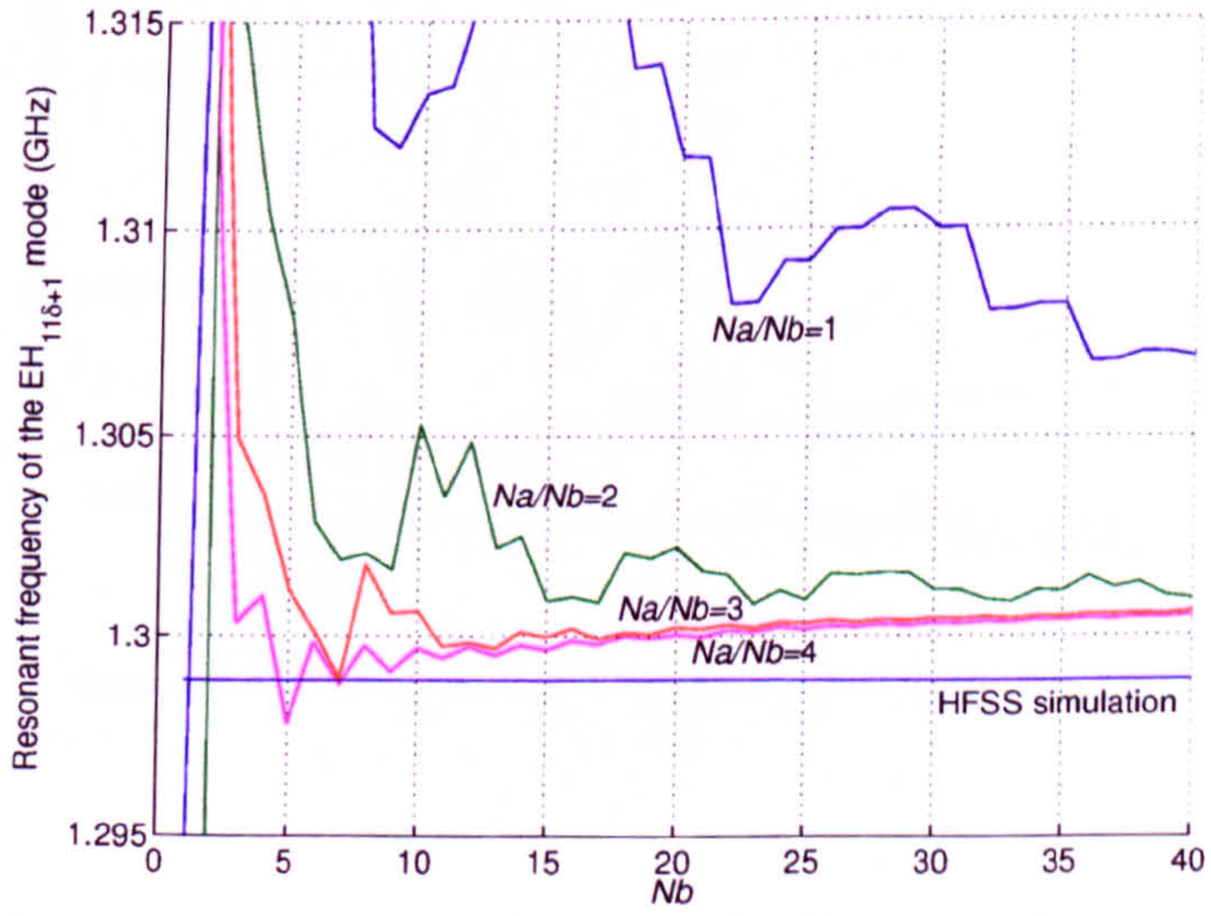

Figure 3.20: Resonant frequency variation with Nb for the $EH_{11\delta+1}$ mode for various Na/Nb. $Nc/Nb = 4$.

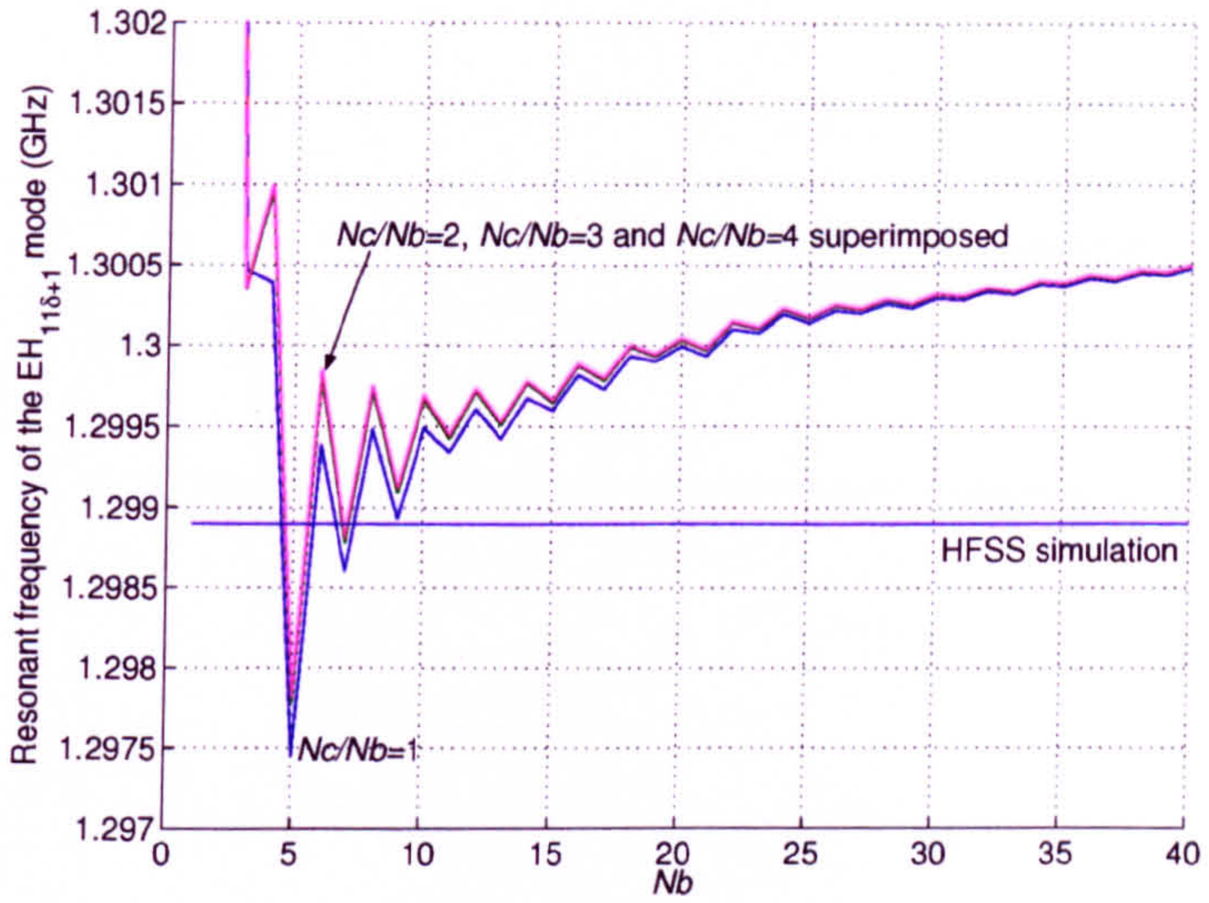

Figure 3.21: Resonant frequency variation with Nb for the $\mathrm{EH}_{11\delta+1}$ mode for various Nc/Nb. $Na/Nb = 4$.

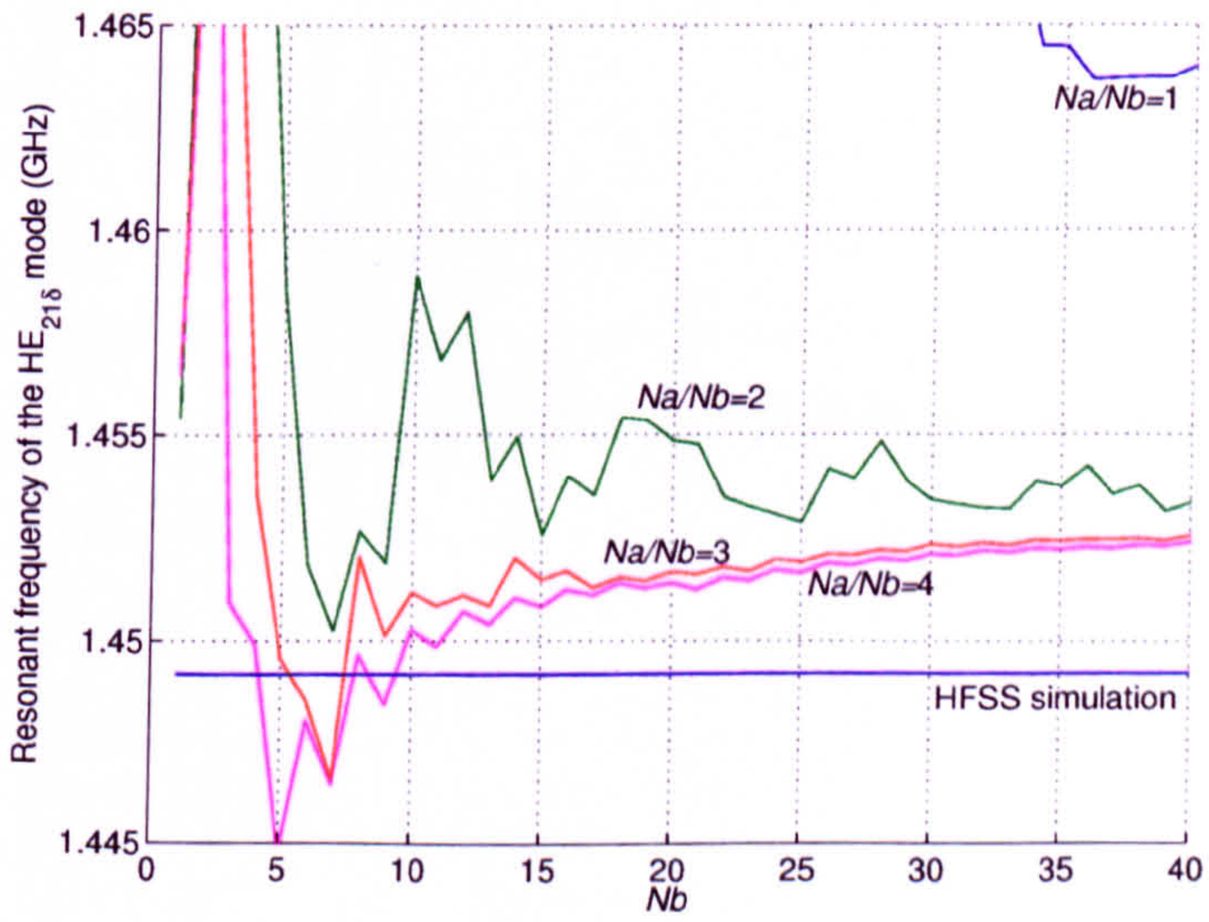

Figure 3.22: Resonant frequency variation with Nb for the $\mathrm{HE}_{21\delta}$ mode for various Na/Nb. $Nc/Nb = 4$.

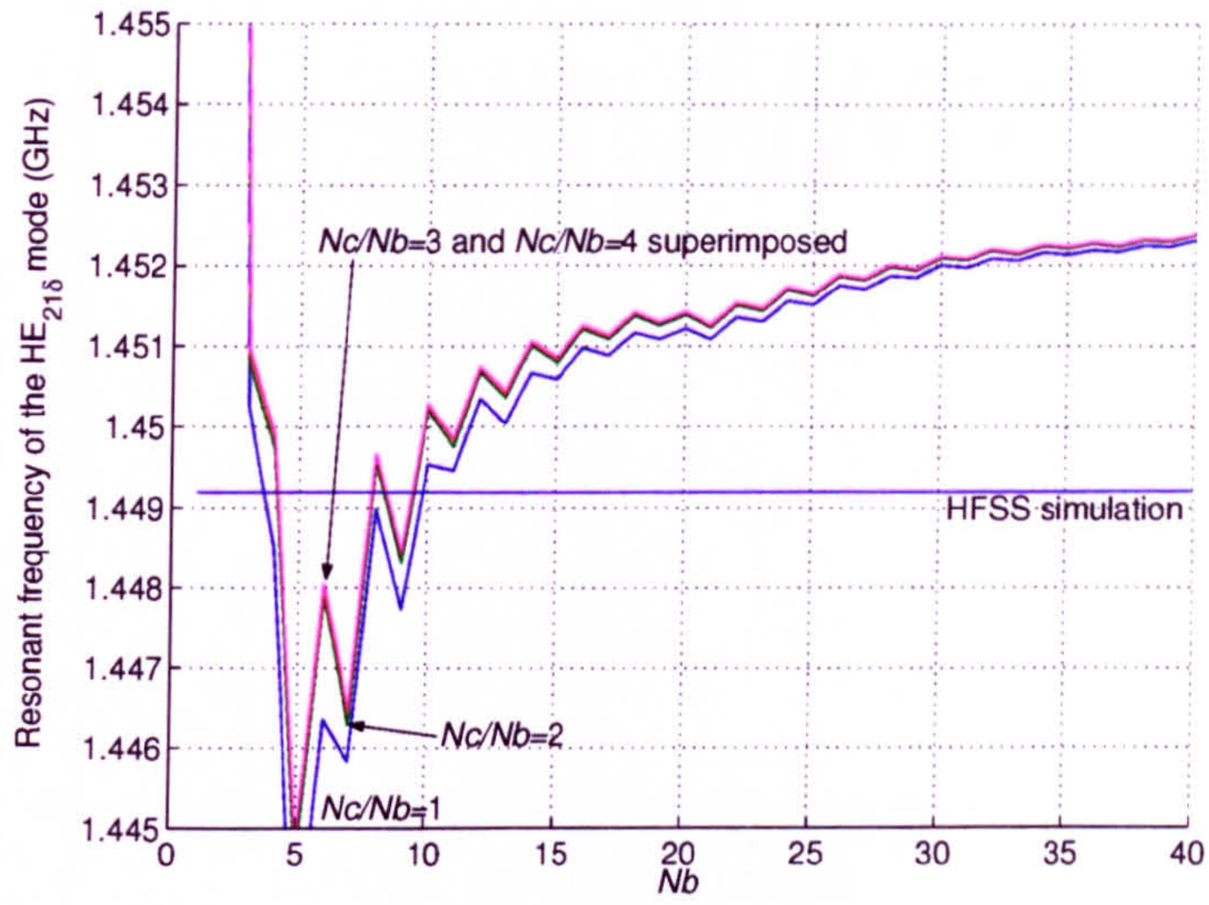

Figure 3.23: Resonant frequency variation with Nb for the $HE_{21\delta}$ mode for various Nc/Nb. $Na/Nb = 4$.

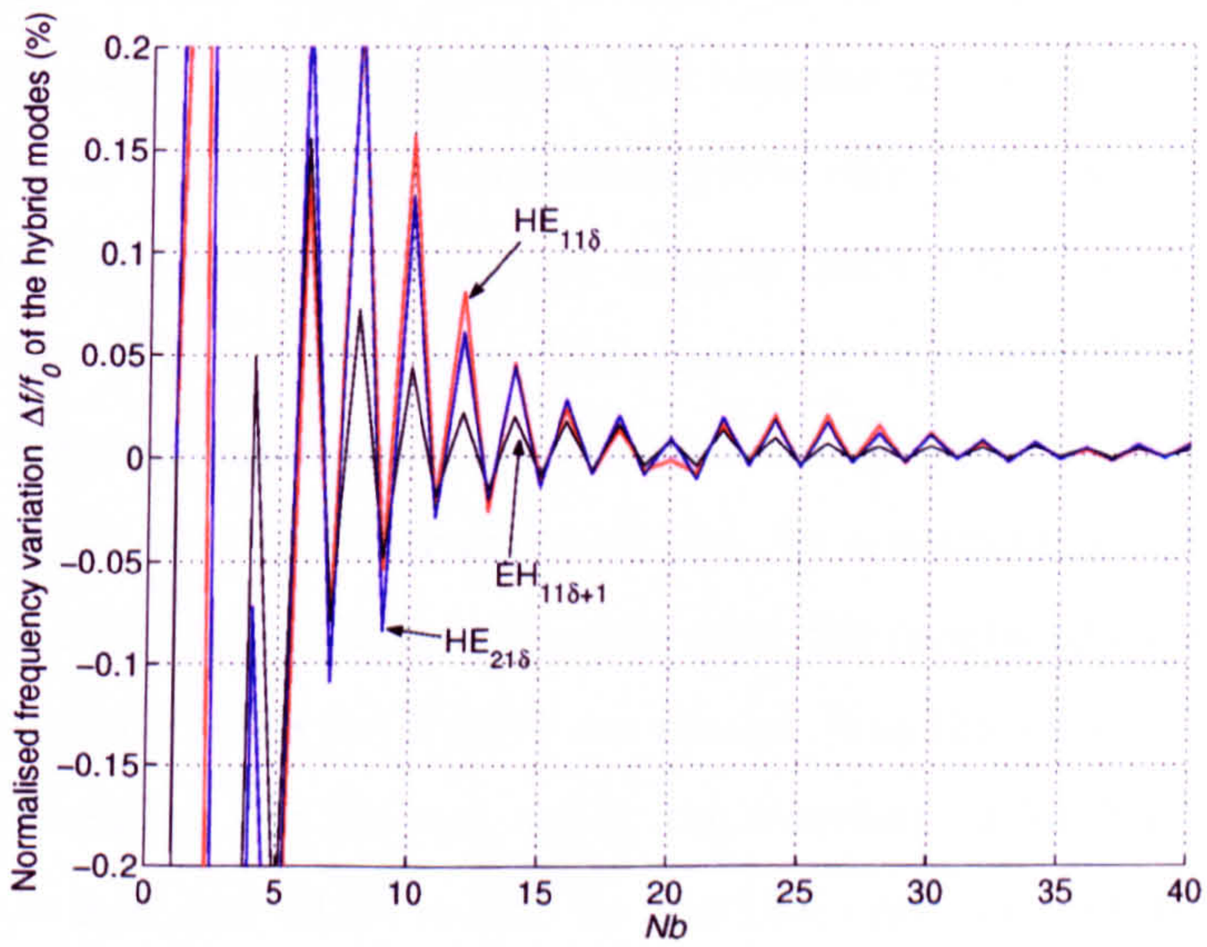

Figure 3.24: Change of resonant frequency over last iteration ($Nb-1 \rightarrow Nb$) versus Nb for the three first hybrid modes. (Na/Nb,Nc/Nb) = (4,4).

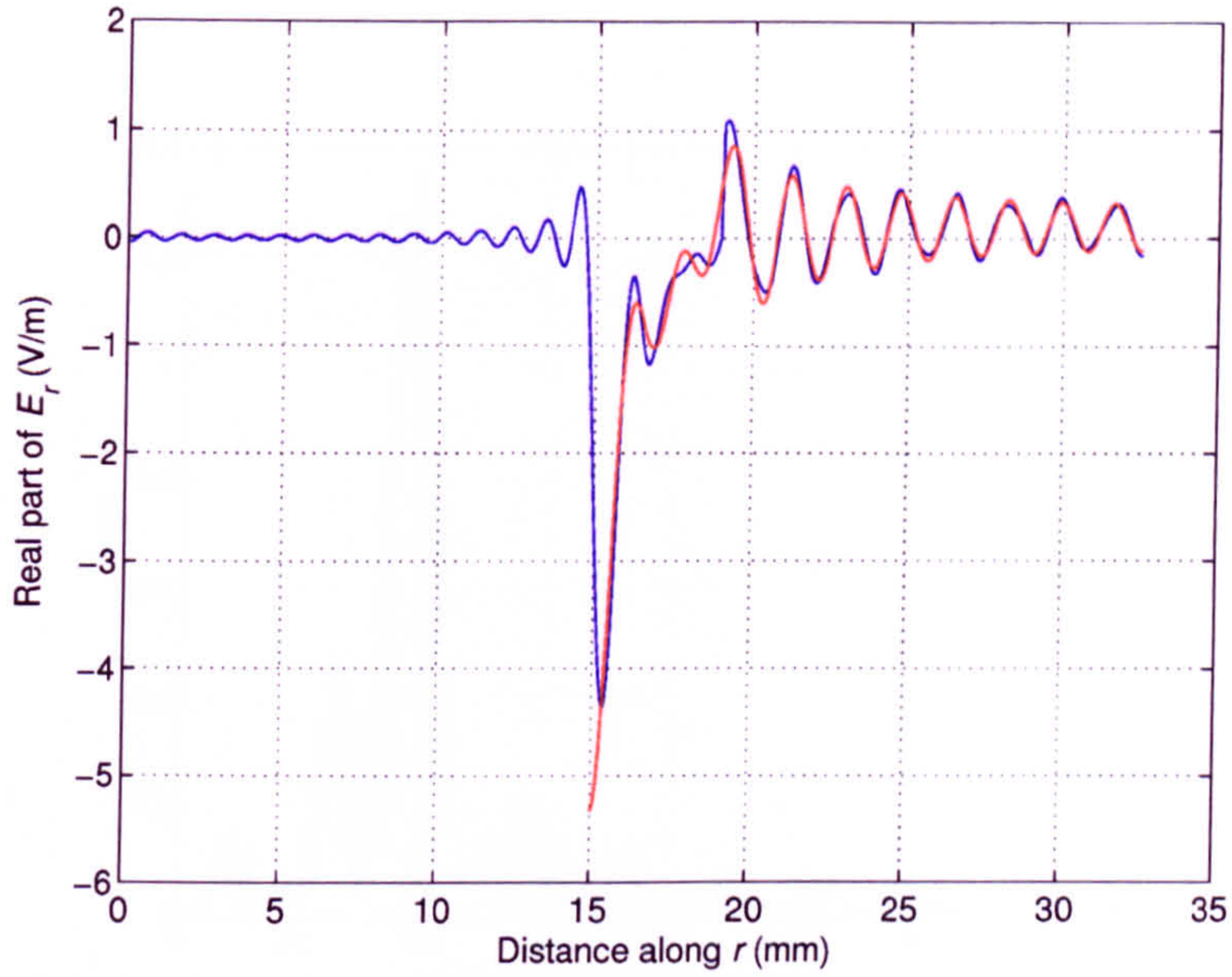

Figure 3.25: E_r of the $\mathrm{EH}_{11\delta+1}$ mode at $z = 0$, $\theta = 0$. $Na = 120$, $Nb = 40$ and $Nc = 80$.

3.3.7 Convergence study of the $\mathrm{TM}_{01\delta}$ and $\mathrm{TE}_{01\delta}$ modes

The convergence of the $\mathrm{TM}_{01\delta}$ mode is expected to be easier to achieve as only the electric fields can have singularities. The correlation distributions are shown in Figs. 3.26 and 3.27. For the same reason as previously with the hybrid modes, the correlation distributions with waveguide A suffer from a similar, but more limited spread than that of Fig. 3.13.a. Fig. 3.28 shows the variation of the Na/Nb ratios with r_1/r_3 for different values of r_2/r_3. Their behaviour is similar to that in Fig. 3.17, although the worst case here only goes over R_{lin} by a maximum of 4 for 10% correlation and 2 for 20%. As in the hybrid mode case, the coaxial to circular interface is well behaved and the ratios for Nc/Nb are similar (less than 10% smaller) to those in the previous section. For the test cavity, the correlations for Na/Nb and Nc/Nb become $60/20 = 3.00$ and $43/20 = 2.15$ for the 10% criterion and $44/20 = 2.20$ and $39/20 = 1.95$ for the 20% criterion. Figs. 3.29 and 3.30 illustrate the convergence for various ratios in waveguide A and C respectively. It is interesting to note that, provided Na/Nb is chosen large enough, the resonant frequency converges by steps as Nb is increased. As these steps always happen for the same values of Nb, independently of the Na/Nb and Nc/Nb ratios, it means that the modes of waveguide

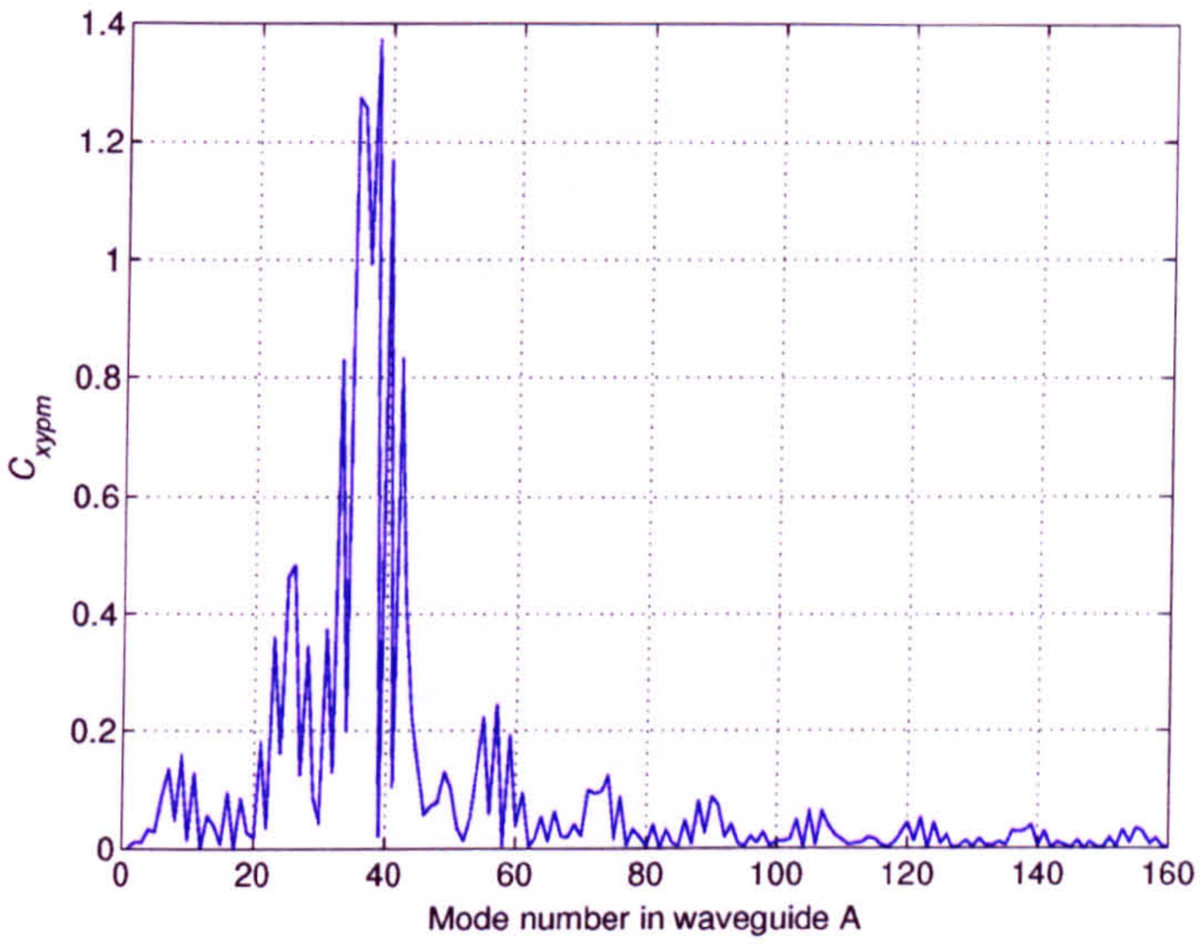

Figure 3.26: Correlation C_{xymp} of 20$^{\text{th}}$ TM mode of waveguide B with TM modes of waveguide A. $n = 0$, $f = 1.342$ GHz.

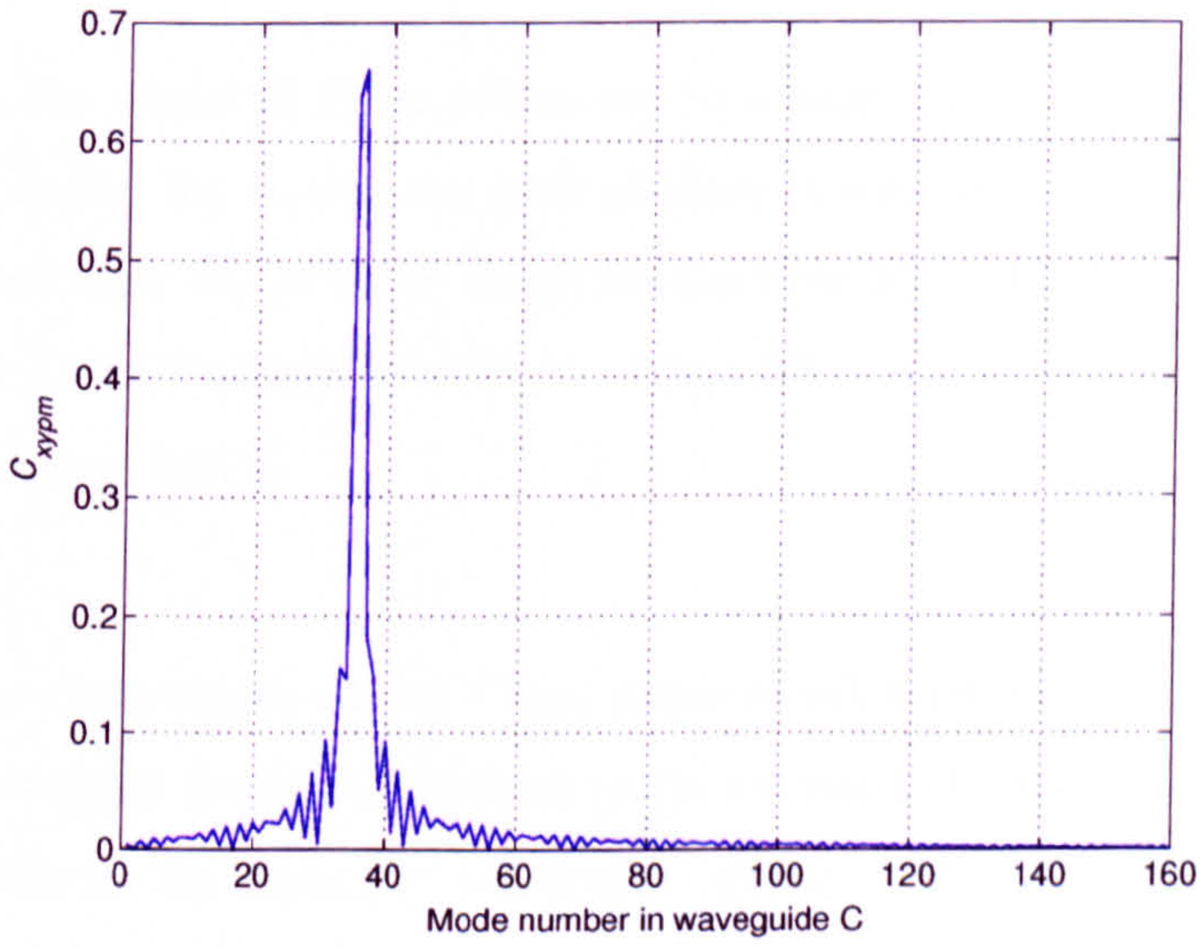

Figure 3.27: Correlation C_{xymp} of 20$^{\text{th}}$ TM mode of waveguide B with TM modes of waveguide C. $n = 0$, $f = 1.342$ GHz.

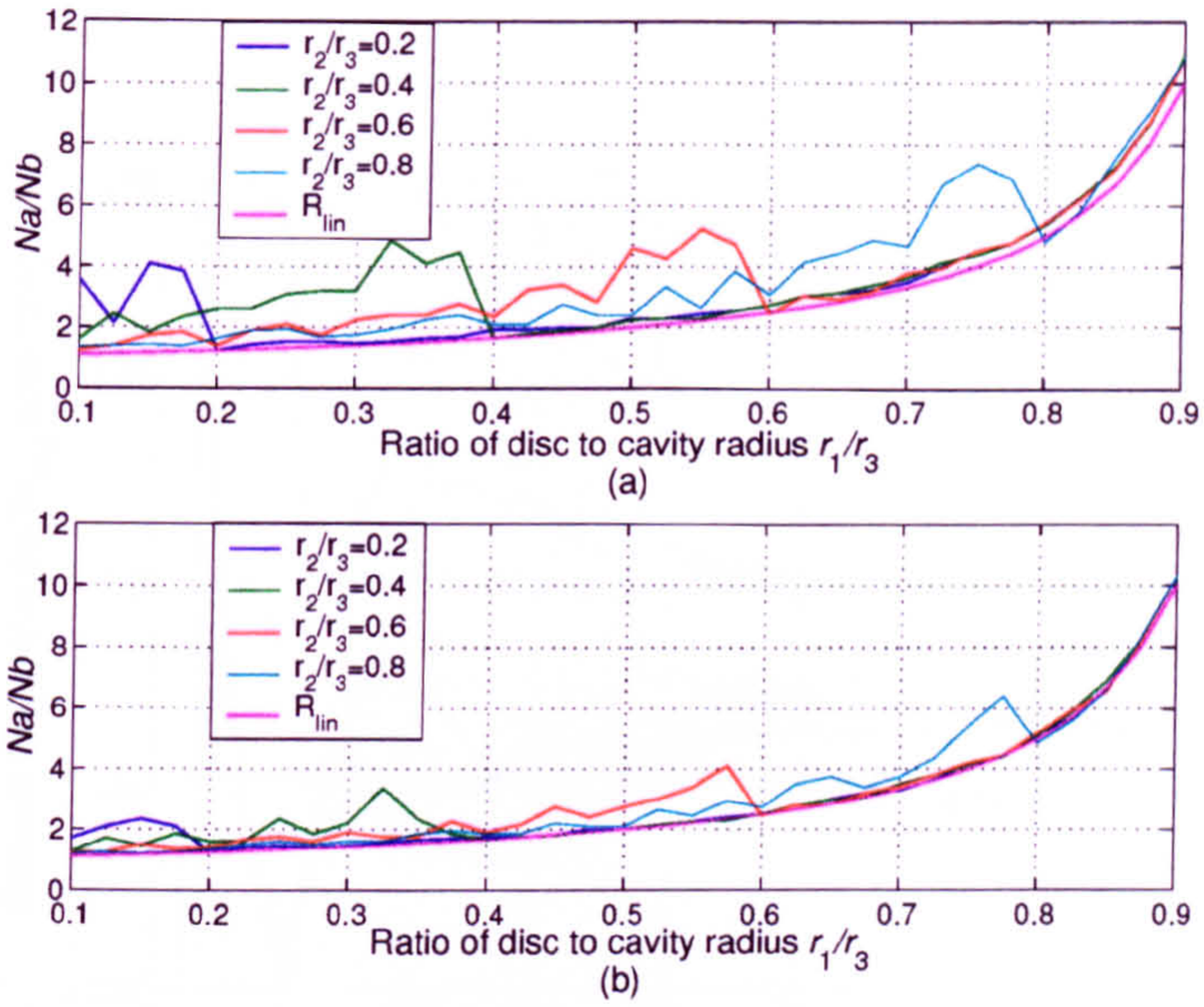

Figure 3.28: Na/Nb ratio variation with the disc to cavity radius ratio r_1/r_3 for different dielectric cylinder to cavity radius r_2/r_3 for the TM modes and $n = 0$. $Nb = 20$, $f = 1.33$ GHz. (a) 10% correlation, (b) 20% correlation.

B included in the model at these points are to a large extent the ones contributing to the $TM_{01\delta}$ mode. So, during the later studies, it will be more efficient to chose a value of Nb just after one of these steps, for example $Nb = 17$. Fig. 3.31 is a plot of the $\Delta f/f_0$ for $(Na/Nb, Nc/Nb) = (3,2)$. After $Nb = 16$, $\Delta f/f_0$ is, for all but one point, always below 0.01%.

Finally, the convergence of the $TE_{01\delta}$ mode is achieved with a minimal number of modes. It presents the least difficulty as its electric field will have no singularity at all. No fields in the dielectric waveguide present a step in amplitude between the air and the dielectric regions, which means that the spread of the correlation distributions is very limited. The Na/Nb and Nc/Nb ratios are the same as for Nc/Nb in the $TM_{01\delta}$ case. Figs. 3.32 and 3.33 show that the correlations have decreased to 10% of the maximum value with Na/Nb and Nc/Nb as small as 2. The convergences are shown in Figs. 3.34 and 3.35.

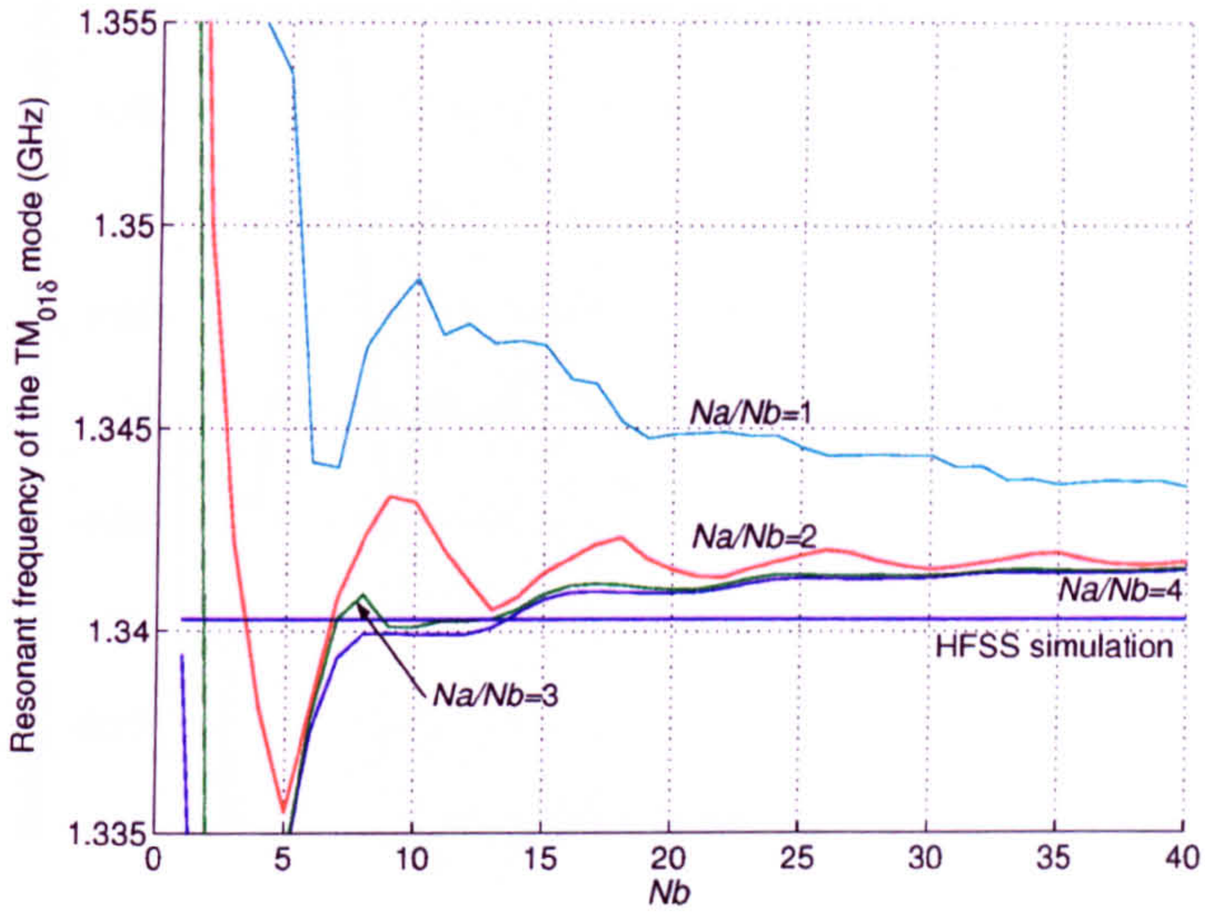

Figure 3.29: Resonant frequency variation with Nb for the $TM_{01\delta}$ mode for various Na/Nb. $Nc/Nb = 4$.

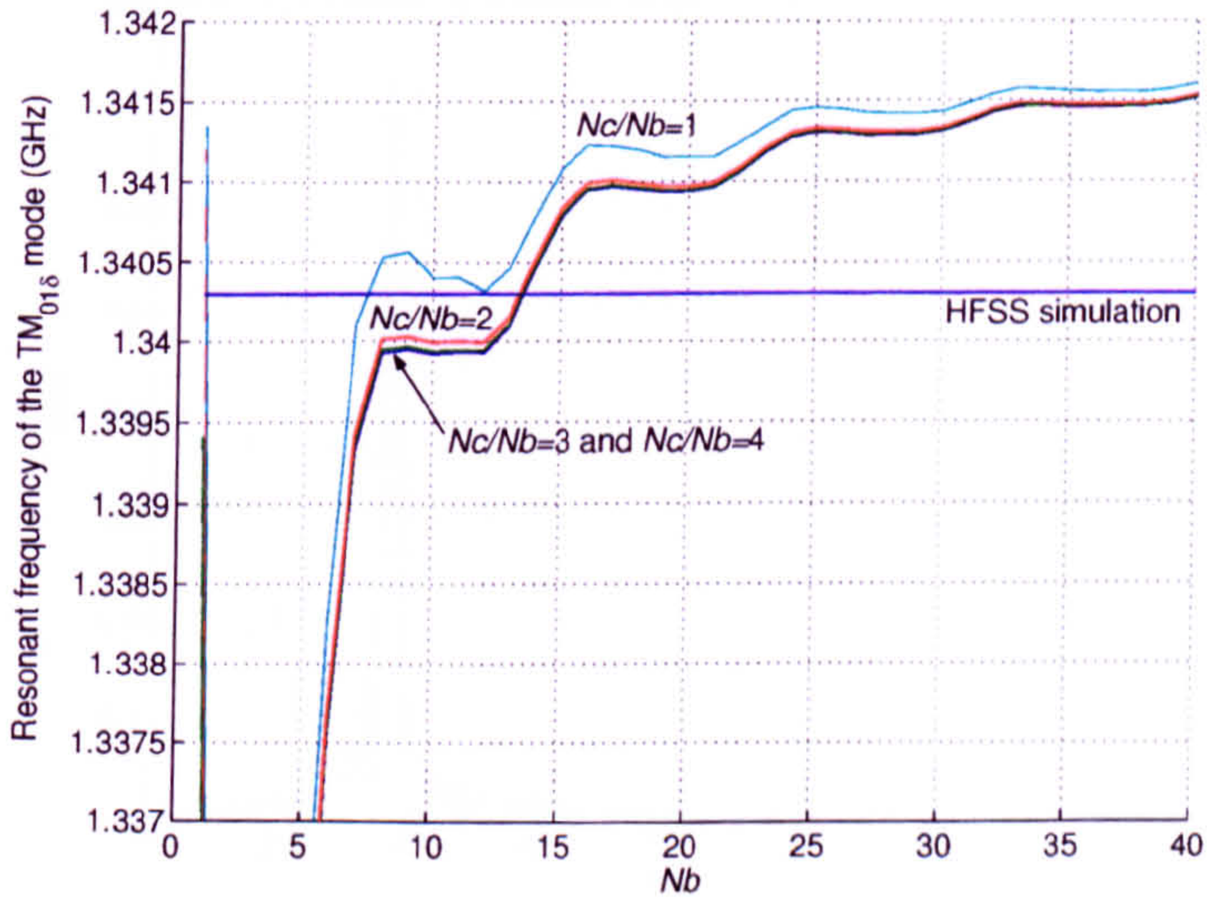

Figure 3.30: Resonant frequency variation with Nb for the $TM_{01\delta}$ mode for various Nc/Nb. $Na/Nb = 4$.

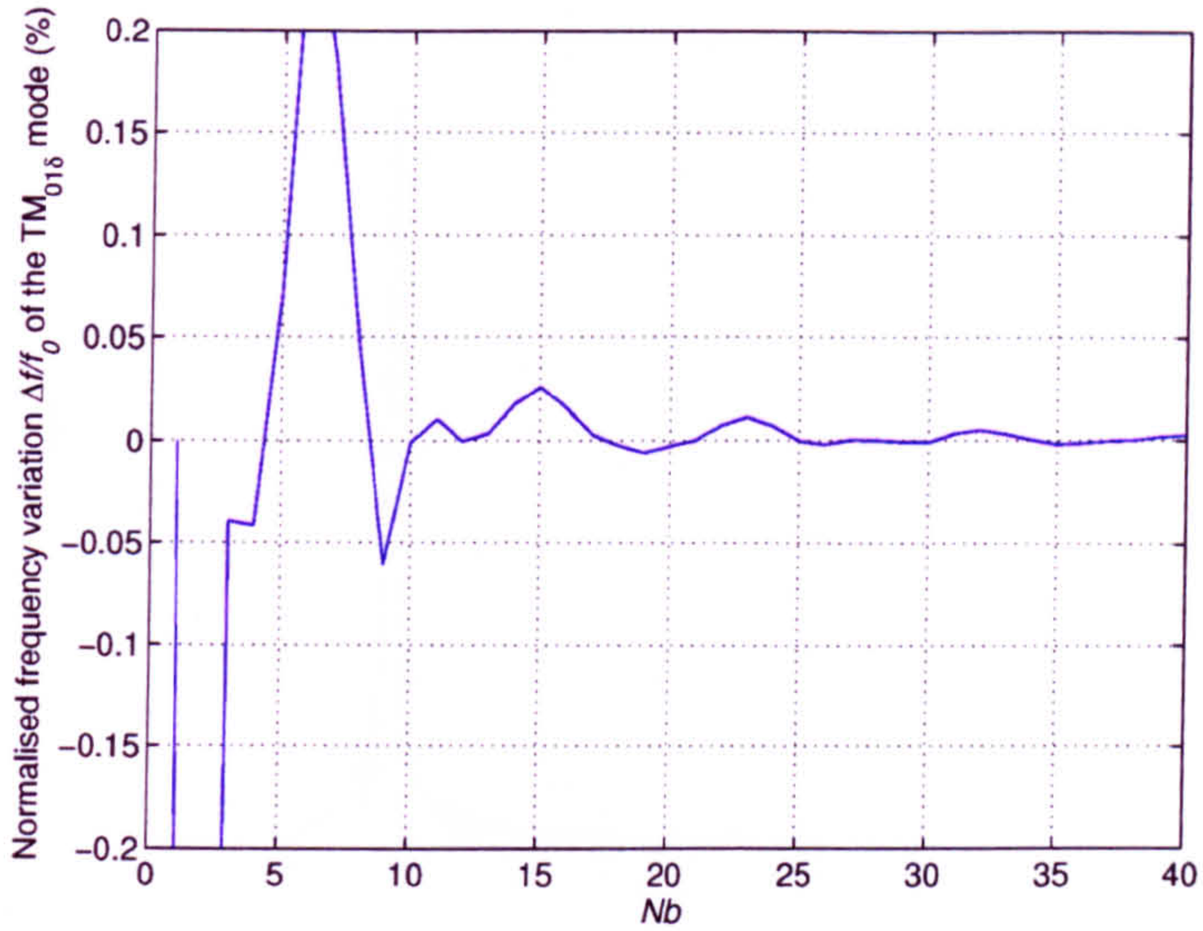

Figure 3.31: Change of resonant frequency over last iteration ($Nb-1 \rightarrow Nb$) versus Nb for the $TM_{01\delta}$ mode. (Na/Nb,Nc/Nb) = (3,2).

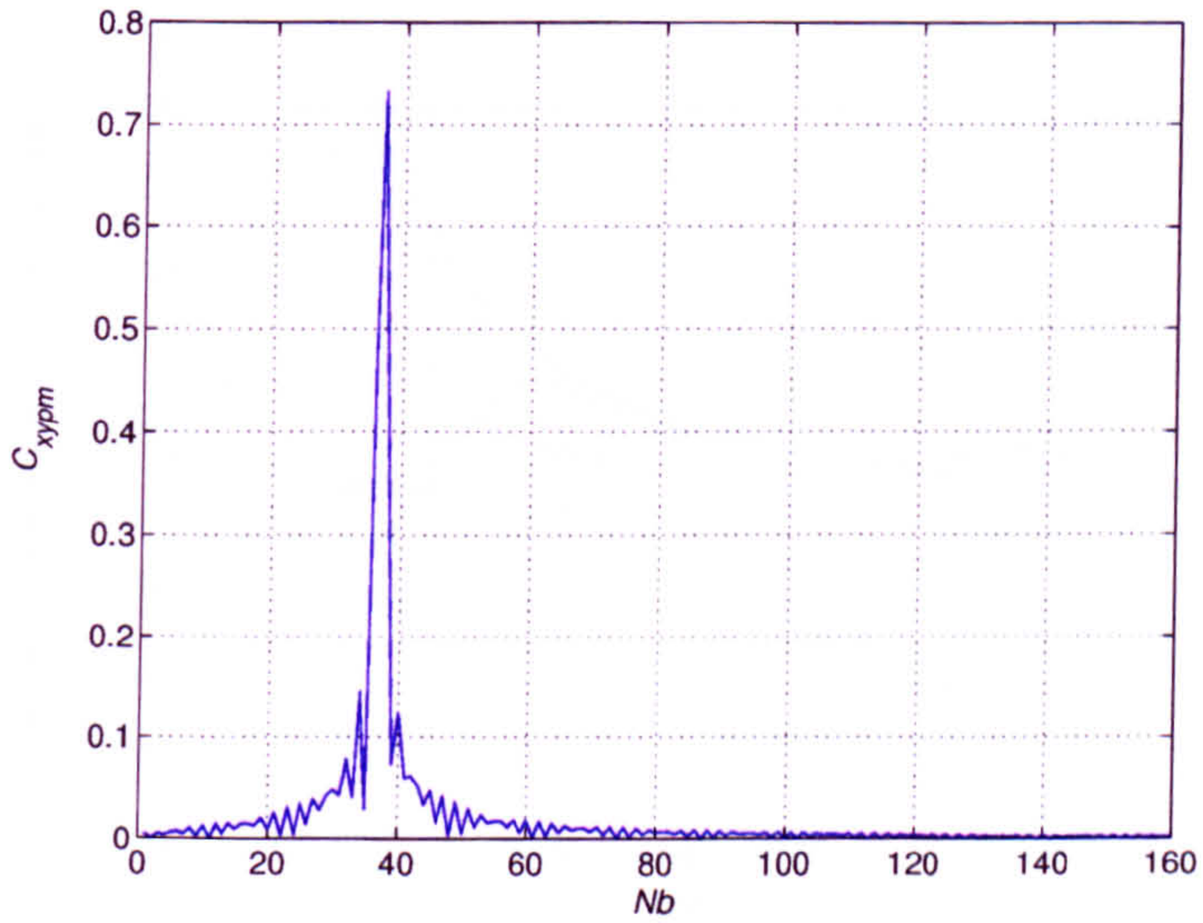

Figure 3.32: Correlation C_{xymp} of 20$^{\text{th}}$ TE mode of waveguide B with TE modes of waveguide A. $n = 0$, $f = 1.4735$ GHz.

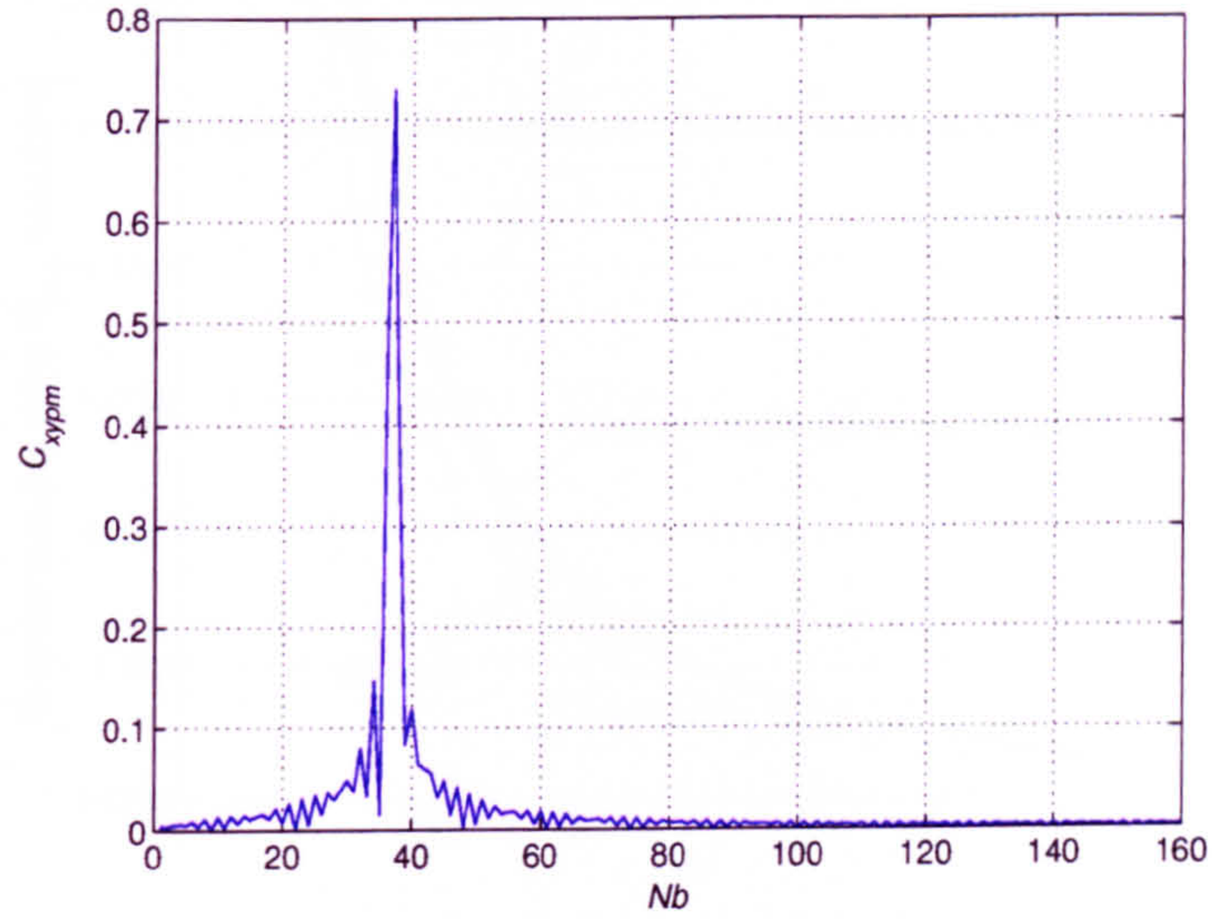

Figure 3.33: Correlation C_{xymp} of 20$^{\text{th}}$ TE mode of waveguide B with TE modes of waveguide C. $n = 0$, $f = 1.4735$ GHz.

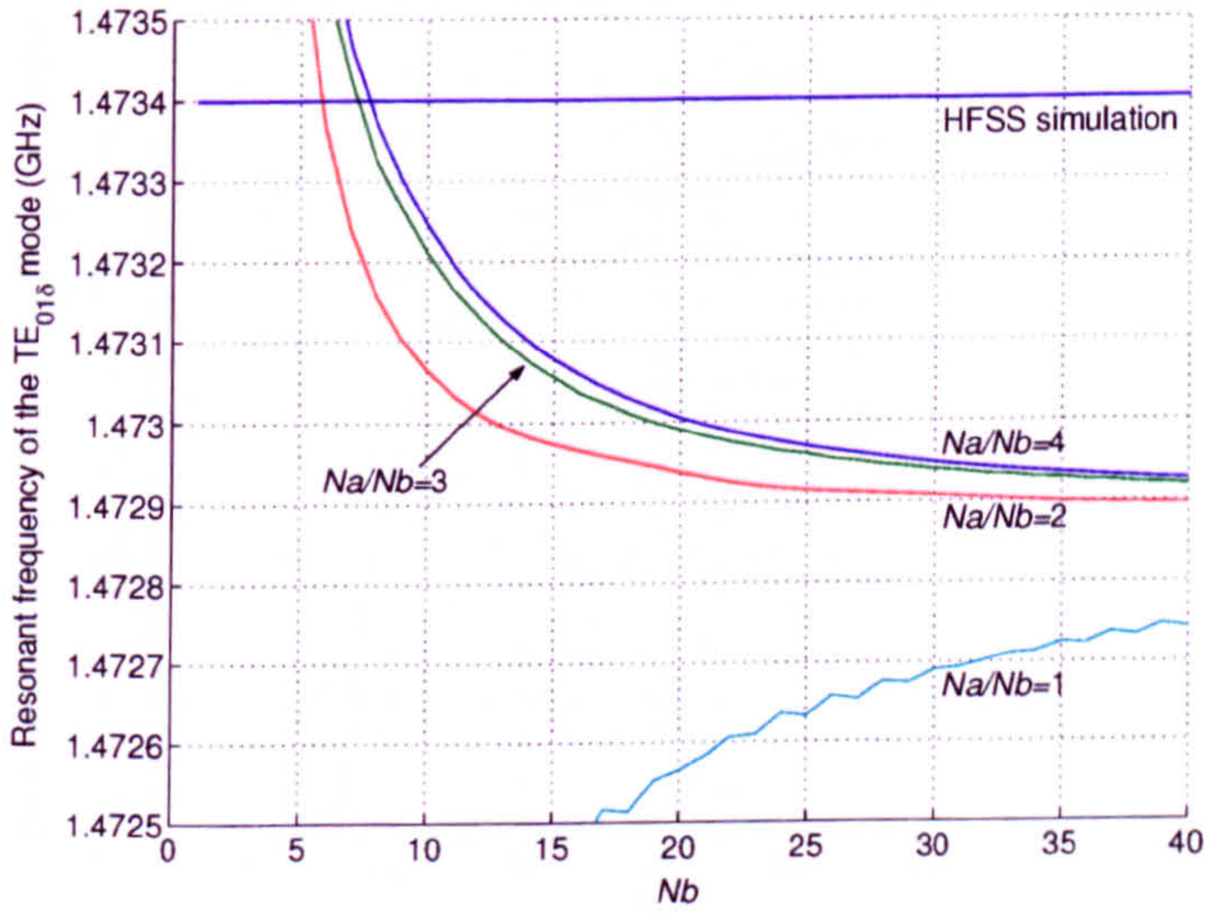

Figure 3.34: Resonant frequency variation with Nb for the $\text{TE}_{01\delta}$ mode for various Na/Nb. $Nc/Nb = 4$.

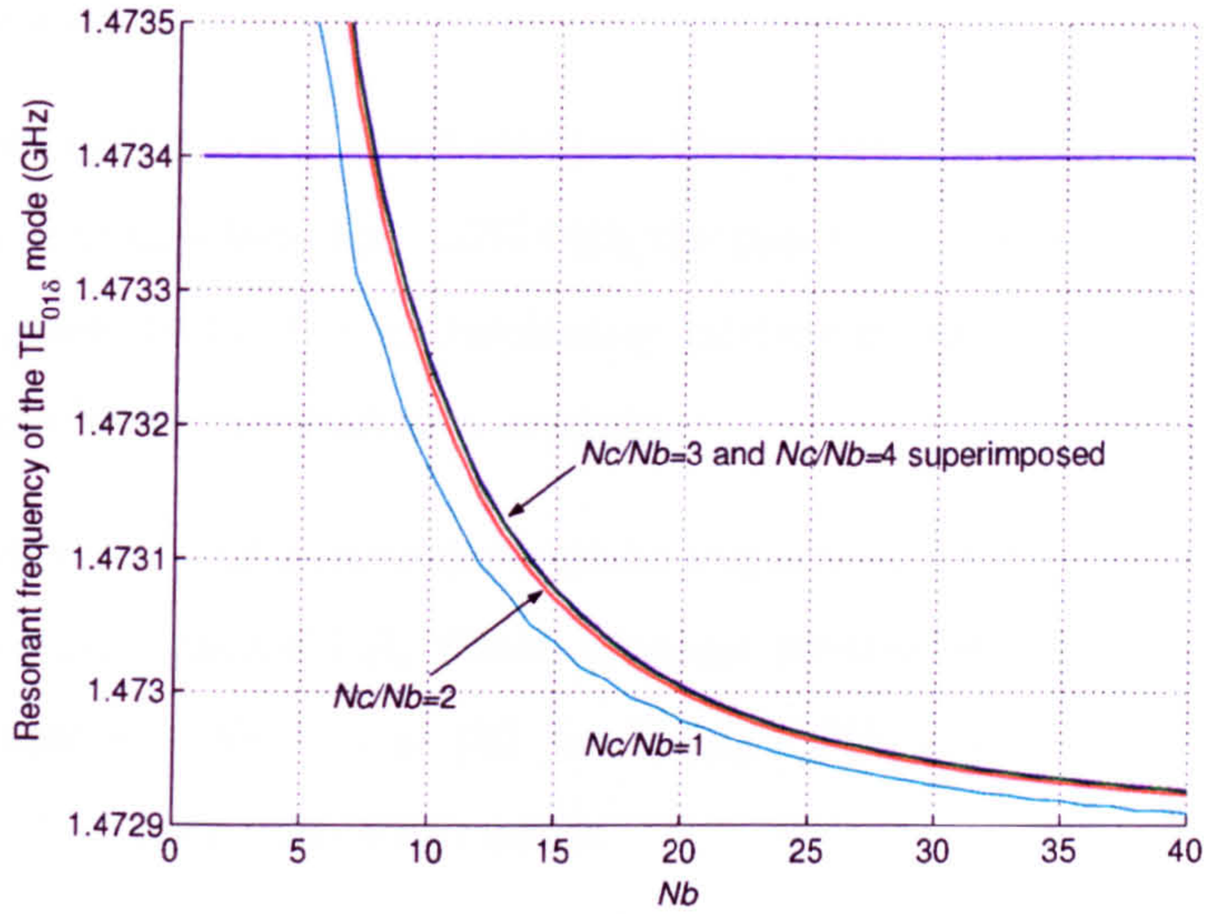

Figure 3.35: Resonant frequency variation with Nb for the $TE_{01\delta}$ mode for various Nc/Nb. $Na/Nb = 4$.

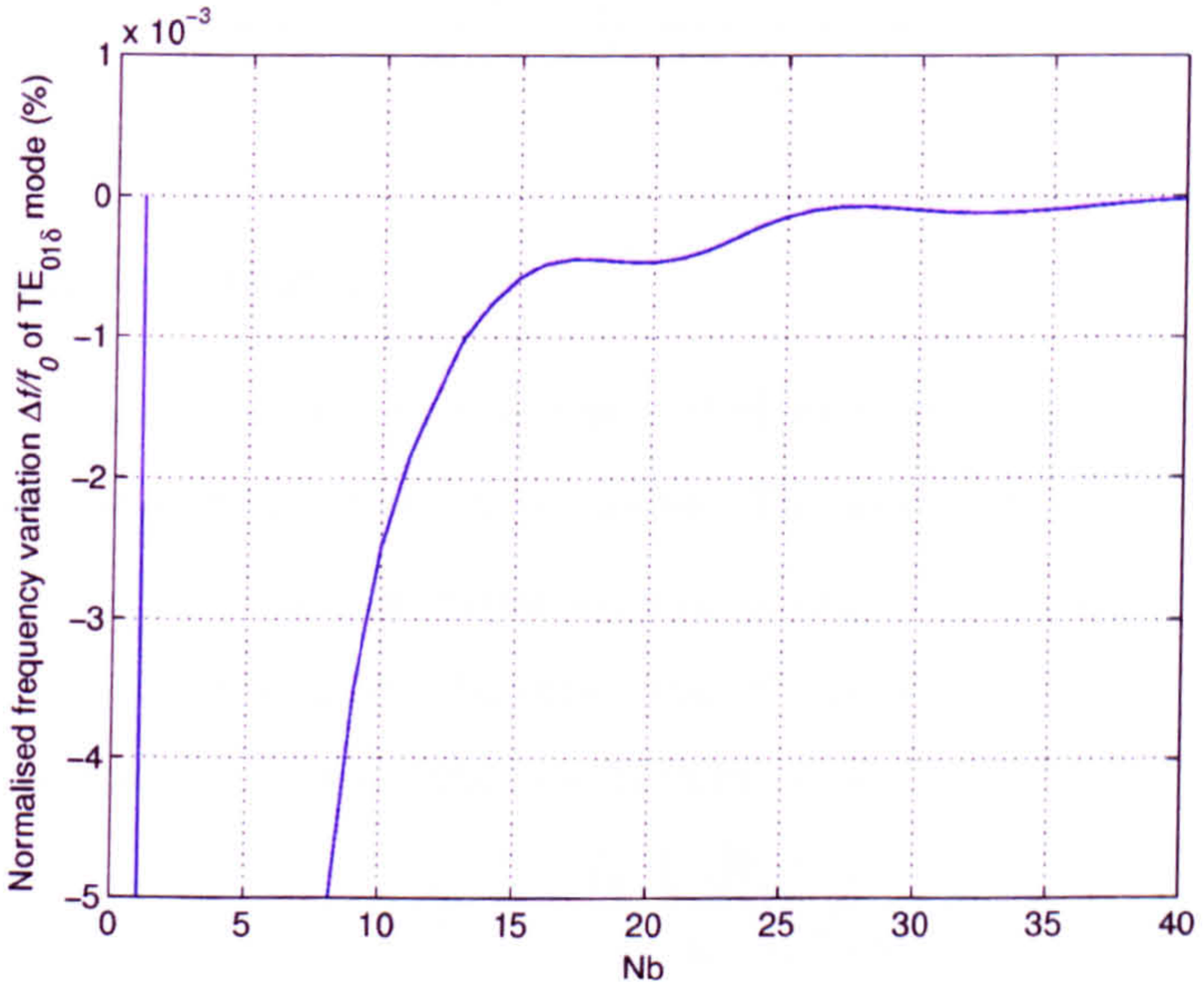

Figure 3.36: Change of resonant frequency over last iteration ($Nb-1 \rightarrow Nb$) versus Nb for the $TE_{01\delta}$ mode. (Na/Nb,Nc/Nb) = (2,2).

3.3.8 Comparison of modelled and measured resonant frequencies

Table 3.2 shows that the measured resonant frequencies of the five first modes of the test cavity agree within less than 3.5% with the mode-matching results. The discrepancies are believed to be due to machining tolerances and above all imperfections such as air gaps between metal and ceramic.

Table 3.2: *Simulated and measured resonant frequencies of the five first modes of the dual-mode conductor-loaded DR. Finite element simulation as in Table 3.1. Mode-matching simulation:* $Na = 120$ *(80 for* $TE_{01\delta}$*),* $Nb = 40$*,* $Nc = 80$*.* df_0 *is the variation from the mode-matching results.*

Mode		$HE_{11\delta}$	$EH_{11\delta+1}$	$TM_{01\delta}$	$HE_{21\delta}$	$TE_{01\delta}$
Mode matching f_0 (GHz)		0.9220	1.300	1.341	1.452	1.473
HFSS^{TM}	f_0 (GHz)	0.9201	1.299	1.340	1.449	1.473
	df_0 (%)	−0.21	−0.08	−0.07	−0.21	$< \pm 0.01$
Measurement	f_0 (GHz)	0.9388	1.312	1.295	1.481	1.461
	df_0 (%)	+1.82	+0.92	−3.43	+2.00	−0.81

3.3.9 Q_u calculations

The Q_u of each resonant mode can be calculated analytically from Eq. 1.3 and the amplitude coefficients of the waveguide modes. The latter are obtained at the resonant frequencies by inverting the linear system of Eq. 1.10 by Gaussian elimination with Matlab^{TM} after arbitrarily choosing one of the coefficient. The Q_u is then calculated from commonly used expressions [138, 174]:

$$\frac{1}{Q_u} = \frac{1}{Q_c} + \frac{1}{Q_d} = \frac{P_c}{\omega_0 W} + \frac{P_d}{\omega_0 W} = \frac{\oint_S R_s \left|\mathbf{H_t}\right|^2 dS}{\omega_0 \int_V \mu_0 \left|\mathbf{H_t}\right|^2 dV} + \frac{\int_{V_d} \epsilon'' \left|\mathbf{E}\right|^2 dV}{\int_V \epsilon_0 \epsilon' \left|\mathbf{E}\right|^2 dV} \tag{3.28}$$

where Q_c and Q_d are the quality factors due to conductor and dielectric losses respectively, related to the respective average powers dissipated P_c and P_d and the total stored energy. R_s is the surface resistivity of the conductor surfaces, $\mathbf{H_t}$ the magnetic field tangential to the conductor surface, $\epsilon = \epsilon' - j\epsilon''$ the complex permittivity at any point in the resonator volume, S the conductor surface area, V the

resonator volume and V_d the dielectric volume. The integrals are similar to those solved for the cross-product calculations. As their expressions are lenghty, they are not included here.

Table 3.3 lists the Q_u's of the five first modes of the test cavity obtained with the mode-matching program, with HFSS^{TM} and by experiment. For $Nb = 40$, the mode-matching results for Q_d agree within 10% with those of HFSS^{TM}. The reason for these discrepancies is not understood. Indeed, the convergences of all five Q_d's modelled by mode-matching are very good: as Nb is doubled from 20 to 40, they all vary by less than 0.06%. Also, if the mode-matching results were inaccurate, one would expect the discrepancies between modes with similar field distributions (e.g. $HE_{11\delta}$ and $HE_{21\delta}$) to be similar. Here, they are quite different and of opposite

Table 3.3: *Q_u factor simulations and measurements for the test cavity. Mode-matching is with $Nb = 40$ and $(Na/Nb, Nc/Nb) = (3, 2)$ for all modes except $TE_{01\delta}$ with $(2, 2)$. Finite element simulations (HFSS^{TM}) are with 8831 tetrahedra.*

Mode		Mode-matching	HFSS^{TM}	Experimental
$HE_{11\delta}$	Q_c	9428	8550	
	Q_d	41,676	41,017	
	Q_u	7689	7075	7230
$EH_{11\delta+1}$	Q_c	7063	6843	
	Q_d	29,028	30,971	
	Q_u	5681	5605	5540
$TM_{01\delta}$	Q_c	13,857	13,760	
	Q_d	38,397	42,649	
	Q_u	10,182	10,403	11,000
$HE_{21\delta}$	Q_c	12,889	11,348	
	Q_d	26,165	28,150	
	Q_u	8635	8088	9390
$TE_{01\delta}$	Q_c	13,294	12,551	
	Q_d	25,587	27,345	
	Q_u	8749	8602	8630

sign. Finally, the $TM_{01\delta}$ mode only disagrees by 3% more than the $HE_{21\delta}$ mode, even though only 72.8% of the electric energy of the former is concentrated within the dielectric region for the $TM_{01\delta}$, compared to more than 97% for all other modes. One would expect the difference of energy distribution to induce different accuracies in the case of an erroneous calculation.

As far as Q_c is concerned, the cases of the $HE_{11\delta}$ and $HE_{21\delta}$ modes represent the major discrepancies between mode-matching and HFSS^{TM} results. Table 3.4 shows that the larger the difference between the two numerical methods, the slower the convergence of Q_c as Nb is increased. In brackets are the variations in Q_c each time Nb is doubled. It has to be noted that, in all cases, the Q_c value modelled by mode-matching converges towards the HFSS^{TM} value. The speed of the Q_c's convergences do not appear to be linked to those of the resonant frequencies. The $EH_{11\delta+1}$ and especially the $TM_{01\delta}$ modes behave much better than in the previous section. On the other hand, the $TE_{01\delta}$ mode convergence is almost comparable to those of the $HE_{11\delta}$ and $HE_{21\delta}$ modes. The reason for this behaviour is difficult to pinpoint as quality factors are the ratios of variables which can themselves converge in different ways. However, the fact that Q_d has converged for all modes, irrespective of their energy distribution, leads to the conclusion that all the energy integrals have also converged. The problem is then believed to be due to the modelling of the conductor loss, primarily in the metal disc, possibly because of the field singularities present at its edges. Figs. 3.37 to 3.45 show the amplitude of each component of the

Table 3.4: *Q_c for the first five modes of the test cavity as Nb is increased. Mode number ratios as in Table 3.3. In brackets, the percentage variation of Q_c obtained by doubling Nb.*

Nb	5	10	20	40
$HE_{11\delta}$	10,303	9992 (−3.02)	9673 (−3.19)	9428 (−2.53)
$EH_{11\delta+1}$	7342	7237 (−1.43)	7133 (−1.44)	7063 (−0.98)
$TM_{01\delta}$	13,754	13,837 (+0.60)	13,847 (+0.07)	13,857 (+0.07)
$HE_{21\delta}$	14,244	13,762 (−3.38)	13,243 (−3.77)	12,888 (−2.68)
$TE_{01\delta}$	14,354	13,937 (−2.91)	13,580 (−2.56)	13,294 (−2.11)

magnetic field on the $r-z$ plane for the different modes, at the value for θ for which the magnitudes are maximum. The fields for the $\mathrm{HE}_{21\delta}$ mode are not pictured, as they are very similar to those of the $\mathrm{HE}_{11\delta}$ mode. In the case of the $\mathrm{HE}_{11\delta}$ mode, the H_r and H_z fields at both edges of the metal disc have large magnitudes. The discontinuity created by the fact that the fields must tend to infinity while approaching the edge of the disc, but also vanish when tangent to the metal surfaces is clear. For the $\mathrm{TE}_{01\delta}$ and $\mathrm{EH}_{11\delta+1}$ modes, the fields are less excited around the top edge of the disc, which coincides with the faster convergence of those two modes. As the $\mathrm{TE}_{01\delta}$ mode converges relatively slower than the $\mathrm{EH}_{11\delta+1}$ mode, one can assume that the modelling of the H_r field component around the top edge of the disc, extremely small in the $\mathrm{TE}_{01\delta}$ case, is not as critical as the H_z field component at the same location. This could be due to the chosen method of mode-matching with interfaces in the $r-\theta$ plane. Finally, the $\mathrm{TM}_{01\delta}$ mode, with no H_r and H_z fields, behaves best.

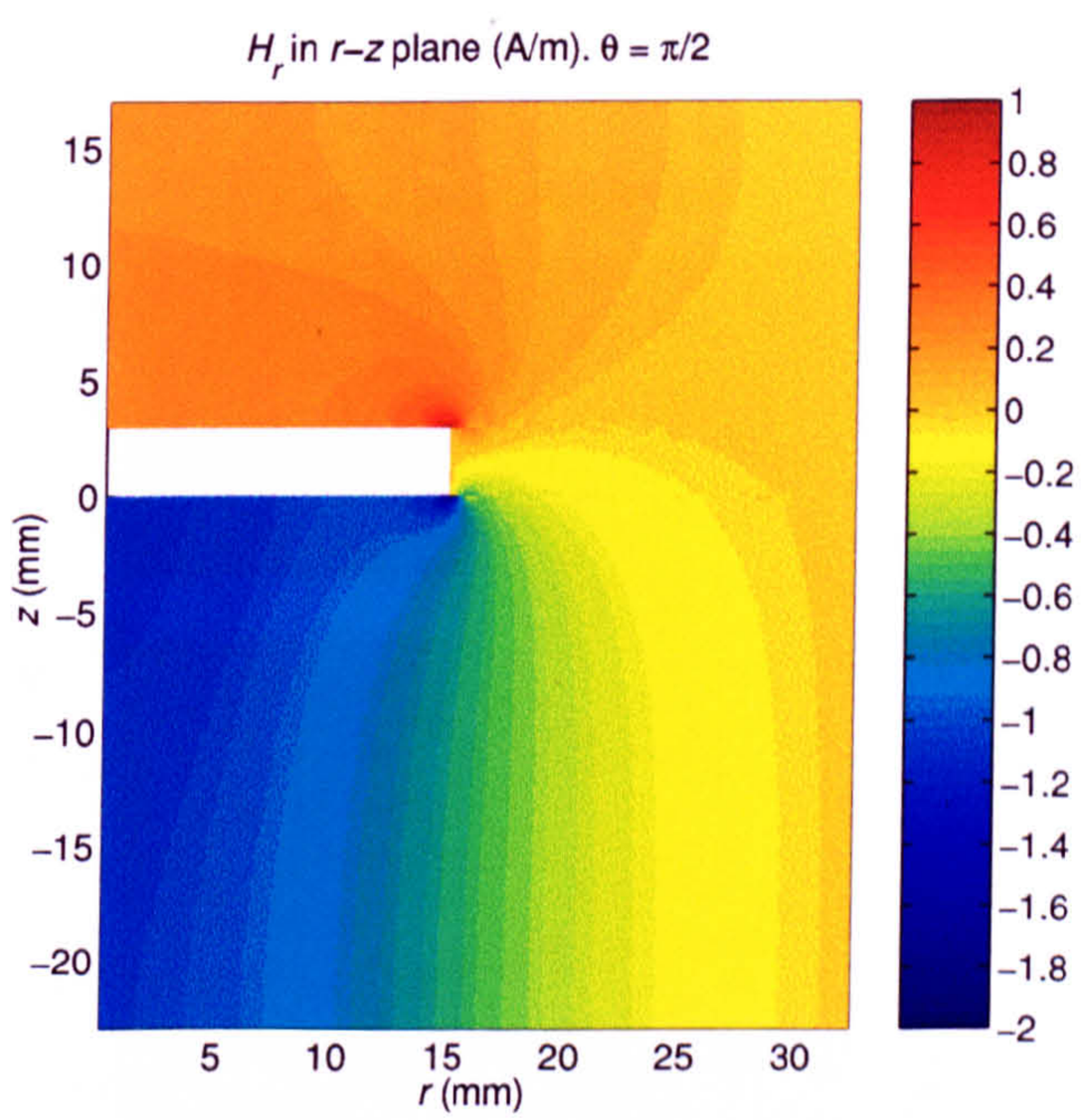

Figure 3.37: H_r of the $\mathrm{HE}_{11\delta}$ mode. $Na = 120$, $Nb = 40$, $Nc = 80$.

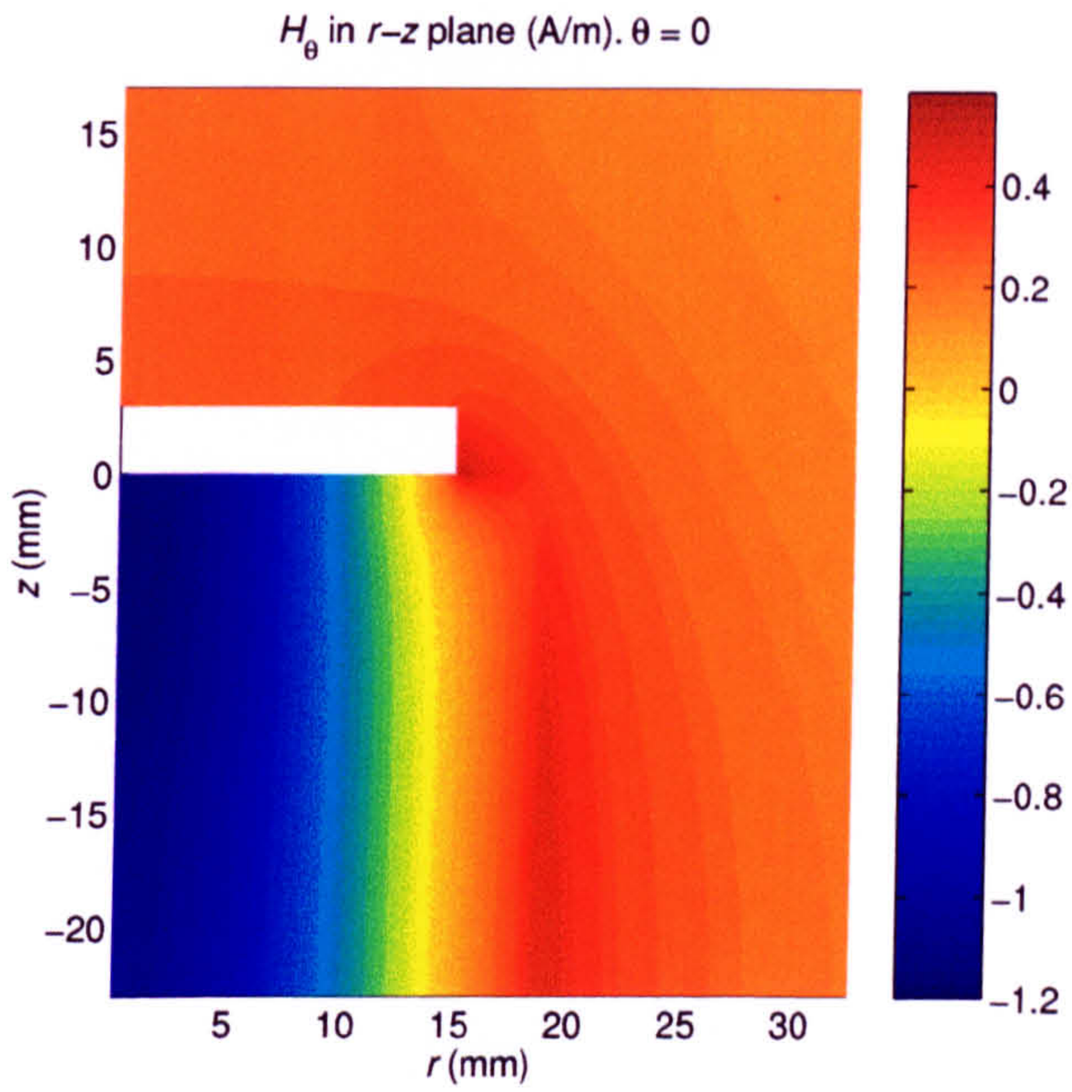

Figure 3.38: H_θ of the $\mathrm{HE}_{11\delta}$ mode. $Na = 120$, $Nb = 40$, $Nc = 80$.

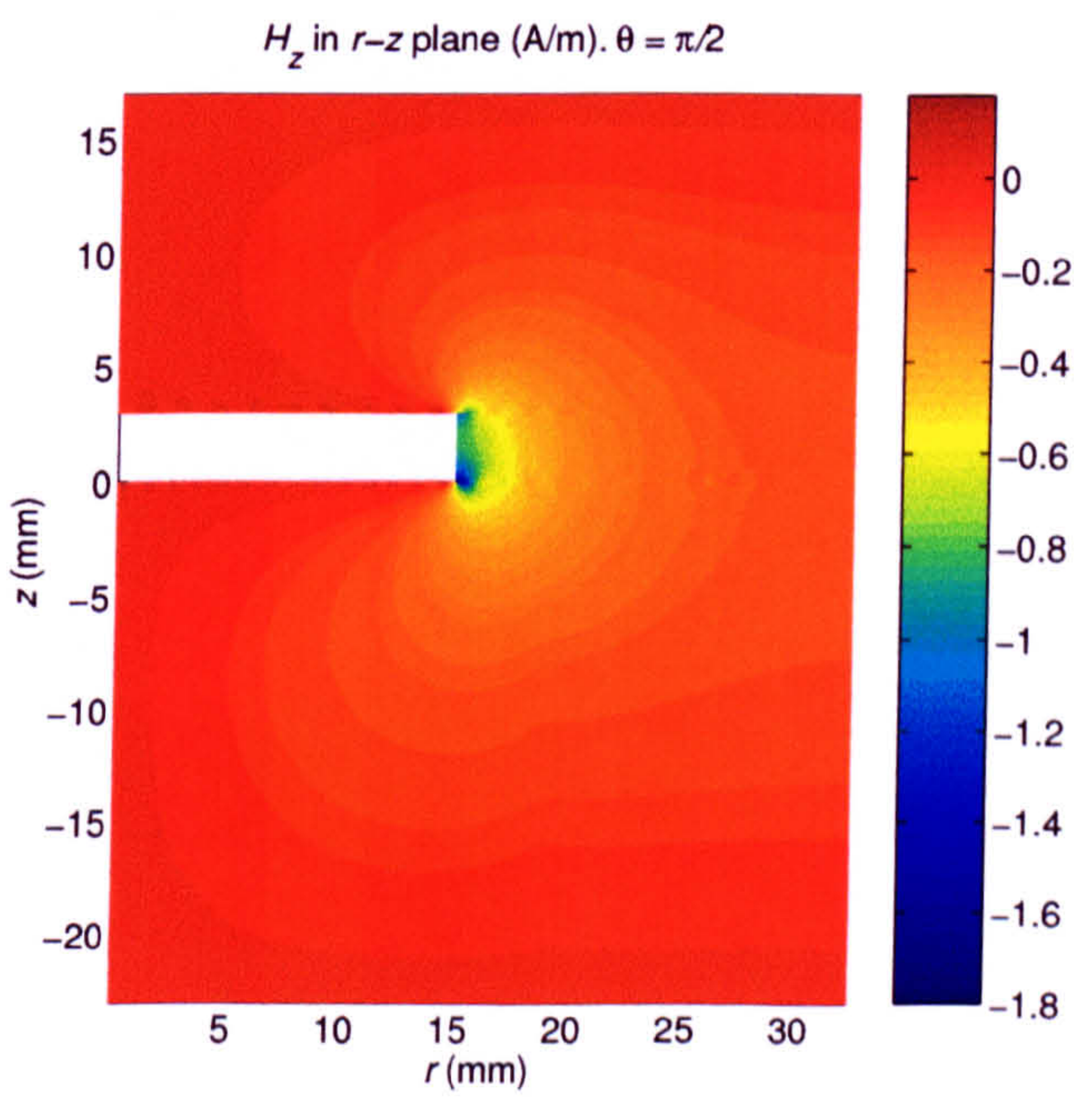

Figure 3.39: H_z of the $\mathrm{HE}_{11\delta}$ mode. $Na = 120$, $Nb = 40$, $Nc = 80$.

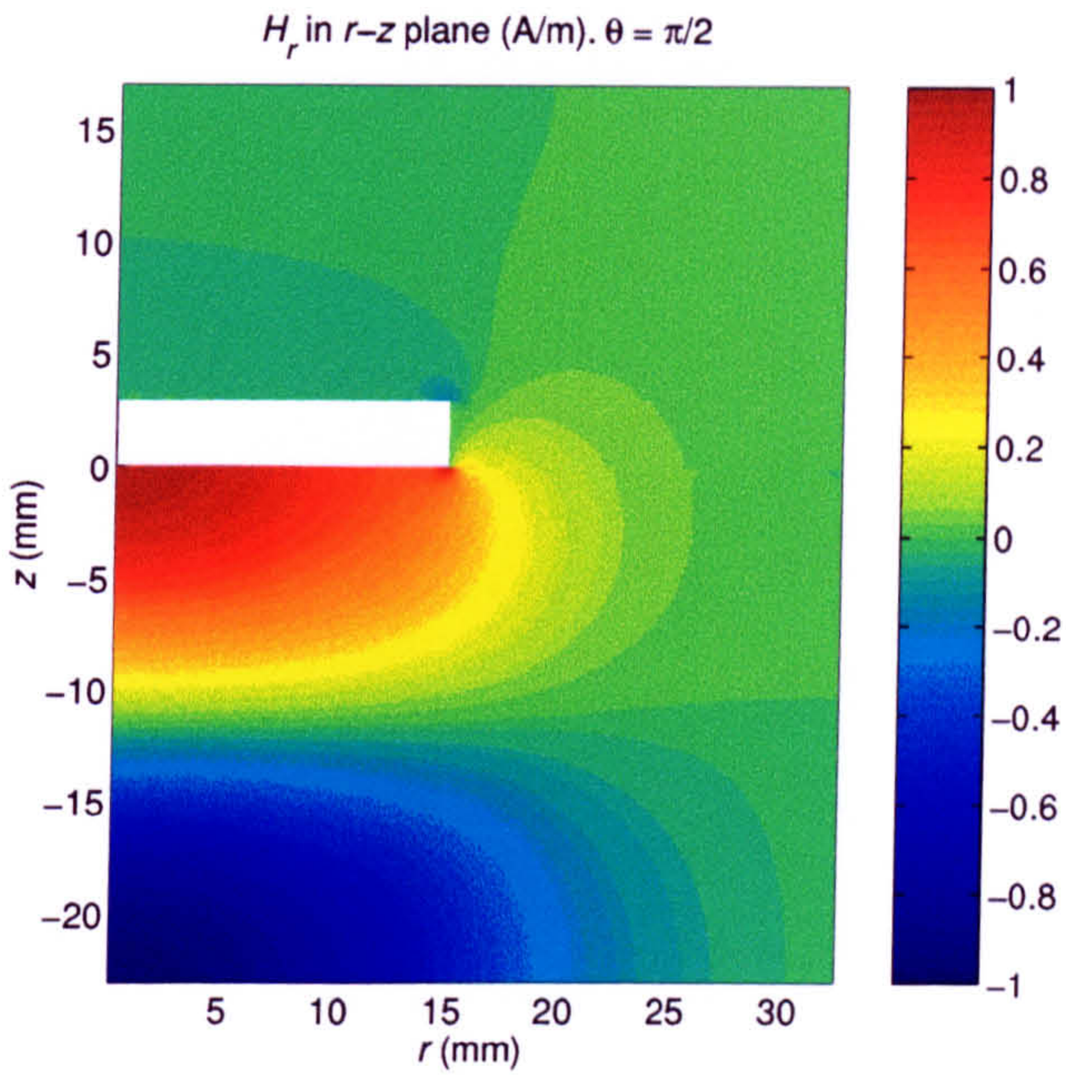

Figure 3.40: H_r of the $\mathrm{EH}_{11\delta+1}$ mode. $Na = 120$, $Nb = 40$, $Nc = 80$.

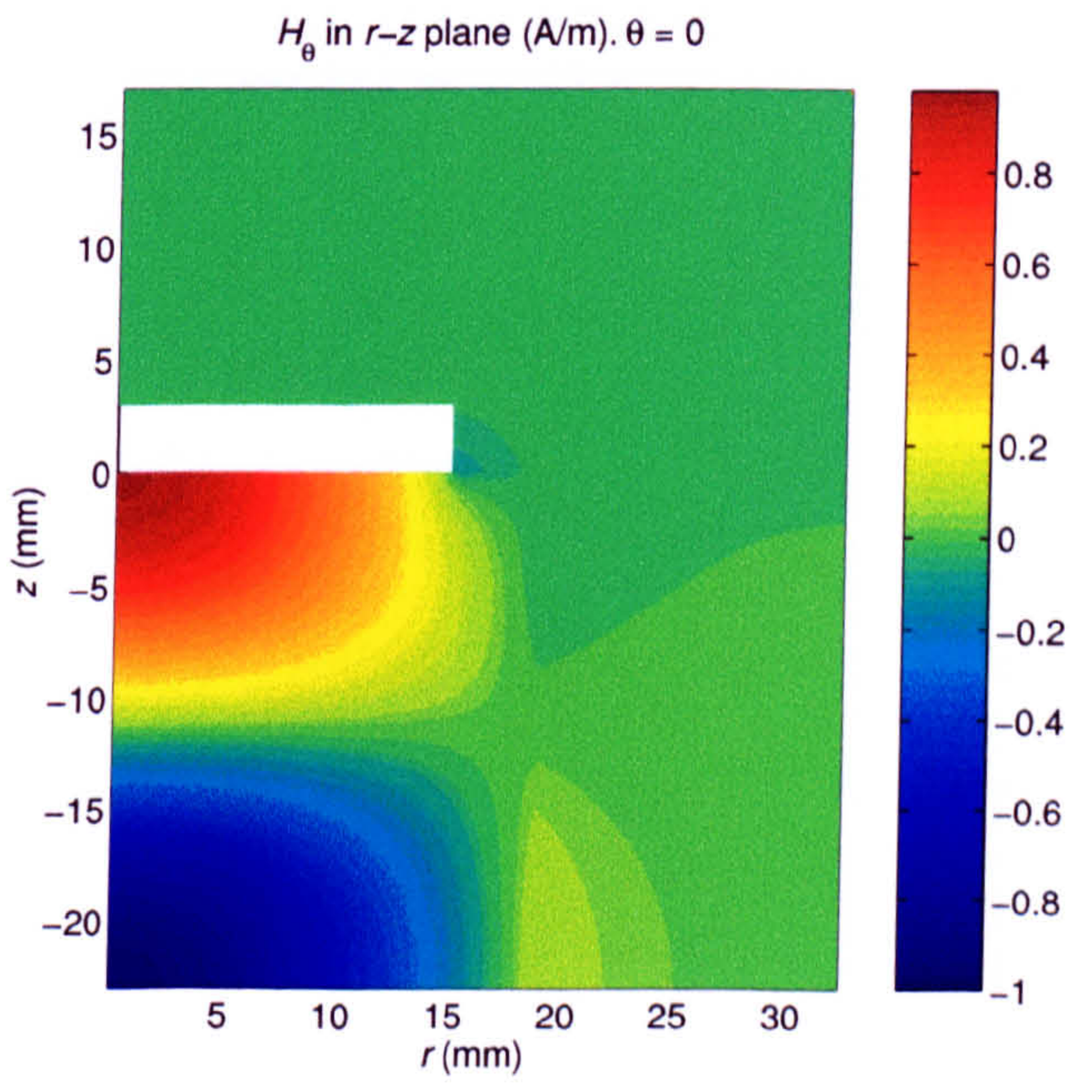

Figure 3.41: H_θ of the $\mathrm{EH}_{11\delta+1}$ mode. $Na = 120$, $Nb = 40$, $Nc = 80$.

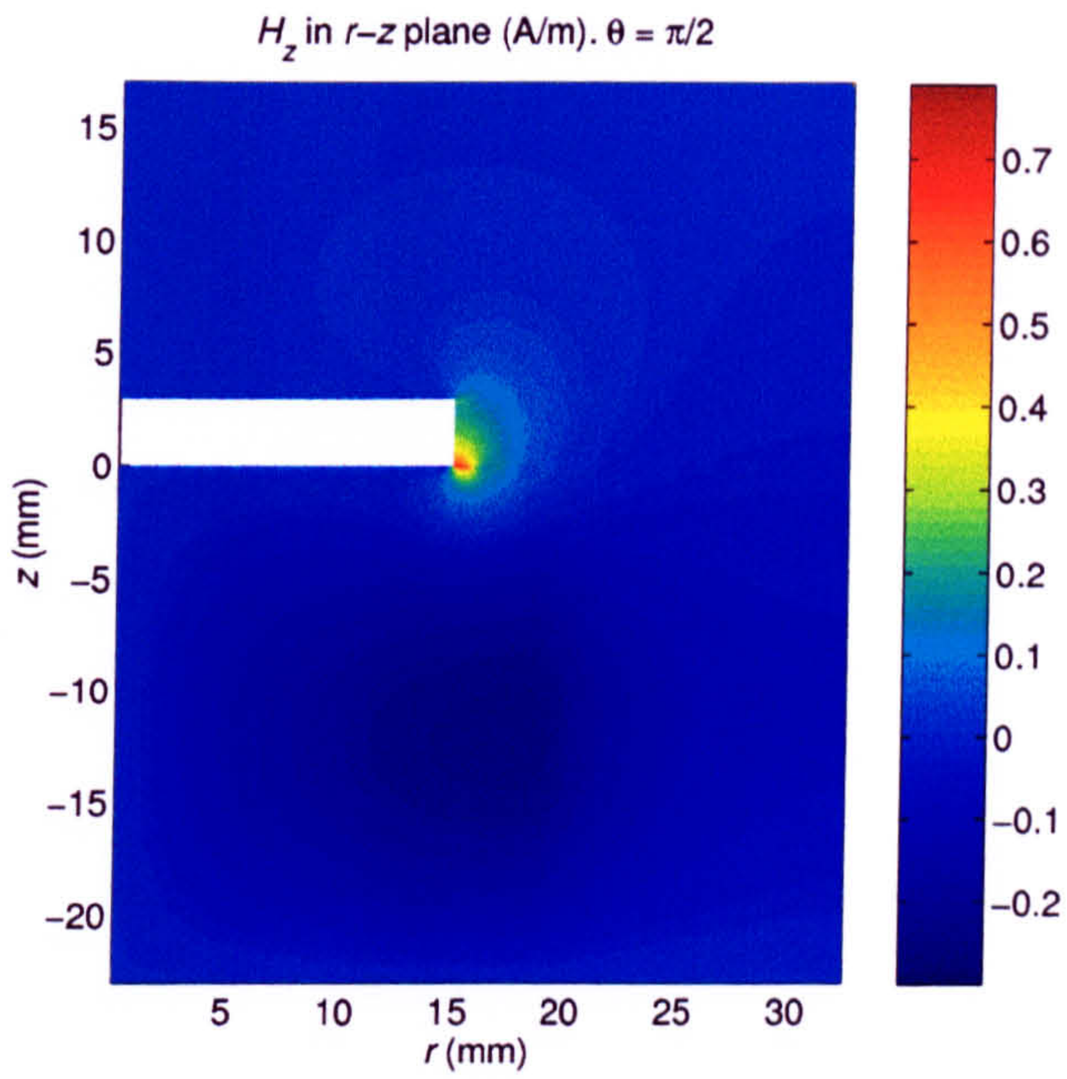

Figure 3.42: H_z of the $\mathrm{EH}_{11\delta+1}$ mode. $Na = 120$, $Nb = 40$, $Nc = 80$.

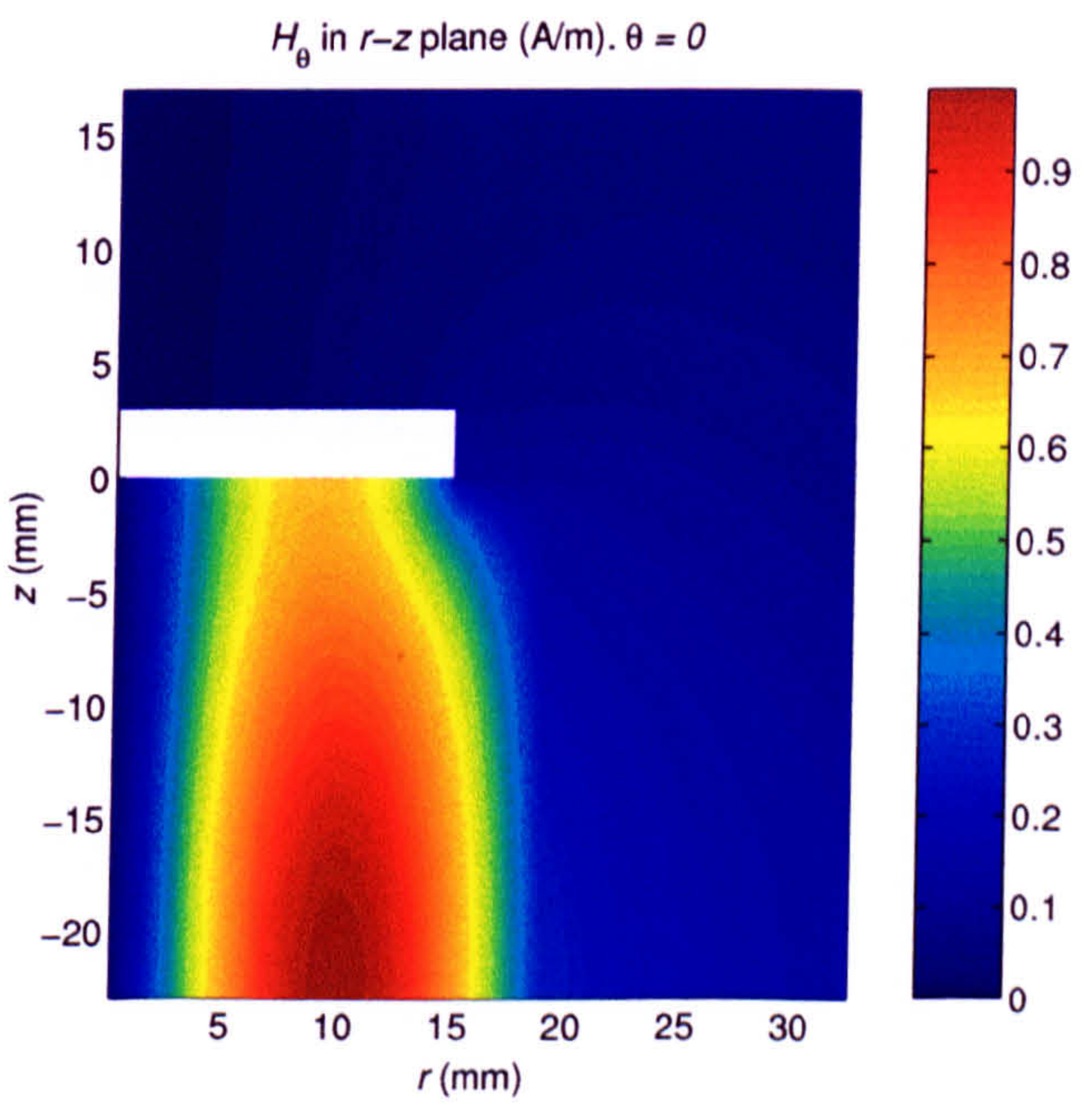

Figure 3.43: H_θ of the $\mathrm{TM}_{01\delta}$ mode. $Na = 120$, $Nb = 40$, $Nc = 80$.

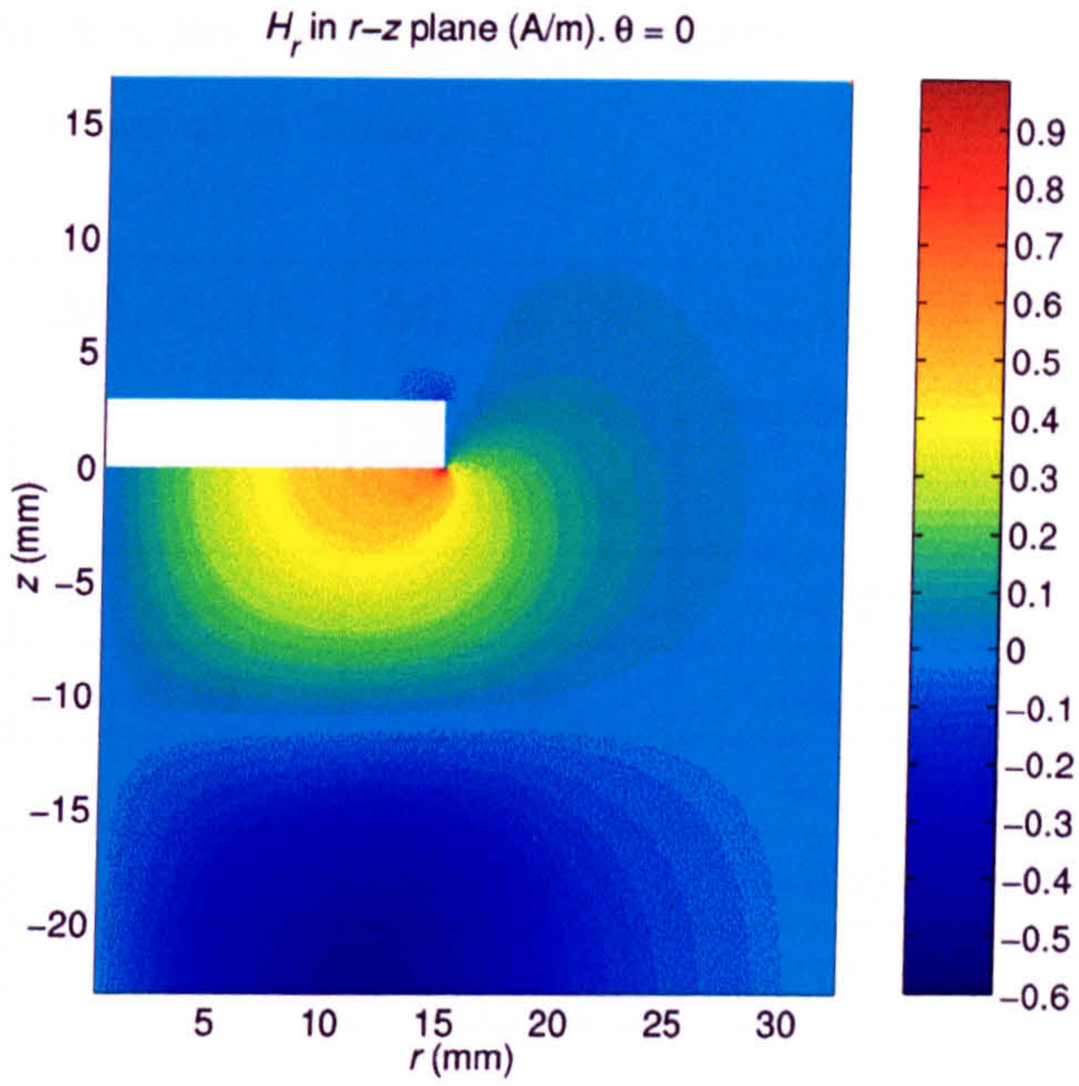

Figure 3.44: H_r of the $\mathrm{TE}_{01\delta}$ mode. $Na = 80$, $Nb = 40$, $Nc = 80$.

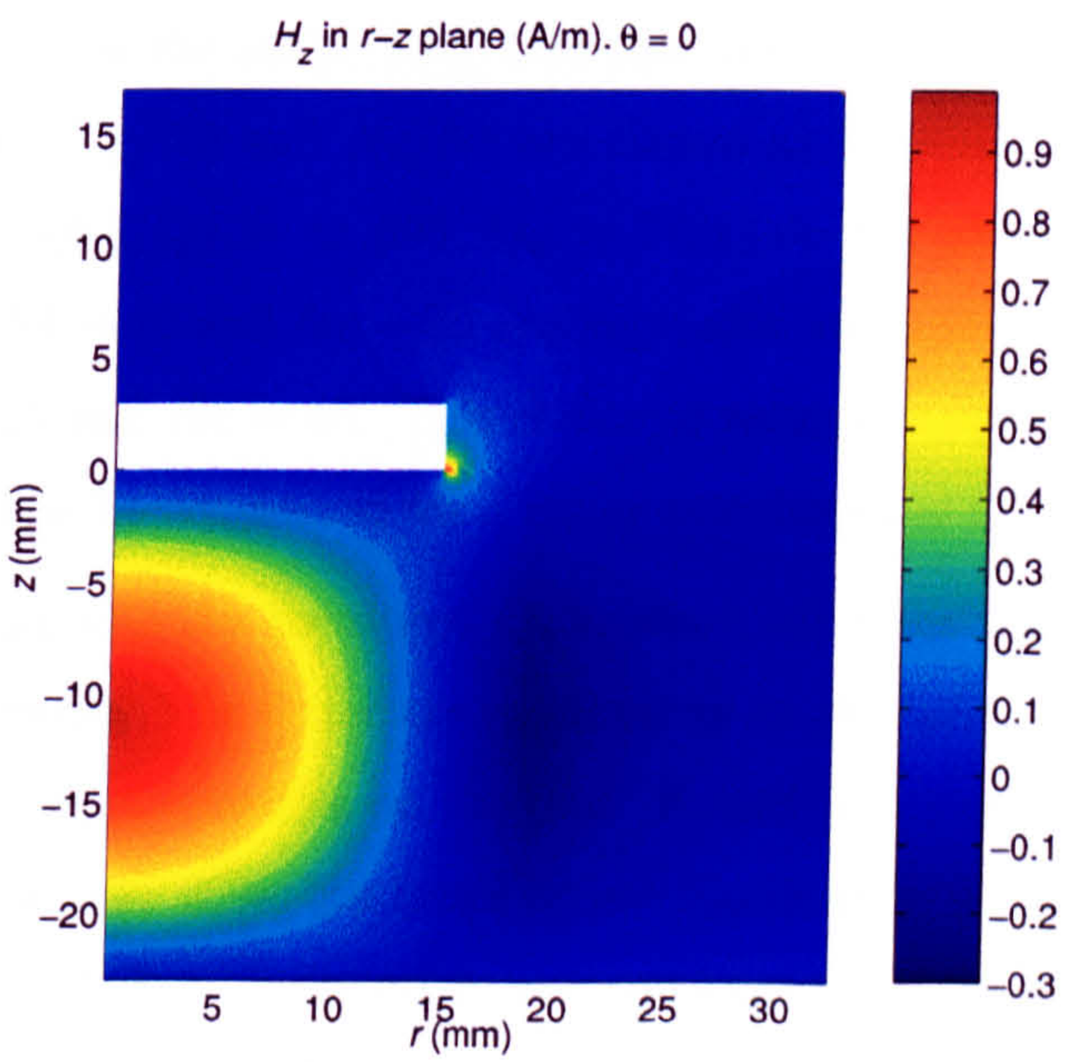

Figure 3.45: H_z of the $\mathrm{TE}_{01\delta}$ mode. $Na = 80$, $Nb = 40$, $Nc = 80$.

Table 3.5: *Variations of Q_c and percentage of P_{cs} compared to total conductor power dissipation for the first five modes of the test cavity as Nb is increased from* 20 *to* 40. *Mode number ratios as in Table 3.3.*

Mode	$\Delta Q_c/Q_c$ (%)	$\Delta Q_c/Q_c$ (%) no loss on edge of disc	$\Delta Q_c/Q_c$ (%) no loss on disc	P_{cs}/P_c (%) (%)
$HE_{11\delta}$	−2.5	−1.2	−0.22	9.2
$EH_{11\delta+1}$	−0.98	−0.46	−0.13	1.8
$TM_{01\delta}$	+0.07	+0.072	+0.10	0.002
$HE_{21\delta}$	−2.7	−1.2	−0.73	9.3
$TE_{01\delta}$	−2.1	−1.1	+0.0045	6.9

In Table 3.5, it can be seen that the modes with slowest convergence are also those with high P_{cs}, power dissipation on the side of the metal disc, which is the region that would be the most influenced by the metal edge singularities. As expected, the convergence is significantly improved by ignoring the losses primarily around the edge of the disc, or on the entire disc. One final remark is that the quality factors change little when Na/Nb and Nc/Nb are chosen as 1: results with $Na = Nb = Nc = 40$ ($Q_c = 9482$, $Q_d = 41,593$, $Q_u = 7721$) do not differ much from those with $Na = 120$, $Nb = 40$ and $Nc = 80$ and represent an improvement over those of $Na = 60$, $Nb = 20$ and $Nc = 40$. This choice of ratio, not optimum for frequency accuracy, could then be considered for a faster calculation of Q_u.

In Table 3.3 are also the measured Q_u's, which all agree within 9.0% with the mode-matching results. The latter are expected to be less accurate for modes with the large magnetic field densities on the disc. Indeed, the method used here is an approximation valid only when the losses do not significantly disturb the field in the resonator. As a result, the results might not converge to the exact value. However, in the case of the $HE_{11\delta}$ and $HE_{21\delta}$ modes, which have very similar characteristics, this convergence is expected to behave in a similar manner. The fact that the Q_u of the former is overestimated (+6.3%) and the latter underestimated (−8.0%) is not explained. Also, the $TM_{01\delta}$ mode should be one of the most accurate modes.

A large part of the discrepancies is thus believed to be due to imperfections at the regions where the dielectric and metal contact. Indeed, no fixation of the dielectric resonator and metal disc was provided and the variations in Q_u created by air gaps and localised currents are believed to be greater than those due to the measurement accuracy or incertainties in the metal conductivity and loss tangent of the ceramic material.

3.4 Conclusions

The mode-matching method has proved to be very accurate for the determination of the resonant frequencies of the first modes of the dual-mode conductor-loaded DR. It is in good agreement with the finite element simulation and measured results. The optimum number of modes to consider has been identified to trade-off speed and accuracy of the modelling. The Q calculations are in good agreement with other simulated results, although the convergence of Q_c can be very slow. However, these values still provide a useful approximation of the experimental results.

Chapter 4

Optimisation of Dual-Mode Conductor-Loaded Dielectric Resonator Filters

In order to gain a better understanding of the new resonator, the variations of the first resonant frequencies and the Q factor of the $HE_{11\delta}$ mode are studied. These results are obtained by using the mode-matching program described in Chapter 3. The aim is to isolate the main parameters governing absolute frequency, spurious separation and Q_u, evaluate the performance of the resonator and optimise its geometry for best Q_u and F_r.

4.1 $HE_{11\delta}$ mode variations

As shown in Fig. 4.1, d_1, d_2 and d_3 are defined as the diameters of the metal disc, the dielectric resonator and the cavity respectively. Also, h_A, h_B and h_C are defined

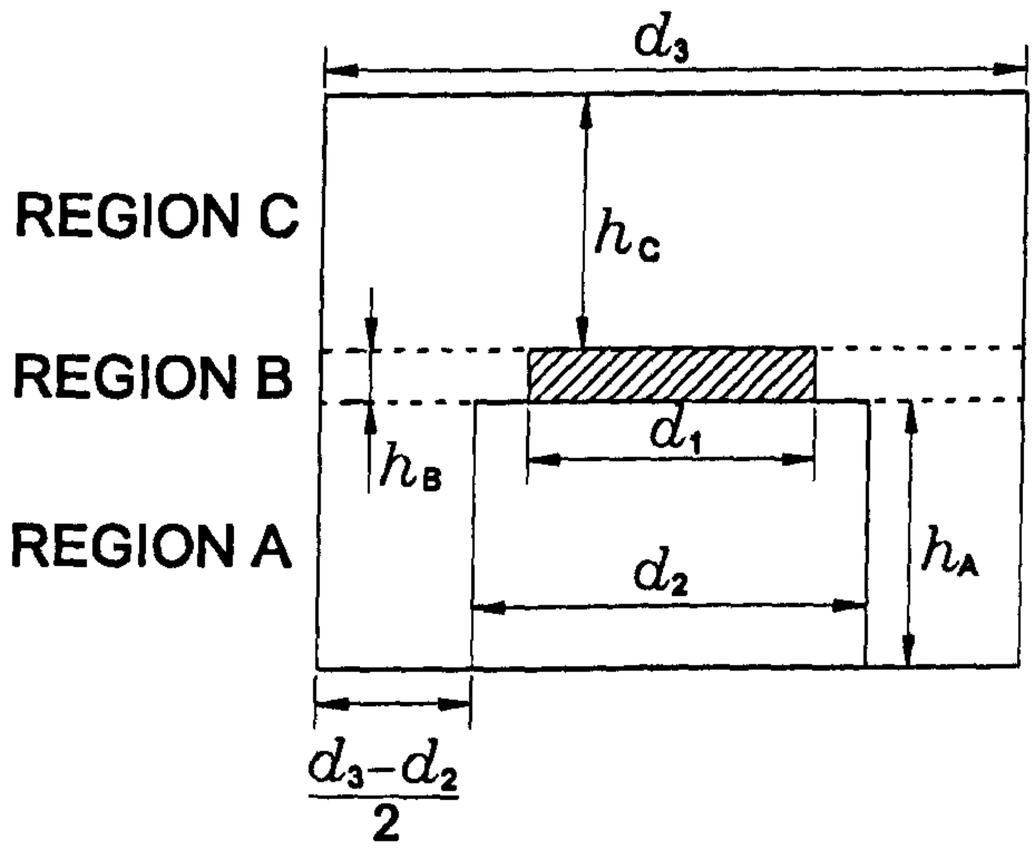

Figure 4.1: Parameters for the study of the dual-mode conductor-loaded DR

respectively as the height of the dielectric resonator, the height of the disc and the gap between the disc and the cavity lid. Figs. 4.2 to 4.7 present the variations of the five first modes with each of these six variables, starting from the dimensions of the test cavity defined in Section 3.2.1. Also in Appendix F the distributions of the electric and magnetic energies are plotted in the different parts of the structure as the parameters are varied.

4.1.1 Variations with dielectric resonator height

As mentioned in Section 3.2.2, the fields of the $HE_{11\delta}$ mode only vary very little along the height of the dielectric cylinder. As h_A is increased, the resonant frequency, shown in Fig. 4.2, increases slowly and in an almost linear manner. Fig. F.1 in Appendix F shows that the proportion of electric energy in the air part of region A increases for values of h_A up to 32 mm. At the same time, the electric energy in the dielectric region and, to a second degree in region B, decreases. The energy in the air part of region A becomes mainly contained by the transverse components of the fields, E_r and E_θ, as h_A is increased. This is illustrated in Table 4.1 for dielectric cylinder heights of 10 and 30 mm. This explains the increase in resonant frequency. As more electric field terminates on the side wall of the cavity, the field pattern of the mode changes away from that of the TM_{110} mode. Figs. 4.8 to 4.11 illustrate the distributions of E_r and E_z at their $r-z$ plane of maximum intensity. The increase of E_r in the air region surrounding the edge of the metal disc can be seen. Also, as h_A is increased, the fields in the top part of the dielectric region are unchanged. The E_r distribution remains close to the metal disc while E_z still extends

Table 4.1: *Distribution of electric energy in region A for different h_A. W_{Ez} is the energy contained in E_z. W_{Et} is the energy contained in E_r and E_θ.*

	$h_A = 10$ mm		$h_A = 30$ mm	
	dielectric region	air region	dielectric region	air region
W_{Ez} (%)	92.31	0.44	95.18	0.69
W_{Et} (%)	7.00	0.26	3.14	0.98
Total	99.31	0.70	98.32	1.67

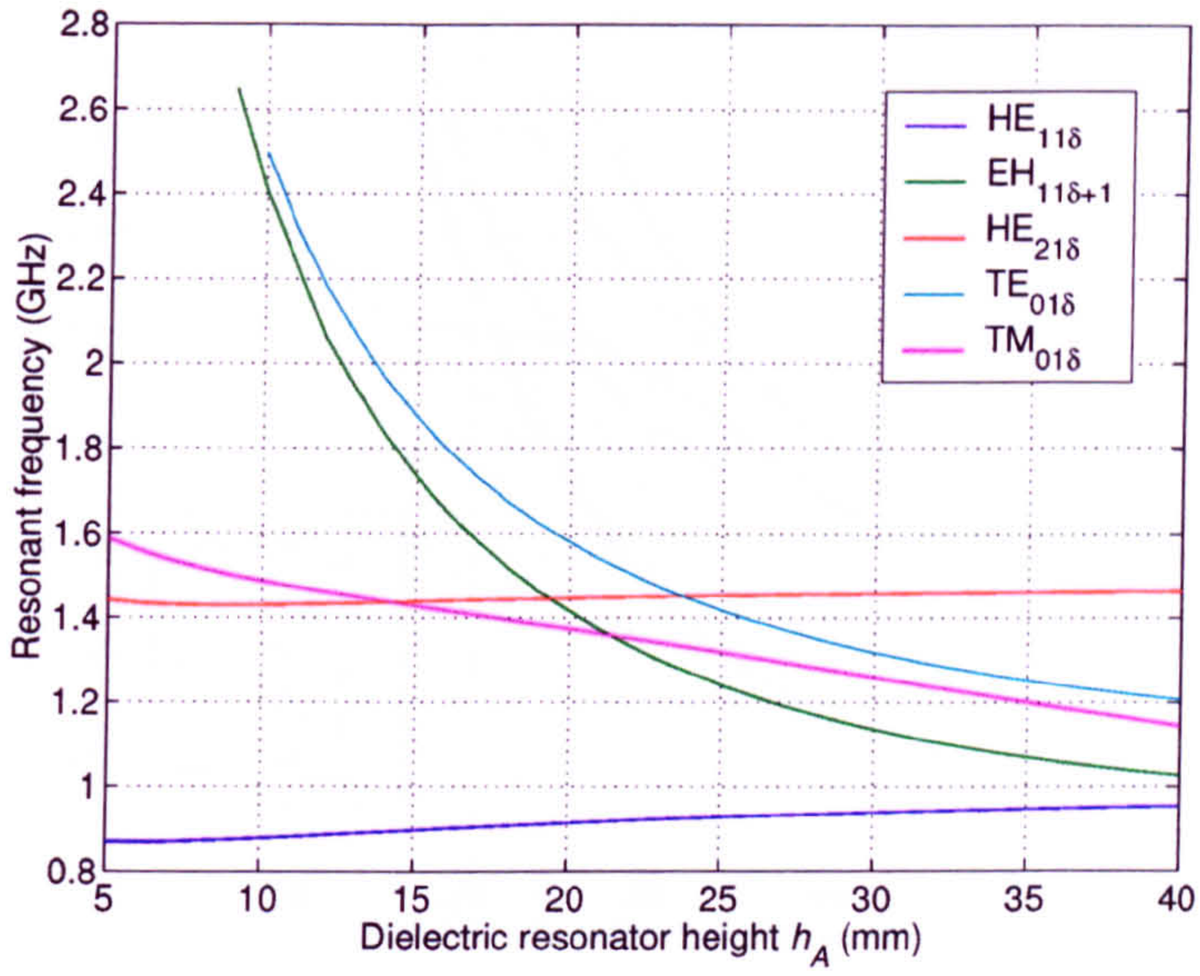

Figure 4.2: Resonant frequency variations with h_A. $h_B = 3$ mm, $h_C = 14$ mm, $d_1 = 30$ mm, $d_2 = 38$ mm, $d_3 = 65$ mm.

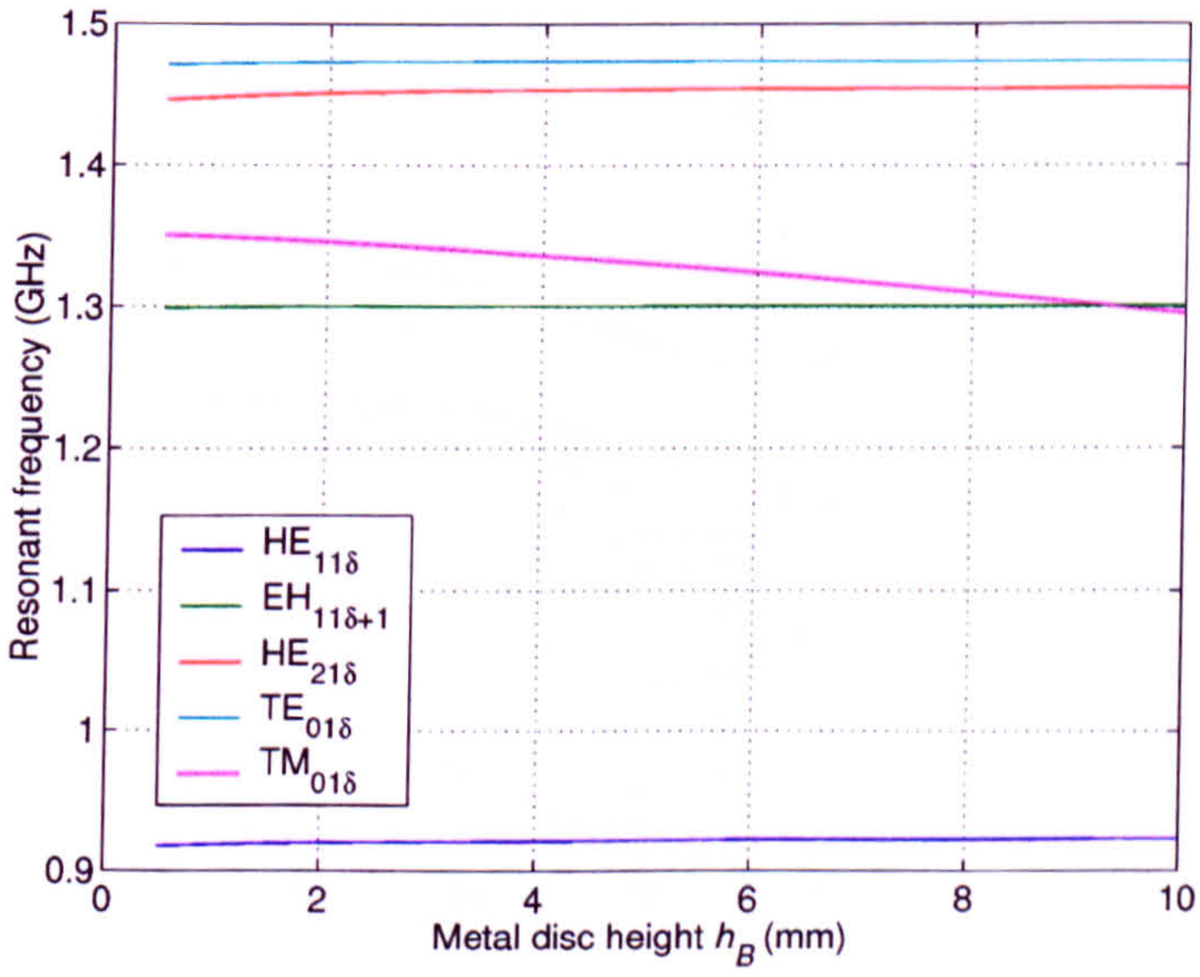

Figure 4.3: Resonant frequency variations with h_B. $h_A = 23$ mm, $h_C = 14$ mm, $d_1 = 30$ mm, $d_2 = 38$ mm, $d_3 = 65$ mm.

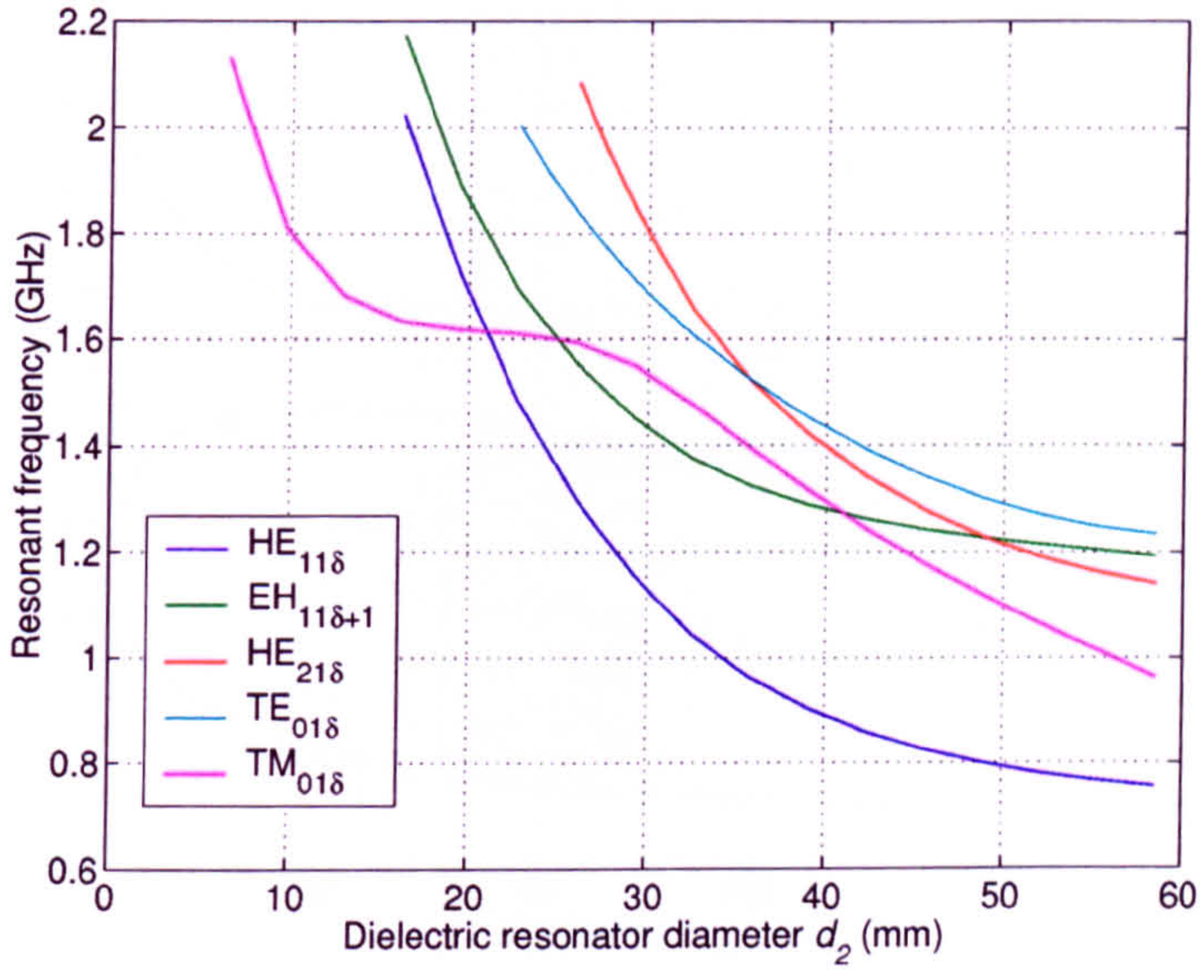

Figure 4.4: Resonant frequency variations with d_2. $h_A = 23$ mm, $h_B = 3$ mm, $h_C = 14$ mm, $d_1 = 30$ mm, $d_3 = 65$ mm.

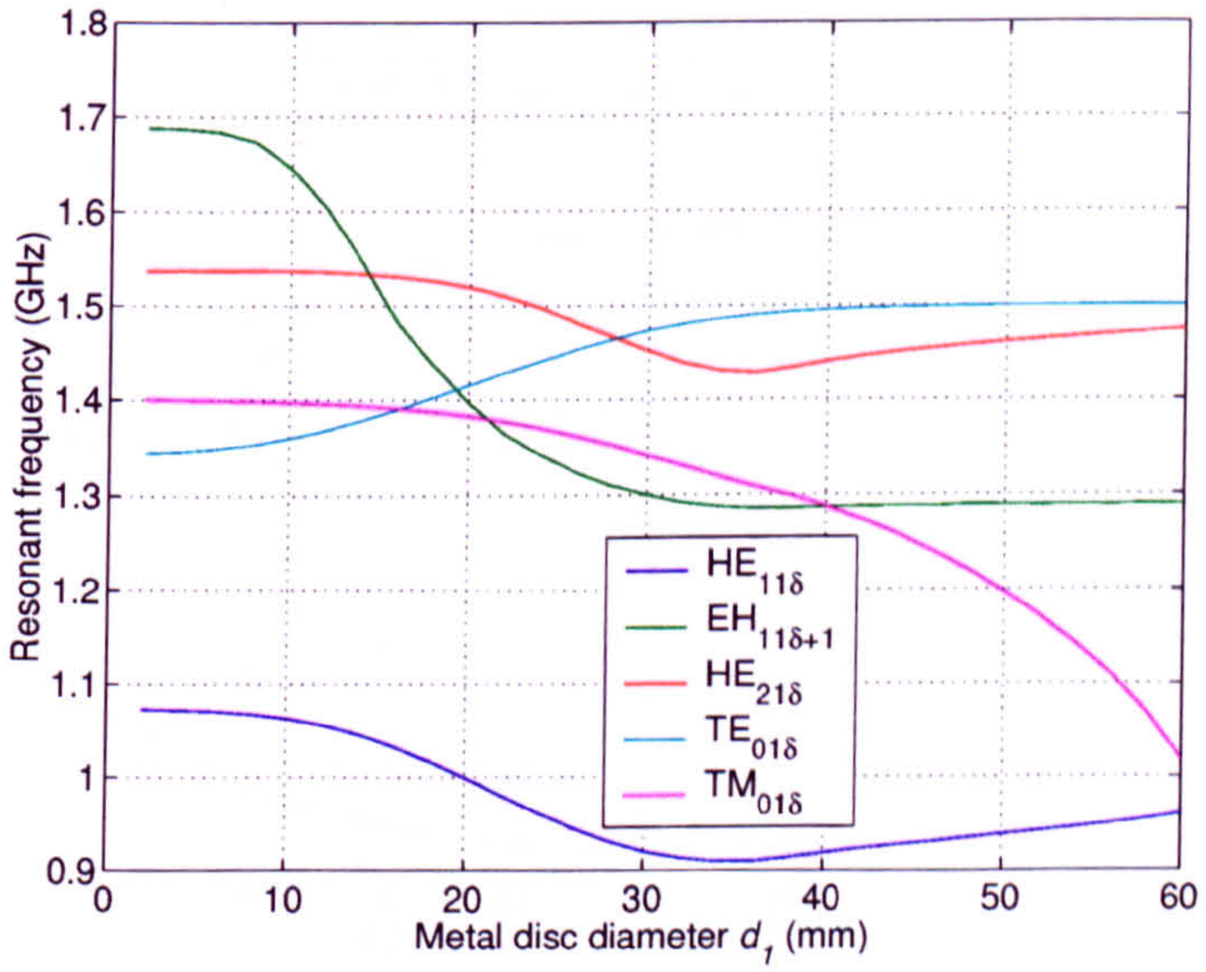

Figure 4.5: Resonant frequency variations with d_1. $h_A = 23$ mm, $h_B = 3$ mm, $h_C = 14$ mm, $d_2 = 38$ mm, $d_3 = 65$ mm.

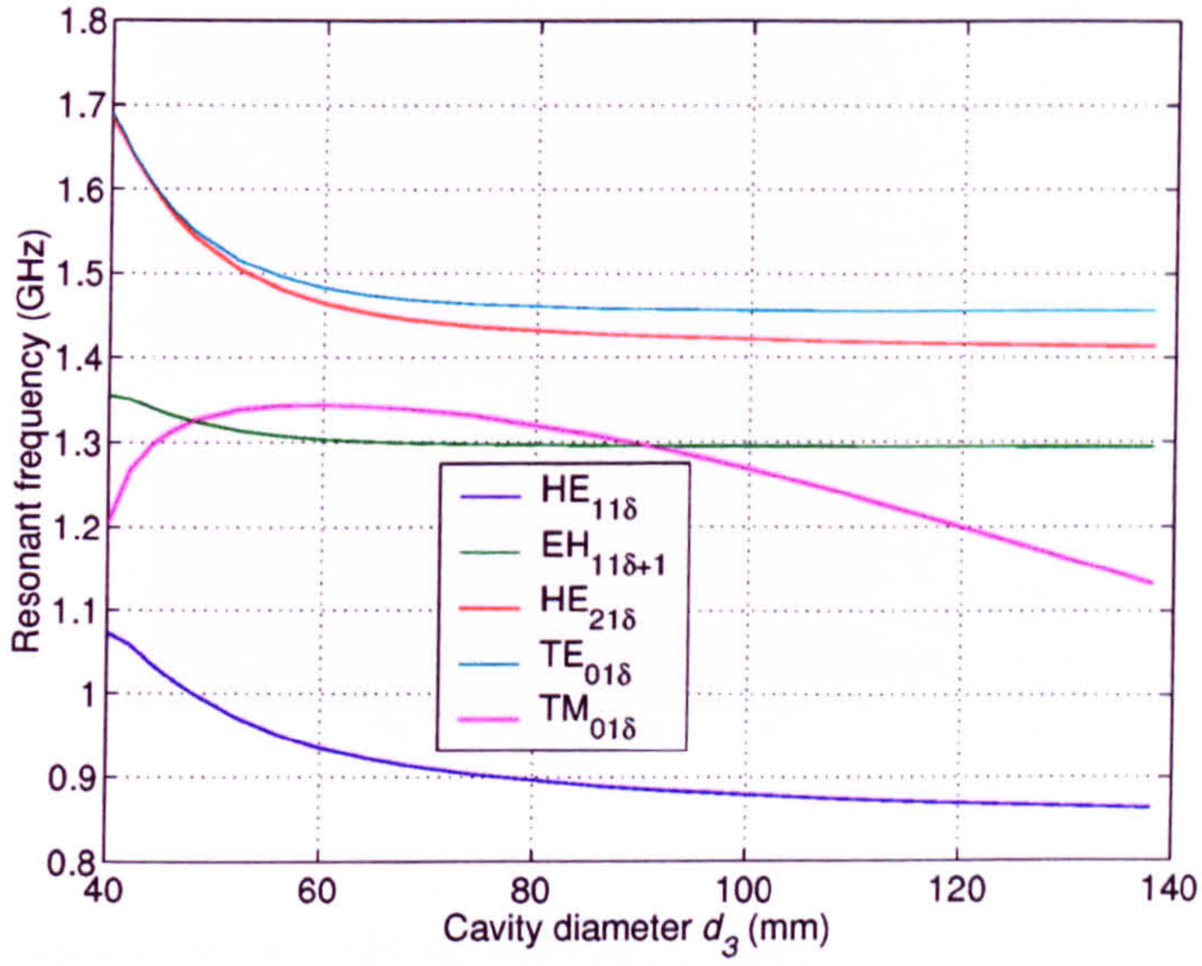

Figure 4.6: Resonant frequency variations with d_3. $h_A = 23$ mm, $h_B = 3$ mm, $h_C = 14$ mm, $d_1 = 30$ mm, $d_2 = 38$ mm.

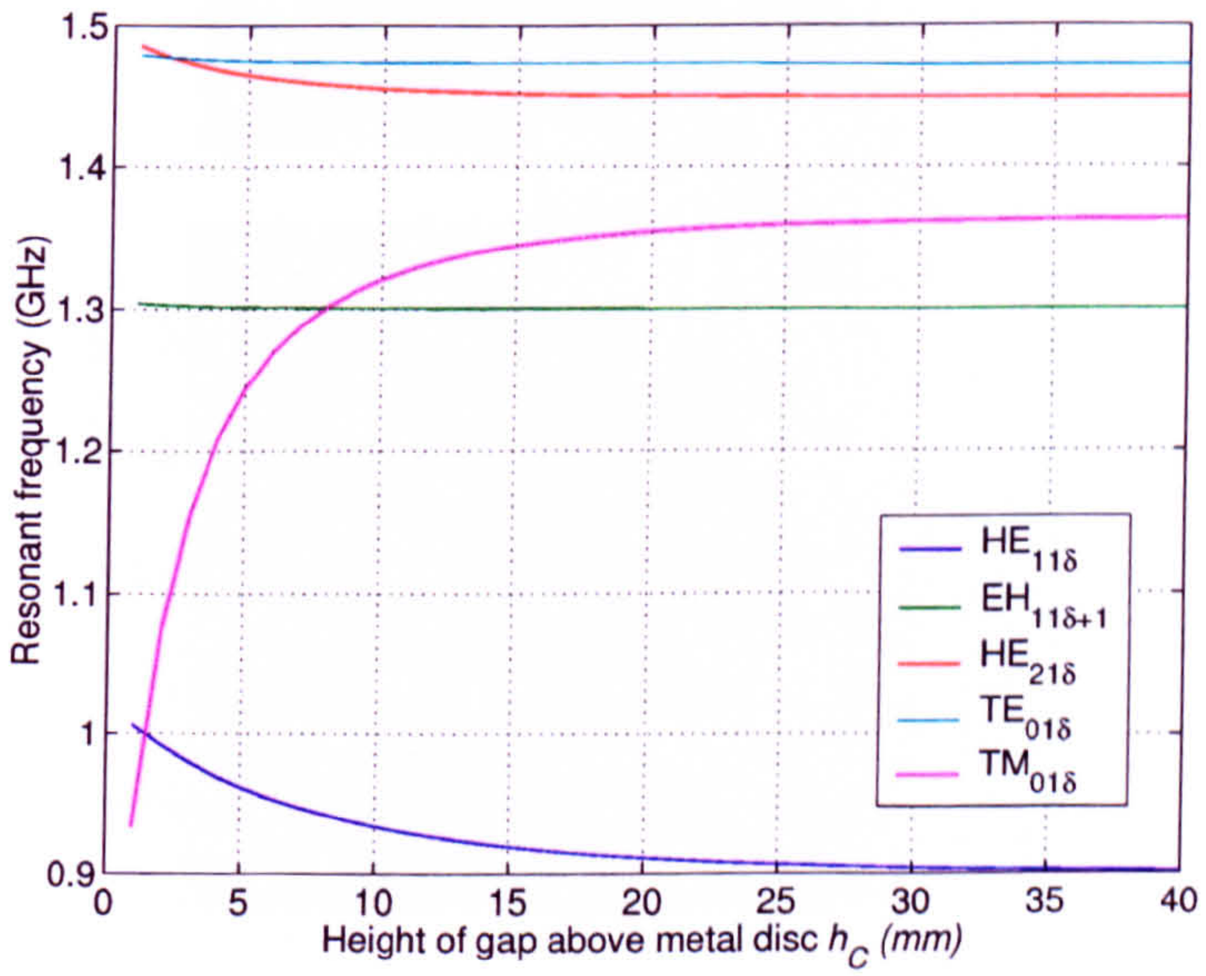

Figure 4.7: Resonant frequency variations with h_C. $h_A = 23$ mm, $h_B = 3$ mm, $d_1 = 30$ mm, $d_2 = 38$ mm, $d_3 = 65$ mm.

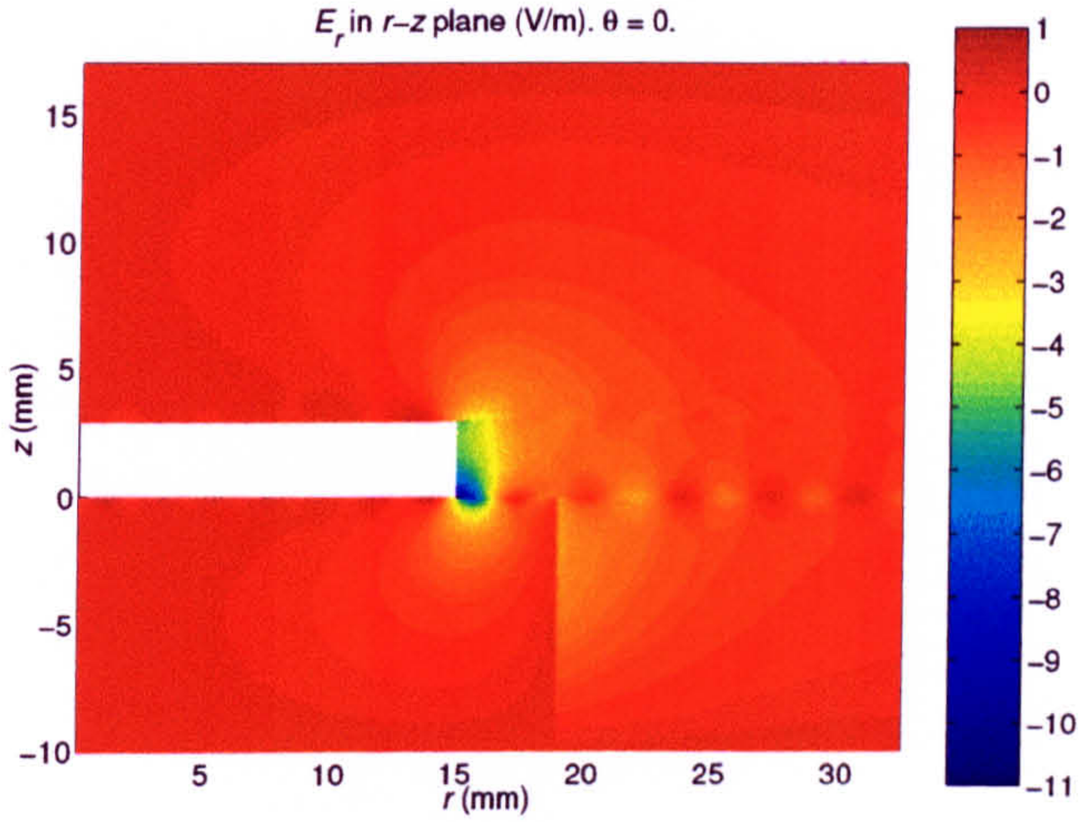

Figure 4.8: Radial electric field of the $\mathrm{HE}_{11\delta}$ mode for $h_A = 10$ mm. $h_B = 3$ mm, $h_C = 14$ mm, $d_1 = 30$ mm, $d_2 = 38$ mm, $d_3 = 65$ mm.

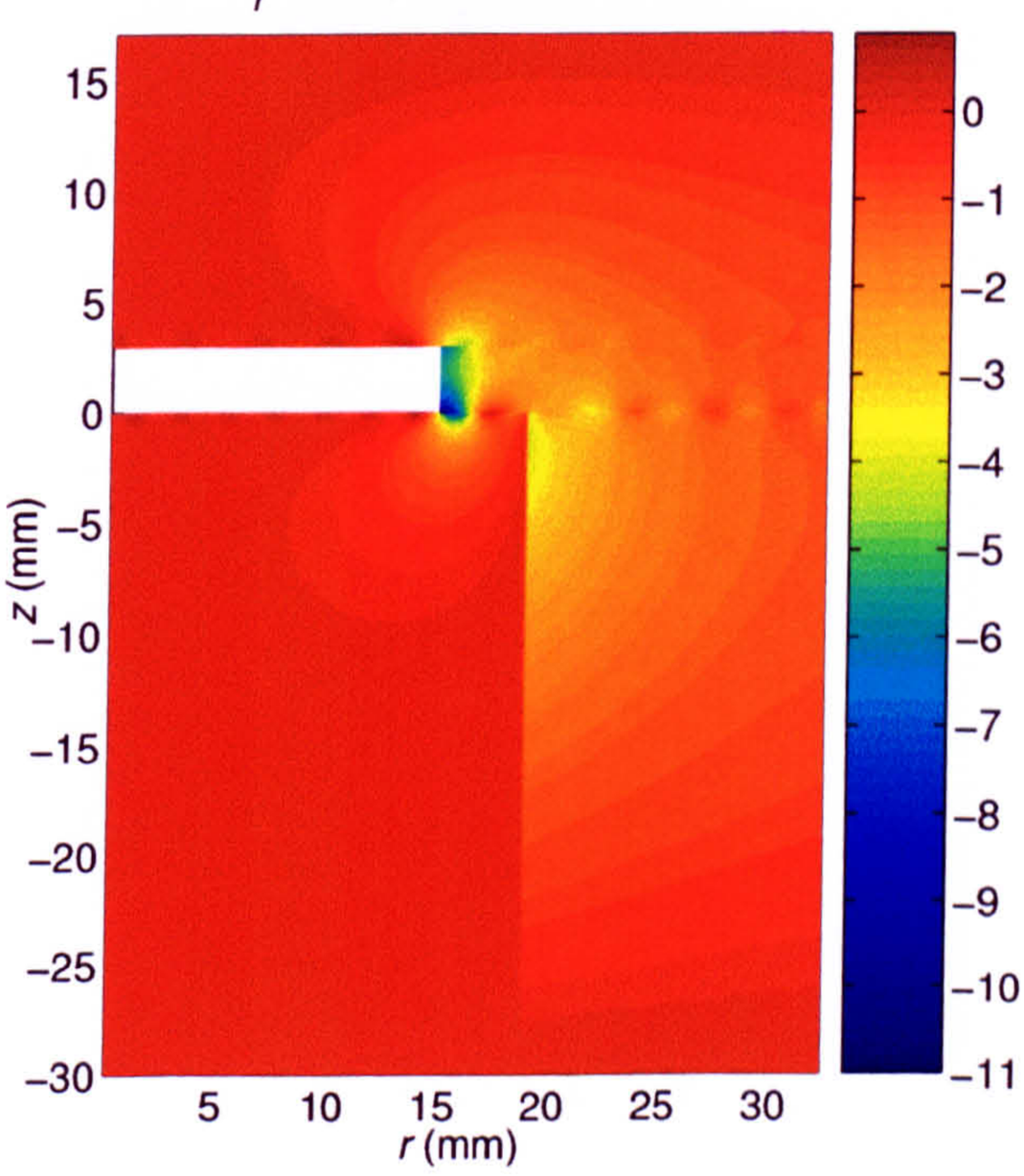

Figure 4.9: Radial electric field of the $\mathrm{HE}_{11\delta}$ mode for $h_A = 30$ mm. $h_B = 3$ mm, $h_C = 14$ mm, $d_1 = 30$ mm, $d_2 = 38$ mm, $d_3 = 65$ mm.

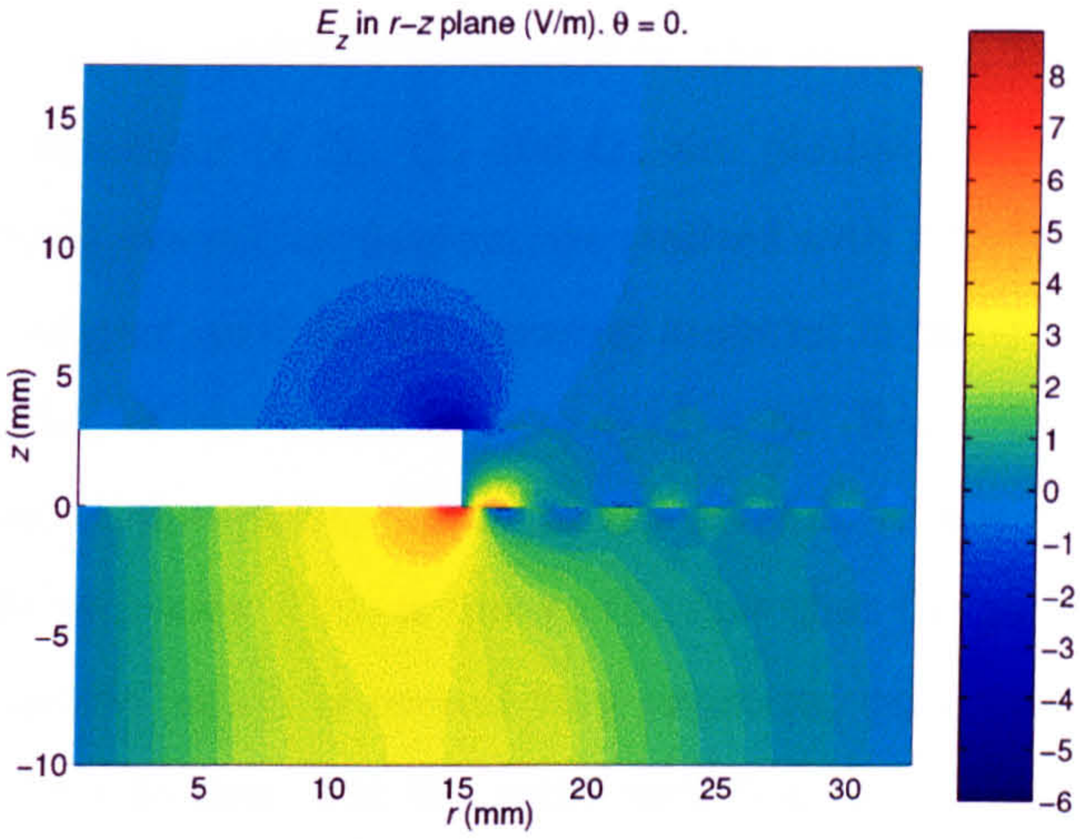

Figure 4.10: Axial electric field of the $\mathrm{HE}_{11\delta}$ mode for $h_A = 10$ mm. $h_B = 3$ mm, $h_C = 14$ mm, $d_1 = 30$ mm, $d_2 = 38$ mm, $d_3 = 65$ mm.

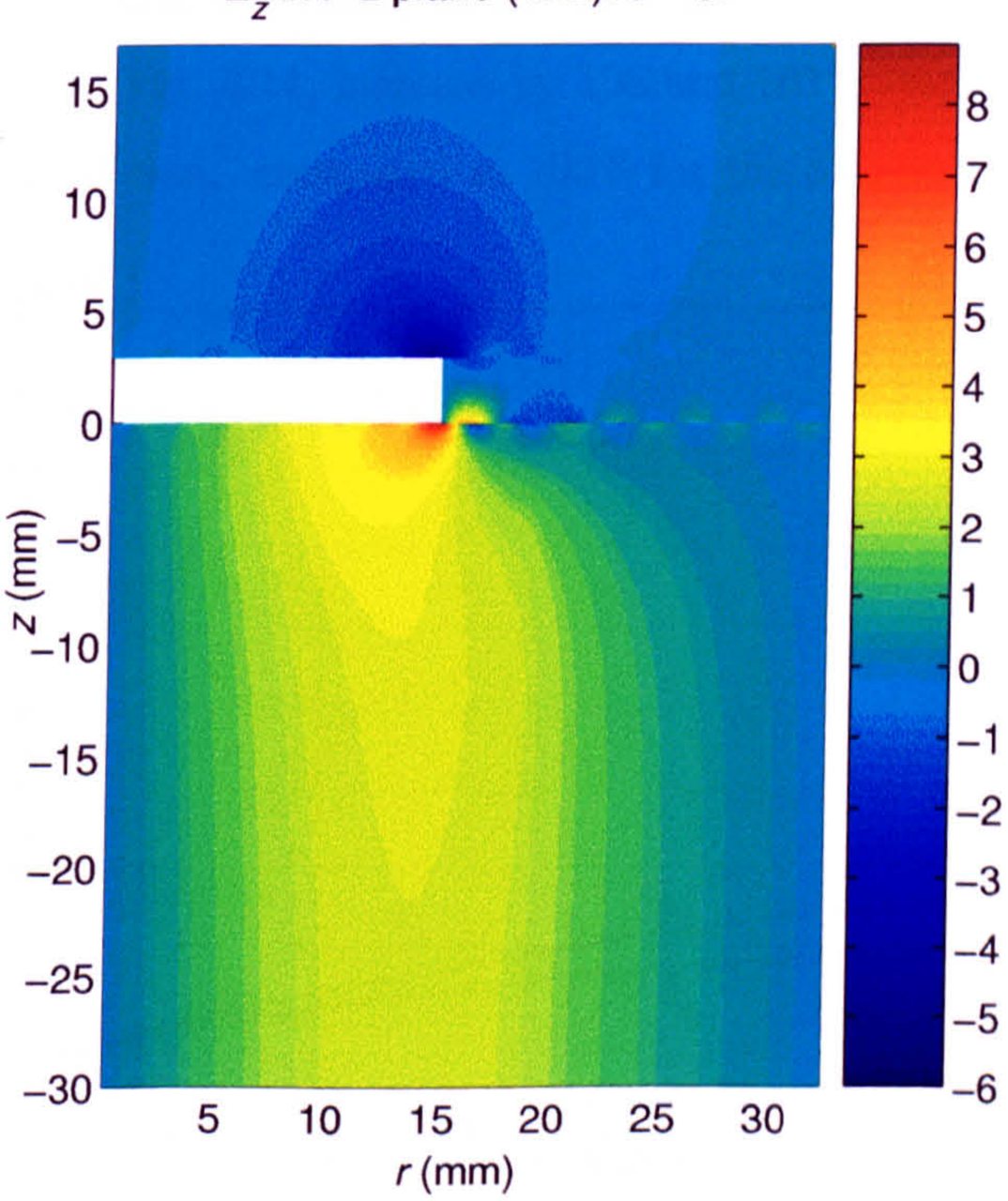

Figure 4.11: Axial electric field of the $\mathrm{HE}_{11\delta}$ mode for $h_A = 30$ mm. $h_B = 3$ mm, $h_C = 14$ mm, $d_1 = 30$ mm, $d_2 = 38$ mm, $d_3 = 65$ mm.

along the whole length of the resonator, which explains why the proportion of W_{Et} (energy contained by E_r and E_θ) decreased in the dielectric region of Table 4.1. In Fig. 4.12, the variations of Q_c, Q_d and Q_u are plotted. These, and all further quality factor calculations in this chapter, are realised with $Nb = 20$ unless otherwise stated. The loss tangent used for the ceramic material is $\tan\delta = f/3.7504 \times 10^{13}$ and the conductivity of the metal is $\sigma = 6.17 \times 10^7$ S/m. The decrease of Q_d follows closely that of the quality factor of the ceramic as the resonant frequency of the $HE_{11\delta}$ mode increases. This is due to the fact that the proportion of electric energy in the dielectric region is overall very constant, only varying by 2% as h_A is increased from 5 to 40 mm. For the same variation in h_A, Q_d drops by a factor 1.08 while the Q of the ceramic drops by a factor 1.09. However, the overall Q_u of the $HE_{11\delta}$ mode still increases due to an increase of Q_c. The variations of Q_c are mainly governed by those of the losses in region A. When h_A is very small, the conductor loss is logically almost equally shared between the base of the cavity and the base of the metal disc (Fig. 4.13). As h_A is increased, the percentage of loss on these two surfaces at first decreases, at about a similar rate. Their corresponding partial Q_c's, shown in Fig. 4.14, increase by 108 and 101% respectively when h_A is doubled from 10 to 20 mm, compared to 100% for the dielectric-loaded waveguide

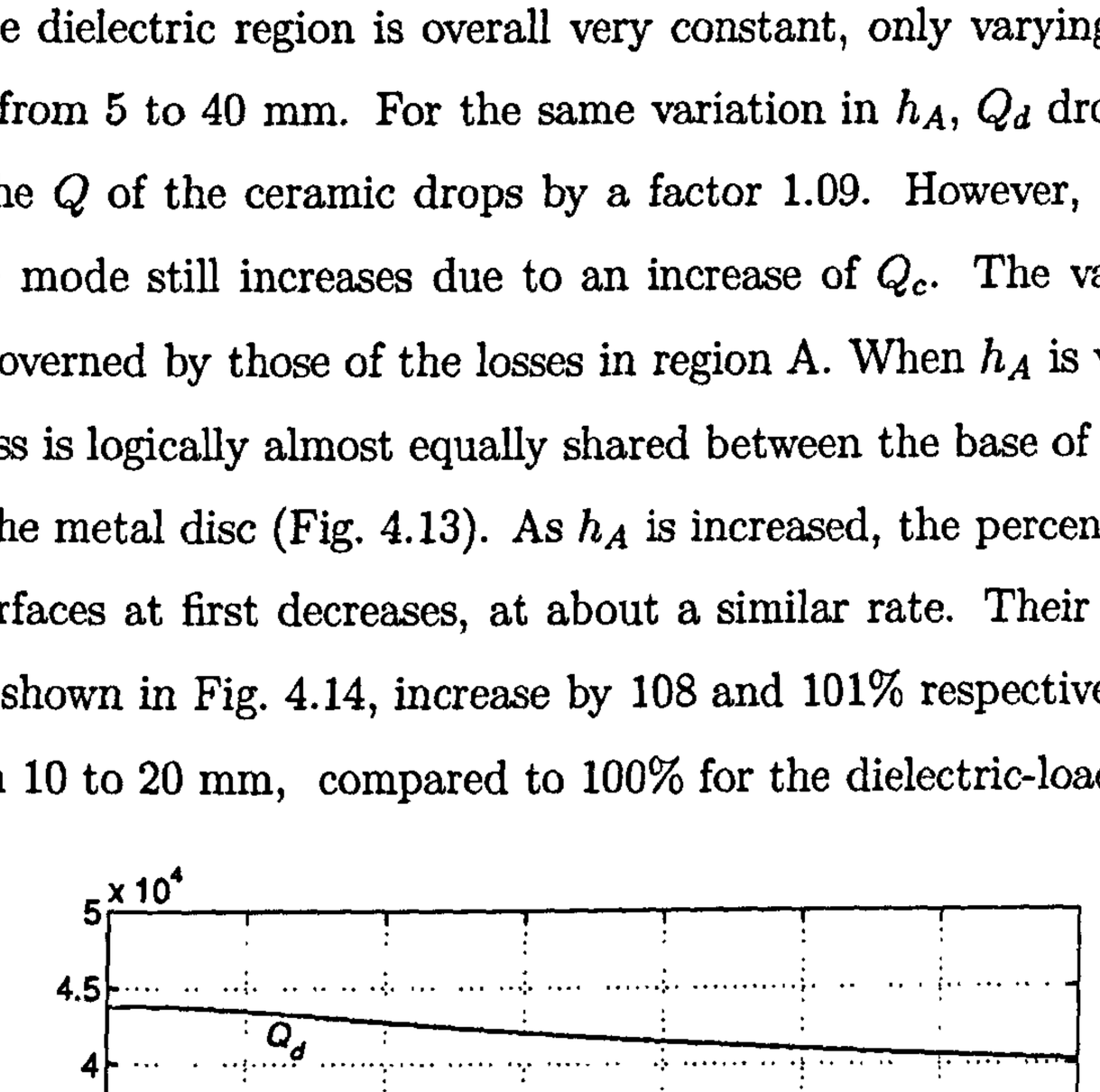

Figure 4.12: Variation of quality factors of the $HE_{11\delta}$ mode with h_A. $h_B = 3$ mm, $h_C = 14$ mm, $d_1 = 30$ mm, $d_2 = 38$ mm, $d_3 = 65$ mm.

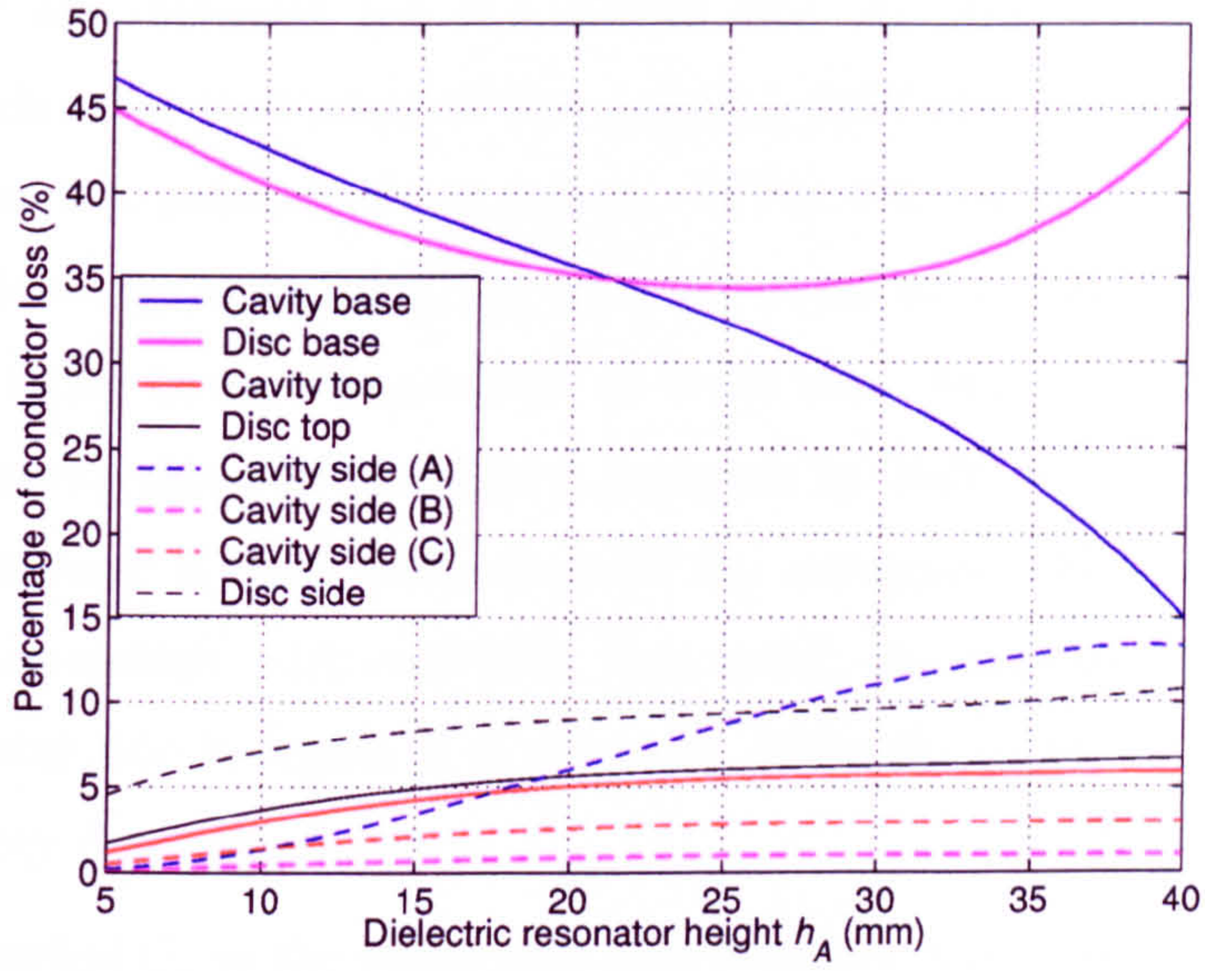

Figure 4.13: Variation of the conductor loss distribution of the $HE_{11\delta}$ mode with h_A. $h_B = 3$ mm, $h_C = 14$ mm, $d_1 = 30$ mm, $d_2 = 38$ mm, $d_3 = 65$ mm.

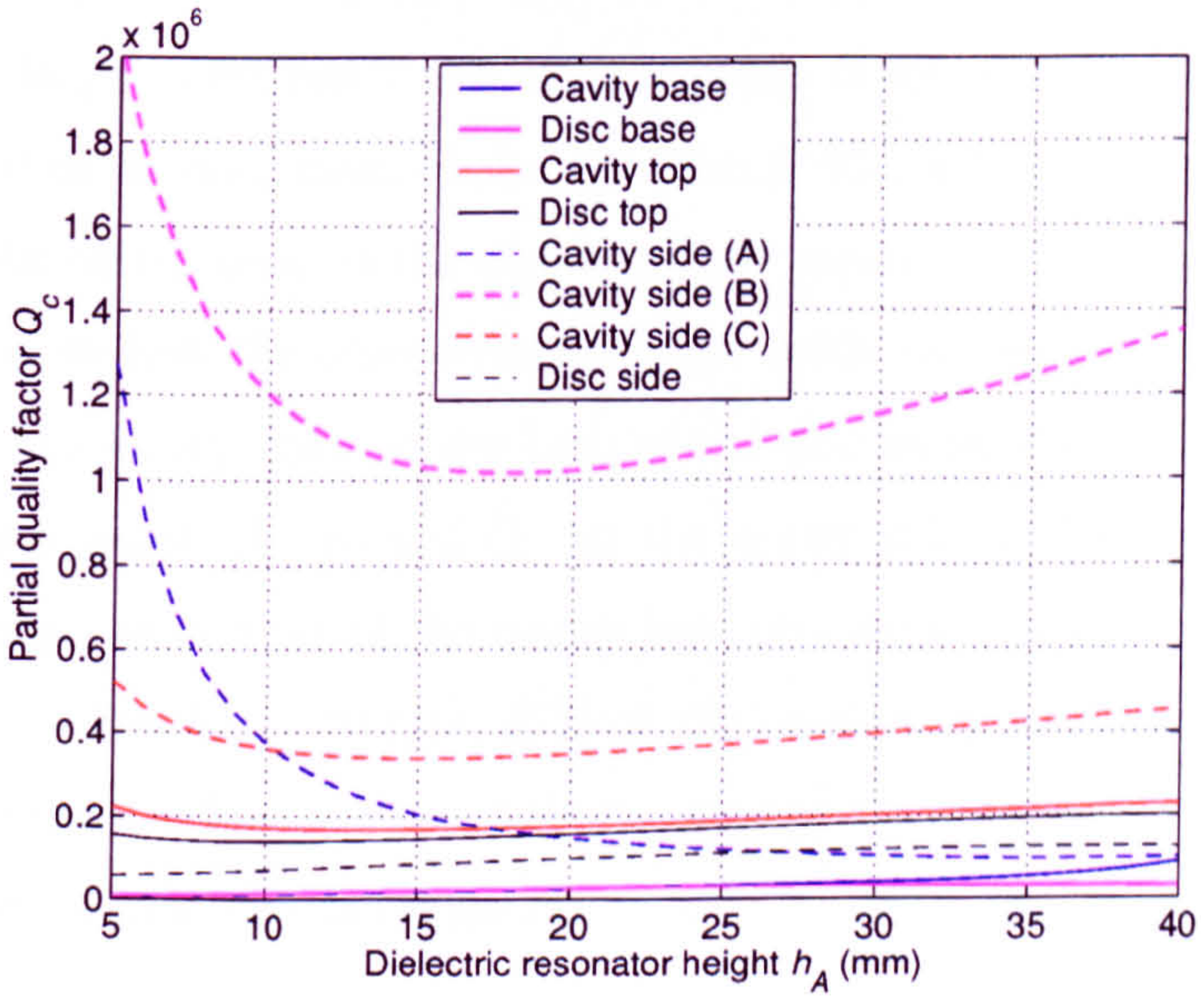

Figure 4.14: Variation of partial quality factors of the $HE_{11\delta}$ mode with h_A. $h_B = 3$ mm, $h_C = 14$ mm, $d_1 = 30$ mm, $d_2 = 38$ mm, $d_3 = 65$ mm.

TM_{110} mode resonator. The partial Q_c corresponding to the loss around the metal disc perimeter also increases, but at a smaller rate. All other partial Q_c's start by decreasing, indicating that some of the magnetic field also moves away from the dielectric region into some of the air regions. In Fig. F.2, the increase in proportion of the magnetic energy in region C, but especially in the air region of A, is significant: +86% for the latter as h_A changes from 10 to 20 mm. As a result, the percentage of loss in the cavity side wall in region A increases by 360% for the same change in height. This increase is much faster than for the waveguide TM_{110} mode resonator of identical cross-section, with only 82%. As a result, the decrease of the partial Q_c due to the cavity side in region A is dramatic, while the corresponding Q_c in the waveguide cavity does not change.

Also, the partial Q_c in the cavity side wall in region A continues to decrease for larger values of h_A, when all other partial Q_c's have started increasing again. At the same time, its loss percentage in Fig. 4.13 continues to increase. In fact, for values of h_A larger than 25 mm, only the proportions of the loss in the cavity side in region A, the cavity base and the disc base significantly change. All others are relatively constant and their corresponding partial Q_c's uniformly increase with h_A. This could be explained by the fact that more energy is stored in region A as the resonator gets larger, with not much of an increase of the losses in region B and C. For h_A larger than 25 mm, most of the variation in Fig. 4.13 occurs from loss being shifted from the cavity base to the disc base and cavity side in region A. Fig. 4.15 and Fig. 4.16 show how the transverse magnetic fields decrease by a larger amount at the base of the cavity than at the base of the disc when h_A is changed from 10 to 30 mm. As a result, the partial Q_c for the cavity side, and eventually the disc base, deteriorates, while that of the cavity base improves at a faster rate than any other partial Q_c. For $h_A = 40$ mm, 45% of the conductor loss is generated in the disc base. The three other main contributions come from the disc top surface, the cavity base and its side wall in region A.

To conclude, it can be said that, in the first approximation, h_A is proportional to the Q_u of the $HE_{11\delta}$ mode, but keeps its resonant frequency constant. As for the TM_{011} mode, the partial Q_u's of the cavity base and disc base both increase significantly as h_A is increased. This leads the overall Q_u to increase, even though the losses in the side walls of the cavity become more important. For large values

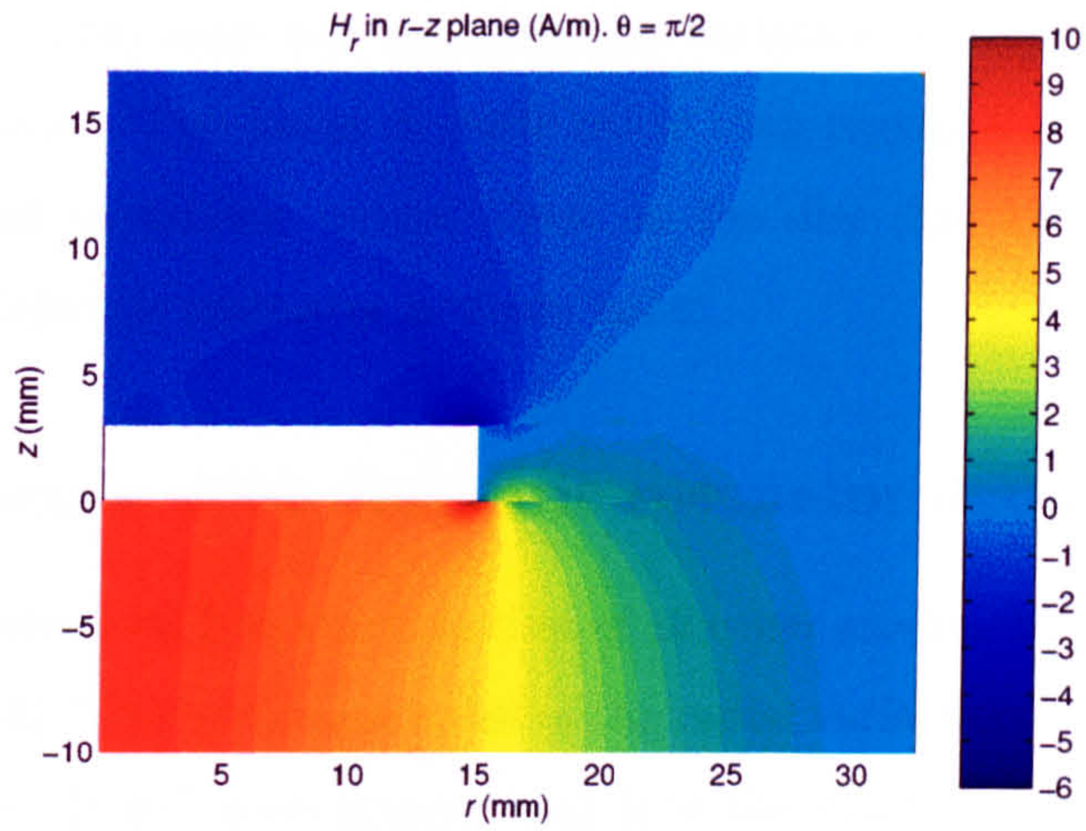

Figure 4.15: Radial magnetic field of the $\mathrm{HE}_{11\delta}$ mode for $h_A = 10$ mm. $h_B = 3$ mm, $h_C = 14$ mm, $d_1 = 30$ mm, $d_2 = 38$ mm, $d_3 = 65$ mm.

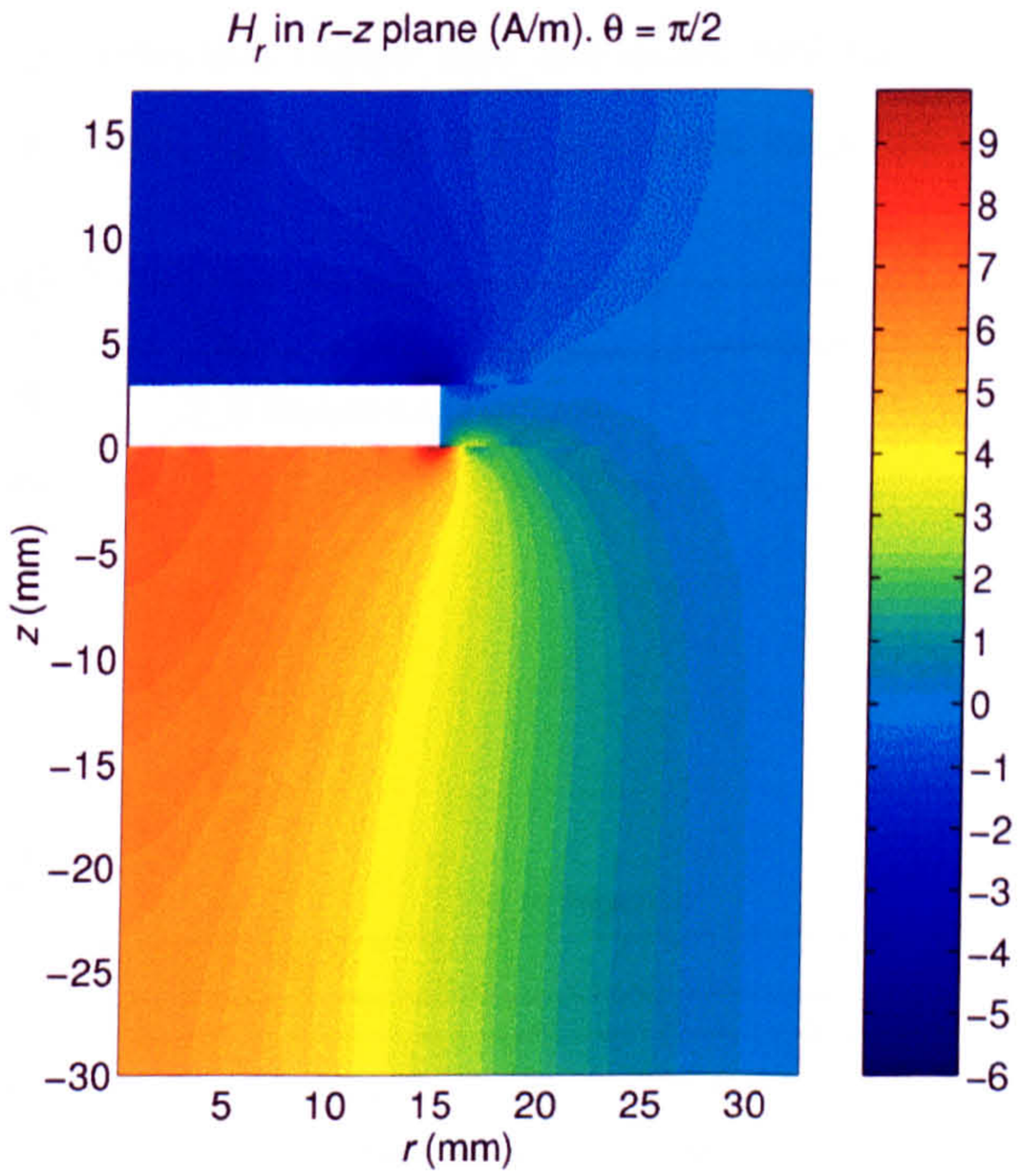

Figure 4.16: Radial magnetic field of the $\mathrm{HE}_{11\delta}$ mode for $h_A = 30$ mm. $h_B = 3$ mm, $h_C = 14$ mm, $d_1 = 30$ mm, $d_2 = 38$ mm, $d_3 = 65$ mm.

of h_A, the process is changed as the losses increase on the disc base but diminish everywhere else. This does not overturn the variation of the overall Q_u, which continues to increase. The losses in parts other than region A never play a major part in the overall variations, except those on the disc side which have a steady increase as the dielectric resonator is made taller.

4.1.2 Variations with dielectric resonator diameter

The $HE_{11\delta}$ mode resonant frequency, as that of all other modes, drops quickly as d_2 is increased (Fig. 4.4). This is because most of the radial variation of their fields occurs over this distance. It will soon appear that it is the main parameter determining the resonant frequency of the dual-mode resonator.

4.1.3 Variations with disc height

The $HE_{11\delta}$ mode resonant frequency is almost constant with h_B, only increasing by 0.43% as h_B changes from 0.5 to 10 mm. The changes in the proportions of electric energy between the dielectric region and the other regions, shown in Fig. F.3 are very small. As a result, Q_d in Fig. 4.17 is almost constant. In Fig. 4.18, it can

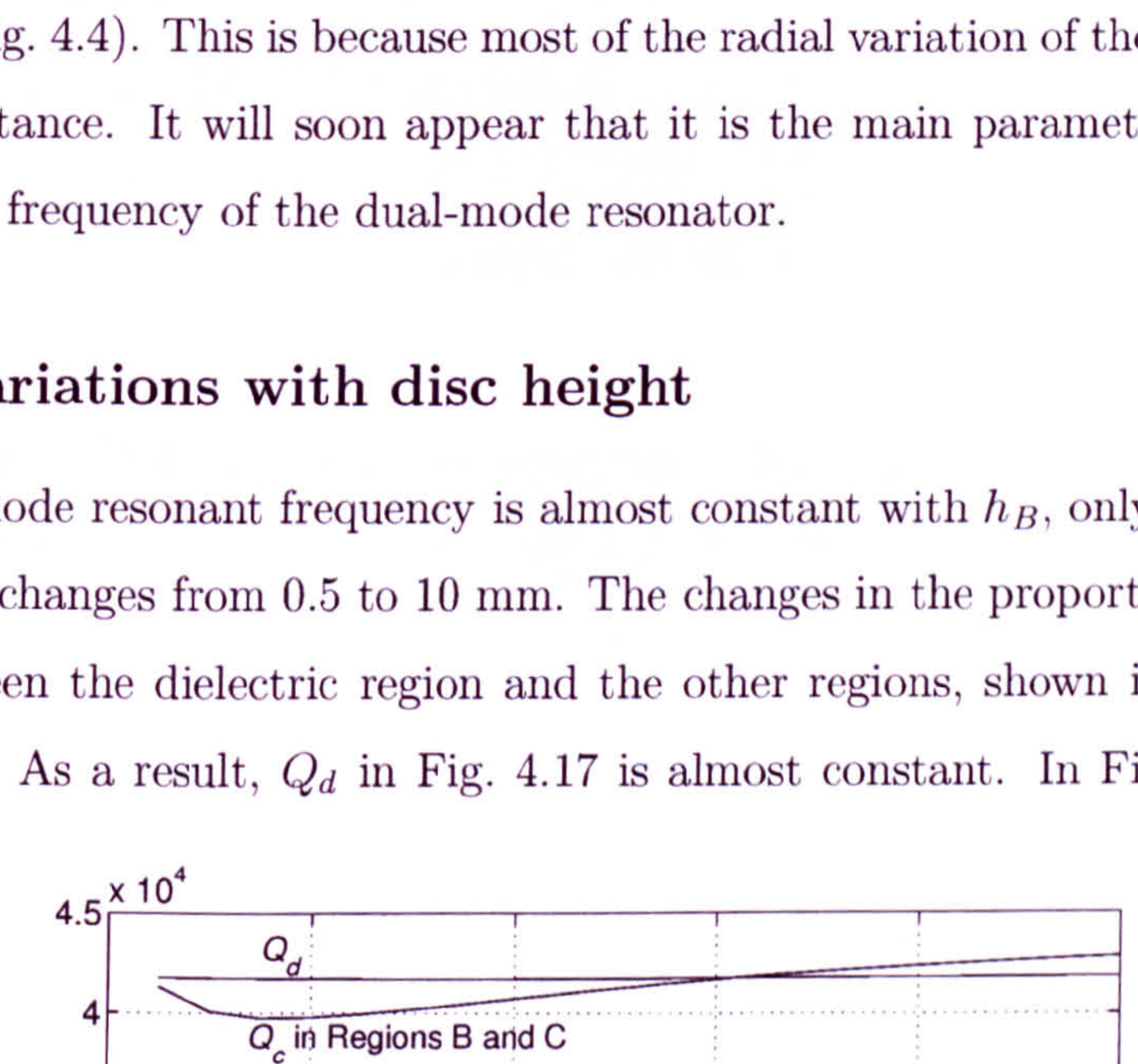

Figure 4.17: Variation of quality factors of the $HE_{11\delta}$ mode with h_B. $h_A = 23$ mm, $h_C = 14$ mm, $d_1 = 30$ mm, $d_2 = 38$ mm, $d_3 = 65$ mm.

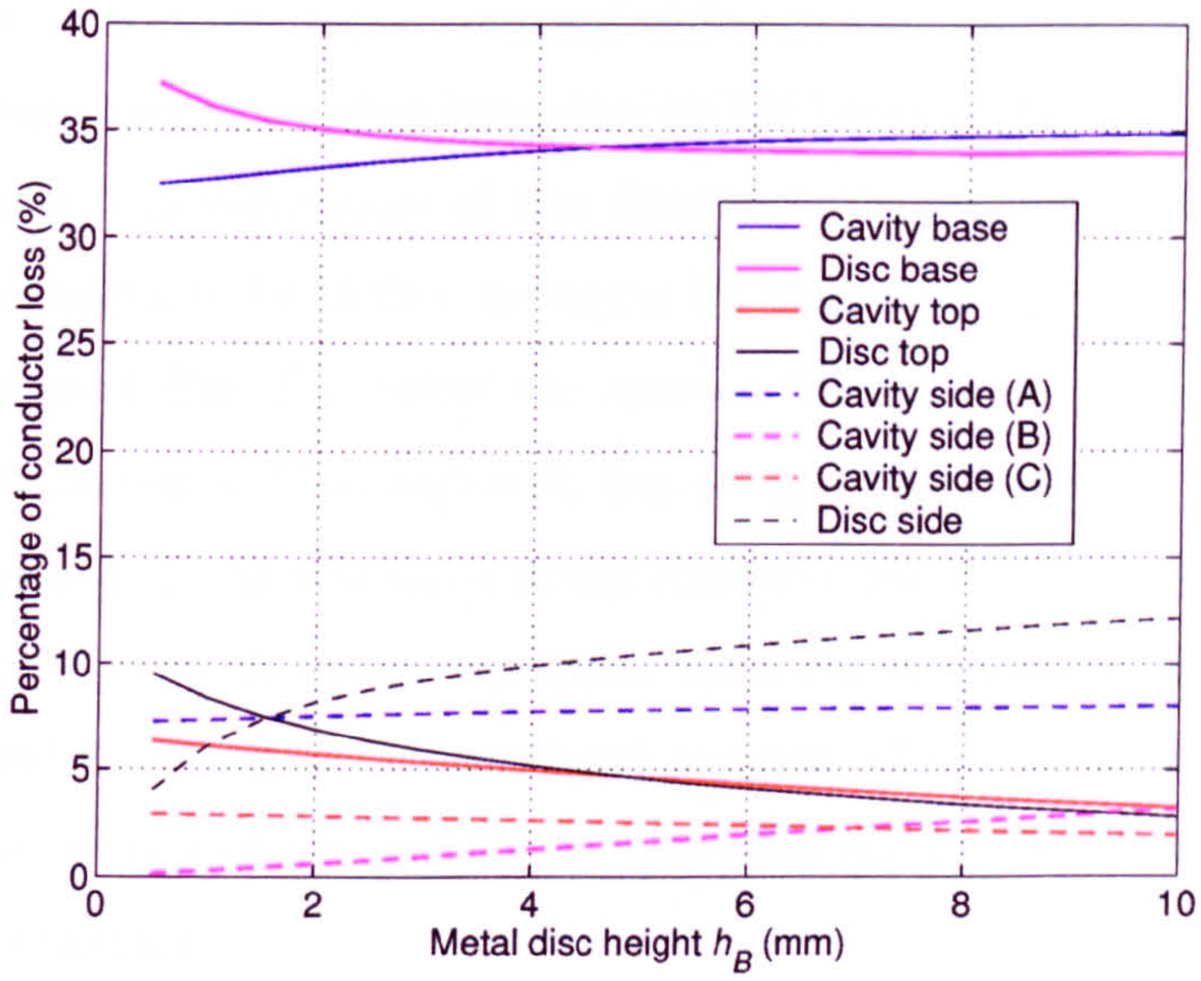

Figure 4.18: Variation of the conductor loss distribution of the $HE_{11\delta}$ mode with h_B. $h_A = 23$ mm, $h_C = 14$ mm, $d_1 = 30$ mm, $d_2 = 38$ mm, $d_3 = 65$ mm.

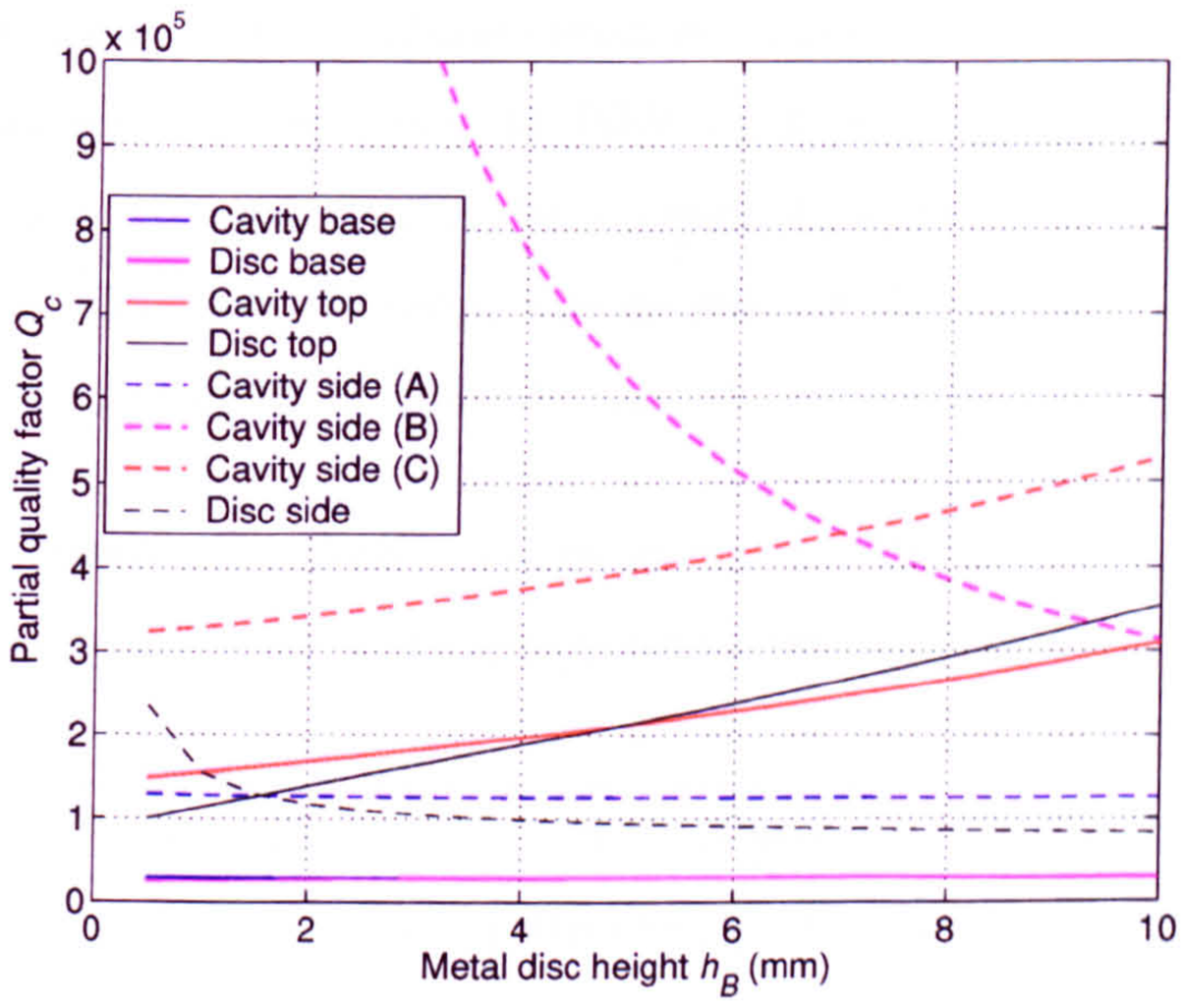

Figure 4.19: Variation of partial quality factors of the $HE_{11\delta}$ mode with h_B. $h_A = 23$ mm, $h_C = 14$ mm, $d_1 = 30$ mm, $d_2 = 38$ mm, $d_3 = 65$ mm.

be seen that the majority of this loss always remains in region A. The percentage of loss in this region stays overall constant although the respective proportions due to the cavity base and metal disc base vary by 6% between $h_B = 1$ and 10 mm. In region C however, the percentage of loss decreases, particularly in the top surface of the disc, and seems to be shifted to region B, mainly on the disc perimeter. The magnetic energies of Fig. F.4 follow the same trends: 8% of the magnetic energy is transferred from region C to region B, but no real change happens for region A. Overall, the amount of loss generated in the resonator for a given stored energy does not change: Q_c in region A varies very little. Also, the variations of the partial Q_c's of regions B and C in Fig. 4.17 cancel out as some of the loss is shifted, mainly from the top to the side of the metal disc, and the total Q_c for these two regions is approximately constant.

4.1.4 Variations with disc diameter

The disc diameter (d_1) is a much more critical parameter for the choice of the optimum resonator geometry. Its effect on the resonant frequency of the $HE_{11\delta}$ mode is significant. As it is increased, it allows the electric fields in the dielectric to be terminated, reducing the longitudinal variations of both electric and magnetic fields and reducing the resonant frequency. In Table 4.2, it can be seen that the proportion of W_{Et} in region A, stored mainly in the top part of the dielectric region, is reduced and that of W_{Ez} increased. However, this decrease of the resonant frequency stops once a certain disc diameter is reached. Indeed, in parallel to the previous effect,

Table 4.2: *Distribution of electric energy in region A for different* d_1. W_{Ez} *is the energy contained in* E_z. W_{Et} *is the energy contained in* E_r *and* E_θ.

	$d_1 = 26$ mm		$d_1 = 34$ mm		$d_1 = 42$ mm	
	dielectric region	air region	dielectric region	air region	dielectric region	air region
W_{Ez} (%)	90.81	0.61	97.08	0.77	97.94	1.06
W_{Et} (%)	7.84	0.74	1.18	0.97	0.12	0.89
Total	98.65	1.35	98.26	1.74	98.05	1.95

the percentage of electric energy contained in the dielectric region also decreases, as shown in Table 4.2 and Fig. F.5. This has the opposite effect of increasing the resonant frequency. In Figs. 4.20 to 4.25, it is observed that, because the point of maximum amplitude of the transverse fields is located almost directly below the edge of the metal disc, W_{Et} is shifted outwards when d_1 is increased. However, as the metal disc diameter is increased beyond the dielectric resonator diameter, it is the longitudinal electric field that becomes predominant in the air part of region A. The transverse electric energy in the air region around the dielectric resonator decreases in Table 4.2 when d_1 is changed from 34 to 42 mm. This agrees with the radial fields shown in Figs. 4.22 and 4.24. Note that, in the limit, as the disc tends towards making contact with the cavity side wall, the $HE_{11\delta}$ mode becomes the TM_{110}. As d_1 reaches values close to d_3, the proximity of the two metal boundaries could start having a significant effect. To quantify this, the frequency variations of each mode are plotted again in Fig. 4.26, with a cavity diameter of 138 mm. the influence of the disc on the dielectric resonator region can then be separated from that on the cavity. The proximity of metal disc and cavity was expected to load the $HE_{11\delta}$ mode and decrease its resonant frequency, as illustrated in [75] for the conductor disc $HE_{11\delta}$ mode resonator. However, in the latter case, the fields are concentrated around the disc edge, instead of being confined below it. As a result, the $HE_{11\delta}$ mode resonant frequency of Fig. 4.26 does not increase any slower than that in Fig. 4.5 for large disc diameters. In fact, the increase of the resonant frequency for large disc diameters is greater.

The Q_d variation with d_1 in Fig. 4.27 follows closely that of the ceramic quality factor, as they increase by 20% and 18% respectively when d_1 is increased from 1 to 18 mm, and then decrease by 2.3% and 2.2% from 18 to 25 mm. Q_c also initially increases with d_1. This is due to an increase of the partial Q_c of the cavity base (Fig. 4.29) because the magnetic fields decrease dramatically on this surface as shown in Figs. 4.30 and 4.31. However, by the time the disc reaches diameters around 20 mm, the partial Q_c due to the loss in the disc base have decreased dramatically and the overall Q_c deteriorates. This happens while the resonant frequency of the $HE_{11\delta}$ mode is still decreasing. In fact, the Q_c variation is not influenced significantly by the change in frequency: in Appendix G, the normalised $Q_c\delta/\lambda_0$ is plotted and shows the same variation. For d_1 above 30 mm, the percentages of the losses stay

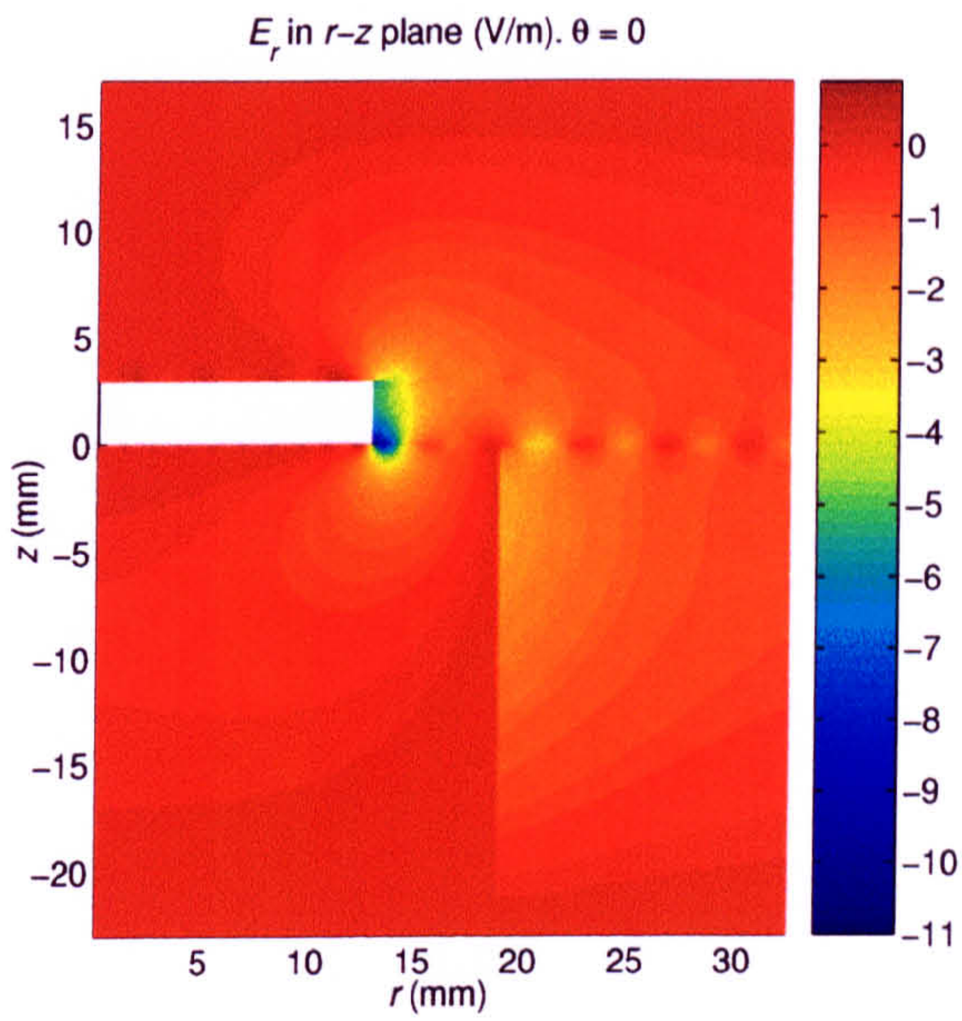

Figure 4.20: Radial electric field of the $\mathrm{HE}_{11\delta}$ mode for $d_1 = 26$ mm. $h_A = 23$ mm, $h_B = 3$ mm, $h_C = 14$ mm, $d_2 = 38$ mm, $d_3 = 65$ mm.

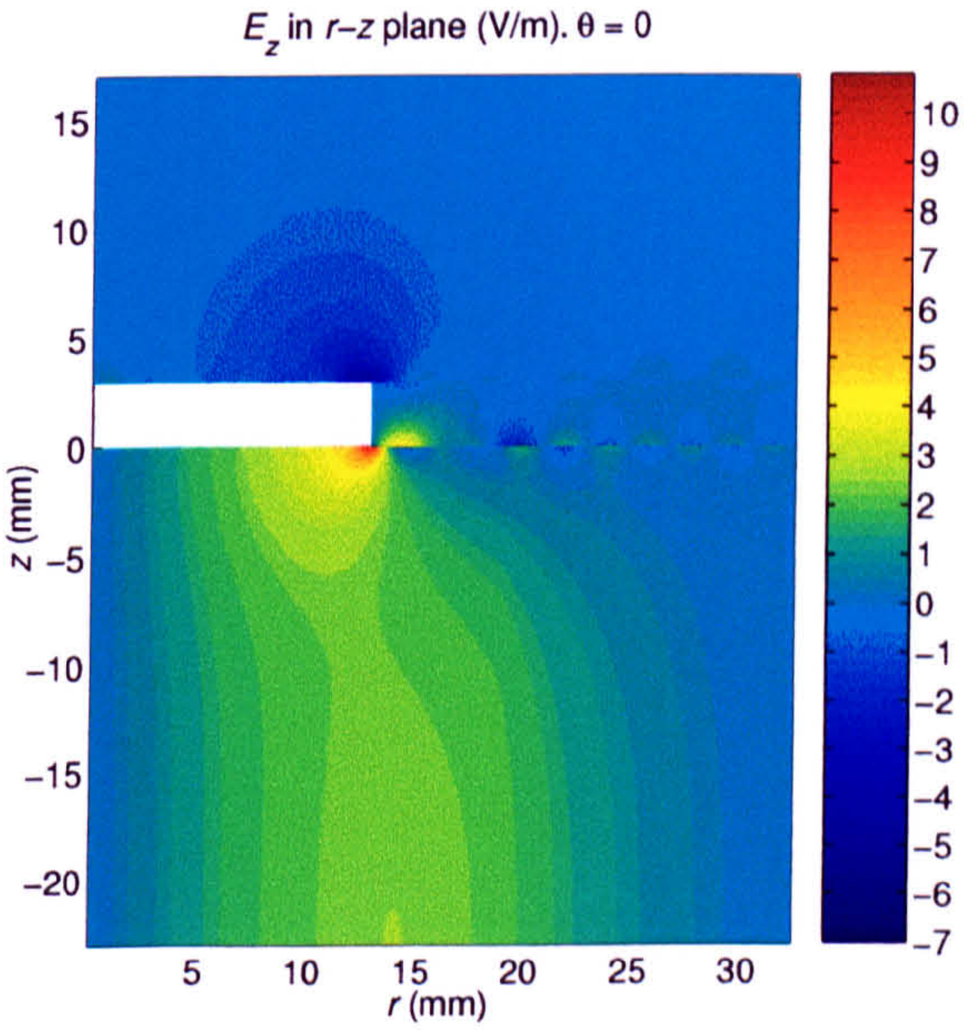

Figure 4.21: Axial electric field of the $\mathrm{HE}_{11\delta}$ mode for $d_1 = 26$ mm. $h_A = 23$ mm, $h_B = 3$ mm, $h_C = 14$ mm, $d_2 = 38$ mm, $d_3 = 65$ mm.

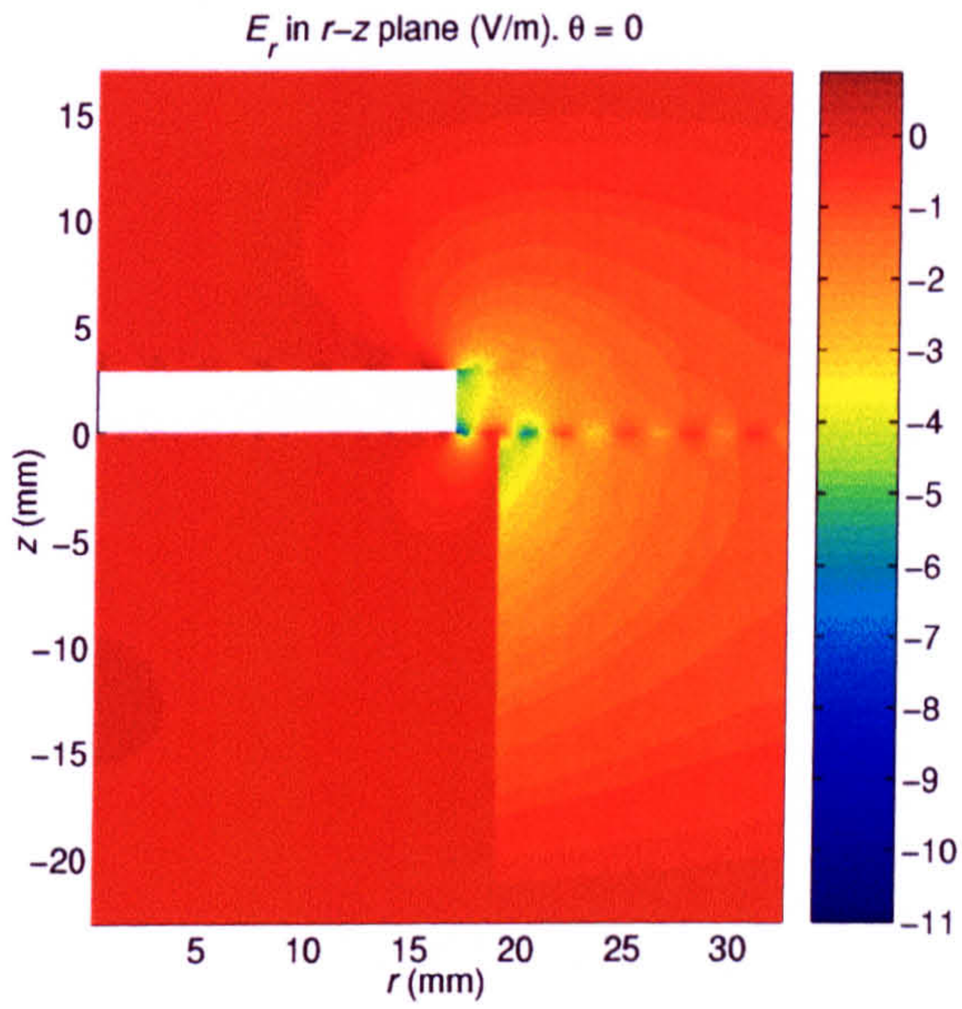

Figure 4.22: Radial electric field of the $\mathrm{HE}_{11\delta}$ mode for $d_1 = 34$ mm. $h_A = 23$ mm, $h_B = 3$ mm, $h_C = 14$ mm, $d_2 = 38$ mm, $d_3 = 65$ mm.

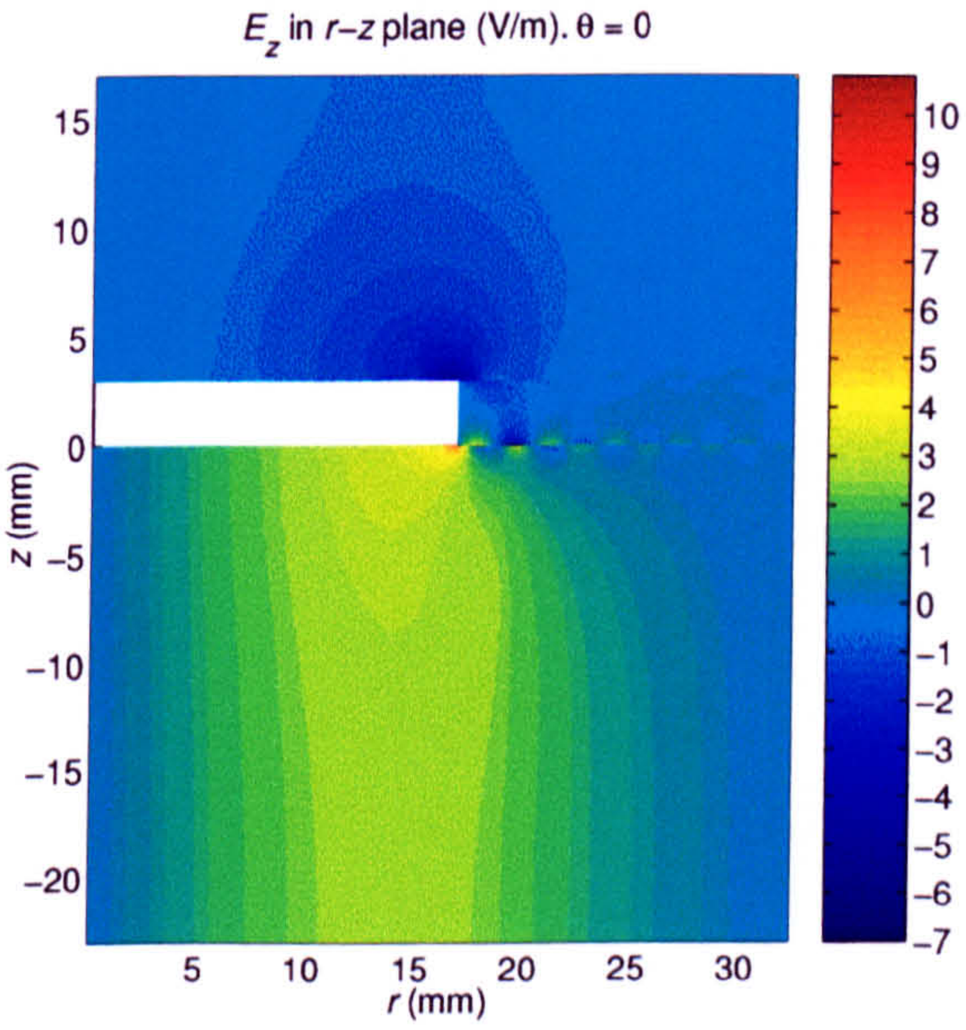

Figure 4.23: Axial electric field of the $\mathrm{HE}_{11\delta}$ mode for $d_1 = 34$ mm. $h_A = 23$ mm, $h_B = 3$ mm, $h_C = 14$ mm, $d_2 = 38$ mm, $d_3 = 65$ mm.

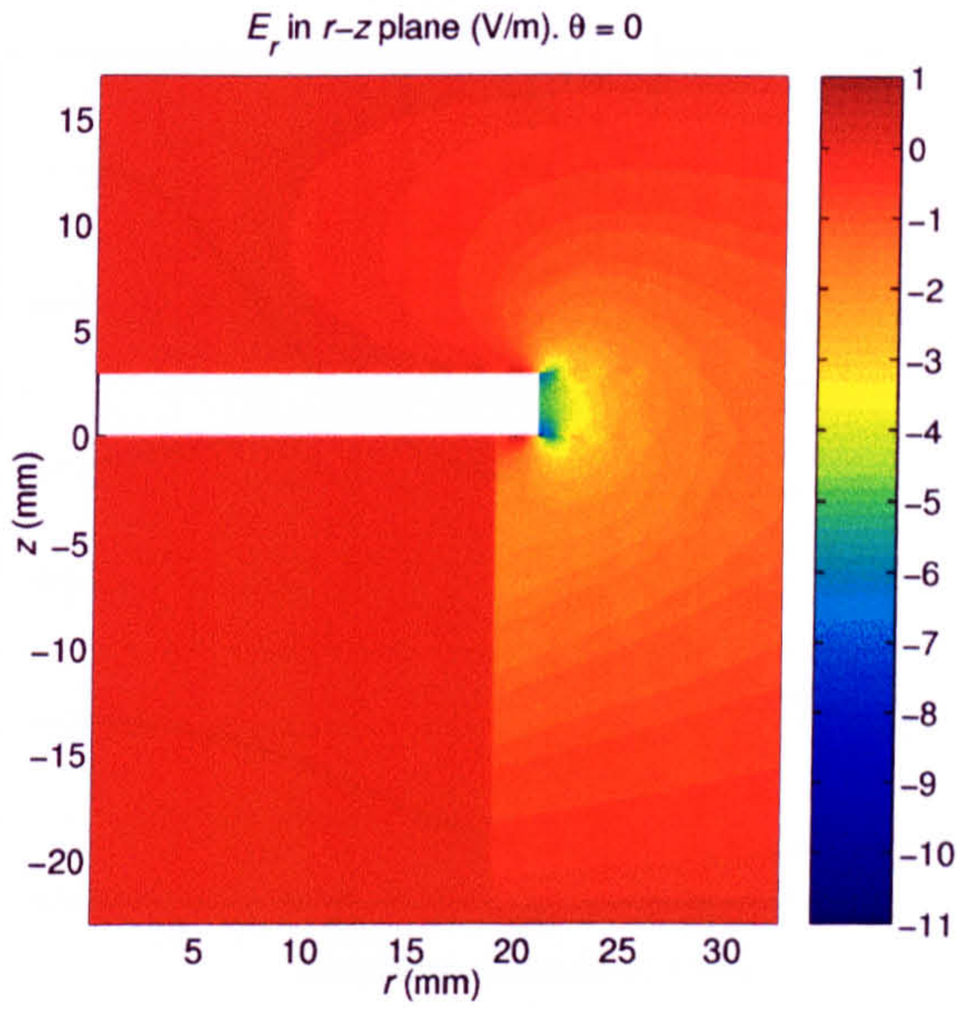

Figure 4.24: Radial electric field of the $\mathrm{HE}_{11\delta}$ mode for $d_1 = 32$ mm. $h_A = 23$ mm, $h_B = 3$ mm, $h_C = 14$ mm, $d_2 = 38$ mm, $d_3 = 65$ mm.

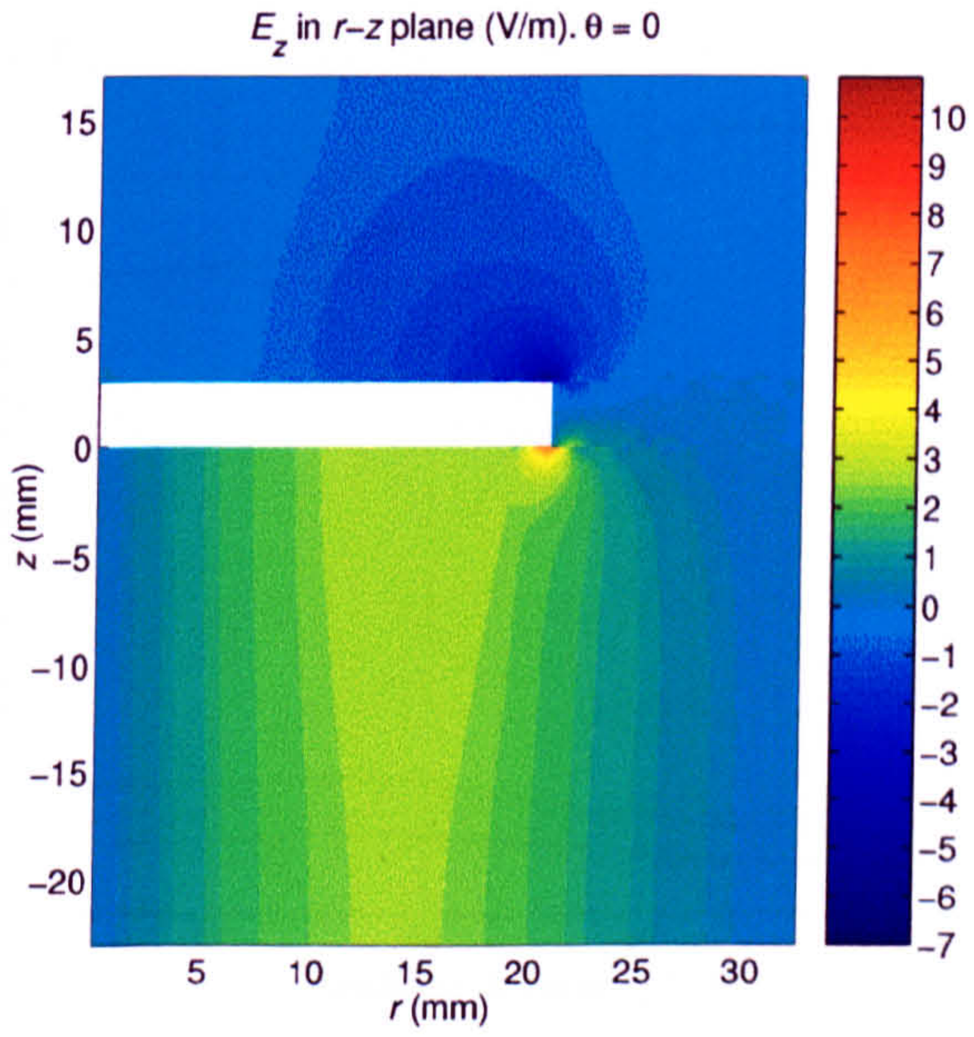

Figure 4.25: Axial electric field of the $\mathrm{HE}_{11\delta}$ mode for $d_1 = 32$ mm. $h_A = 23$ mm, $h_B = 3$ mm, $h_C = 14$ mm, $d_2 = 38$ mm, $d_3 = 65$ mm.

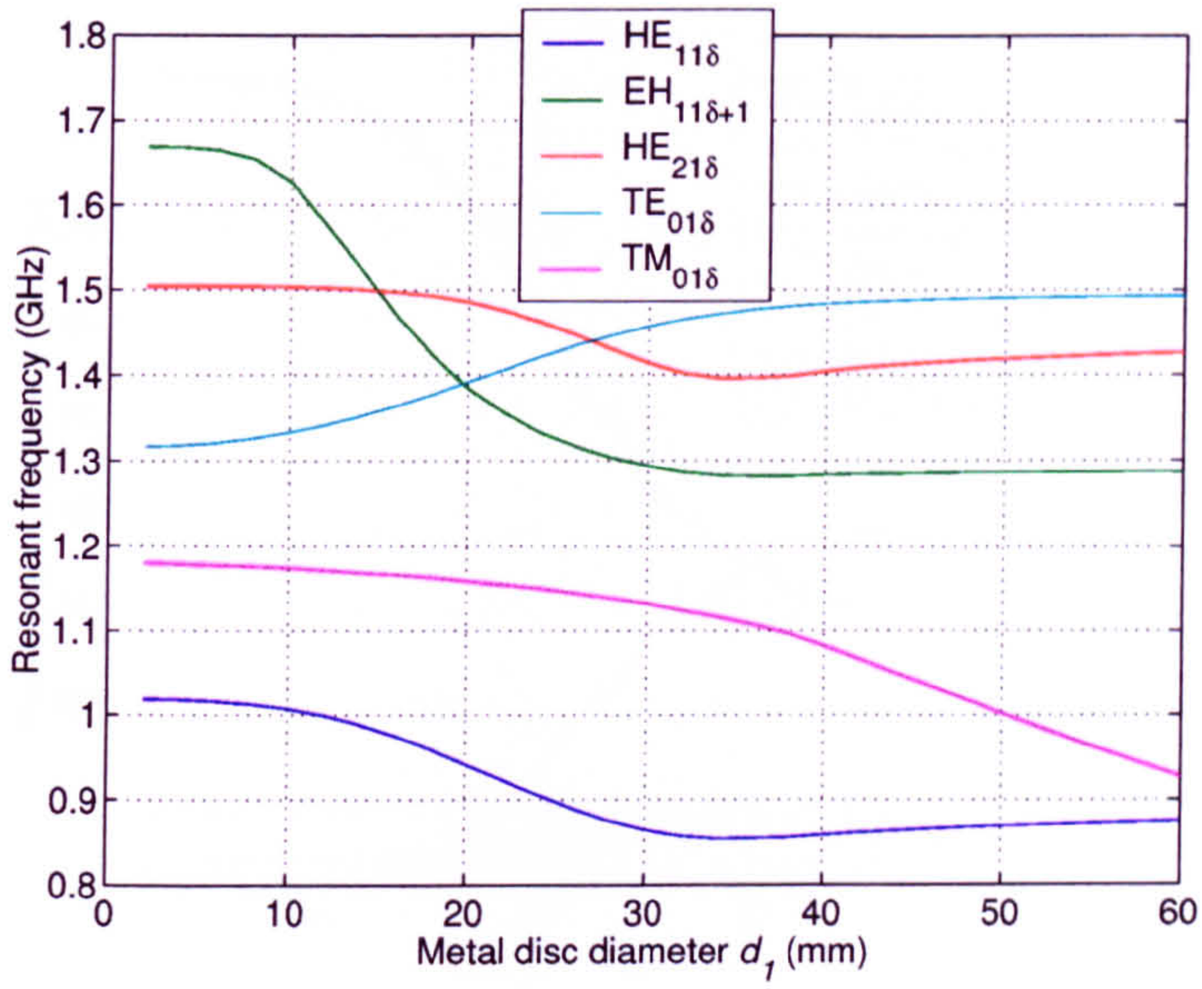

Figure 4.26: Resonant frequency variations with d_1. $h_A = 23$ mm, $h_B = 3$ mm, $h_C = 14$ mm, $d_2 = 38$ mm, $d_3 = 138$ mm.

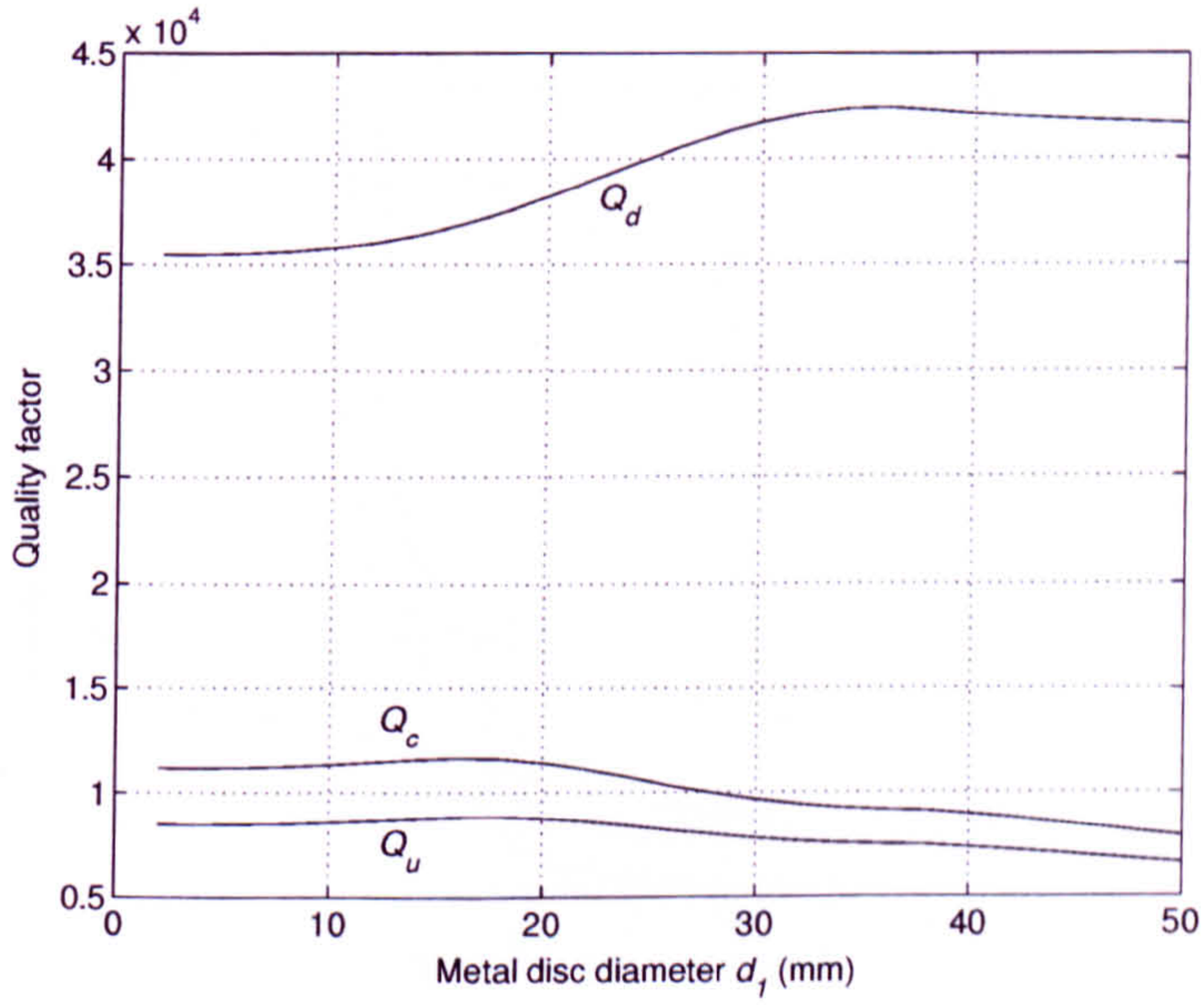

Figure 4.27: Variation of quality factors of the $\mathrm{HE}_{11\delta}$ mode with d_1. $h_A = 23$ mm, $h_B = 3$ mm, $h_C = 14$ mm, $d_2 = 38$ mm, $d_3 = 65$ mm.

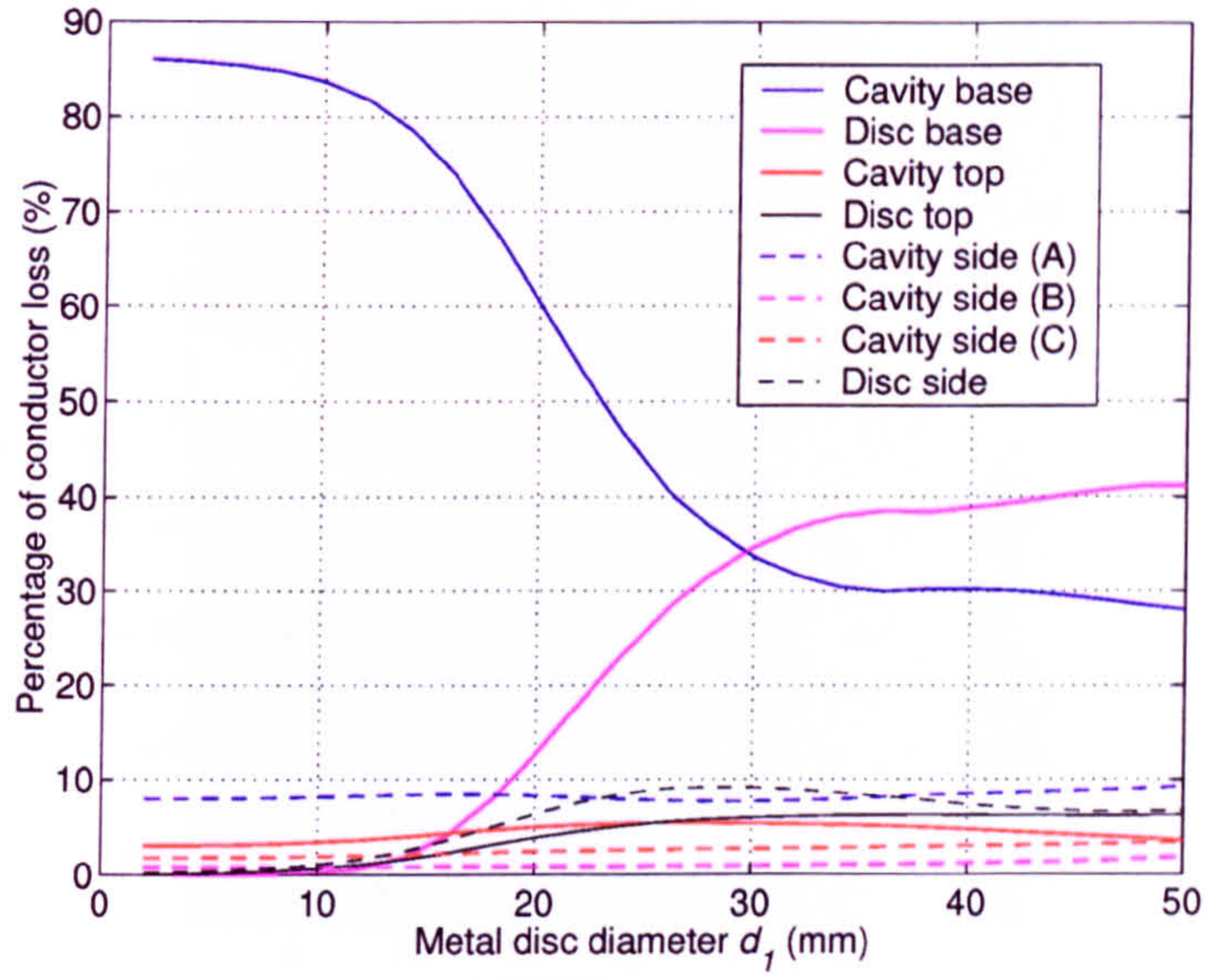

Figure 4.28: Variation of the conductor loss distribution of the $HE_{11\delta}$ mode with d_1. $h_A = 23$ mm, $h_B = 3$ mm, $h_C = 14$ mm, $d_2 = 38$ mm, $d_3 = 65$ mm.

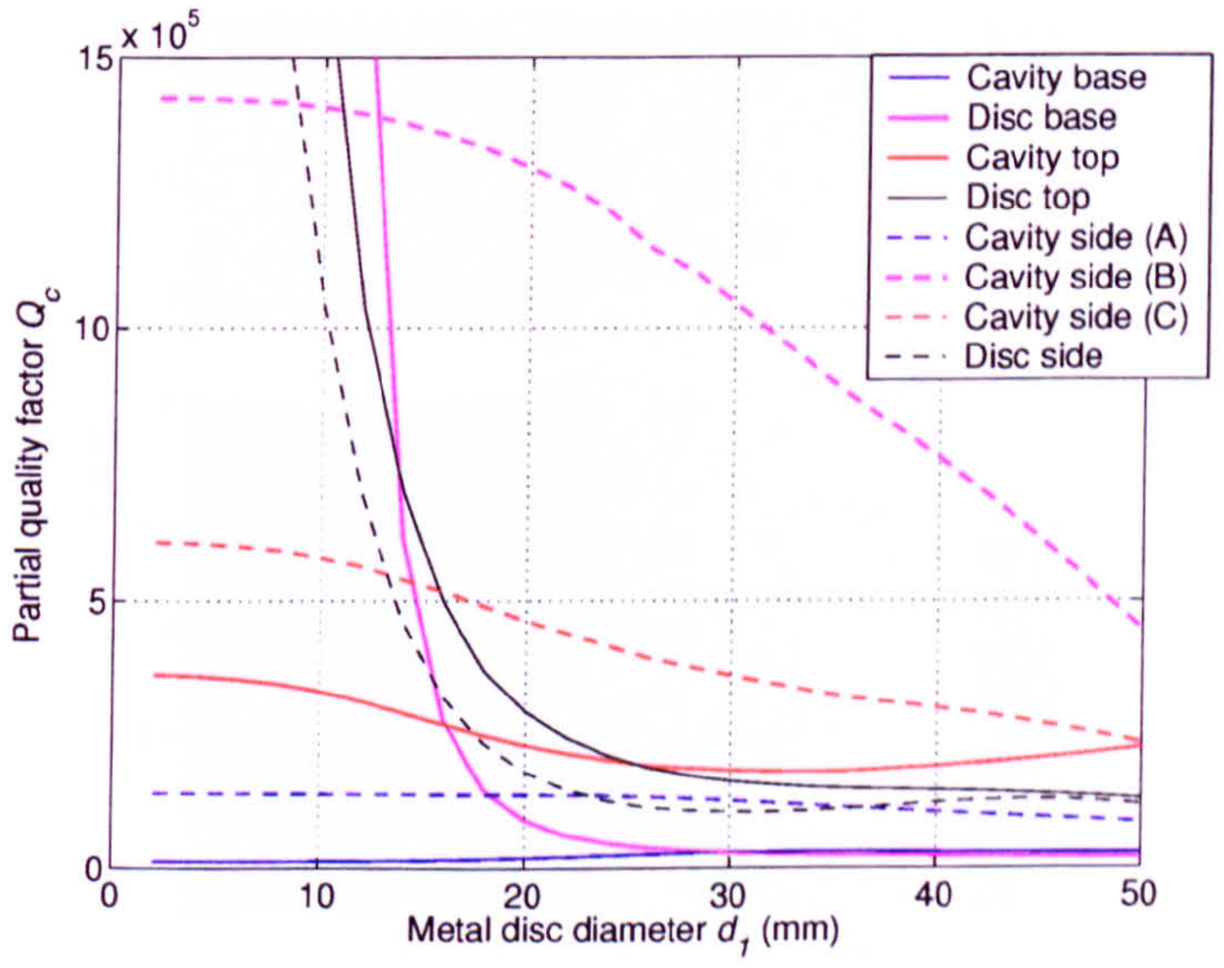

Figure 4.29: Variation of partial quality factors of the $HE_{11\delta}$ mode with d_1. $h_A = 23$ mm, $h_B = 3$ mm, $h_C = 14$ mm, $d_2 = 38$ mm, $d_3 = 65$ mm.

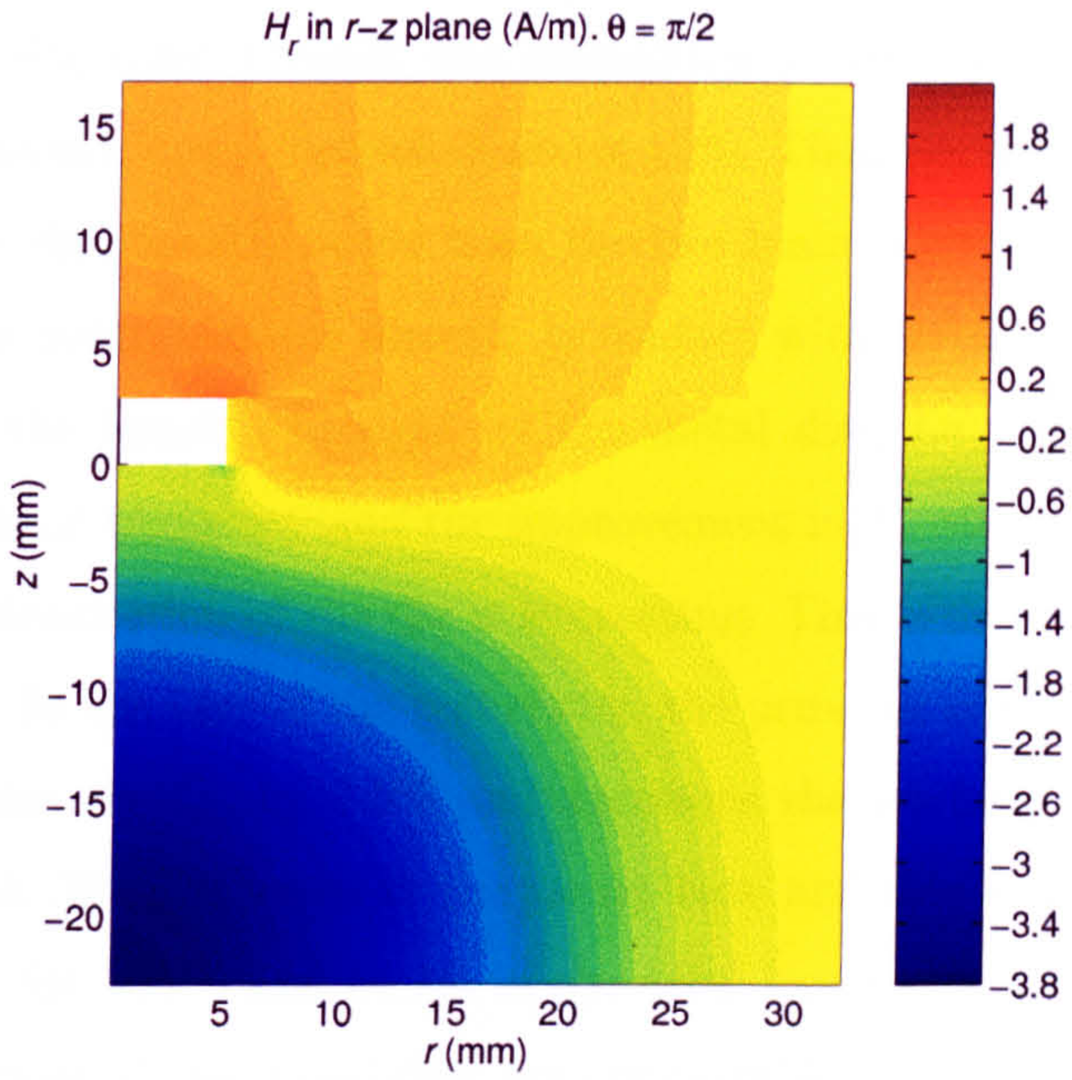

Figure 4.30: Radial magnetic field of the $\mathrm{HE}_{11\delta}$ mode for $d_1 = 10$ mm. $h_A = 23$ mm, $h_B = 3$ mm, $h_C = 14$ mm, $d_2 = 38$ mm, $d_3 = 65$ mm.

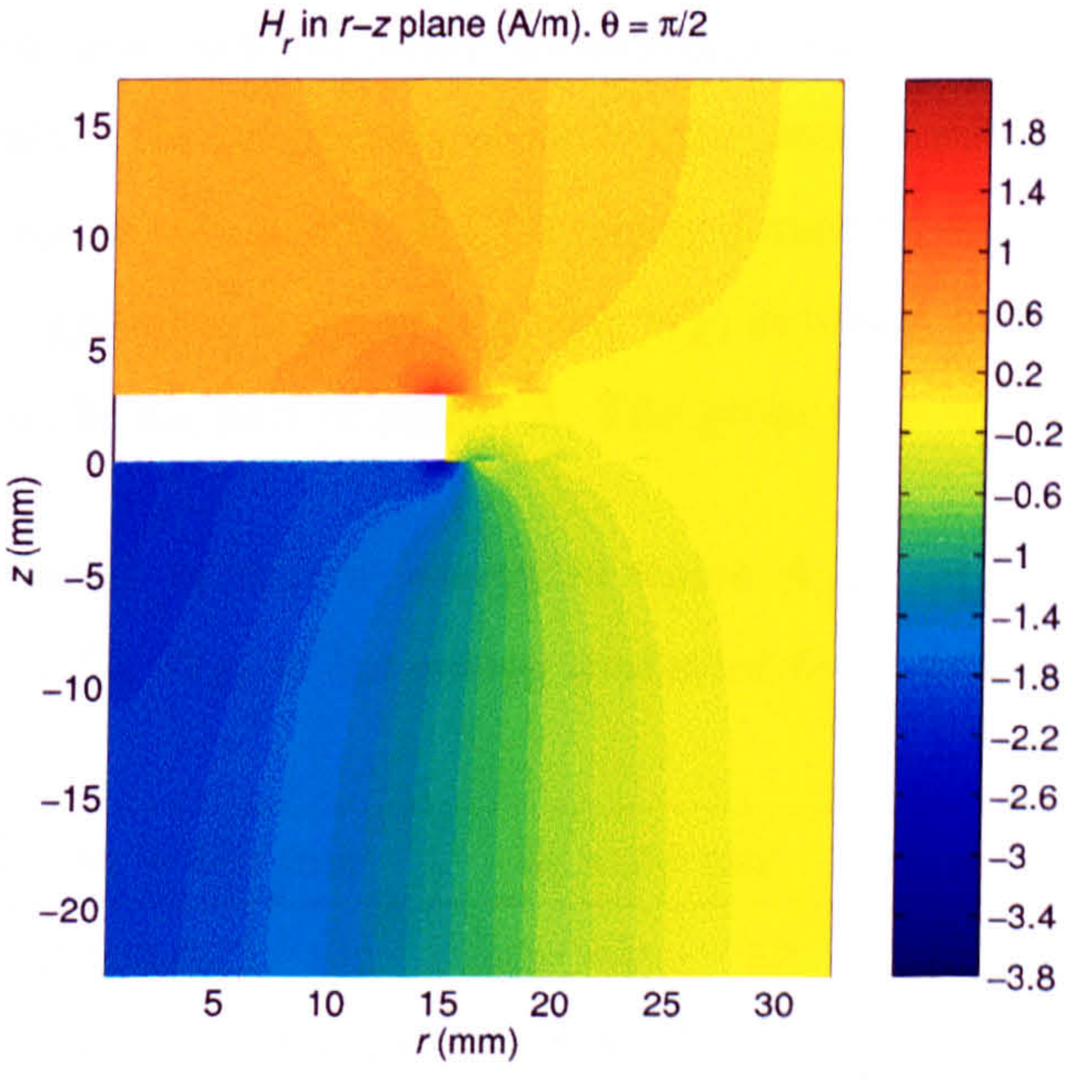

Figure 4.31: Radial magnetic field of the $\mathrm{HE}_{11\delta}$ mode for $d_1 = 30$ mm. $h_A = 23$ mm, $h_B = 3$ mm, $h_C = 14$ mm, $d_2 = 38$ mm, $d_3 = 65$ mm.

overall constant except for those around the perimeter of the disc and in the lid of the cavity which decrease. Overall, the proportion of the losses in the cavity side walls is fairly constant, never increasing above 10%. Their partial Q_c's, in Fig. 4.29, decrease but stay significantly larger than the two main contributors to the overall Q_u, which are the metal surfaces directly in contact with the dielectric.

To conclude, the benefits brought by the metal disc, i.e. the decrease of the $HE_{11\delta}$ mode resonant frequency and the improvement in F_r can be compromised by the significant deterioration of the Q_u it is creating. This is due to the loss created in the metal disc. In the case of the test cavity, the presence of the 30 mm diameter metal disc degrades the Q_u by 7.5% and decreases the resonant frequency of the $HE_{11\delta}$ mode by 14.1%. The losses in the cavity base and disc base are then almost equal, accounting for 33.7% and 34.7% of the total loss respectively. Losses in the side and top surfaces of the metal disc are comparable to those in the rest of the cavity walls, with 15.1% and 16.6% respectively.

4.1.5 Variations with cavity diameter

As for the dielectric-loaded waveguide TM_{110} resonator, decreasing the cavity diameter d_3 increases the resonant frequency of the $HE_{11\delta}$ mode and, for cavity diameters above a certain value, the proportion of its electric energy within the dielectric region. The latter can be seen in Fig. F.7 for cavity diameters larger than 70 mm and in Table 4.3, which gives the detail of W_{Ez} and W_{Et} in region A. The main variations however happen in the air part of region A. The proportion of W_{Ez} there decreases

Table 4.3: *Distribution of electric energy in region A for different* d_3. W_{Ez} *is the energy contained in* E_z. W_{Et} *is the energy contained in* E_r *and* E_θ.

	$d_3 = 100$ mm		$d_3 = 65$ mm		$d_3 = 48$ mm	
	dielectric region	air region	dielectric region	air region	dielectric region	air region
W_{Ez} (%)	94.601	1.43	94.81	0.67	93.19	0.20
W_{Et} (%)	3.42	0.55	3.67	0.84	4.68	1.93
Total	98.02	1.98	98.48	1.52	97.87	2.13

sharply, but more importantly that of W_{Et} increases significantly. Overall, the electric energy in the air part of region A increases again for gaps between dielectric resonator and cavity smaller than 10 mm. This also contributes to the increase of the resonant frequency.

Fig. 4.32 shows the variations of Q_d, Q_c and Q_u with the cavity diameter. When the gap between cavity and dielectric cylinder is reduced to very small values, the percentage of electric energy in the dielectric decreases, which, when it outweighs the effect due to the increase of the resonant frequency, results in an increase of Q_d. Otherwise, Q_d simply increases with d_3 at the rate followed by the ceramic quality factor. Q_c also increases with d_3. All partial Q_c's corresponding to losses in the cavity side walls logically increase rapidly, as shown in Fig. 4.34. So do those due to the disc side and top surfaces, and for larger d_3, the cavity top. For d_3 smaller than 60 mm, the partial Q_c of the latter actually deteriorates with increasing d_3, as its corresponding percentage of conductor loss in Fig. 4.33 increases. However, by far the largest relative loss increase is that of the cavity base. For a 1 mm gap between cavity and dielectric, only 6.3% of the loss is generated in this area. As the gap is increased to 50 mm, this increases to 46.4%. The fields inside the dielectric become more uniform in the axial direction and the intensity of the transverse

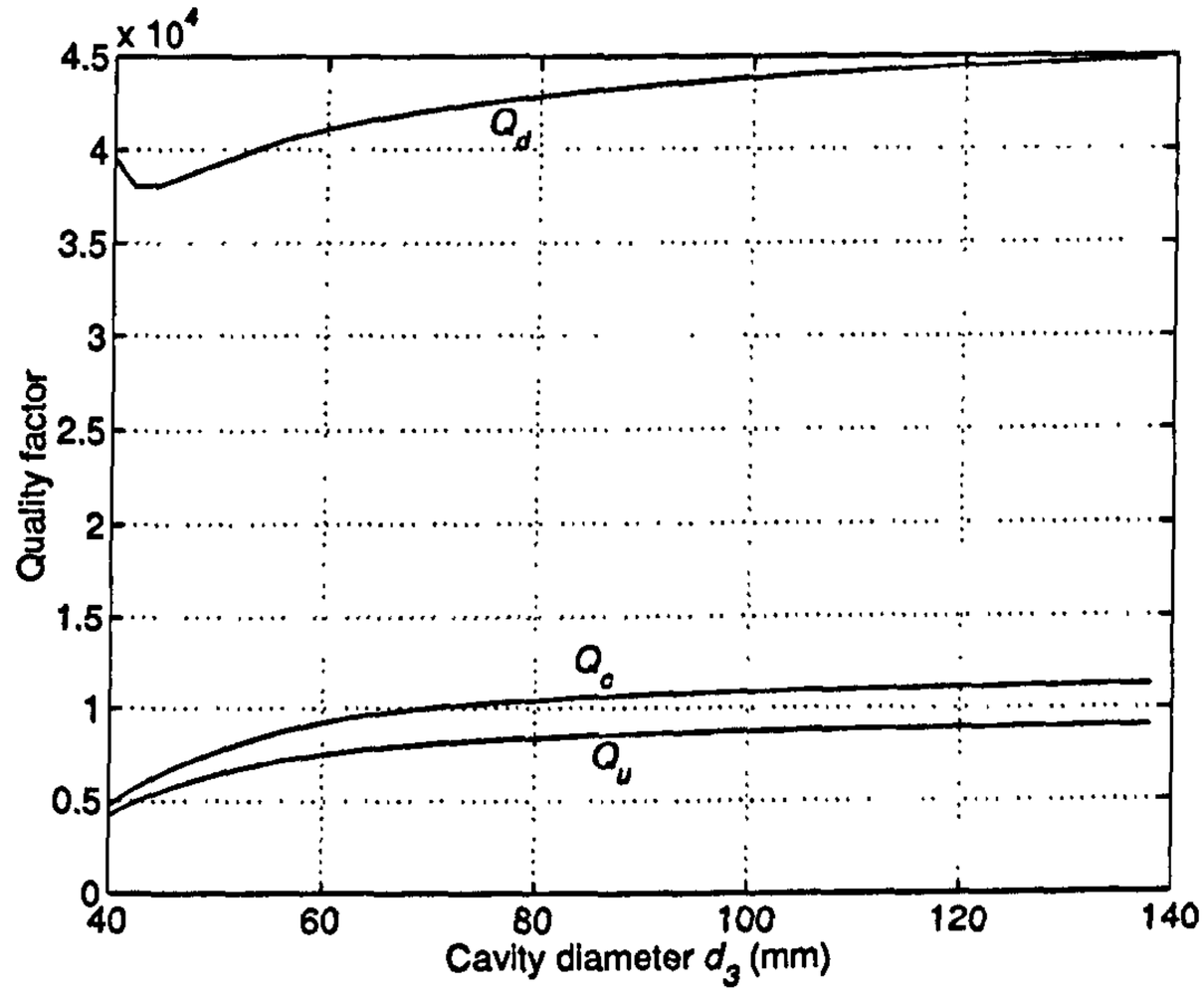

Figure 4.32: Variation of quality factors of the $HE_{11\delta}$ mode with d_3. $h_A = 23$ mm, $h_B = 3$ mm, $h_C = 14$ mm, $d_1 = 30$ mm, $d_2 = 38$ mm.

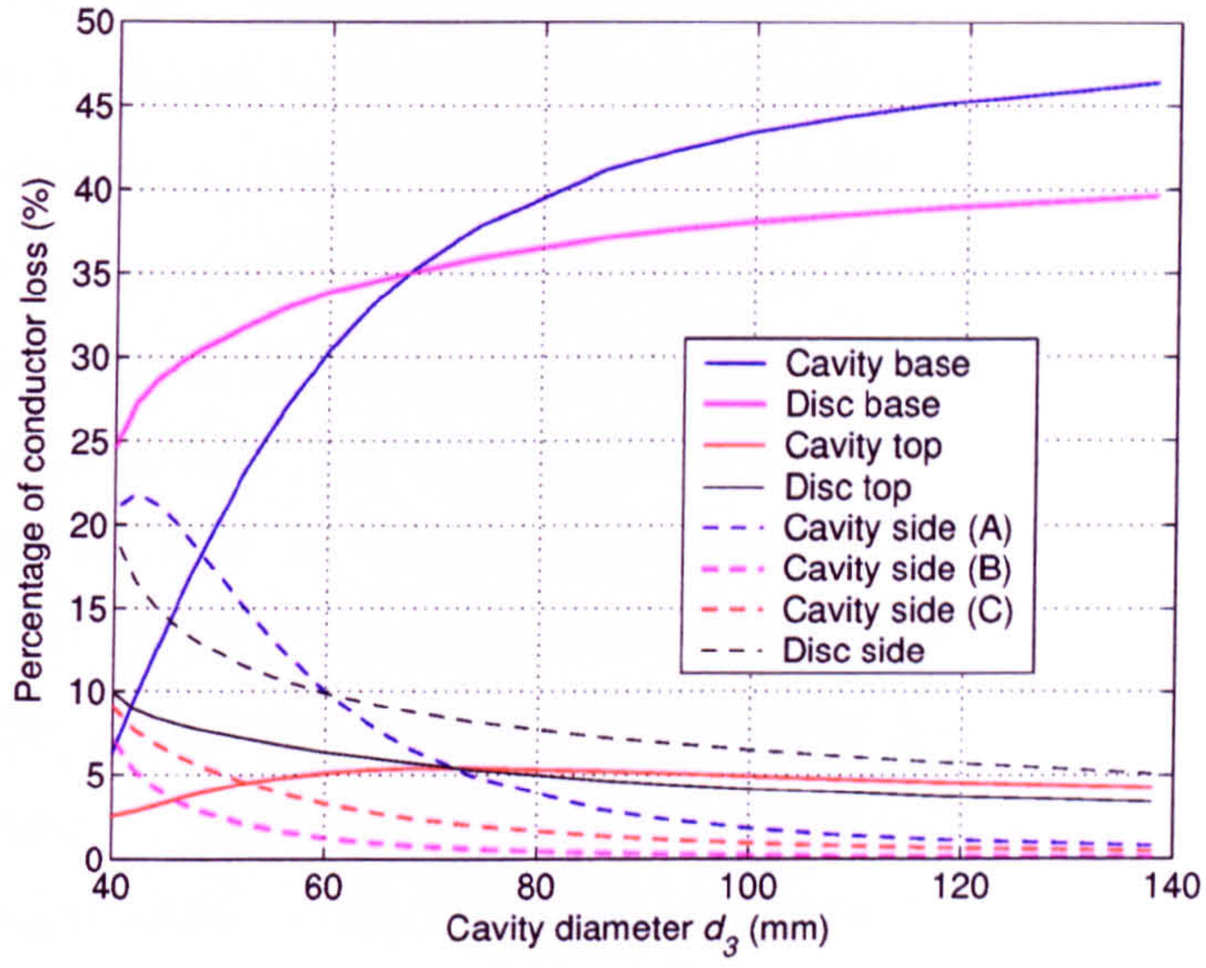

Figure 4.33: Variation of the conductor loss distribution of the $HE_{11\delta}$ mode with d_3. $h_A = 23$ mm, $h_B = 3$ mm, $h_C = 14$ mm, $d_1 = 30$ mm, $d_2 = 38$ mm.

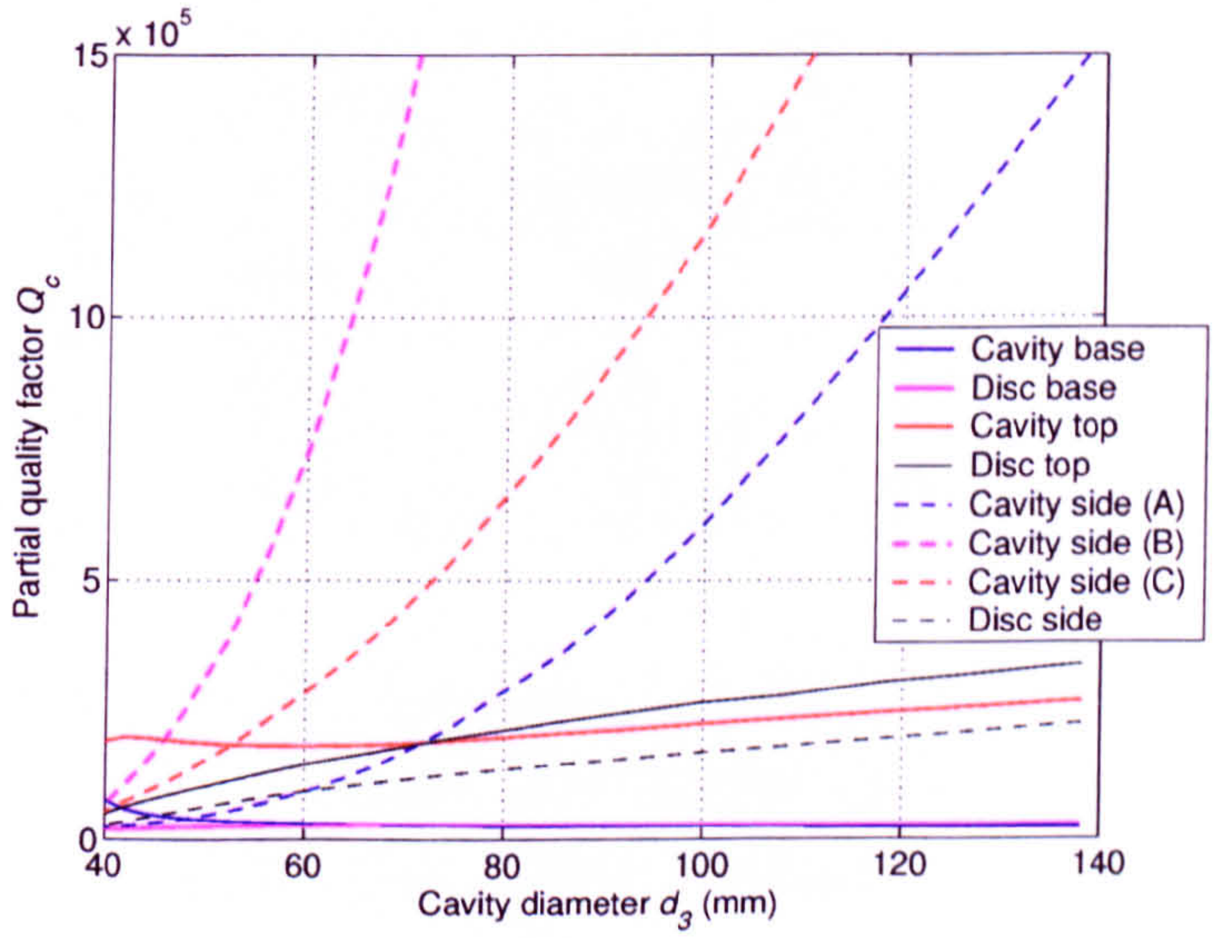

Figure 4.34: Variation of partial quality factors of the $HE_{11\delta}$ mode with d_3. $h_A = 23$ mm, $h_B = 3$ mm, $h_C = 14$ mm, $d_1 = 30$ mm, $d_2 = 38$ mm.

magnetic fields at the base of the cavity increases, as shown in Figs. 4.35 to 4.38. As a result, the partial Q_c corresponding to the loss in the cavity base decreases rapidly (Fig. 4.34). Even though a larger proportion of the conductor loss is also present in the disc base for increasing values of d_3, this is only because its absolute value, relative to the stored energy, decreases slower than that of every other part except the cavity base. Indeed, its partial Q_u is actually increasing.

To conclude, leaving a gap of 10 to 15 mm between the dielectric resonator and the outside diameter of the cavity ensures that the Q_u is not degraded too significantly. The resonant frequency of the $HE_{11\delta}$ mode is lower than for smaller gaps, but the plot of the normalised Q_c in Fig. G.5 of Appendix G shows that even when scaled down to retain the same resonant frequency, the Q_u of the cavity can be increased significantly. Indeed, the extra loss created in the base of the cavity is outweighed by that eliminated in the rest of the cavity and disc surfaces.

4.1.6 Variations with cavity height

Table 4.4: *Distribution of electric energy in region A for different h_C. W_{Ez} is the energy contained in E_z. W_{Et} is the energy contained in E_r and E_θ.*

	$h_C = 5$ mm		$h_C = 14$ mm	
	dielectric region	air region	dielectric region	air region
W_{Ez} (%)	95.74	0.63	94.81	0.67
W_{Et} (%)	3.24	0.39	3.67	0.84
Total	98.98	1.02	98.49	1.51

Similarly to increasing d_3, decreasing h_C pushes the electric fields back into the dielectric region (see Fig. F.9) but also increases the resonant frequency, as the proportion of transverse fields in the dielectric decreases and the fields become more uniform. In the limit, in the case of a very thin metal disc, decreasing h_C to zero should force the $HE_{11\delta}$ mode back into a TM_{110} mode. As a result, the transverse electric fields should reduce, as illustrated in Table 4.4.

In Fig. 4.39, Q_d increases at a faster rate than the ceramic quality factor as h_C is increased, because of the decrease of the percentage of electric energy contained

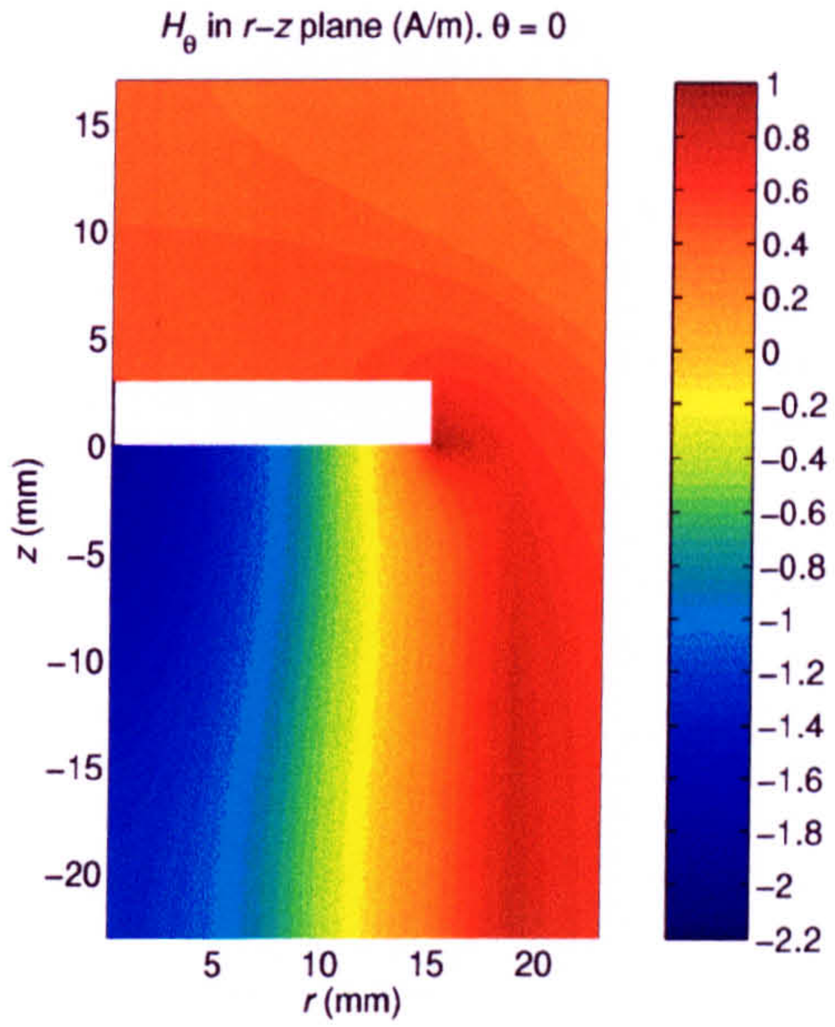

Figure 4.35: Angular magnetic field of the $\mathrm{HE}_{11\delta}$ mode for $d_3 = 46$ mm. $h_A = 23$ mm, $h_B = 3$ mm, $h_C = 14$ mm, $d_1 = 30$ mm, $d_2 = 38$ mm.

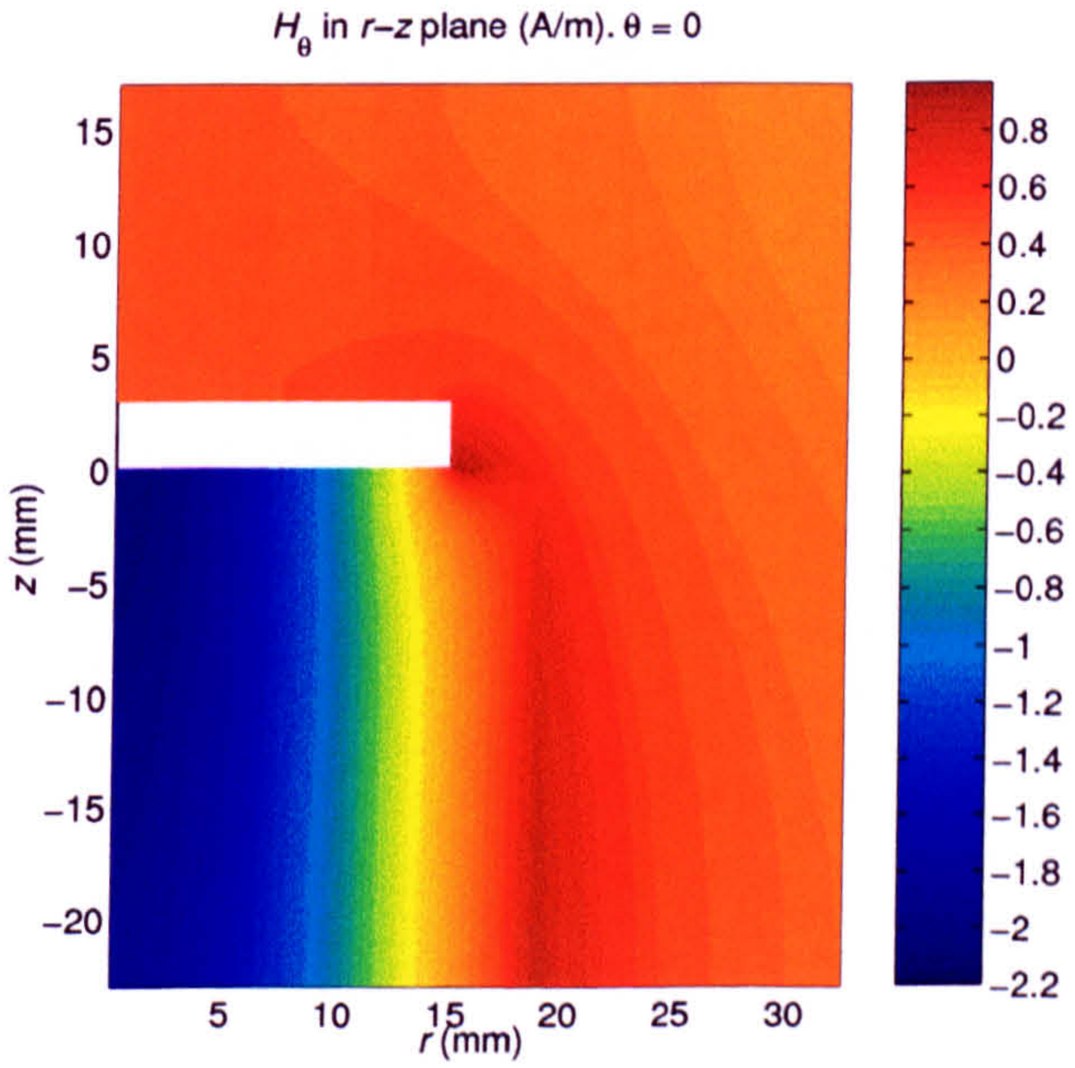

Figure 4.36: Angular magnetic field of the $\mathrm{HE}_{11\delta}$ mode for $d_3 = 65$ mm. $h_A = 23$ mm, $h_B = 3$ mm, $h_C = 14$ mm, $d_1 = 30$ mm, $d_2 = 38$ mm.

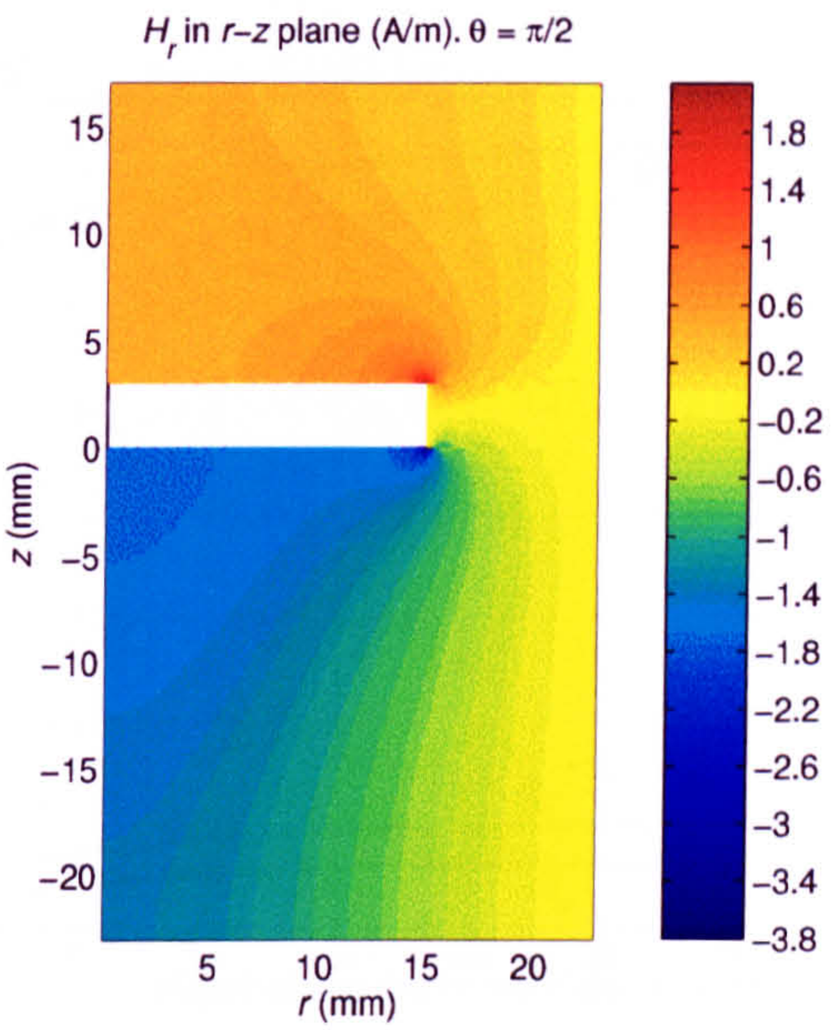

Figure 4.37: Radial magnetic field of the $\mathrm{HE}_{11\delta}$ mode for $d_3 = 46$ mm. $h_A = 23$ mm, $h_B = 3$ mm, $h_C = 14$ mm, $d_1 = 30$ mm, $d_2 = 38$ mm.

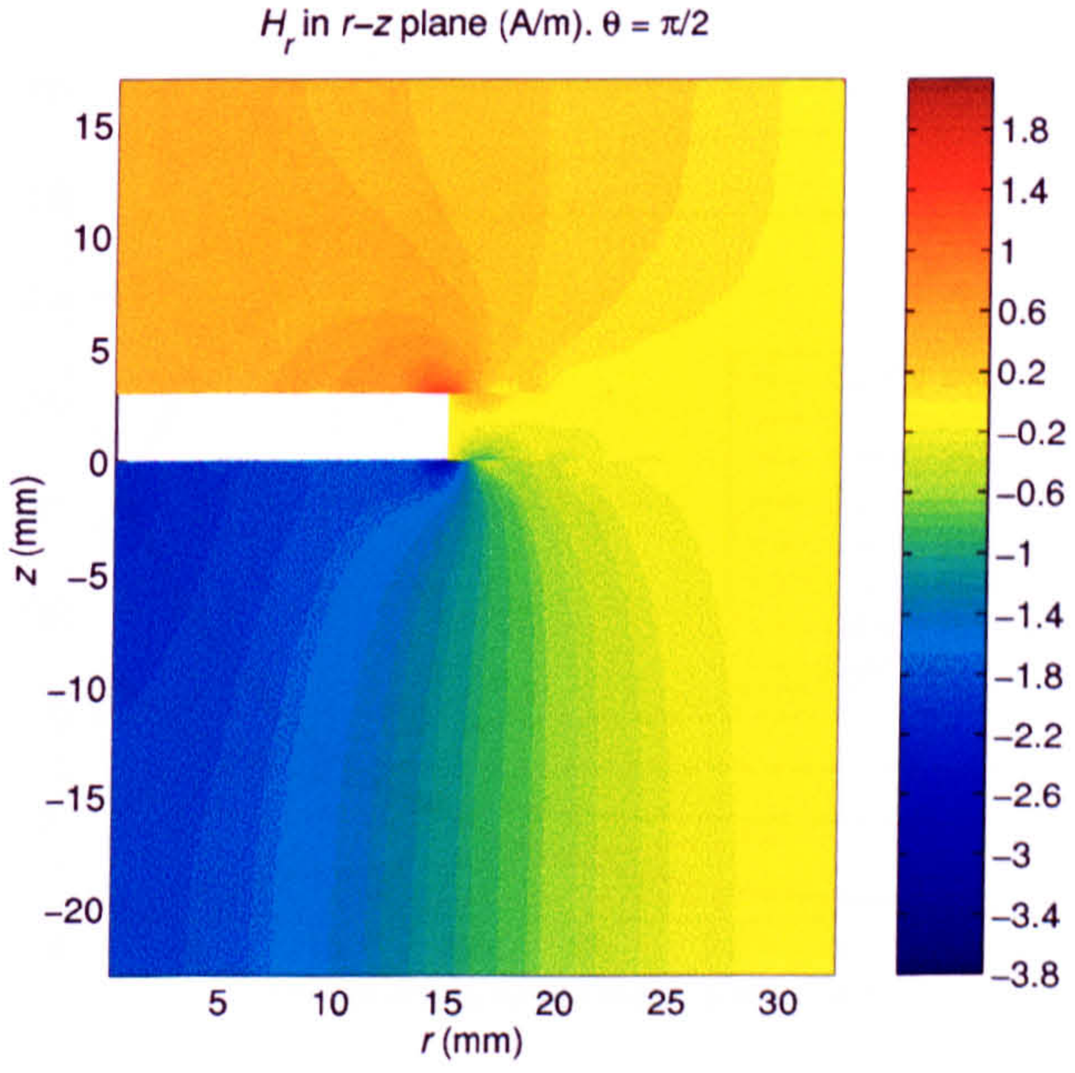

Figure 4.38: Radial magnetic field of the $\mathrm{HE}_{11\delta}$ mode for $d_3 = 65$ mm. $h_A = 23$ mm, $h_B = 3$ mm, $h_C = 14$ mm, $d_1 = 30$ mm, $d_2 = 38$ mm.

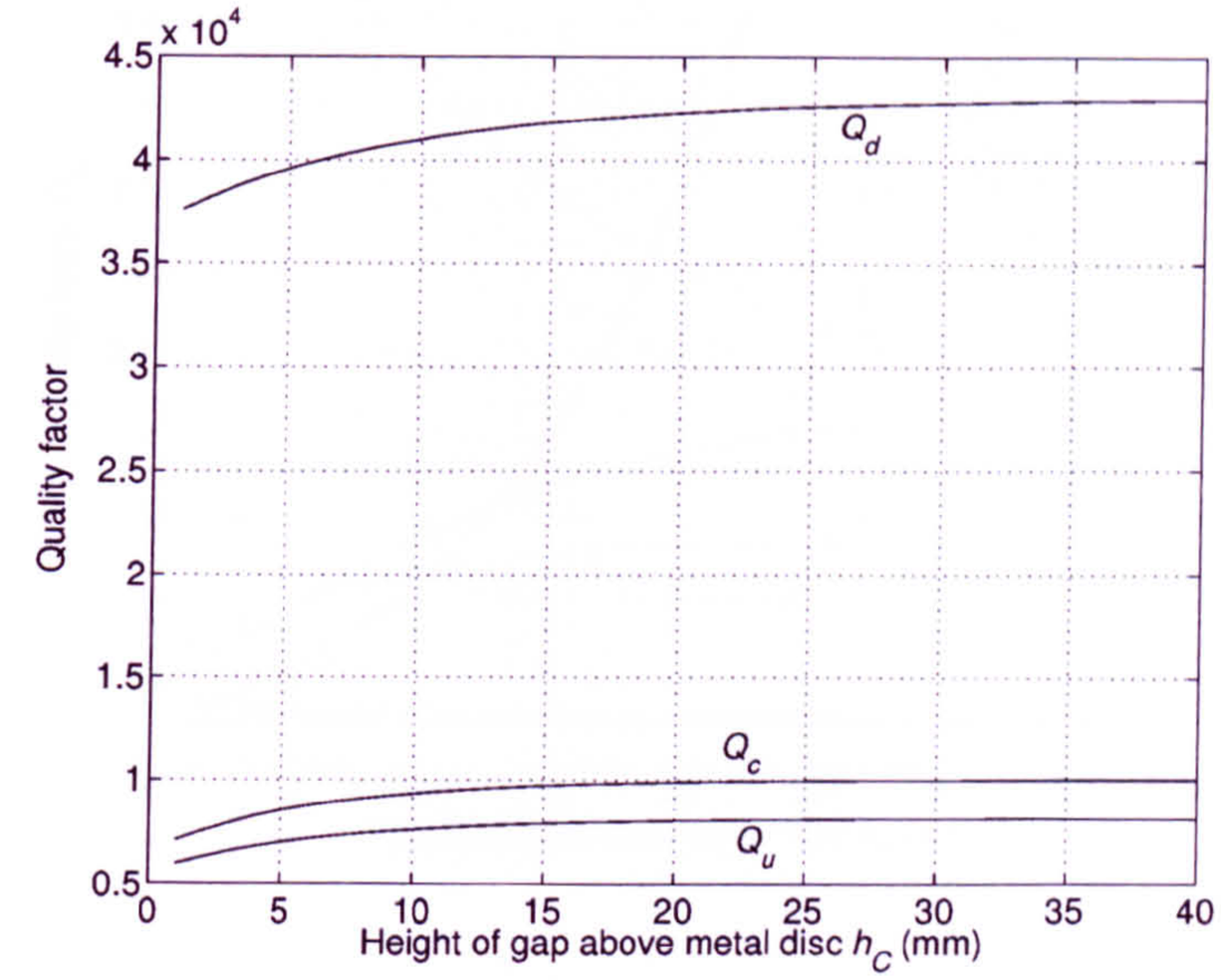

Figure 4.39: Variation of quality factors of the $HE_{11\delta}$ mode with h_C. $h_A = 23$ mm, $h_B = 3$ mm, $d_1 = 30$ mm, $d_2 = 38$ mm, $d_3 = 65$ mm.

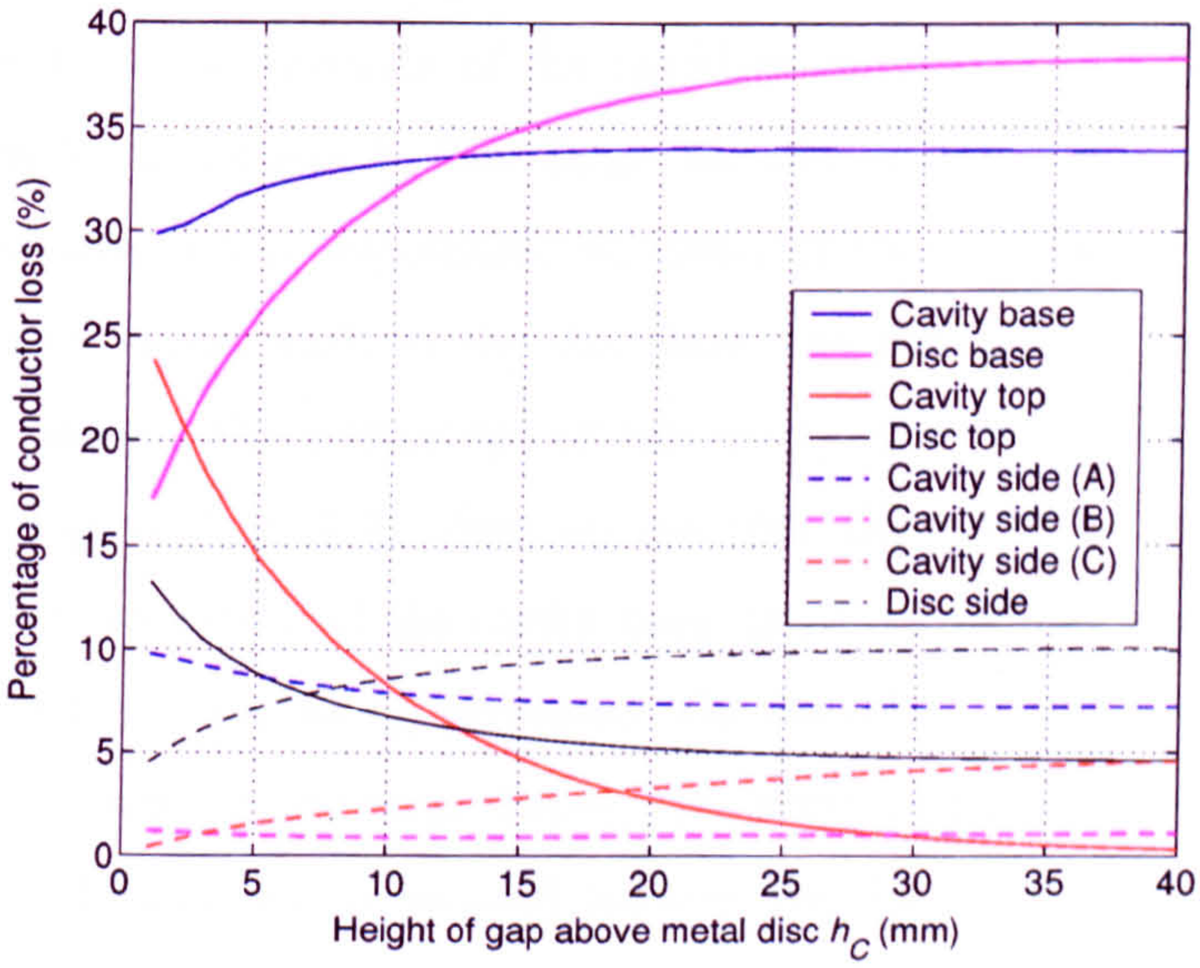

Figure 4.40: Variation of the conductor loss distribution of the $HE_{11\delta}$ mode with h_C. $h_A = 23$ mm, $h_B = 3$ mm, $d_1 = 30$ mm, $d_2 = 38$ mm, $d_3 = 65$ mm.

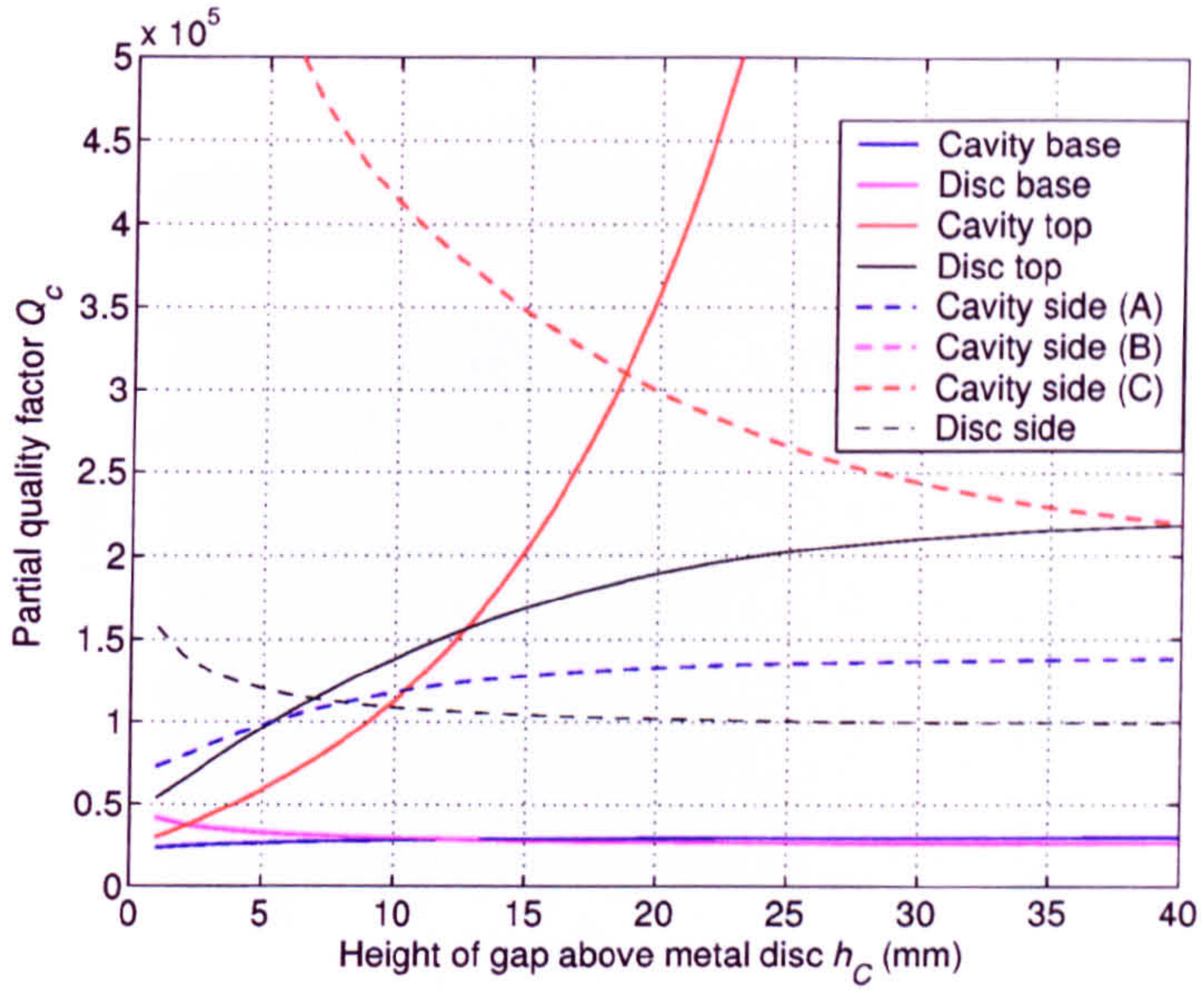

Figure 4.41: Variation of partial quality factors of the $HE_{11\delta}$ mode with h_C. h_A = 23 mm, $h_B = 3$ mm, $d_1 = 30$ mm, $d_2 = 38$ mm, $d_3 = 65$ mm. Q_c of the cavity side in B is off scale.

within the dielectric. As far as conductor loss is concerned, the fastest increases of Q_c happen in Fig. 4.41 for the top of the cavity and the top of the metal disc. In Figs. 4.42 and 4.43, the intensity of the radial magnetic field in region C decrease significantly as h_C is increased. The large decrease in the loss proportions of the cavity top and disc top is responsible for some of the increase of the proportion of losses in some regions such as the disc base, the cavity base and the disc side in Fig. 4.40. Indeed, the partial Q_c of the cavity base is actually improving in Fig. 4.41. In Fig. 4.42 to 4.45, one can see that the intensity of the transverse magnetic field at the centre of the cavity base decreases slightly as h_C is increased and the corresponding partial Q_c improves. On the other hand, the partial Q_c's of the disc base and side deteriorates. Indeed, the areas of large radial magnetic field intensity in Fig. 4.42 appear to expand towards the disc edge in Fig. 4.43 and the field becomes more uniform along the disc radius. Figs. 4.44 and 4.45 show how the intensity of the angular magnetic field close to the edge of the ceramic region is largest for the smaller value of h_C. This is in agreement with Fig. F.10, where the ratio of magnetic energy contained in the air part of region A with respect to that in the dielectric part is shown to decrease. As a result, the partial Q_c of the side wall

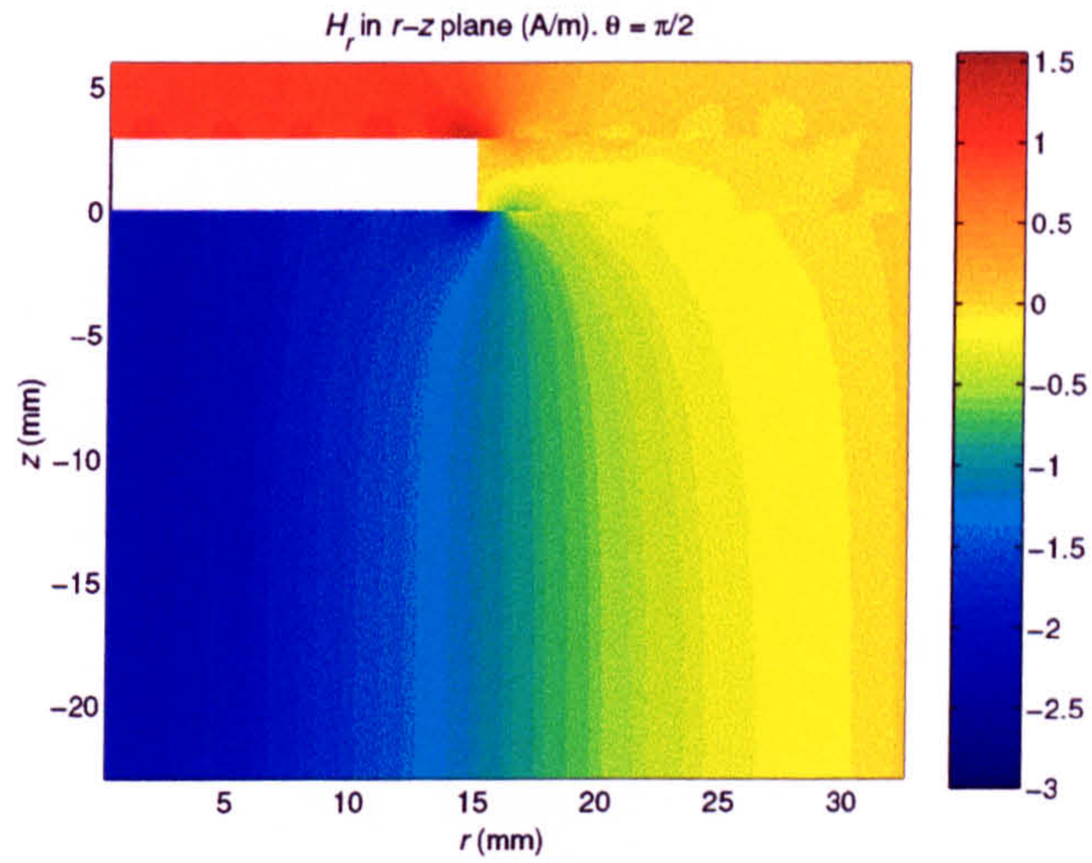

Figure 4.42: Radial magnetic field of the $\mathrm{HE}_{11\delta}$ mode for $h_C = 3$ mm. $h_A = 23$ mm, $h_B = 3$ mm, $d_1 = 30$ mm, $d_2 = 38$ mm, $d_3 = 65$ mm.

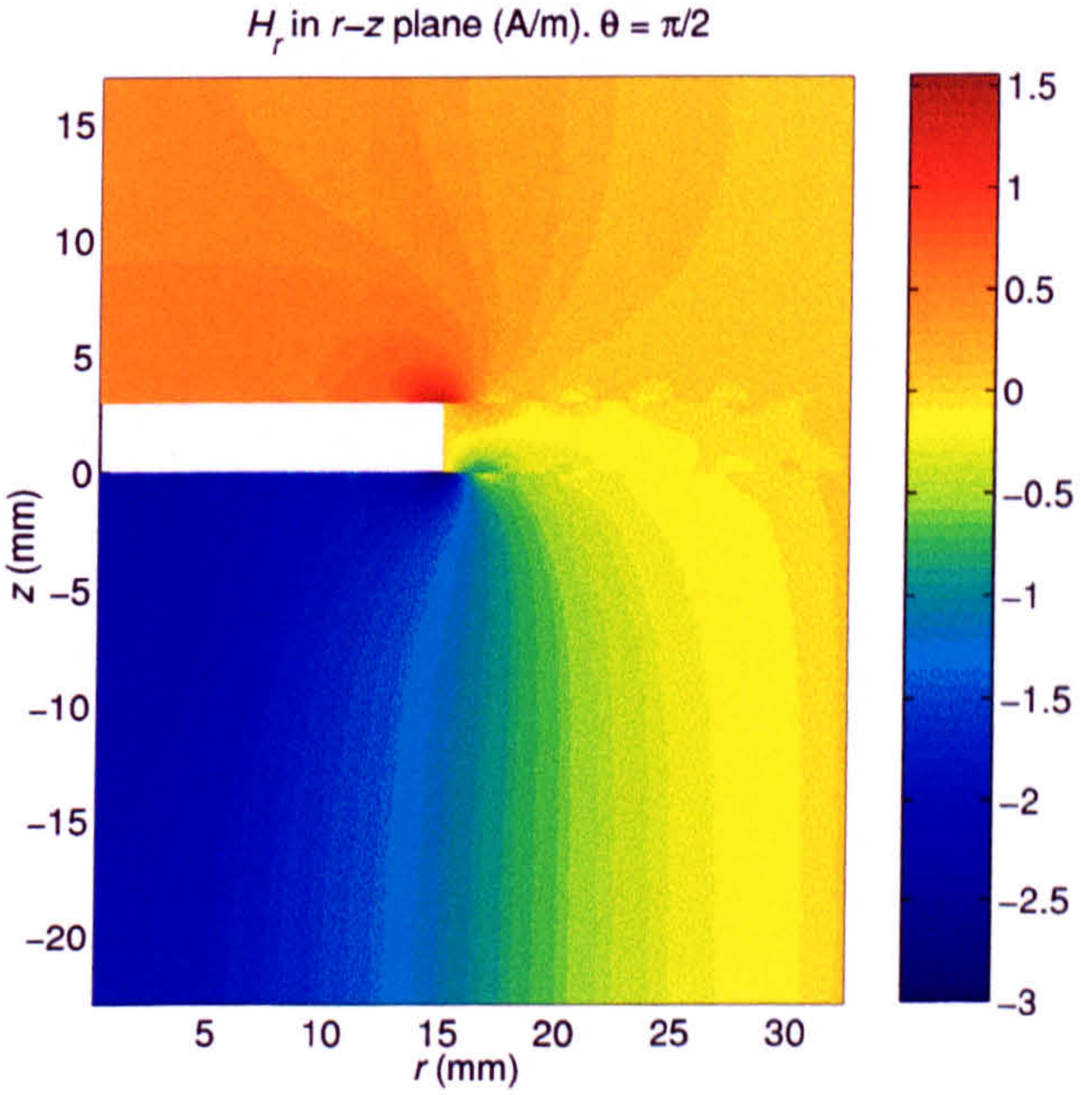

Figure 4.43: Radial magnetic field of the $\mathrm{HE}_{11\delta}$ mode for $h_C = 14$ mm. $h_A = 23$ mm, $h_B = 3$ mm, $d_1 = 30$ mm, $d_2 = 38$ mm, $d_3 = 65$ mm.

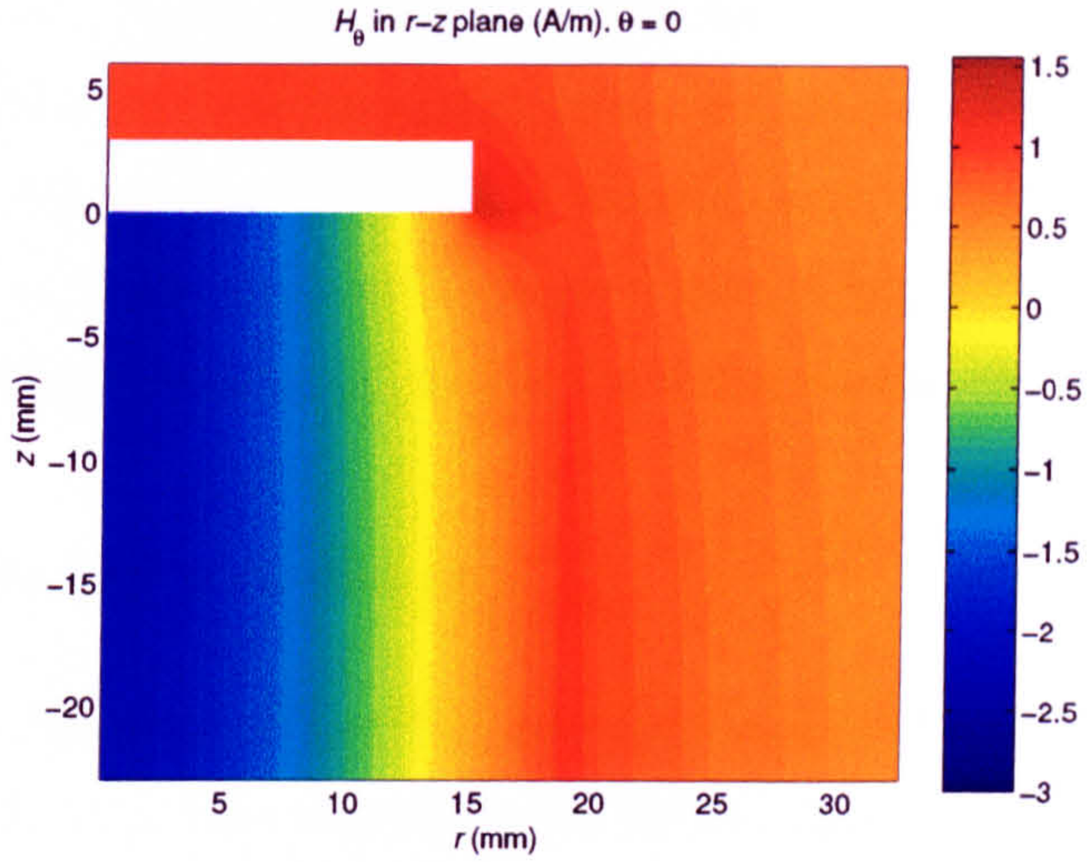

Figure 4.44: Angular magnetic field of the $\mathrm{HE}_{11\delta}$ mode for $h_C = 3$ mm. $h_A = 23$ mm, $h_B = 3$ mm, $d_1 = 30$ mm, $d_2 = 38$ mm, $d_3 = 65$ mm.

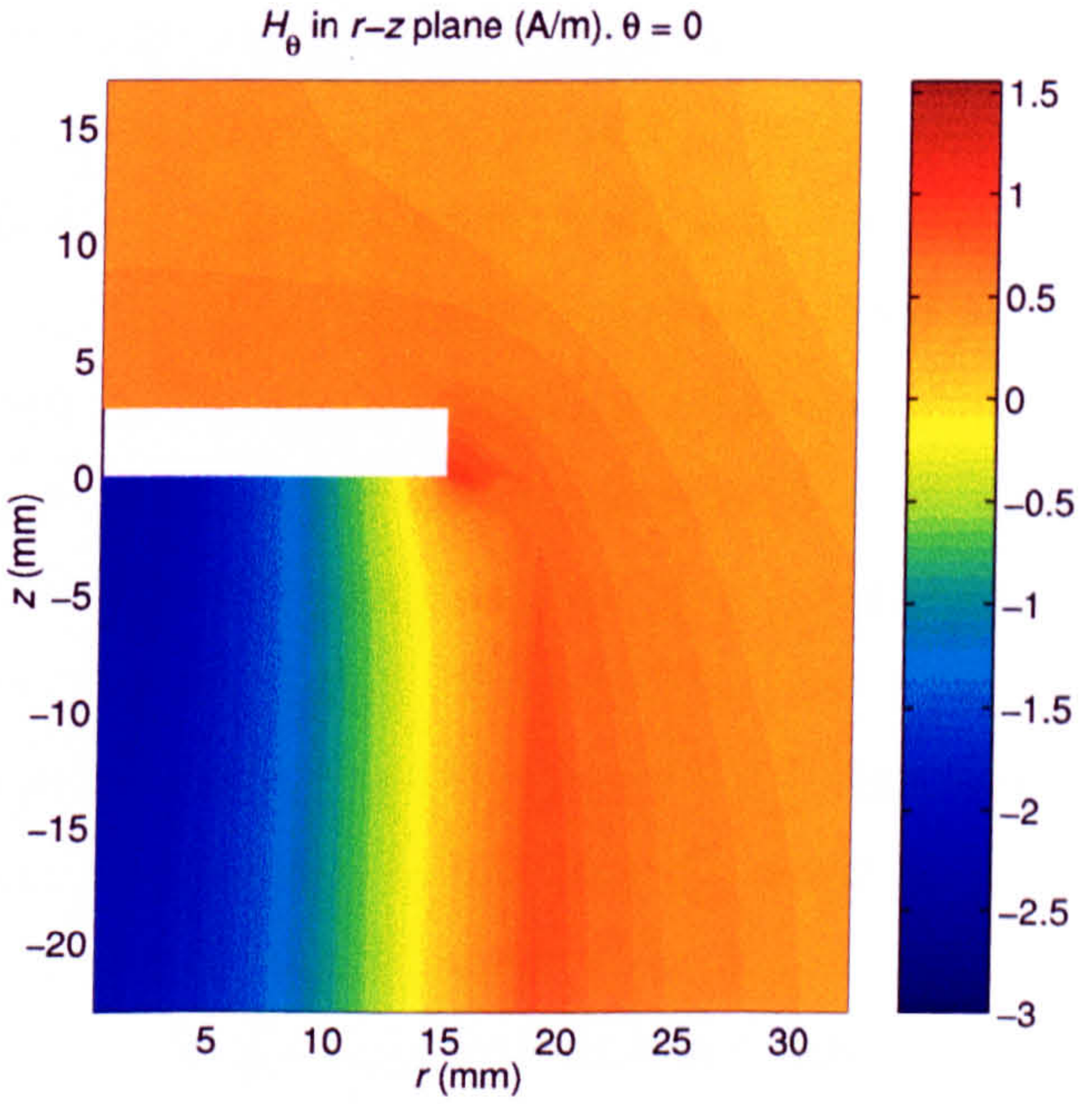

Figure 4.45: Angular magnetic field of the $\mathrm{HE}_{11\delta}$ mode for $h_C = 14$ mm. $h_A = 23$ mm, $h_B = 3$ mm, $d_1 = 30$ mm, $d_2 = 38$ mm, $d_3 = 65$ mm.

in region A improves. In region B, it stays very large, while in region C, it decreases as the corresponding surface area expands with h_C.

The conclusion is very similar to that for d_3: the resonant frequency of the $HE_{11\delta}$ mode decreases and its Q_u is improved by ensuring that the gap between the metal disc and cavity lid is not too small. As previously, a gap between 10 and 15 mm significantly reduces the losses, created in the cavity lid and the disc top.

4.2 $HE_{21\delta}$ mode variations

As expected, the variations of the $HE_{21\delta}$ mode in Fig. 4.2-4.7 are very similar to those of the $HE_{11\delta}$ mode. The separation between the two modes stays in the majority of cases between 500 and 550 MHz as, for example, when h_B or h_A are varied. As far as h_C is concerned, reducing the gap to 1 mm does reduce the separation to 400 MHz as shown in Fig. 4.7. By opposition, the $HE_{11\delta}$ mode is pushed down slightly further in frequency than the $HE_{21\delta}$ mode as d_1 is increased in Fig. 4.5. This is explained by the fact that the proportion of transversal fields in the dielectric in the absence of a metal disc is smaller in the case of the $HE_{21\delta}$ mode: 17.3% of the total electric energy is in the dielectric region instead of 35.8%. Finally, the total energy storage in the dielectric region is greater for the $HE_{21\delta}$ mode than for the $HE_{11\delta}$ mode: 98.7% for the electric energy instead of 97.6% and 74.5% for the magnetic energy instead of 66.5% in the case of the test cavity. As a result, as d_2 is decreased, the separation between the two modes improves, from 400 to 670 MHz for dielectric resonators of diameter 55 and 30 mm respectively. For the same reason, reducing the gap between the dielectric region and the cavity perimeters initially reduces the separation between the two modes. But when the gap is smaller than 4 mm, the resonant frequency of the $HE_{21\delta}$ mode increases faster than that of the $HE_{11\delta}$ mode, slightly improving the separation to 580 MHz. To conclude, the $HE_{21\delta}$ mode is not prone to any fast variation relative to the $HE_{11\delta}$ mode. As a result, it should not prove too restrictive when optimising the resonator dimensions.

4.3 $EH_{11\delta+1}$ mode variations

The $EH_{11\delta+1}$ variations are more difficult to compare to those of the two other hybrid modes as their field patterns are significantly different. As for the $HE_{11\delta}$ and $HE_{21\delta}$

modes, the thickness of the metal disc has extremely little effect on the $EH_{11\delta+1}$ mode resonant frequency. As far as the cavity height and diameter are concerned, the $EH_{11\delta+1}$ mode varies in the same direction, but by a smaller amount than the two other hybrid modes, deteriorating the spurious separation of smaller cavities. Indeed, in the case of the test cavity, 99.34% of the electric energy and 92.26% of the magnetic energy of the $EH_{11\delta+1}$ mode are concentrated within the dielectric. Also, the fields are less prone to expand into the air regions of the structures. Looking at the electric fields of the $EH_{11\delta+1}$ mode in the dielectric region in Figs. 4.46 and 4.47, one can observe that the fields terminating on the two parallel metal planes sandwiching the resonator quickly curve to cross the resonator radially. The sign of the radial fields are then of opposite sign to those surrounding the edge of the disc and extending in the air region in the case of the $HE_{11\delta}$ and $HE_{21\delta}$ modes.

As for the $HE_{11\delta}$ mode, the metal disc terminates the electric fields of the $EH_{11\delta+1}$ mode and restricts the longitudinal variation of its fields within the dielectric. With no metal disc, 96.70% and 93.25% of the electric and magnetic energies respectively are concentrated within the dielectric region. In the case of the $HE_{11\delta}$ mode, these values actually decreased from 98.58% and 73.17% to 97.60% and 66.52%. This explains why the effect of increasing d_1 is much more important on the resonant

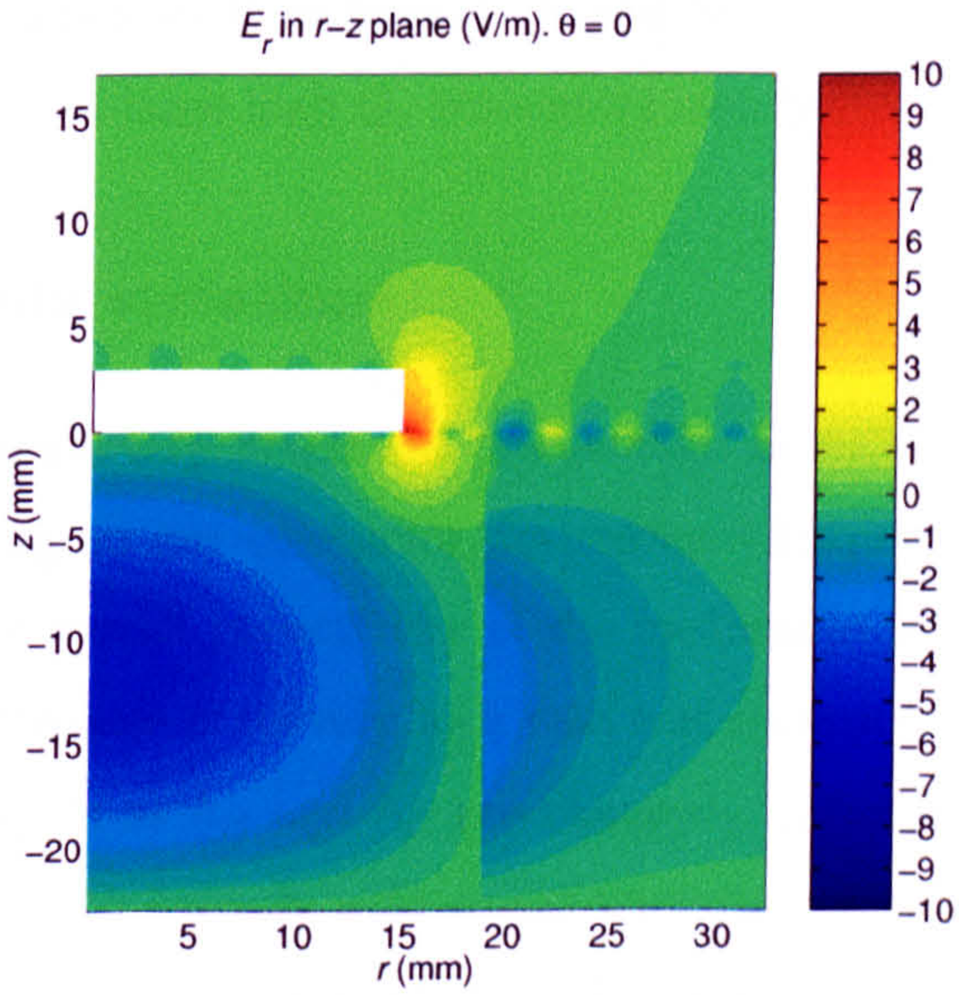

Figure 4.46: Radial electric field of the $EH_{11\delta+1}$ mode for the test cavity. h_A = 23 mm, $h_B = 3$ mm, $h_C = 14$ mm, $d_1 = 30$ mm, $d_2 = 38$ mm, $d_3 = 65$ mm.

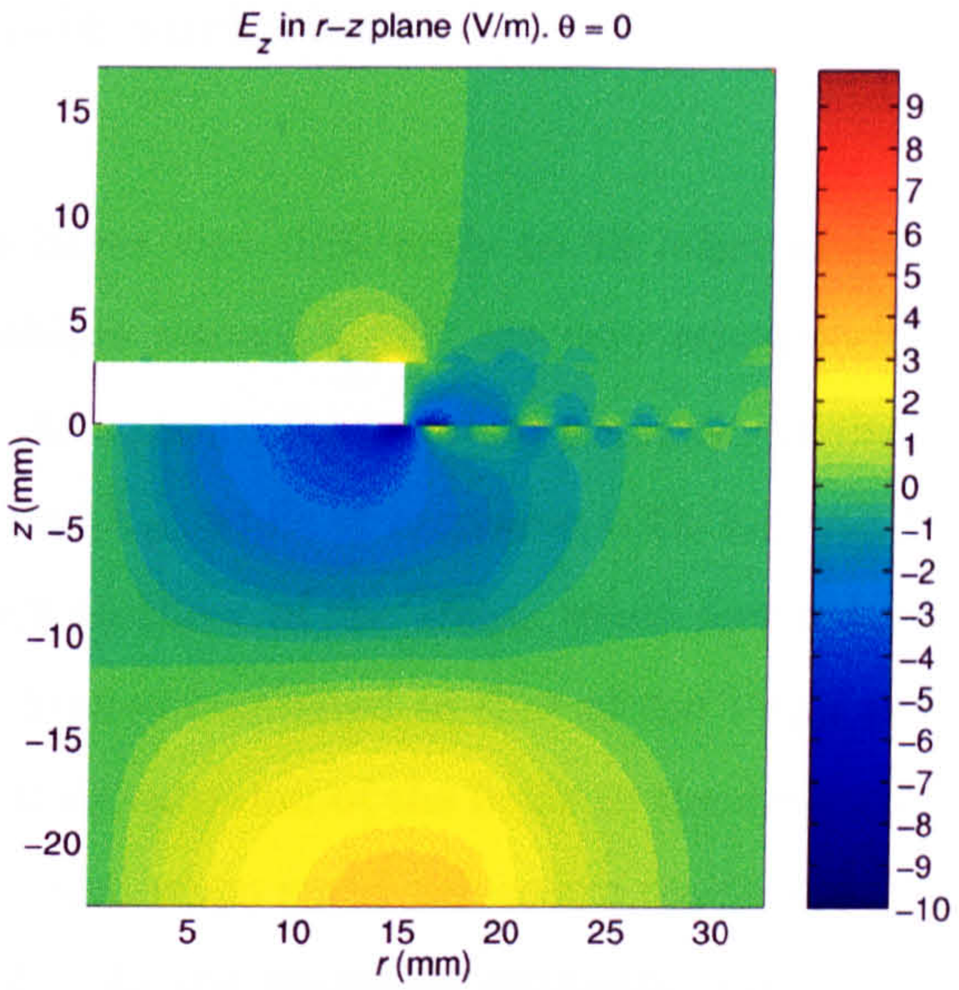

Figure 4.47: Axial electric field of the $\mathrm{EH}_{11\delta+1}$ mode for the test cavity. h_A = 23 mm, $h_B = 3$ mm, $h_C = 14$ mm, $d_1 = 30$ mm, $d_2 = 38$ mm, $d_3 = 65$ mm.

frequency of the $\mathrm{HE}_{11\delta}$ mode than on that of the $\mathrm{EH}_{11\delta+1}$ mode. Finally, with a full cosine variation along the longitudinal axis, the $\mathrm{EH}_{11\delta+1}$ mode is very dependent on h_A, very much like the $\mathrm{TE}_{01\delta}$ mode, which has a full sine variation. h_A is then the parameter which will have to be controlled to ensure that the degradation that the $\mathrm{EH}_{11\delta+1}$ mode causes to F_r is limited. It can be foreseen that it will limit the spurious performance of large high Q_u resonators mainly.

4.4 $\mathrm{TE}_{01\delta}$ mode variations

The $\mathrm{TE}_{01\delta}$ variations are very simple and predictable. Being a H mode, with no electric fields terminating on any conductor, its resonant frequency decreases as soon as the volume or the overall permittivity of the medium in which its fields are distributed increases. Because of its very high field concentration within the dielectric, variations are negligible as h_B and h_C are changed. Increasing h_A decreases the resonant frequency, which severely reduces the separation with the $\mathrm{HE}_{11\delta}$ mode, the latter moving in the direction opposite to the $\mathrm{TE}_{01\delta}$ mode. Like the $\mathrm{HE}_{11\delta}$ mode, the $\mathrm{TE}_{01\delta}$ mode resonant frequency also decreases with larger d_2 and d_3, but increases with d_1 and is the only mode to do so, as the fields are then forced further down into the dielectric, until the disc completely covers the dielectric cylinder.

4.5 $TM_{01\delta}$ mode variations

The $TM_{01\delta}$ mode behaves very differently to all other modes. Its fields, like those of the dielectric combline resonator [80], are very reminiscent to those of the metal combline resonator. As a result, the resonant frequency of the $TM_{01\delta}$ mode decreases with increasing h_A and h_B, while it increases with h_C. All three variations are in the opposite direction to those of the $HE_{11\delta}$ mode and reduce the separation. The variation with h_A is limited compared to that of the $TE_{01\delta}$ and $EH_{11\delta+1}$ modes, due to the small longitudinal variation of the fields in the dielectric. However, the variation with h_C is very rapid when small values are reached and the capacitive loading increases dramatically. As the resonator geometry tends towards a waveguide resonator, there will always be value for h_C so that the $HE_{11\delta}$ and $TM_{01\delta}$ modes cross over, whatever the cross section of the resonator.

As d_1 tends towards d_3 in Fig. 4.5, the loading also increases, but less significantly than for h_C, due to the smaller surface area involved. The effect is less, but still important, when the cavity diameter is more than doubled (see Fig. 4.26). The same loading is visible in Fig. 4.6 as d_3 is reduced for a constant d_1, for gaps between disc and cavity smaller than about 15 mm. For larger gaps, another effect predominates: similarly to all the other modes, reducing the cavity diameter constraints the fields within a smaller volume. As a fairly large proportion of electric energy is stored in the air region surrounding the dielectric (9.09% in the case of the $TM_{01\delta}$ compared to less than 1.5% for all other modes in the test cavity), the variation is more important.

Finally, the variation with d_2 shows a region of slower decrease of the resonant frequency, when the dielectric resonator diameter is slightly smaller than that of the metal disc. This effect is not explained.

To conclude, the separation of the $TM_{01\delta}$ mode degrades rapidly when the cavity becomes close to the metal disc. As a result, it will limit the spurious performance of the smaller, lower Q_u resonators.

4.6 Geometry optimisation for spurious separation

4.6.1 Procedure

In this section, a range of resonators is optimised with a view to give a general understanding of the spurious separation obtainable by the geometry studied in this chapter. The best spurious separation F_r obtainable will depend on the volume of the resonator. As a result, an attempt is made to highlight the trends followed by the best achievable F_r as the cavity volume is varied. The variations of F_r, deduced from the frequency plots Figs. 4.2 to 4.7, are given in Figs. 4.48 to 4.52. These show the spurious behaviour as each variable of the geometry is changed from its value in the test cavity. However, these plots do not cover the full range of resonator geometries and a more complete study is necessary. In order to simplify the problem, the number of variables defining the resonator geometry is reduced. To start with, there are seven variables: d_1, d_2, d_3, h_A, h_B, h_C and ε_r. Let us restrict the study by setting the latter to 44. Also, as Fig. 4.49 shows that F_r is very insensitive to the metal disc height, h_B can be kept constant and equal to 1 mm. Moreover, it was decided to keep constant the diameter of the dielectric resonator, decreasing the number of variables to 4. Indeed, it was clear in the previous section that the resonator frequency of the $HE_{11\delta}$ mode is primarily dependent on d_2. As a result, its variations are expected to be limited as all parameters other than the resonator diameter are varied.

The study is made at approximately 900 MHz. The resonator diameter d_2 is set to 38 mm. Two cavity volumes are considered: 125 and 75 cm^3. It would have been desirable to widen the study to a larger range of cavity volumes. However, the computation time necessary for each optimisation made it impractical to do so with the current the mode-matching program. Also, it is believed that the general trends are still shown and that the two examples presented would cover geometries suitable for a wide range of requirements. For each volume, cavity diameter and height are linked, reducing the number of variables to 3. They are d_3/h_C, d_1 and h_A. As the latter is the main parameter defining the Q_u of the resonator, it was felt that a separate optimisation of F_r for different values of h_A would offer some valuable extra information. For three values of h_A (10, 15 and 20 mm), the two remaining variables are optimised for best F_r.

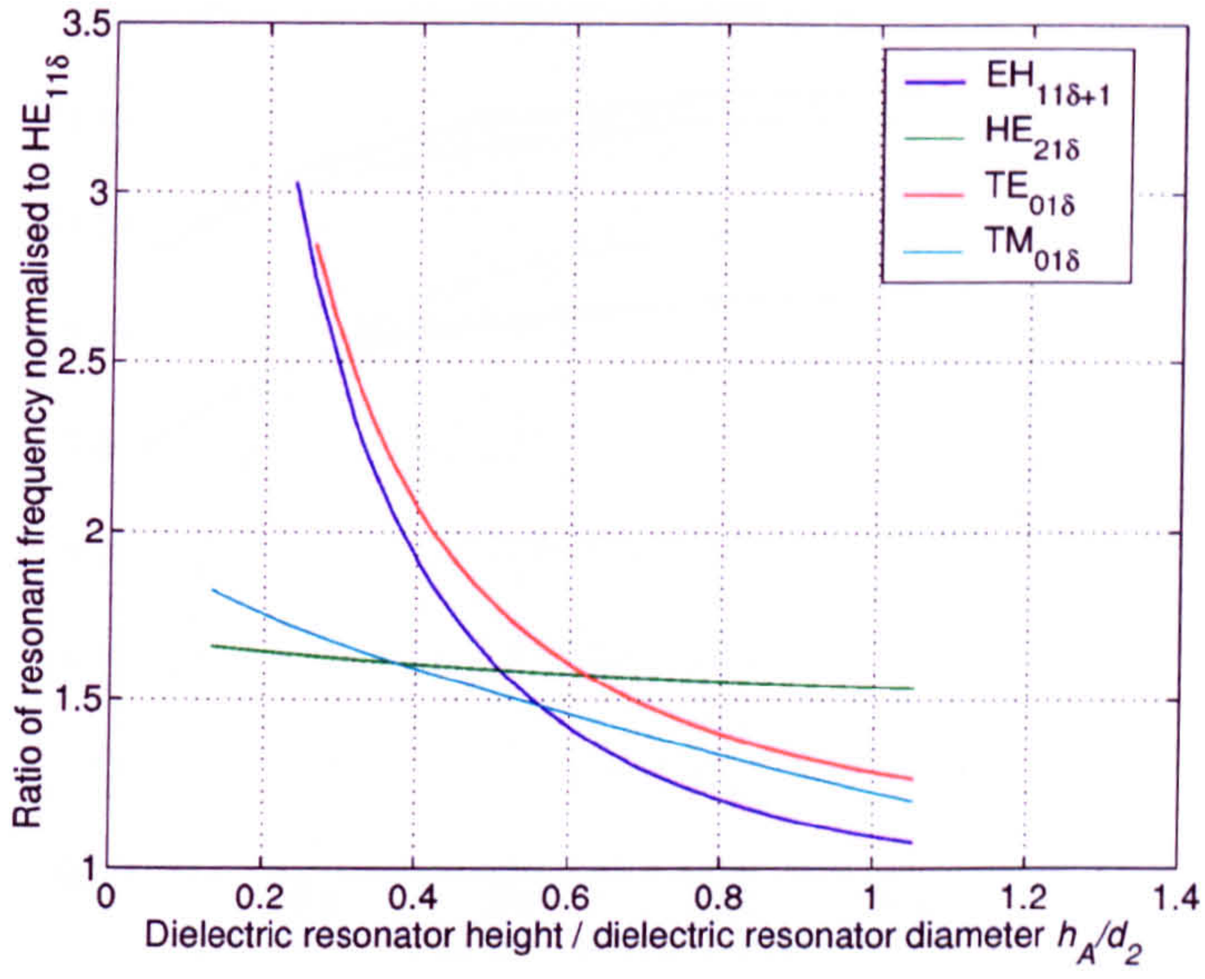

Figure 4.48: Variations of resonant frequencies normalised to that of the $HE_{11\delta}$ mode with h_A/d_2. $h_B/d_2 = 0.079$, $h_C/d_2 = 0.368$, $d_1/d_2 = 0.789$, $d_3/d_2 = 1.71$.

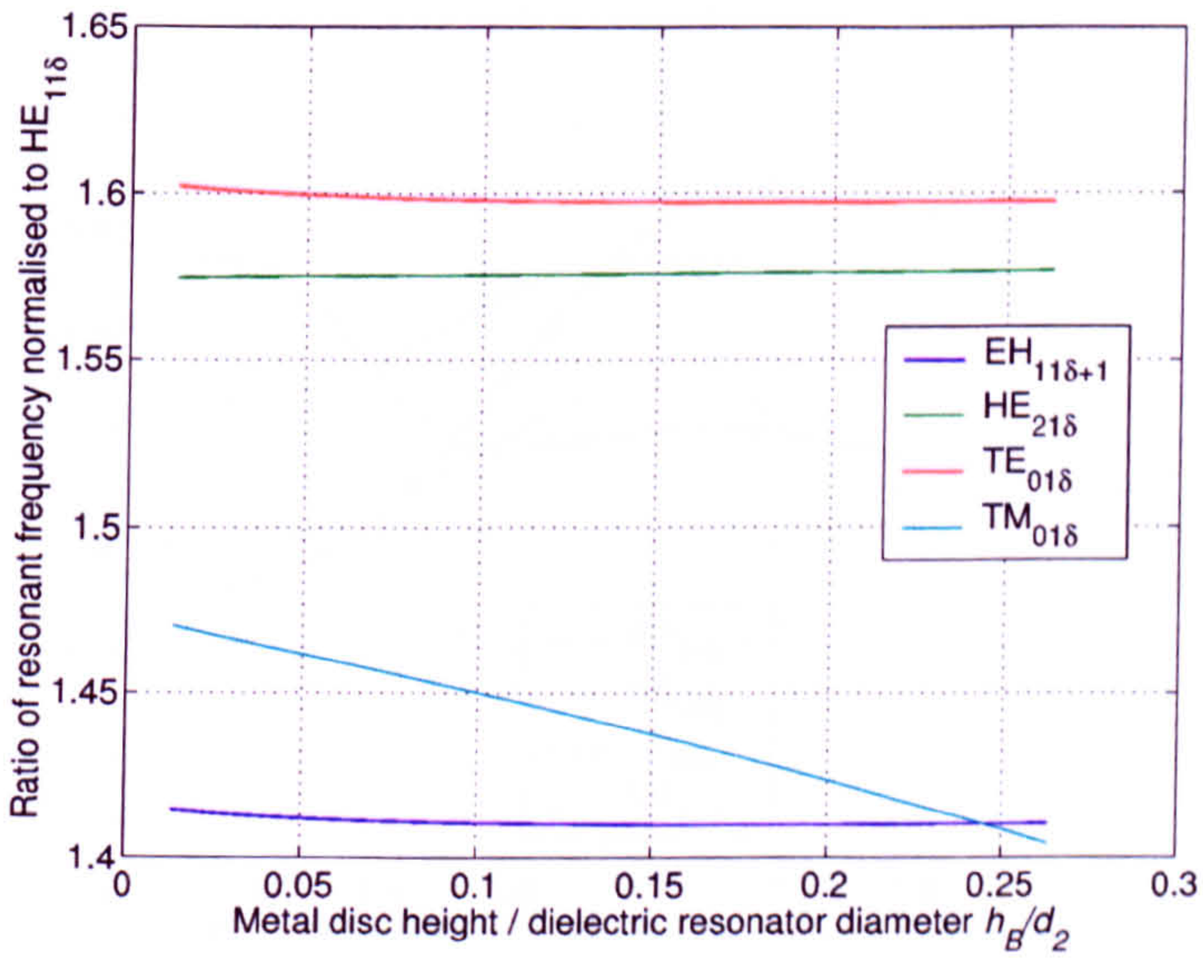

Figure 4.49: Variations of resonant frequencies normalised to that of the $HE_{11\delta}$ mode with h_B/d_2. $h_A/d_2 = 0.605$, $h_C/d_2 = 0.368$, $d_1/d_2 = 0.789$, $d_3/d_2 = 1.71$.

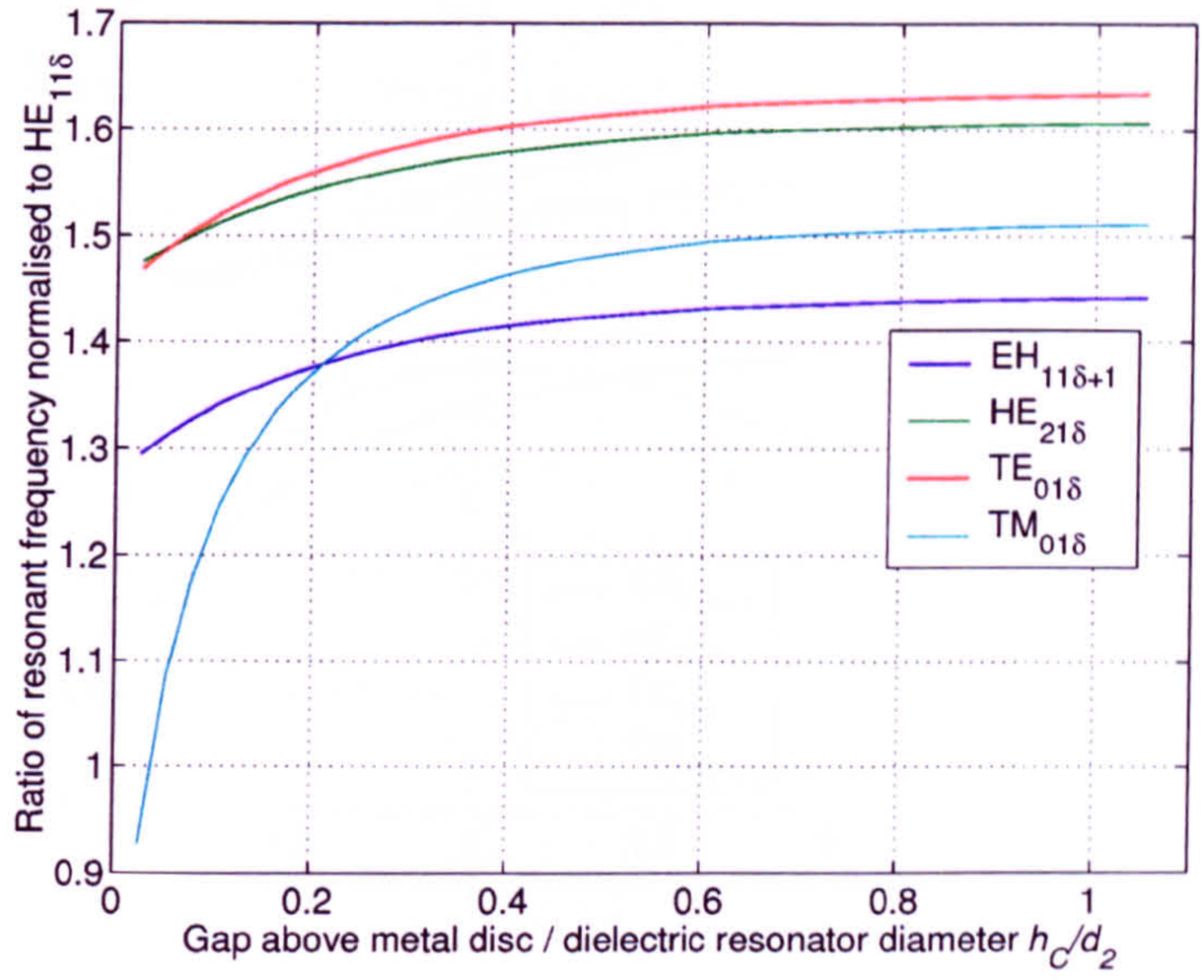

Figure 4.50: Variations of resonant frequencies normalised to that of the $HE_{11\delta}$ mode with h_C/d_2. $h_A/d_2 = 0.605$, $h_B/d_2 = 0.079$, $d_1/d_2 = 0.789$, $d_3/d_2 = 1.71$.

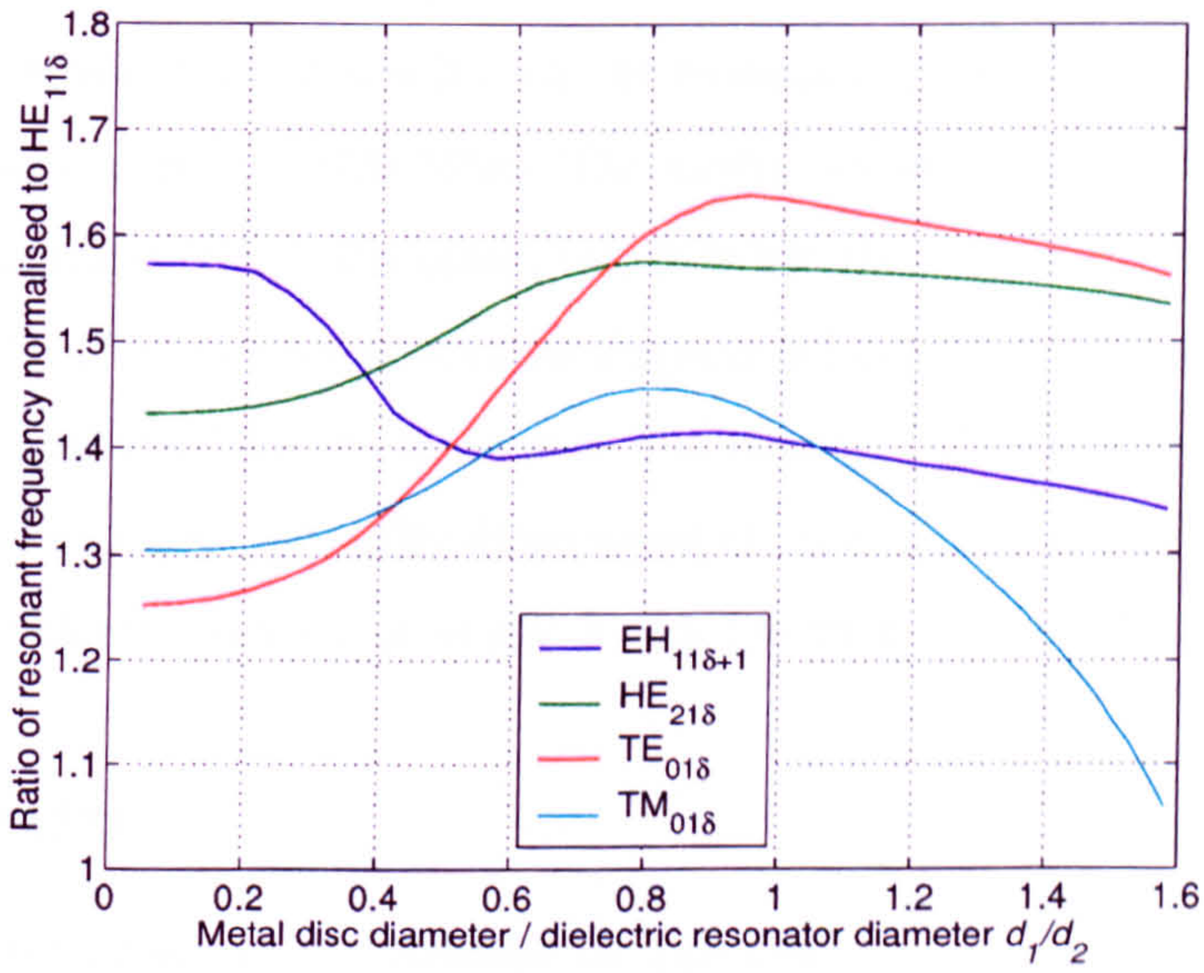

Figure 4.51: Variations of resonant frequencies normalised to that of the $HE_{11\delta}$ mode with d_1/d_2. $h_A/d_2 = 0.605$, $h_B/d_2 = 0.079$, $h_C/d_2 = 0.368$, $d_3/d_2 = 1.71$.

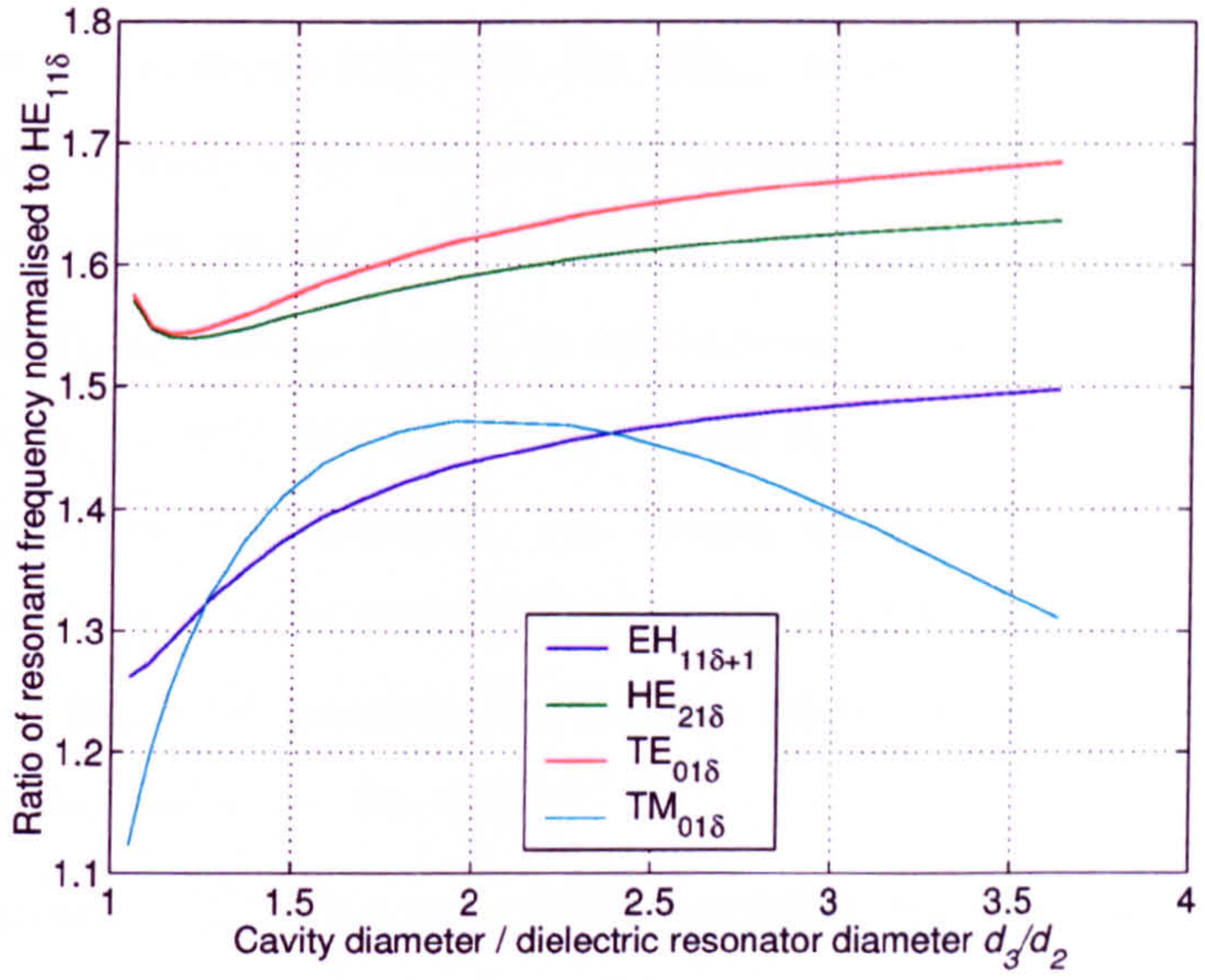

Figure 4.52: Variations of resonant frequencies normalised to that of the $HE_{11\delta}$ mode with d_3/d_2. $h_A/d_2 = 0.605$, $h_B/d_2 = 0.079$, $h_C/d_2 = 0.368$, $d_1/d_2 = 0.789$.

Even though d_2 is the main parameter determining the resonant frequency of the $HE_{11\delta}$ mode, the other variables also have a small effect. As a result, the final resonant frequency after each optimisation is not exactly 920 MHz. In order to better compare the different results, all the resonator dimensions are scaled for the $HE_{11\delta}$ mode to resonate at 920 MHz. The cavity volumes and dielectric resonator diameters then differ from each other, but it is felt that the general trends are still illustrated. The Q of the resonator of each optimised geometry is then calculated. In each case, the optimised cavity dimensions and resulting Q factors are also presented in a normalised manner. All cavity dimensions are normalised to d_2. The normalised values of the dielectric resonator height h_A/d_2 are then 0.263, 0.395 and 0.526.

4.6.2 Results

Results for nominal cavity volume of 125 cm^3

Table 4.5 presents the results for cavities with a volume of approximately 125 cm^3. Although all cavity volumes differ slightly when scaled, they all still have $\sqrt[3]{V}/d_2 = 1.11$.

In the case of $h_A/d_2 = 0.526$, the first spurious is the $TM_{01\delta}$ mode. From

Figs. 4.50 and 4.52, it can be seen that small values of d_3 or h_C both lead to a rapid decrease of its separation with the $HE_{11\delta}$ mode. The best F_r will happen for a cavity aspect ratio away from the two extremes. To find this optimum value, d_1/d_2 is first set to be 30/38 = 0.789. This is because, in Fig. 4.51, the separation between the $TM_{01\delta}$ and $HE_{11\delta}$ modes, as well as between the $HE_{21\delta}$ and $HE_{11\delta}$ modes, appears optimum around this value. d_3/h_C and d_1/d_2 are then optimised in turns until convergence for F_r is reached. The results are shown in the first column in Table 4.5. For h_A/d_2 = 0.395 and 0.263, the method is the same but this time with the $HE_{21\delta}$ mode as lowest spurious. Indeed, the behaviours of the $TM_{01\delta}$ and $HE_{21\delta}$ modes with d_3/h_C and d_1/d_2 are similar.

It can be noted that, for h_A/d_2 = 0.526 and 0.395, the converged geometries are very similar in terms of cross-sections, although the first spurious mode is actually a different mode in the two cases. For h_A/d_2 = 0.263 (third column of Table 4.5), the optimum values for spurious separation for d_1/d_2 and d_3/d_2 increase to 1.079 and 1.711 respectively. However, if d_1/d_2 is kept close to 0.8 as in the first two columns, then the best F_r is only slightly degraded to 1.656 and d_3/d_1 is reduced back to a value comparable to those of columns 1 and 2 (see fourth column). As a result, it can be concluded that, for cavities with $\sqrt[3]{V}/d_2$ = 1.11, d_1/d_2 and d_3/d_2 can be fixed to 0.8 and 1.6 respectively and lead to a F_r very close to optimum. Only h_C changes, to compensate for the change in h_A. From Fig. 4.52, it is expected that better separations are possible between the $HE_{11\delta}$ and $HE_{21\delta}$ modes for smaller values of d_3/d_2. Indeed, for h_A/d_2 = 0.263 and d_3/d_2 = 1.053, the ratio between the $HE_{11\delta}$ and $HE_{21\delta}$ modes is 1.077. However, as d_3 is decreased, so is the resonant frequency of the $TM_{01\delta}$ mode, which eventually becomes the first spurious and quickly deteriorates the separation.

In Table 4.5, it can be seen that, as h_A/d_2 is reduced, F_r improves at first rapidly and then more slowly. A study for h_A/d_2 = 0.132 showed very little improvement as the optimised F_r only increased to 1.678. This general trend can be understood by looking at Fig. 4.48. For values of h_A/d_2 above 0.37, the first spurious is the $TM_{01\delta}$ mode. For lower values of h_A/d_2, it is replaced by the $HE_{21\delta}$ mode. The separation of the latter with the $HE_{11\delta}$ mode improves less rapidly than that of the $TM_{01\delta}$ mode. It can be noted that, because the cavity volume in Table 4.5 is quite large, the variations of F_r in this table and in Fig. 4.48 are almost equal. The fact that

Table 4.5: *Details of geometries optimised with respect to F_r for different h_A/d_2. Nominal cavity volume:* 125 cm^3. $\sqrt[3]{V}/d_2 = 1.11$.

Normalised results				
h_A/d_2	0.526	0.395	0.263	0.263
d_1/d_2	0.829	0.816	1.079	0.789
d_3/d_2	1.658	1.605	1.711	1.632
h_C/d_2	0.503	0.705	0.702	0.800
F_r	1.542	1.630	1.662	1.656
First spurious mode	$TM_{01\delta}$	$HE_{21\delta}$	$HE_{21\delta}$	$HE_{21\delta}$
$\sqrt[3]{V}f$ (m×MHz)	44.85	43.75	41.86	42.93
$Q_c\ \delta/\lambda_0$	0.05474	0.04379	0.02844	0.03132
$Q_d\ \tan\delta$	1.027	1.026	1.030	1.020
Results scaled to 920 MHz				
Volume (cm^3)	115.8	107.5	94.2	101.6
d_2 (mm)	37.0	36.1	34.6	35.5
h_A (mm)	19.5	14.3	9.1	9.3
d_1 (mm)	30.7	29.5	37.3	28.0
d_3 (mm)	61.4	58.0	59.2	57.9
h_C (mm)	18.6	25.5	24.3	28.4
h_B (mm)	0.97	0.95	0.91	0.93
Q_c	8444.4	6754.6	4387.4	4831.7
Q_d	41,874	41,825	42,008	41,560
Q_u	7027.3	5815.4	3972.5	4328.5
Q_u/volume per mode (cm^{-3})	121.3	108.2	84.3	85.2

the cavity volume has to be kept constant for the F_r results in Table 4.5, unlike in Fig. 4.48, does not influence F_r considerably. Looking at the Q_u values in Table 4.5, it seems that, for a given volume, the crossover point between the two spurious modes will offer a F_r close to its maximum value for a limited drop in Q_u/volume.

Results for nominal cavity volume of 75 cm^3

For smaller cavities, as those presented in Table 4.6 ($\sqrt[3]{V}/d_2 = 0.90$), the $TM_{01\delta}$ mode is the first spurious mode for a larger range of h_A/d_2. For both $h_A/d_2 = 0.526$ and 0.395, its F_r can be optimised as previously with respect to cavity aspect ratio and disc diameter. In both cases, the optimum d_1/d_2 is 0.789. As h_A/d_2 is increased from 0.395 to 0.526, both d_3 and h_C decrease. In the case of $\sqrt[3]{V}/d_2 = 1.11$ (Table 4.5), only h_C decreased. It is assumed that this is because the effect of the loading of the $TM_{01\delta}$ mode to the cavity lid is limited for $\sqrt[3]{V}/d_2 = 1.11$. Both d_3 and h_C would decrease in Table 4.5 if h_A/d_2 became sufficiently large, i.e. above 0.526.

As h_A/d_2 is decreased from 0.526 to 0.395, F_r is improved, but not up to the value reached for the same h_A/d_2 in Table 4.5. However, the decrease in Q_u is again quite limited. In fact, the Q_u/volume ratio is larger for the thinner resonator, indicating that the proximity of the cavity to the resonator, or to the metal disc, was limiting the Q_u significantly. By decreasing h_A/d_2 to smaller values still, e.g. 0.263, F_r can be improved further, up to values close to those reached in the larger cavities. As the aspect ratio of the cavity is changed in order to find the best F_r, it is found that the best separation happens, for most values of d_1/d_2, at the cross-over between the $HE_{21\delta}$ and $TM_{01\delta}$ modes. Indeed, the separation with the former decreases with increasing d_3/h_C while that of the latter increases. Because of this, the optimum geometry cannot be found by successive optimisations of cavity aspect ratio and disc diameter. Rather, d_3/h_C is repeatedly optimised for various d_1/d_2. The optimum F_r is located once again at $d_1/d_2 = 0.789$ and is equal to 1.646 (case A of Table 4.6). The resulting cavity is tall and of small diameter. d_3/d_2 is in fact decreased as h_A/d_2 is decreased from 0.395 to 0.263, possibly because the separation with the $HE_{21\delta}$ mode is less sensitive to the proximity of the cavity side than that of the $TM_{01\delta}$ mode. However, the Q_u/volume is by then relatively low. By increasing d_3/d_2 slightly from its value in case A, the Q_u/volume can be improved significantly,

Table 4.6: *Details of geometries optimised with respect to F_r for different h_A/d_2. Nominal cavity volume:* 75 cm^3. $\sqrt[3]{V}/d_2 = 0.90$.

Normalised results					
h_A/d_2	0.526	0.395	0.263 (A)	0.263 (B)	0.263 (C)
d_1/d_2	0.789	0.789	0.789	0.789	1.053
d_3/d_2	1.368	1.447	1.211	1.368	1.658
h_C/d_2	0.377	0.410	0.898	0.640	0.344
F_r	1.447	1.573	1.646	1.642	1.628
First spurious mode(s)	$TM_{01\delta}$	$TM_{01\delta}$	$TM_{01\delta}$ and $HE_{21\delta}$	$HE_{21\delta}$	$TM_{01\delta}$ and $HE_{21\delta}$
$\sqrt[3]{V}f$ (m×MHz)	40.20	38.49	38.22	37.26	36.14
Q_c δ/λ_0	0.04923	0.04245	0.02898	0.03054	0.02861
Q_d $\tan\delta$	0.9109	0.9878	1.0050	1.0205	1.1225
Results scaled to 920 MHz					
Volume (cm^3)	83.40	73.25	71.70	66.43	60.62
d_2 (mm)	39.4	37.7	37.4	36.5	35.4
h_A (mm)	20.7	14.9	9.8	9.6	9.3
d_1 (mm)	31.1	29.8	29.5	28.8	37.3
d_3 (mm)	53.9	54.6	45.3	49.9	58.7
h_C (mm)	14.8	15.4	33.6	23.3	12.2
h_B (mm)	1.04	0.99	0.99	0.96	0.93
Q_c	7594.9	6548.3	4470.9	4710.6	4413.6
Q_d	73,134	40,266	40,969	41,600	45,759
Q_u	6305.3	5632.3	4031.0	4231.5	4025.3
Q_u/volume per mode (cm^{-3})	151.2	153.8	112.4	127.4	132.8

while the degradation of F_r is limited (case B). It can be noted that using a larger d_1/d_2 as in Table 4.5 is not optimum in the case of this smaller cavity volume. Choosing $d_1/d_2 = 1.05$ (case C), F_r is restricted to 1.628, once again because of the increased loading of the $TM_{01\delta}$ mode. However, the Q_u/volume is better than that of case B.

Comparison of 125 cm^3 and 75 cm^3 results

Comparing the results of Tables 4.5 and 4.6, some conclusions can be drawn. The best F_r obtainable with the dual-mode conductor-loaded dielectric resonator is around 1.67. d_1/d_2 is not critical, and in all cases 0.8 is close to optimum. The optimum choice of the d_3/d_2 is more complex. It will only stay relatively constant with respect to h_A/d_2 provided the cavity volume is large enough and the dielectric resonator height small enough. Maximum F_r's are achieved with ratios of 1.6 for $\sqrt[3]{V}/d_2 = 1.11$ and between 1.2 and 1.4 for $\sqrt[3]{V}/d_2 = 0.90$. A wider study would be necessary to check that the behaviour of the d_1/d_2 and d_3/d_2 ratios is similar for smaller and larger values of $\sqrt[3]{V}/d_2$.

A F_r higher than 1.64 can be reached at least for a range of volumes between 66 and 104 cm^3 at 920 MHz. In these two volumes, a F_r of 1.64 is achieved with $h_A/d_2 = 0.26$ and 0.34 respectively. In the latter case, Q_u's of around 5400 are then achievable. In the former, they are restricted to 4200. If the lower value of 1.54 for F_r is sufficient for a filter application, then the respective maximum Q_u's become 7000 in 115 cm^3 and 5850 in 76 cm^3. There is then a trade-off between good spurious and good Q_u/volume. More simulations would be necessary to fully evaluate the performance of the resonator for larger Q applications. However, the results available here show that it will be necessary to use larger volumes still to combine Q_u's comparable to that of the test cavity (7850 with $Nb = 20$) and maximum F_r. The Q_u/volume of the resonator will then be less than 90 cm^{-3} per mode. However, for many applications, obtaining the maximum Q_u from the geometry will be critical and the spurious separation can be traded-off. The next section presents a study of the optimum geometry for Q_u and its impact on F_r.

4.7 Geometry optimisation for Q_u

Finding the geometry that gives the maximum Q_u in a given volume also requires optimising all the resonator dimensions. The figures in Appendix G present the variations of the normalised Q_d tan δ and Q_c δ/λ_0 deduced from the plots in Section 4.1. A study is realised at 920 MHz, initially for two cavity volumes: 75 and 125 cm^3. h_B is set to 3 mm, which is small enough not to use the cavity space inefficiently, as Fig. G.2 indicates little improvement as h_B is increased. It is also thick enough to be reliably manufactured and to realise the very good contact needed with the ceramic resonator. Although Fig. G.4 points at a ratio of 0.4 for d_1/d_2 for maximum Q_c, a value of 0.8 was chosen. This is because the spurious separation proved optimum with this ratio and that a much smaller ratio would tend towards the case of a dielectric resonator sitting on the cavity floor. Some results are already available for this geometry, which is a limiting case of the shielded dielectric cylinder resonator on a grounded substrate [175, 174, 86]. If a particular application calls for a smaller metal disc diameter, the study which follows can be repeated. Given these two constraints, the absolute best Q_u is found by optimising h_A, h_C and d_3. The ratios h_C/h_A, h_A/d_3 and h_C/d_3 are optimised in turn, while each time d_2 is adjusted to retain a frequency of 920 MHz. Because Q_d is much larger than Q_c, the difference between the optimum dimensions for Q_c and Q_u is smaller than the steps, of about 1 mm, used for converging towards the final geometry. The optimisation is realised with $Nb = 10$, and the final quality factors are then calculated again with $Nb = 20$ for more precision. It was checked in several cases that the optimum ratios were the same for both values of Nb.

In the case of 125 cm^3, the maximum Q_u is 7,983 and is found for $h_A = 29.5$ mm and, noticeably, equal gaps of 10.4 mm above the disc (h_C) and around the dielectric resonator ($(d_3-d_2)/2$). If h_A is reduced to 10 mm, h_C is then larger than $(d_3-d_2)/2$, but only by 1.8 mm or 10%. In the case of 75 cm^3, the maximum Q_u is 5,988 and happens for h_A of 19 mm. h_C and $(d_3 - d_2)/2$ are 10 and 7.3 mm respectively. However, using the same value for h_A and equal gaps only drops the Q_u by 0.7%. As a result, it is felt that equal gaps can be used to simplify the study and still lead to values very close to the maximum achievable Q_u. This simplification might not be valid for cavity volumes much larger than 125 cm^3. As the cavity volume is

increased, the maximum Q_u happens for larger values of h_A. The loss in the cavity side wall then increases dramatically, as explained in Section 4.1.1, and $(d_3 - d_2)/2$ might become more critical. However, this will only happen for cavity volumes too large to offer a very attractive Q_u/volume as shown later in this section. In Fig. 4.53, Q_u is plotted against h_A for volumes between 50 and 150 cm^3 and equal gaps. The Q_u's initially increase almost linearly as in Fig. 4.12, before slowing down and finally decrease as the loss in the cavity walls becomes more important. The case of $h_A = 20$ mm in 50 cm^3 is not plotted because a resonant frequency as low as 920 MHz cannot be realised in such a small volume. In Table 4.7 the spurious separation of the geometries of Fig. 4.53 are given. They show the deterioration of F_r as the distances between the dielectric resonator and the cavity are reduced.

From the turning points in Fig. 4.53, the maximum Q_u's (Fig. 4.54) and the corresponding resonator heights and gaps' dimensions (Fig. 4.55) can be plotted against cavity volume. All have very similar variations, which is an almost linear increase slowing down as the cavity volume becomes large. Doubling the volume does not double the Q_u, which means that the Q_u/volume (Fig. 4.56) deteriorates for larger cavity volumes.

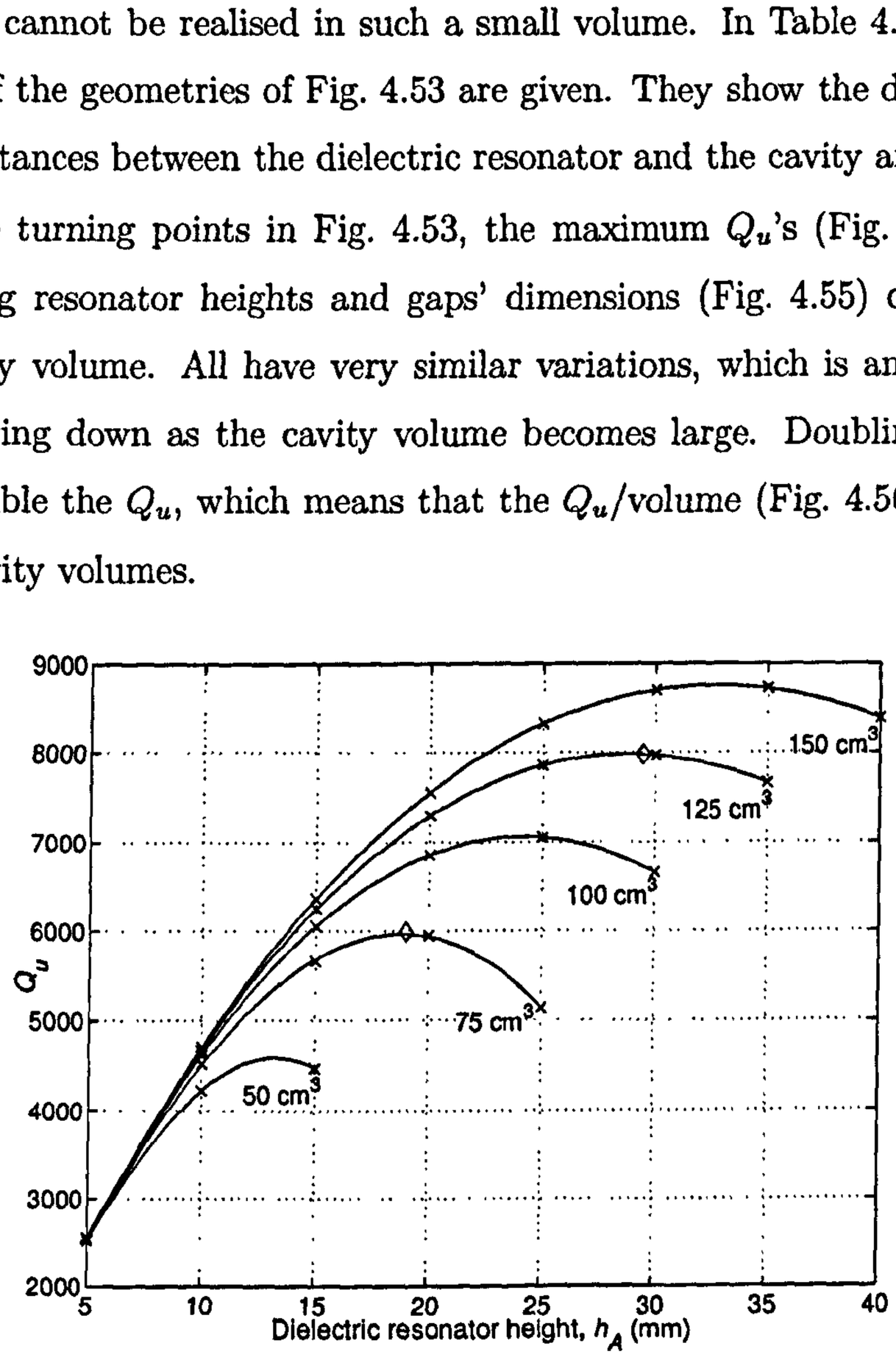

Figure 4.53: Variations of Q_u with h_A for different cavity volumes and equal gaps at 920 MHz. The two markers indicate the maximum Q_u (within the constraints imposed on the metal disc) for 75 and 125 cm^3.

Table 4.7: *F_r for the geometries in Fig. 4.53.*

h_A	Cavity volume (cm^3)				
(mm)	50	75	100	125	150
5	1.642 $HE_{21\delta}$	1.657 $HE_{21\delta}$	1.662 $HE_{21\delta}$	1.666 $HE_{21\delta}$	1.668 $HE_{21\delta}$
10	1.586 $HE_{21\delta}$	1.621 $HE_{21\delta}$	1.636 $HE_{21\delta}$	1.644 $HE_{21\delta}$	1.651 $HE_{21\delta}$
15	1.380 $TM_{01\delta}$	1.533 $TM_{01\delta}$	1.585 $TM_{01\delta}$	1.612 $TM_{01\delta}$	1.626 $HE_{21\delta}$
20		1.382 $TM_{01\delta}$	1.467 $TM_{01\delta}$	1.506 $TM_{01\delta}$	1.529 $TM_{01\delta}$
25		1.180 $TM_{01\delta}$	1.321 $EH_{11\delta+1}$	1.335 $EH_{11\delta+1}$	1.346 $EH_{11\delta+1}$
30			1.180 $EH_{11\delta+1}$	1.202 $EH_{11\delta+1}$	1.215 $EH_{11\delta+1}$
35				1.111 $EH_{11\delta+1}$	1.127 $EH_{11\delta+1}$
40					1.068 $EH_{11\delta+1}$

The spurious separations of the geometries with maximum Q_u for the different volumes are listed in Table 4.8. It can be seen that the maximum Q_u achievable in a given volume cannot be obtained at the same time as the maximum F_r, at least for cavity volumes well below 50 cm^3. In a 75 cm^3 cavity, h_A has to be decreased by about 9 mm, or 48% of its value for maximum Q_u. Assuming that the the best geometry for Q_u is closely approximated by using equal gaps h_C and $(d_3 - d_2)/2$, the degradation of the Q_u is then of 25%, from 5988 to 4500. In the case of a 125 cm^3 cavity, h_A is reduced by 16.5 mm, or 56% of h_A for maximum Q_u, and degrades the Q_u from 7980 to 5800, which represents a 27% decrease.

It is clear that the large cavities optimised for Q_u have the poorest spurious separation. However, as the first spurious is then the $EH_{11\delta+1}$ mode or the $TM_{01\delta}$ mode, one can trade-off a small percentage of the Q_u for a significant improvement in

Table 4.8: *F_r for the geometries for maximum Q_u.*

	Cavity volume (cm^3)				
	50	75	100	125	150
F_r	1.474	1.421	1.352	1.233	1.166
	$TM_{01\delta}$	$TM_{01\delta}$	$EH_{11\delta+1}$	$EH_{11\delta+1}$	$EH_{11\delta+1}$

F_r. This is simply done by choosing a dielectric resonator height up to 15% smaller than the optimum height for a given cavity volume, given in Fig. 4.55. Taking the example of a 125 cm^3 cavity, reducing h_A from 29.5 mm to 25 mm improves F_r from 1.233 to 1.335, but only degrades the Q_u by 1.5%. After having chosen h_A, one may also improve F_r slightly by readjusting h_C and $(d_3 - d_2)/2$. Comparing the data for a 15 mm tall dielectric resonator in a 75 cm^3 cavity, the geometry for best F_r in Table 4.6 has a F_r of 1.573 compared to 1.533 for the geometry with equal gaps (see Table 4.7). However, their Q_u's are very close.

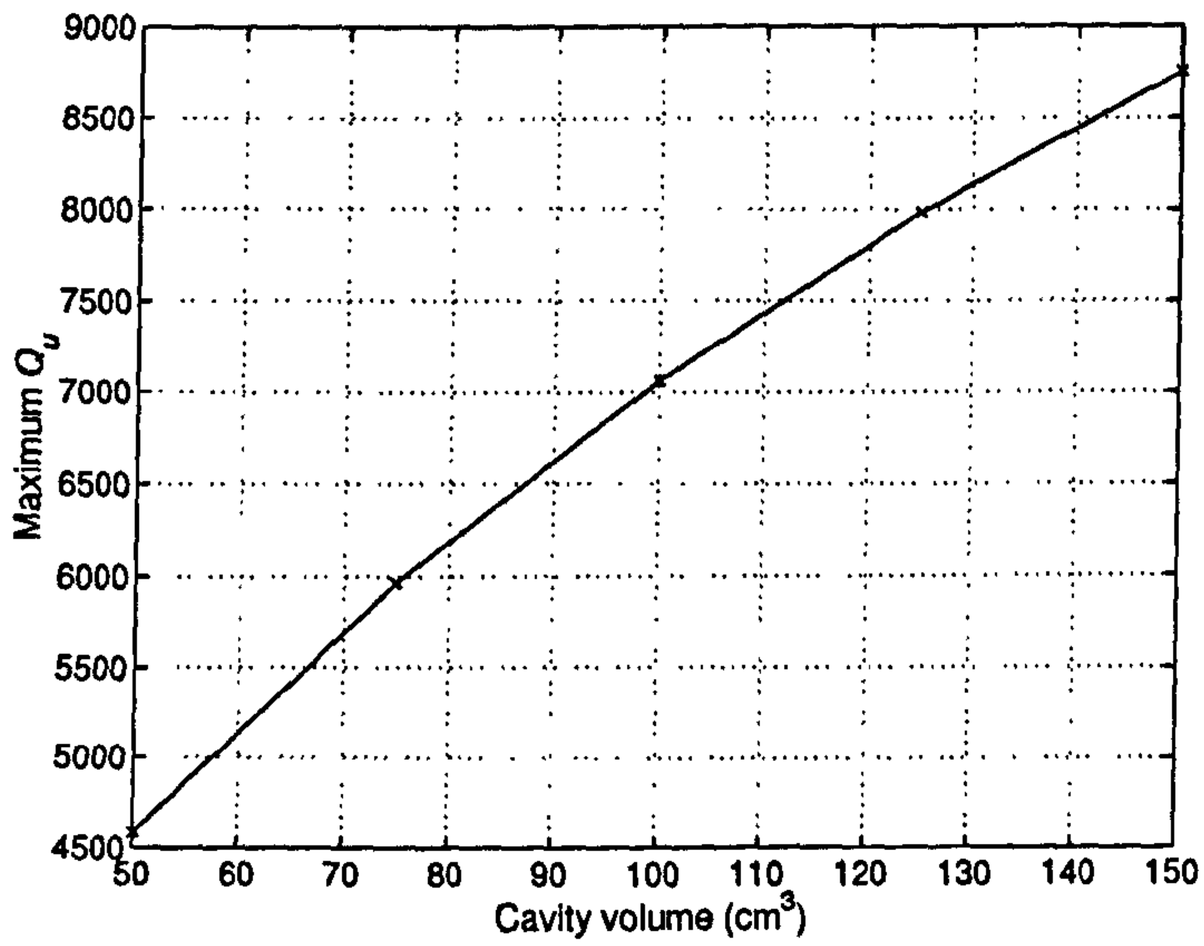

Figure 4.54: Variations of Q_u with cavity volume for the maximum Q_u geometries at 920 MHz.

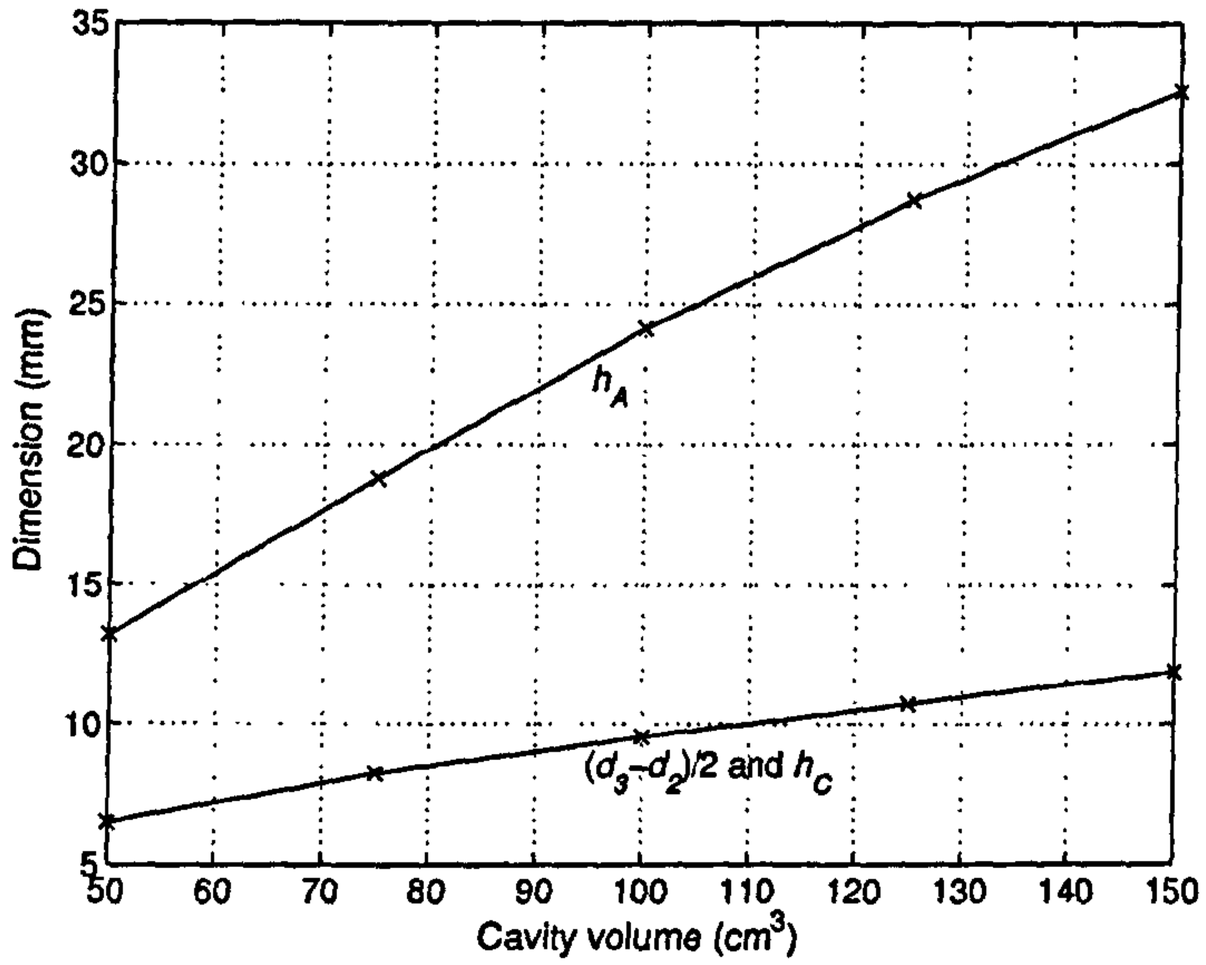

Figure 4.55: Variations of h_A and $(d_3 - d_2)/2$ with cavity volume for the maximum Q_u geometries at 920 MHz.

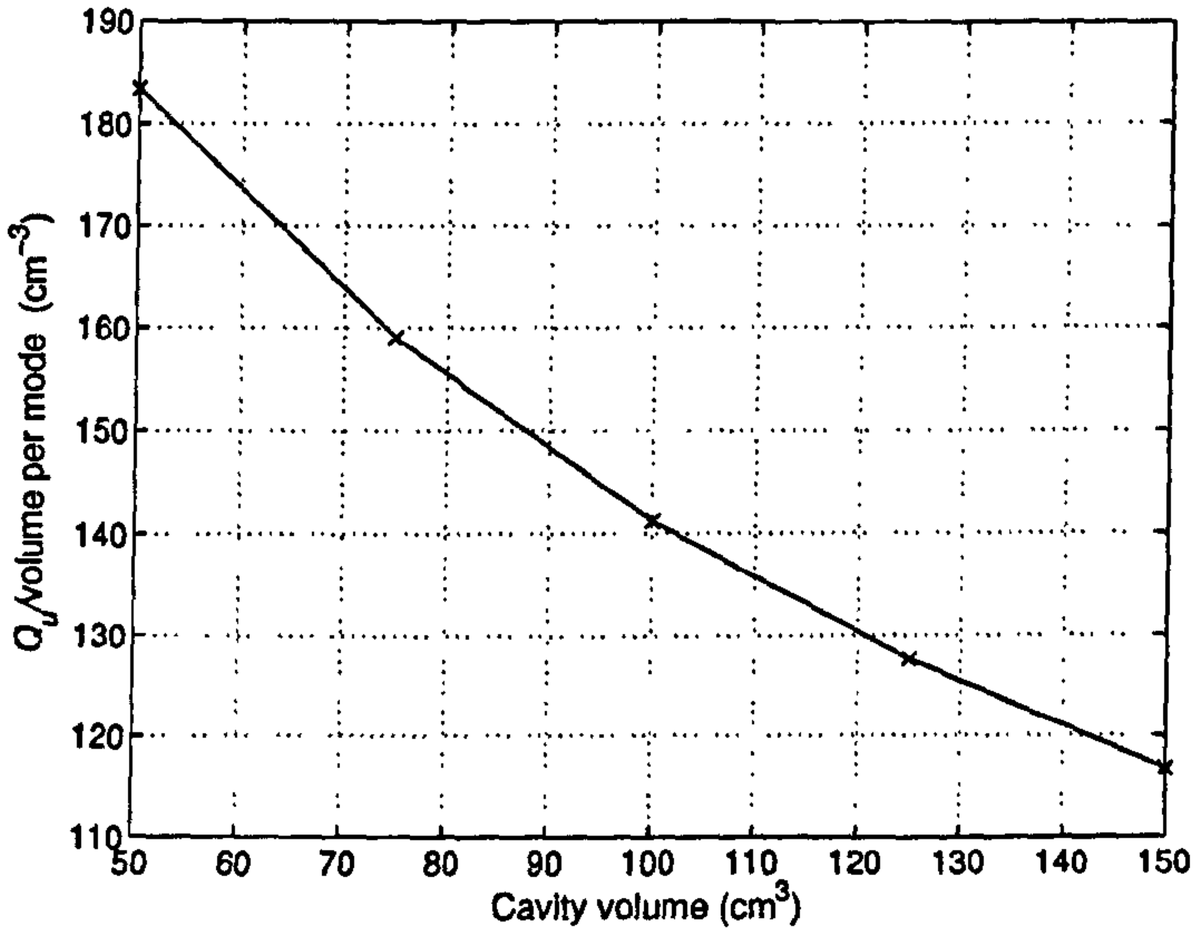

Figure 4.56: Variations of Q_u/volume per mode with cavity volume for the maximum Q_u geometries at 920 MHz.

4.8 Conclusion

In this chapter, the dual-mode conductor-loaded DR, using the $HE_{11\delta}$ mode, was studied using the mode-matching program developed in Chapter 3. All the parameters of the resonator geometry were varied in order to understand their effect on the resonant frequency, Q and field distributions of the $HE_{11\delta}$ mode. It was verified that the unloaded Q is always mainly determined by conductor losses rather than dielectric losses. It also appears that the resonant frequency and Q_u are primarily governed by the dimensions of the dielectric cylinder. Changing its height has a direct effect on the Q_u while retaining the resonant frequency relatively constant. The latter is instead strongly affected by the diameter of the dielectric resonator. The role of the metal disc, which is to improve the spurious separation, is entirely determined by its diameter. Neither the resonant frequencies of the first modes, nor the Q_u of the $HE_{11\delta}$ mode are strongly influenced by its thickness. The diameter of the disc also reduces the resonant frequency of the $HE_{11\delta}$ mode, until it reaches a diameter comparable to that of the dielectric resonator. Unfortunately, the Q_u is also degraded. Finally, increasing the cavity diameter to create an adequate gap around the dielectric cylinder ensures that the Q_u is not significantly degraded. This also decreases the resonant frequency of the $HE_{11\delta}$ mode. The effect of the cavity lid is similar on both frequency and Q_u.

The resonant frequencies and field distributions of the first four spurious modes were also investigated and a range of cavities were optimised for maximum spurious separation using the mode matching program. The best separation achievable is approximately 1.6 and happens for small dielectric resonator heights in large enough cavities, where the first spurious is the $HE_{21\delta}$ mode. As the dielectric cylinder height is increased, the separation of the $HE_{11\delta}$ mode with two other spurious modes degrades, thus imposing a trade-off between Q_u and spurious separation. The $EH_{11\delta+1}$ mode is likely to be the lowest spurious in the case of large high Q_u cavities, while the $TM_{01\delta}$ mode is the lowest in the case of smaller cavities. If the separation with the $TM_{01\delta}$ mode is limited, care has to be taken when designing the frequency and coupling tuning mechanisms which will be inserted in the cavity as this mode is easily capacitively loaded and its frequency could drift down further.

The resonator was also optimised for best Q_u for a range of cavity volumes.

As expected, the spurious separation of the resulting geometries were significantly degraded from the case where the geometries were optimised for spurious separation. As an example, a F_r of 1.64 was obtained in 66 cm^3 with a Q_u of 4200. In the same volume, optimising the geometry to reach a Q_u of 5500 degrades F_r to 1.43. Also, as the cavity volume is increased to reach larger values of maximum Q_u, F_r degrades quickly. In 150 cm^3, a Q_u of 8750 can be obtained, but F_r is only 1.17.

Trading-off between Q_u and F_r, for example by slightly decreasing the dielectric resonator height from its optimum value for Q_u, the typical performance of the dual-mode conductor-loaded DR can be presented for different values of Q_u and compared to other types of resonators. For example, a Q_u of 3000 can be obtained with a Q_u/volume of 170 cm^{-3}, compared with 55 cm^{-3} for a combline resonator and 83 cm^{-3} for a single-mode TM_{010} resonator [23]. The spurious performance is F_r =1.6 instead of 2.1 for the TM_{010} resonator, which is inferior but still quite adequate. A Q_u of 5000 is obtained with a Q_u/volume of 154 cm^{-3}, instead of 39 cm^{-3} for a combline resonator and 73 cm^{-3} for a single-mode TM_{010} resonator. The spurious performances are similar as for $Q_u = 3000$. As a result, the dual-mode conductor-loaded DR is seen as a suitable resonator for Q_u's around the 3000-5000 range.

In the case of $Q_u = 7000$, the Q_u/volume of the dual-mode conductor-loaded DR is 112 cm^{-3}. This is again significantly better than those of the combline and TM_{010} resonators, with 26 cm^{-3} and 65 cm^{-3} respectively. However, F_r is then 1.33. Improving F_r to 1.48 degrades the Q_u/volume to 80 cm^{-3}, which is less attractive. If a spurious separation around 1.2-1.3 is acceptable, then the dual [84] or triple [85] TM_{010} mode resonators are more attractive. Indeed they have a Q_u/volume of 150 cm^{-3} and 230 cm^{-3} respectively but with a F_r of 1.21 and 1.26. The advantage of the dual-mode conductor-loaded DR is then its layout, as the dielectric is in contact with one side of the cavity, which simplifies the mounting of the resonator and the access for filter tuning. The design of a typical base-station transmit filter is detailed in [157]. The dual-mode conductor-loaded DR would then be interesting for applications with Q_u's of approximately 7000, if its spurious performance could be improved while keeping a good Q_u/volume. In [157], an improvement was made by using a ring shaped dielectric resonator. This increased F_r to 1.54 for a resonator Q_u of 6000 in a Q_u/volume of 90 cm^{-3}.

Chapter 5

Cross-coupled Dielectric-Loaded TE_{011} Filters

5.1 Introduction

The TE_{011} dielectric-loaded waveguide resonator was introduced by Kobayashi *et al.* [81] in 1978. It was presented in Section 1.4.7 as the TM_{010} DR with cylindrical coordinates. Fig. 5.1 shows the resonator structure in the case of a rectangular cavity and dielectric slab. The cases of the cylindrical [81, 176] and rectangular [23] resonator have been studied, in most cases concentrating on a cavity Q_u around 8000 at 900 MHz. The present chapter complements this data by considering the particular application of this technology to microcell base-station filters at PCN-PCS frequencies.

Work on TE_{011} filter modeling has been reported [3, 23, 81, 176] and various TE_{011} mode bandpass filters have been developed. Different filter structures have been studied, varying the angle between each consecutive dielectric slab [3]. The in-line configuration appears to be the most suited for the type of applications considered here. However, filters using this configuration have only been reported with symmetrical cross-couplings [3, 23]. A more general investigation of the filter design with asymmetrical couplings is necessary, including the study of the couplings between two cavities out of line, with a non-square cross-section or even with off-centred resonators. Because of this, the rectangular coordinate system is chosen. Also, all the data given in the references for the coupling between resonators considers a material of relative permittivity 36. This study will concentrate on $\varepsilon_r = 44$, which gives, as it will be pointed out, resonators with better performance.

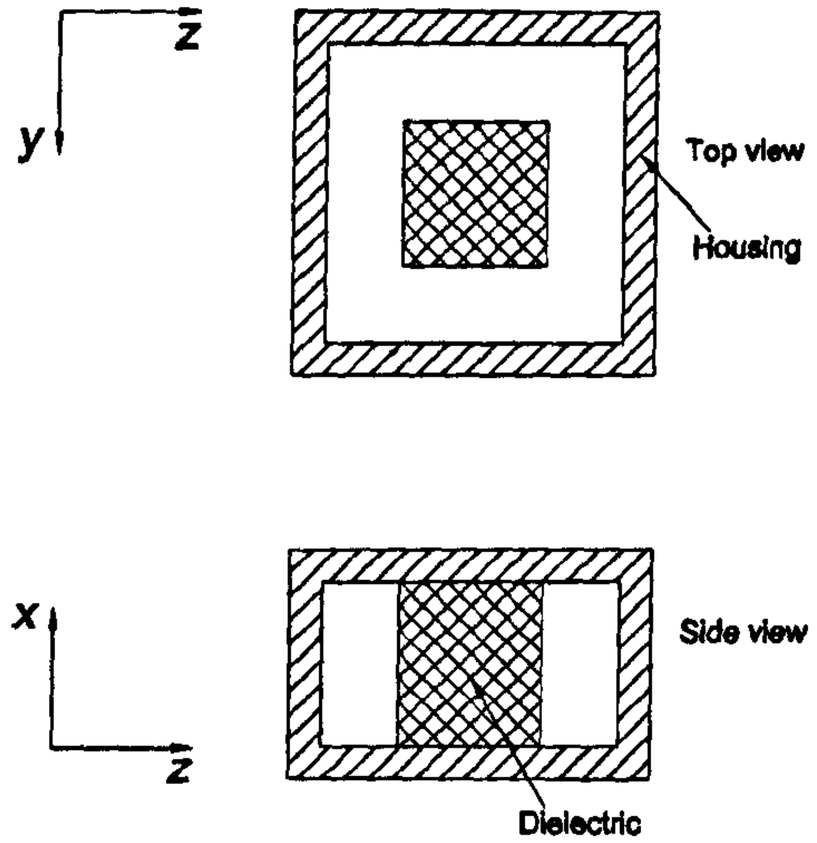

Figure 5.1: Dielectric-loaded TE_{011} resonator geometry

5.2 Mode-matching geometry

Although the maximum volume reduction of a TE_{011} waveguide resonator is obtained by a complete dielectric loading of the cavity, the Q_u values of the resulting resonator are then fairly small. Optimal Q_u/volume ratios happen for a partial dielectric loading localised in the centre of the cavity, which maximises the amount of field concentrated away from the lateral walls. For a single cavity, Q_u and resonant frequency can be calculated to a high degree of precision using the mode-matching procedure of Section B.1 in Appendix B. The partitioning of the resonator is shown in Fig. 5.2. The fields in each waveguide are expanded as a series of TE_{0n} modes.

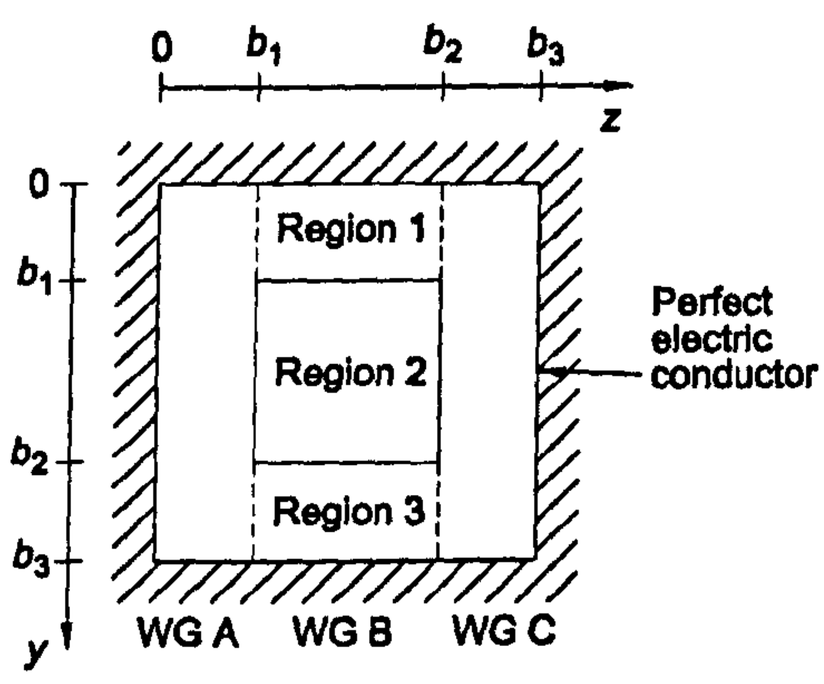

Figure 5.2: Dielectric-loaded TE_{011} resonator mode-matching geometry

Table 5.1: *Theoretical and measured resonant frequencies and* Q_u *for centrally loaded silver plated cavity of dimensions* $9\times20\times20$ mm, $\varepsilon_r = 44$, $\tan\delta = 5.55\times10^{-5}$ *at* 2 GHz, $Rs(silver) = 2.52\times10^{-7}\sqrt{f}$

Theoretical resonant frequency (Mode matching) (GHz)	2.0000
Measured resonant frequency (GHz)	2.0001
Theoretical Q_u (Mode matching)	3543
Theoretical Q_u (MicrowaveLab^{TM})	3560
Measured Q_u	2530

In waveguides A and C, their variations are simply defined, as the wave number of mode i in the y direction is simply $k_{yi} = i\pi/b_3$. In waveguide B, the characteristic equation [177]

$$-e^{jk_{y2}(b_2-b_1)}\left(-j\frac{k_{y3}}{k_{y2}}\cot(k_{y3}(b_3-b_2))+1\right)\left(-j\frac{k_{y1}}{k_{y2}}\cot(k_{y1}b_1)+1\right)$$
$$+\,e^{jk_{y2}(b_1-b_2)}\left(j\frac{k_{y3}}{k_{y2}}\cot(k_{y3}(b_3-b_2))+1\right)\left(j\frac{k_{y1}}{k_{y2}}\cot(k_{y1}b_1)+1\right)=0 \qquad (5.1)$$

has to be solved numerically with $k_{yn} = \sqrt{\omega^2\mu_0\varepsilon_0\varepsilon_{rn}+\gamma^2}$, where k_{y1}, k_{y2} and k_{y3} are the wave numbers in the y direction in regions 1, 2 and 3 respectively. ε_{rn} is the corresponding relative permittivity. The expressions of the self and cross-products used in the mode-matching resolution are detailed in Appendix H.

Table 5.1 shows predictions and measurements for Q_u and resonant frequency of a test cavity of length 20 mm and height 9 mm. To ensure a reliable measurement by avoiding any air gap (see Section 5.4), the dielectric slab is plated and soldered to the base of the cavity and a flexible lid. The purpose of the Q_u simulation by MicrowaveLab^{TM} is to validate the result obtained by mode matching. The discrepancy between theoretical and experimental Q_u is believed to be mainly due to the resistivity of the plating being higher than that of perfect silver. The soldering is also responsible for some of the loss. It was simulated with the mode matching program by 0.3 mm wide regions of higher resistivity conductor ($R_s(solder) = 7.56\times10^{-7}\sqrt{f}$) surrounding the base and the top of the dielectric slab. This decreased the Q_u by 330. The experimental Q_u of 2530 in a volume of 3.6 cm^3 represents a 3.0:1 improvement in Q_u/volume over a combline resonator, which can achieve Q_u of 2500 in a volume of 10.7 cm^3.

5.3 Study of dielectric-loaded TE_{011} cavities

Table 5.2: *Performance of dielectric-loaded cavities with different* ϵ_r, $f_0 = 2$ GHz, *Cavity volume :* 3.6 cm^3

ϵ_r	29	35	44
cavity height (mm)	8.0	9.2	10.7
cavity length (mm)	21.2	19.8	18.3
dielectric length (mm)	13.1	11.4	9.7
Q_c	3745	4099	4531
Q_c/volume (cm^{-3})	1040	1139	1259
tan δ ($\times 10^{-5}$)	2.08	6.25	5.55
Q_d	48278	16114	18160
Q_u	3475	3267	3624
Q_u/volume (cm^{-3})	965.3	907.5	1007

In the following study, the cavity and dielectric slab are of square cross-sections and the dielectric slab is located at the centre of the cavity unless stated otherwise.

Table 5.2 shows the calculated Q_u's for three cavities of identical volume but with different ϵ_r. The integrals for Q_u are calculated analytically from the modes coefficients and field expressions, as in Chapter 3. Values are given considering conductor and dielectric losses separately. It can be seen that a dielectric loading of high permittivity offers the double advantage of a better Q_c/volume ratio as well as needing a smaller amount of ceramic. For a given frequency, volume and dielectric constant, the mode-matching program provides charts from which the optimum geometry can be found. At 2 GHz for example, the optimum cavity height is first deduced from Fig. 5.3, in turn leading to the cavity length. The dielectric slab length then follows from Fig. 5.4.

The variations of the Q_u, Q_u/volume and geometry dimensions of the optimal resonator are shown in Figs. 5.5 to 5.7 as the cavity volume is increased. It can be seen in Fig. 5.7 that, as the cavity volume is increased, the cross-sectional dimensions vary less than the height of the cavity. This is reminiscent of the case of the dual-mode conductor-loaded DR in Chapter 4. By increasing the height of the dielectric

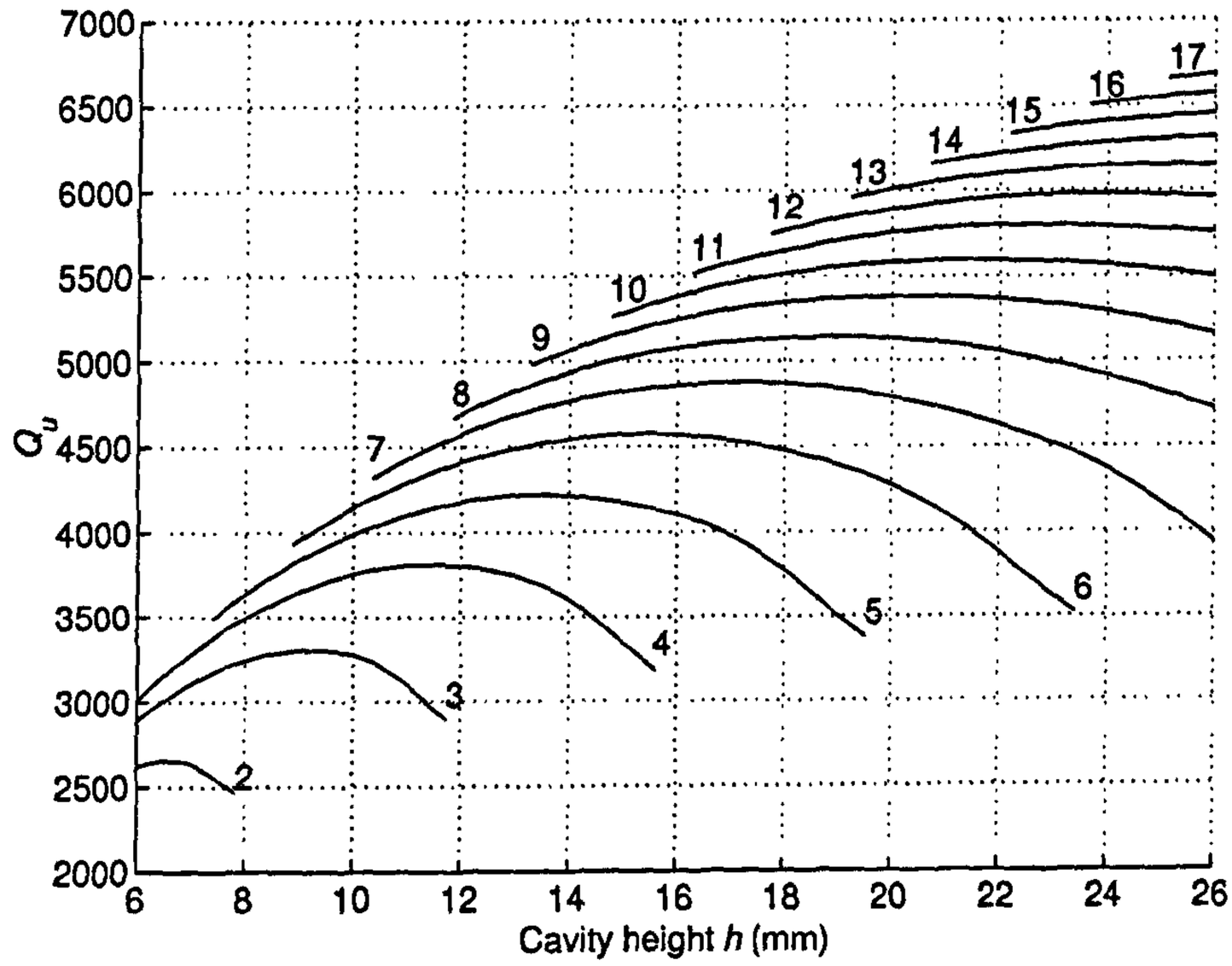

Figure 5.3: Variation of the Q_u with cavity height for different cavity volumes (in cm^3) ($\varepsilon_r = 44$, $f_0 = 2$ GHz)

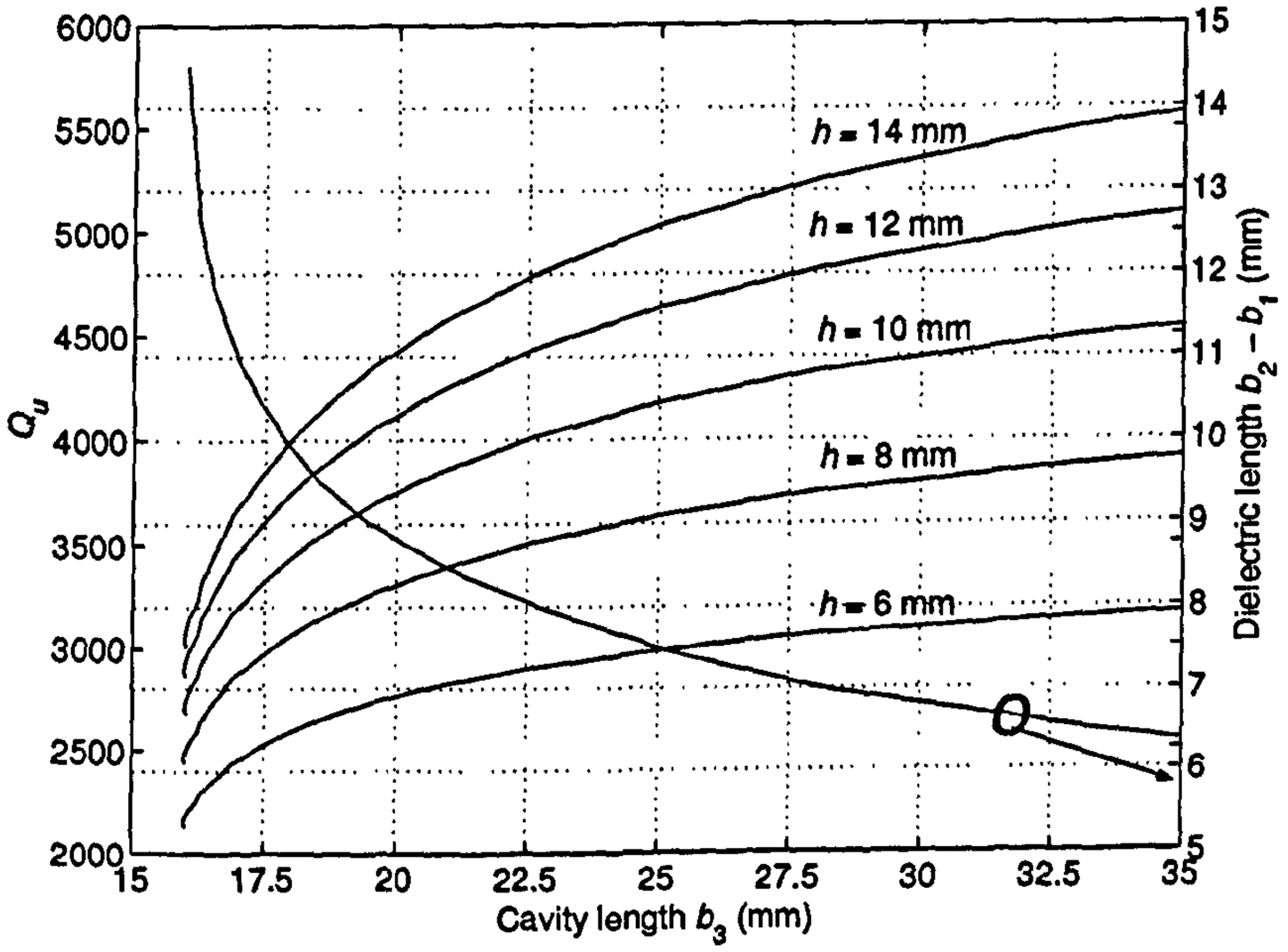

Figure 5.4: Variation of the Q_u and dielectric slab length with cavity length (h = cavity height, $\varepsilon_r = 44$, $f_0 = 2$ GHz)

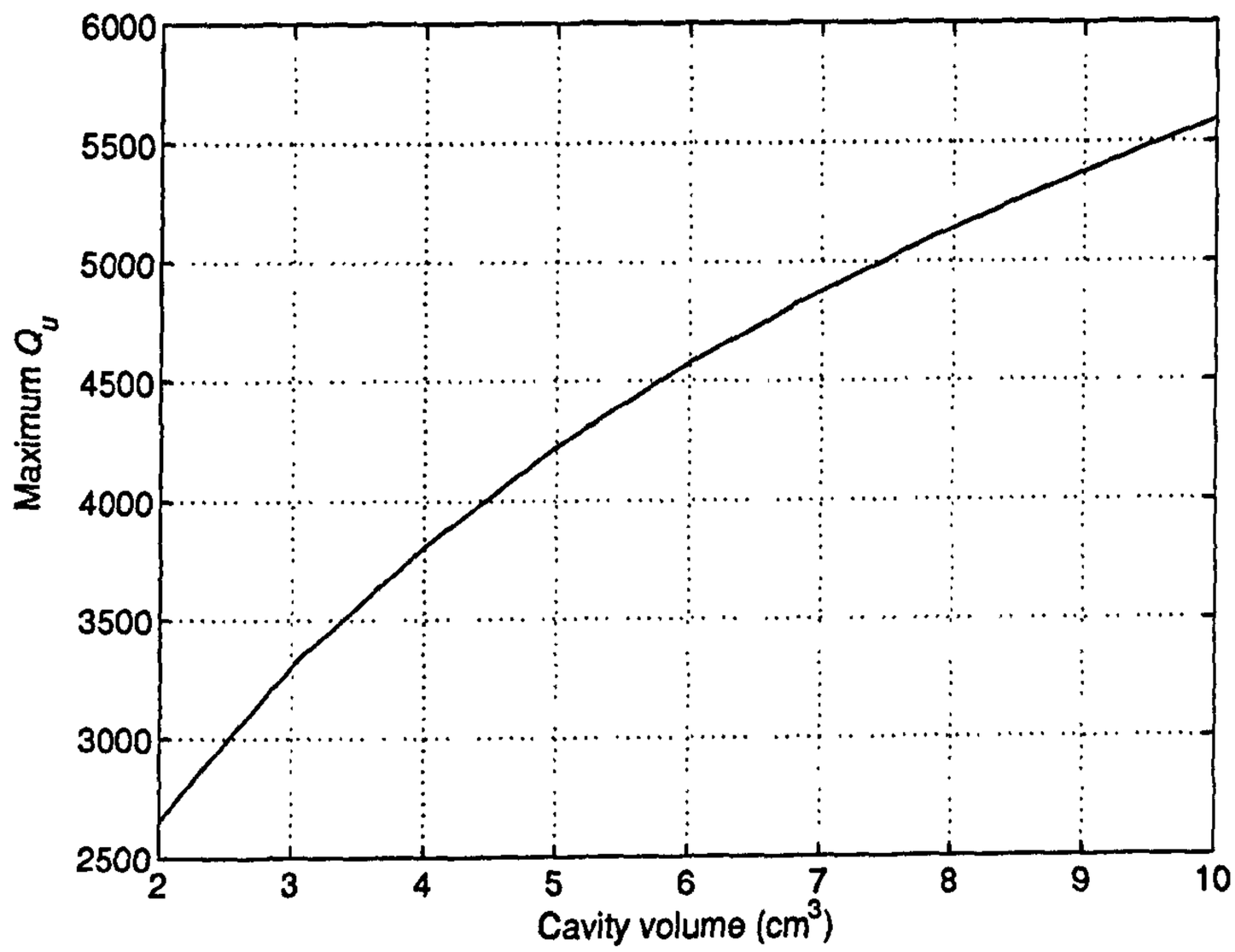

Figure 5.5: Variation of the maximum Q_u obtainable in a given cavity volume ($\epsilon_r = 44$, $f_0 = 2$ GHz)

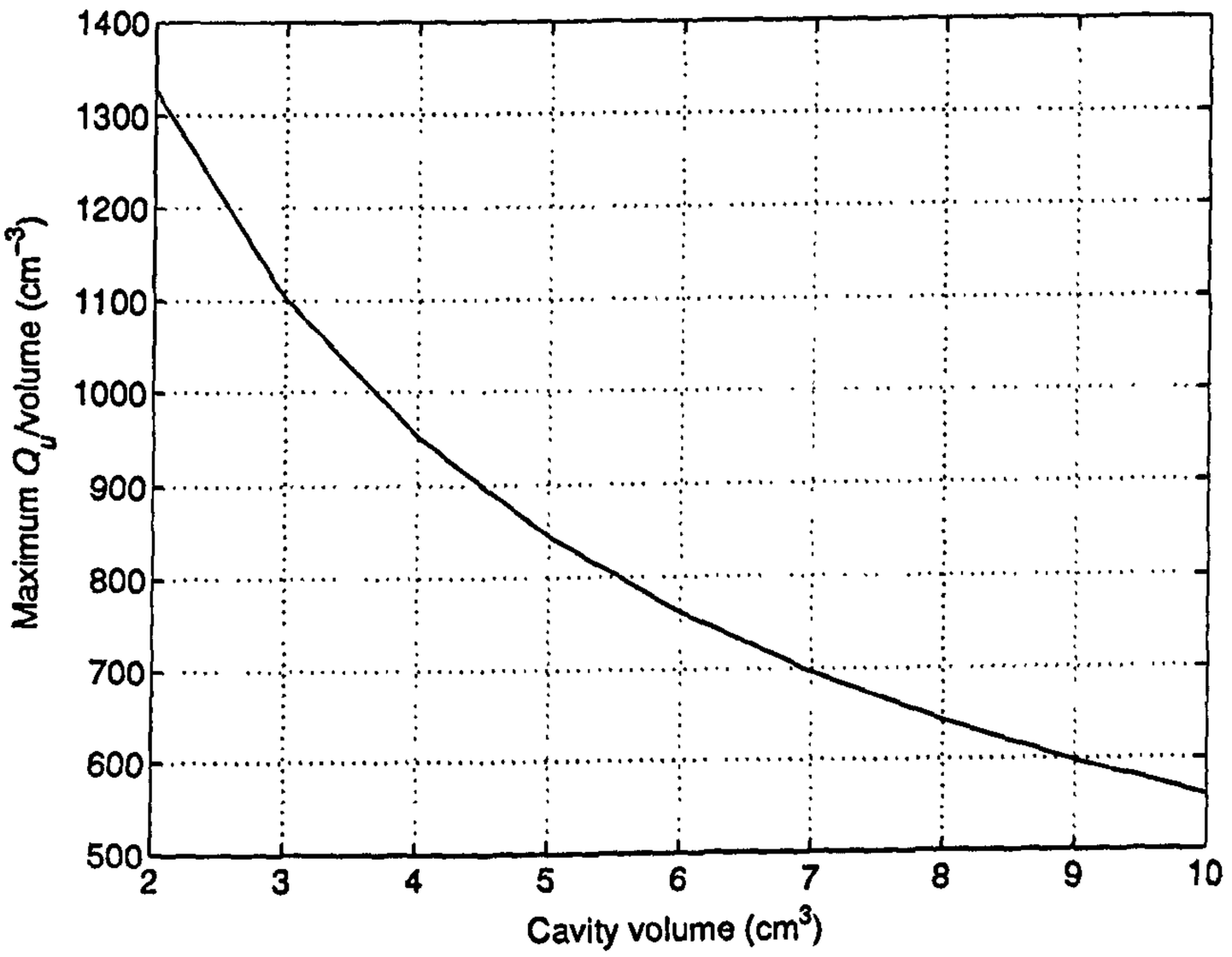

Figure 5.6: Variations of maximum Q_u/volume with cavity volume ($\epsilon_r = 44$, $f_0 = 2$ GHz)

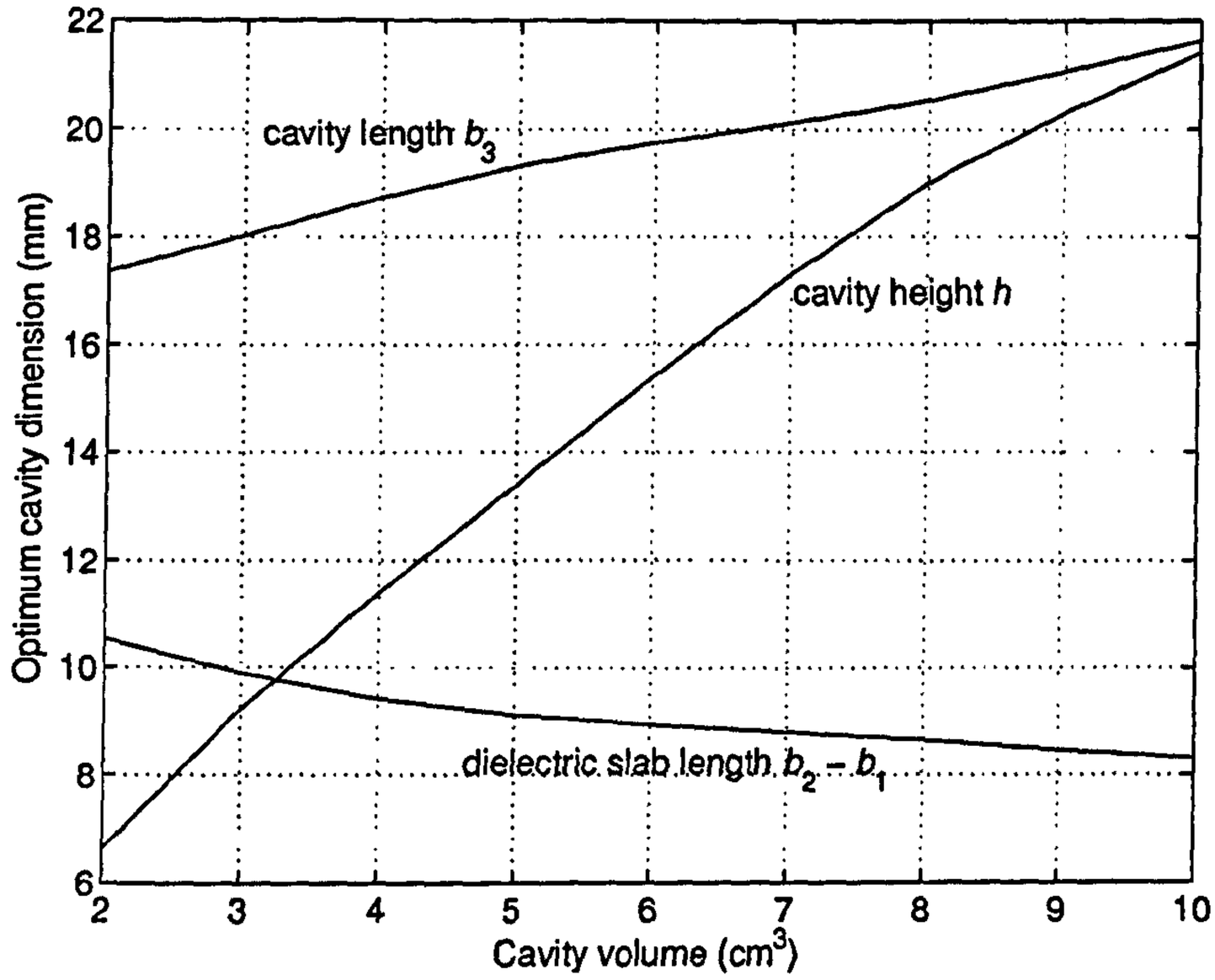

Figure 5.7: Dimensions of the geometry with maximum Q_u in a given cavity volume ($\varepsilon_r = 44$, $f_0 = 2$ GHz)

resonator, along which there is little or no field variation, the increase in stored energy is maximised compared to the extra loss created in the side cavity walls. As a result, at 2 GHz, a Q_u within 95% of the optimum can be obtained for cavity volumes between 2 and 10 cm^3 by using a dielectric slab and cavity length of 9.5 mm and 18.6 mm respectively. As the cavity height increases much faster than its length, the optimum resonator geometry for high Q_u applications then strongly resembles that of the dielectric combline [80], except that, in the latter case, the long and thin dielectric rod is only shorted at one end. The short distance between the top of the dielectric and the lid forces the fields to have some variation along the length of the rod. In the case of very long rods, the resulting increase of the resonant frequency is limited and can be corrected by modifying the diameter of the rod. The dielectric combline resonator then offers slightly better Q_u/volume than the dielectric-loaded TE_{011} resonator. For example, the optimum dielectric-loaded TE_{011} resonator in a 30 cm^3 cavity volume and using $\varepsilon_r = 44$ has a height of 39 mm and a Q_u of 8145. Keeping the same cavity height but creating a 1 mm gap between the dielectric slab and the lid and retuning the resonant frequency, the resulting dielectric combline

resonator has a Q_u of 8670. The dielectric combline also has the advantage of requiring mounting only on one side of the dielectric rod. However, this mounting has to be of equally good quality in both cases. In the case of lower Q_u cavities, the optimum height of the rod is much smaller and the frequency increase created by any gap at the top of the resonator is far too large. Indeed, a 1 mm gap only increases the resonant frequency of the TE_{011} mode by 15% in the case of the 30 cm^3 cavity. For a 4 cm^3 cavity, the increase is 72% and the dielectric-loaded TE_{011} resonators is the optimum geometry.

A study of the normalised spurious separation has been presented for $\varepsilon_r = 10$ and 36 [81]. It was shown that, in the case of high Q_u resonators, the higher value of ε_r was needed to improve the separation with the TM_{011} and HE_{111} modes (in cylindrical coordinates) and achieve a value of F_r as large as 2. The separation of lower Q_u resonators is less critical because the resonant frequency of the two previous modes is increased due to the smaller resonator height. The spurious separation is studied again here in the case of $\varepsilon_r = 44$. It is realised for two cavity heights using the finite element analysis software, MicrowaveLab^{TM}. The results are shown in Fig. 5.8. The spurious performance improves as the loading is reduced, because the fields of the spurious modes are less concentrated at the centre of the cavity than for the fundamental mode. This is true up to very big cavity lengths, at which point the resonant frequency of modes which have most of their fields contained in the air region starts decreasing. The resonators with small cavity lengths, which have the limited spurious separations, are also those with the largest inter-cavity couplings. This limitation will be discussed in Section 5.5.2.

The best separation is for cavity heights below a certain value, for which the first spurious is the dual TM_{110} mode (TE_{021} and TE_{012} modes in rectangular coordinates). For cavities filled with dielectric of relative permittivity 44, this value is fairly constant and around 12 mm for a large range of cavity lengths including those optimum for Q_u/volume in Fig. 5.7. For larger heights, the spurious performance is degraded as the HE_{111} mode becomes the first spurious. In the case of the geometry for optimum Q_u/volume, this happens for cavity volumes larger than 4.3 cm^3, i.e. with Q_u's above 3900 (see Figs. 5.7 and 5.5). This deterioration will have to be taken into account especially when considering using particularly high cavities, optimum for larger Q_u values.

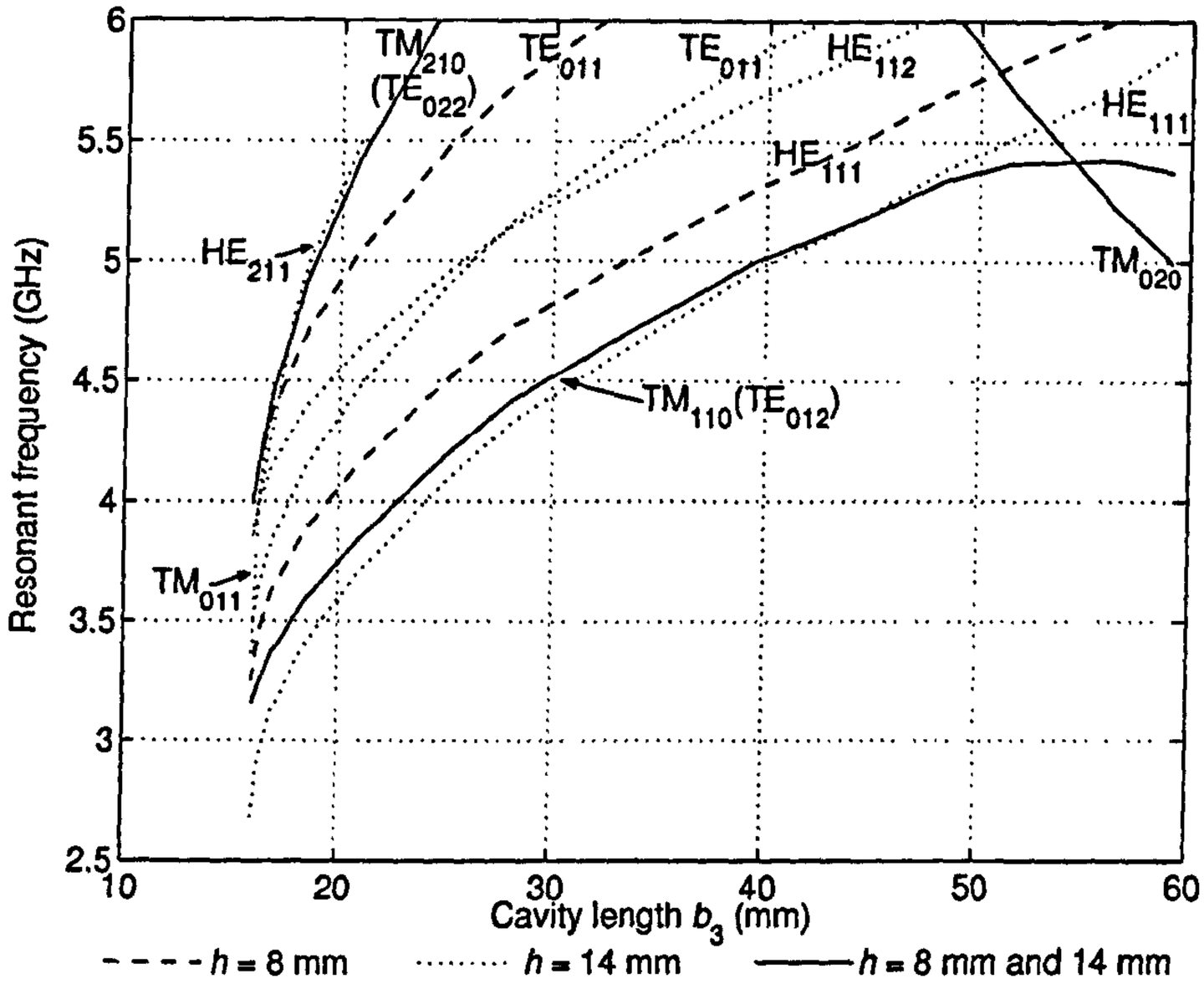

Figure 5.8: Variation of the first spurious frequencies with cavity length ($h = 8$ and 14 mm, $\varepsilon_r = 44$, fundamental resonant frequency: 2 GHz). Names in cylindrical coordinates (rectangular coordinates in brackets).

5.4 Resonator mounting

The resonator mounting technique has to be mechanically and electrically reliable as well as easy to manufacture. This is difficult to achieve especially over a range of temperatures as the presence of air gaps between dielectric slab and cavity makes the resonant frequency unrepeatable and uncontrollable. Solutions were proposed by Kobayashi *et al.* [81] and Nishikawa *et al.* [176]. The former consists in fitting the dielectric cylinder through holes at both extremities of the cavity. As their diameter is relatively small, these holes behave as waveguides below their cut-off frequency and the resonator fields do not leak out of the cavity. The latter method covers the inside of the cavity with a temperature stable plated dielectric shield. These methods require either high precision manufacturing or a high degree of machining of the ceramic material. The technique adopted in this paper uses cylindrical ceramic slabs fitting through holes in the base of the cavities. The top and bottom faces of the slabs are silver plated and soldered to the cavity. This realises a good mechanical support of the slab, providing frequency stability over temperature as well as good

electrical contact resulting in reliable Q_u values.

The results obtained with the mode matching technique with rectangular coordinates are still usable when using cylindrical resonators. Indeed, simulations using the finite element analysis software have shown that changing from a square to a cylindrical piece of ceramic only changes the resonant frequency very slightly, provided the volume of dielectric material is kept constant. In the case of the cavity in Table 5.1, the resonant frequency is decreased by −0.6% for a cylindrical resonator. This variation is small enough to be recovered by tuning. The Q_u variation is negligible as the FEM simulations of the two resonators differ by less than 0.1%. Also, the inter-cavity coupling bandwidth through a 10 mm iris between two cavities of Table 5.1 changes by less than 0.2%.

5.5 Filter design

The following filter specifications, typical for microcells applications, were considered:

- Centre frequency :	$f_0 =$ 1.9 GHz	
- Bandwidth :	80 MHz	
- Insertion loss :	1 dB	over the 80 MHz bandwidth
- Rejection :	60 dB	for $f > f_0 + 56.2$ MHz
		or $f < f_0 - 56.2$ MHz

The filter was designed as a degree 6 generalised Chebyshev bandpass prototype [10]. The prototype uses two cross-couplings, each realised by a cascaded trisection [178]. The required coupling bandwidths are shown in Table 5.3.

5.5.1 Cross-coupling configurations

With inductive coupling naturally existing through irises between cavities, the high side cross-coupling configuration simply consists in arranging the three resonators in a triangle as shown in Fig. 5.9. A low side cross-coupling is realised by inverting the sign of the in-line coupling. A probe connecting the top of the first cavity to the base of the second [3], illustrated in Fig. 5.10, provides such an inversion. However, the tuning of such a coupling is difficult. A reliable answer is to machine an iris next to the wire which, by tuning, cancels a small amount of the negative coupling.

Table 5.3: *Filter coupling bandwidths*

Nodes	Coupling BW (MHz)	Nodes	Coupling BW (MHz)
input-1	80.335		
1-2	58.634	1-3	33.437
2-3	40.141		
3-4	46.747		
4-5	43.669	4-6	25.956
5-6	62.308		
6-output	80.335		

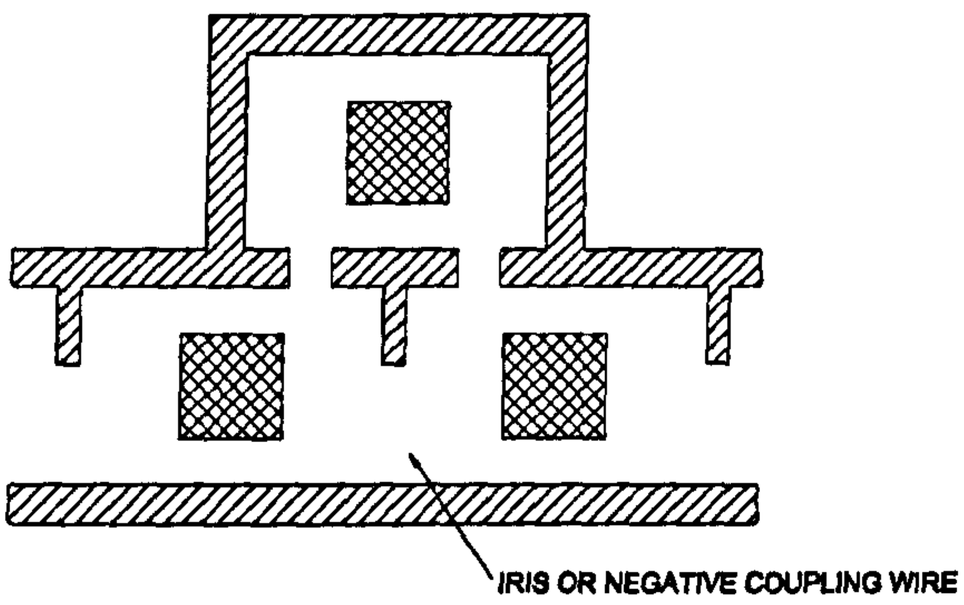

Figure 5.9: Layout for cross-coupling realisation

5.5.2 Evaluation of intercavity couplings

Irises between directly adjacent cavities generally create enough coupling to satisfy base-station filter bandwidth specifications. However, when cross-couplings across three resonators are needed, the main path irises can be too small and the resonators too far apart to get the amount of coupling needed. The maximum coupling available can be computed once again by mode-matching, but this time using a 7 section structure as shown in Fig. 5.11.

The first option to increase the coupling is to increase the dielectric size (i.e. decrease the cavity surface area). This means going away from the optimal cavity height/length ratio as calculated in Section 5.3, which will decrease the Q_u. Fig. 5.12

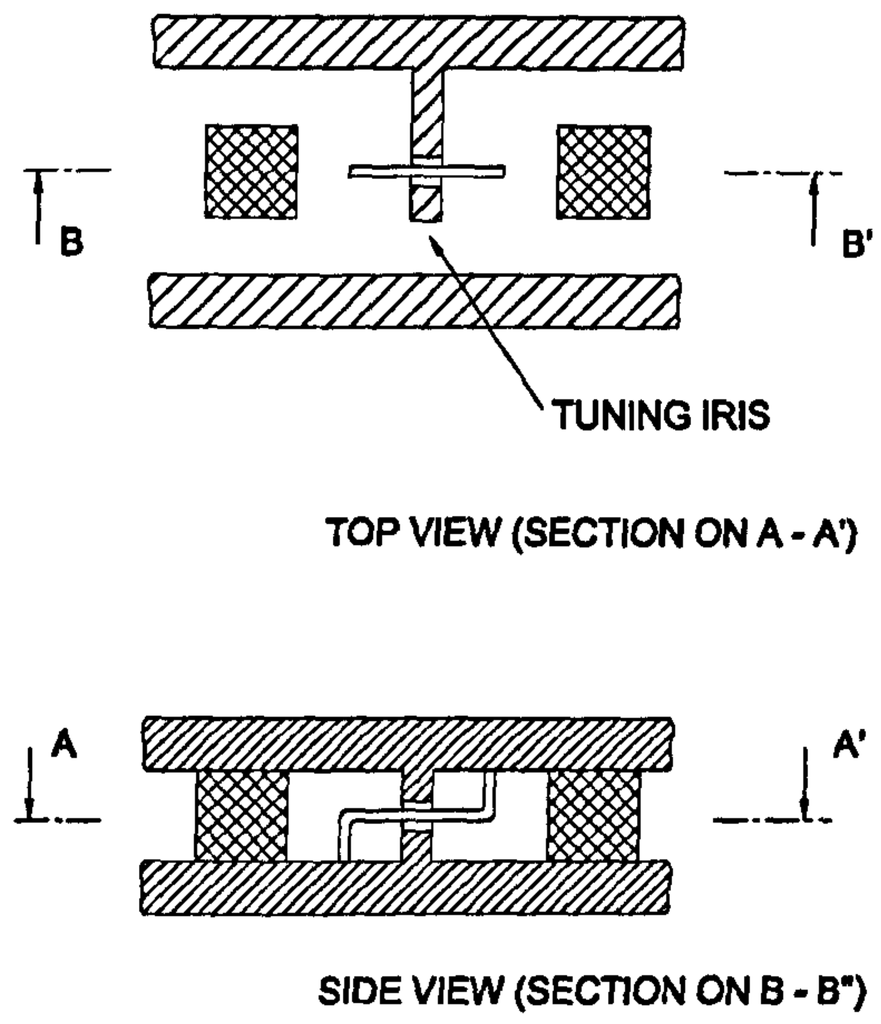

Figure 5.10: Inverted sign coupling mechanism [3]

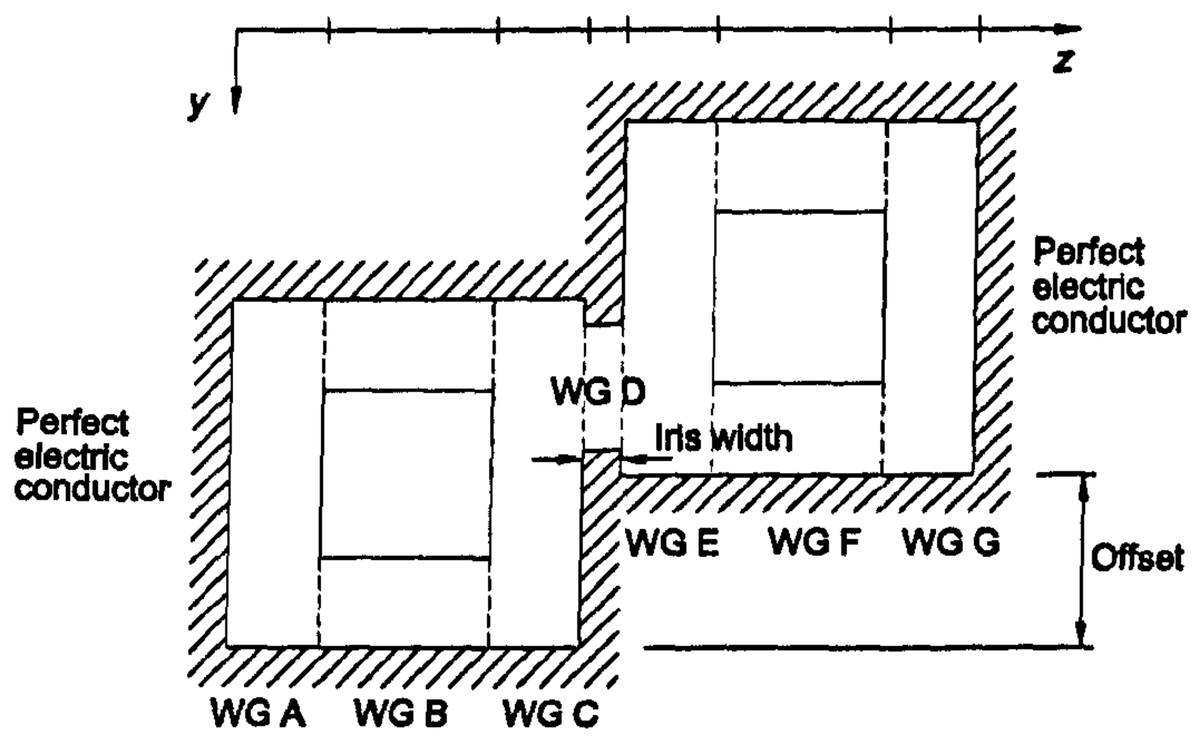

Figure 5.11: Mode-matching geometry for calculation of adjacent coupling

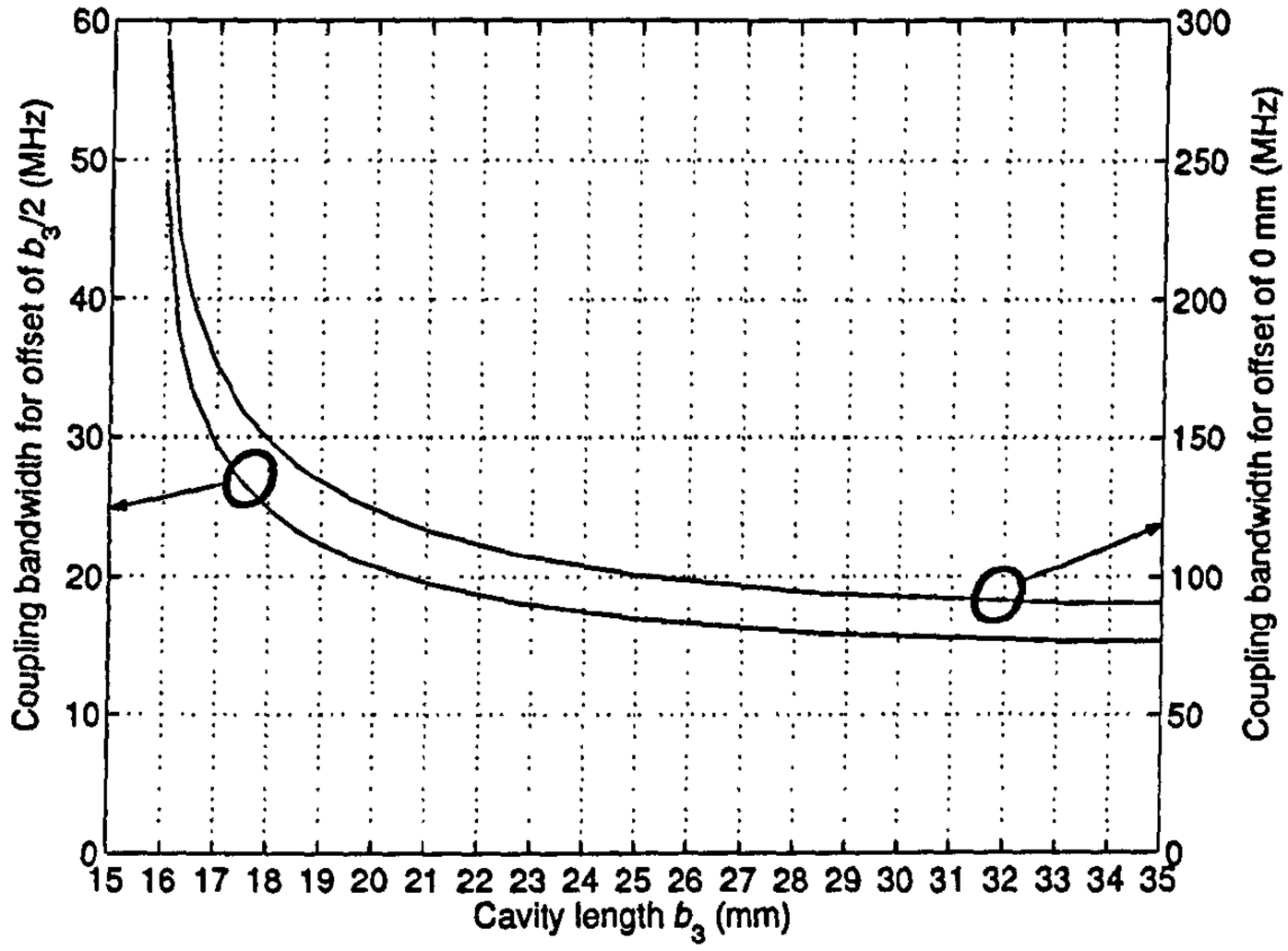

Figure 5.12: Simulated coupling bandwidths as cavity length b_3 is varied. $f_0 =$ 2 GHz. Iris thickness is 1 mm and the iris width is maximum. $\varepsilon_r = 44$.

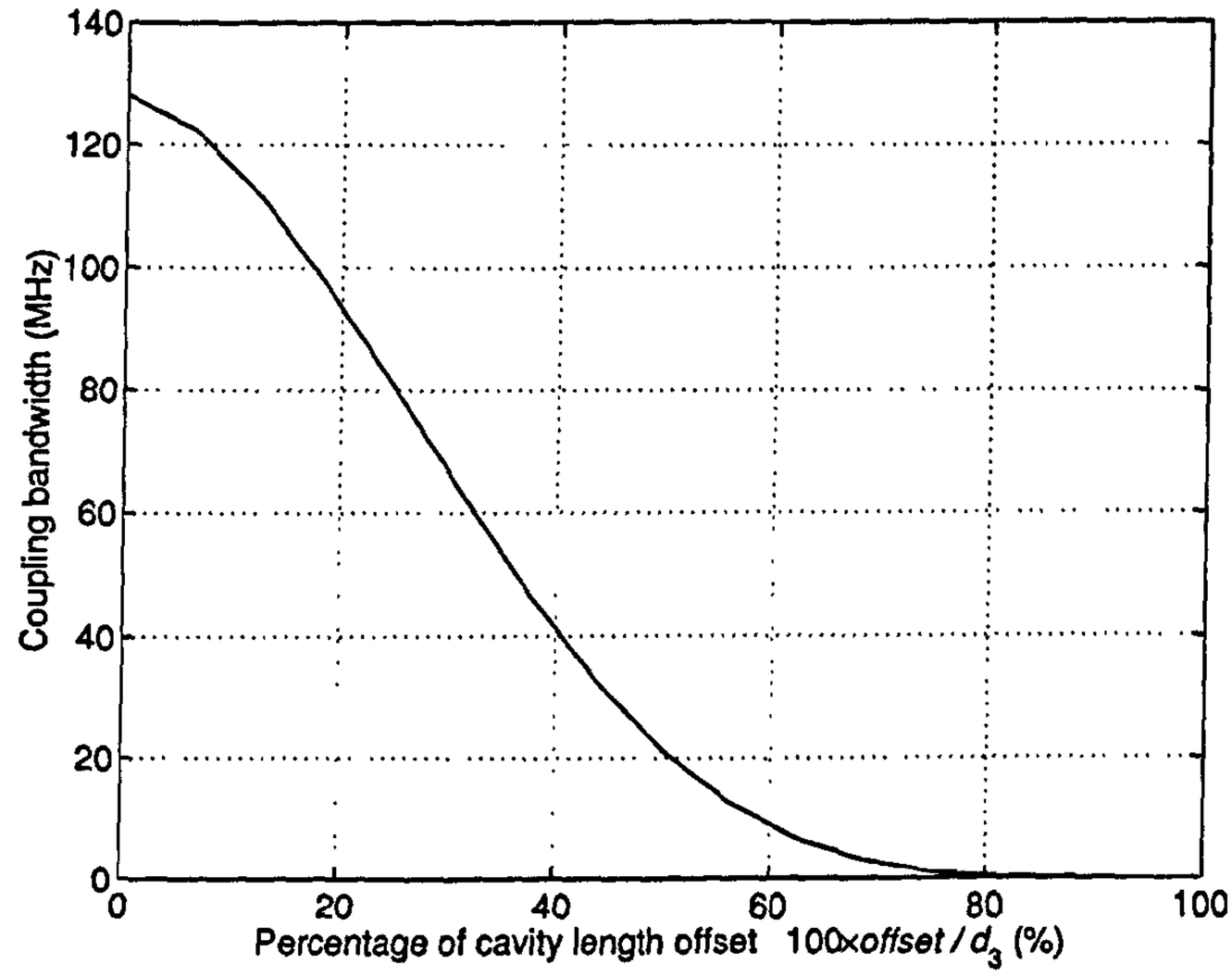

Figure 5.13: Simulated coupling bandwidths as the offset between cavities is varied. Cavity length $b_3 = 19.6$ mm, dielectric slab length $b_2 - b_1 = 9.0$ mm. Iris thickness is 1 mm and the iris width is maximum. $\varepsilon_r = 44$.

shows the variation of the coupling bandwidths between two resonators at 2 GHz as the cavity length is increased. It is computed in both cases of in-line cavities and cavities offseted by half their side length. Fig. 5.13 illustrates the variation of the coupling bandwidth as the offset is increased, for a particular resonator cross-section. Let us consider two cavities loaded with $\varepsilon_r = 44$ as in Table 5.2. With an iris width of 1 mm and an offset of $b_3/2$, the maximum coupling is 23.6 MHz. To get 38.3 MHz of coupling, the cavity side length needs to be reduced by 2.1 mm. If the cavity volume is kept constant, the height of the cavity can then be increased but the Q_u still drops from 3624 to 3238. At the same time, the spurious performance is made worse, with the HE_{111} as the first spurious at 2.898 GHz instead of 3.561 GHz. It is actually more optimal to move the slabs towards each other in the z axis by reducing the lengths of waveguides C and E and keep the cavity height constant. This is for two reasons:

- the drop in Q_u is greatly reduced. With this approach, 39.4 MHz of coupling can be obtained in the same cavity volume by moving the slabs in the z axis by 1.3 mm and the Q_u is still 3573.

- A finite element analysis shows that the spurious performance does not decrease as much as previously. The first spurious is the TE_{012} mode at 3.504 GHz and the HE_{111} mode does not cause any problem.

Fig. 5.14 shows the coupling bandwidth variations as the distance between both the dielectric slabs and the iris is varied. The distances between the dielectric slab and the cavity walls in the three other directions remain equal. The cavity cross-section areas and heights are kept constant. The dielectric slab lengths are slightly adjusted to keep the resonant frequency constant. The degradation of the Q_u due to the offseting of the slabs is shown in Fig. 5.15 in the case of the cross-section area of 3.44 cm^2. The cavity height considered is the one for maximum Q_u/volume before offseting, i.e. 10.88 mm.

5.5.3 Frequency tuning

Considering the small size of the resonators, the use of dielectric plungers [23] was discarded for frequency tuning. 1/4" metal screws inserted from the side wall of the cavity [3] do provide sufficient tuning, but also deteriorate the Q_u significantly. An

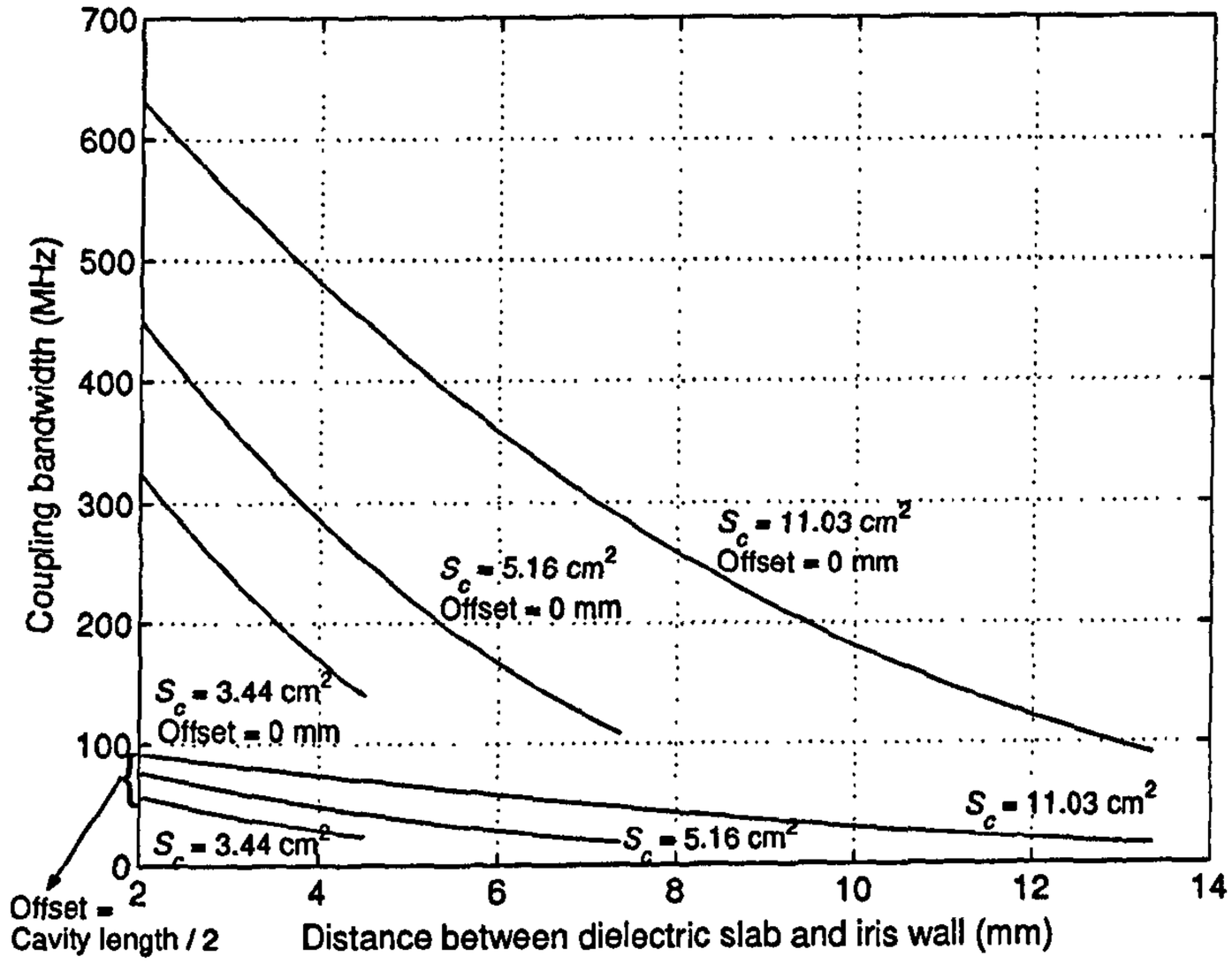

Figure 5.14: Simulated coupling bandwidths as the distance between dielectric slabs is varied. Iris thickness is 1 mm and the iris width is maximum. $\varepsilon_r = 44$.

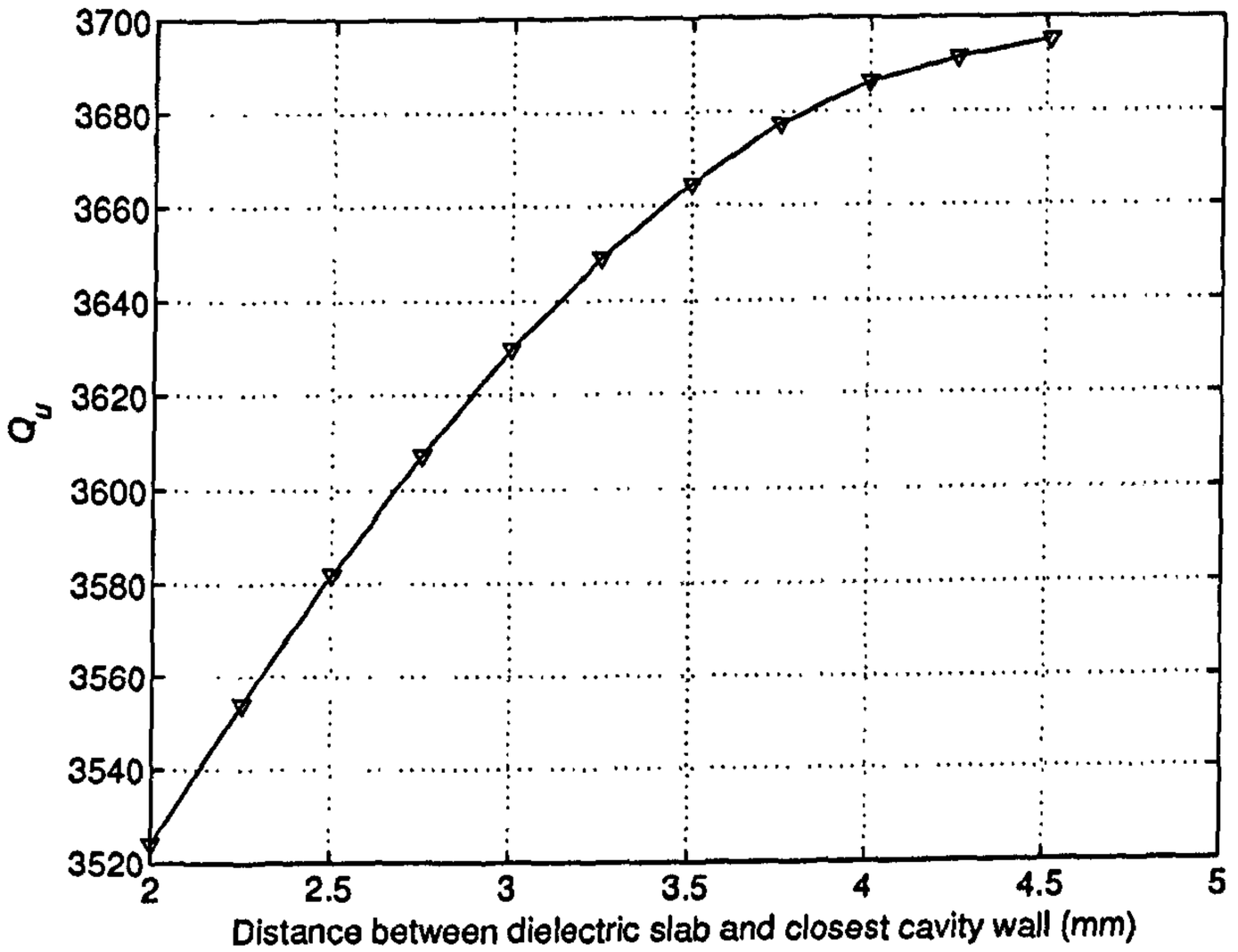

Figure 5.15: Variation of Q_u as the distance between dielectric slabs is varied. Cavity cross-section area $S_c = 3.44$ cm^2. Cavity height $h = 10.88$ mm.

experiment showed that the Q_u of a cavity as in Table 5.1 decreases by 21.6% when the frequency is tuned up by 55 MHz. A better method is to insert a metal screw in a hole machined in the top of the slab as described in Fig. 5.16. The positioning at the top of the cavity is optimal to give an easy access to all tuning screws. The metal screw decreases the resonant frequency of the cavity, as for a TEM resonator. The Q_u degradation is only of 6.2% when the frequency is tuned down by 50 MHz. The drawback of this method is that some of the initial Q_u is lost (about 5% for a through hole) and the resonant frequency increased as the slab is drilled. However, the tuning range with a through hole in the slab is by far more than needed and the hole can be limited to half the depth of the resonator.

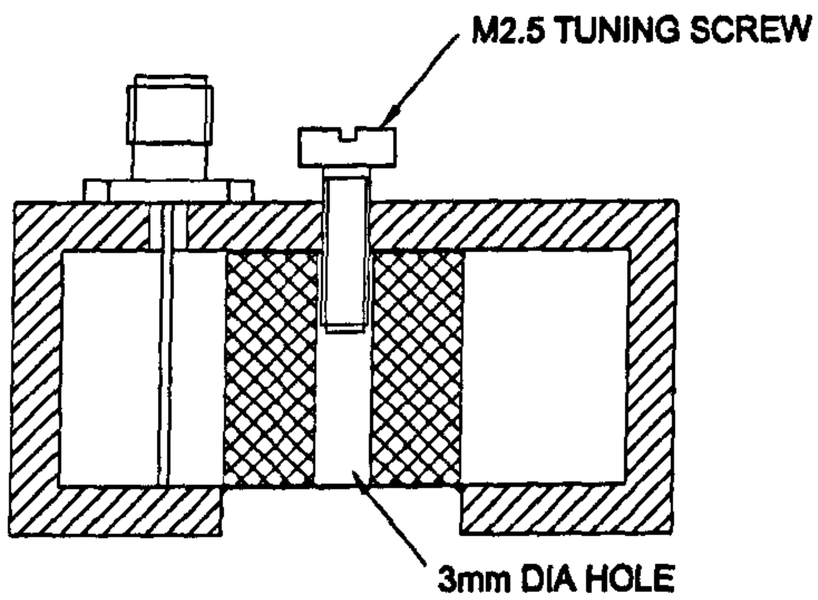

Figure 5.16: Frequency tuning and input coupling mechanism

5.5.4 Input coupling

As 1.0% of the electric energy and 73.2% of the magnetic energy is outside the dielectric for the cavity in Table 5.1, enough input coupling can only be achieved by coupling into the magnetic field.

The method presented in Fig. 5.16 is quite sensitive to the positioning of the connector pin and no tuning is possible, but experiments have shown that the tolerances on the housing make the coupling repeatable enough for the input coupling not to require tuning. Fig. 5.17 shows the variation of the Q_u of the resonator as the input coupling is increased.

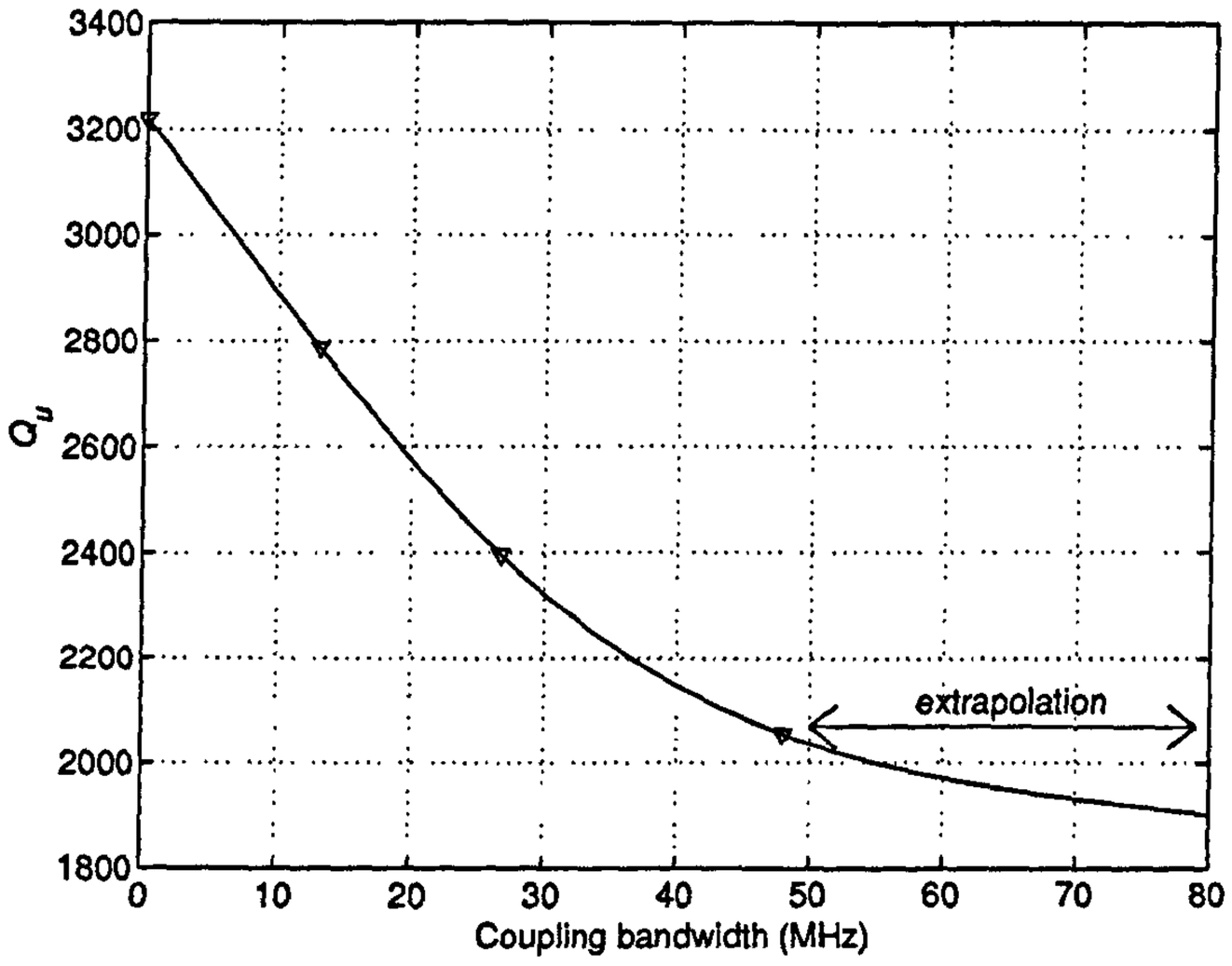

Figure 5.17: Variation of the Q_u of the input cavity of the filter with the amount of input coupling, adjusted by the distance from the connector to the slab (values obtained experimentally).

5.5.5 Practical filter results

The cavity size is chosen as $21.4 \times 26 \times 10$ mm with dielectric slabs of 10 mm diameter, giving a theoretical Q_u by mode-matching analysis of 3780 (perfect silver). The dielectric slabs are slightly offset to the side. The resulting degradation in Q_u from the central position is only of 6.6%. F_r is 1.89 with the first spurious at 3.65 GHz. The filter with positive cross-couplings and its response are shown in Figs. 5.18 to 5.21. The insertion loss at centre frequency is 0.25 dB and 0.84 dB at the upper bandedge (−25 dB return loss). The overall Q_u was estimated to be around 2800. This corresponds very well to a combined Q_u of 1900 for the input-output cavities as estimated from Fig. 5.17, and 3200 for the others, as measured with a test cavity. The latter value represents 85 % of the theoretical value.

The temperature coefficient of the filter was measured to be 7.1 ppm/°C. This is comparable to the one obtained by Kobayashi *et al.* [81]. A finite element model of the cavity showed that this drift is solely due to the expansion of the cavity in the H plane and that the tuning screws have no major effect. A filter with negative cross-couplings was also made with similar dimensions and had the expected performance.

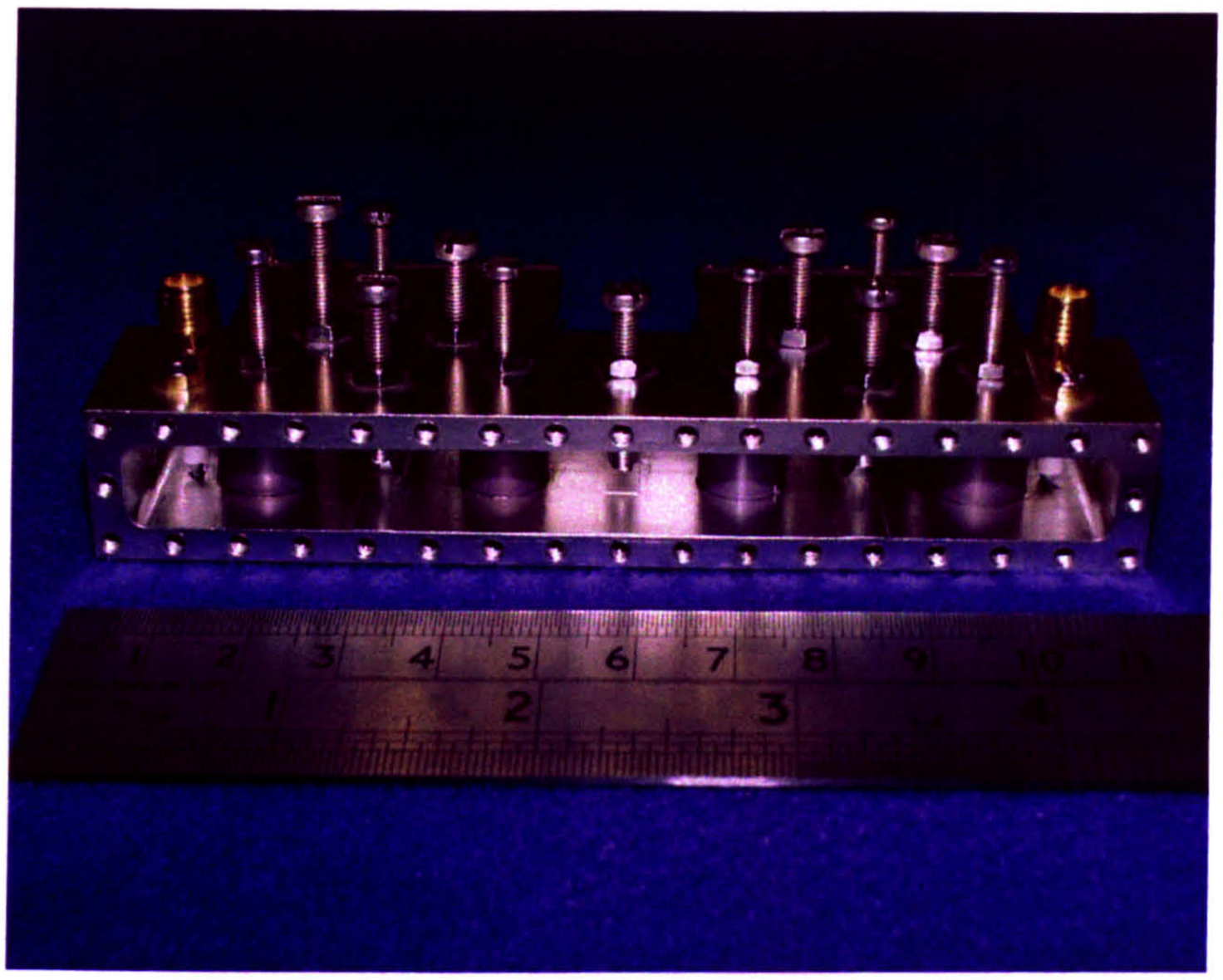

Figure 5.18: Filter with positive cross-couplings

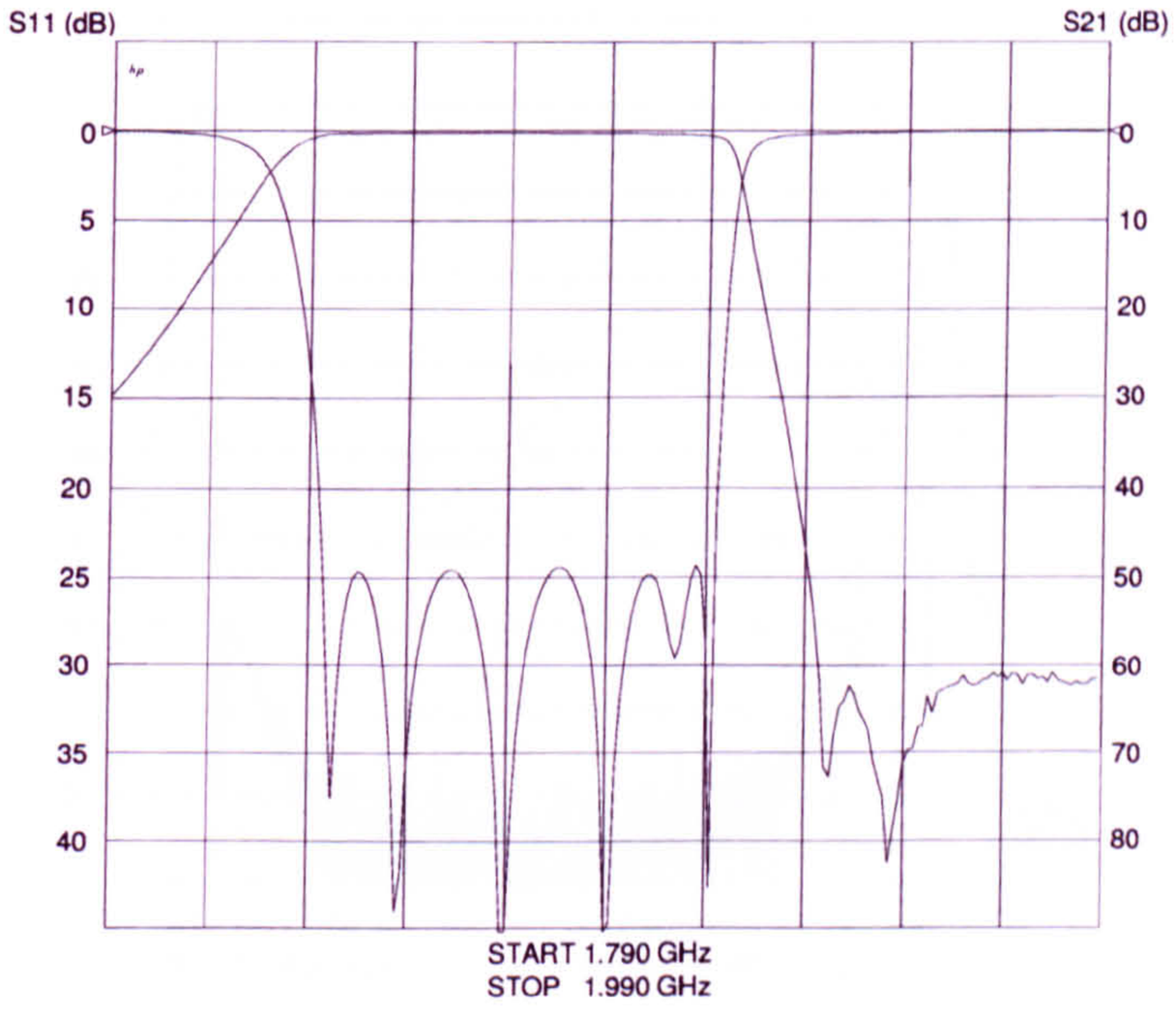

Figure 5.19: Response of the filter with positive cross-couplings

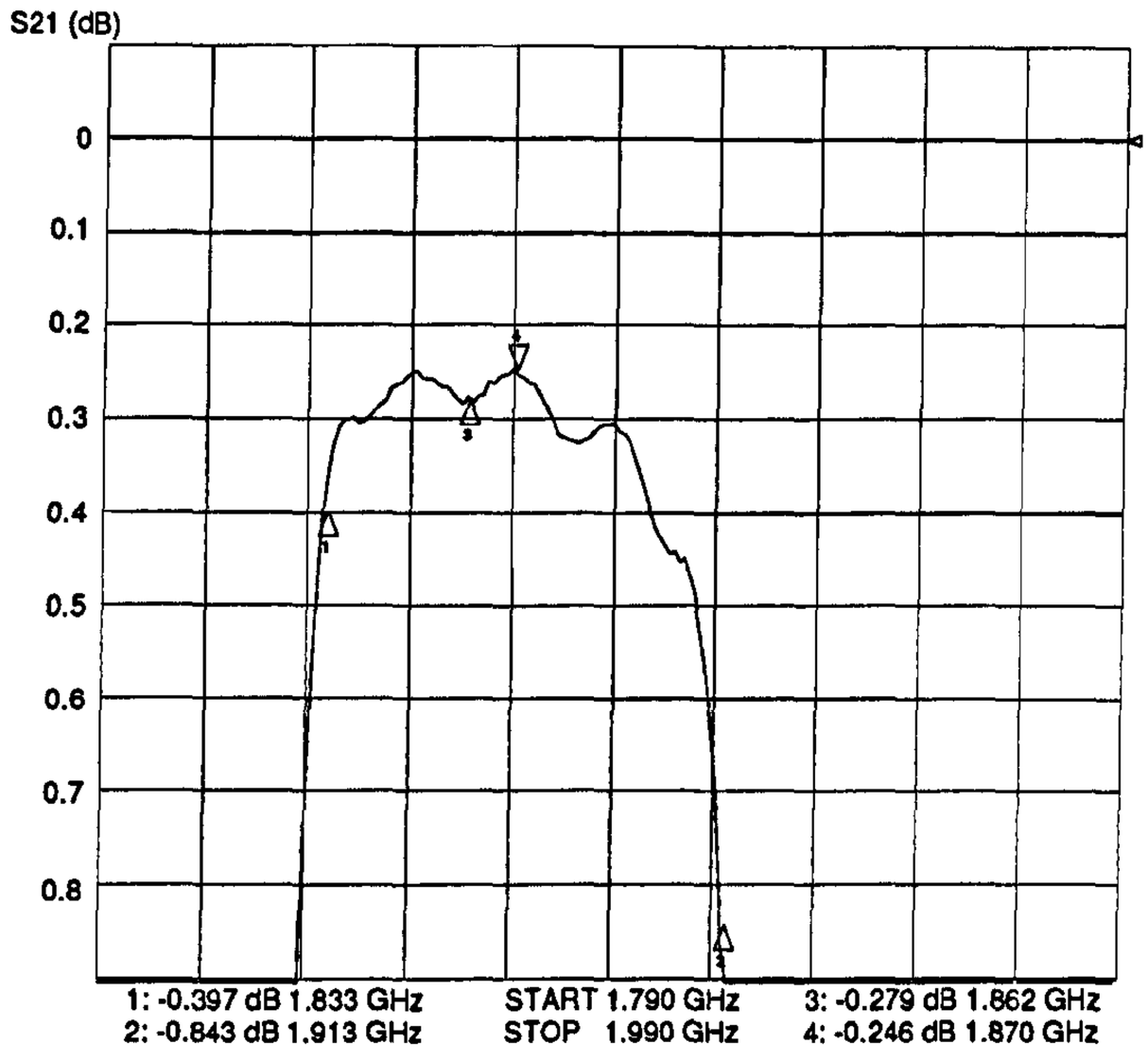

Figure 5.20: Insertion loss of the filter with positive cross-couplings

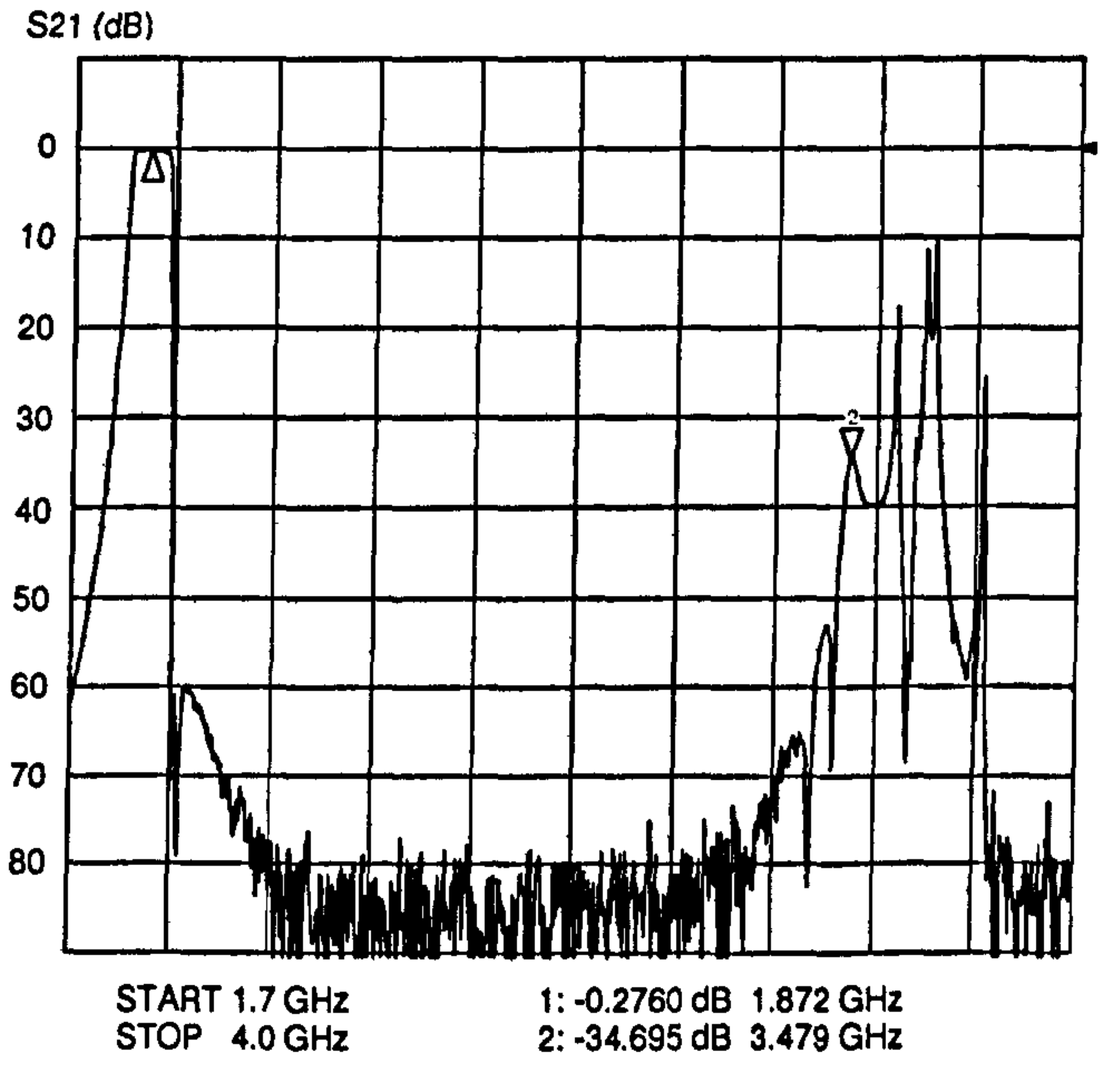

Figure 5.21: Wideband response of the filter with positive cross-couplings

5.6 Conclusion

The electrical performance of the rectangular TE_{011} dielectric-loaded resonator has been investigated at 2 GHz. For maximum Q_u/volume, the cross-section of the resonator varies little. The height of the resonator is increased to reach large Q_u values. However, this limits the spurious performance. As a result, the TE_{011} dielectric-loaded resonator seems optimum for applications with Q_u's of a few thousands. It then combines good Q_u/volume and good spurious separation. For example, a theoretical Q_u of 3000 and F_r of 1.75 are obtained in 2.5 cm^3. The volume of a combline resonator with comparable Q_u is 13.3 cm^3. For larger Q_u values, the separation can be improved by increasing the cross-section of the resonator, although this limits the inter-cavity coupling available. A reliable method of mounting the resonators was demonstrated giving in excess of 80% of the calculated Q_u for perfect silver.

Cross-coupled triplets were used to design typical microcells base-station filters. The coupling between cavities decreases quickly as the cavities are offset, although the dielectric slabs can be moved towards each other and recover some coupling with only a limited Q_u degradation. The amount of frequency tuning and input coupling necessary for the application considered here are also achievable. However, experiments showed that the technique used to realise the latter reduces significantly the Q_u of the resonator. A filter with positive cross-couplings was presented, which has an overall Q_u of 2800 in an internal volume of 35.3 cm^3. This represents a 2.0:1 improvement over the combline technology.

Chapter 6

Conclusions and further work

6.1 Conclusions

This work has concentrated on the study of novel dielectric resonators, all for use in different cellular base-station applications. The performance of each resonator was studied by means of different modelling methods. Filter designs have also been realised to prove the suitability of the resonators for various filter specifications. The results of the previous four chapters and the conclusions that follow are summarised here.

In Chapter 2, the simple shaped triple-mode cubic $TE_{01\delta}$ resonator was studied. It was demonstrated that this resonator is most suited for use in filters requiring Q_u's above 13000 at 2 GHz and 25000 at 900 MHz. A spurious separation above 1.20 is then assured, which is similar to that of the interlocking disc triple-mode $TE_{01\delta}$ resonator. For lower Q_u values, the superiority of the $TM_{01\delta}$ modes over the $TE_{01\delta}$ modes was pointed out.

A novel type of filter, the even-odd mode hybrid reflection filter, was also introduced. It allows the realisation of any symmetrical filter response without the need for cross-couplings. The filter theory was proven with the design of a degree 6 elliptic filter at 900 MHz, using the triple-mode cubic $TE_{01\delta}$ resonator. For such a resonator, the advantage of the new type of filter is maximum, as no cross-couplings are needed inside the individual cavity, but also and more importantly between the cavities. Adding a phase shifter on the input of the even and odd mode networks also eliminated the input-output coupling.

In the case of a degree 6 symmetrical filter, the insensitivity of the response to most spurious couplings was demonstrated. The coupling from the input to the third

mode of the filter sub-network resonator was proven to be the only one that could not be totally cancelled, unless its magnitude was less than a few percent than that of the intentional input coupling. However, drawbacks were also found to the new filter type, namely the high sensitivity of the filter response to a slight detuning of the resonant frequency of any mode and the limited bandwidth of the hybrid. Also, the rejection level of the bandstop filter is limited to the usual bandpass return loss levels, i.e. a maximum of 30 dB.

The suitability of the cubic triple-mode $TE_{01\delta}$ resonator for the realisation of a wide range of conventional highly selective and narrowband bandpass filters was demonstrated for the first time by developing typical 5 MHz wide degree 6 filters at 2 GHz. A significant size reduction of 67% over single-mode $TE_{01\delta}$ resonator filters was obtained. Practical and repeatable means for tuning the filter responses were devised. A method to identify the sign of cross-couplings was established. The magnitude of the two spurious couplings between cavities occurring through irises in two different locations was evaluated experimentally. It was found that, for the same amount of intentional coupling, the minimal amount of spurious coupling was created, for both pairs of modes, through an iris located at the edge of the dividing wall. For a 5 MHz wide filter, the spurious couplings were 3.4% and 0.7% of the main coupling. In the case of a Chebyshev filter response, the sequencing of the modes can be arranged so that the effect of these couplings on the frequency response is minimum. However, this poses restrictions on the filter layout. Also, in the general case, if a cross-coupling in the form of a quadruplet is needed, the order of the modes cannot be chosen. The amount of spurious coupling then increases to prohibitive levels. It was concluded that the realisation of the most general filter response would necessitate the use of additional coupling paths, which would not consist of irises. An example, using electrical probe coupling, was demonstrated.

Chapters 3 and 4 were concerned with the evaluation of a novel resonator, the dual-mode conductor-loaded DR, for macrocell applications at 900 MHz. Simple approximation models were found to be insufficient to predict the frequency of its first resonant modes, typically giving less than 10% accuracy for its fundamental mode. The mode-matching technique was then used. The code of the mode-matching program is available on request. This technique gave very good results. However, in order to give the best accuracy with the least computing time, the numbers of modes

included in each region of the geometry have to be carefully chosen. The study of the correlation between modes in adjacent waveguides allowed the selection of the optimum ratios of modes for good modelling accuracy and limited matrix size. These were found to vary with the type of the propagating modes and, as expected, with the relative dimensions of the regions. It was shown that including modes with less than 20% correlation with all modes used in the central, and smaller, region of the structure gave very little improvement. The optimum ratio of modes between the coaxial and empty regions was found to be close to the ratio of the radial dimensions of the two regions, R_{lin}. This was true for all types of modes. However, this was not the case for the optimum ratio between the dielectric-loaded and coaxial regions. The correlation plots of the hybrid modes in the dielectric-loaded region with a TE mode in the coaxial region were similar to that of the previous interface. The correlation plots with a TM mode, however, had a larger spread in the case of disc diameters smaller than the dielectric cylinder diameter. This increase of the spread was worst as the difference between the two diameters decreased. As a result, a larger ratio of modes was needed for this interface in the case of the modelling of the hybrid and the $TM_{01\delta}$ resonant modes. A minimum of $R_{lin} + 4$ was found to the necessary for the hybrid modes and $R_{lin} + 2$ for the $TM_{01\delta}$ mode, when the two diameters differ by less than 5%. The convergences of the resonant frequency results appeared to be linked to the singularities of the fields at the edges of the dielectric resonator and metal disc: they are worst for the hybrid modes and the $TM_{01\delta}$ mode. The electric fields of these modes present two discontinuities at a very short distance from each other. The convergences of the Q_u simulations were found to be slower and behave quite differently to those of the resonant frequencies. They were linked to the magnitude of the magnetic field tangential to the metal disc in the regions of the singularities. The convergence of the conductor loss on the side of the metal disc was worst for the $HE_{11\delta}$, $HE_{21\delta}$ and $TE_{01\delta}$ modes. For the fundamental mode, the normalised variation $\Delta Q_c/Q_c$ obtained by increasing Nb from 20 to 40 was 2.5%. By comparison, the corresponding normalised frequency variation $\Delta f/f_0$ was 0.06%.

The mode-matching program was used to draw plots from which the main geometry parameters governing resonant frequencies and Q_u were extracted. The Q_u of the fundamental $HE_{11\delta}$ mode was found to be primarily related to the height of the dielectric cylinder. Another important contribution to the Q_u is the loss created

by the metal disc, which is dependent on the disc diameter, but not its height. The loss in the cavity walls is more limited: in the case of comparable disc and dielectric cylinder diameters, it is only more important than the loss in the metal disc if the cavity side and lid are located less than a few millimeters away from the resonator.

The resonant frequency of the $HE_{11\delta}$ mode is, to the first approximation, determined by the diameter of the dielectric cylinder. The effect of the dielectric height is smaller. Also, as the dielectric height is increased, the resonant frequency increases because the field patterns of the $HE_{11\delta}$ mode change away from those of the TM_{110} mode. The opposite happens as the surface of the metal disc is increased. However, as the metal disc diameter reaches values close to that of the dielectric cylinder, the resonant frequency increases again. More generally, reducing the gap between the cavity walls and the resonator increases the resonant frequency. However, this also decreases the frequency of the $TM_{01\delta}$ mode. This limits the spurious performance of average to small size cavities. For larger cavity sizes, the limiting mode becomes the $EH_{11\delta+1}$ mode, which has a resonant frequency that strongly depends on the dielectric cylinder height. Away from these situations, the spurious is the $HE_{21\delta}$ mode, which separation with the $HE_{11\delta}$ mode is not critical on the resonator geometry. It gives the best achievable F_r by the dual-mode conductor-loaded resonator, around 1.67. For cavity volumes between $\sqrt[3]{V}/d_2 = 0.9$ and 1.1, with d_2 the dielectric cylinder diameter and for a wide range of dielectric cylinder heights, the optimum disc to dielectric diameter ratio was shown to be 0.8. The optimum cavity to dielectric ratio varied from 1.2 to 1.6.

The resonator dimensions for maximum Q_u/volume were also calculated at 900 MHz for a wide range of cavity volumes. Maximum Q_u and F_r are more incompatible for larger cavity volumes. However, even in very small cavities, the maximum Q_u/volume and maximum F_r cannot be obtained simultaneously. For a wide range of cavity volumes, the Q_u has to be decreased by 25% from its maximum value to achieve maximum F_r. In 85 cm^3, the maximum Q_u, of 6400, is achieved by trading-off F_r to the lower value of 1.4. Overall, the spurious separation becomes restrictive for filter designs requiring Q_u's of 7000 and above. This is also the case of existing multi-mode resonators such as the dual and triple-mode TM_{010} mode resonators. For Q_u values below 7000, however, the new resonator offers good performance.

In Chapter 5, it was concluded that the TE_{011} mode dielectric-loaded resonator

was best suited for microcell base-station filters at 2 GHz. For higher Q_u values, the limitation comes from the height of the resonator, which becomes large for optimum Q_u/volume geometries. At 2 GHz, the spurious performance of the resonator degrades for cavity heights above 12 mm. The cross-section dimensions of the resonator for optimum Q_u/volume were found to vary little as the cavity volume is changed. 9.5 mm and 18.6 mm for the dielectric slab and cavity lengths respectively were found to give close to optimum results for a wide range of cavity volumes. For cavity heights below 12 mm, these dimensions determined the spurious separation, with $F_r = 1.81$. The TE_{011} mode dielectric-loaded resonator displayed most of the advantages of the combline resonator, for example the ease of frequency and coupling tuning or the possibility of using a two dimensional layout. The magnitude of the inter-cavity coupling bandwidths realisable was also sufficient for full-band filter specifications, except in the case of off-line cavities. However, using off-centred dielectric slabs to increase the couplings did not degrade the resonator performance considerably.

6.2 Suggestions for further work

As the bandwidth of the triple-mode $TE_{01\delta}$ mode bandpass transmission filters of Section 2.4 is increased, it is expected that the spurious couplings will increase and that the resonant frequency of the $TM_{01\delta}$ will decrease. A knowledge of the maximum bandwidth practically realisable could be useful.

It would be useful to study methods of improving the spurious performance of the cubic $TE_{01\delta}$ mode resonator filters. One possible method might be to increase (or decrease) the dimension of the resonator in one of the three directions. In order to keep all three $TE_{01\delta}$ resonances degenerate, the cavity dimension in that same direction could be decreased (or increased) accordingly. The spurious $TM_{01\delta}$ modes would then occur at different frequencies and their transmission through the filter should be limited. Also, the new resonator could be oriented so that the modes with the larger field intensities at the cavity wall are used to realise the largest of the inter-cavity couplings required. This would minimise the spurious couplings. The effect of changing the permittivity on the spurious performance could also be studied.

In [170] and [168], the knowledge of the field variation at the singularity regions of a waveguide discontinuity, obtained from the edge condition, are used to improve the modelling of the fields at this discontinuity. Such methods could be investigated to improve the convergence of the mode-matching modelling of the dual-mode conductor-loaded DR, in particular that of the Q_u calculations.

Some fundamental changes could also be made to the dual-mode conductor-loaded DR to improve its spurious performance. In [157], it was showed that a ring shaped dielectric cylinder would improve the separation between the $HE_{11\delta}$ and $EH_{11\delta+1}$ modes. Also, using a ring shaped metal disc could decrease the loading of the $TM_{01\delta}$ mode while having a minimum effect on the $HE_{11\delta}$ mode. Both changes could be implemented in the mode-matching program and the new geometry could be re-optimised. For both modifications, the mode-matching geometry would still consist of three regions. However, one has to take into account the fact that new singularities would then appear, both at the dielectric and the metal inner edges. This will most certainly have an impact on the efficiency of the mode-matching modelling.

The possibility of using the dual-mode conductor-loaded DR as a triple-mode resonator could be investigated. In particular, the resonant frequency of the $TM_{01\delta}$ mode could be decreased to coincide with that of the $HE_{11\delta}$ mode. This could be realised by increasing the metal disc diameter or decreasing the cavity dimensions. Alternatively, a metallic boss could be added on top of the disc, which would limit the degradation in Q_u of the $HE_{11\delta}$ mode. The tuning of the $TM_{01\delta}$ mode would be realised from the centre point of the cavity lid. This mode would also offer larger coupling bandwidths, desirable in particular for inter-cavity couplings.

Appendix A

Field expressions and characteristic equations for partially dielectric loaded, coaxial and homogeneously filled circular waveguides

Let us consider a waveguide as a medium with no free charges or convection currents and where the permittivity and permeability are scalar constants. The waves in this waveguide are considered to be time-harmonic i.e. of variation $e^{(j\omega t-\gamma z)}$. Their electric and magnetic fields then satisfy the Helmholtz equations for phasor fields:

$$\nabla^2\mathbf{E} = -k^2\mathbf{E} \qquad \text{and} \qquad \nabla^2\mathbf{H} = -k^2\mathbf{H} \tag{A.1}$$

with $k^2 = \omega^2\varepsilon\mu$ where ω is the angular frequency, ε the permittivity of the medium and μ its permeability. In both rectangular and cylindrical coordinate systems, the left-hand part of Eq. A.1 can be separated into a transverse and a longitudinal part:

$$\nabla^2 = \nabla_t^2 + \frac{\partial^2}{\partial z^2} \tag{A.2}$$

This leads to:

$$\nabla_t^2\mathbf{E} = \nabla^2\mathbf{E} - \frac{\partial\mathbf{E}^2}{\partial z^2} = -(\gamma^2 + k^2)\mathbf{E} \tag{A.3}$$

$$\nabla_t^2\mathbf{H} = \nabla^2\mathbf{H} - \frac{\partial\mathbf{H}^2}{\partial z^2} = -(\gamma^2 + k^2)\mathbf{H} \tag{A.4}$$

The transverse variations of two components of the fields (e.g. E_z and H_z) are deduced by solving Eqs. A.3 and A.4, using the separation of variables method. The other components are then derived using the curl equations $\nabla \times \mathbf{E} = -\mathrm{j}\omega\mu\mathbf{H}$ and $\nabla \times \mathbf{H} = -\mathrm{j}\omega\mu\mathbf{E}$.

A.1 Partially dielectric-loaded circular waveguide

The field expressions of the normal modes and their corresponding characteristic equations in a dielectric rod loaded circular waveguide can be found in the literature [146, 30, 31, 179]. The general case of a multilayered coated waveguide has also been published [180].

The wave numbers in the dielectric and air regions (named region 1 and 2 respectively) are then:

$$k_1 = \sqrt{\omega\mu_0\epsilon_0\epsilon_{r1}} \qquad k_2 = \sqrt{\omega\mu_0\epsilon_0\epsilon_{r2}} \tag{A.5}$$

where μ_0 and ϵ_0 are the vacuum permeability and permittivity. ϵ_i is the relative permittivity of region i. The wave numbers in the radial direction for a mode with a propagation constant γ are then:

$$\xi_1 = \sqrt{k_1^2 + \gamma^2} \qquad \xi_2 = -j\zeta_2 = \sqrt{k_2^2 + \gamma^2} \tag{A.6}$$

Let us consider a waveguide with a dielectric rod radius r_2 and enclosure radius r_3.

A.1.1 Hybrid modes

In region 1, the fields expressions are:

$$E_z = J_n(\xi_1 r)\cos n\theta \tag{A.7}$$

$$H_z = \frac{\kappa\gamma}{j\omega\mu_o} J_n(\xi_1 r)\sin n\theta \tag{A.8}$$

$$E_r = \frac{-\gamma}{\xi_1^2}[\xi_1 J_n'(\xi_1 r) + \frac{\kappa n}{r} J_n(\xi_1 r)]\cos n\theta \tag{A.9}$$

$$E_\theta = \frac{\gamma}{\xi_1^2}[\frac{n}{r} J_n(\xi_1 r) + \kappa\xi_1 J_n'(\xi_1 r)]\sin n\theta \tag{A.10}$$

$$H_r = \frac{1}{j\omega\mu_0\xi_1^2}[\frac{nk_1^2}{r} J_n(\xi_1 r) - \kappa\gamma^2\xi_1 J_n'(\xi_1 r)]\sin n\theta \tag{A.11}$$

$$H_\theta = \frac{-1}{j\omega\mu_0\xi_1^2}[-k_1^2\xi_1 J_n'(\xi_1 r) + \frac{\kappa\gamma^2 n}{r} J_n(\xi_1 r)]\cos n\theta \tag{A.12}$$

In region 2, if ξ_2 is real,

$$E_z = R_n(\xi_2 r)\cos n\theta \tag{A.13}$$

$$H_z = \frac{\kappa\gamma}{j\omega\mu_o} P_n(\xi_2 r)\sin n\theta \tag{A.14}$$

$$E_r = \frac{-\gamma}{\xi_2^2}[\xi_2 R_n'(\xi_2 r) + \frac{\kappa n}{r} P_n(\xi_2 r)]\cos n\theta \tag{A.15}$$

$$E_\theta = \frac{\gamma}{\xi_2^2}[\frac{n}{r}R_n(\xi_2 r) + \kappa\xi_2 P_n'(\xi_2 r)]\sin n\theta \tag{A.16}$$

$$H_r = \frac{1}{j\omega\mu_0\xi_2^2}[\frac{nk_2^2}{r}R_n(\xi_2 r) - \kappa\gamma^2\xi_2 P_n'(\xi_2 r)]\sin n\theta \tag{A.17}$$

$$H_\theta = \frac{-1}{j\omega\mu_0\xi_2^2}[-k_2^2\xi_1 R_n'(\xi_2 r) + \frac{\kappa\gamma^2 n}{r}P_n(\xi_2 r)]\cos n\theta \tag{A.18}$$

with J_n and Y_n Bessel functions of the first and second kind of order n and

$$R_n(\xi_2 r) = J_n(\xi_1 r_2)\left[\frac{Y_n(\xi_2 r)J_n(\xi_2 r_3) - J_n(\xi_2 r)Y_n(\xi_2 r_3)}{Y_n(\xi_2 r_2)J_n(\xi_2 r_3) - J_n(\xi_2 r_2)Y_n(\xi_2 r_3)}\right] \tag{A.19}$$

$$P_n(\xi_2 r) = J_n(\xi_1 r_2)\left[\frac{Y_n(\xi_2 r)J_n'(\xi_2 r_3) - J_n(\xi_2 r)Y_n'(\xi_2 r_3)}{Y_n(\xi_2 r_2)J_n'(\xi_2 r_3) - J_n(\xi_2 r_2)Y_n'(\xi_2 r_3)}\right] \tag{A.20}$$

Ensuring the continuity of E_θ and H_θ at $r = r_2$ gives the expression for κ and the characteristic equation.

$$\kappa = \frac{-nJ_n(\xi_1 r_2)\left(\frac{1}{\xi_1^2 r_2^2} - \frac{1}{\xi_2^2 r_2^2}\right)}{\frac{J_n'(\xi_1 r_2)}{\xi_1 r_2} - \frac{P_n'(\xi_2 r_2)}{\xi_2 r_2}} \tag{A.21}$$

$$\frac{1}{J_n^2(\xi_1 r_2)}\left(\frac{J_n'(\xi_1 r_2)}{\xi_1 r_2} - \frac{P_n'(\xi_2 r_2)}{\xi_2 r_2}\right)\left(\varepsilon_{r1}\frac{J_n'(\xi_1 r_2)}{\xi_1 r_2} - \varepsilon_{r2}\frac{R_n'(\xi_2 r_2)}{\xi_2 r_2}\right) + \frac{\gamma^2 n^2}{k_0^2}\left(\frac{1}{\xi_1^2 r_2^2} - \frac{1}{\xi_2^2 r_2^2}\right)^2 = 0 \tag{A.22}$$

If $\zeta_2 = j\xi_2$ is real, Eqs. A.13 to A.18 become:

$$E_z = S_n(\zeta_2 r)\cos n\theta \tag{A.23}$$

$$H_z = \frac{\kappa\gamma}{j\omega\mu_o}T_n(\zeta_2 r)\sin n\theta \tag{A.24}$$

$$E_r = \frac{\gamma}{\zeta_2^2}[\zeta_2 S_n'(\zeta_2 r) + \frac{\kappa n}{r}T_n(\zeta_2 r)]\cos n\theta \tag{A.25}$$

$$E_\theta = \frac{-\gamma}{\zeta_2^2}[\frac{n}{r}S_n(\zeta_2 r) + \kappa\zeta_2 T_n'(\zeta_2 r)]\sin n\theta \tag{A.26}$$

$$H_r = \frac{-1}{j\omega\mu_0\zeta_2^2}[\frac{nk_2^2}{r}S_n(\zeta_2 r) - \kappa\gamma^2\zeta_2 T_n'(\zeta_2 r)]\sin n\theta \tag{A.27}$$

$$H_\theta = \frac{1}{j\omega\mu_0\zeta_2^2}[-k_2^2\zeta_2 S_n'(\zeta_2 r) + \frac{\kappa\gamma^2 n}{r}T_n(\zeta_2 r)]\cos n\theta \tag{A.28}$$

with I_n and K_n modified Bessel functions of order n and

$$S_n(\zeta_2 r) = J_n(\xi_1 r_2)\left[\frac{K_n(\zeta_2 r)I_n(\zeta_2 r_3) - I_n(\zeta_2 r)K_n(\zeta_2 r_3)}{K_n(\zeta_2 r_2)I_n(\zeta_2 r_3) - I_n(\zeta_2 r_2)K_n(\zeta_2 r_3)}\right] \tag{A.29}$$

$$T_n(\zeta_2 r) = J_n(\xi_1 r_2)\left[\frac{K_n(\zeta_2 r)I_n'(\zeta_2 r_3) - I_n(\zeta_2 r)K_n'(\zeta_2 r_3)}{K_n(\zeta_2 r_2)I_n'(\zeta_2 r_3) - I_n(\zeta_2 r_2)K_n'(\zeta_2 r_3)}\right] \tag{A.30}$$

The characteristic equation is then

$$\frac{1}{J_n^2(\xi_1 r_2)}\left(\frac{J_n'(\xi_1 r_2)}{\xi_1 r_2}+\frac{T_n'(\zeta_2 r_2)}{\zeta_2 r_2}\right)\left(\varepsilon_{r1}\frac{J_n'(\xi_1 r_2)}{\xi_1 r_2}+\varepsilon_{r2}\frac{S_n'(\zeta_2 r_2)}{\zeta_2 r_2}\right) + \frac{\gamma^2 n^2}{k_0^2}\left(\frac{1}{\xi_1^2 r_2^2}-\frac{1}{\zeta_2^2 r_2^2}\right)^2 = 0 \quad \text{(A.31)}$$

with

$$\kappa = \frac{nJ_n(\xi_1 r_2)\left(\frac{1}{\xi_1^2 r_2^2}+\frac{1}{\zeta_2^2 r_2^2}\right)}{\frac{J_n'(\xi_1 r_2)}{\xi_1 r_2}+\frac{T_n'(\zeta_2 r_2)}{\zeta_2 r_2}} \quad \text{(A.32)}$$

A.1.2 TE modes

In region 1

$$H_z = \frac{\gamma}{j\omega\mu_o}J_0(\xi_1 r)\sin n\theta \quad \text{(A.33)}$$

$$E_\theta = \frac{\gamma}{\xi_1}J_0'(\xi_1 r)\sin n\theta \quad \text{(A.34)}$$

$$H_r = \frac{-\gamma^2}{j\omega\mu_o\xi_1}J_0'(\xi_1 r)\sin n\theta \quad \text{(A.35)}$$

In region 2, if ξ_2 is real,

$$H_z = \frac{\gamma}{j\omega\mu_o}P_0(\xi_2 r)\sin n\theta \quad \text{(A.36)}$$

$$E_\theta = \frac{\gamma}{\xi_2}P_0'(\xi_2 r)\sin n\theta \quad \text{(A.37)}$$

$$H_r = \frac{-\gamma^2}{j\omega\mu_o\xi_2}P_0'(\xi_2 r)\sin n\theta \quad \text{(A.38)}$$

The characteristic equation becomes

$$\frac{1}{J_0(\xi_1 r_2)}\left(\frac{J_0'(\xi_1 r_2)}{\xi_1 r_2}-\frac{P_0'(\xi_2 r_2)}{\xi_2 r_2}\right)=0 \quad \text{(A.39)}$$

If ζ_2 is real,

$$H_z = \frac{\gamma}{j\omega\mu_o}T_0(\zeta_2 r)\sin n\theta \quad \text{(A.40)}$$

$$E_\theta = \frac{-\gamma}{\zeta_2}T_0'(\zeta_2 r)\sin n\theta \quad \text{(A.41)}$$

$$H_r = \frac{\gamma^2}{j\omega\mu_o\zeta_2}T_0'(\zeta_2 r)\sin n\theta \quad \text{(A.42)}$$

and the characteristic equation is

$$\frac{1}{J_0(\xi_1 r_2)}\left(\frac{J_0'(\xi_1 r_2)}{\xi_1 r_2}+\frac{T_0'(\zeta_2 r_2)}{\zeta_2 r_2}\right)=0 \quad \text{(A.43)}$$

A.1.3 TM modes

In region 1

$$E_z = J_0(\xi_1 r)\cos n\theta \tag{A.44}$$

$$E_r = \frac{-\gamma}{\xi_1} J_0'(\xi_1 r)\cos n\theta \tag{A.45}$$

$$H_\theta = \frac{k_1^2}{j\omega\mu_o\xi_1} J_0'(\xi_1 r)\cos n\theta \tag{A.46}$$

In region 2, if ξ_2 is real,

$$E_z = R_0(\xi_2 r)\cos n\theta \tag{A.47}$$

$$E_r = \frac{-\gamma}{\xi_2} R_0'(\xi_2 r)\cos n\theta \tag{A.48}$$

$$H_\theta = \frac{k_2^2}{j\omega\mu_o\xi_2} R_0'(\xi_2 r)\cos n\theta \tag{A.49}$$

and characteristic equation is

$$\frac{1}{J_0(\xi_1 r_2)}\left(\frac{\varepsilon_{r1} J_0'(\xi_1 r_2)}{\xi_1 r_2} - \frac{\varepsilon_{r2} R_0'(\xi_2 r_2)}{\xi_2 r_2}\right) = 0 \tag{A.50}$$

If $\zeta_2 =$ is real,

$$E_z = R_0(\zeta_2 r)\cos n\theta \tag{A.51}$$

$$E_r = \frac{\gamma}{\zeta_2} S_0'(\zeta_2 r)\cos n\theta \tag{A.52}$$

$$H_\theta = \frac{-k_2^2}{j\omega\mu_o\zeta_2} S_0'(\zeta_2 r)\cos n\theta \tag{A.53}$$

and the characteristic equation is

$$\frac{1}{J_0(\xi_1 r_2)}\left(\frac{\varepsilon_{r1} J_0'(\xi_1 r_2)}{\xi_1 r_2} + \frac{\varepsilon_{r2} S_0'(\zeta_2 r_2)}{\zeta_2 r_2}\right) = 0 \tag{A.54}$$

A.2 Homogeneously filled coaxial waveguide

Let us note r_1 and r_3 the inner and outer radii of the waveguide respectively, and ε_r the relative permittivity of the waveguide filling material such that $k = \sqrt{\omega\mu_0\varepsilon_0\varepsilon_r}$. ξ is the wave number in the radial direction.

A.2.1 TE modes

$$H_z = \frac{\gamma}{j\omega\mu_0}[-\frac{Y_n'(\xi r_1)}{J_n'(\xi r_1)}J_n(\xi r) + Y_n(\xi r)]\sin n\theta \tag{A.55}$$

$$E_r = \frac{-\gamma n}{\xi^2 r}[-\frac{Y_n'(\xi r_1)}{J_n'(\xi r_1)}J_n(\xi r) + Y_n(\xi r)]\cos n\theta \tag{A.56}$$

$$E_\theta = \frac{\gamma}{\xi}[-\frac{Y_n'(\xi r_1)}{J_n'(\xi r_1)}J_n'(\xi r) + Y_n'(\xi r)]\sin n\theta \tag{A.57}$$

$$H_r = \frac{-\gamma^2}{j\omega\mu_0\xi}[-\frac{Y_n'(\xi r_1)}{J_n'(\xi r_1)}J_n'(\xi r) + Y_n'(\xi r)]\sin n\theta \tag{A.58}$$

$$H_\theta = \frac{-\gamma^2 n}{j\omega\mu_0\xi^2 r}[-\frac{Y_n'(\xi r_1)}{J_n'(\xi r_1)}J_n(\xi r) + Y_n(\xi r)]\cos n\theta \tag{A.59}$$

The characteristic equation is

$$J_n'(\xi r_1)Y_n'(\xi r_3) - Y_n'(\xi r_1)J_n'(\xi r_3) = 0 \tag{A.60}$$

A.2.2 TM modes

$$E_z = [-\frac{Y_n(\xi r_1)}{J_n(\xi r_1)}J_n(\xi r) + Y_n(\xi r)]\cos n\theta \tag{A.61}$$

$$E_r = \frac{-\gamma}{\xi}[-\frac{Y_n(\xi r_1)}{J_n(\xi r_1)}J_n'(\xi r) + Y_n'(\xi r)]\cos n\theta \tag{A.62}$$

$$E_\theta = \frac{\gamma n}{\xi^2 r}[-\frac{Y_n(\xi r_1)}{J_n(\xi r_1)}J_n(\xi r) + Y_n(\xi r)]\sin n\theta \tag{A.63}$$

$$H_r = \frac{nk^2}{j\omega\mu_0\xi^2 r}[-\frac{Y_n(\xi r_1)}{J_n(\xi r_1)}J_n(\xi r) + Y_n(\xi r)]\sin n\theta \tag{A.64}$$

$$H_\theta = \frac{k^2}{j\omega\mu_0\xi}[-\frac{Y_n(\xi r_1)}{J_n(\xi r_1)}J_n'(\xi r) + Y_n'(\xi r)]\cos n\theta \tag{A.65}$$

The characteristic equation is

$$J_n(\xi r_1)Y_n(\xi r_3) - Y_n(\xi r_1)J_n(\xi r_3) = 0 \tag{A.66}$$

A.2.3 TEM mode

$$E_r = \frac{1}{r} \tag{A.67}$$

$$H_\theta = \sqrt{\frac{\epsilon_0\epsilon_r}{\mu_0}}\frac{1}{r} \tag{A.68}$$

The characteristic equation is

$$\gamma^2 = -k^2 \tag{A.69}$$

A.3 Homogeneously filled circular waveguide

Let us note r_3 the radius of the waveguide and ε_r the relative permittivity of the waveguide filling material such that $k = \sqrt{\omega\mu_0\varepsilon_0\varepsilon_r}$. Again, ξ is the wave number in the radial direction.

A.3.1 TE modes

$$H_z = \frac{\gamma}{j\omega\mu_0} J_n(\xi r)\sin n\theta \tag{A.70}$$

$$E_r = \frac{-\gamma n}{\xi^2 r} J_n(\xi r)\cos n\theta \tag{A.71}$$

$$E_\theta = \frac{\gamma}{\xi} J'_n(\xi r)\sin n\theta \tag{A.72}$$

$$H_r = \frac{-\gamma^2}{j\omega\mu_0\xi} J'_n(\xi r)\sin n\theta \tag{A.73}$$

$$H_\theta = \frac{-\gamma^2 n}{j\omega\mu_0\xi^2 r} J_n(\xi r)\cos n\theta \tag{A.74}$$

The characteristic equation is

$$J'_n(\xi r_3) = 0 \tag{A.75}$$

A.3.2 TM modes

$$E_z = J_n(\xi r)\cos n\theta \tag{A.76}$$

$$E_r = \frac{-\gamma}{\xi} J'_n(\xi r)\cos n\theta \tag{A.77}$$

$$E_\theta = \frac{\gamma n}{\xi^2 r} J_n(\xi r)\sin n\theta \tag{A.78}$$

$$H_r = \frac{nk^2}{j\omega\mu_0\xi^2 r} J_n(\xi r)\sin n\theta \tag{A.79}$$

$$H_\theta = \frac{k^2}{j\omega\mu_0\xi} J'_n(\xi r)\cos n\theta \tag{A.80}$$

The characteristic equation is

$$J_n(\xi r_3) = 0 \tag{A.81}$$

Appendix B

Preliminaries on Mode-Matching

The concept behind the mode-matching technique is described in Section 1.5.3. The aim of this appendix is to define the terminology and underline the main steps of the procedure followed to find the resonant frequencies of the particular geometries studied in this thesis. The procedure is detailed for a three section structure used in two different cases in Chapter 3, 4 and 5 and a seven section structure used for coupling simulations in Chapter 5. One restriction of the method presented here is that the cross-section of every second waveguide has to be totally overlapped by those of the two adjacent waveguides. The total overlapping is due to the choice of the testing functions used to realise the vector products [181, 121, 128].

The first step is to expand the transverse fields in each waveguide section of the structure as an infinite series of the fields of the waveguide modes. Each waveguide mode is an independent solution to the Helmholtz equations for phasor fields, also satisfying the boundary conditions and electrical properties of the waveguide cross-section. As these modes form a complete orthogonal set, the total fields in the waveguide are described in a unique manner as a weighted sum of the mode fields. Let us express the transverse part of the field of the mode i of a particular waveguide as

$$\hat{\mathbf{e}}_i(x,y,z) = \overline{\mathbf{e}}_i(x,y)e^{\pm\gamma_i z} \qquad \hat{\mathbf{h}}_i(x,y,z) = \overline{\mathbf{h}}_i(x,y)e^{\pm\gamma_i z} \tag{B.1}$$

in rectangular coordinates and

$$\hat{\mathbf{e}}_i(r,\theta,z) = \overline{\mathbf{e}}_i(r,\theta)e^{\pm\gamma_i z} \qquad \hat{\mathbf{h}}_i(r,\theta,z) = \overline{\mathbf{h}}_i(r,\theta)e^{\pm\gamma_i z} \tag{B.2}$$

in cylindrical coordinates.

In the subsequent text, the spatial dependence symbols (e.g. (x,y,z)) will be

omitted. The total transverse electric field in the waveguide can be written as

$$\mathbf{E_t} = \sum_{i=1}^{\infty} \overline{\mathbf{e}}_\mathbf{i}(a_i^+ e^{-\gamma_i z} + a_i^- e^{+\gamma_i z}) \tag{B.3}$$

and to satisfy the curl equations $\nabla \times \mathbf{E} = -\mathrm{j}\omega\mu\mathbf{H}$ and $\nabla \times \mathbf{H} = -\mathrm{j}\omega\mu\mathbf{E}$, $\mathbf{H_t}$ is:

$$\mathbf{H_t} = \sum_{i=1}^{\infty} \overline{\mathbf{h}}_\mathbf{i}(a_i^+ e^{-\gamma_i z} - a_i^- e^{+\gamma_i z}) \tag{B.4}$$

with a_i^+ and a_i^- the forward and reverse coefficients of the mode i in the waveguide and γ_i the propagation constant of this mode. The latter can be calculated for a given frequency by solving the characteristic equation of the waveguide.

B.1 Three section mode-matching procedure

The first geometry presented here is a cascade of three waveguide sections, short-circuited at both extremities, as shown in Fig. B.1.

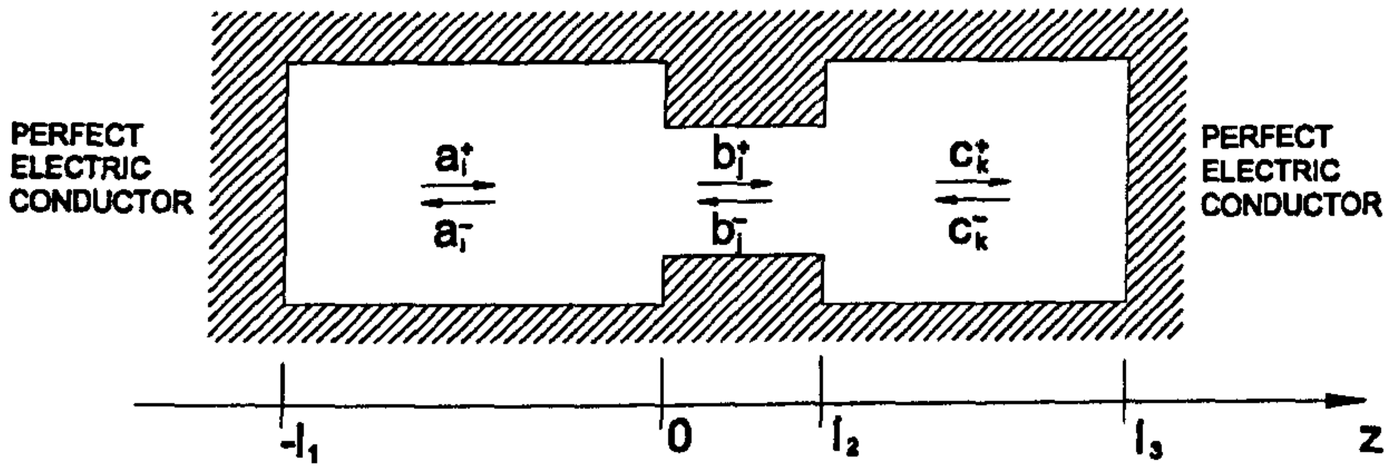

Figure B.1: Three section waveguide geometry

The transverse fields are matched at each interface between two consecutive waveguides. This gives

$$\sum_{i=1}^{\infty} \overline{\mathbf{e}}_{\mathbf{ai}}(a_i^+ + a_i^-) = \sum_{j=1}^{\infty} \overline{\mathbf{e}}_{\mathbf{bj}}(b_j^+ + b_j^-) \tag{B.5}$$

$$\sum_{i=1}^{\infty} \overline{\mathbf{h}}_{\mathbf{ai}}(a_i^+ - a_i^-) = \sum_{j=1}^{\infty} \overline{\mathbf{h}}_{\mathbf{bj}}(b_j^+ - b_j^-) \tag{B.6}$$

$$\sum_{j=1}^{\infty} \overline{\mathbf{e}}_{\mathbf{bj}}(b_j^+ e^{-\gamma_{bj} l_2} + b_j^- e^{+\gamma_{bj} l_2}) = \sum_{k=1}^{\infty} \overline{\mathbf{e}}_{\mathbf{ck}}(c_k^+ e^{-\gamma_{ck} l_2} + c_k^- e^{+\gamma_{ck} l_2}) \tag{B.7}$$

$$\sum_{j=1}^{\infty} \overline{\mathbf{h}}_{\mathbf{bj}}(b_j^+ e^{-\gamma_{bj} l_2} - b_j^- e^{+\gamma_{bj} l_2}) = \sum_{k=1}^{\infty} \overline{\mathbf{h}}_{\mathbf{ck}}(c_k^+ e^{-\gamma_{ck} l_2} - c_k^- e^{+\gamma_{ck} l_2}) \tag{B.8}$$

where the first and second subscripts of $\overline{\mathbf{e}}$, $\overline{\mathbf{h}}$ and γ denote the waveguide and the mode number respectively. The six sets of unknown coefficients a_i^+, a_i^-, b_j^+, b_j^-, c_k^+ and c_k^- are the forward and reverse coefficients of the modes in region A, B and C respectively.

Next, Eqs. B.5-B.8 are broken down into four infinite sets of equations by applying the orthogonality property of the modes within each waveguide:

$$\int_S \overline{\mathbf{e}}_{\mathbf{xi}} \times \overline{\mathbf{h}}_{\mathbf{xj}} dS = 0 \qquad i \neq j \tag{B.9}$$

with S the cross-section of waveguide x. The vector products of Eq. B.5 with $\overline{\mathbf{h}}_{\mathbf{aI}}$, and Eq. B.7 with $\overline{\mathbf{h}}_{\mathbf{aK}}$ are formed and both are integrated over S_B, cross-section of the smaller (middle) waveguide. This gives

$$\sum_{i=1}^{\infty}(a_i^+ + a_i^-) \int_{S_B} \overline{\mathbf{e}}_{\mathbf{aI}} \times \overline{\mathbf{h}}_{\mathbf{aI}} dS = \sum_{j=1}^{\infty}(b_j^+ + b_j^-) \int_{S_B} \overline{\mathbf{e}}_{\mathbf{bJ}} \times \overline{\mathbf{h}}_{\mathbf{aI}} dS \tag{B.10}$$

$$\sum_{j=1}^{\infty}(b_j^+ e^{-\gamma_{bj} l_2} + b_j^- e^{+\gamma_{bj} l_2}) \int_{S_B} \overline{\mathbf{e}}_{\mathbf{bJ}} \times \overline{\mathbf{h}}_{\mathbf{cK}} dS =$$

$$\sum_{k=1}^{\infty}(c_j^+ e^{-\gamma_{ck} l_2} + c_k^- e^{+\gamma_{ck} l_2}) \int_{S_B} \overline{\mathbf{e}}_{\mathbf{cK}} \times \overline{\mathbf{h}}_{\mathbf{cK}} dS \tag{B.11}$$

The integrals on the left-hand side of Eq. B.10 and the right-hand side of Eq. B.11 can be extended over the full cross-sections of waveguides A and C respectively, since the transverse electric fields vanish over the perfect conductor surfaces ($z = 0$ and $z = l_2$), giving:

$$\sum_{i=1}^{\infty} \overline{\mathbf{e}}_{\mathbf{aI}}(a_i^+ + a_i^-) = 0 \tag{B.12}$$

$$\sum_{k=1}^{\infty} \overline{\mathbf{e}}_{\mathbf{ck}}(c_k^+ e^{-\gamma_{ck} l_2} + c_k^- e^{+\gamma_{ck} l_2}) = 0 \tag{B.13}$$

Finally, by applying the boundary conditions at both extremities of the structure, the number of unknown sets of coefficients can be decreased from six to four. In this example, the extremities are perfect electric conductors and give the following equations:

$$a_i^- = -a_i^+ e^{2\gamma_{ai} l_1} \qquad \textit{and} \qquad c_k^+ = -c_k^- e^{2\gamma_{ck} l_3} \tag{B.14}$$

The resulting equations are then

$$a_I^+(1 - e^{2\gamma_{aI} l_1}) \int_{S_A} \overline{\mathbf{e}}_{\mathbf{aI}} \times \overline{\mathbf{h}}_{\mathbf{aI}} dS = \sum_{j=1}^{\infty}(b_j^+ + b_j^-) \int_{S_B} \overline{\mathbf{e}}_{\mathbf{bJ}} \times \overline{\mathbf{h}}_{\mathbf{aI}} dS \tag{B.15}$$

$$\sum_{j=1}^{\infty}(b_j^+ e^{-\gamma_{bj}l_2} + b_j^- e^{+\gamma_{bj}l_2}) \int_{S_B} \bar{\mathbf{e}}_{\mathbf{bJ}} \times \bar{\mathbf{h}}_{\mathbf{cK}} dS =$$

$$c_K^- e^{\gamma_{cK}l_2}(1 - e^{2\gamma_{cK}l_2}) \int_{S_C} \bar{\mathbf{e}}_{\mathbf{cK}} \times \bar{\mathbf{h}}_{\mathbf{cK}} dS \tag{B.16}$$

Similarly, Eqs. B.6 and B.8 are vector multiplied by $\bar{\mathbf{e}}_{\mathbf{bJ}}$ and the result is integrated over S_B to give

$$\sum_{i=1}^{\infty} a_i^+(1 + e^{2\gamma_{ai}l_1}) \int_{S_B} \bar{\mathbf{e}}_{\mathbf{bJ}} \times \bar{\mathbf{h}}_{\mathbf{aI}} dS = (b_J^+ - b_J^-) \int_{S_B} \bar{\mathbf{e}}_{\mathbf{bJ}} \times \bar{\mathbf{h}}_{\mathbf{bJ}} dS \tag{B.17}$$

$$(b_J^+ e^{-\gamma_{bJ}l_2} - b_J^- e^{+\gamma_{bJ}l_2}) \int_{S_B} \bar{\mathbf{e}}_{\mathbf{bJ}} \times \bar{\mathbf{h}}_{\mathbf{bJ}} dS =$$

$$\sum_{k=1}^{\infty} c_k^- e^{\gamma_{ck}l_2}(-1 - e^{2\gamma_{ck}l_3}) \int_{S_B} \bar{\mathbf{e}}_{\mathbf{bJ}} \times \bar{\mathbf{h}}_{\mathbf{ck}} dS \tag{B.18}$$

Eqs. B.15 to B.18 can be simplified by noting

$$\int_S \bar{\mathbf{e}}_{\mathbf{xp}} \times \bar{\mathbf{h}}_{\mathbf{xp}} dS = P_{xp} \tag{B.19}$$

$$\int_{S_x} \bar{\mathbf{e}}_{\mathbf{xp}} \times \bar{\mathbf{h}}_{\mathbf{ym}} dS = P_{xypm} \tag{B.20}$$

to give the following system:

$$a_I^+(1 - e^{2\gamma_{aI}l_1})P_{aI} = \sum_{j=1}^{\infty}(b_j^+ + b_j^-)P_{bajI} \tag{B.21}$$

$$\sum_{j=1}^{\infty}(b_j^+ e^{-\gamma_{bj}l_2} + b_j^- e^{+\gamma_{bj}l_2})P_{bcjK} = c_K^- e^{\gamma_{cK}l_2}(1 - e^{2\gamma_{cK}l_3})P_{cK} \tag{B.22}$$

$$\sum_{i=1}^{\infty} a_i^+(1 + e^{2\gamma_{ai}l_1})P_{baJi} = (b_J^+ - b_J^-)P_{bJ} \tag{B.23}$$

$$(b_J^+ e^{-\gamma_{bJ}l_2} - b_J^- e^{+\gamma_{bJ}l_2})P_{bJ} = \sum_{k=1}^{\infty} c_k^- e^{\gamma_{ck}l_2}(-1 - e^{2\gamma_{ck}l_3})P_{bcJk} \tag{B.24}$$

This system can finally be put in a matrix form:

$$[\mathbf{M}] \begin{bmatrix} \mathbf{a}^+ \\ \mathbf{b}^+ \\ \mathbf{b}^- \\ \mathbf{c}^- \end{bmatrix} = 0 \tag{B.25}$$

with $\mathbf{M}$ a square matrix and $\mathbf{a}^+$, $\mathbf{b}^+$, $\mathbf{b}^-$ and $\mathbf{c}^-$ column vectors containing the infinite sets of mode coefficients. Only at the resonant frequencies of the structures, for which $\det(\mathbf{M}) = 0$, will non-trivial solutions exist. The order of the linear system is then decreased by 1 and all field coefficients can be found by Gaussian elimination after one of the field coefficients is fixed to an arbitrary value [133, 19].

B.2 Seven section mode-matching procedure

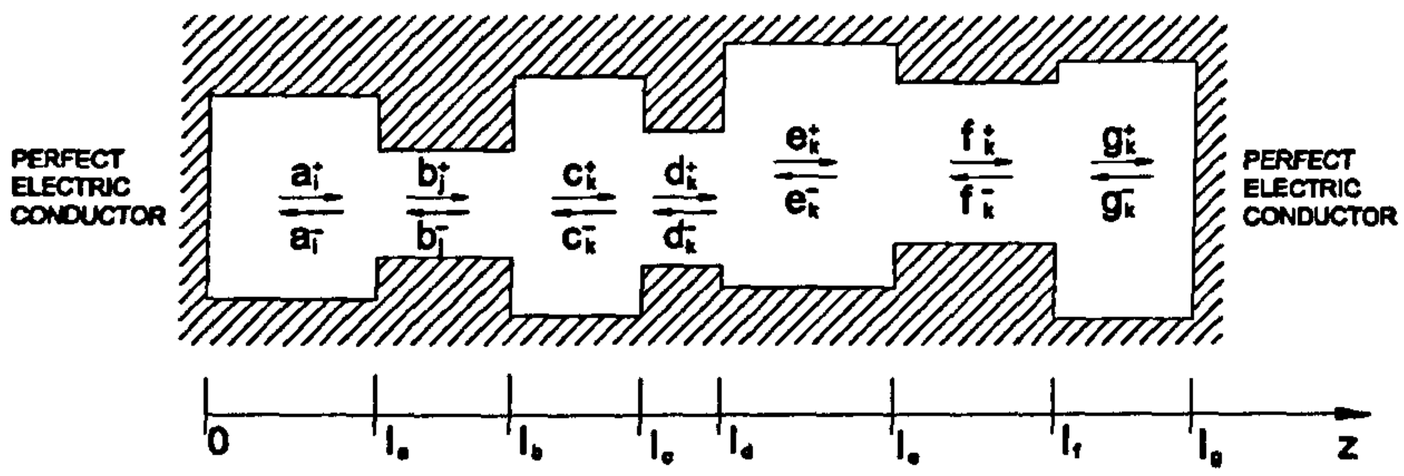

Figure B.2: Seven section waveguide geometry

A seven section cascade is necessary for the calculation of the coupling between two dielectric-loaded cavities as in Chapter 5. As in the previous section, the transverse fields are equated at each interface between two consecutive waveguides. For example, for mode i and j in region p and m respectively:

$$\sum_{i=1}^{\infty} \overline{\mathbf{e}}_{\mathbf{pi}}(p_i^+ e^{-\gamma_{pi} l_{pm}} + p_i^- e^{+\gamma_{pi} l_{pm}}) = \sum_{j=1}^{\infty} \overline{\mathbf{e}}_{\mathbf{mj}}(m_j^+ e^{-\gamma_{mj} l_{pm}} + m_j^- e^{+\gamma_{mj} l_{pm}}) \qquad \text{(B.26)}$$

$$\sum_{i=1}^{\infty} \overline{\mathbf{h}}_{\mathbf{pi}}(p_i^+ e^{-\gamma_{pi} l_{pm}} - p_i^- e^{+\gamma_{pi} l_{pm}}) = \sum_{j=1}^{\infty} \overline{\mathbf{h}}_{\mathbf{mj}}(m_j^+ e^{-\gamma_{mj} l_{pm}} - m_j^- e^{+\gamma_{mj} l_{pm}}) \qquad \text{(B.27)}$$

with l_{pm} the z coordinate of the interface between regions p and m.

The transverse electric fields on both sides of each interface are then vector multiplied with the transverse magnetic field of the larger of the two waveguides. Also, the transverse magnetic fields are vector multiplied with the transverse electric fields of the smaller waveguide. All are integrated over the smaller waveguide cross-section. Using the orthogonality condition (Eq. B.9) and the fact that the total transverse electric field vanishes on perfect electric conductors yields six sets of equations:

$$(p_I^+ e^{\gamma_{pI} l_{pm}} + p_I^- e^{\gamma_{pI} l_{pm}}) P_{pI} = \sum_{j=1}^{\infty} (m_j^+ e^{\gamma_{mj} l_{pm}} + m_j^- e^{\gamma_{mj} l_{pm}}) P_{mpjI} \qquad \text{(B.28)}$$

$$\sum_{i=1}^{\infty} (p_i^+ e^{\gamma_{mJ} l_{pm}} - p_i^- e^{\gamma_{mJ} l_{pm}}) P_{mpJi} = (m_J^+ e^{\gamma_{mJ} l_{pm}} - m_J^- e^{\gamma_{mJ} l_{pm}}) P_{mJ} \qquad \text{(B.29)}$$

with p being regions A, C, E and G and with m being regions B, D and F. In the two equations above, we write

$$\int_S \overline{\mathbf{e}}_{\mathbf{xk}} \times \overline{\mathbf{h}}_{\mathbf{xk}} dS = P_{xk} \qquad \text{(B.30)}$$

with S the cross section of waveguide x, and

$$\int_{S_m} \overline{\mathbf{e}}_{\mathbf{mi}} \times \overline{\mathbf{h}}_{\mathbf{pj}} dS = P_{mpji} \tag{B.31}$$

with S_m the cross section of the smaller waveguide m.

Finally, the boundary conditions at $z = 0$ and $z = l_g$ are applied:

$$a_i^- = -a_i^+ \qquad \text{and} \qquad g_i^+ = -g_i^- e^{2\gamma_{gi} l_g} \tag{B.32}$$

to give the matrix equation of the form:

$$[\mathbf{M}] \begin{bmatrix} \mathbf{a}^+ \\ \mathbf{b}^+ \\ \mathbf{b}^- \\ \mathbf{c}^- \\ \mathbf{c}^+ \\ \mathbf{d}^- \\ \mathbf{d}^+ \\ \mathbf{e}^- \\ \mathbf{e}^+ \\ \mathbf{f}^- \\ \mathbf{f}^+ \\ \mathbf{g}^- \end{bmatrix} = 0 \tag{B.33}$$

Appendix C

Self-coupling coefficients for the conductor-loaded dual-mode DR

Recalling Eq. 3.20, the self-coupling power coefficient of mode p in waveguide x, defined by Eq. B.19, is, in cylindrical coordinates:

$$P_{xp} = \int_S (\overline{e}_{r\,xp} \times \overline{h}_{\theta\,xp} - \overline{h}_{r\,xp} \times \overline{e}_{\theta\,xp}) r dr d\theta \tag{C.1}$$

with S the cross-section of the waveguide.

Let us note r_1, r_2 and r_3 as the inner radius of the coaxial region, the radius of the dielectric region, and the radius of the cavity respectively. γ_x and ξ_x are the propagation constant and wave number of the mode in waveguide x respectively. We call the dielectric-loaded waveguide, the coaxial waveguide and the circular waveguide waveguides A, B and C respectively. For the dielectric-loaded waveguide, the additional 1 and 2 in the subscripts refer to the dielectric and the air regions respectively.

C.1 Partially dielectric-loaded waveguide

C.1.1 Case 1: Modes with no angular variation

Let us note

$$A_0(\xi r) = \frac{r^2}{2}\left[J_1'(\xi r)^2 + \left(1 - \frac{1}{\xi^2 r^2}\right) J_1(\xi r)^2\right] \tag{C.2}$$

$$B_0(\xi r) = \frac{r^2}{2}\left[J_1'(\xi r) Y_1'(\xi r) + \left(1 - \frac{1}{\xi^2 r^2}\right) J_1(\xi r) Y_1(\xi r)\right] \tag{C.3}$$

$$C_0(\xi r) = \frac{r^2}{2}\left[Y_1'(\xi r)^2 + \left(1 - \frac{1}{\xi^2 r^2}\right) Y_1(\xi r)^2\right] \tag{C.4}$$

Then for TE modes,

$$P_{ap} = \frac{2\pi\gamma_a^3}{j\omega\mu_0}\left\{\frac{A_0(\xi_{1a}r_2)}{\xi_{1a}^2} + \frac{1}{\xi_{2a}^2}\left(\frac{J_0(\xi_{1a}r_2)}{Y_0(\xi_{2a}r_2)J_0'(\xi_{2a}r_3) - J_0(\xi_{2a}r_2)Y_0'(\xi_{2a}r_3)}\right)^2 \times\left[J_0'(\xi_{2a}r_3)^2 C_0(\xi_{2a}r) + Y_0'(\xi_{2a}r_3)^2 A_0(\xi_{2a}r) - 2J_0'(\xi_{2a}r_3)Y_0'(\xi_{2a}r_3)B_0(\xi_{2a}r)\right]_{r_2}^{r_3}\right\} \quad \text{(C.5)}$$

and for TM modes:

$$P_{ap} = \frac{-2\pi\gamma_a}{j\omega\mu_0}\left\{\frac{k_{1a}^2 A_0(\xi_{1a}r_2)}{\xi_{1a}^2} + \frac{k_{2a}^2}{\xi_{2a}^2} \times\left(\frac{J_0(\xi_{1a}r_2)}{Y_0(\xi_{2a}r_2)J_0(\xi_{2a}r_3) - J_0(\xi_{2a}r_2)Y_0(\xi_{2a}r_3)}\right)^2 \times\left[J_0(\xi_{2a}r_3)^2 C_0(\xi_{2a}r) + Y_0(\xi_{2a}r_3)^2 A_0(\xi_{2a}r) - 2J_0(\xi_{2a}r_3)Y_0(\xi_{2a}r_3)B_0(\xi_{2a}r)\right]_{r_2}^{r_3}\right\} \quad \text{(C.6)}$$

C.1.2 Case 2: Modes with angular variation

For hybrid modes,

$$\begin{aligned} P_{ap} = {} & \frac{\pi\gamma_a}{j\omega\mu_0\xi_{1a}^2}\left\{(\kappa^2\gamma_a^2 - k_{1a}^2)A_n(\xi_{1a}r_2) + \frac{n\kappa}{\xi_{1a}^2}(\gamma_a^2 - k_{1a}^2)\left[J_n(\xi_{1a}r)^2\right]_0^{r_2}\right\} \\ & + \frac{\pi\gamma_a}{j\omega\mu_0\xi_{2a}^2}\left\{\left(\frac{-k_{2a}J_0(\xi_{1a}r_2)}{Y_0(\xi_{2a}r_2)J_0(\xi_{2a}r_3) - J_0(\xi_{2a}r_2)Y_0(\xi_{2a}r_3)}\right)^2 \times \right. \\ & \left[J_n(\xi_{2a}r_3)^2 C_n(\xi_{2a}r) + Y_n(\xi_{2a}r_3)^2 A_n(\xi_{2a}r) - 2J_n(\xi_{2a}r_3)Y_n(\xi_{2a}r_3)B_n(\xi_{2a}r)\right]_{r_2}^{r_3} \\ & + \left(\frac{\kappa\gamma_a J_0(\xi_{1a}r_2)}{Y_0(\xi_{2a}r_2)J_0'(\xi_{2a}r_3) - J_0(\xi_{2a}r_2)Y_0'(\xi_{2a}r_3)}\right)^2 \times \left[J_n'(\xi_{2a}r_3)^2 C_n(\xi_{2a}r) \right. \\ & \left. \left. + Y_n'(\xi_{2a}r_3)^2 A_n(\xi_{2a}r) - 2J_n'(\xi_{2a}r_3)Y_n'(\xi_{2a}r_3)B_n(\xi_{2a}r)\right]_{r_2}^{r_3} \right. \\ & \left. + n\kappa\frac{(-k_{2a}^2 + \gamma_a^2)}{\xi_{2a}^2}\left[P_n(\xi_{2a}r)Q_n(\xi_{2a}r)\right]_{r_2}^{r_3}\right\} \end{aligned} \quad \text{(C.7)}$$

with

$$A_n(\xi r) = \frac{r^2}{2}\left[J_{n-1}'(\xi r)^2 + \left(1 - \frac{(n-1)^2}{\xi^2 r^2}\right)J_{n-1}(\xi r)^2\right] - n\frac{J_n(\xi r)^2}{\xi^2} \quad \text{(C.8)}$$

$$\begin{aligned} B_n(\xi r) = {} & \frac{r^2}{2}\left[J_{n-1}'(\xi r)Y_{n-1}'(\xi r) + \left(1 - \frac{(n-1)^2}{\xi^2 r^2}\right)J_{n-1}(\xi r)Y_{n-1}(\xi r)\right] \\ & - n\frac{J_n(\xi r)Y_n(\xi r)}{\xi^2} \end{aligned} \quad \text{(C.9)}$$

$$C_n(\xi r) = \frac{r^2}{2}\left[Y_{n-1}'(\xi r)^2 + \left(1 - \frac{(n-1)^2}{\xi^2 r^2}\right)Y_{n-1}(\xi r)^2\right] - n\frac{Y_n(\xi r)^2}{\xi^2} \quad \text{(C.10)}$$

$$Q_n(\xi_{2a}r) = J_n(\xi_{1a}r_2)\left[\frac{Y_n(\xi_{2a}r)J_n(\xi_{2a}r_3) - J_n(\xi_{2a}r)Y_n(\xi_{2a}r_3)}{Y_n(\xi_{2a}r_2)J_n(\xi_{2a}r_3) - J_n(\xi_{2a}r_2)Y_n(\xi_{2a}r_3)}\right] \tag{C.11}$$

$$P_n(\xi_{2a}r) = J_n(\xi_{1a}r_2)\left[\frac{Y_n(\xi_{2a}r)J'_n(\xi_{2a}r_3) - J_n(\xi_{2a}r)Y'_n(\xi_{2a}r_3)}{Y_n(\xi_{2a}r_2)J'_n(\xi_{2a}r_3) - J_n(\xi_{2a}r_2)Y'_n(\xi_{2a}r_3)}\right] \tag{C.12}$$

C.2 Coaxial waveguide

C.2.1 Case 1: Modes with no angular variation

- TEM mode:

$$P_{bp} = 2\pi\sqrt{\frac{\epsilon_0}{\mu_0}}[\ln(r_3) - \ln(r_1)] \tag{C.13}$$

With A_0, B_0 and C_0 defined as in Eqs. C.2-C.4, we have:

- TE modes:

$$P_{bp} = \frac{2\pi\gamma_b^3}{j\omega\mu_0\xi_b^2}\left[\frac{Y'_0(\xi_b r_1)^2}{J'_0(\xi_b r_1)^2}A_0(\xi_b r) - 2\frac{Y'_0(\xi_b r_1)}{J'_0(\xi_b r_1)}B_0(\xi_b r) + C_0(\xi_b r)\right]_{r_1}^{r_3} \tag{C.14}$$

- TM modes:

$$P_{bp} = \frac{-2\pi\gamma_b k_0^2}{j\omega\mu_0\xi_b^2}\left[\frac{Y_0(\xi_b r_1)^2}{J_0(\xi_b r_1)^2}A_0(\xi_b r) - 2\frac{Y_0(\xi_b r_1)}{J_0(\xi_b r_1)}B_0(\xi_b r) + C_0(\xi_b r)\right]_{r_1}^{r_3} \tag{C.15}$$

C.2.2 Case 2: Modes with angular variation

With A_n, B_n and C_n defined as in Eqs. C.8-C.10, we have:

- TE modes:

$$P_{bp} = \frac{\pi\gamma_b^3}{j\omega\mu_0\xi_b^2}\left[\frac{Y'_n(\xi_b r_1)^2}{J'_n(\xi_b r_1)^2}A_n(\xi_b r) - 2\frac{Y'_n(\xi_b r_1)}{J'_n(\xi_b r_1)}B_n(\xi_b r) + C_n(\xi_b r)\right]_{r_1}^{r_3} \tag{C.16}$$

- TM modes:

$$P_{bp} = \frac{-\pi\gamma_b k_0^2}{j\omega\mu_0\xi_b^2}\left[\frac{Y_n(\xi_b r_1)^2}{J_n(\xi_b r_1)^2}A_n(\xi_b r) - 2\frac{Y_n(\xi_b r_1)}{J_n(\xi_b r_1)}B_n(\xi_b r) + C_n(\xi_b r)\right]_{r_1}^{r_3} \tag{C.17}$$

C.3 Circular empty waveguide

C.3.1 Case 1: Modes with no angular variation

With A_0, B_0 and C_0 defined as in Eqs. C.2-C.4, we have:

- TE modes:

$$P_{cp} = \frac{2\pi\gamma_c^3}{j\omega\mu_0\xi_c^2} A_0(\xi_c r_3) \tag{C.18}$$

- TM modes:

$$P_{cp} = \frac{-2\pi\gamma_c k_0^2}{j\omega\mu_0\xi_c^2} A_0(\xi_c r_3) \tag{C.19}$$

C.3.2 Case 2: Modes with angular variation

With A_n, B_n and C_n defined as in Eqs. C.8-C.10, we have:

- TE modes:

$$P_{cp} = \frac{\pi\gamma_c^3}{j\omega\mu_0\xi_c^2} A_n(\xi_c r_3) \tag{C.20}$$

- TM modes:

$$P_{cp} = \frac{-\pi\gamma_c k_0^2}{j\omega\mu_0\xi_c^2} A_n(\xi_c r_3) \tag{C.21}$$

Appendix D

Cross-coupling coefficients for the conductor-loaded dual-mode DR

Recalling Eq. 3.23, the cross-coupling power coefficient between modes p and m in waveguide x and y respectively, defined by Eq. B.20, is, in cylindrical coordinates:

$$P_{xypm} = \int_{S_x} (\overline{e}_{r\ xp} \times \overline{h}_{\theta\ ym} - \overline{h}_{r\ ym} \times \overline{e}_{\theta\ xp}) r dr d\theta \tag{D.1}$$

with S_x the cross-section of waveguide x.

Let us note r_1, r_2 and r_3 as the inner radius of the coaxial region, the radius of the dielectric region, and the radius of the cavity respectively. γ_x and ξ_x are the propagation constant and wave number of a mode in waveguide x respectively. We call the dielectric-loaded waveguide, the coaxial waveguide and the circular waveguide waveguides A, B and C respectively. For the dielectric-loaded waveguide, the additional 1 and 2 in the subscripts refer to the dielectric and the air regions respectively. If $r_1 > r_2$, the part of the integrals between r_1 and r_2 is zero and the part between r_2 and r_3 has to be realised between r_1 and r_3 instead.

The following notations will be used in the rest of this appendix:

$$Q_n(\xi_{2a} r) = J_n(\xi_{1a} r_2) \left[\frac{Y_n(\xi_{2a} r) J_n(\xi_{2a} r_3) - J_n(\xi_{2a} r) Y_n(\xi_{2a} r_3)}{Y_n(\xi_{2a} r_2) J_n(\xi_{2a} r_3) - J_n(\xi_{2a} r_2) Y_n(\xi_{2a} r_3)} \right] \tag{D.2}$$

$$P_n(\xi_{2a} r) = J_n(\xi_{1a} r_2) \left[\frac{Y_n(\xi_{2a} r) J'_n(\xi_{2a} r_3) - J_n(\xi_{2a} r) Y'_n(\xi_{2a} r_3)}{Y_n(\xi_{2a} r_2) J'_n(\xi_{2a} r_3) - J_n(\xi_{2a} r_2) Y'_n(\xi_{2a} r_3)} \right] \tag{D.3}$$

$$U_n(\xi, r) = J'_n(\xi r) J_n(\xi_b r) \xi_b - J'_n(\xi_b r) J_n(\xi r) \xi \tag{D.4}$$

$$V_n(\xi, r) = J'_n(\xi r) Y_n(\xi_b r) \xi_b - Y'_n(\xi_b r) J_n(\xi r) \xi \tag{D.5}$$

$$W_n(\xi, r) = Q'_n(\xi r) J_n(\xi_b r) \xi_b - J'_n(\xi_b r) Q_n(\xi r) \xi \tag{D.6}$$

$$X_n(\xi,r) = Q_n'(\xi r)Y_n(\xi_b r)\xi_b - Y_n'(\xi_b r)Q_n(\xi r)\xi \tag{D.7}$$

$$S_n(\xi,r) = P_n'(\xi r)J_n(\xi_b r)\xi_b - J_n'(\xi_b r)P_n(\xi r)\xi \tag{D.8}$$

$$Z_n(\xi,r) = P_n'(\xi r)Y_n(\xi_b r)\xi_b - Y_n'(\xi_b r)P_n(\xi r)\xi \tag{D.9}$$

D.1 Partially dielectric-loaded waveguide to coaxial waveguide

D.1.1 Case 1: Modes with no angular variation

- TM in A, TEM in B:

$$P_{bapm} = \frac{2\pi}{j\omega\mu_0}\left\{\frac{k_{1a}^2}{\xi_{1a}^2}\Big(J_0(\xi_{1a}r_2) - J_0(\xi_{1a}r_1)\Big) + \frac{k_{2a}^2}{\xi_{2a}^2}\Big(Q_0(\xi_{2a}r_2) - Q_0(\xi_{2a}r_1)\Big)\right\} \tag{D.10}$$

- TE in A, TEM in B:

$$P_{bapm} = 0 \tag{D.11}$$

- TM in A, TM in B:

$$\begin{aligned} P_{bapm} = {} & \frac{2\pi\gamma_b}{j\omega\mu_0\xi_b}\left\{\frac{k_{1a}^2}{\xi_{1a}(\xi_b^2-\xi_{1a}^2)}\Big[r\Big(\frac{Y_0(\xi_b r_1)}{J_0(\xi_b r_1)}U_0(\xi_{1a},r) - V_0(\xi_{1a},r)\Big)\Big]_{r_1}^{r_2}\right. \\ & \left. + \frac{k_{2a}^2}{\xi_{2a}(\xi_b^2-\xi_{2a}^2)}\Big[r\Big(\frac{Y_0(\xi_b r_1)}{J_0(\xi_b r_1)}W_0(\xi_{2a},r) - X_0(\xi_{2a},r)\Big)\Big]_{r_2}^{r_3}\right\} \end{aligned} \tag{D.12}$$

- TE in A, TE in B:

$$\begin{aligned} P_{bapm} = {} & \frac{2\pi\gamma_b}{j\omega\mu_0\xi_b}\left\{\frac{\gamma_a^2}{\xi_{1a}(\xi_b^2-\xi_{1a}^2)}\Big[r\Big(-\frac{Y_0'(\xi_b r_1)}{J_0'(\xi_b r_1)}U_0(\xi_{1a},r) + V_0(\xi_{1a},r)\Big)\Big]_{r_1}^{r_2}\right. \\ & \left. + \frac{\gamma_a^2}{\xi_{2a}(\xi_b^2-\xi_{2a}^2)}\Big[r\Big(-\frac{Y_0'(\xi_b r_1)}{J_0'(\xi_b r_1)}S_0(\xi_{2a},r) - Z_0(\xi_{2a},r)\Big)\Big]_{r_2}^{r_3}\right\} \end{aligned} \tag{D.13}$$

- TM in A, TE in B:

$$P_{bapm} = 0 \tag{D.14}$$

- TE in A, TM in B:

$$P_{bapm} = 0 \tag{D.15}$$

D.1.2 Case 2: Modes with angular variation

- HE in A, TM in B:

$$P_{bapm} = \frac{\pi\gamma_b}{j\omega\mu_0\xi_b}\Bigg\{\frac{\gamma_a^2 n\kappa}{\xi_{1a}^2\xi_b}\Bigg[-\frac{Y_n(\xi_b r_1)}{J_n(\xi_b r_1)}J_n(\xi_{1a}r)J_n(\xi_b r) + J_n(\xi_{1a}r)Y_n(\xi_b r)\Bigg]_{r_1}^{r_2}$$
$$+\frac{k_{1a}^2}{\xi_{1a}(\xi_b^2-\xi_{1a}^2)}\Bigg[r\Bigg(\frac{Y_n(\xi_b r_1)}{J_n(\xi_b r_1)}U_n(\xi_{1a},r) - V_n(\xi_{1a},r)\Bigg)\Bigg]_{r_1}^{r_2}$$
$$+\frac{\gamma_a^2 n\kappa}{\xi_{2a}^2\xi_b}\Bigg[\frac{-Y_n(\xi_b r_1)}{J_n(\xi_b r_1)}P_n(\xi_{2a}r)J_n(\xi_b r) + P_n(\xi_{2a}r)Y_n(\xi_b r)\Bigg]_{r_2}^{r_3}$$
$$+\frac{k_{2a}^2}{\xi_{2a}(\xi_b^2-\xi_{2a}^2)}\Bigg[r\Bigg(\frac{Y_n(\xi_b r_1)}{J_n(\xi_b r_1)}W_n(\xi_{2a},r) - X_n(\xi_{2a},r)\Bigg)\Bigg]_{r_2}^{r_3}\Bigg\} \qquad \text{(D.16)}$$

- HE in A, TE in B:

$$P_{bapm} = \frac{\pi\gamma_b}{j\omega\mu_0\xi_b}\Bigg\{\frac{k_{1a}^2 n}{\xi_{1a}^2\xi_b}\Bigg[\frac{Y_n'(\xi_b r_1)}{J_n'(\xi_b r_1)}J_n(\xi_{1a}r)J_n(\xi_b r) - J_n(\xi_{1a}r)Y_n(\xi_b r)\Bigg]_{r_1}^{r_2}$$
$$+\frac{\gamma_a^2\kappa}{\xi_{1a}(\xi_b^2-\xi_{1a}^2)}\Bigg[r\Bigg(-\frac{Y_n'(\xi_b r_1)}{J_n'(\xi_b r_1)}U_n(\xi_{1a},r) + V_n(\xi_{1a},r)\Bigg)\Bigg]_{r_1}^{r_2}$$
$$+\frac{k_{2a}^2 n}{\xi_{2a}^2\xi_b}\Bigg[\frac{Y_n'(\xi_b r_1)}{J_n'(\xi_b r_1)}Q_n(\xi_{2a}r)J_n(\xi_b r) - Q_n(\xi_{2a}r)Y_n(\xi_b r)\Bigg]_{r_2}^{r_3}$$
$$+\frac{\gamma_a^2\kappa}{\xi_{2a}(\xi_b^2-\xi_{2a}^2)}\Bigg[r\Bigg(-\frac{Y_n'(\xi_b r_1)}{J_n'(\xi_b r_1)}S_n(\xi_{2a},r) + Z_n(\xi_{2a},r)\Bigg)\Bigg]_{r_2}^{r_3}\Bigg\} \qquad \text{(D.17)}$$

D.2 Coaxial waveguide to empty waveguide

D.2.1 Case 1: Modes with no angular variation

- TEM in B, TM in C:

$$P_{bcpm} = \frac{2\pi k_c^2}{j\omega\mu_0\xi_c^2}\Big[J_0(\xi_c r_3) - J_0(\xi_c r_1)\Big] \qquad \text{(D.18)}$$

- TEM in B, TE in C:

$$P_{bcpm} = 0 \qquad \text{(D.19)}$$

- TM in B, TM in C:

$$P_{bcpm} = \frac{-2\pi\gamma_b k_c^2}{(\xi_c^2-\xi_b^2)\xi_b\xi_c j\omega\mu_0}\Bigg[r\Bigg(\frac{Y_0(\xi_b r_1)}{J_0(\xi_b r_1)}U_0(\xi_c,r) - V_0(\xi_c,r)\Bigg)\Bigg]_{r_1}^{r_3} \qquad \text{(D.20)}$$

- TE in B, TE in C:

$$P_{bcpm} = \frac{2\pi\gamma_b\gamma_c^2}{(\xi_c^2-\xi_b^2)\xi_b\xi_c j\omega\mu_0}\Bigg[r\Bigg(\frac{Y_0'(\xi_b r_1)}{J_0'(\xi_b r_1)}U_0(\xi_c,r) - V_0(\xi_c,r)\Bigg)\Bigg]_{r_1}^{r_3} \qquad \text{(D.21)}$$

- TM in B, TE in C:

$$P_{bcpm} = 0 \tag{D.22}$$

- TE in B, TM in C:

$$P_{bcpm} = 0 \tag{D.23}$$

D.2.2 Case 2: Modes with angular variation

- TM in B, TM in C:

$$P_{bcpm} = \frac{-\pi\gamma_b k_c^2}{(\xi_c^2 - \xi_b^2)\xi_b\xi_c j\omega\mu_0}\left[r\left(\frac{Y_n(\xi_b r_1)}{J_n(\xi_b r_1)}U_n(\xi_c, r) - V_n(\xi_c, r)\right)\right]_{r_1}^{r_3} \tag{D.24}$$

- TE in B, TE in C:

$$P_{bcpm} = \frac{\pi\gamma_b\gamma_c^2}{(\xi_c^2 - \xi_b^2)\xi_b\xi_c j\omega\mu_0}\left[r\left(\frac{Y_n'(\xi_b r_1)}{J_n'(\xi_b r_1)}U_n(\xi_c, r) - V_n(\xi_c, r)\right)\right]_{r_1}^{r_3} \tag{D.25}$$

- TM in B, TE in C:

$$P_{bcpm} = 0 \tag{D.26}$$

- TE in B, TM in C:

$$P_{bcpm} = \frac{-\pi\gamma_b k_c^2 n}{\xi_b^2\xi_c^2 j\omega\mu_0}\left[J_n(\xi_c r)\left(-\frac{Y_n'(\xi_b r_1)}{J_n'(\xi_b r_1)}J_n(\xi_b r) + Y_n(\xi_b r)\right)\right]_{r_1}^{r_3} \tag{D.27}$$

Appendix E

Variations of electric and magnetic fields of the $HE_{11\delta}$ mode at the interfaces of the mode-matching regions

For all figures, $Na = 180$, $Nb = 60$ and $Nc = 120$. The curves in blue show the fields in waveguides A and C (i.e. $z = 0^-$ and $z = l_2^+$). Those in red show the fields in waveguide B (i.e. $z = 0^+$ and $z = l_2^-$).

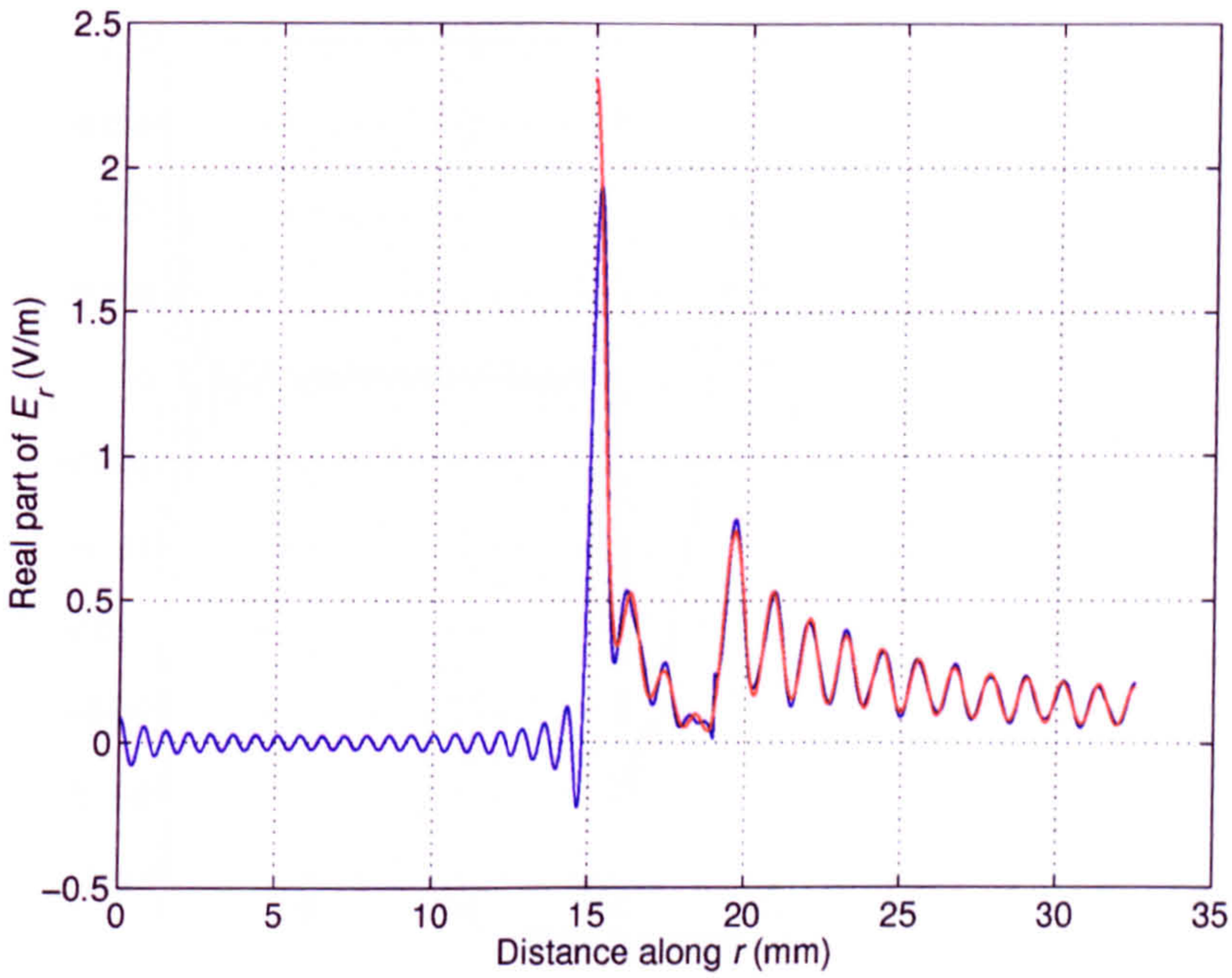

Figure E.1: E_r of the $\mathrm{HE}_{11\delta}$ mode at $z = 0$, $\theta = 0$.

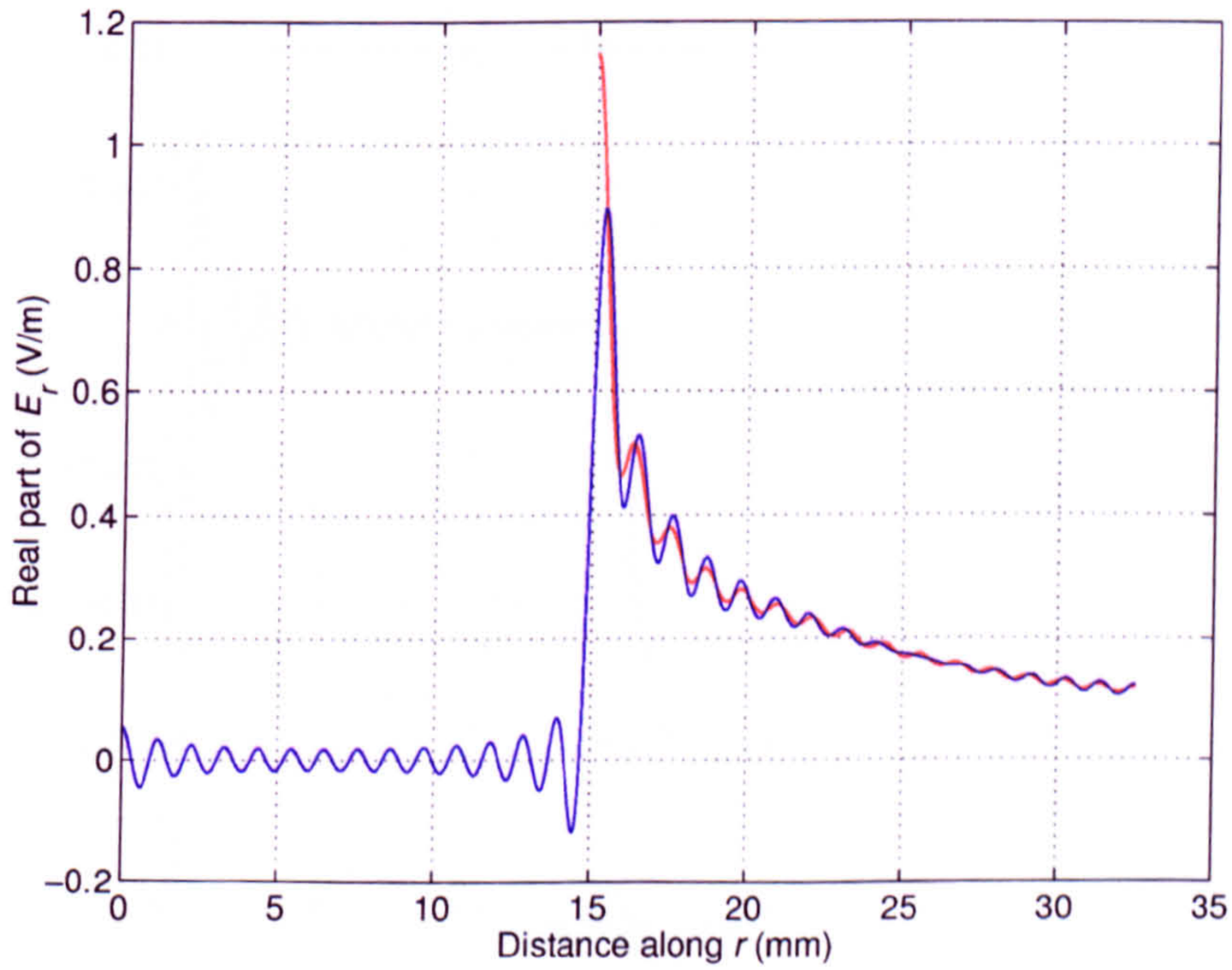

Figure E.2: E_r of the $\mathrm{HE}_{11\delta}$ mode at $z = l_2$, $\theta = 0$.

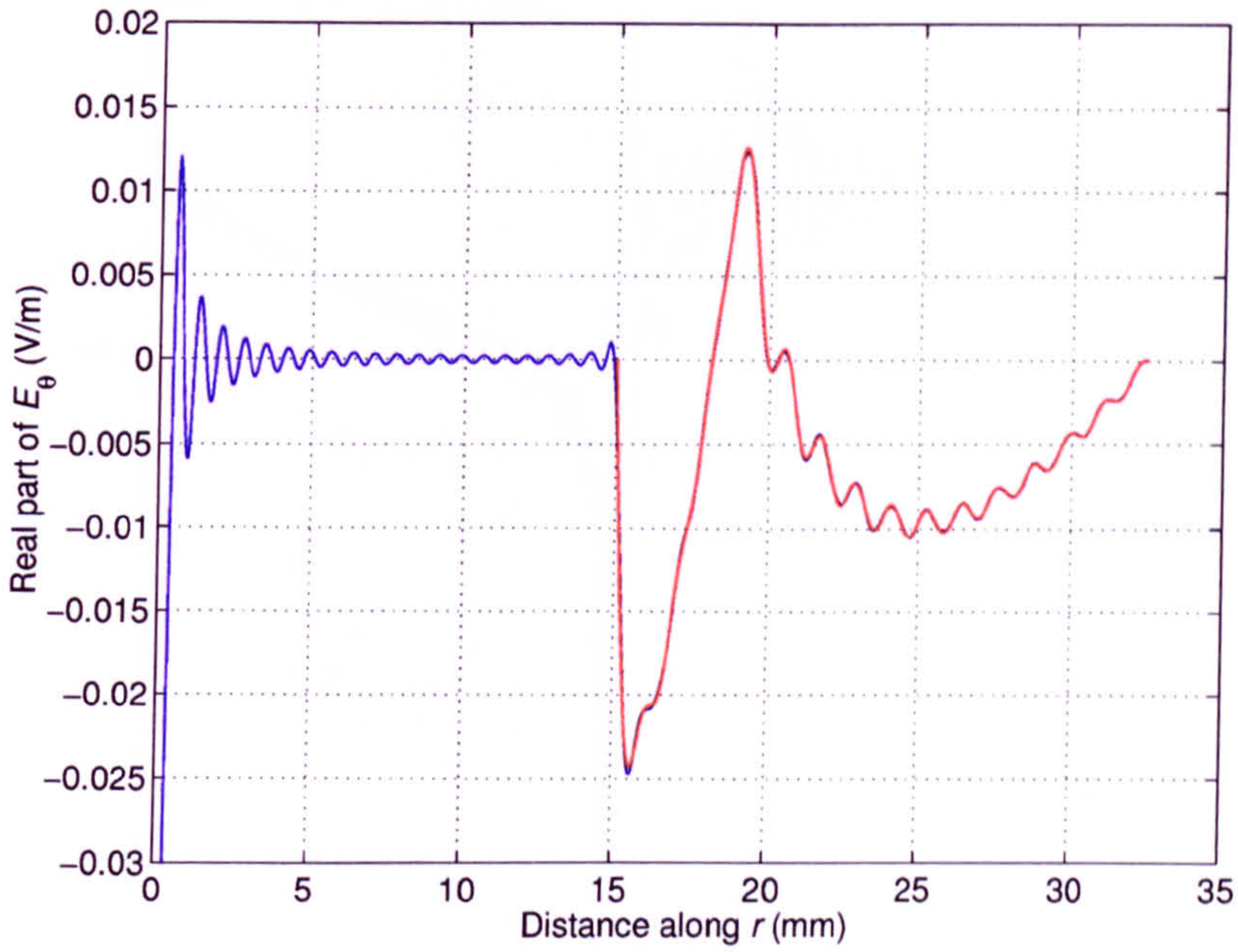

Figure E.3: E_θ of the $\mathrm{HE}_{11\delta}$ mode at $z = 0$, $\theta = \pi/2$.

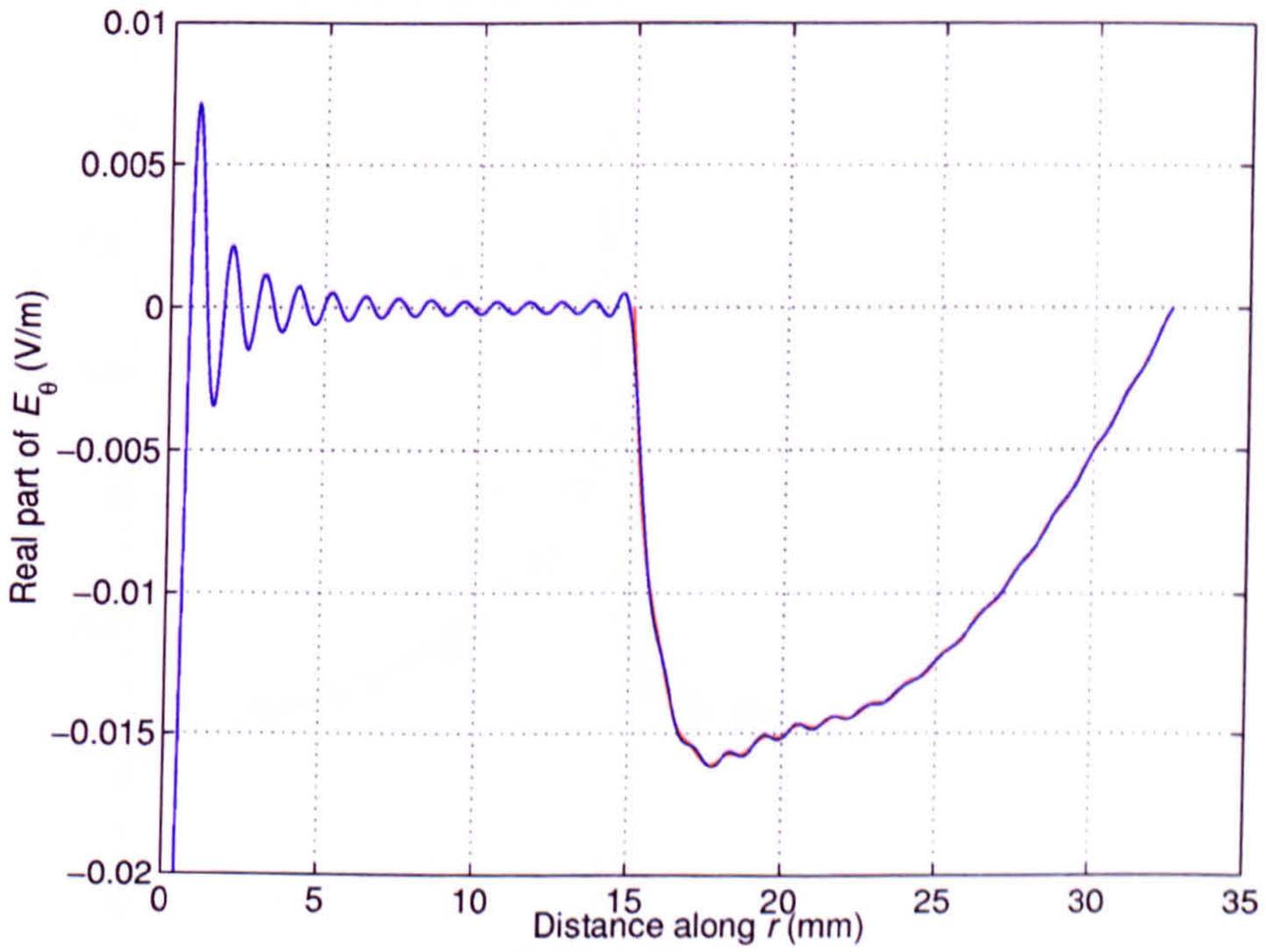

Figure E.4: E_θ of the $\mathrm{HE}_{11\delta}$ mode at $z = l_2$, $\theta = \pi/2$.

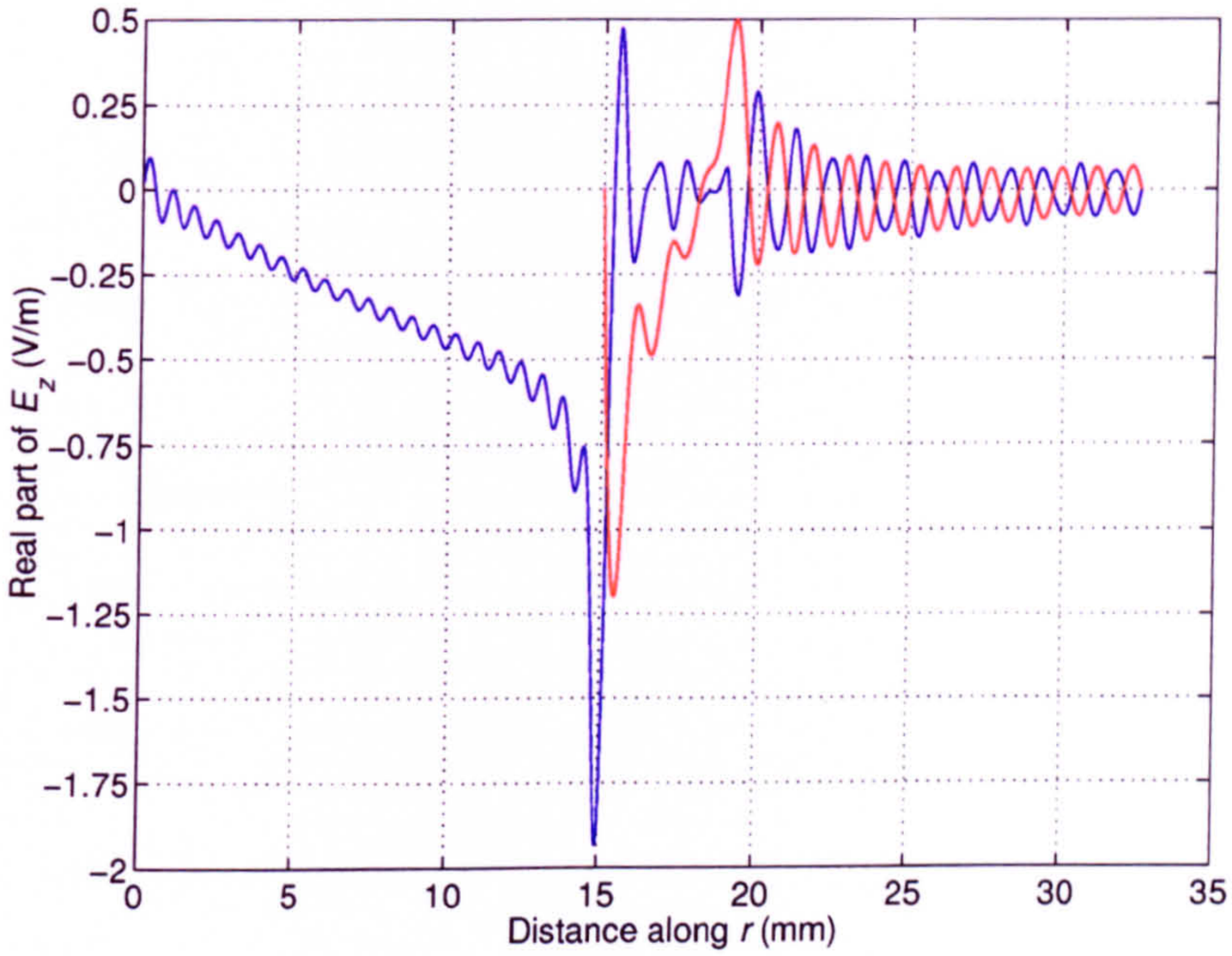

Figure E.5: E_z of the $\mathrm{HE}_{11\delta}$ mode at $z = 0$, $\theta = 0$.

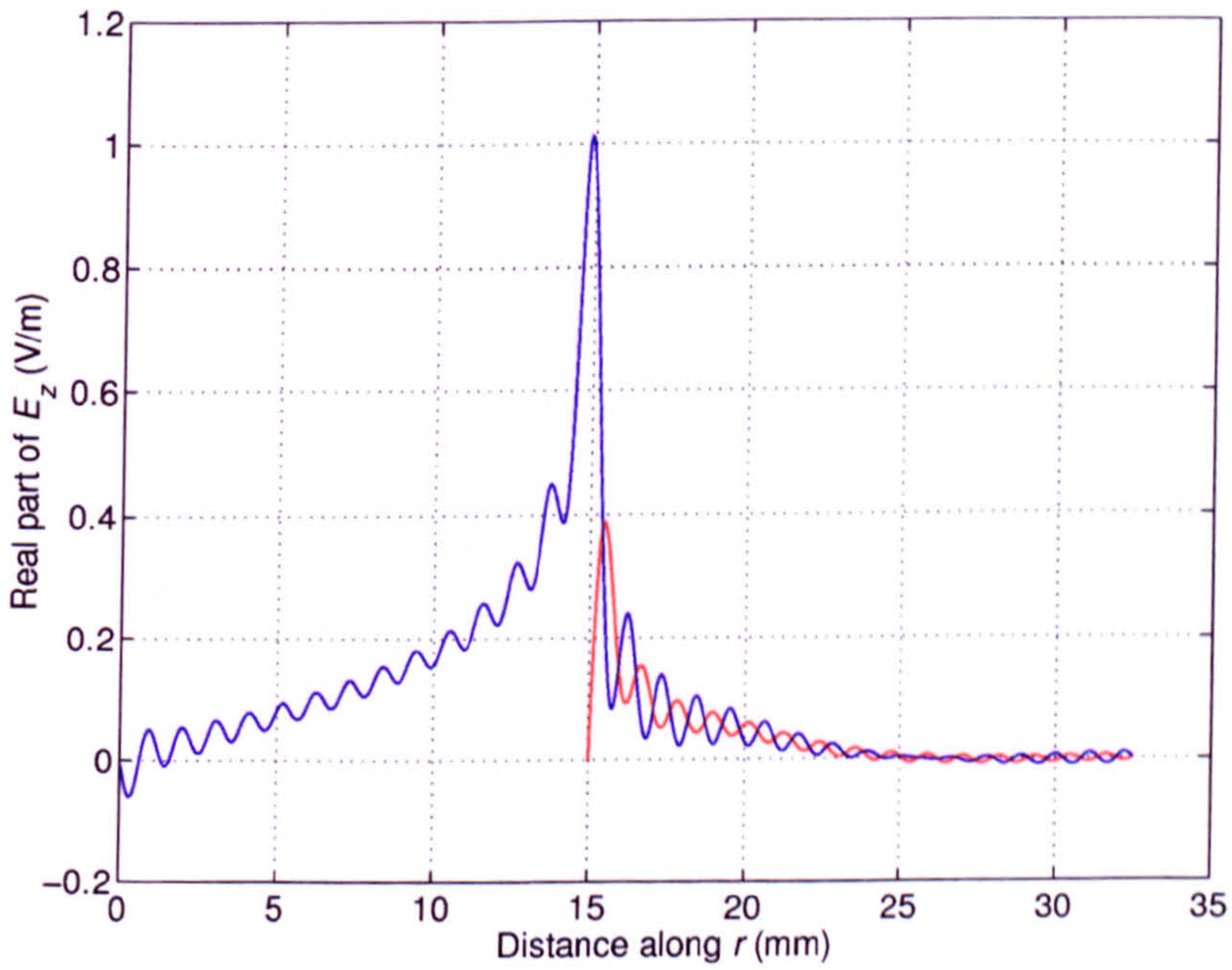

Figure E.6: E_z of the $\mathrm{HE}_{11\delta}$ mode at $z = l_2$, $\theta = 0$.

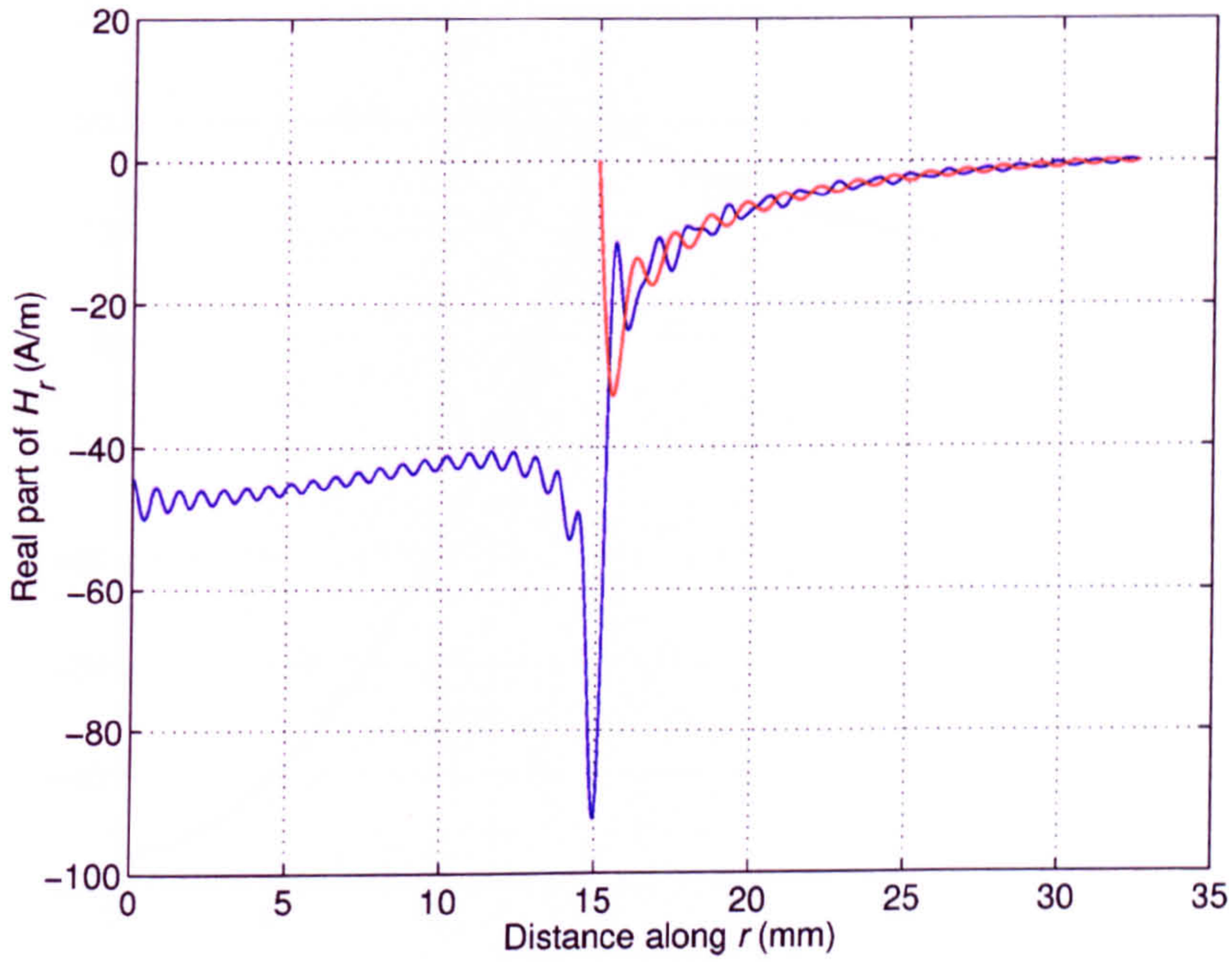

Figure E.7: H_r of the $\mathrm{HE}_{11\delta}$ mode at $z = 0$, $\theta = \pi/2$.

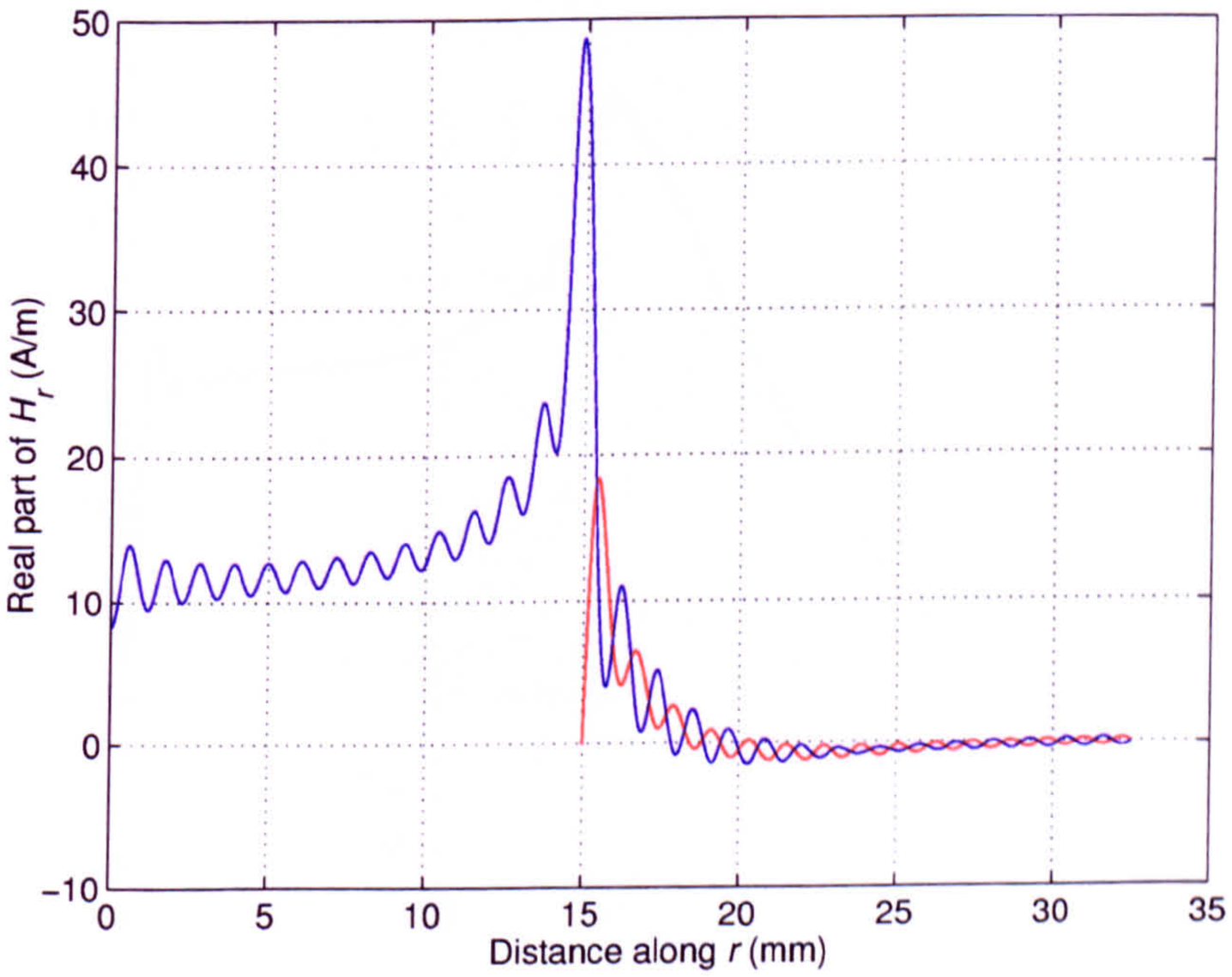

Figure E.8: H_r of the $\mathrm{HE}_{11\delta}$ mode at $z = l_2$, $\theta = \pi/2$.

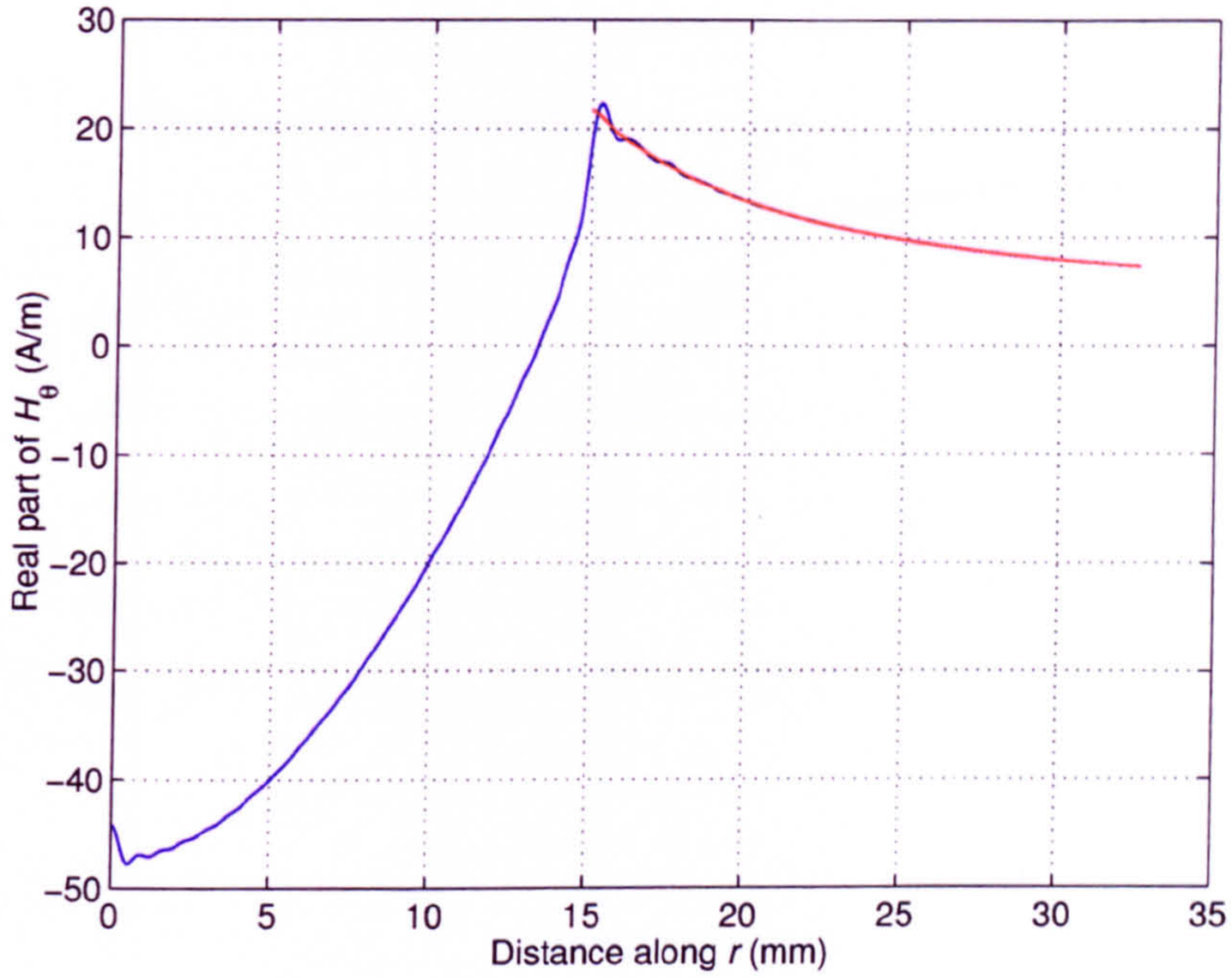

Figure E.9: H_θ of the $\mathrm{HE}_{11\delta}$ mode at $z = 0$, $\theta = 0$.

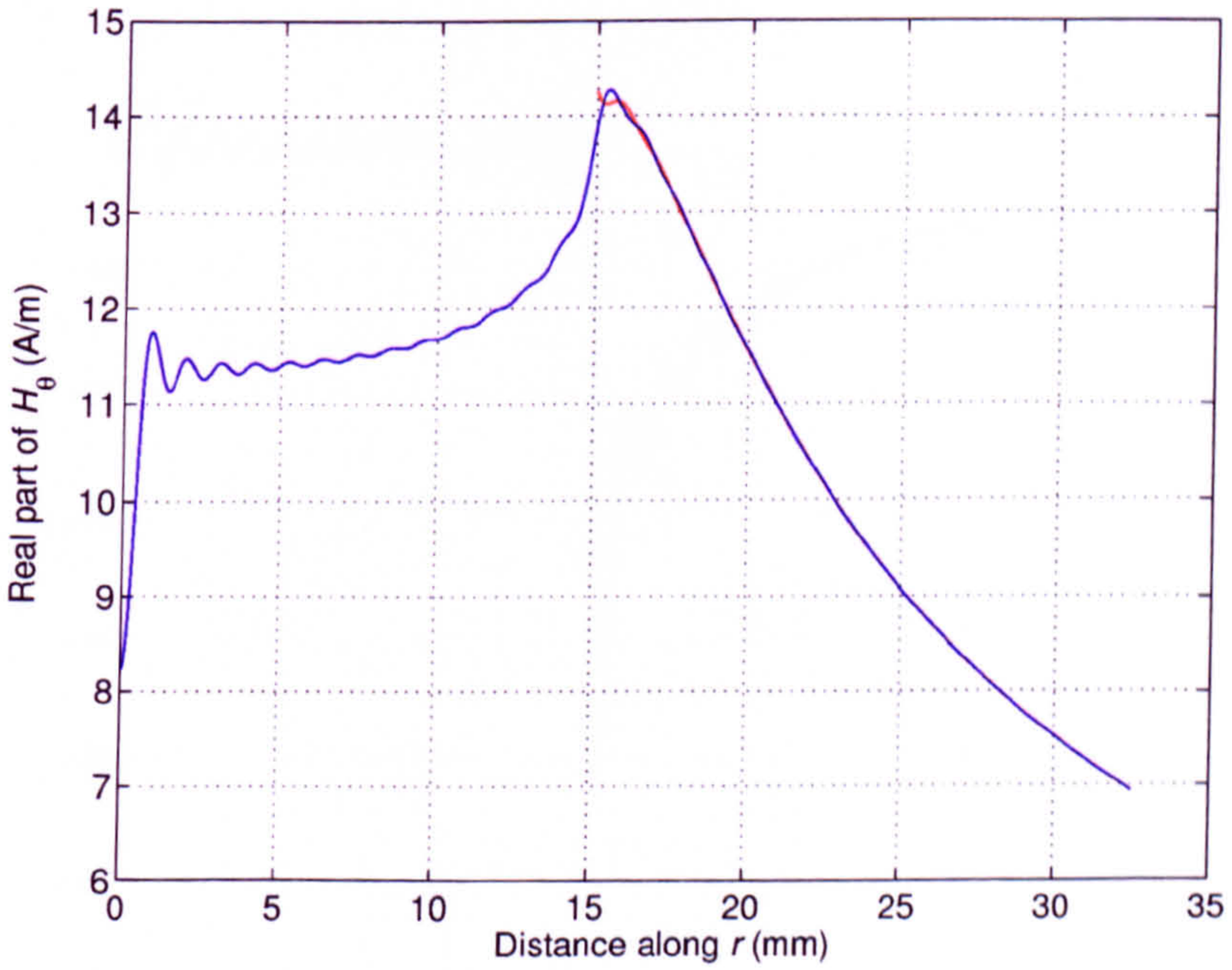

Figure E.10: H_θ of the $\mathrm{HE}_{11\delta}$ mode at $z = l_2$, $\theta = 0$.

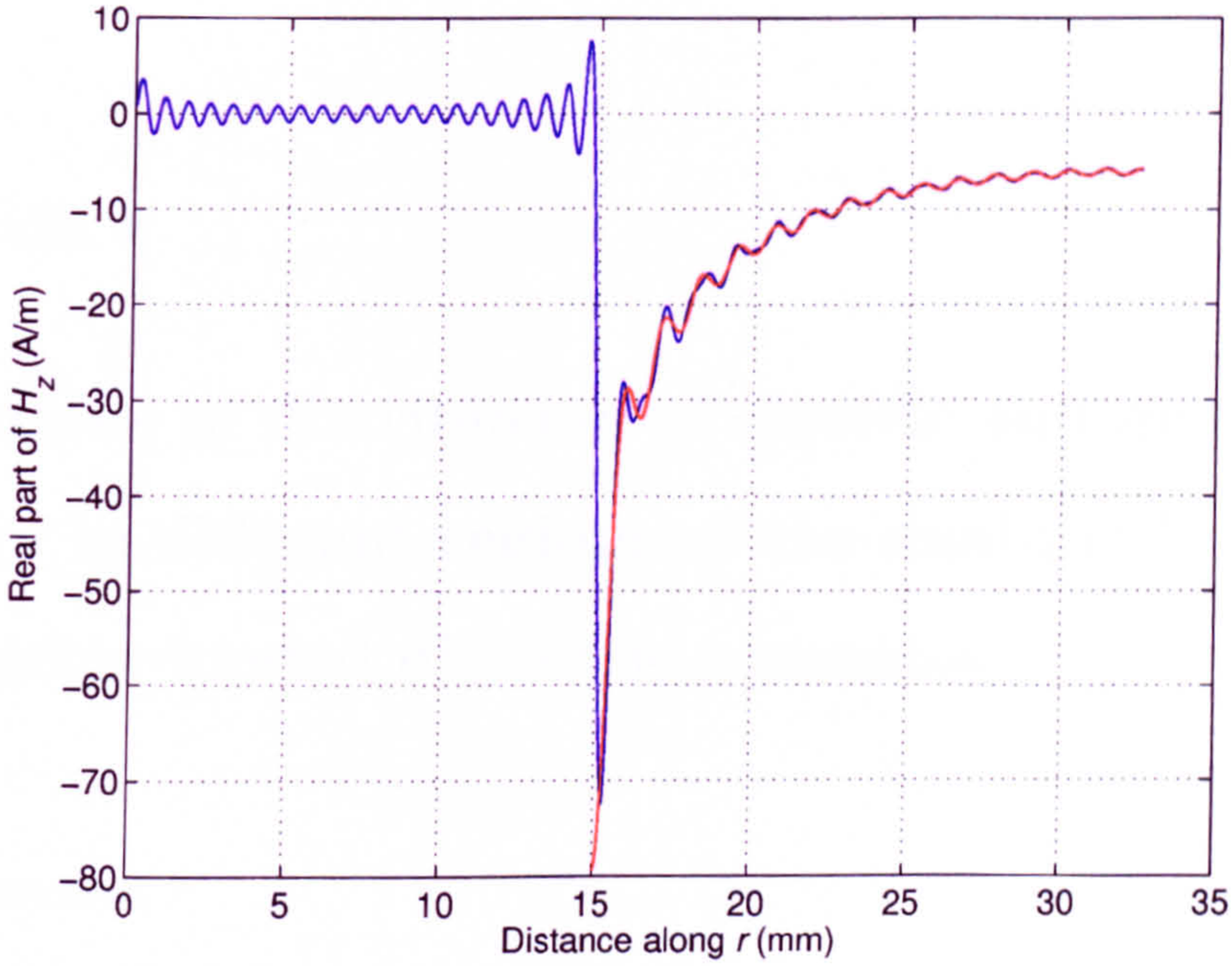

Figure E.11: H_z of the $\mathrm{HE}_{11\delta}$ mode at $z = 0$, $\theta = \pi/2$.

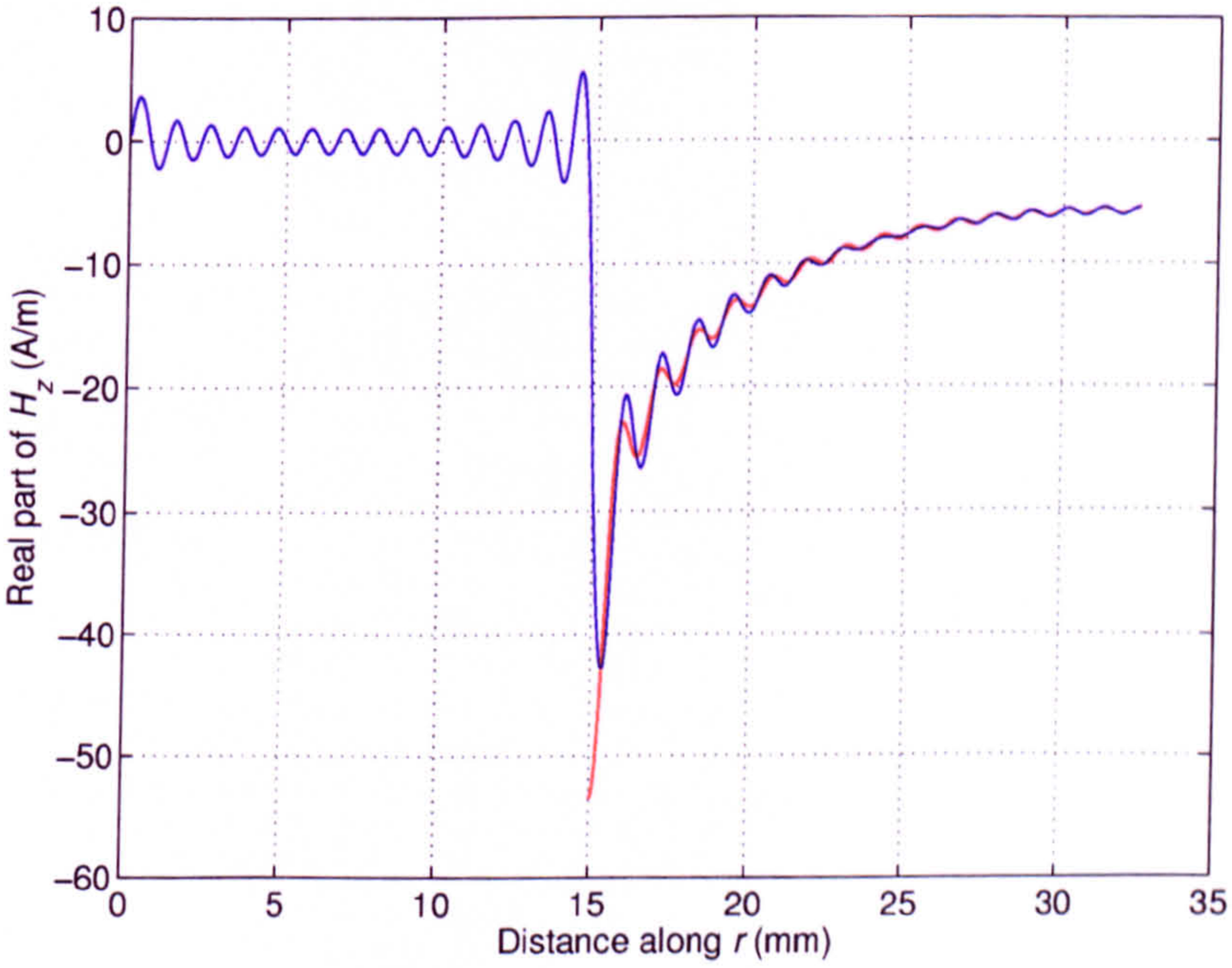

Figure E.12: H_z of the $\mathrm{HE}_{11\delta}$ mode at $z = l_2$, $\theta = \pi/2$.

Appendix F

Variations of distribution of electric and magnetic energy in different regions of the dual-mode conductor-loaded dielectric resonator

Please turn over.

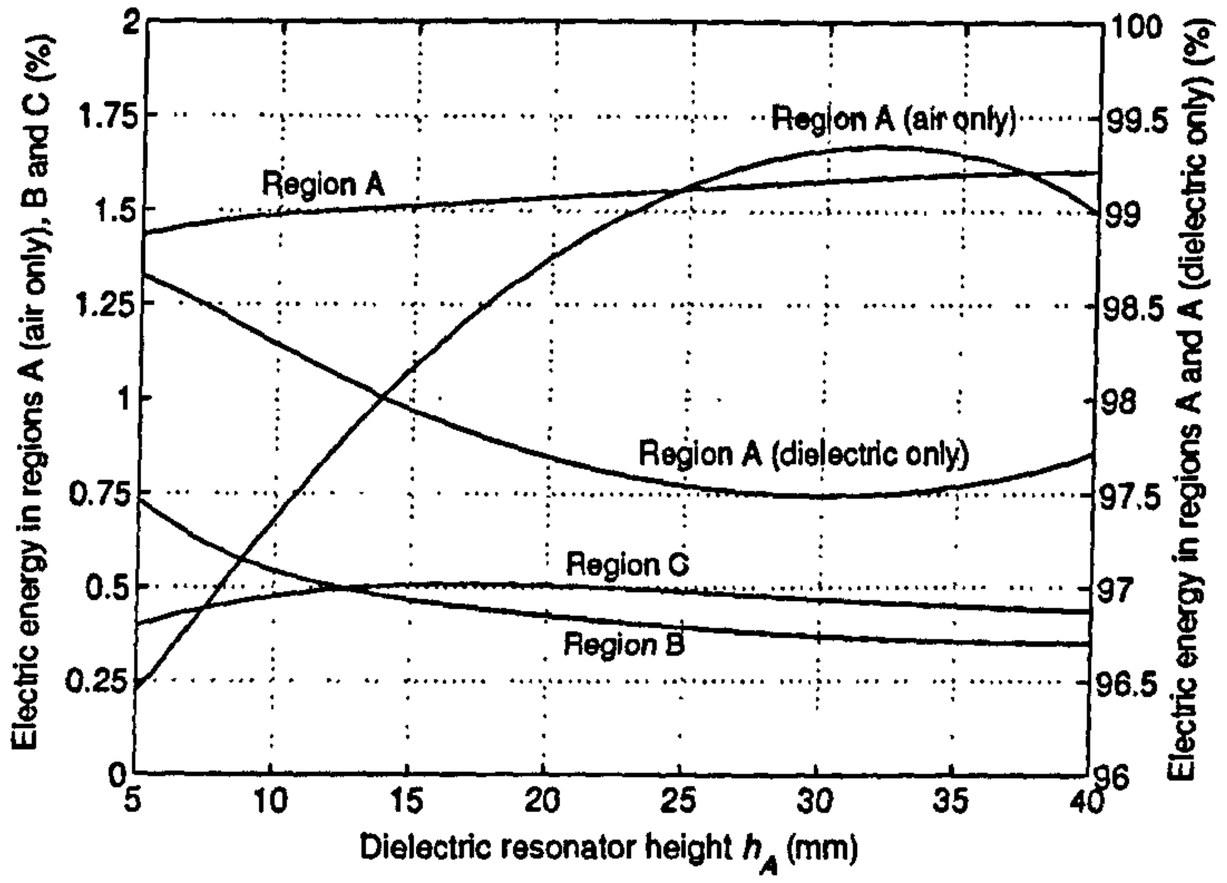

Figure F.1: Variations of electric energy with h_A. $h_B = 3$ mm, $h_C = 14$ mm, $d_1 = 30$ mm, $d_2 = 38$ mm, $d_3 = 65$ mm.

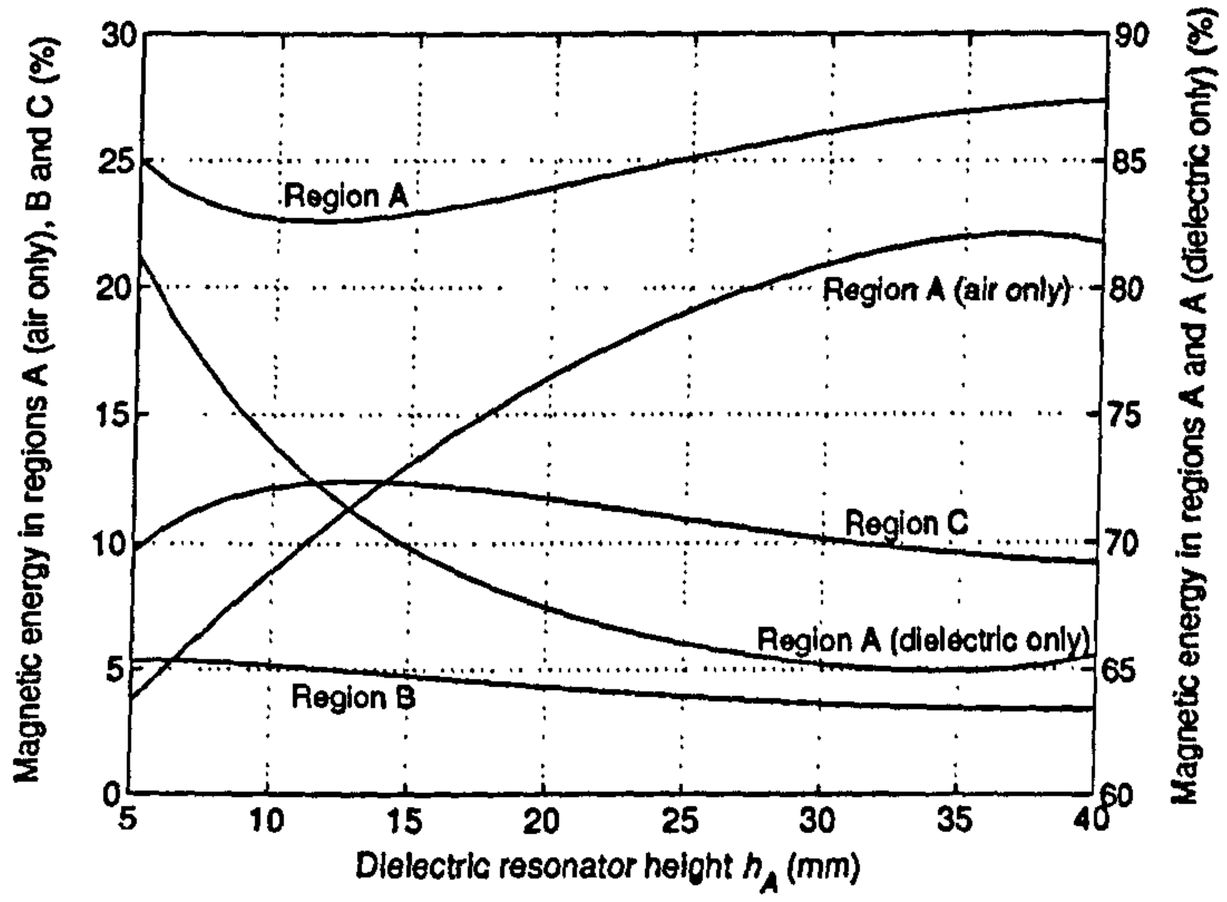

Figure F.2: Variations of magnetic energy with h_A. $h_B = 3$ mm, $h_C = 14$ mm, $d_1 = 30$ mm, $d_2 = 38$ mm, $d_3 = 65$ mm.

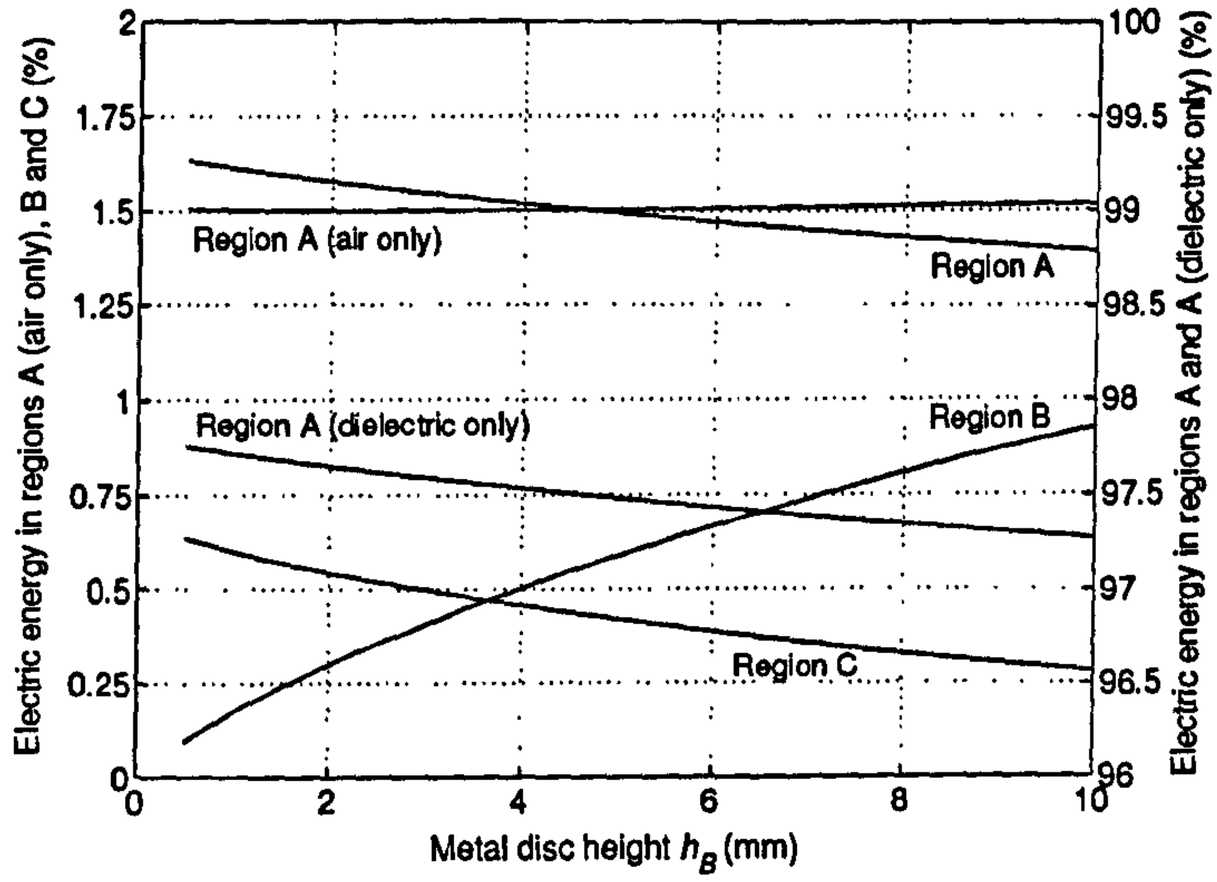

Figure F.3: Variations of electric energy with h_B. $h_A = 23$ mm, $h_C = 14$ mm, $d_1 = 30$ mm, $d_2 = 38$ mm, $d_3 = 65$ mm.

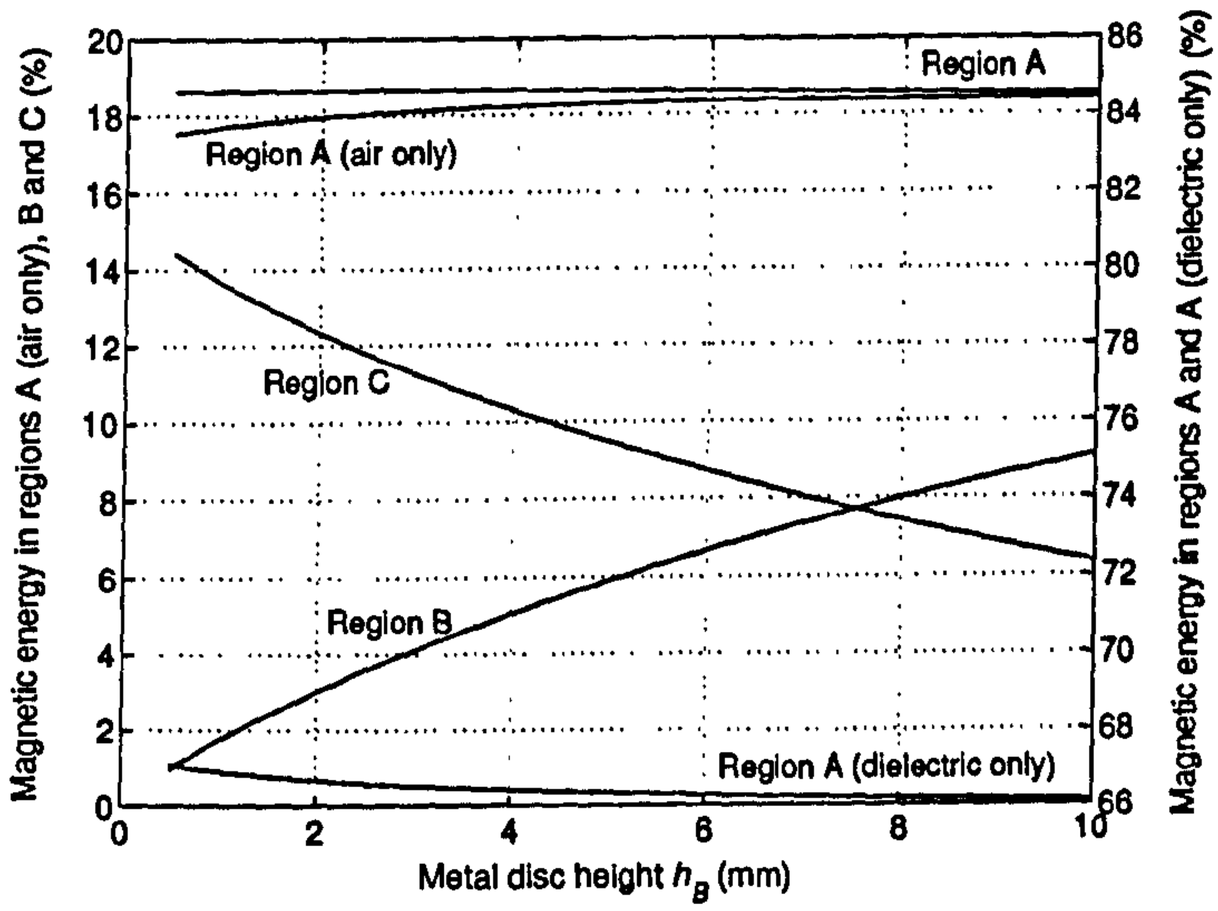

Figure F.4: Variations of magnetic energy with h_B. $h_A = 23$ mm, $h_C = 14$ mm, $d_1 = 30$ mm, $d_2 = 38$ mm, $d_3 = 65$ mm.

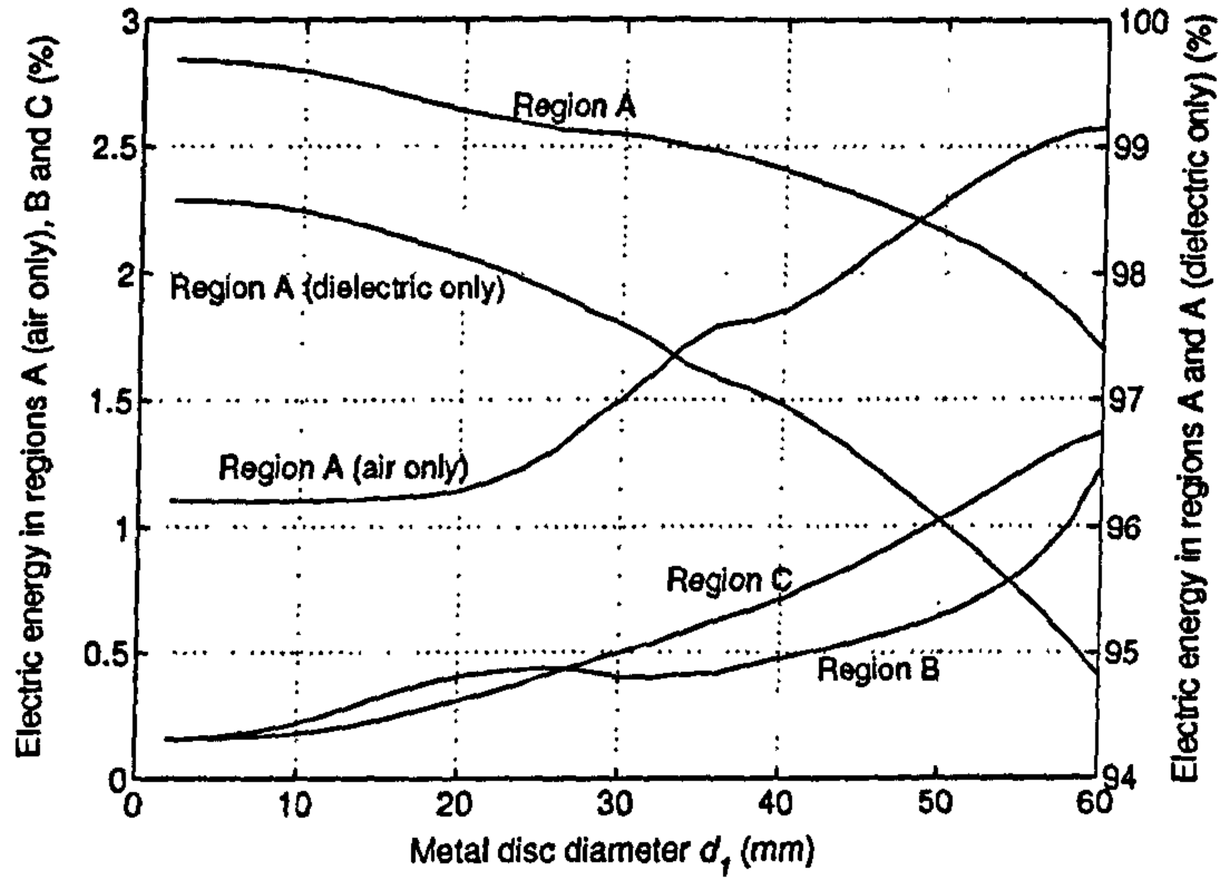

Figure F.5: Variations of electric energy with d_1. $h_A = 23$ mm, $h_B = 3$ mm, $h_C = 14$ mm, $d_2 = 38$ mm, $d_3 = 65$ mm.

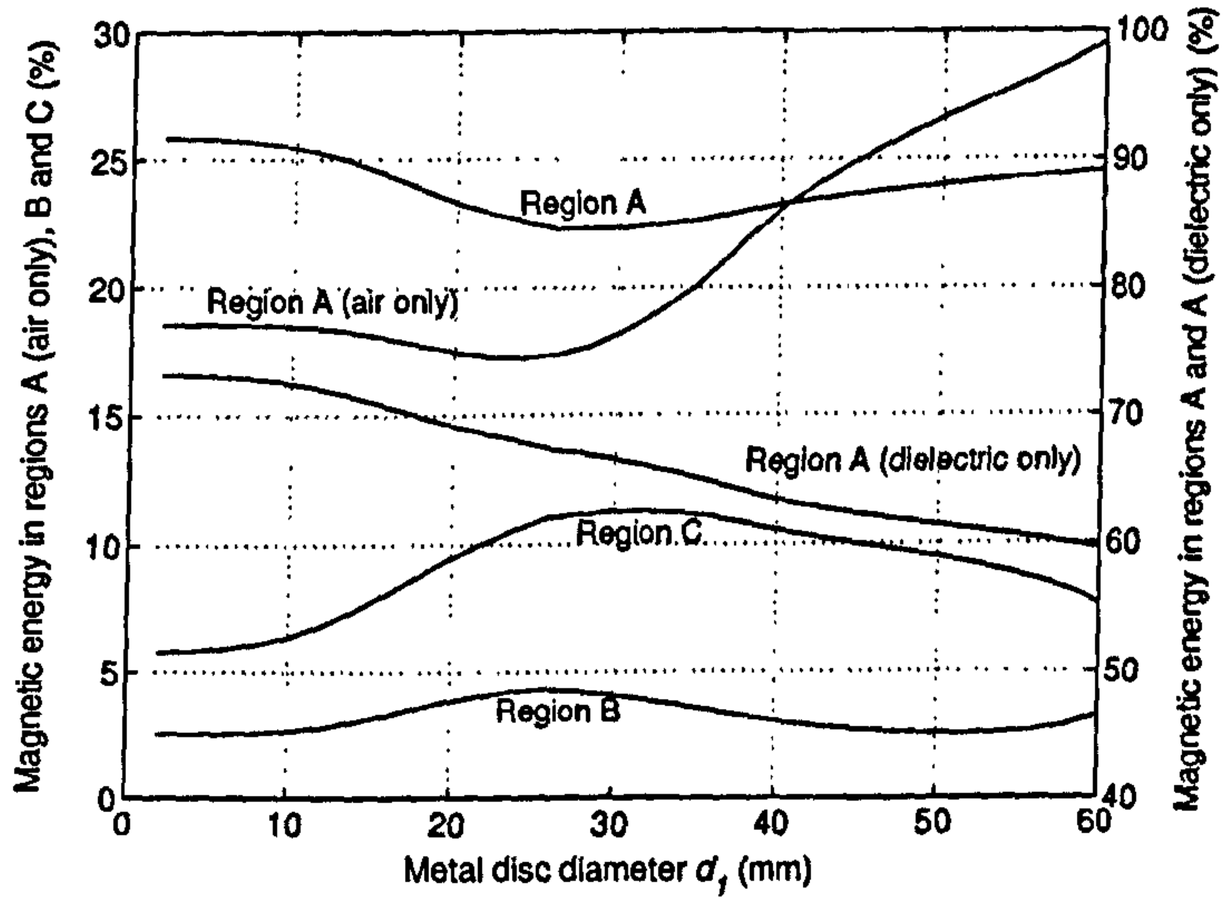

Figure F.6: Variations of magnetic energy with d_1. $h_A = 23$ mm, $h_B = 3$ mm, $h_C = 14$ mm, $d_2 = 38$ mm, $d_3 = 65$ mm.

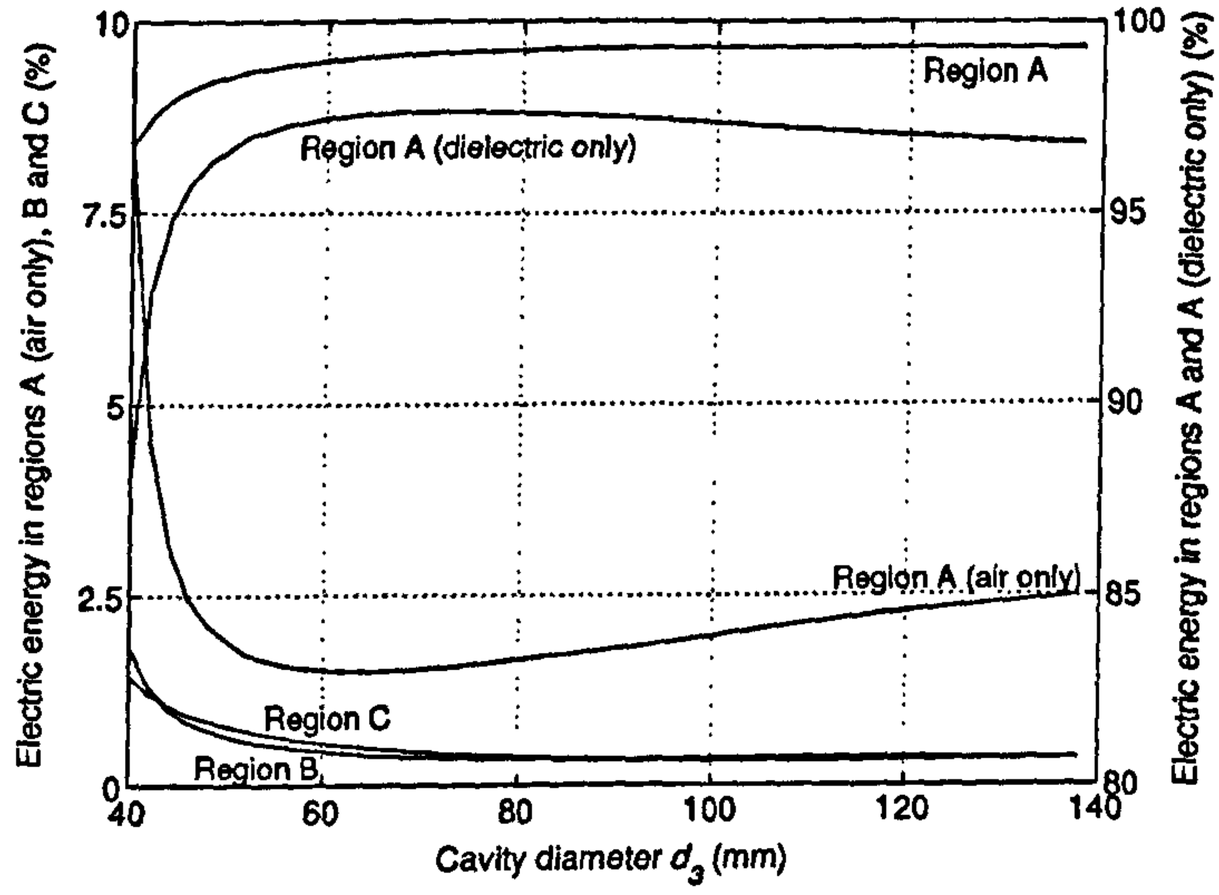

Figure F.8: Variations of electric energy with d_3. $h_A = 23$ mm, $h_B = 3$ mm, $h_C = 14$ mm, $d_1 = 30$ mm, $d_2 = 38$ mm.

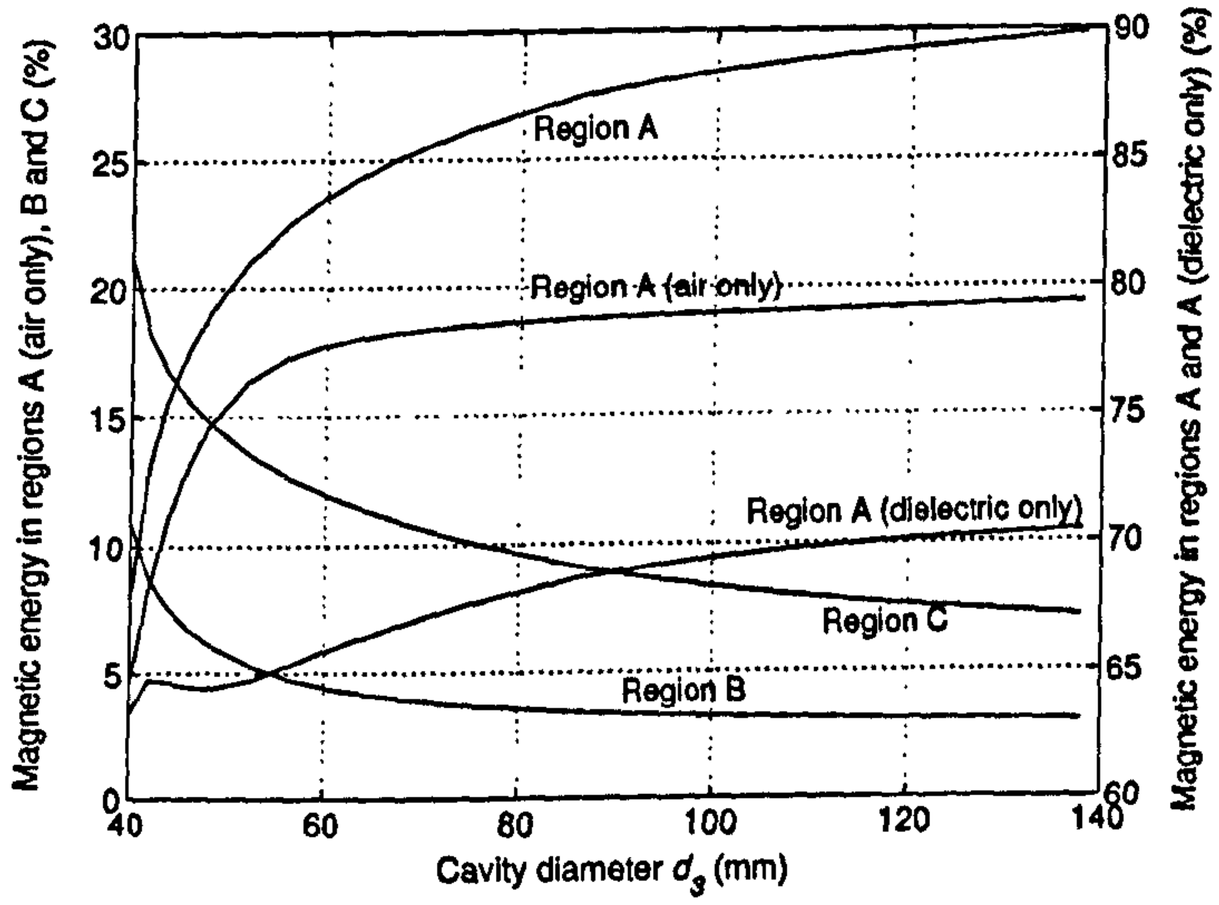

Figure F.8: Variations of magnetic energy with d_3. $h_A = 23$ mm, $h_B = 3$ mm, $h_C = 14$ mm, $d_1 = 30$ mm, $d_2 = 38$ mm.

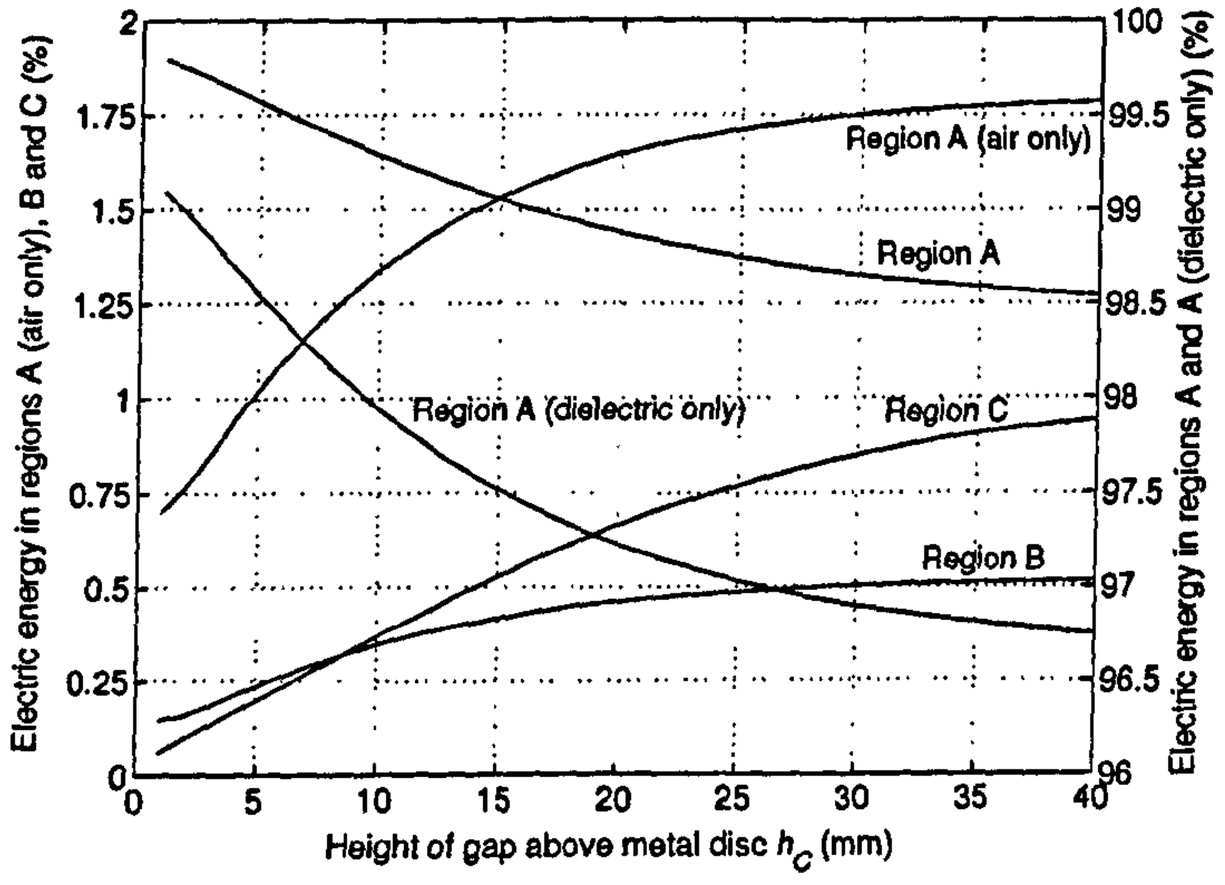

Figure F.9: Variations of electric energy with h_C. $h_A = 23$ mm, $h_B = 3$ mm, $d_1 = 30$ mm, $d_2 = 38$ mm, $d_3 = 65$ mm.

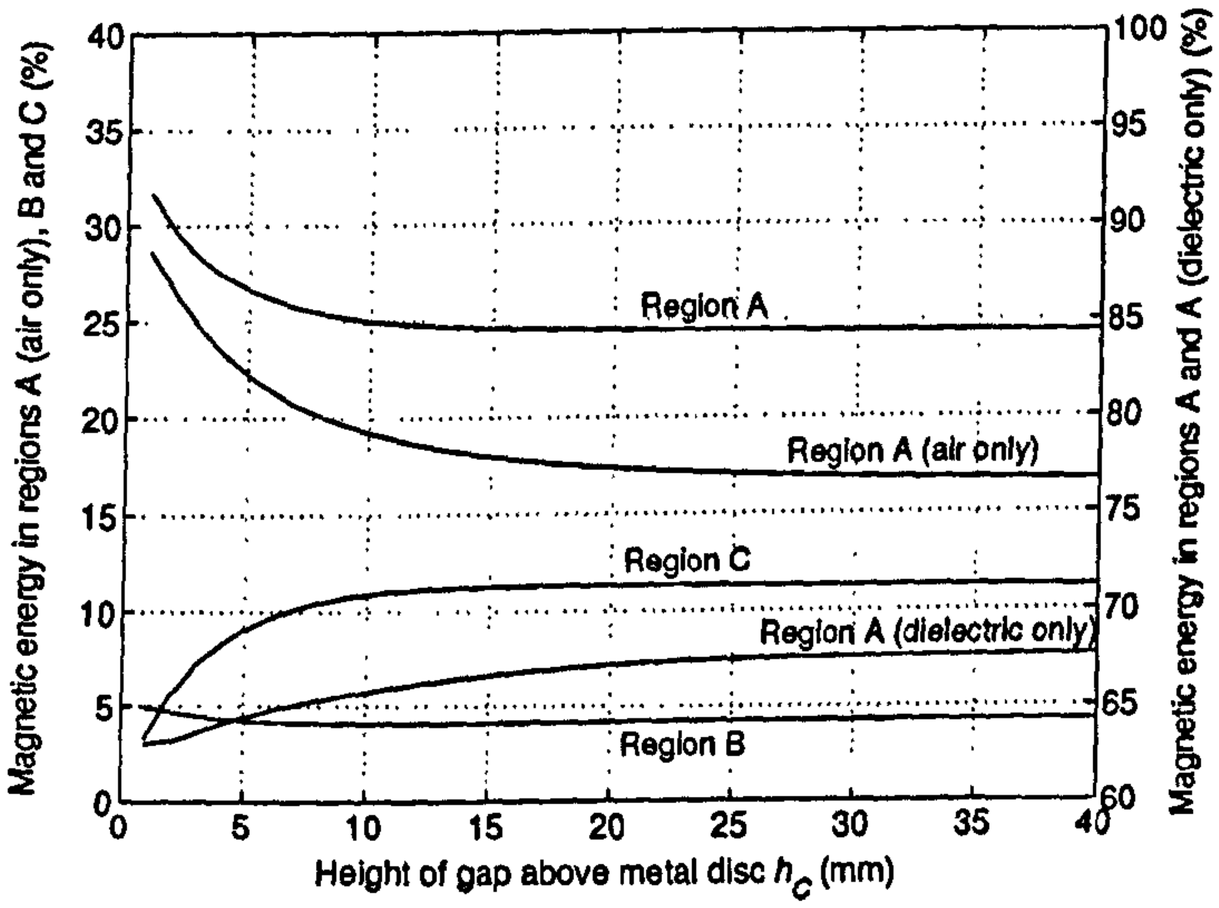

Figure F.10: Variations of magnetic energy with h_C. $h_A = 23$ mm, $h_B = 3$ mm, $d_1 = 30$ mm, $d_2 = 38$ mm, $d_3 = 65$ mm.

Appendix G

Variations of normalised Q factors with resonator dimensions

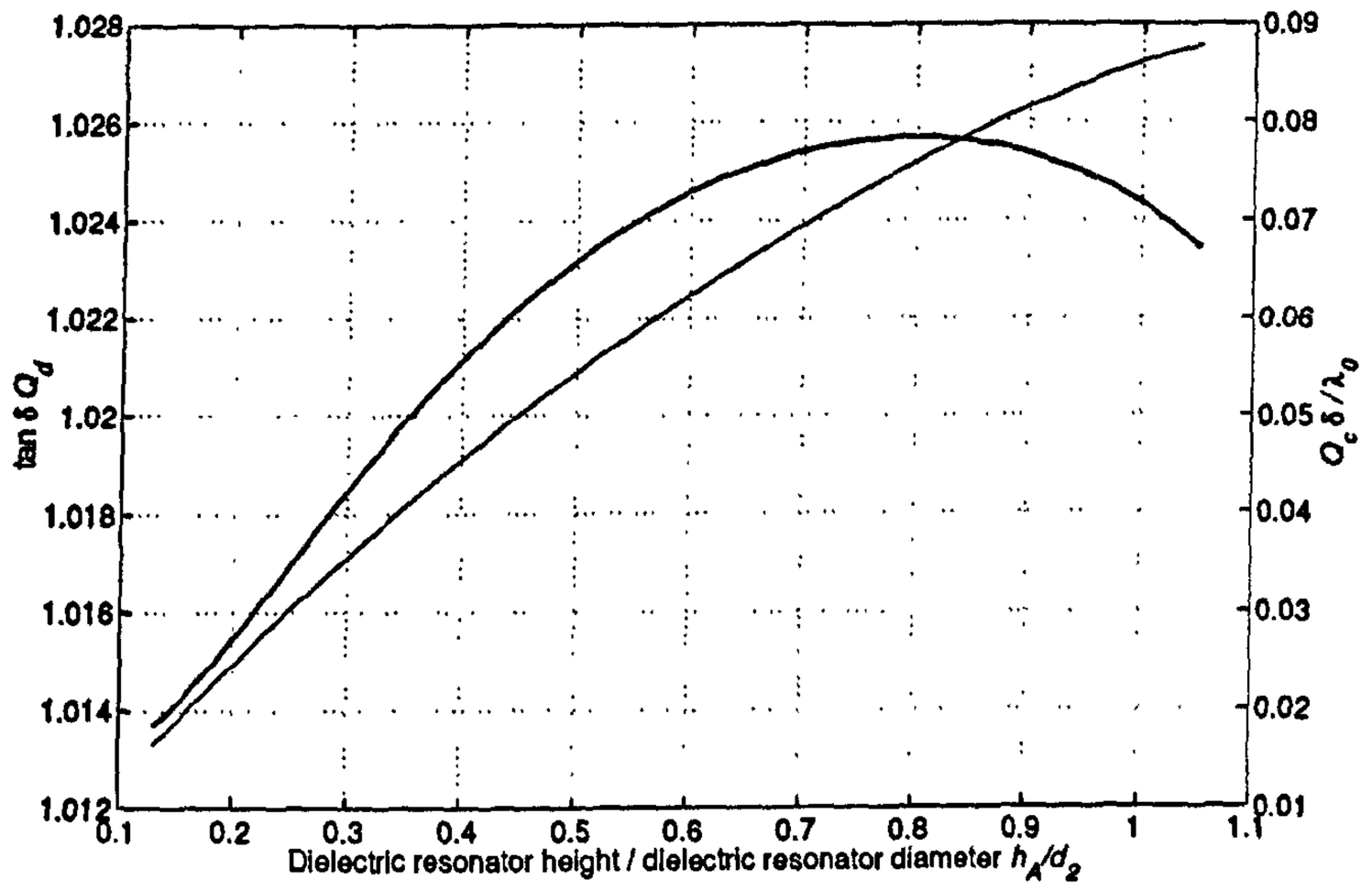

Figure G.1: Variations of normalised Q_c and Q_d of the $HE_{11\delta}$ mode with h_A/d_2. $h_B/d_2 = 0.079$, $h_C/d_2 = 0.368$, $d_1/d_2 = 0.789$, $d_3/d_2 = 1.71$.

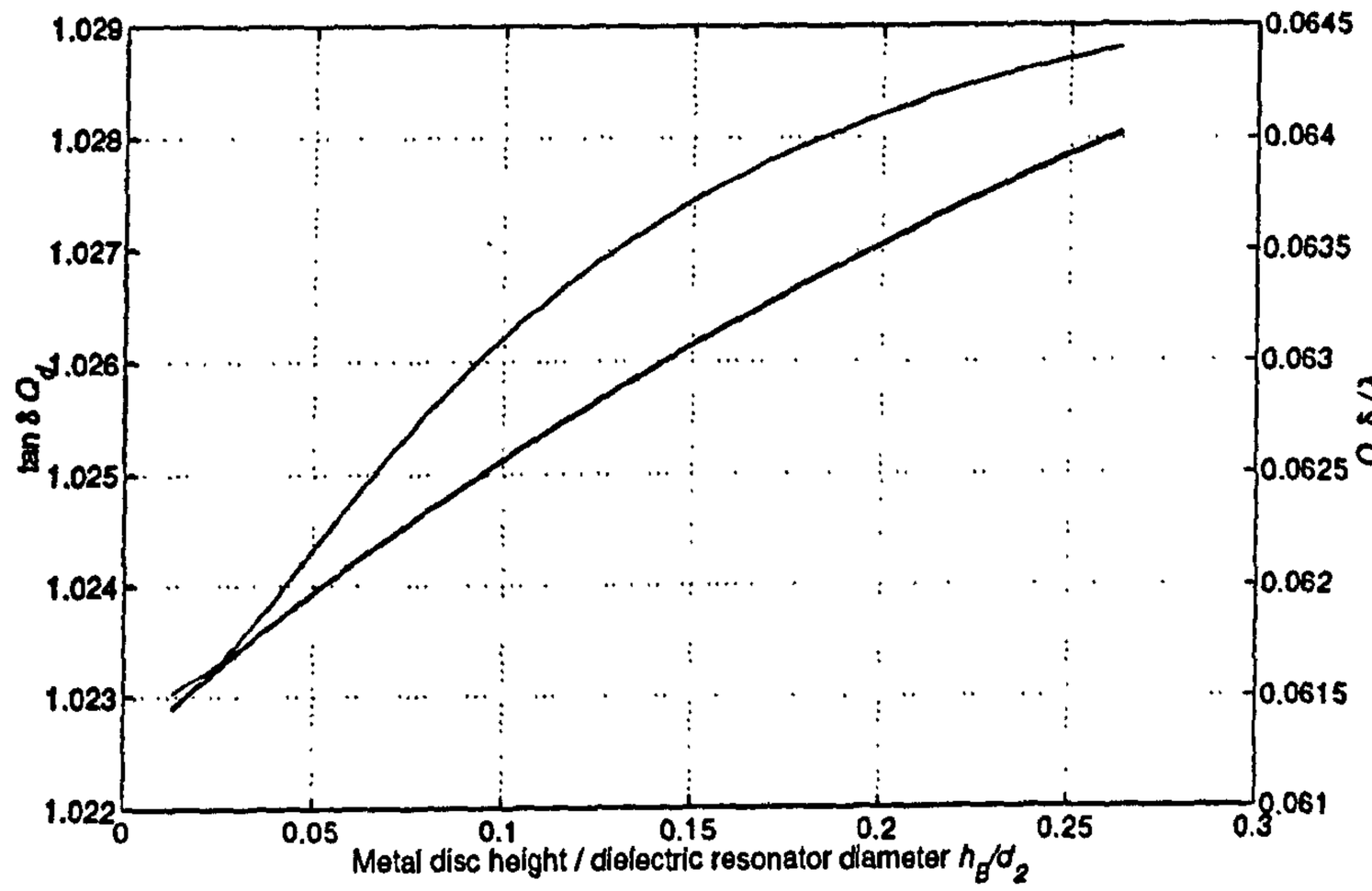

Figure G.2: Variations of normalised Q_c and Q_d of the $HE_{11\delta}$ mode with h_B/d_2. $h_A/d_2 = 0.605$, $h_C/d_2 = 0.368$, $d_1/d_2 = 0.789$, $d_3/d_2 = 1.71$.

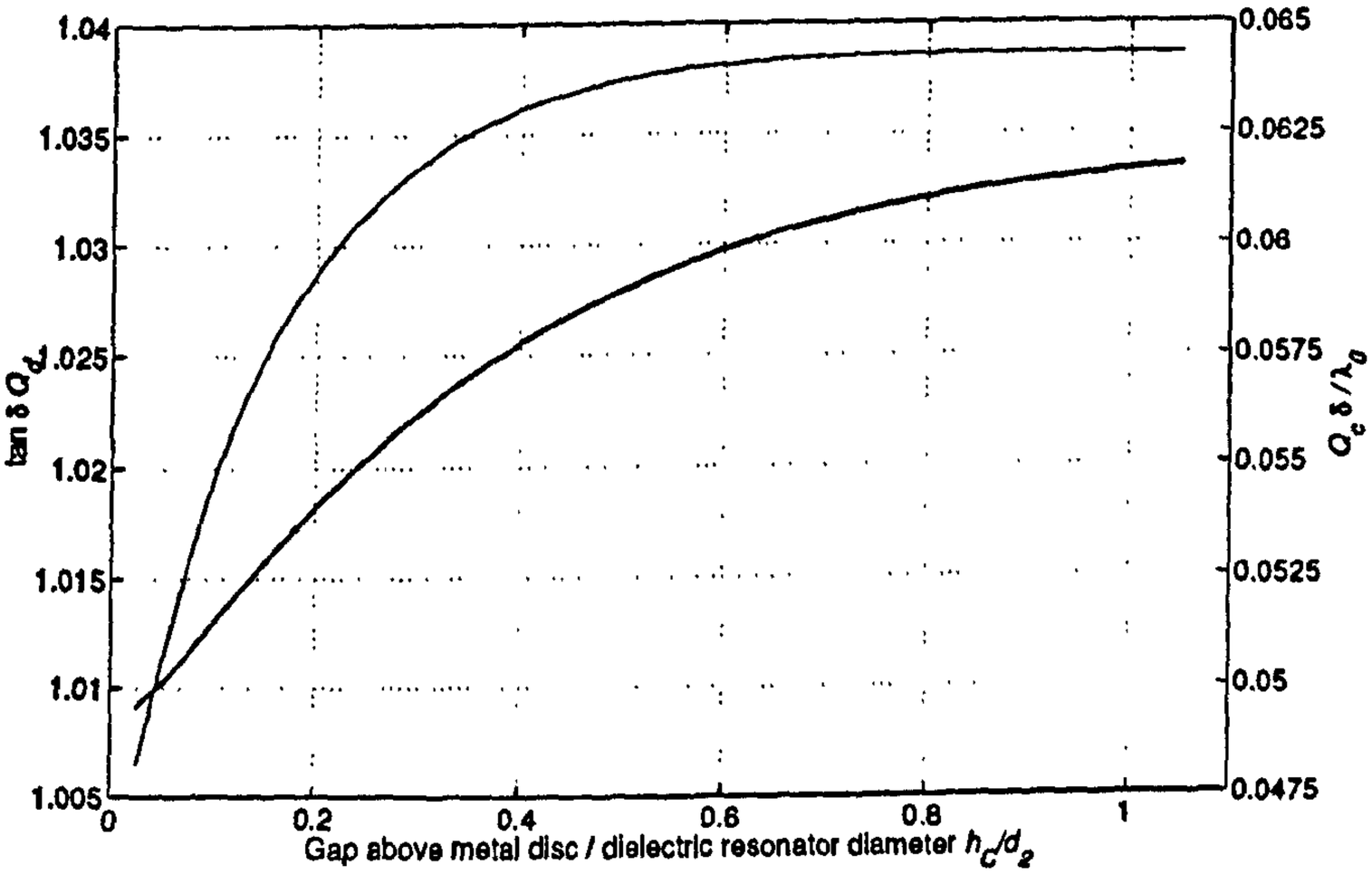

Figure G.3: Variations of normalised Q_c and Q_d of the $HE_{11\delta}$ mode with h_C/d_2. $h_A/d_2 = 0.605$, $h_B/d_2 = 0.079$, $d_1/d_2 = 0.789$, $d_3/d_2 = 1.71$.

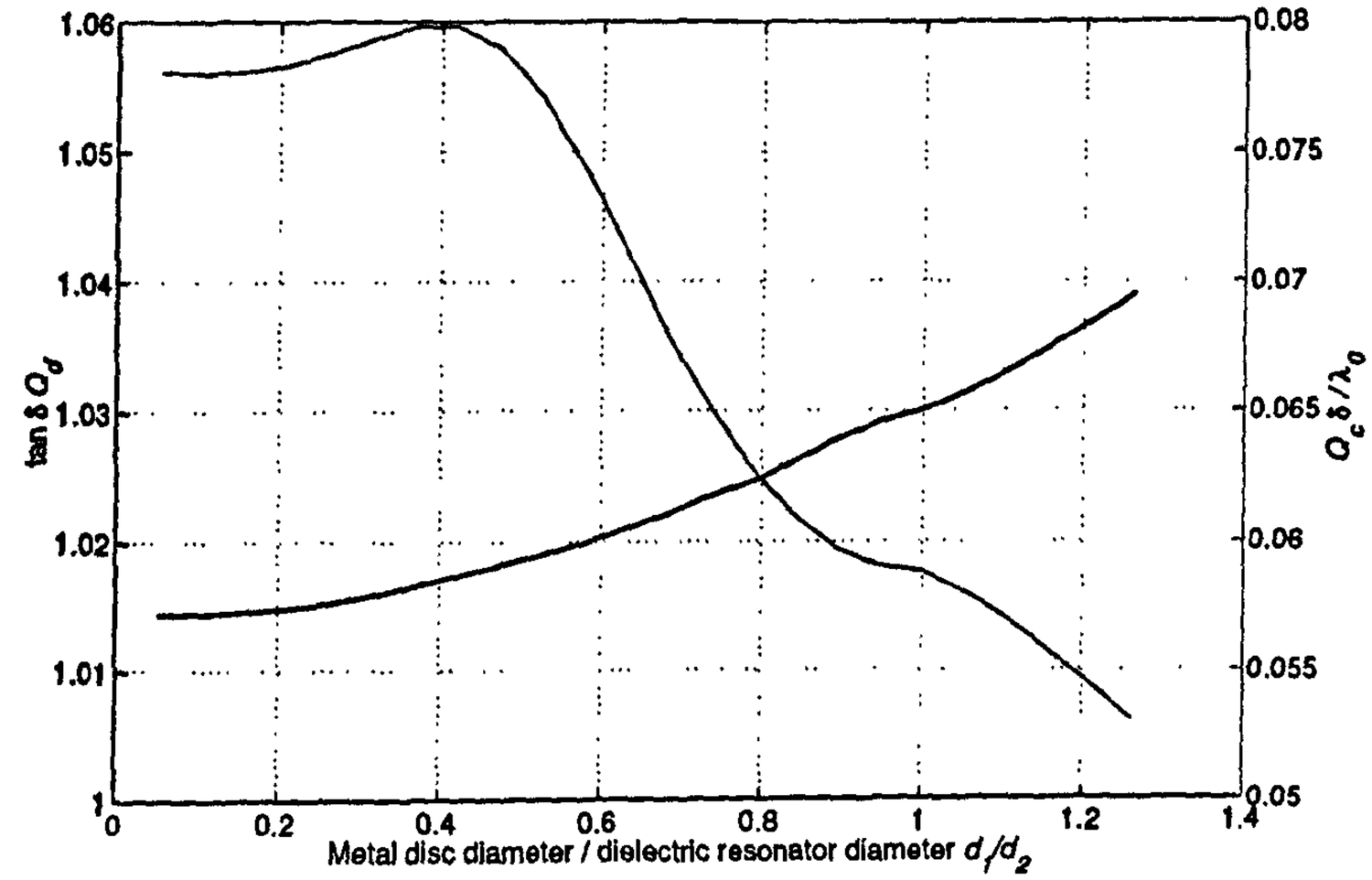

Figure G.4: Variations of normalised Q_c and Q_d of the $HE_{11\delta}$ mode with d_1/d_2. $h_A/d_2 = 0.605$, $h_B/d_2 = 0.079$, $h_C/d_2 = 0.368$, $d_3/d_2 = 1.71$.

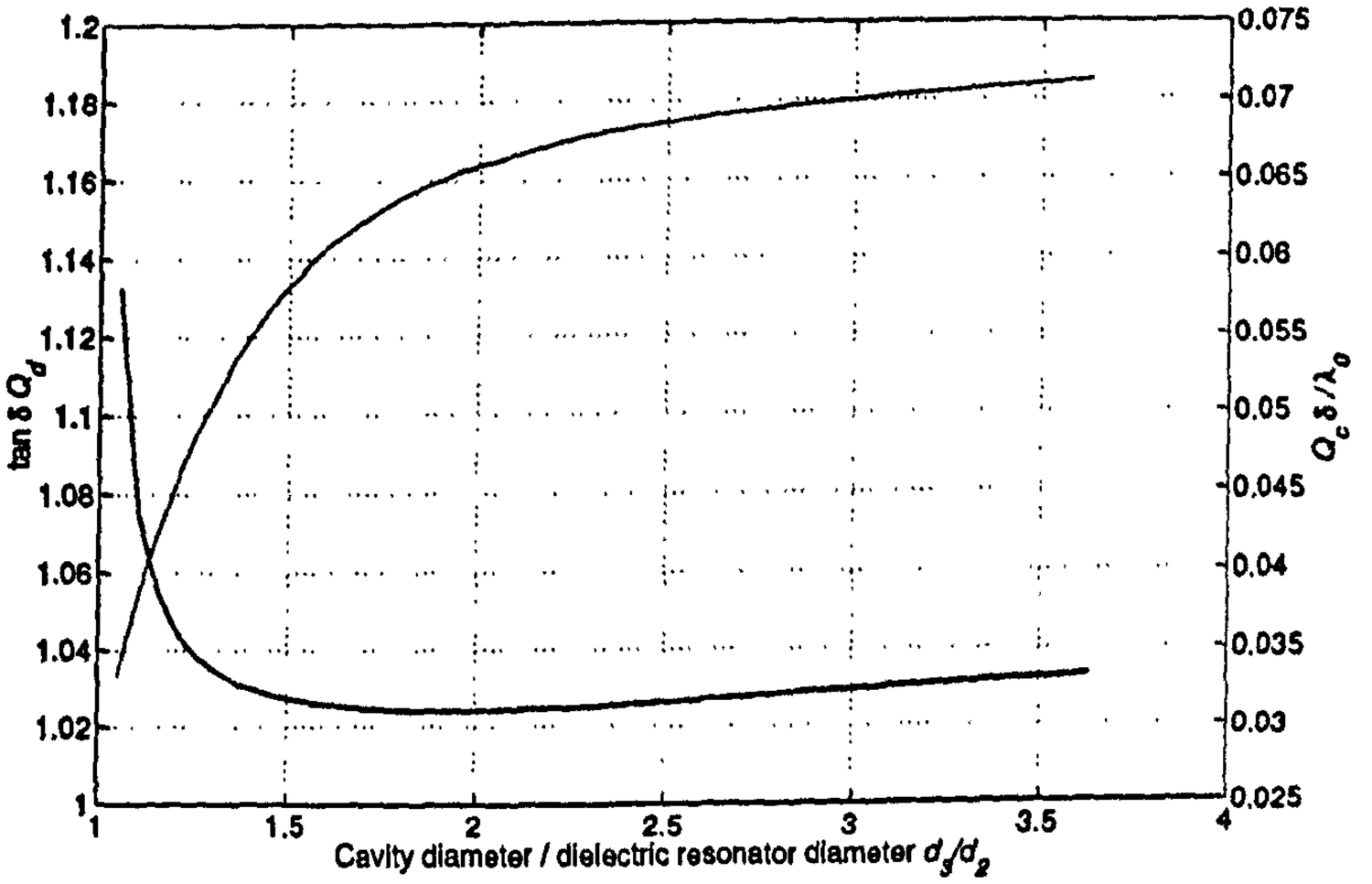

Figure G.5: Variations of normalised Q_c and Q_d of the $HE_{11\delta}$ mode with d_3/d_2. $h_A/d_2 = 0.605$, $h_B/d_2 = 0.079$, $h_C/d_2 = 0.368$, $d_1/d_2 = 0.789$.

Appendix H

Self and cross-coupling coefficients for the dielectric loaded TE_{011} resonator

Throughout this appendix, the notations of Chapter 5 are used.

H.1 Self-coupling coefficients

The self-coupling power coefficient of mode p in waveguide i, defined by Eq. B.19, is, in rectangular coordinates:

$$P_{ip} = \int_S (\overline{e}_{x\,ip} \times \overline{h}_{y\,ip} - \overline{h}_{x\,ip} \times \overline{e}_{y\,ip}) dxdy \tag{H.1}$$

with S the cross-section of the waveguide.

In region A and C,

$$P_{ip} = \frac{j\omega\mu_0 h\gamma_i}{{k_{yi}}^2}\left(\frac{b_3}{2} - \frac{\sin(2k_{yi}b_3)}{4k_{yi}}\right) \tag{H.2}$$

In region B, let us note

$$A_f = \frac{-k_{y1i}\cos(k_{y1i}b_1) + jk_{y2i}\sin(k_{y1i}b_1)}{2k_{y1i}e^{-jk_{y2i}b_1}} \tag{H.3}$$

$$A_r = \frac{k_{y1i}\cos(k_{y1i}b_1) + jk_{y2i}\sin(k_{y1i}b_1)}{2k_{y1i}e^{jk_{y2i}b_1}} \tag{H.4}$$

$$A_3 = \frac{k_{y3i}e^{jk_{y2i}b_2}\left(k_{y1i}\cos(k_{y1i}b_1) + jk_{y2i}\sin(k_{y1i}b_1)\right)}{k_{y1i}e^{jk_{y2i}b_1}\left(k_{y3i}\cos(k_{y3i}(b_3 - b_2)) - jk_{y2i}\sin(k_{y3i}(b_3 - b_2))\right)} \tag{H.5}$$

Then,

$$P_{bp} = j\omega\mu_0 h\gamma_i\left[\frac{1}{{k_{y1b}}^2}\left(\frac{b_1}{2} - \frac{\sin(2k_{y1b}b_1)}{4k_{y1b}}\right) - \frac{2A_fA_r(b_2 - b_1)}{{k_{y2b}}^2}\right.$$

$$- jA_f{}^2 \frac{e^{-2jk_{y2b}b_2} - e^{-2jk_{y2b}b_1}}{2k_{y2b}{}^3} + jA_r{}^2 \frac{e^{+2jk_{y2b}b_2} - e^{+2jk_{y2b}b_1}}{2k_{y2b}{}^3}$$
$$+ \frac{A_3{}^2}{k_{y3b}{}^2}\left(\frac{(b_3 - b_2)}{2} - \frac{\sin(2k_{y3b}(b_3 - b_2))}{4k_{y3b}}\right)\Bigg] \tag{H.6}$$

H.2 Cross-coupling coefficients

The cross-coupling power coefficient between modes p and m in waveguide i and l respectively, defined by Eq. B.20, is, in rectangular coordinates:

$$P_{ilpm} = \int_{S_i} (\overline{e}_{x\,ip} \times \overline{h}_{y\,lm} - \overline{h}_{x\,lm} \times \overline{e}_{y\,ip}) dxdy \tag{H.7}$$

with S_i the cross-section of waveguide i.

Then,

$$P_{blpm} = \frac{h\gamma_a \mu_o \omega}{2k_{yl}}\Bigg[\frac{j}{k_{y1b}}\left(\frac{\sin((k_{y1b} - k_{yl})b_1)}{k_{y1b} - k_{yl}} - \frac{\sin((k_{y1b} + k_{yl})b_1)}{k_{y1b} + k_{yl}}\right)$$
$$+ \frac{A_f}{k_{y2b}}\left(\frac{e^{j(-k_{y2b}+k_{yl})b_2} - e^{j(-k_{y2b}+k_{yl})b_1}}{k_{y2b} - k_{yl}} - \frac{e^{-j(k_{y2b}+k_{yl})b_2} - e^{-j(k_{y2b}+k_{yl})b_1}}{k_{y2b} + k_{yl}}\right)$$
$$+ \frac{A_r}{k_{y2b}}\left(-\frac{e^{j(k_{y2b}+k_{yl})b_2} - e^{j(k_{y2b}+k_{yl})b_1}}{k_{y2b} + k_{yl}} + \frac{e^{j(k_{y2b}-k_{yl})b_2} - e^{j(k_{y2b}-k_{yl})b_1}}{k_{y2b} - k_{yl}}\right)$$
$$- \frac{jA_3}{k_{y3b}}\left(\frac{\sin(k_{y3b}b_3 - (k_{y3b} + k_{yl})b_2)}{k_{y3b} + k_{yl}} - \frac{\sin(k_{y3b}b_3 + (-k_{y3b} + k_{yl})b_2)}{k_{y3b} - k_{yl}}\right)\Bigg] \tag{H.8}$$

References

[1] Y. Kobayashi and C. Inoue, "Bandpass and bandstop filters using dominant $TM_{01\delta}$ mode dielectric rod resonators", *IEEE Microwave Theory and Techniques Symposium Digest*, vol. 2, pp. 793–796, 1997.

[2] J.-F. Liang and W. D. Blair, "High-Q $TE_{01\delta}$ mode DR filters for PCS wireless base stations", *IEEE Transactions on Microwave Theory and Techniques*, vol. 46, no. 12, pp. 2493–2500, Dec. 1998.

[3] Y. Kobayashi and H. Furukawa, "Elliptic bandpass filters using four TM_{010} dielectric rod resonators", *IEEE Microwave Theory and Techniques Symposium Digest*, vol. 1, pp. 353–356, 1986.

[4] I. C. Hunter, *Theory and Design of Microwave Filters*, Institution of Electrical Engineers, 2001.

[5] J. Helszajn, *Synthesis of Lumped Element, Distributed and Planar Filters*, McGraw-Hill, 1990.

[6] I. C. Hunter and S.R. Chandler, "Intermodulation distortion in active microwave filters", *IEE Proc. Antennas Propag.*, vol. 145, no. 1, pp. 7–12, Feb. 1998.

[7] S. C. Cripps, *RF Power Amplifiers for Wireless Communications*, Artech House, 1999.

[8] J. O. Scanlan and R. Levy, *Circuit Theory, Volume Two*, Oliver and Boyd, 1973.

[9] J. D. Rhodes, *Theory of Electrical Filters*, John Wiley and Sons, 1976.

[10] R. J. Cameron, "General prototype network synthesis methods for microwave filters", *ESA Journal*, vol. 6, pp. 193–206, 1982.

[11] S. B. Cohn, "Dissipation loss in multiple-coupled-resonator filters", *Proceedings of the IEEE*, vol. 47, no. 8, pp. 1342–1348, Aug. 1959.

[12] C. M. Kudsia and V. O'Donovan, *Microwave Filters for Communications Systems*, Artech House, 1974.

[13] J. O. Scanlan, "Theory of microwave coupled-line networks", *Proceedings of the IEEE*, vol. 68, no. 2, pp. 209–231, Feb. 1980.

[14] T. J. Price, D. M. Iddles, and D. S. Cannell, "The design and selection of ceramic $TE_{01\delta}$ resonators for filters and combiners, A general guide to good practice", *Internal Filtronic Comtek Document*, 1998.

[15] S. Ramo, J. R. Whinnery, and T. Van Duzer, *Fields and Waves in Communication Systems*, John Wiley and Sons, 1994.

[16] T. J. Price, D. M. Iddles, and D. S. Cannell, "Progress in the understanding, design and processing of new and improved ceramic resonator filters", *Internal Filtronic Comtek Document*, 1999.

[17] Y. Konishi, "Novel dielectric waveguide components - microwave applications of new ceramic materials", *Proceedings of the IEEE*, vol. 79, no. 6, pp. 726–740, June 1991.

[18] K. Wakino, "Miniaturization techniques of microwave components for mobile communications systems - using low loss dielectrics -", *Ferroelectrics Review*, vol. 2/1-2, pp. 1–49, 2000.

[19] D. Kajfez and P. Guillon, *Dielectric Resonators*, Artech House, 1986.

[20] Y. Kobayashi and S. Nakayama, "Design charts for shielded dielectric rod and ring resonators", *IEEE Microwave Theory and Techniques Symposium Digest*, vol. 1, pp. 241–244, 1986.

[21] Y. Kobayashi and M. Minegishi, "Precise design of a bandpass filter using high Q dielectric ring resonators", *IEEE Transactions on Microwave Theory and Techniques*, vol. 35, no. 12, pp. 1156–1160, Dec. 1987.

[22] T. Nishikawa, K. Wakino, K. Tsunoda, and Y. Ishikawa, "Dielectric high-power bandpass filter using quarter-cut $TE_{01\delta}$ image resonator for cellular base stations", *IEEE Transactions on Microwave Theory and Techniques*, vol. 35, no. 12, pp. 1150–1155, Dec. 1987.

[23] T. Nishikawa, K. Wakino, T. Hiratsuka, and Y. Ishikawa, "800 MHz high power bandpass filter using TM_{110} dielectric resonators for cellular base stations", *IEEE Microwave Theory and Techniques Symposium Digest*, vol. 1, pp. 519–522, 1988.

[24] J. K. Plourde and D. P. Linn, "Microwave dielectric resonator filters utilizing $Ba_2Ti_9O_{20}$ ceramics", *IEEE Microwave Theory and Techniques Symposium Digest*, vol. 1, pp. 290–293, 1977.

[25] I. M. Reaney and R. Ubic, "Talking microwaves: A review of ceramics at the heart of the telecommunications network", *International Ceramics*, vol. no. 1, pp. 48–52, 2000.

[26] P. J. B. Clarricoats, "Propagation along unbounded and bounded dielectric loaded rods. part1. propagation along an unbounded dielectric rod", *I.E.E. Monograph*, vol. No 409E, pp. 170–176, Oct. 1960.

[27] E. Snitzer, "Cylindrical dielectric waveguide modes", *J. Opt. Soc. Am.*, vol. 51, pp. 491–498, May 1961.

[28] G. Biernson and D. J. Kinsley, "Generalized plots of mode patterns in a cylindrical dielectric waveguide applied to retinal cones", *IEEE Transactions on Microwave Theory and Techniques*, vol. 13, no. 3, pp. 345–356, May 1965.

[29] P. J. B. Clarricoats, "Circular waveguide backward wave structures", *Proc. IEE*, vol. 110, no. 2, pp. 261–270, Feb. 1963.

[30] K. A. Zaki and C. Chen, "Intensity and distribution of hybrid-mode fields in dielectric-loaded waveguide", *IEEE Transactions on Microwave Theory and Techniques*, vol. 33, no. 12, pp. 1442–1447, Dec. 1985.

[31] P. J. B. Clarricoats and B. C. Taylor, "Evanescent and propagating modes of dielectric-loaded circular waveguide", *Proc. IEE*, vol. 111, no. 12, pp. 1951–1956, Dec. 1964.

[32] R. D. Richtmyer, "Dielectric resonators", *Journal of Applied Physics*, vol. 10, pp. 391–398, June 1939.

[33] A. Karp, H. J. Shaw, and D. K. Winslow, "Circuit properties of microwave dielectric resonators", *IEEE Transactions on Microwave Theory and Techniques*, vol. 16, no. 10, pp. 818–828, Oct. 1968.

[34] A. Okaya and L. F. Barash, "The dielectric microwave resonator", *Proc. IRE*, vol. 50, pp. 2081–2092, Oct. 1962.

[35] W. R. Day, "Dielectric resonators as microstrip circuit elements", *IEEE Microwave Theory and Techniques Symposium Digest*, vol. 1, pp. 24–28, 1970.

[36] M. Verplanken and J. Van Bladel, "The electric-dipole resonances of ring resonators of very high permittivity", *IEEE Transactions on Microwave Theory and Techniques*, vol. 24, no. 2, pp. 108–112, Feb. 1976.

[37] M. Verplanken and J. Van Bladel, "The magnetic-dipole resonances of ring resonators of very high permittivity", *IEEE Transactions on Microwave Theory and Techniques*, vol. 27, no. 4, pp. 328–333, April 1979.

[38] Y. Kobayashi and M. Miura, "Optimum design of shielded dielectric rod and ring resonators for obtaining the best mode separation", *IEEE Microwave Theory and Techniques Symposium Digest*, vol. 1, pp. 184–186, 1984.

[39] S. B. Cohn, "Microwave bandpass filters containing high-Q dielectric resonators", *IEEE Transactions on Microwave Theory and Techniques*, vol. 16, no. 4, pp. 218–227, April 1968.

[40] W. E. Harrison, "A miniature high Q bandpass filter employing dielectric resonators", *IEEE Transactions on Microwave Theory and Techniques*, vol. 16, no. 4, pp. 210–218, April 1968.

[41] T. D. Iveland, "Dielectric resonator filters for applications in microwave integrated circuits", *IEEE Transactions on Microwave Theory and Techniques*, vol. 19, no. 7, pp. 643–652, July 1971.

[42] S. Fiedziuszko and A. Jelenski, "Double dielectric resonator", *IEEE Transactions on Microwave Theory and Techniques*, vol. 19, no. 9, pp. 779–781, Sept. 1971.

[43] M. A. Gerdine, "A frequency-stabilized microwave band rejection filter using high dielectric constant resonators", *IEEE Transactions on Microwave Theory and Techniques*, vol. 17, no. 7, pp. 354–359, July 1969.

[44] K. Wakino, T. Nishikawa, S. Tamura, and Y. Ishikawa, "Microwave bandpass filters containing dielectric resonators with improved temperature stability and spurious response", *IEEE Microwave Theory and Techniques Symposium Digest*, vol. 1, pp. 63–66, 1975.

[45] Y. Kobayashi, T. Aoki, and Y. Kabe, "Influence of conductor shields on the Q-factors of the TE_0 dielectric resonator", *IEEE Microwave Theory and Techniques Symposium Digest*, vol. 1, pp. 281–284, 1985.

[46] Y. Kobayashi, Y. Kabe, Y. Kogami, and T. Yamagishi, "Frequency and low-temperature characteristics of high-Q dielectric resonators", *IEEE Microwave Theory and Techniques Symposium Digest*, vol. 3, pp. 1239–1242, 1989.

[47] M. Mizumura, H. Sei, T. Konishi, M. Sakai, and I. Haga, "Dielectric resonator band pass filters for microwave communication systems", *NEC Internal Document*, Year Unknown.

[48] C.-L. Ren, "Waveguide bandstop filter utilizing $Ba_2Ti_9O_{20}$ resonators", *IEEE Microwave Theory and Techniques Symposium Digest*, vol. 1, pp. 227–229, 1978.

[49] P. Guillon, J. P. Balabaud, and Y. Garault, "TM_{01p} tubular and cylindrical dielectric resonator mode", *IEEE Microwave Theory and Techniques Symposium Digest*, vol. 1, pp. 163–166, 1981.

[50] B. Byzery and P. Guillon, "$TM_{0\gamma\delta}$ mode of cylindrical dielectric resonators applications to microwave filters", *IEEE Microwave Theory and Techniques Symposium Digest*, vol. 1, pp. 515–518, 1985.

[51] P. Skalicky, "Direct coupling between two dielectric resonators", *Electronics Letters*, vol. 18, no. 8, pp. 332–334, April 1982.

[52] Y. Kobayashi and M. Minegishi, "A low loss bandpass filter using electrically coupled high-Q $TM_{01\delta}$ dielectric rod resonators", *IEEE Transactions on Microwave Theory and Techniques*, vol. 36, no. 12, pp. 1727–1732, Dec. 1988.

[53] G. Macchiarella and G. B. Stracca, "An accurate design approach for TM mode dielectric resonator filters in circular waveguide below cutoff", *IEEE Transactions on Microwave Theory and Techniques*, vol. 42, no. 7, pp. 1321–1329, July 1994.

[54] G. Macchiarella and S. Cavalieri D'Oro, "Design criteria and performance evaluation of TM_{01} dielectric resonators cavities for cellular base station filters", *Proc. of the 29th European Microwave Conference*, pp. 47–50, 1999.

[55] W. Lin, "Microwave filters employing a single cavity excited in more than one mode", *Journal of Applied Physics*, vol. 22 no. 8, pp. 989–1001, Aug. 1951.

[56] A. E. Atia and A. E. Williams, "Narrow-bandpass waveguide filters", *IEEE Transactions on Microwave Theory and Techniques*, vol. 20, no. 4, pp. 258–265, April 1972.

[57] P. Guillon, Y. Garault, and J. Farenc, "Dielectric resonator dual modes filter", *Electronics Letters*, vol. 16, no. 17, pp. 646–647, Aug. 1980.

[58] S. J. Fiedziuszko, "Dual-mode dielectric resonator loaded cavity filters", *IEEE Transactions on Microwave Theory and Techniques*, vol. 30, no. 9, pp. 1311–1316, Dec. 1982.

[59] S. J. Fiedziuszko, ""Engine Block" dual mode dielectric resonator loaded cavity filter with nonadjacent cavity couplings", *IEEE Microwave Theory and Techniques Symposium Digest*, vol. 1, pp. 285–287, 1984.

[60] Y. Kobayashi and K. Kubo, "Canonical bandpass filters using dual-mode dielectric resonators", *IEEE Microwave Theory and Techniques Symposium Digest*, vol. 1, pp. 137–140, 1987.

[61] K. A. Zaki, C. Chen, and A. E. Atia, "Canonical and longitudinal dual-mode dielectric resonator filters without iris", *IEEE Transactions on Microwave Theory and Techniques*, vol. 35, no. 12, pp. 1130–1135, Dec. 1987.

[62] A. E. Williams and A. E. Atia, "Dual-mode canonical waveguide filters", *IEEE Transactions on Microwave Theory and Techniques*, vol. 25, no. 12, pp. 1021–1026, April 1977.

[63] S.-W. Chen and K. A. Zaki, "A novel coupling method for dual-mode dielectric resonators and waveguide filters", *IEEE Transactions on Microwave Theory and Techniques*, vol. 38, no. 12, pp. 1885–1893, April 1990.

[64] D. R. Jachowski, "Alternative designs for dual-mode filters", *IEEE Microwave Theory and Techniques Symposium Digest*, vol. 2, pp. 1087–1090, 1997.

[65] K. Wakino, T. Nishikawa, and Y. Ishikawa, "Miniaturization technologies of dielectric resonator filters for mobile communications", *IEEE Transactions on Microwave Theory and Techniques*, vol. 42, no. 7, pp. 1295–1300, July 1994.

[66] C. Wang, W. Wilber, and B. Engst, "A practical triple-mode monoblock bandpass filter for base station applications", *IEEE Microwave Theory and Techniques Symposium Digest*, vol. 3, pp. 1783–1786, 2001.

[67] W. C. Tang, J. Sferrazza, B. Beggs, and D. Siu, "Dielectric resonator output multiplexer for C-band satellite applications", *IEEE Microwave Theory and Techniques Symposium Digest*, vol. 1, pp. 343–345, 1985.

[68] Z. Gan, Y. Li, C. Feng, and S. Yang, "Triple-mode dielectric resonator loaded cavity", *IEEE Microwave Theory and Techniques Symposium Digest*, vol. 2, pp. 687–690, 1991.

[69] D. Siu, "Realization of an exact 5-pole elliptic function filter employing dielectric loaded triple-dual-mode cavity structure", *IEEE Microwave Theory and Techniques Symposium Digest*, vol. 1, pp. 357–359, 1986.

[70] J. Hattori, H. Wakamatsu, H. Kubo, and Y. Ishikawa, "2GHz band triple mode dielectric resonator duplexer for digital cellular base station", *Microwave Conference 2000 - Asia-Pacific, 2000*, pp. 1315–1318, 2000.

[71] J.-F. Liang, K. A. Zaki, and R. Levy, "Dual-mode dielectric-loaded resonators with cross-coupling flats", *IEEE Microwave Theory and Techniques Symposium Digest*, vol. 2, pp. 509–512, 1995.

[72] R. R. Mansour, "Dual-mode dielectric resonator filters with improved spurious performance", *IEEE Microwave Theory and Techniques Symposium Digest*, vol. 1, pp. 439–442, 1993.

[73] R. V. Snyder, "Dielectric resonator filters with wide stopbands", *IEEE Transactions on Microwave Theory and Techniques*, vol. 40, no. 11, pp. 2100–2103, Nov. 1992.

[74] H. Hwang, N. Park, Y. Cho, S. Yun, and I. Chang, "The design of band-pass filters made of both dielectric and coaxial resonators", *IEEE Microwave Theory and Techniques Symposium Digest*, vol. 2, pp. 805–808, 1997.

[75] C. Wang, K. A. Zaki, and A. E. Atia, "Dual-mode conductor-loaded cavity filters", *IEEE Transactions on Microwave Theory and Techniques*, vol. 45, no. 8, pp. 1240–1246, Aug. 1997.

[76] C. Wang, K. A. Zaki, and A. E. Atia, "Dual mode combined dielectric and conductor loaded cavity filters", *IEEE Microwave Theory and Techniques Symposium Digest*, vol. 2, pp. 1103–1107, 1997.

[77] J.-F. Liang, K. A. Zaki, and A. E. Atia, "Mixed modes dielectric resonator filters", *IEEE Transactions on Microwave Theory and Techniques*, vol. 42, no. 12, pp. 2449–2454, Dec. 1994.

[78] C. Wang, H.-W. Yao, K. A. Zaki, and R. R. Mansour, "Mixed modes cylindrical planar dielectric resonator filters with rectangular enclosure", *IEEE Transactions on Microwave Theory and Techniques*, vol. 43, no. 12, pp. 2817–2823, Dec. 1995.

[79] R. V. Snyder and C. Alvarez, "Filters using a new type resonator: The partially-metallized dielectric slug", *IEEE Microwave Theory and Techniques Symposium Digest*, vol. 3, pp. 1029–1032, 1999.

[80] C. Wang, K. A. Zaki, A. E. Atia, and T. Dolan, "Dielectric combline resonators and filters", *IEEE Transactions on Microwave Theory and Techniques*, vol. 46, no. 12, pp. 2501–2506, Dec. 1998.

[81] Y. Kobayashi and S. Yoshida, "Bandpass filters using TM_{010} dielectric rod resonators", *IEEE Microwave Theory and Techniques Symposium Digest*, vol. 1, pp. 233–235, 1978.

[82] J. Hattori, H. Kubo, S. Abe, T. Nishiyama, and Y. Ishikawa, "Compact transmitting dielectric resonator filter using capacitive loaded dual mode method for PCS microcellular base station", *IEEE Microwave Theory and Techniques Symposium Digest*, vol. 3, pp. 1631–1634, 1996.

[83] V. Madrangeas, M. Aubourg, P. Guillon, S. Vigneron, and B. Theron, "Analysis and realization of L-band dielectric resonator microwave filters", *IEEE Transactions on Microwave Theory and Techniques*, vol. 40, no. 1, pp. 120–127, Jan. 1992.

[84] Y. Ishikawa, J. Hattori, M. Andoh, and T. Nishikawa, "800 MHz high power duplexer using TM dual mode dielectric resonators", *IEEE Microwave Theory and Techniques Symposium Digest*, vol. 3, pp. 1617–1620, 1992.

[85] T. Nishikawa, K. Wakino, H. Wada, and Y. Ishikawa, "800 MHz band dielectric channel dropping filter using TM_{110} triple mode resonance", *IEEE Microwave Theory and Techniques Symposium Digest*, vol. 1, pp. 289–292, 1985.

[86] X.-P. Liang and K. A. Zaki, "Modeling of cylindrical dielectric resonators in rectangular waveguides and cavities", *IEEE Transactions on Microwave Theory and Techniques*, vol. 41, no. 12, pp. 2174–2181, Dec. 1993.

[87] X. Zhang, C. Wang, K. A. Zaki, and K. S. Harshavardhan, "Dual mode patch superconductor cavity filters", *IEEE Microwave Theory and Techniques Symposium Digest*, vol. 3, pp. 1725–1728, 1997.

[88] A. R. Weily and A. S. Mohan, "Microwave filters with improved spurious performance based on sandwiched conductor dielectric resonators", *IEEE Transactions on Microwave Theory and Techniques*, vol. 49, no. 8, pp. 1501–1507, Aug. 2001.

[89] K. Wakino, T. Nishikawa, H. Matsumoto, and Y. Ishikawa, "Miniaturized band pass filters using half wave dielectric resonators with improved spurious

response", *IEEE Microwave Theory and Techniques Symposium Digest*, vol. 1, pp. 230–232, 1978.

[90] K. Wakino, T. Nishikawa, H. Matsumoto, and Y. Ishikawa, "Quarter wave dielectric transmission line diplexer for land mobile communications", *IEEE Microwave Theory and Techniques Symposium Digest*, vol. 1, pp. 278–280, 1979.

[91] K. Wakino, T. Nishikawa, and Y. Ishikawa, "Miniaturized diplexer for land mobile communication using high dielectric resonators", *IEEE Microwave Theory and Techniques Symposium Digest*, vol. 1, pp. 185–187, 1981.

[92] H. Matsumoto, H. Ogura, and T. Nishikawa, "A miniaturized dielectric monoblock band-pass filter for 800MHz band cordless telephone system", *IEEE Microwave Theory and Techniques Symposium Digest*, vol. 1, pp. 249–252, 1994.

[93] H.-W. Yao, C. Wang, and K. A. Zaki, "Analysis of quarter wavelength ceramic combline filters", *IEEE Microwave Theory and Techniques Symposium Digest*, vol. 2, pp. 473–476, 1996.

[94] A. Fukasawa, T. Sato, and K. Hosoda, "Miniaturized microwave filter construction with dielectric-loaded resonator and space coupling", *IEEE Microwave Theory and Techniques Symposium Digest*, vol. 1, pp. 209–211, 1981.

[95] K. Hano, H. Kohriyama, and K-I. Sawamoto, "A direct-coupled $\lambda/4$-coaxial resonator bandpass filter for land mobile communications", *IEEE Transactions on Microwave Theory and Techniques*, vol. 34, no. 9, pp. 972–976, Sept. 1986.

[96] S. Yamashita and M. Makimoto, "Miniaturized coaxial resonator partially loaded with high-dielectric-constant microwave ceramics", *IEEE Transactions on Microwave Theory and Techniques*, vol. 31, no. 9, pp. 697–703, Sept. 1983.

[97] T. Ishizaki, M. Fujita, H. Kagata, T. Uwano, and H. Miyake, "A very small dielectric planar filter for portable telephones", *IEEE Transactions on Microwave Theory and Techniques*, vol. 42, no. 11, pp. 2017–2022, Nov. 1994.

[98] S. Kobayashi and K. Saito, "A miniaturized ceramic bandpass filter for cordless phone systems", *IEEE Microwave Theory and Techniques Symposium Digest*, vol. 2, pp. 391–394, 1995.

[99] S. J. Fiedziuszko and R. S. Kwok, "Novel helical resonator filter structures", *IEEE Microwave Theory and Techniques Symposium Digest*, vol. 3, pp. 1323–1326, 1998.

[100] Y. Tagushi, S.-I. Seki, K. Onishi, O. Kawasaki, and K. Eda, "A balanced-type SAW filter for PCN and PCS systems", *IEEE Microwave Theory and Techniques Symposium Digest*, vol. 2, pp. 837–840, 1997.

[101] R. Ruby, P. Bradley, J. D. Larson III, and Y. Oshmyansky, "PCS 1900MHz duplexer using thin film bulk acoustic resonators (FBARs)", *Electronics Letters*, vol. 35, no. 10, pp. 794–795, May 1999.

[102] H. Y. Hwang, S.-W. Yun, and I.-S. Chang, "A design of planar elliptic bandpass filter using SMD type partially metallized rectangular dielectric resonators", *IEEE Microwave Theory and Techniques Symposium Digest*, vol. 3, pp. 1483–1486, 2001.

[103] H. Kubo, H. Yamashita, and I. Awai, "Analysis of dielectric E-plane waveguides and design of filters", *IEEE Transactions on Microwave Theory and Techniques*, vol. 46, no. 8, pp. 1085–1090, Aug. 1998.

[104] J. Liang, X. Liang, K. A. Zaki, and A. E. Atia, "Dual mode dielectric or air-filled rectangular waveguide filters", *IEEE Transactions on Microwave Theory and Techniques*, vol. 42, no. 7, pp. 1330–1336, July 1994.

[105] A. Abdelmonem, J. Liang, H. Yao, and K. A. Zaki, "Full-wave design of spurious free D.R. TE mode band pass filters", *IEEE Transactions on Microwave Theory and Techniques*, vol. 43, no. 4, pp. 744–752, April 1995.

[106] K. Sano and M. Miyashita, "Dielectric waveguide filter with low profile and low insertion loss", *IEEE Transactions on Microwave Theory and Techniques*, vol. 47, no. 12, pp. 2299–2303, Dec. 1999.

[107] A. C. Kundu and I. A. Awai, "Resonant frequency and quality factors of a silver-coated $\lambda/4$ dielectric waveguide resonator", *IEEE Transactions on Microwave Theory and Techniques*, vol. 46, no. 8, pp. 1124–1131, Dec. 1998.

[108] M. Reppel, *Novel HTS Microstrip Resonator Configurations for Microwave Bandpass Filters*, PhD thesis, University of Bergischen Wuppertal, 2000.

[109] J. A. Curtis, S. J. Fiedziuszko, and S. C. Holme, "Hybrid dielectric/HTS resonators and their applications", *IEEE Microwave Theory and Techniques Symposium Digest*, vol. 2, pp. 447–450, 1991.

[110] S. J. Fiedziuszko, J. A. Curtis, S. C. Holme, and R. S. Kwok, "Low loss multiplexers with planar dual mode HTS resonators", *IEEE Transactions on Microwave Theory and Techniques*, vol. 44, no. 7, pp. 1248–1257, July 1996.

[111] H. Y. Yee, "Natural resonant frequencies of microwave dielectric resonators", *IEEE Transactions on Microwave Theory and Techniques*, vol. 13, no. 2, pp. 256, Feb. 1965.

[112] J. C. Sethares and S. J. Naumann, "Design of microwave dielectric resonators", *IEEE Transactions on Microwave Theory and Techniques*, vol. 14, no. 1, pp. 2–6, Jan. 1966.

[113] S. J. Fiedziuszko, "The influence of conducting walls on resonant frequencies of the dielectric microwave resonator", *IEEE Transactions on Microwave Theory and Techniques*, vol. 19, no. 9, pp. 778–779, Sept. 1971.

[114] Y. Konishi, N. Hoshino, and Y. Utsumi, "Resonant frequency of a $TE_{01\delta}$ dielectric resonator", *IEEE Transactions on Microwave Theory and Techniques*, vol. 24, no. 2, pp. 112–114, Feb. 1976.

[115] R. F. Harrington, *Time-Harmonic Electromagnetic Fields*, McGraw-Hill, 1961.

[116] T. Itoh and R. S. Rudokas, "New method for computing the resonant frequencies of dielectric resonators", *IEEE Transactions on Microwave Theory and Techniques*, vol. 25, no. 1, pp. 52–54, Jan. 1977.

[117] K. K. Chow, "On the solution and field patterns of cylindrical dielectric resonators", *IEEE Transactions on Microwave Theory and Techniques*, vol. 14, no. 9, pp. 439, Sept. 1966.

[118] R. K. Mongia and B. Bhat, "Accurate resonant frequencies of cylindrical dielectric resonators using a simple analytical technique", *Electronics Letters*, vol. 21, no. 11, pp. 479–480, May 1985.

[119] P. Guillon and Y. Garault, "Accurate resonant frequencies of dielectric resonators", *IEEE Transactions on Microwave Theory and Techniques*, vol. 25, no. 11, pp. 916–922, Nov. 1977.

[120] R. F. Harrington, *Field Computation by Moment Method*, The Macmillan Company, 1968.

[121] A. Wexler, "A solution of waveguide discontinuities by modal analysis", *IEEE Transactions on Microwave Theory and Techniques*, vol. 15 No 9, pp. 508–517, Sept. 1967.

[122] T. Itoh, *Numerical Techniques for Microwave and Millmeter-Wave Passive Structures*, Wiley Interscience, 1989.

[123] W. J. R. Hoefer, "The transmission-line matrix method - theory and applications", *IEEE Transactions on Microwave Theory and Techniques*, vol. 33, no. 10, pp. 882–893, Oct. 1985.

[124] D. H. Choi and W. J. R. Hoefer, "The finite-difference - time-domain method and its application to eigenvalue problems", *IEEE Transactions on Microwave Theory and Techniques*, vol. 34, no. 12, pp. 1464–1470, Dec. 1986.

[125] N. Marcuvitz, *Waveguide Handbook*, Peter Peregrinus on Behalf of the Institution of Electrical Engineers, 1993.

[126] R. Mittra and S. W. Lee, *Analytical Techniques in the Theory of Guided Waves*, Macmillan , New York, 1971.

[127] R. Mittra, T. Itoh, and T. Li, "Analytical and numerical studies of the relative convergence phenomenon arising in the solution of an integral equation by the

moment method", *IEEE Transactions on Microwave Theory and Techniques*, vol. 20, no. 2, pp. 96–103, Feb. 1972.

[128] P. J. B. Clarricoats and K. R. Slinn, "Numerical solution of waveguide-discontinuity problems", *Proc.IEE*, vol. 114, no. 7, pp. 878–886, July 1967.

[129] P. H. Masterman and P. J. B. Clarricoats, "Computer field-matching solution of waveguide transverse discontinuities", *Proc. IEE*, vol. 118, no. 1, pp. 51–62, Jan. 1971.

[130] S. Wu Lee, W. R. Jones, and J. J. Campbell, "Convergence of numerical solutions of the iris type discontinuity problems", *IEEE Transactions on Microwave Theory and Techniques*, vol. 19, no. 6, pp. 528–536, June 1971.

[131] Y. C. Shih and K. G. Gray, "Convergence of numerical solutions of step-type waveguide discontinuity problems by modal analysis", *IEEE Microwave Theory and Techniques Symposium Digest*, vol. 1, pp. 233–235, 1983.

[132] W. J. English, "The circular waveguide step-discontinuity mode transducer", *IEEE Transactions on Microwave Theory and Techniques*, vol. 21, no. 10, pp. 633–636, Oct. 1973.

[133] K. A. Zaki, S. Chen, and C. Chen, "Modeling discontinuities in dielectric-loaded waveguides", *IEEE Transactions on Microwave Theory and Techniques*, vol. 36, no. 12, pp. 1804–1810, Dec. 1988.

[134] R. Schmidt and P. Russer, "Modeling of cascaded coplanar waveguide discontinuities by the mode-matching approach", *IEEE Transactions on Microwave Theory and Techniques*, vol. 43, no. 12, pp. 2910–2917, Dec. 1995.

[135] A. S. Omar and K. F. Schünemann, "The effects of complex modes at finline discontinuities", *IEEE Transactions on Microwave Theory and Techniques*, vol. 34, no. 12, pp. 1508–1514, Dec. 1986.

[136] T. Chu, T. Itoh, and Y. Shih, "Comparative study of mode matching formulations for microstrip discontinuity problems", *IEEE Transactions on Microwave Theory and Techniques*, vol. 33, no. 10, pp. 1018–1023, Oct. 1985.

[137] X-P. Liang, K. A. Zaki, and A. E. Atia, "A rigorous three plane mode-matching technique for characterizing waveguide t-junctions, and its application in multiplexer design", *IEEE Transactions on Microwave Theory and Techniques*, vol. 39, no. 12, pp. 2138–2147, Dec. 1991.

[138] S. Chen, *Analysis and Modeling of Dielectric Loaded Resonators*, PhD thesis, University of Maryland, College Park, 1990.

[139] A. S. Omar and K. Schünemann, "Formulation of the singular integral equation technique for planar transmission lines", *IEEE Transactions on Microwave Theory and Techniques*, vol. 33, no. 12, pp. 1313–1322, Dec. 1985.

[140] K. Raghavan, *Modal Matching Technique Applied to Dielectric Loaded and Smooth-Walled Conical Horns*, Report, Department of Electronic Engineering, Queen Mary and Westfield College, April 1987.

[141] A. D. Olver, P. J. B. Clarricoats, P. A. Kishk, and L. Shafai, *Microwave Horns and Feeds*, IEEE Press, New York, 1994.

[142] C. Wang, K. A. Zaki, A. E. Atia, and T. Dolan, "Conductor loaded resonator filters with wide spurious free stop band", *IEEE Transactions on Microwave Theory and Techniques*, vol. 45 no. 12, pp. 2387–2392, Dec. 1997.

[143] C. Wang, H. Yao, and K. A. Zaki, "Modeling of conductor loaded resonators and filters", *IEEE Transactions on Microwave Theory and Techniques*, vol. 45 no. 12, pp. 2479–2485, Dec 1997.

[144] S. Maj and M. Pospieszalski, "A composite, multilayered cylindrical dielectric resonator", *IEEE Microwave Theory and Techniques Symposium Digest*, vol. 1, pp. 190–192, 1984.

[145] K. A. Zaki and C. Chen, "New results in dielectric-loaded resonators", *IEEE Transactions on Microwave Theory and Techniques*, vol. 34, no. 7, pp. 815–824, July 1986.

[146] K. A. Zaki and A. E. Atia, "Modes in dielectric loaded waveguides and resonators", *IEEE Transactions on Microwave Theory and Techniques*, vol. 31, no. 12, pp. 1039–1045, Dec. 1983.

[147] Y. Kobayashi and T. Senju, "Resonant modes in shielded uniaxial-anisotropic dielectric rod resonators", *IEEE Transactions on Microwave Theory and Techniques*, vol. 41, no. 12, pp. 2198–2205, Dec. 1993.

[148] S.-W. Chen and K. A. Zaki, "Dielectric ring resonators loaded in waveguides and on substrate", *IEEE Transactions on Microwave Theory and Techniques*, vol. 39, no. 12, pp. 2069–2076, Dec. 1991.

[149] J. D. Rhodes and I. C. Hunter, "Synthesis of reflection mode filters with dissipative circuit elements", *IEE Proc. Antennas Propag.*, vol. 144, no. 6, pp. 437–442, 1997.

[150] J. D. Rhodes and P. D. Sleigh, *Hybrid Notch Filters*, U.K. patent 2284311, May 1995.

[151] J. D. Rhodes, "Waveguide bandstop elliptic function filters", *IEEE Transactions on Microwave Theory and Techniques*, vol. 20, no. 1, pp. 715–718, Nov. 1972.

[152] J. D. Rhodes and I. H. Zabalawi, "Synthesis of symmetrical dual mode in-line prototype networks", *International Journal of Circuit Theory and its Applications*, vol. 8, pp. 145–160, 1980.

[153] W. C. Tang and S. K. Chaudhuri, "Triple-mode true elliptic-function filter realization for satellite transponders", *IEEE Microwave Theory and Techniques Symposium Digest*, vol. 1, pp. 83–85, 1983.

[154] U. Rosenberg and D. Wolk, "New possibilities of cavity-filter design by a novel te-tm- mode iris-coupling", *IEEE Microwave Theory and Techniques Symposium Digest*, vol. 3, pp. 1155–1158, 1989.

[155] Z. J. Csendes and P. Silvester, "Numerical solution of dielectric loaded waveguides: Ii-modal approximation technique", *IEEE Transactions on Microwave Theory and Techniques*, vol. 19, no. 6, pp. 504–509, June 1971.

[156] C. Wang and K. A. Zaki, "Generalized multilayer anisotropic dielectric resonators", *IEEE Microwave Theory and Techniques Symposium Digest*, vol. 1, pp. 233–236, 1998.

[157] I. C. Hunter, J. D. Rhodes, and V. Dassonville, "Dual mode filters with conductor loaded dielectric resonators", *IEEE Transactions on Microwave Theory and Techniques*, vol. 42 no. 12, pp. 2304–2311, Dec. 1999.

[158] D. M. Pozar, *Microwave Engineering*, Addison-Wesley, 1990.

[159] A. S. Omar and K. F. Schünemann, "Complex and backward wave modes in inhomogeneously and anistotropically filled waveguides", *IEEE Transactions on Microwave Theory and Techniques*, vol. 35, no. 3, pp. 268–275, March 1987.

[160] L. Costa da Silva, "Determination of the roots of the characteristic equation for corrugated and dielectric loaded circular waveguides", *IEEE Transactions on Microwave Theory and Techniques*, vol. 45, no. 3, pp. 298–301, March 1997.

[161] R. L. Burden and J. D. Faires, *Numerical Analysis*, PWS-KENT, 1989.

[162] J. Strube and F. Arndt, "Rigorous hybrid-mode analysis of the transition from rectangular waveguide to shielded dielectric image guide", *IEEE Transactions on Microwave Theory and Techniques*, vol. 33, no. 5, pp. 391–401, May 1985.

[163] C. J. Railton and T. Rozzi, "Complex modes in boxed microstrip", *IEEE Transactions on Microwave Theory and Techniques*, vol. 36, no. 5, pp. 865–874, May 1988.

[164] M. Mrozowski and J. Mazur, "Matrix theory approach to complex waves", *IEEE Transactions on Microwave Theory and Techniques*, vol. 40, no. 4, pp. 781–785, April 1992.

[165] T. Rozzi, L. Pierantoni, and M. Farina, "General constraints on the propagation of complex waves in closed lossless isotropic waveguides", *IEEE Transactions on Microwave Theory and Techniques*, vol. 46, no. 5, pp. 512–515, May 1998.

[166] S. B. Rayevskiy, "Some properties of complex waves in a double-layer circular shielded waveguide", *Radio Eng. Electron. Phys.*, vol. 21, pp. 36–39, 1976.

[167] C. Chen and K. A. Zaki, "Resonant frequencies of dielectric resonators containing guided complex modes", *IEEE Transactions on Microwave Theory and Techniques*, vol. 36, no. 10, pp. 1455–1457, Oct. 1988.

[168] H. Shigesawa and M. Tsuji, "Mode propagation through a step discontinuity in dielectric planar waveguide", *IEEE Transactions on Microwave Theory and Techniques*, vol. 34, no. 2, pp. 205–212, Feb. 1986.

[169] E. G. Royer and R. M. Mittra, "The diffraction of electromagnetic waves by dielectric steps in waveguides", *IEEE Transactions on Microwave Theory and Techniques*, vol. 20, no. 4, pp. 273–279, April 1972.

[170] C. Vassallo, "On a direct use of edge condition in modal analysis", *IEEE Transactions on Microwave Theory and Techniques*, vol. 24, no. 4, pp. 208–212, April 1976.

[171] M. Leroy, "On the convergence of numerical results in modal analysis", *IEEE Transactions on Antennas and Propagation*, vol. 31, no. 4, pp. 655–659, July 1983.

[172] J. Meixner, "The behaviour of electromagnetic fields at edges", *IEEE Transactions on Antennas and Propagation*, vol. 20, no. 4, pp. 442–446, July 1972.

[173] J. B. Andersen and V. V. Solodukhov, "Field behaviour near a dielectric wedge", *IEEE Transactions on Antennas and Propagation*, vol. 26, pp. 598–602, July 1978.

[174] M. Zinieris and R. Sloan, "Unloaded Q factors, energy storage, and power dissipation of axially symmetric and asymmetric modes of shielded dielectric resonators", *Electromagnetics*, vol. 20, no. 3, pp. 187–203, 2000.

[175] X.-P. Liang, H.-C. Chang, and K. A. Zaki, "Unloaded Q's of hybrid mode dielectric resonators on grounded or suspended substrates", *Journal of Electromagnetic Waves and Applications*, vol. 5, no. 3, pp. 281–299, 1991.

[176] T. Nishikawa, K. Wakino, and Y. Ishikawa, "800 MHz band channel dropping filter using TM_{010} mode dielectric resonator", *IEEE Microwave Theory and Techniques Symposium Digest*, vol. 1, pp. 199–201, 1984.

[177] R. E. Collin, *Field Theory of Guided Waves. Second Edition.*, IEEE Press, 1991.

[178] R. Hershtig, R. Levy, and K. A. Zaki, "Synthesis and design of cascaded trisection (ct) dielectric resonator filters", *Proceedings of the European Conference on Microwaves.*

[179] P. J. B. Clarricoats, "Propagation along unbounded and bounded dielectric loaded rods. part2. propagation along a dielectric rod contained in a circular waveguide", *I.E.E. Monograph*, vol. No 410E, pp. 177–186, Oct. 1960.

[180] R. Chou and S. Lee, "Modal attenuation in multilayered coated waveguides", *IEEE Transactions on Microwave Theory and Techniques*, vol. 36, no. 7, pp. 1167–1178, July 1988.

[181] G. V. Eleftheriades, A. S. Omar, L. P. B Katehi, and G. M. Rebiez, "Some important properties of waveguide junction generalised scattering matrices in the context of the mode matching technique", *IEEE Transactions on Microwave Theory and Techniques*, vol. 42, no. 10, pp. 1896–1903, Oct. 1994.

Publications

Part of the results of this research were published in the following publications :

- I. C. Hunter, J. D. Rhodes and V. Dassonville, "Triple Mode Dielectric Resonator Hybrid Reflection Filters", *IEE Proc. Antennas Propag.*, vol. 145, no. 4, pp. 337-343, Aug. 1998.

- V. Walker and I. C. Hunter, "Design of Triple Mode $TE_{01\delta}$ Resonator Transmission Filters", *IEEE Microwave and Wireless Components Letters*, vol. 12, no. 6, pp. 215-217, June 2002.

- V. Walker and I. C. Hunter, "Design of Cross-coupled Dielectric-Loaded Waveguide Filters", *IEE Proc. Antennas Propag.*, vol. 148, no. 2, pp. 91-96, April 2001.

Other publications :

- I. C. Hunter, J. D. Rhodes and V. Dassonville, "Dual Mode Filters with Conductor Loaded Dielectric Resonators", *IEEE Transactions on Microwave Theory and Techniques*, vol. 42, no. 12, pp. 2304-2311, Dec. 1999.

- I. C. Hunter and V. Walker, "Ceramic Filters in Mobile Communications", *Proceedings of the IEE Electronics and Communications Symposium on Microwave Filters and Diplexers*, Nov. 2000.